



SENSORDEVICES 2015

The Sixth International Conference on Sensor Device Technologies and
Applications

ISBN: 978-1-61208-426-8

August 23 - 28, 2015

Venice, Italy

SENSORDEVICES 2015 Editors

Sergey Yurish, IFSA, Spain

Vítor Carvalho, IPCA / Minho University-Algorithmi R&D, Portugal

SENSORDEVICES 2015

Foreword

The Ninth International Conference on Sensor Device Technologies and Applications (SENSORDEVICES 2015), held between August 23-28, 2015 in Venice, Italy, continued a series of events focusing on sensor devices themselves, the technology-capturing style of sensors, special technologies, signal control and interfaces, and particularly sensors-oriented applications. The evolution of the nano-and microtechnologies, nanomaterials, and the new business services make the sensor device industry and research on sensor-themselves very challenging.

We take here the opportunity to warmly thank all the members of the SENSORDEVICES 2015 Technical Program Committee, as well as the numerous reviewers. The creation of such a high quality conference program would not have been possible without their involvement. We also kindly thank all the authors who dedicated much of their time and efforts to contribute to SENSORDEVICES 2015. We truly believe that, thanks to all these efforts, the final conference program consisted of top quality contributions.

Also, this event could not have been a reality without the support of many individuals, organizations, and sponsors. We are grateful to the members of the SENSORDEVICES 2015 organizing committee for their help in handling the logistics and for their work to make this professional meeting a success. We hope that SENSORDEVICES 2015 was a successful international forum for the exchange of ideas and results between academia and industry and for the promotion of progress in the area of sensor device technologies and applications.

We are convinced that the participants found the event useful and communications very open. We hope Venice provided a pleasant environment during the conference and everyone saved some time for exploring this beautiful city.

SENSORDEVICES 2015 Chairs:

SENSORDEVICES Advisory Chairs

Sergey Yurish, IFSA - Barcelona, Spain

Petre Dini, Concordia University, Canada / China Space Agency Center, China

Elena Gaura, Coventry University, UK

Vittorio Ferrari, Università di Brescia, Italy

SENSORDEVICES 2015 Research/Industry Chairs

Raluca - Ioana Stefan-van Staden, National Institute of Research for Electrochemistry and Condensed Matter, Bucharest, Romania

Alberto Yúfera, Centro Nacional de Microelectronica (CNM-CSIC) - Sevilla, Spain

SENSORDEVICES Special Area Chairs

Ultrasonic and piezoelectric sensors

Thomas Herzog, Fraunhofer Institute for Non-Destructive Testing IZFP - Dresden, Germany

Henning Heuer, Fraunhofer Institute for Non-Destructive Testing IZFP - Dresden, Germany

Optical sensors

Vítor Carvalho, IPCA / Minho University-Algoritmi R&D, Portugal

Irinela Chilibon, National Institute of Research and Development for Optoelectronics - Bucharest, Romania

Gas sensors

Dongfang Yang, National Research Council Canada - London, Canada

Testing and validation

Ksenia V. Sapozshnikova D.I. Mendeleyev Institute for Metrology - St. Petersburg, Russia

Vibration sensors

Subodh Kumar Singhal, National Physical Laboratory, New Delhi, India

SENSORDEVICES 2015

Committee

SENSORDEVICES Advisory Chairs

Sergey Y. Yurish, International Frequency Sensor Association (IFSA), Spain
Petre Dini, Concordia University, Canada / China Space Agency Center, China
Elena Gaura, Coventry University, UK
Vittorio Ferrari, Università di Brescia, Italy

SENSORDEVICES 2015 Research/Industry Chairs

Raluca - Ioana Stefan-van Staden, National Institute of Research for Electrochemistry and Condensed Matter, Bucharest, Romania
Alberto Yúfera, Centro Nacional de Microelectronica (CNM-CSIC) - Sevilla, Spain

SENSORDEVICES Special Area Chairs

Ultrasonic and piezoelectric sensors

Thomas Herzog, Fraunhofer Institute for Non-Destructive Testing IZFP - Dresden, Germany
Henning Heuer, Fraunhofer Institute for Non-Destructive Testing IZFP - Dresden, Germany

Optical sensors

Vítor Carvalho, IPCA / Minho University-Algoritmi R&D, Portugal
Irinela Chilibon, National Institute of Research and Development for Optoelectronics - Bucharest, Romania

Gas sensors

Dongfang Yang, National Research Council Canada - London, Canada

Nanosensors

TBA

Testing and validation

Ksenia V. Sapozhnikova D.I. Mendeleev Institute for Metrology - St. Petersburg, Russia

Vibration sensors

Subodh Kumar Singhal, National Physical Laboratory, New Delhi, India

SENSORDEVICES 2015 Technical Program Committee

Jesús B. Alonso Hernández, University of Las Palmas de Gran Canaria, Spain
Farid Amirouche, University of Illinois at Chicago, USA
Ammar Aryan, Université de Caen Basse-Normandie, France
Selcuk Atalay, Inonu University - Malatya, Turkey
Francisco Javier Arcega Solsona, University of Zaragoza, Spain

Debjyoti Banerjee, Texas A&M University, U.S.A.
Yoseph Bar-Cohen, Jet Propulsion Laboratory (JPL) - NASA, USA
Matthias Bartholmai, BAM Federal Institute for Materials Research and Testing, Germany
Sukumar Basu, Jadavpur University - Kolkata, India
Juarez Bento da Silva, Universidade Federal de Santa Catarina, Brazil
Daniel Berckmans, Katholieke Universiteit Leuven, Belgium
Partha Bhattacharyya, Bengal Engineering and Science University, West Bengal, India
Virginie Blondeau-Patissier, Université de Franche-Comté, France
Michal Borecki, Warsaw University of Technology, Poland
Jaime Calvo-Gallego, University of Salamanca - Zamora, Spain
John Canning, University of Sydney, Australia
Cristina Carmona-Duarte, University of Las Palmas de Gran Canaria, Spain
Vitor Carvalho, IPCA / Minho University-Algorithmi R&D, Portugal
Gustavo Cerda-Villafaña, University of Guanajuato, Mexico
Sudhir Chandra, Indian Institute of Technology Delhi - New Delhi, India
Irinela Chilibon, National Institute of R&D for Optoelectronics - Bucharest-Magurele, Romania
Jeong-Woo Choi, Sogang University - Seoul, Korea
Caterina Ciminelli, Politecnico of Bari, Italy
Alberto Corigliano, Politecnico di Milano, Italy
Rodrigo P.B. Costa-Felix, INMETRO, Brazil
Anna Cysewska-Sobusiak, Poznan University of Technology, Poland
Boris Zaitsev Davydovich, Russian Academy of Sciences - Saratov Branch, Russia
Francesco De Leonardis, Politecnico di Bari, Italy
Matthieu Denoual, GREYC-ENSICAEN, France
Dermot Diamond, Dublin City University, Ireland
Alexandar Djordjevich, City University of Hong Kong, Hong Kong
Marco Dominietto, University of Basel / University Hospital Basel, Switzerland
Jimmy Efir, East Carolina Heart Institute, USA
Alessandro Fantoni, UNINOVA-CTS, Portugal
Miguel Fernandes, UNINOVA - Caparica, Portugal
Vittorio Ferrari, Università di Brescia, Italy
Anselmo Frizera Neto, Federal University of Espírito Santo, Brazil
Masato Futagawa, Shizuoka University, Japan
Noureddine Gabouze, CRTSE (exUDTS), Algeria
Juan Carlos García García, University of Alcalá, Spain
Arfan Ghani, University of Bolton, UK
Friederike Gruhl, Karlsruhe Institute of Technology (KIT), Germany
Vinod Kumar Gupta, Indian Institute of Technology Roorkee, India
Jan Havlík, Czech Technical University in Prague, Czech Republic
Thomas Herzog, Fraunhofer Institute for Non-Destructive Testing IZFP - Dresden, Germany
Henning Heuer, Fraunhofer Institute for Non-Destructive Testing IZFP - Dresden, Germany
Eiji Higurashi, University of Tokyo, Japan
Gotan Hiralal Jain, KTHM College, India
Sandeep K. Jha, Indian Institute of Technology Delhi, India
Vladan Koncar, ENSAIT Research, France
Daniel Lai, Victoria University, Australia
Alan K. T. Lau, Hong Kong Polytechnic University, Hong Kong SAR
Vladimir Laukhin, Institució Catalana de Recerca i Estudis Avançats (ICREA / Institut de Ciència de

Materials de Barcelona (ICMAB-CSIC) - Barcelona, Spain
Elena Laukhina, Networking Research Center on Bioengineering, Biomaterials and Nanomedicine (CIBER-BBN) - Bellaterra, Spain
Yann-Aël Le Borgne, Université Libre de Bruxelles, Belgium
Kevin Lee, Murdoch University, Australia
Hongen Liao, Tsinghua University, China
Diego Liberati, National Research Council of Italy, Italy
Aihua Liu, Qingdao Institute of Bioenergy & Bioprocess Technology, Chinese Academy of Sciences, China
Kenneth J. Loh, University of California - Davis, USA
Salvatore A. Lombardo, CNR-IMM - Catania, Italy
Jerzy P. Lukaszewicz, Nicholas Copernicus University - Torun, Poland
Mai S. Mabrouk, Misr University for Science and Technology, Egypt
Ryutaro Maeda, UMEMSME / AIST, Japan
Emanuela Marasco, West Virginia University, USA
Stefano Mariani, Politecnico di Milano, Italy Iren Kuznetsova, Russian Academy of Sciences - Saratov Branch, Russia
Hamed Sadeghian Marnani, Delft University of Technology, The Netherlands
Marek Miskowicz, AGH University of Science and Technology - Cracow, Poland
Tarek Mohammad, University of Western Ontario - London, Canada
Gaidi Mounir, Centre de Recherches et des Technologies de l'Energie (CRTE), Tunisie
António J. R. Neves, University of Aveiro, Portugal
Eros Pasero, Politecnico di Torino, Italy
François Pérès, ENIT-INPT, France
Radislav A. Potyrailo, GE Global Research Center, U.S.A.
Konandur Rajanna, Indian Institute of Science - Bangalore, India
Càndid Reig, University of Valencia, Spain
Teresa Restivo, University of Porto, Portugal
Marcos A Rodrigues, Sheffield Hallam University, UK
Aldo Romani, University of Bologna, Italy
Nicholas Ruth, Ryerson University, Canada
Mounir Bousbia Salah, University of Annaba, Algeria
Ksenia V. Sapozhnikova D.I. Mendeleev Institute for Metrology - St. Petersburg, Russia
Majid Sarrafzadeh, University of California Los Angeles, U.S.A.
Tapio Seppänen, University of Oulu, Finland
Subodh Kumar Singhal, National Physical Laboratory - New Delhi, India
Junho Song, Sunnybrook Research Institutes/University of Toronto, Canada
Nickolaj Starodub, National University of Life and Environmental Sciences of Ukraine, / T. Shevchenko Kiev State University of Ukraine, Ukraine
Arndt Steinke, CiS Forschungsinstitut für Mikrosensorik und Photovoltaik GmbH - Erfurt, Germany
Raluca - Ioana Stefan-van Staden, National Institute of Research for Electrochemistry and Condensed Matter, Bucharest, Romania
Chelakara S. Subramanian, Florida Institute of Technology - Melbourne, USA
Roman Szewczyk, Warsaw University of Technology, Poland
Roald Taymanov, D.I. Mendeleev Institute for Metrology, Russia
Reshef Tenne, Weizmann Institute, Israel
Wen-Miin Tian, National Sun Yet-sen University, Taiwan
Vicente Traver Salcedo, ITACA-Universitat Politècnica de València, Spain
Carlos M. Travieso, University of Las Palmas de Gran Canaria, Spain

Pankaj Vadgama, Queen Mary University of London, U.K.
Antonio Valente, University of Trás-os-Montes and Alto Douro (UTAD) - Vila Real, Portugal
Fernando Vidal Verdú, Universidad de Málaga, Spain
Manuela Vieira, UNINOVA/ISEL, Portugal
Winfried Vonau, Kurt-Schwabe-Institut für Mess- und Sensortechnik e.V. Meinsberg, Germany
Dongfang Yang, National Research Council Canada - London, Canada
Alberto Yúfera, Seville Microelectronics Institute (IMSE-CNM), Spain
Sergey Y. Yurish, International Frequency Sensor Association (IFSA), Spain
Cyrus Zamani, University of Barcelona, Spain
Dan Zhang, University of Ontario Institute of Technology, Canada
Weiping Zhang, Shanghai Jiao Tong University, P. R. China
Ya-Pu Zhao, Chinese Academy of Sciences - Beijing, China
Daniele Zonta, University of Trento, Italy

Copyright Information

For your reference, this is the text governing the copyright release for material published by IARIA.

The copyright release is a transfer of publication rights, which allows IARIA and its partners to drive the dissemination of the published material. This allows IARIA to give articles increased visibility via distribution, inclusion in libraries, and arrangements for submission to indexes.

I, the undersigned, declare that the article is original, and that I represent the authors of this article in the copyright release matters. If this work has been done as work-for-hire, I have obtained all necessary clearances to execute a copyright release. I hereby irrevocably transfer exclusive copyright for this material to IARIA. I give IARIA permission to reproduce the work in any media format such as, but not limited to, print, digital, or electronic. I give IARIA permission to distribute the materials without restriction to any institutions or individuals. I give IARIA permission to submit the work for inclusion in article repositories as IARIA sees fit.

I, the undersigned, declare that to the best of my knowledge, the article does not contain libelous or otherwise unlawful contents or invading the right of privacy or infringing on a proprietary right.

Following the copyright release, any circulated version of the article must bear the copyright notice and any header and footer information that IARIA applies to the published article.

IARIA grants royalty-free permission to the authors to disseminate the work, under the above provisions, for any academic, commercial, or industrial use. IARIA grants royalty-free permission to any individuals or institutions to make the article available electronically, online, or in print.

IARIA acknowledges that rights to any algorithm, process, procedure, apparatus, or articles of manufacture remain with the authors and their employers.

I, the undersigned, understand that IARIA will not be liable, in contract, tort (including, without limitation, negligence), pre-contract or other representations (other than fraudulent misrepresentations) or otherwise in connection with the publication of my work.

Exception to the above is made for work-for-hire performed while employed by the government. In that case, copyright to the material remains with the said government. The rightful owners (authors and government entity) grant unlimited and unrestricted permission to IARIA, IARIA's contractors, and IARIA's partners to further distribute the work.

Table of Contents

Characterization and Simulation of PbS Photoconductors Prepared by Chemical Bath Deposition <i>Said Kouissa, Amor Djemel, Mohammed Salah Aida, and Mohammed Abdou Djouadi</i>	1
Automation and Control in Engineering: A Global Approach with Educational Kits <i>Filomena Soares, Celina Leao, Jose Machado, and Vitor Carvalho</i>	7
Simple and Precise Analog Arcsine Synthesis Applied to Amplitude to Phase Conversion for Hall Effect Position Sensors <i>Mohieddine Benammar and Antonio Jr. Gonzales</i>	13
An Intelligent and Customized Electrical Conductivity Sensor to Evaluate the Response Time of a Direct Injection System <i>Heitor Mercaldi, Caio Fujiwara, Elmer Penaloza, Vilma Oliveira, and Paulo Cruvinel</i>	19
Underwater Oil Spill Imaging via UV LED-induced Fluorescence <i>Sangwoo Oh and Moonjin Lee</i>	26
New Methods for the Preparation of Partial Selective Redox Electrodes for the Determination of H ₂ O ₂ <i>Winfried Vonau, Manfred Decker, Jens Zosel, Kristina Ahlborn, Frank Gerlach, and Steffen Weissmantel</i>	28
Design, Analysis and Modelling of a Capacitive-Based Collision Detector for 3-DOF Hybrid Robotic Manipulator <i>Dan Zhang and Bin Wei</i>	31
Capillary Rise Multiparametric Sensor for Testing of Diesel and Biodiesel Fuel <i>Michal Borecki, Jan Szmidt, Michael L. Korwin-Pawlowski, Andrzej Kociubinski, Mariusz Duk, Jaroslaw Frydrych, and Przemyslaw Prus</i>	37
UV Irradiation to Increase the Spectral Sensitivity of a-SiC:H pi'n/pin Photodiode Beyond the Visible Spectrum Light <i>Manuela Vieira, Manuel Augusto Vieira, Vitor Silva, Paula Louro, Alessandro Fantoni, and Isabel Rodrigues</i>	44
Silicon Based Temperature Sensors with Extended Temperature Range and Simple One-point Calibration <i>Ingo Tobehn, Arndt Steinke, Andreas Albrecht, Horst Hansch, Michael Kunze, and Thomas Ortlepp</i>	50
Performance Analysis of Commercial Accelerometers of Different Technologies <i>Stephan Elies and Stefan Ebenhoch</i>	54
2D and 3D Phononic Crystals - A New Class of (Bio)Chemical Microsensors and Sensor Networks <i>Ralf Lucklum, Mikhail Zubtsov, Yan Pennec, and Frieder Lucklum</i>	60
A Dual Grating Fiber Sensor to Discriminate Axial and Radial Strains	62

Romain Guyard, Dominique Leduc, Yann Lecieux, and Cyril Lupi

A Multi-directional Thermal Flow Sensor Fabricated on Flexible Substrate 68
Anastasios Moschos, Dimitrios Barmpakos, and Grigoris Kaltsas

Development of a Novel Approach for Detecting Wood Decays in Living Trees Using Gas-Sensor Arrays 72
Manuela Baietto, Sofia Aquaro, Alphas Dan Wilson, Letizia Pozzi, and Daniele Bassi

Bayesian Inference using Spike Latency Codes for Quantification of Health Endangering Formaldehyde 78
Muhammad Hassan, Amine Bermak, Amine Ait Si Ali, and Abbes Amira

Application of Cavity Enhanced Absorption Spectroscopy in Detection of Selected Gas Pollutants 82
Zbigniew Bielecki, Jacek Wojtas, Janusz Mikolajczyk, and Sylwester Chojnowski

Reducing System Response Time and Noise of Electrochemical Gas Sensors - Discussed for Propofol Monitoring in Breathing Gas 84
Dammon Ziaian, Philipp Rostalski, Andreas Hengstenberg, and Stefan Zimmermann

Early Detection of Emissions Preceding Fires from Overloaded Electric Cables: Approach with Thermo-Cyclically Operated MOG Sensor Arrays and Numerical Signal Analysis 90
Rolf Seifert, Hubert Keller, Navas Illyaskutty, Jens Knoblauch, and Heinz Kohler

Highly Sensitive Pt-TiO₂-Pt Sandwich-type Metal Oxide Gas Sensors of Hydrogen 96
Ondrej Krsko, Tomas Plecenik, Azhar ALi Haidry, Pavol Durina, Martin Truchly, Branislav Grancic, Maros Gregor, Tomas Roch, Leonid Satrapinsky, Marian Mikula, Peter Kus, Andrej Plecenik, Martin Mosko, and Antonia Moskova

High Frequency Thick Film Ultrasonic Transducers Used for Flow-mediated Vasodilatation of the Radial Artery 98
Andrzej Nowicki, Marcin Lewandowski, Ihor Trots, and Robert Olszewski

Figuring Out Conscientious Degree from Brightness Distribution in IADL 100
Shota Shimayoshi, Shun Okamura, Yusuke Kajiwara, and Hiromitsu Shimakawa

Tactile Handle for an Instrumented Cane 106
Andres Trujillo-Leon, Ragou Ady, Fernando Vidal-Verdu, and Wael Bachta

Analysis of the Effect of Visuals on the Stabilization of Trunk Muscles During Rotational Motion 110
Nika Zolfaghari, Kristiina M. Valter McConville, and Shahini Sirikantharajah

Controlled Cryogenic Ablation Using Ultrasonic Sensing 115
Assaf Sharon and Gabor Kosa

Key Features to Classify Shopping Customer Status from Gait Vector Acquired with RFID Technology 120

<i>Yoshihiro Uemura, Yusuke Kajiwara, and Hiromitsu Shimakawa</i>	
EEG Sensor Based Semi-Supervised Inattention Prediction Framework For Unmanned Aerial Vehicles <i>Yerim Choi, Jonghun Park, and Dongmin Shin</i>	126
A GSM-based System for the Tracking of Birds <i>Samuel Matos, Raul Morais, Pedro Araujo, Paulo Tenreiro, Paulo Ferreira, and Manuel Reis</i>	130
The Experimental Study of Moving Targets Radio Shadows using GPS Signals <i>Christo Kabakchiev, Ivan G. Garvanov, Vera Behar, and Dorina Kabakchieva</i>	137
Synthesis of Amide Functionalized Graphene Oxide for Humidity Sensing Application <i>Dinesh Kumar and Sumita Rani</i>	141
Navigating for Visually Handicapped to Walk Alone with RFID Technologies <i>Masayoshi Asano, Yusuke Kajiwara, and Hiromitsu Shimakawa</i>	145
Identification of Personal Actions with Brightness Distribution Sensors to Harmonize Domestic Affairs <i>Nobuaki Takaoka, Yusuke Kajiwara, and Hiromitsu Shimakawa</i>	151
Macropixel Compressive Sensing Reconstruction of Spectral Images Sensed by Multispectral Filter Array-based Sensors <i>Yuri Mejia, Fernando Rojas, and Henry Arguello</i>	157
Receiver Design of Passive UHF RFID Sensor Platform for Gas Identification <i>Muhammad Ali Akbar, Amine Ait Si Ali, Abbes Amira, Mohieddine Benammar, Faycal Bensaali, Mohamed Zgaren, Mohamad Sawan, and Amine Bermak</i>	163
Inspection and Visualization Method for the Internal Structure of Spot-Welded Three-Steel Sheet Using Eddy Current Testing <i>Keisyu Shiga, Song Nannan, Kenji Sakai, Toshihiko Kiwa, and Keiji Tsukada</i>	169
Development of the Detecting System for Steel Plate with Backside Defect Using an Array of AMR Sensor <i>Koji Morita, Keishu Shiga, Yuta Haga, Kenji Sakai, Toshihiko Kiwa, and Keiji Tsukada</i>	173
Analysis of the Planar Electrode Morphology for Capacitive Chemical Sensors <i>Luiz Eduardo Bento Ribeiro and Fabiano Fruett</i>	178

Characterization and Simulation of PbS Photoconductors Prepared by Chemical Bath Deposition.

S. Kouissa, A. Djemel, M. S. Aida

Department of Physics, University of Constantine1,
Constantine, Algeria

E.mail: skouissa@yahoo.fr, djemelamor@yahoo.fr,
aida_2salah@yahoo.fr

M.A.Djouadi

Laboratoire ID2M, Institut des Matériaux Jounh-Rouxel-
CNRS, Université de Nantes
Nantes, France.

E.mail: Abdou.djouadi@cnrs-immn.fr

Abstract — The present work deals with the characterization and simulation of lead sulfide (PbS) photoconductors infrared detectors growth by Chemical Bath Deposition (CBD) method. Three different solutions bath are used in order to explore the doping effect and oxidant agent on detection capabilities. Photoelectrical characterization indicates that detectors performances depend strongly on oxidant and doping agents. A simulation study with surface state model is also presented. The physical parameters are deduced and are found to be in agreement with those published in the literature.

Keywords- Chemical Bath Deposition; photoconductors; infrared detectors; surface state model; PbS.

I. INTRODUCTION

Thin film lead sulfide detectors have been widely used over the past years for radiation sensing in 1 to 3 μ m spectral region. They are mainly very useful in academic, commercial and military applications. In military application, PbS detectors are used for both tactical and strategic systems, with a very strong emphasis towards an increasing requirement for large area multiple element arrays.

Unlike most other semiconductors IR detectors, lead sulfide materials are used in the form of polycrystalline films approximately 1 μ m thick and with individual crystallites ranging in size from approximately 0.1 μ m to 1 μ m. They are usually prepared by chemical bath deposition (CBD), which generally yields better uniformity of response and more stable results than the evaporate methods [1]-[5].

As-deposited PbS films exhibit very low photoconductivity, however, a post deposition process are used to achieve final sensitization. To obtain high performance detectors, lead chalcogenide films need to be sensitized by oxidation. This oxidation may be carried out using additives in the deposition bath, post-deposition heat treatment in the presence of oxygen, or chemical oxidation of the films.

Others impurities added to the chemical-deposition solution for PbS have a considerable effect on photosensitivity films characteristics [5]-[9]. They may increase the photosensitivity by some order of magnitude more than films prepared without these impurities [8] [9].

This work deals with characterization and simulation of PbS photoconductors infrared detectors prepared by CBD. The effect of oxidant agent and Bismuth Nitrate additives on

the performances of PbS detectors is also examined. Finally, a simulation study with surface state model proposed in [10] [11] is also presented. This paper is organized as follows: Section I presents the particularities associated with PbS infrared photo- detectors development. Section II details the experimental procedure for devices fabrication and characterization. After analysis of surface morphology and film structure in subsection III.A, we performed optical measurements (III.B) in order to understand the effect of additives of oxidation and doping on structural and optical properties of deposited PbS films. Based on surface state model reviewed in subsection III.C, a comparison between photoelectrical measurements of developed PbS photoconductors and theoretical prediction is proposed in subsection III.D. The conclusions and perspectives are described in Section IV.

II. EXPERIMENTAL DETAILS

The setup deposition of *E. Pentia et al* [9] was used for growing the PbS films over three bath solutions, summarized in Table I. The bath 1 contain the basic precursors which are Lead Nitrate Pb(NO₃)₂, Sodium Hydroxide (NaOH) and Thiourea SC(NH₂)₂, the bath 2 contain in addition an oxidant agent, named Hydroxylamine Hydrochloride (NH₂OH-HCl), and the bath 3 contain in addition to bath 2, the Bismuth Nitrate Bi(NO₃)₃ as doping agent.

Aqueous solution of 0.069 M lead nitrate, 0.69 M NaOH and 0.24 M thiourea were used. In order to prepare PbS films, the following procedure was adopted: 20 ml of lead nitrate solution was mixed with 20 ml of NaOH with constant stirring. The initial color solution was milky, after it became transparent, 20 ml of thiourea solution was gradually added followed by addition of oxidant with 20 ml of 0.086 M Hydroxylamine Hydrochloride (NH₂OH.HCL), again with constant stirring, the global solution was diluted with 20 ml of water. Finally, a small quantity of Bismuth nitrate with 1.5 ml of 2.0610⁻⁴ M was added to some reactions. The PbS films were deposited on microscope glass substrate cleaned, for about 48 h, in a mixture of (HNO₃, (K₂Cr₂O₇: H₂SO₄; 1:10), 1% EDTA followed by rinsing in distilled water.

TABLE I. SOLUTIONS BATH

Bath 1	Pb(NO ₃) ₂	NaOH	SC(NH ₂) ₂		
Bath 2	Pb(NO ₃) ₂	NaOH	SC(NH ₂) ₂	NH ₂ OH. HCl	
Bath 3	Pb(NO ₃) ₂	NaOH	SC(NH ₂) ₂	NH ₂ OH. HCl	Bi(NO ₃) ₃

After drying, one facet of this substrate was stuck with an inert paste on a support having T format introduced vertically in the reaction bath containing the chemical mixture. After some time, the transparent color solution started to change to become completely black after one (01) hour.

The measured film thicknesses, using DEKTAK profilometer, were about 150 nm for both films elaborated with and without oxidant. Thicker films were obtained by repeated deposition. Gold electrodes were evaporated on the surface of PbS films for electric and photoelectric measurements in a coplanar configuration. The films characterizations were performed after annealing in air at 80° C for approximately 70 h.

Structural properties were evaluated by x-rays diffraction using a D5000 Siemens diffractometer. The scans were carried out at room temperature, in the conventional $\theta/2\theta$ mode using Cu-K α radiation (0.1542 nm). The morphology was observed by scanning electron microscopy (SEM) using a JEOL 6400F microscope. The optical properties were studied with a CARY 5000 UV-Vis-NIR double beam spectrometer. The photoconductivity measurements were performed with a system constituted by a standard IR light source, an Oriel MS257 monochromator operated in the range 1-20 μ m, a chopper fixed at 400 Hz and the acquisition equipment composed with spectrum analyzer, lock-in amplifier and oscilloscope.

III. RESULTS AND DISCUSSIONS

A. Surface morphology and films structures

Figures 1 and 2 show SEM micrographs of PbS films deposited with and without oxidant. It appears that the average grain size increases with the used oxidant. Concerning the films structural properties, Figures 3 and 4 show the effect of annealing treatment (T=80°C, for 72h) and Bismuth doping on the XRD (X Rays Diffraction) patterns of deposited PbS films. As can be seen, films deposited with hydroxylamine hydrochloride additive are less textured when compared to films prepared without this additive, which are (200) preferentially oriented, the grains become oriented quasi-equally with (200) and (111) crystallographic direction. The effect of annealing at 80°C for 72h and doping with bismuth nitrate, affects in opposite manner the XRD patterns. As seen, the annealing increases, while the doping decreases the films texture.

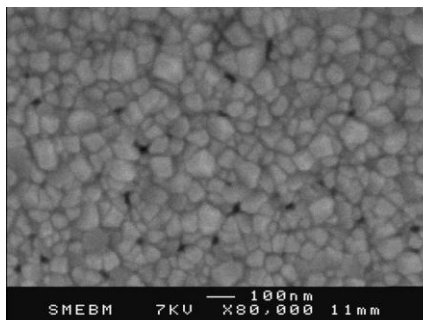


Figure 1. SEM image of PbS films prepared without oxidant agent

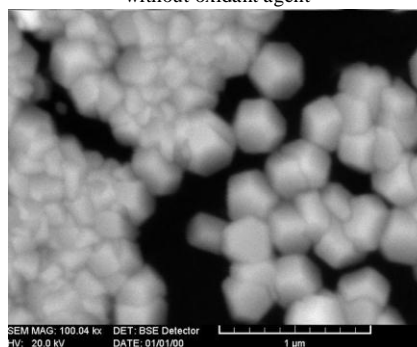


Figure 2. SEM image of PbS films prepared with oxidant agent

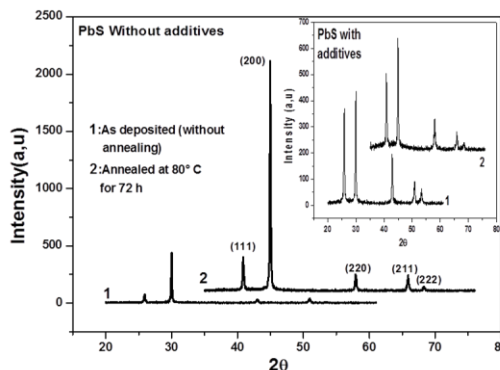


Figure 3. Effect of annealing on the XRD patterns of PbS films

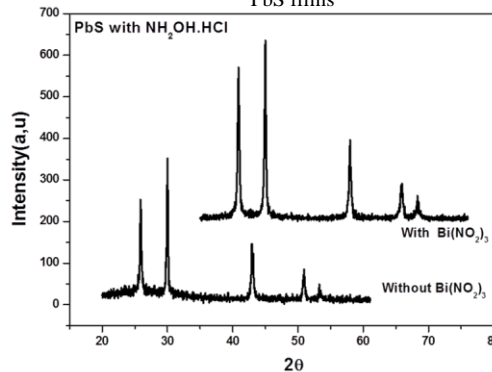


Figure 4. Effect of doping with Bi(NO₃)₃ on the XRD patterns of PbS films

B. Optical properties

Figures 5 and 6 show the transmittances (T_{corr}) and $(\alpha hv)^2$ plots of PbS films prepared with different baths and annealed at 80° C for 72 h respectively. The inset shows the absorption coefficient of these films. As shown, oxidant and doping affect the optical properties. The optical band gap was calculated from the spectral absorption near the fundamental absorption edge. The direct band gap of all synthesized PbS films was estimated using the Tauc relation given as follow

$$\alpha hv = A(hv - E_g)^{\frac{1}{2}} \quad (1)$$

where ‘A’ is the parameter which depends on the transition probability. For direct transition in the fundamental absorption, $(\alpha hv)^2$ have linear dependence on the photon energy (hv). The intercept on energy axis gives the direct band gap energy. Based on the optical transmission measurements, we have obtained the direct band gap energy for PbS films grown by different baths, which is 0.42 eV for films prepared without additive (referred as 1), it becomes 0.5 eV for films prepared with oxidant (referred as 2) and 0.56 eV for films prepared with doping agent (referred as 3).

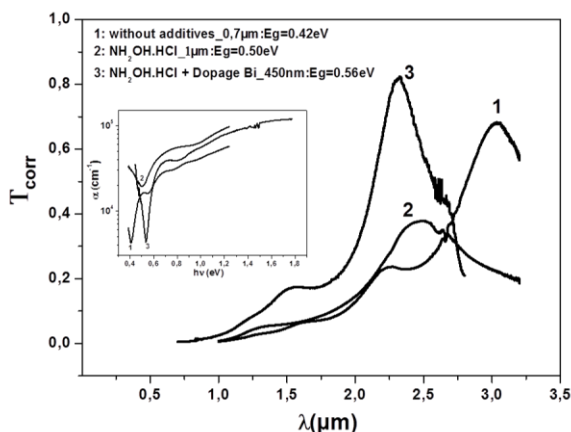


Figure 5. Transmittances of PbS thin films prepared with different bath solution

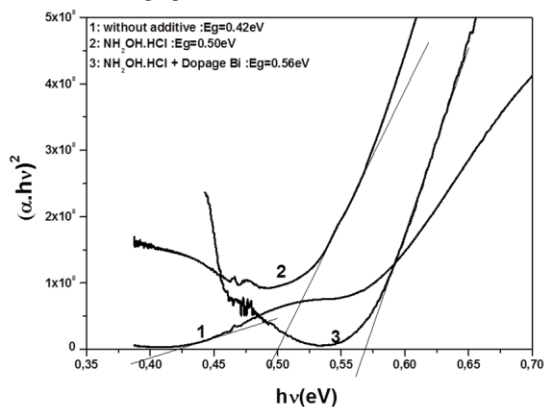


Figure 6. Plot of $(\alpha hv)^2$ for PbS thin films prepared with different bath solution

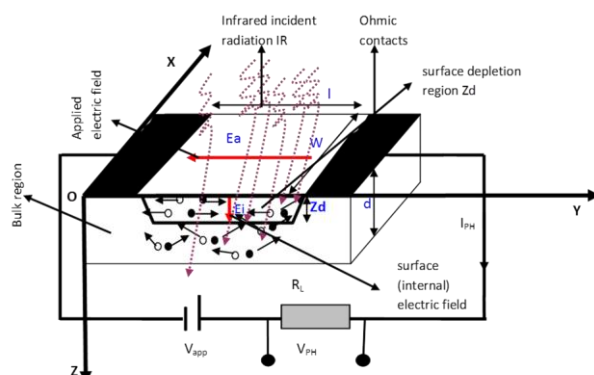


Figure 7. Schematic structure of surface state model [10]

C. Surface state model

Photoconductivity in PbS films can be explained by two models depending upon whether the semiconductor is single-crystalline or polycrystalline, which are recombination and barrier models respectively. The recombination model assumes that change in conductivity on illumination results from the change in the number of conducting electrons or holes per unit volume. In the barriers model, it is assumed that illumination produces little or no change in the density of charge carriers but an increase in their effective mobility. A large number of surface defects are produced along the crystalline boundaries. These surface defects capture electrons from the interior of the single-crystalline and produce space charge barriers. Illumination reduces the number of electrons in the surface defects and thereby lowers the barrier height. In real polycrystalline material, the observed photoconductivity may be due to a combination of both recombination and barrier processes. One of these combination models is the surface state model proposed by [10] [11] (figure 7).

This model treats the free surface with different manner of precedent model [12] [13]. It was characterized by surface state density (N_s), unique energy level (E_s) associated with defect localized in the forbidden gap and effective cross section (σ) rather than the surface recombination velocity. In this model, the barrier height at the semiconductor free surface is modified under photonic excitation. It was suggested that recombination influence directly the quantum efficiency of detector. All models accept that, the role of oxidant is assumed to introduce a trapping state that inhibits recombination; these traps capture the minority carriers and thereby extending the life time of material. As mentioned above, without the sensitization step, lead sulfide has very short life time and a low response.

The concentration of excess carriers density; the key parameter of this model, allows us to explore all the theoretical equations of detectors figure of merit. This parameter is calculated with a self-consistent way, taking into account the resolution of continuity equation of majority and minority carriers in the depletion and neutral (Bulk) region of material, given by [10][11];

$$\Delta n(z) = B_n \exp\left[-\left(\frac{z - z_d}{L_n}\right)\right] + \frac{L_n}{2D_n} \int_{z_d}^z G(z') \left\{ \exp\left[-\frac{|z - z_d|}{L_n}\right] - \exp\left[-\frac{(z + z' + 2z_d)}{L_n}\right] \right\} dz' \quad (2)$$

Where B_n is the concentration of excess carriers density at free surface ($z=0$), which is determined by the appropriate conditions of limits [14], Z_d , L_n , D_n and $G(z)$ are width of depletion region, diffusion length, diffusion coefficient and generation rate respectively. Detailed calculation of the surface analysis, optical generation and photoconductor performances (Signal, Spectral response or responsivity and specific detectivity) is presented respectively in the appendix.

D. Photo-detection performances measurement and simulation

In order to investigate the influence of oxidant and doping on detection and capabilities of PbS films, three photoconductive detectors prepared with and without additives (table I) have been analyzed. To avoid the Flicker noise, manifested at low frequency, the chopping frequency at 400 Hz and the total polarization voltage at 50 V have been fixed. The test set used provides radiant flux in a very narrow spectral band centered about any desired wavelength (λ). There are three functional controls on the monochromator:

- The centered λ of the exciting beam;
- The width of the spectral interval centered at λ ;
- The amount of flux passing through the monochromator.

A constant flux per unit λ interval should be maintained for any selected λ center in the interval of [1-4 μm]. According to application data sheet of the infrared source, the power of infrared radiation is calculated manually by assuming the IR source as a blackbody at 1230° C (the IR source is a Silicon Carbide SiC emitted in the range of 0.7-28 μm , the irradiance of this source is nearly the same of blackbody heated at 1230°C, particularly in 0.7-3 μm spectral range) [15].

It is interesting to notice, here, that the noise is measured in the absence of light, with lock-in amplifier and spectrum analyzer under equivalent noise band width of $\Delta f=50$, the effective value of noise is done by $V_n / (\Delta f)^{1/2}$ [16]. The values of V_n (noise voltage in rms) for photoconductors prepared with three baths are 55.15, 86.3 and 63.6 μV respectively.

This measurement of noise is crucial in the calculating of spectral specific detectivity, which depends of the ratio of spectral response and noise.

Figures 8, 9 and 10 show the signal, spectral response and specific detectivity of these photoconductive detectors fitted with surface state model [10] [11]. The oxidant enhances the capabilities of detection comparatively to detectors prepared without oxidant. The doping increases again these capabilities and decreases the peak wavelength.

The best adjustments are obtained with the data reported in Table II. It should be noted that, the confrontation between experimental and calculated data of signal is excellent, but a small discrepancy in spectral response and specific detectivity for the first point of measurement is observed. It is probably due to high fluctuation of signal at low wavelength. Also, the parameters issued with this simulation are in agreement with the published ones in the literature [17] [18].

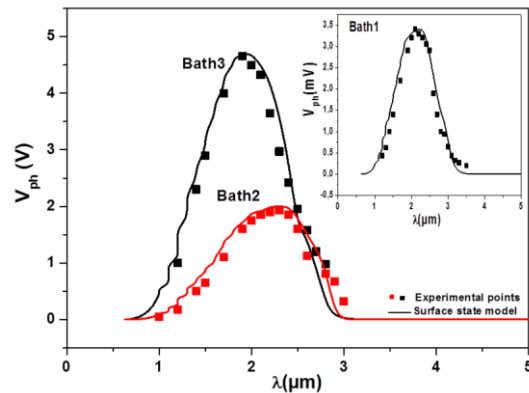


Figure 8. Simulation of signal with surface state model

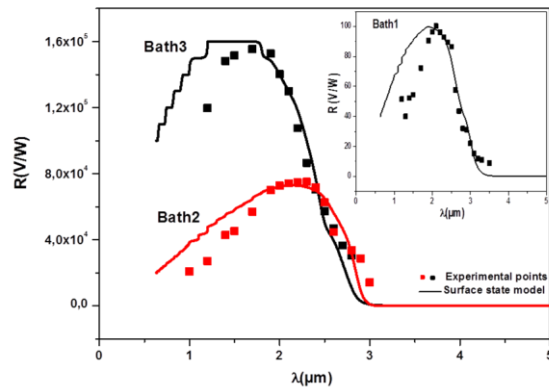


Figure 9. Simulation of spectral response with surface state model

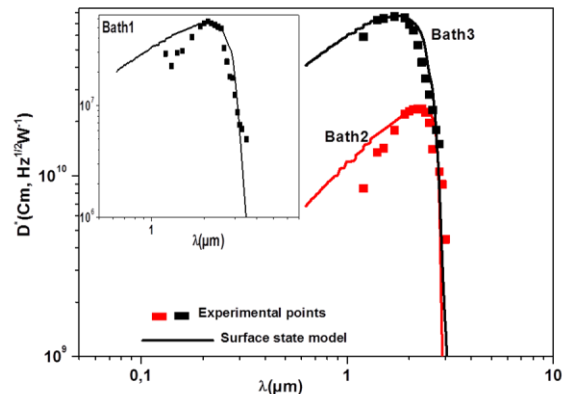


Figure 10. Simulation of spectral detectivity with surface state model

TABLE II. SIMULATION RESULTS

Detector	Bath 1	Bath 2	Bath 3
Simulated parameters			
E_g (eV)	0.43	0.43	0.48
L_p (μm)	500	500	400
Z_d (nm)	30	10	10
N_a (cm^{-3})	510^{17}	510^{17}	510^{17}
E_i (eV)	0.42	0.42	0.47
σ (cm^2)	2.5510^{-14}	3.410^{-16}	2.4510^{-17}
N_r (cm^{-2})	1.510^{12}	510^{11}	510^{11}
Introduced parameters			
d (μm)	0.7	1	0.45
A_d (cm^2)	0.4	0.3	0.4
R_L (M Ω)	0.1	0.1	0.25

IV. CONCLUSION

In the present work, detectors based on sensitized thin films, growth by chemical bath deposition are studied. The photoelectrical characterization allowed that, detectors developed without oxidant has approximately very low performances (Signal, Responsivity and Specific Detectivity) compared with those developed with oxidant. The use of doping agent increases again these performances along with decreasing the peak position wavelength of detector.

A simulation study of proposed IR photoconductors, using surface state model, has been also presented. The plots show the ability of this model to adjust their performance behavior.

The extracted physical parameters are in agreement with those published in literature.

REFERENCES

[1] S. Kumar, T. P. Sharma, M. Zulfequar and M. Husain, "Characterization of vacuum evaporated PbS thin films", Physica B, volume 325, 2003, p8.
 [2] J. N. Humphrey, "Optimum utilization of lead sulphide detectors under diverse operating conditions", Appl. Opt, volume 4, 1965, p 665.
 [3] T. H. Johnson, H. T. Cozine, and B. N. McLean, "Lead selenide detector for ambient temperature operation", Appl. Opt, volume 4, 1965, p 693.
 [4] D. E. Bode, "Physics of Thin Films", Vol 3, Academic Press, New York, 1966.
 [5] T. S. Moss, G. J. Burrell, and B. Ellis, "Semiconductor Optoelectronics", Butterworths, London, 1973.

[6] E. Pentia, L. Pintilie, C. Tivarus, I. Pintilie and T. Botila, "Influence of Sb^{3+} ions on photoconductive properties of chemically deposited PbS films", Materials Science and Engineering, B80, 2001, p23.
 [7] R. Dalven, "A review of semiconductor properties of PbTe, PbSe, PbS and PbO", Infrared Physics, 9, 1969, p 141.
 [8] V. M. Simic and Z. B. Marinkomc, "Influence of impurities on photosensitivity in chemically deposited lead sulphide layers", Infrared Physics, Vol. 8, 1968, p189.
 [9] E. Pentia, L. Pintilie, T. Botila, I. Pintilie, A. Chaparro and C. Maffiotte, "Bi influence on growth and physical properties of chemical deposited PbS films", Thin Solid Films, 434, 2003, p162.
 [10] S. Kouissa, M. S. Aida and A. Djemel, "Surface state simulation model for photoconductors infrared detectors", J Mater Sci: Mater Electron, 20, 2009, S400-S406.
 [11] S. Kouissa, A. Djemel and M. S. Aida, "Surface state dependence of PbS and PbSe infrared noise and detectivity", J Mater Sci: Mater Electron, 23, 2012, p2083-2088.
 [12] J. C. Slater, "Barrier theory of the photoconductivity of lead sulfide" Phys. Rev, Vol 103, N°6, 1956, p1631.
 [13] R. L. Petritz, "Theory of photoconductivity in semiconductors films", Phys. Rev, Vol 104, N°6, 1956, p 1508.
 [14] A Djemel, R J Taronto, J Castnaing, Y Marfaing, and A Nouiri, "Study of electronic surface properties of GaAs in cathodoluminescence experiment", phys. stat. solid (a), 1998, p168.
 [15] Infrared Industries, INC, Application Data Sheet, "Calculation of Radiant Flux for Restricted Wavelength Regions", SLS. APP 0005, 1989 (Private Document).
 [16] J. D. Vincent, "Fundamentals of Infrared Detector Operation and Testing", Wiley-Interscience Publication, Santa Barbara Research Center, California, 1990.
 [17] E. Dereniak, and G. D. Boreman, "Infrared Detector and Systems", Edition Wiley interscience Publication, 1996.
 [18] N. B. Kotaiya, A. J. Kothari, D. Tiwari and T. K. Chaudhuri, "Photoconducting nanocrystalline lead sulphide thin films obtained by chemical bath deposition", Appl. phys A, volume 108, 2012, p 819.
 [19] A. Rogalski, "Infrared photon detectors", edit SPIE Press, 1995.
 [20] W. Z. Shen and A. G. U. Perera, "Low frequency noise and interface states in GaAs homojunction far- infrared detectors", IEEE Trans-Electron Devices, Vol 46, N° 4, 1999, p811.
 [21] E. Rosencher and B. Vinter, "Optoelectronique", edit Masson, 1998.

APPENDIX

A. Surface analysis

Assuming that Q is the absolute charge at the surface absorber material, then

$$Q = eZ_d N_a = eN_t(1-f)$$

$$\Downarrow$$

$$Z_d = \frac{N_t}{N_a}(1-f) \quad (\text{A1})$$

Where Z_d is the depletion region width and f the occupation probability of the donor energy level given by [10] [14]:

$$f = \frac{\Delta n(0) + n_0 + n_i \exp\left(\frac{E_t - E_i}{kT}\right)}{\Delta n(0) + n_0 + \Delta p(0) + p_0 + 2n_i \cosh\left(\frac{E_t - E_i}{kT}\right)} \quad (\text{A2})$$

Where $\Delta n(0)$ ($\Delta p(0)$), n_i , E_t and N_t are the electron (holes) excess carriers concentrations at the surface, intrinsic carriers concentration, energy level of surface states and surface states density, respectively.

The electron (hole) concentration at the surface n_0 (p_0) is given by:

$$n_0 = \frac{n_i^2}{N_a} \exp\left(\frac{E_b}{kT}\right) \quad (\text{A3})$$

$$p_0 = N_a \exp\left(-\frac{E_b}{kT}\right) \quad (\text{A4})$$

The barriers height is given by:

$$E_b = \frac{eN_a}{2\varepsilon} Z_d^2 \quad (\text{A5})$$

B. Optical Generation

The optical generation rate is given by:

$$G_{ph}(z) = F_f \alpha \eta e^{-\alpha z} \quad (\text{A6})$$

Where F_f is the front surface flux modeled by Plank function, α is the absorption coefficient and the η is the quantum efficiency calculated by [19]:

$$\eta = \frac{(1-r) \cdot [1 - e^{-\alpha d}] \tau_{eff}}{1 - r \cdot e^{-\alpha d} \tau} \quad (\text{A7})$$

In which r is the reflection coefficient and τ_{eff} is the effective lifetime given by [19]:

$$\frac{1}{\tau_{eff}} = \frac{1}{\tau} + \frac{1}{\tau_s \cdot Z_d} \quad (\text{A8})$$

With τ , and τ_s are the bulk and surface electron lifetime respectively.

C. Signal, Responsivity and Detectivity

The conductance of film (Figure 7) is given by:

$$\Delta g = \frac{Z\mu_n e}{l} \int_0^d \Delta n(z) dz \quad (\text{A9})$$

The signal in current and voltage is given by:

$$I_{ph} = \Delta g \cdot V$$

$$V_{ph} = I_{ph} \cdot R_L \quad (\text{A10})$$

Where V is the bias voltage

The spectral response is given by:

$$R = \frac{R_0}{\sqrt{1 + (2\pi f \tau)^2}} \quad (\text{V/W}) \quad (\text{A11})$$

Where R_0 :

$$R_0 = \frac{V_{ph}}{P_{inc}} \quad (\text{V/W}) \quad (\text{A12})$$

f is the modulation frequency and τ the bulk carrier lifetime ($\tau = L_p^2/D_p$)

The specific detectivity is given by:

$$D^* = \frac{R_i \sqrt{A_d \Delta f}}{i_n} = \frac{R_V \sqrt{A_d \Delta f}}{V_n} \quad (\text{A13})$$

The total noise expression is done by

$$i_n^2 = i_{G-R}^2 + i_{1/f}^2 + i_{jph}^2 \quad (\text{A14})$$

$$i_n^2 = 4G^2 q(q\eta E_d A_d + qg_{th} d \cdot A_d) \Delta f +$$

$$\frac{B_{1/f} \bar{i}^2}{f} \Delta f + \frac{4kT}{R_d} \Delta f \quad (\text{A15})$$

The $1/f$ noise is given by [20] where $B_{1/f} = \frac{C}{N_t A_d}$,

$C=0.1$, A_d is the detector area, N_t is the surface state density and Δf is the electrical bandwidth of detector.

At room temperature and high modulation frequency, the dominant compound of noise is the thermal generated-recombination part given by [21]:

$$i_n^2 = 4 q g i_0 \Delta f \quad (\text{A16})$$

Where i_0 is the dark current, Δf is the noise equivalent frequency bandwidth given by $1/(2t_{int})$ where t_{int} is electronic integration time and g is the gain of photoconduction.

Automation and Control in Engineering

A Global Approach with Educational Kits

Filomena Soares, Celina P. Leão
 Centro Algoritmi R&D
 University of Minho, Guimarães,
 Portugal
 email:(fsoares@dei,cpl@dps).uminho.
 pt

José Machado
 MEtRICs R&D Centre
 University of Minho, Guimarães,
 Portugal
 email: jmachado@dem.uminho.pt

Vítor Carvalho
 School of Technology & Centro
 Algoritmi R&D
 Polytechnic Institute of Cávado and
 Ave (IPCA) & University of Minho
 Barcelos & Guimarães, Portugal
 email:vcarvalho@ipca.pt

Abstract— The well-known paradigm learning by doing is particularly important in engineering courses. Still, in some situations, there is a lack of real-world didactic workbenches due to the absence of financial support, human resources or maintenances restrictions. Following this trend, the authors have been trying to overcome this difficulty designing and implementing virtual and remote laboratories in Process Monitoring, Control and Automation teaching applied to Mechanical, Electronics and Biomedical Engineering. The goal of this paper is to review and present the work developed regarding the real-world workbenches to be used in automation and control practical classes as an integrated virtual and remote laboratory. Some important points include the modelling and control of Discrete Event Systems, Continuous Systems and Real-Time Systems as well as Industrial Control Networks. The physical parts were developed and connected, in a closed-loop configuration, with the respective controllers. The developed kits and systems were geared towards the engineering students' needs. This integrated approach is very useful for providing students with a global set of skills in this domain. Quantitative and qualitative studies are continuously applied not only for obtaining students feedback but also to gather information to devise strategies for future virtual and remote laboratory applications development suitable for the target public. The positive results achieved so far are very encouraging.

Keywords-*automation; control design; control engineering; control equipment; engineering education.*

I. INTRODUCTION

The design of new teaching/learning methodologies implies the definition of tools and environments that promote students and teachers' engagement in the knowledge acquisition process. These tools will serve as a complement to the traditional face-to-face lectures.

In engineering courses the laboratory work is very important since it is when students have the opportunity to apply the theoretical concepts learned earlier. So, to install and maintain several working positions in the laboratory is sometimes a challenge: the equipment is expensive, laboratorial space and qualified personnel are not enough. And this problem is replicated at each school.

The virtual and remote (V&R) laboratories may overcome this limitation [1-6]. The students may access the V&R laboratory at any time and place testing the real-world case-study through a graphical animation or a remote webcam.

Nevertheless, a good understanding of the pedagogical aspects is crucial for an efficient remote labs use [7]. Remote laboratories can also be used as a link between the University and the Industry, by providing remote monitoring for some industrial applications [8].

With this in mind and regarding Automation and Control education, a multidisciplinary group of teachers with different backgrounds, from the University of Minho (UM) and from the Polytechnic Institute of Cávado and Ave (IPCA), at North of Portugal, have been centering their attention in designing and developing workbenches in order to enable a practical learning environment. The goal was to provide to the engineering students different pedagogical tools/examples in order to have real-world interactive situations, for instance virtual processes and interactive animations, as well as local and remote experiences.

Considering the main domains, concerning Control and Automation, considered at UM and IPCA - namely: Discrete Event Systems modeling and control, Continuous Systems modeling and control, Real-Time Systems modeling and control and control industrial networks - several workbenches have been developed. For teaching these domains several software tools and controllers can be used. It was, in this spirit, that the workbenches were developed. Also, the physical part of the workbenches were developed and connected, in a closed-loop configuration, with the respective controllers.

Some (five) of the developed solutions include: the velocity control of a Direct Current (DC) motor (modeled as a Continuous System, controlled by a microcontroller in which was implemented a discrete Proportional, Integral, Derivative (PID) algorithm); two examples of systems controlled by Programmable Logic Controller (PLC): an automation workbench for testing and simulating PLC programs (modeled as a Discrete Event System), and the implementation of a small intelligent house (modeled as a Real-Time System); and, finally, two workbenches controlled by Industrial Computers modeled, both, as Real-Time Systems: one, of them - the level control of a two-tank

system - using LabVIEW, and the other one - the acquisition of physiological signals – using, first, LabVIEW and, finally, C# and Java. This paper presents the developed solutions as an integrated V&R laboratory. Among others, this approach allows students to support and consolidate the traditional classes’ model allowing an efficient learning methodology in the specific areas of Control, Automation, Domotics, and Biomedical Data Acquisition fully integrated in one laboratory.

In this way, in order to describe the work developed and exchanged experience on best practice in the use of V&R laboratory for educational purpose over several years this paper is organized as follows: Section 2 presents the five developed real-world didactic kits used in the work, Section 3 describes the qualitative and quantitative students feedback obtained during the experiments and finally, Section 4 enunciates the final remarks.

II. REAL-WORLD DIDACTIC KITS

The real-world engineering problems are from automation and control areas. The goal was to provide students with practical real-world examples previously learned at class. These examples were used in engineering courses of different areas Mechanical, Electronics and Biomedical, at two institutions, Minho University (Braga and Guimarães, Portugal) and IPCA (Barcelos, Portugal) with 3rd and 4th year’s students. In the next subsections there are presented five developed kits: the velocity control of a DC motor, controlled by a Microcontroller; two examples of systems controlled by PLC: an automation workbench for testing and simulating PLC programs and the implementation of a small intelligent house; and, finally, two workbenches controlled by Industrial Computers: the level control of a two-tank system and the acquisition and treatment of physiological signals. The booking of students to access the developed kits is done by a queue defined by a set of conditions for proper priority (i.e., role of the participant – administrator or general user, user with/without previous scheduled access, etc).

A. Velocity Control of a DC Motor

A remote controlled DC motor velocity was developed for undergraduate control studies [9], allowing discrete PID algorithm testing and simulation [10]. A DC Motor “Maxon RE36” is inserted with an encoder “HEDS-5540 A11” for velocity measurement. The control methodology was implemented in a microcontroller. Four different digital versions of the PID algorithm are available. The microcontroller PIC16F876 from Microchip is used to directly control the motor; the control board is linked to the local personal computer by a serial RS-232 communication link for monitoring.

The user interface was developed in a LabVIEW (Figure 1). Twelve motor velocity values can be selected (from 7m/min to 335m/min). The user must select the PID algorithm to be tested as well as the proportional, integral and derivative controller parameters.

B. Automation Workbench

The main focus of the workbench is to allow faster testing and validation of PLC programs, modeled as discrete event systems. The global goal of the developed system is to simulate and test the control programs in order to be sure that, when tested on the real system, those programs will not damage the physical part of the platform. It must be highlighted that this platform can be accessed from outside by different users – using Internet access - from different origins.

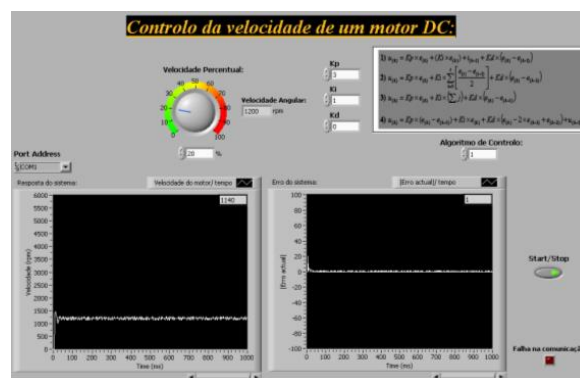


Figure 1. User interface [9].

Thus, it was decided to use a PLC as the controller device and another PLC that will interact with the first one, using a developed network for that, as the plant simulator. For this purpose, the PLC that will run the program that simulates the plant behavior generates all the input signals for the PLC that runs the program of the controller.

The best configuration to meet the needs of the proposed workbench is presented in Figure 2. OMRON equipment was used due to its availability in the laboratory. Both the controller and the plant models were implemented in the controllers OMRON CP1L M30 with CX-Programmer. The physical connection between components (the convertor MDW-45 and Personal Computer, PC and the converter and the PLC) was done using a serial port RS-422; in the connection PC-Converter an adaptor USB to serial port RS-232 was included.

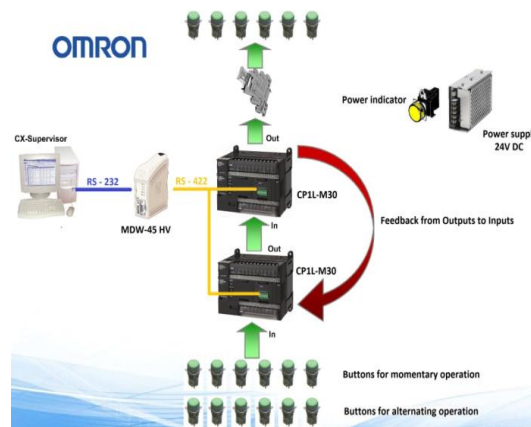


Figure 2. Hardware In the Loop Workbench circuit.

There were used the CX-One software and CX-Supervisor from OMRON. CX-One allows using CX-Programmer to edit and simulate programs and CX-Designer that allows creation of simulation scenarios (drawings, schemes, among others) and using these scenarios associated to the program developed in CX-Programmer the user can understand the simulation of the system. Together with these tools, CX-Supervisor is devoted to the design and operation of PC visualization and machine control. It allows interaction between the user and the PLC program that is running on the controller and also the interaction with the program that is in the PLC that simulates the plant.

C. Small Intelligent House

A test kit for a “small intelligent house” [2] with the following functionalities was developed: alarm control, temperature control, entrance door open/close, and illumination control (Figure 3). The sensors were positioned in order to allow control of alarm intrusion, main and internal illumination, main door opening/closing and attic temperature, using the PLC CQM1H-CPU61 from Omron. The simulation of the “small intelligent” house was developed in LabVIEW (Figure 4). The LabVIEW interface enables both simulation and “small intelligent” house monitoring and actuation, but direct control is performed by the PLC. The interface allows also monitoring and testing different proportional, integral and derivative parameters of the attic temperature control algorithm, as well as real time monitoring using a Webcam.



Figure 3. Small Intelligent House Kit.

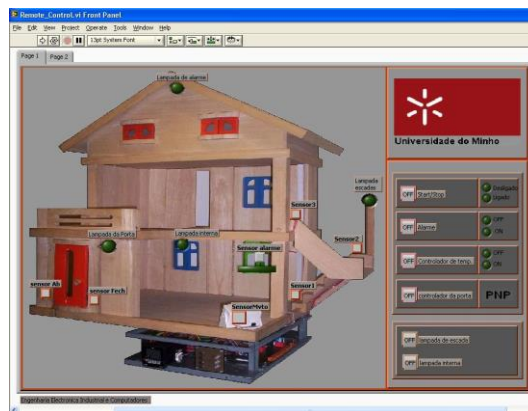


Figure 4. User interface.

D. Level Control of a Two-Tanks System

This work considers the objective of the design and implementation of a remote experiment for controlling the water level in a two-tank system (Figure 5) [7].

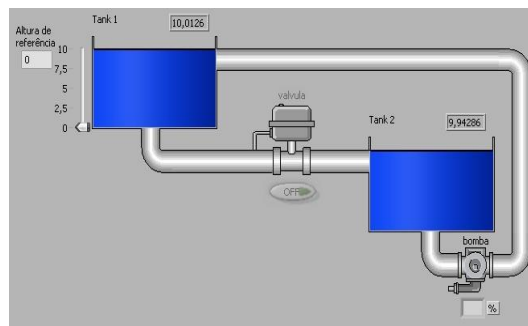


Figure 5. Two tanks system Layout [7].

The system includes two tanks made in acrylic, a pump to circulate the water from the lower to the upper tank, two ultrasonic sensors for measuring both tank levels, an electrovalve to stop the flow between the upper and the lower level tank and a manual valve for security purposes. The upper tank is being controlled and the lower tank serves as a buffer.

An 8-bit Atmega16 microcontroller from Atmel is used for data acquisition, control and pump actuation. A custom made LabVIEW tool, the Watch Tank, was developed for monitoring purposes. The control algorithms, on-off and PID are implemented in the microcontroller that is connected to a PC by a RS232 protocol.

The user interface, Watch Tank, developed in LabVIEW allows the monitoring of the system (Figure 6). In the Watch Tank program, the user must select the PID type algorithm to be tested, as well as the controller parameters, Kp, Ki and Kd, the proportional, integral and derivatives constants, respectively.

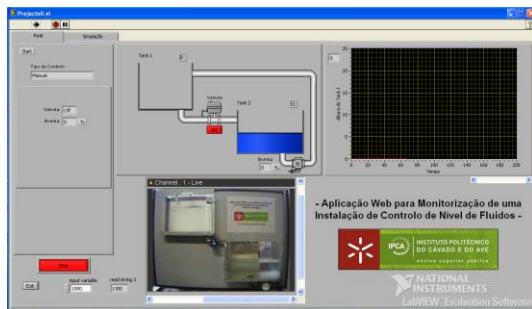


Figure 6. User interface [7].

The user can test the digital algorithms and parameters, change level reference values and register the output data. The system can be set available with either local or remote control configurations for teaching/learning purposes. A Webcam is used for real-time monitoring.

E. Remote Physiological Signals

The study of human physiology allows understanding the human body’s structure and the processes that are carried out within it, which involves mechanical, electrical and chemical forces. So, and in order to support the biomedical engineering undergraduate students’ learning process on physiological data acquisition studies, an innovative remote laboratory has been developed: RePhyS (Remote Physiological Systems) laboratory. RePhyS is capable of engaging biomedical engineering students, providing the real-time remote acquisition of physiological signals from the human body through a web platform. The educational goals should be achieved, namely the knowledge of acquisition methods, the recognition of the signals and the identification of important components of each one [11].

RePhyS was developed using the commercial BioStarter® kit, with sensors’ modules: Electrocardiogram (ECG), Electromyography (EMG), Galvanic Skin Response (GSR), Strain Gauge and an accelerometer. The system includes different remote experiments for the acquisition and study of different physiological signals [12]. The data processing, storage and transmission are made by a computer Bluetooth connection. The general architecture of the RePhyS lab is presented in Figure 7. The ShimmerTM device captures the data through the electrodes placed on the human body. The Bluetooth (IEEE 802.15.1) connection established between the computer, in the real laboratory, and the experiment allows the control and the configuration of the device, and the transfer of measured physiological data. The students, located in a distance place, access the experience through an interface, on an Internet browser, facilitating the interaction with the device through various control buttons. A webcam allows monitoring of the experience.



Figure 7. General architecture of RePhyS.

Figure 8 shows the user interface for the acquisition of ECG remote data acquisition. The experiments developed were initially implemented with LabVIEW being others user-side solutions (C and Java) under development [12].

Thus, the student/user can acquire, visualize and analyze, in real-time, the results of practical experiences being able to interact and to control the measurement parameters. The stored data is always available for further processing.

Currently, the architecture defined for the first version of the remote laboratory is being improved. Thus, RePhyS will allow simultaneous access up to three users, each having a control experiment, and will also allow the simultaneous use of several modules that is, in the same experiment, able to study various physiological conditions of the system.

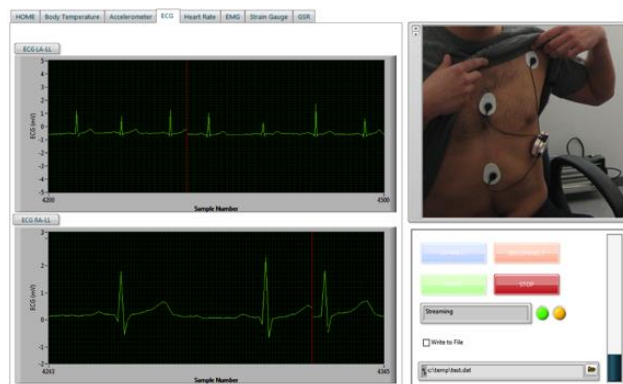


Figure 8. RePhyS user interface during an ECG remote acquisition.

III. QUALITATIVE AND QUANTITATIVE STUDENTS FEEDBACK

For all kits and systems described herein, and in order to obtain the feedback of students, questionnaires were always presented and results analyzed by the teachers involved in the process. The studies also allow the identification of students learning style in order to develop a platform suitable for the engineering learners. The detailed results can be found elsewhere [9, 13].

The use of these questionnaires (n=200, number of students) enabled the improvement of the educational kits in order to accomplish their objective. The questionnaires had open questions in order to obtain students feedback towards specific points as well as quantitative questions defined in

the Likert scale (1, strongly disagree, to 5, completely agree). The analysis was performed using SPSS software.

The questionnaires were divided in sections: after the student characterization, close, open and multiple choices responses, and the evaluation of several statements for the experiment evaluation, the simulator assessment, and to analyze students' perspectives, fillings and knowledge before and after carried out the experiment were used.

The students that participated in this study were from Mechanical, Electronics and Biomedical engineering courses, having an average of 21 years old, of which 20% were female (Biomedical presents the highest percentage of female students with 40%). Concerning the experiment evaluation, on average, students evaluate it with a positive score (values higher than 3 for Q1, Q2, Q4, Q5, Q6 and lower than 3 for Q3), as described in Table I.

TABLE I. KITS AVERAGE STUDENTS' EVALUATION BY ITEM

Item	Average
Q1: In general, I was motivated for the use of these kits in the course context.	4.4
Q2: In general, I can say that the performance of the kits...	
1: ... helped me assimilate the concepts presented during the course	3.6
2: ... made my learning more objective	3.7
3: ... increased my chances of getting a high final evaluation	3.5
4: ... motivated me towards the course	3.8
5: ... raised my expectations relative to the assessment	3.5
Q3: Running the kits had nothing to do with my motivation and my interest in this course.	2.2
Q4: The kits are suitable for my Control/Automation learning process.	4.2
Q5: I recommend the implementation of these kits and activities, in the next school year, as a teaching/learning tool.	4.3
Q6: The implementation of the remote experiment ...	
1: ... has increased understanding of the operation of an on-off controller.	3.5
2: ... has increased understanding of the operation of the PID controller.	3.1
3: ... allow the visualization of the effect of the off-set reduced when going from a controller P to PI.	3.0
4: motivated to learn the subjects under study.	3.5

Based on a protocol, Biomedical engineering students performed several remote experiments in physiological signals acquisition (RePhyS: ECG, body acceleration and body temperature acquisition). All students understood the ECG signal acquisition and they were able to identify all the waves' constituents during the data real-time visualization (as demonstrated in Figure 8). For the other two experiments, 89% identified to have understood and visualized the experiments.

Recently students' perception in relation to their own learning style and the learning style employed during the experiment performance, in accordance with the students' perspective, has been considered. The analysis of this factor becomes an important indicator on how these kits or the V&R laboratories procedure is appropriate for the students' learning process.

In short, it is possible to observe that, and based on the Biomedical engineering students, 67% prefer to process information more actively (2nd and 3th quadrants, Figure 9),

and 67% also prefer to understand the concepts through concrete experiences (1st and 2nd quadrant, Figure 9). This behavior (expected in some way) is coherent to an engineering behavior: motivated to investigate how situations are processed and to put into practice ideas. This information is important as it suggests that the development efforts of these didactics kits meet engineering students' learning styles.

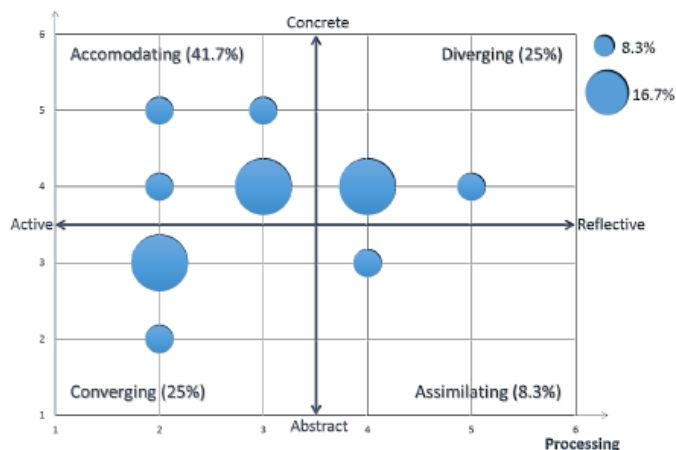


Figure 9. Learning Styles diagram obtained: 1st quadrant – diverging style, 2nd quadrant – accomodating style, 3rd quadrant – covengent style, 4th quadrant – assimilating style.

The qualitative analysis of the data helped to recognize the necessity of devising and implementing new learning strategies to fulfill students' needs. The students replied to the questionnaire on a voluntary basis and according to the experiment conducted. A majority if not all students who performed the experience have accepted this challenge.

The strategy designed V&R laboratory development is appropriated for the target public's learning style (converging learning style) where students do the things in an active way and they have a more abstract perception of the situations.

In general, the students' feedback about the use of the kits and system in Automation and Control Engineering studies is very positive stating that these kits and activities should be used in the coming years, and being suitable for the Automation and Control learning process. The majority of students felt encouraged in using these kits and sentences like: "an innovative and useful tool"; "easy to understand", and "rewarding experience" were found.

The less positive issues pointed out by students were concerned to more technical aspects, like specific problems with the Internet connection, real-time monitoring of an experiment. For a continuous improvement, new alternatives are under studied to overcome the identified problems. The feedback from students to these real-world engineering problems was very positive allowing the researchers to continue and improve this methodology.

IV. FINAL REMARKS

This work describes the work undertaken at two Higher Education Institutions, from north of Portugal, on the development of V&R laboratories as facilitators in the students' study. The students can be from different engineering branches, aiming towards a final objective of optimizing their learning about different important subjects that must be highlighted in the context of teaching of Control and Automation for different future Engineers in many areas, including mechanical engineering, biomedical engineering, and electronics engineering that will need Control and Automation knowledge during their professional life.

Although some of the didactics kits developed and presented in this paper could be considered comparable to some described in the literature (while it has been authors' choice to include as they are part of the automation and control laboratory described), the acquisition and treatment of physiological signals correspond to an innovative remote laboratory. So, this paper describes the development of the virtual and remote laboratory since its creation until today, highlighting the strengths of the didactics kits selected.

A real added value of this project is the use of dedicated workbenches – covering, in a complementary way, the domains related with teaching of control and automation fields - for dedicated needs of real learning, as commercial tools available are very specific mismatching important concepts, together, in the Control and Automation domains.

Based on the different views expressed by students, the final users of the kits and system in Automation and Control Engineering studies, alongside positive points, there are also a few negative points to be identified. The positive points state that these kits and activities are suitable for the Automation and Control learning process and should be used in the coming years. The less positive point identified is concerned to technical aspects, namely specific problems with the Internet connection and real-time monitoring of an experiment.

Finally, it is important to highlight that strong physical and human resources have been optimized because students from both institutions can use this remote access laboratory and experiences have been developed taking into account their specific Curricular Unit's needs.

ACKNOWLEDGMENT

The authors are grateful to the students that participated in

this project as designers and as end users.

This work has been supported by FCT – “Fundação para a Ciência e Tecnologia” in the scope of the project: PEst-UID/CEC/00319/2013.

REFERENCES

- [1] L. Gomes and S. Bogosyan, “Trends in Remote Laboratories”, IEEE Transactions on Industrial Electronics, vol. 56, issue 12, Dec. 2009, pp. 4744-4756.
- [2] P.M. Silva, P.C. Oliveira, N.C. Carvalho, C.P. Leão, and F. Soares, “Virtual and Remote Control: an experience by students for students”, International Conference on Remote Engineering and Virtual Instrumentation (REV07), Porto, Portugal, Jun. 2007, p.3.
- [3] S. Santos, B. Alves, and F. Soares, “Remote Laboratory for Control Studies – A Case-study Developed by Students for Students”, 9th Portuguese Conference on Automatic Control (Controlo2010), Coimbra, Portugal, Set. 2010.
- [4] T. Karakasidis, “Virtual and remote labs in higher education distance learning of physical and engineering sciences”, IEEE Global Engineering Education Conference (EDUCON2013), Berlin, Germany, March 13-15, 2013, p. 798-807.
- [5] T. Machet and D. Lowe, “Issues Integrating Remote Laboratories into Virtual Worlds”, 30th Australian Society for Computers in Learning in Tertiary Education (ASCILITE 2013), Sydney, Australia, 1-4 December, 2013, p. 521-525.
- [6] X. Chen, G. Song, and Y. Zhang, Y., “Virtual and Remote Laboratory Development: A Review”, Earth and Space, 2010, pp. 3843-3852.
- [7] N. Brito et al., “A Remote System for Water Tank Level Monitoring and Control - a Collaborative Case-study”, 3rd IEEE International Conference on e-Learning in Industrial Electronics (ICELIE 2009), Porto, Portugal, Nov. 2009, pp. 19-23.
- [8] A. Mokhtar, G. R. Mikhail, and C. Seong-Joo, “A Survey on Remote Laboratories for E-learning and Remote Experimentation”, Contemporary Engineering Sciences, vol. 7, issue 29, 2014, pp. 1617-1624.
- [9] F. Soares, C.P. Leão, V. Carvalho, R.M. Vasconcelos, and S. Costa, “Automation & Control Remote Laboratory: A Pedagogical Tool”, International Journal of Electrical Engineering Education, vol. 51 issue 1, Jan. 2014, pp. 54-67.
- [10] K. Ogata, Modern Control Engineering, 4th ed., Prentice-Hall: New York, 2001.
- [11] C. Barros, C. P. Leão, F. Soares, G. Minas, and J. Machado, “RePhyS: A Multidisciplinary Experience in Remote Physiological Systems Laboratory”, International Journal of Online Engineering, vol. 9, no. S5, Jun. 2013, pp. 21-24.
- [12] C. Barros, C. P. Leão, F. Soares, G. Minas, and J. Machado, “Issues in remote laboratory developments for biomedical engineering education”, International Conference on Interactive Collaborative Learning (ICL2013), Kazan, Russia, Sep. 2013, pp. 293-298.
- [13] C. Barros et al., “Assessing Remote Physiological Signals Acquisition experiments”, International Mechanical Engineering Congress & Exposition (IMECE2014), Montreal, Canada, Nov. 2014, pp. V005T05A049-7.

Simple and Precise Analog Arcsine Synthesis Applied to Amplitude to Phase Conversion for Hall Effect Position Sensors

Mohieddine Benammar & Antonio Jr. Gonzales
 Dept. of Electrical Engineering, College of Engineering
 Qatar University
 Doha, Qatar

e-mail: mhenammar@qu.edu.qa; antoniojr.gonzales@qu.edu.qa

Abstract — Sinusoidal encoders, including Hall effect sensors, are position sensors that provide analog sine and cosine signals of angular position. All schemes used for converting these signals into measure of the angle require either trigonometric or inverse trigonometric function implementation. The proposed converter is based on the use of the alternating pseudo-linear segments of the sensor signals together with a simple and effective linearization technique. The theoretical absolute error of non-linearity of the converter is 0.05 degree over the full 360 degree range. The converter may be implemented numerically or electronically. The paper describes the proposed method, full details of its analog implementation, and experimental results obtained with a Hall effect sensor. Results demonstrate agreement between theory and experimental results.

Keywords — amplitude-phase conversion, inverse sine synthesis, linearization, position measurement, sinusoidal encoder, Hall effect sensor.

I. INTRODUCTION

Rotational speed and position measurement and control is often required in various applications in industry, military, avionics, communication and other fields. Sinusoidal encoders whether operating on optical, inductive, Hall effect or magnetoelectric principles produce quadrature electrical signals in which the unknown angle is encoded [1]-[10]. In practice, it is common to observe phase and amplitude imbalances in the sensor signals; therefore the sensor outputs may be written as:

$$\begin{cases} U_s(\theta) = A \times \sin(\theta) \\ U_c(\theta) = A(1 + \alpha) \times \cos(\theta + \beta) \end{cases} \quad (1)$$

where A is the maximum amplitude of the sinusoidal component of $U_s(\theta)$, θ is the shaft angle of the rotor of the sensor, and α and β are amplitude and phase imbalances respectively. Note that some sensors may produce signals with dc offset components; however, these may easily be removed before further processing. Amplitude and phase balancing may be achieved in a number of ways [11]-[14]. In this work, we propose balancing by generating a perfect cosine signal, from $U_s(\theta)$ and $U_c(\theta)$, with the same amplitude as the sine signal,

$$\begin{cases} \hat{U}_s(\theta) = U_s(\theta) = A \times \sin(\theta) \\ \hat{U}_c(\theta) = \frac{U_c(\theta)}{(1 + \alpha)\cos\beta} + \tan\beta \times U_s(\theta) = A \times \cos(\theta) \end{cases} \quad (2)$$

The resolver requires a suitable converter in order to determine θ from its signals (2); many open loop and closed loop conversion schemes have been described in literature. Some open loop converters based on the linearization of the pseudo-linear segments of sinusoidal signals have been described [10][15]-[22]. Ratiometric techniques based on arctangent method are also used in open loop converters [23]-[26]; these require the use of look up tables or linearization techniques. Other open loop converters based on the use of reference ac signals and time measurement techniques have also been described [8][9][27]-[29]. Closed loop converters employ the phase-locked loop (PLL) technique [30]-[37].

In the present work, we present an open-loop amplitude-to-phase converter that uses a simple arcsine synthesis technique which can be easily implemented with few standard electronic components. The remainder of the paper is organized as follows. In Section II, the principle and theory of operation of the proposed converter, including a novel linearization technique, are described in details. A dedicated signal shaping technique used for implementing the converter is also described. In Section III, the practical implementation of the converter and experimental results are described. Section IV concludes the paper.

II. PROPOSED CONVERTER

The basic principle of the proposed converter (Figure 1) is based on making use of the alternating pseudo-linear segments of the sensors signals (2) in order to produce a signal $U_0(\theta)$ which is almost proportional to the unknown angle θ in each of its four quadrants (Figure 2), as has been reported in previous works [5]-[19]. The four quadrants are identifiable using two binary outputs whose states depend on the signs of the sum and difference of the transducer signals (i.e., LOW state for negative and HIGH state for positive values):

$$\begin{cases} Bit1(\theta) = \overline{\text{sign}(\hat{U}_s(\theta) + \hat{U}_c(\theta))} \\ Bit0(\theta) = Bit1(\theta) \oplus \text{sign}(\hat{U}_s(\theta) - \hat{U}_c(\theta)) \end{cases} \quad (3)$$

The signal $Bit0(\theta)$ is used to control the multiplexer that selects the pseudo-linear segments of the sensor signal to produce $U_o(\theta)$,

$$U_o(\theta) = (Bit0(\theta) \times \hat{U}_c(\theta)) + (\overline{Bit0(\theta)} \times \hat{U}_s(\theta)) \quad (4)$$

The sign of $\hat{U}_s(\theta) - \hat{U}_c(\theta)$ is used together with a synchronous rectifier to generate a rectified signal $U_{OR}(\theta)$, a sawtooth-like waveform made up of four identical and positive-slope sections as shown in Figure 1 and Figure 2. The signal $U_{OR}(\theta)$ requires further linearization in order to obtain a piecewise linear output $U_{ORL}(\theta)$. The angle may be determined from the linearize signal $V_{ORL}(\theta)$ using a simple linear equation within each quadrant of input angle with minimal non-linearity error. Within the full 360 degree range, the computed angle noted θ_c (in degree) is determined from:

$$\theta_c = 45^\circ \times \left[\left(\sqrt{2}/A \right) \times U_{ORL}(\theta) + 2 \times Bit0(\theta) + 4 \times Bit1(\theta) \right] \quad (5)$$

Note that in the range 315 to 360 degree, the angle determined using (5) is negative (i.e., measured clockwise). Evidently, the residual error ($\theta_c - \theta$) depends on the quality of linearization scheme. Previous works have presented various linearization methods with different degrees of complexity and precision [10][15]-[22]. These schemes that uses multipliers/dividers add complexity and cost, particularly, in analog implementation. In this work, the proposed linearization method is based on signal shaping techniques.

Signal shaping networks are usually associated with trigonometric and inverse trigonometric function synthesis. In this application, the pseudo-linear segments of $V_{OR}(\theta)$ belong to sinusoidal signals. Hence, linearization requires arcsine function synthesis, or in other words sine-to-triangle conversion. It is well known that signal shaping can be implemented using well established piece-wise linear approximation techniques involving diodes and/or transistors [38]-[40]. Other techniques based on differential pairs of transistors offer attractive and simpler solutions that closely approximate sine function [41]-[47]. In the present application, a signal converter based on the non-linear I-V characteristics of the base-emitter junction of low power bipolar junction transistors. The circuit diagram of the proposed linearization scheme is shown in Figure 4. This is a translinear sine-triangle converter inspired from the triangle-sine scheme presented in [47].

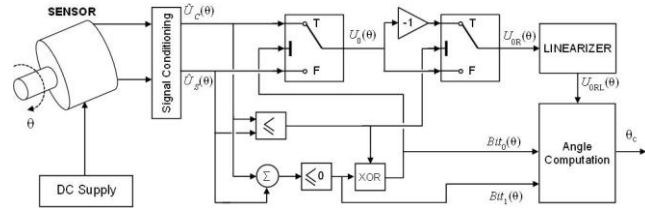


Figure 1. Basic diagram of the proposed converter.

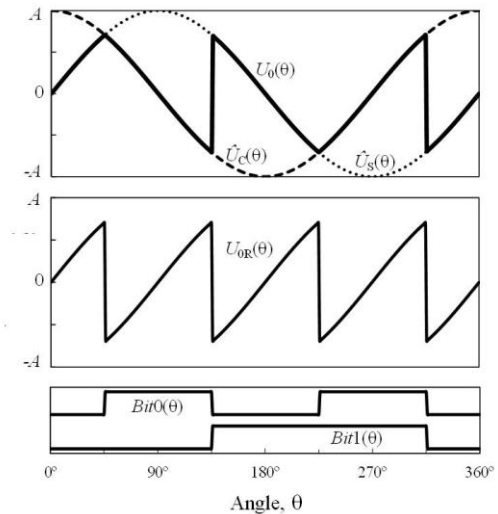


Figure 2. Converter signals: input signals $\hat{U}_s(\theta)$ and $\hat{U}_c(\theta)$, non-linearized signals $U_{OR}(\theta)$ and $U_{ORL}(\theta)$ and binary outputs $Bit0(\theta)$ and $Bit1(\theta)$.

The following analysis assumes that the transistors in the scheme of Figure 4 are matched. Because of symmetry, the current source of magnitude $2I$ ensures that the individual bias currents I in the two trans-diodes are equal. The sinusoidal segments of the rectified voltage $U_{OR}(\theta)$ applied to the linearization circuit result in a current $i = U_{OR}(\theta)/R$. Note that this current should always be lower than I ; the maximum value should correspond to the maximum amplitude A of the sinewaves from which the segments of $U_{OR}(\theta)$ are extracted and therefore $i_{max} = A/R = I$. By invoking the Shockley equation for the base-emitter junctions of the transistors, we can write:

$$\begin{aligned} U_{ORL} &= -\left(1 + \frac{R_2}{R_1}\right) \times \left[2(R_1 // R_2) i + V_{BE1} - V_{BE2}\right] \\ &\approx -\frac{2R_2}{R} V_{OR} - \left(1 + \frac{R_2}{R_1}\right) V_T \ln \left[\frac{1 + U_{OR}/(IR)}{1 - U_{OR}/(IR)} \right] \end{aligned} \quad (6)$$

where V_T is the thermal voltage ($\approx 26\text{mV}$ at room temperature). The Maclaurin series expansion of (6) yields:

$$\begin{aligned} U_{ORL} &= -\frac{2R_2}{R} U_{OR} - 2 \left(1 + \frac{R_2}{R_1}\right) V_T \sum_{n=0}^{\infty} \frac{(U_{OR}/(IR))^{2n+1}}{2n+1} \\ &= -\frac{2U_{OR}}{R} \left[R_2 I + \left(1 + \frac{R_2}{R_1}\right) V_T \right] - 2 \left(1 + \frac{R_2}{R_1}\right) V_T \left[\frac{1}{3} \left(\frac{U_{OR}}{RI}\right)^3 + \frac{1}{5} \left(\frac{U_{OR}}{RI}\right)^5 + \dots \right] \end{aligned} \quad (7)$$

The objective is to convert the sinusoidal signal $U_{OR}(\theta)$ into a sinusoidal current which is in turn converted into a triangular output voltage $U_{ORL}(\theta)$; therefore:

$$U_{ORL} = -K_1 \times \arcsin(U_{OR}/(RI)) = -K_1 \sum_{n=0}^{\infty} \frac{(2n!)}{4^n (n!)^2 (2n+1)} (U_{OR}/(RI))^{2n+1} \quad (8)$$

$$= -K_1 \times \left[\left(\frac{U_{OR}}{RI} \right) + \frac{1}{6} \left(\frac{U_{OR}}{RI} \right)^3 + \frac{3}{40} \left(\frac{U_{OR}}{RI} \right)^5 + \dots \right]$$

By comparing (7) and (8), and considering the first three terms of the expansions, we can deduce the conditions for a successful conversion:

$$\begin{cases} \left(1 + \frac{R_2}{R_1} \right) V_T + R_2 I = K_1 / 2 \\ U_{ORLmax} = K_1 \pi / 4 \\ K_1 / 6 = 2 \left(1 + \frac{R_2}{R_1} \right) V_T / 3 \quad \text{or} \quad 3 K_1 / 40 = 2 \left(1 + \frac{R_2}{R_1} \right) V_T / 5 \end{cases} \quad (9)$$

Note that the maximum amplitude of $U_{ORL}(\theta)$ occurs at the peak of $U_{OR}(\theta)$ which is equal to $2^{-1/2}A$; therefore $U_{ORLmax} = K_1 \times \arcsin(2^{1/2}A/(RI)) = K_1 \pi / 4$. If we keep K_1 within the boundaries defined by the last condition of (9):

$$4(1 + R_2/R_1)V_T \leq K_1 \leq 80(R_2/R_1)V_T/15 \quad (10)$$

Straightforward analysis shows that when considering (10), the two conditions in (9) may be re-written as:

$$\begin{cases} \frac{V_T}{I} \leq R_1 // R_2 \leq \frac{25V_T}{15I} \\ \frac{15U_{ORLmax}}{20\pi V_T} - 1 \leq \frac{R_2}{R_1} \leq \frac{U_{ORLmax}}{\pi V_T} - 1 \end{cases} \quad (11)$$

Assuming operation at room temperature ($V_T=26mV$), a current $I=0.25mA$, sensor signals amplitude $A=10V$, and choosing a peak output voltage $U_{ORLmax}=10V$, simple analysis yields:

$$\begin{cases} 104\Omega \leq R_1 // R_2 \leq 173\Omega \\ 90 \leq R_2/R_1 \leq 126 \end{cases} \quad (12)$$

Since $A=RI$, the required value for $R=10V/0.25mA=40k\Omega$. Simulation of $U_{ORL}(\theta)$ according to (6) suggest that with $R=40.04k\Omega$, $R_1=130\Omega$ and $R_2=14130\Omega$, the residual error in the determination of θ using (5) is within $\pm 0.048^\circ$ in the full 360° range as shown in Figure 3.

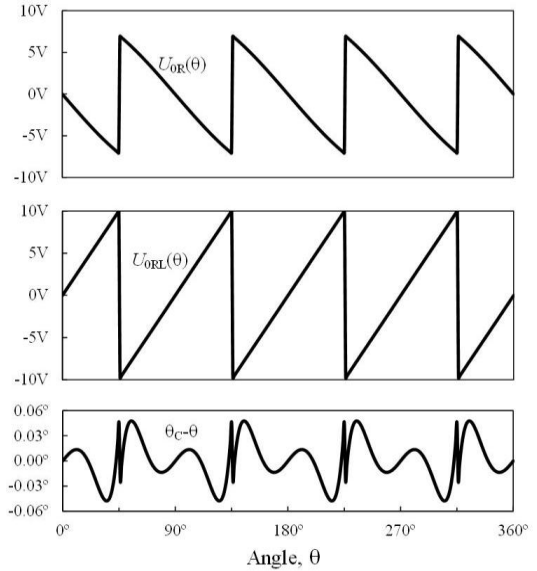


Figure 3. Simulation of the performance of the proposed linearization scheme. $U_{ORL}(\theta)$ is computed according to approximation in (6) with $A=10V$, $I=0.25mA$, $R=40.04k\Omega$, $R_1=130\Omega$, $R_2=14130\Omega$, and $V_T=26mV$.

Note that (i) the inversion of $U_{ORL}(\theta)$ with respect to $U_{OR}(\theta)$ is due to the inverting configuration of the operational amplifier, and (ii) the amplitude A of the sensor signals is assumed to be $20V_{pp}$ and therefore $U_{OR}(\theta)$ is $20/2^{1/2} V_{pp}$. It is important to note that the operating temperature usually affects signal shaping schemes; this can be seen in (6) through the thermal voltage term. However, some degree of temperature compensation is achieved in the present scheme by selecting a suitable current source element with appropriate positive temperature coefficient.

It is important to note that since the proposed scheme is open loop, the bandwidth is only limited by the dynamics of the components used, mainly the operational amplifiers and analog switches. In all cases, the bandwidth should be much higher than what is required in practical positioning applications: e.g., for a maximum rotational speed of 24000rpm (i.e., considered to be very high for real applications), the corresponding frequency would be $24000/60=400Hz$ only which does not pose any problem even for standard components.

III. EXPERIMENT

The practical converter is a straightforward implementation of the scheme of Figure 1 using few standard electronic components. Figure 4 depicts the detailed circuit diagram. Matched dual NPN transistors (MAT01) and adjustable current sources (LM334) have been used in the implementation of the linearizer. The offset cancellation, amplification, amplitude equalization and phase correction of the encoder output signals are not shown. The amplitudes of the converter's input signals $\dot{U}_c(\theta)$ and $\dot{U}_s(\theta)$ are $20V_{pp}$, and the linearized output is $20V_{pp}$.

The encoder used in the present work is a Hall effect sensor (model HSCB22). This sensor produces two

quadrature sine and cosine signals with a nominal peak-to-peak amplitude of 4V and an offset of 2.5V. Appropriate analog signal conditioning is applied to the sensor signals in order to (i) remove the offset, (ii) correct the phase between its signals using (2) and (iii) adjust their amplitudes to 20Vpp. The sensor was driven with a dc motor through a 100:1 reduction gear.

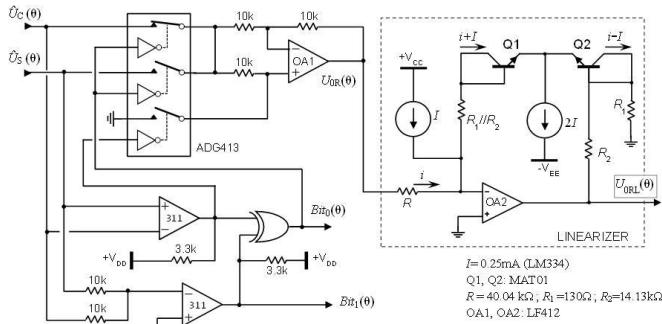


Figure 4. Basic implementation of the proposed open loop converter.

Figure 5 depicts the amplified sensor signals (1) together with the balanced signals (2); the offset in the sensor signals has been removed in the amplification stage generating (1) and the sensor was driven at 37rpm. Figure 6 shows plots of $U_s(\theta)$ versus $U_c(\theta)$ and $\hat{U}_s(\theta)$ versus $\hat{U}_c(\theta)$, and illustrates the effectiveness of phase and amplitude equalization.

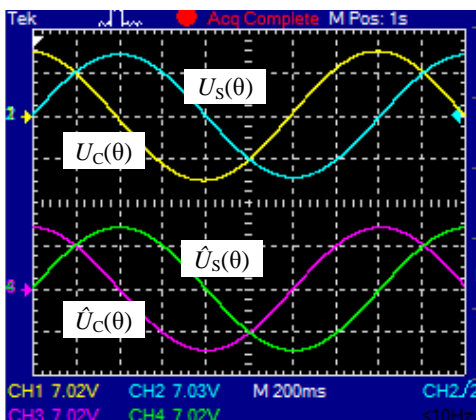


Figure 5. Unbalanced (upper) and balanced (lower) sensor signals at 37rpm.

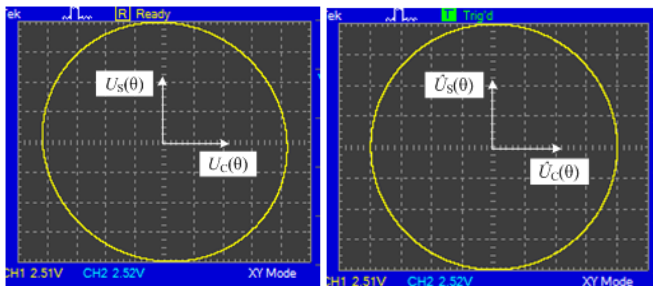


Figure 6. Sine versus cosine sensor signals before (left) and after (right) balancing.

Figure 7 shows the converter input signals $\hat{U}_s(\theta)$ and $\hat{U}_c(\theta)$, the signal $U_0(\theta)$ obtained from the multiplexer, the rectified signal $U_{0R}(\theta)$ and the linearized analog output $U_{0RL}(\theta)$ and binary outputs $Bit0(\theta)$ and $Bit1(\theta)$; the sensor was driven at a fixed rotational speed of 37 rpm. Figure 8 shows the converter signals by driving the sensor at the maximum rotational speed 240rpm; this is the maximum rotational speed that the setup allowed. It is clear, however, that because of its open loop nature, the converter should work at much higher speeds.

The characterization of the converter is shown in Figure 9 where the sensor was mounted on a miniature rotary table (model A5990TS with an integral 90:1 gear ratio and 100 arc-second accuracy) that enabled precise control of the angle θ .

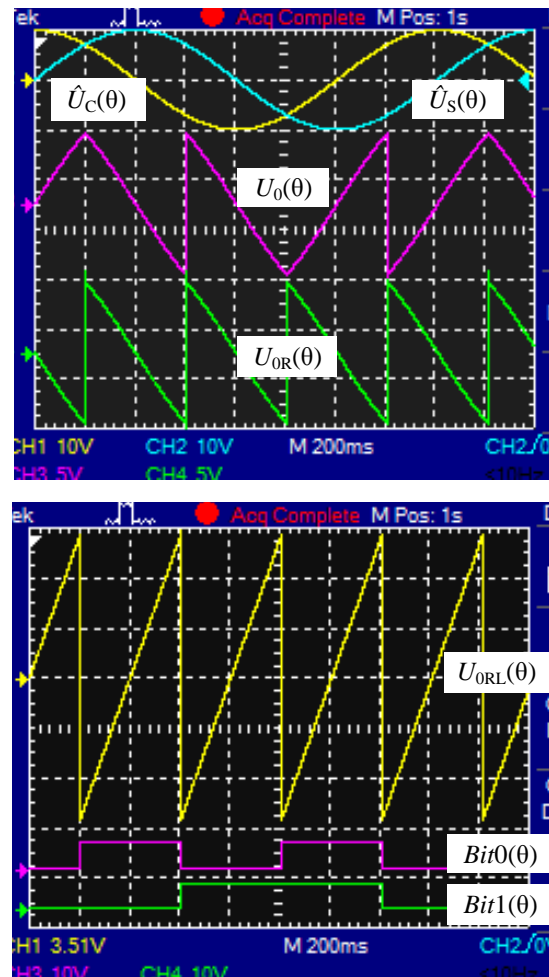


Figure 7. Converter signals at 37rpm.

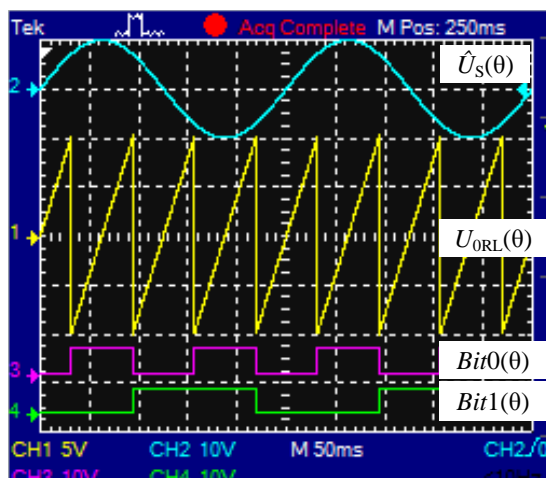


Figure 8. Converter signals at 240rpm.

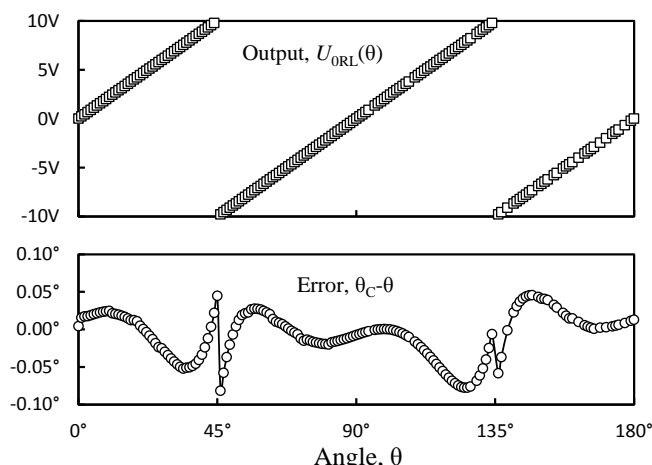


Figure 9. Characterization of the converter by controlling θ using a precision miniature rotary table.

The overall error in the determination of the angle θ_c from the converter signals was lower than 0.09° in the range 0 to 180° of input angle; this compares well with the theoretical error estimated above in Figure 3. Despite the simplicity and low cost of the proposed scheme, its error compares well with those of other more complex closed loop and open loop schemes reported in literature, e.g., 0.01° in [15], 0.10° in [17], 0.04° in [20], 0.18° in [37].

IV. CONCLUSIONS

In this paper, low-cost and simple-to-implement open-loop method for amplitude-to-phase conversion was proposed for use with sinusoidal Hall effect sensors. The conversion was based on a simple and effective linearization technique, full theory of which was given. The theoretical error of non-linearity of the converter is below 0.05° . The scheme was implemented using standard electronic components and was experimentally tested. The results have been excellent and showed that the proposed scheme can be used to measure angles in the full 360° range with an overall error lower than 0.09° .

REFERENCES

- [1] N.H. Duc, B.D. Tu, N.T. Ngoc, V.D. Lap, and D.T.H. Giang, "Metglas/PZT-Magnetolectric 2-D Geomagnetic Device for Computing Precise Angular Position," *IEEE Transactions on Magnetics*, vol.49, no. 8, 2013, pp. 4839 – 4842.
- [2] D. T. Huong Giang, P. A. Duc, N. T. Ngo, N. T. Hien, and N. H. Duc. "Spatial angular positioning device with three-dimensional magnetolectric sensors," *Rev. Sci. Instrum.* Vol. 83 (095006), 2012, doi: 10.1063/1.4752763.
- [3] Y. Netzer, "Linear electric encoder with facing transmitter and receiver," US Patent US2004/02525032A1, Dec. 16, 2004
- [4] P. Kejik, S. Reymond, and R. S. Popovic, "Purely CMOS angular position sensor based on a new hall microchip," in *Proc. IEEE Ind. Electron.*, Orlando, FL, Nov. 10–13, 2008, pp. 1777–1781.
- [5] P. Kejik, S. Reymond, and R. S. Popovic, "Circular hall transducer for angular position sensing," in *Proc. Transducers Eurosensors XXI Conf.*, Lyon, France, Jun. 10–14, 2007, pp. 2593–2596.
- [6] K. Bienczyk, "Angle measurement using a miniature hall effect position sensor," in *Proc. IEEE Electrodyn. Mechatron.*, Opole, Poland, May 19–21, 2009, pp. 21–22.
- [7] D. Wang, J. Brown, T. Hazelton, and J. Daughton, "360° angle sensor using spin valve materials with SAF structure," *IEEE Trans. Magn.*, vol. 41, no. 10, Oct. 2005, pp.3702–3705.
- [8] C. S. Anoop and B. George, "Electronic Scheme for Computing Inverse-Cosine and its Application to a GMR Based Angle Sensor," *IEEE Trans. Instrum. Meas.*, vol. 61, no. 7, July 2012, pp. 1991-1999.
- [9] C.S. Anoop, B. George, and J. Kumar V, "Tunneling Magneto-Resistor based Angle Transducer," in *Proc. Fifth International Conf. on Sensing Technology (ICST)*, Palmerston North, NewZealand, Nov. 28 - Dec. 1, 2011, pp. 431-435.
- [10] G. Ye, et.al, "Design of a precise and robust linearized converter for optical encoders using a ratiometric technique," *Meas. Sci. Technol.*, vol. 25, 2014, pp. 125003-125011.
- [11] D. C. Hanselman, "Techniques for Improving Resolver-to-Digital Conversion Accuracy," *IEEE Trans. Ind. Electron.*, Vol. 38, no. 6, Dec. 1991, pp. 501-504.
- [12] A. Bünte and S. Beineke, High-performance speed measurement by suppression of systematic resolver and encoder errors, *IEEE Trans. Ind. Electron.*51, 2004, pp. 49-53.
- [13] J. Zhang and Z. Wu, "Automatic calibration of resolver signals via state observers," *Meas. Sci. Technol.* Vol. 25, no. 9, 2014, doi: 10.1088/0957-0233/25/9/095008
- [14] S. Balemi, "Automatic Calibration Of Sinusoidal Encoder Signals", *Proceedings of IFAC World Congress*, Prague, Jul. 2005, doi: 10.3182/20050703-6-CZ-1902.01190
- [15] M. Benammar, L. Ben-Brahim, and M. A. Alhamadi, "A high precision resolver-to-DC converter," *IEEE Trans. Instrum. Meas.*, vol. 54, no. 6, Dec. 2005, pp. 2289–2296.
- [16] M. Benammar, L. Ben-Brahim, and Mohd A. Alhamadi, "A Novel Resolver-to-360 Degree Linearized Converter" *IEEE Sensors J.*, vol.4, no. 1, 2004, pp. 96-101.
- [17] M. Benammar, "A novel amplitude-to-phase converter for sine/cosine position transducers," *Int. J. of Electronics*, vol. 94, 2007, pp. 353-365.
- [18] M. Benammar, M. Bagher, and M. Al Kaisi, "Digitally-tuned resolver converter," *Procedia Chemistry*, vol. 1, 2009, pp. 449 – 452.
- [19] D. Živanović, J. Lukić, and D. Denić, "A Novel Linearization Method of Sin/Cos Sensor Signals Used for Angular Position

- Determination,” *J. Electr. Eng. Technol.*, vol. 9, no. 4, 2014, pp. 1437-1445.
- [20] M. Benammar, L. Ben-Brahim, M. A. Alhamadi, and M. Al-Naemi, “A novel method for estimating the angle from analog co-sinusoidal quadrature signals”, *Sensors and Actuators-A*, vol. 142, March 2008, pp. 225-231.
- [21] V. Riewruja and A. Kaewpoonsuk, “OTA-based sine-to-triangular wave converter,” *Circuits Systems Signal Processing*, vol 25, 2006, pp.753-765.
- [22] A. Kaewpoonsuk, W. Petchmaneelumka, A. Rerkratn, S. Tammaruckwattana, and V. Riewruja, “A novel resolver-to-DC converter based on OTA-based inverse-sine function circuit,” in *Proc. SICE Annual Conf.*, Japan, 20-22 Aug, 2008, pp. 609 – 614.
- [23] M. Benammar, M. Bagher, and M. Al Kaisi, “Novel Linearizer for Tangent/Cotangent Converter,” in *Proc. The 16th IEEE International Conf. on Electronics, Circuits, and Systems (ICECS 2009)*, Hammamet, Tunisia, 13-16 Dec., 2009, pp. 575-578.
- [24] S. C. M. Reddy and K. N. Raju, “Inverse Tangent Based Resolver to Digital Converter - A Software Approach,” *Int. J. Adv. Eng. and Tech.*, vol. 4, no. 2, Sept. 2012, pp. 228-235.
- [25] A. Attaianese and G. Tomasso, “Position measurement in industrial drives by means of low-cost resolver-to digital converter,” *IEEE Trans. Instrum.Meas.*, vol. 56, no. 6, Dec. 2007, pp. 2155–2159.
- [26] S. Sarma, V. K. Agrawal, and S. Udupa, “Software-based resolver-to-digital conversion using a DSP,” *IEEE Trans. Ind. Electron.*, vol. 55, no. 1, Jan. 2008, pp. 371–379.
- [27] L. Ben-Brahim, M. Benammar, and M. A. Alhamadi, “A resolver angle estimator based on its excitation signal,” *IEEE Trans. Ind. Electron.*, vol. 56, no. 2, Feb. 2009, pp. 574–580.
- [28] L. Ben-Brahim, M. Benammar, M. Alhamadi, N. Alhamadi, and M. Alhitmi, “A new low cost linear resolver converter,” *IEEE Sensors J.*, vol. 8, no. 10, Oct. 2008, pp. 1620–1627.
- [29] M. Benammar, L. Ben-Brahim, and K. Besbes, “An apparatus for the determination of the angle from its sine/cosine values,” *UK Patent Application 2471458 (A)*, Jan. 5, 2011.
- [30] J. Bergas-Jané, C. Ferrater-Simón, G. Gross, R. Ramírez-Pisco, S. Galceran-Arellano, and J. Rull-Duran, “High-Accuracy All-Digital Resolver-to-Digital Conversion,” *IEEE Trans. Ind. Electron.*, vol. 59, no. 1, 2012, pp. 326 – 333.
- [31] G. A. Woolvet, “Digital transducers,” *J. Phys. E, Sci. Instrum.*, vol. 15, no. 12, Dec. 1982, pp. 1271–1280.
- [32] C.H. Yim, I. J. Ha and M. S. Ko, “A resolver-to-digital conversion method for fast tracking,” *IEEE Trans. Ind. Electron.*, vol. 39, no. 5, Oct. 1992, pp. 369–378.
- [33] D.A. Khaburi, “Software-Based Resolver-to-Digital Converter for DSP-Based Drives Using an Improved Angle-Tracking Observer,” *IEEE Trans. Instrum. Meas.*, vol. 61, no. 4, April 2012, pp. 922-929.
- [34] N. Noori and D.A. Khaburi, “A new software-based method for rotor angle calculation,” in *Proc. The 5th Power Electronics, Drive Systems and Technologies Conference (PEDSTC 2014)*, Teheran, Iran, 5-6 Feb., 2014, pp. 305-310.
- [35] L. Idkhajine, E. Monmasson, M. W. Naouar, A. Prata, and K. Bouallaga, “Fully Integrated FPGA-Based Controller for Synchronous Motor Drive,” *IEEE Trans. Ind. Electron.*, vol. 56, no. 10, Oct. 2009, pp. 4006 – 4017.
- [36] L. Ben-Brahim and M. Benammar, “A New PLL Method for Resolvers,” in *Proc. The International Power Electronics Conference (IPEC2010)*, Sapporo, Japan, 21-24 June, 2010, pp. 299-305.
- [37] N. Al-Emadi, L. Ben-Brahim, and M. Benammar, “A New Tracking Technique for Mechanical Angle Measurement,” *Measurement*, vol. 54, 2014, pp. 58–64.
- [38] C.J. Paull and W.A. Evans, “Waveform shaping techniques for the design of signal sources,” *Radio and Electronic Engineer*, Vol. 44, No. 10, 1974, pp. 523–532.
- [39] V. Schiffer and W.A. Evans, “Approximations in sinewave generation and synthesis,” *Radio and Electronic Engineer*, Vol. 48, No. 3, 1978, pp. 113-121.
- [40] D. Kubanek, “Diode piecewise-linear function approximation circuit with current input and output,” *34th International Conference on Telecommunications and Signal Processing (TSP 2011)*, 2011, pp. 284–287.
- [41] B. Gilbert, “Circuits for the Precise Synthesis of the Sine Function,” *Electronics Letters*, Vol. 13, August 1977, pp. 506-508.
- [42] O. Ishizuka, Z. Tang, and H. Matsumoto, “MOS Sine Function Generator Using Exponential-Law Technique,” *Electronics Letters*, Vol. 27, October 1991, pp. 1937-1939.
- [43] W.A. Evans and V. Schiffer, “A low distortion tri-wave to sine converter,” *Radio and Electronic Engineer*, Vol. 47, No. 5, 1977, pp. 217 – 224.
- [44] C. A. dos Reis Filho, M.P. Pessatti, and J.P.C. Cajueiro, “Analog triangular-to-sine converter using lateral-pnp transistors in analogue pCMOS process,” *9th International Conference on Electronics, Circuits and Systems*, 2002, Vol. 1, 2002, pp. 253 – 256.
- [45] H. Hassan, “FET differential amplifier as a tri-wave to sine converter,” *Proceedings of the 36th Southeastern Symposium on System Theory*, 2004, pp. 427–430.
- [46] S. Galecki, “Multiphase sine-shaper circuit,” *IEEE Journal of Solid-State Circuits*, Vol. 32, No. 1, pp. 126–129, 1997
- [47] R.G. Meyer, W.M.C. Sansen, S. Lui, and S. Peeters, “The differential pair as a triangle-sine converter,” *IEEE Journal of Solid-state Circuits*, Vol. 11, No. 3, 1976, pp. 418-420.

An Intelligent and Customized Electrical Conductivity Sensor to Evaluate the Response Time of a Direct Injection System

Heitor V. Mercaldi*[§], Caio H. Fujiwara*[§], Elmer A. G. Peñaloza*[§], Vilma A. Oliveira[§] and Paulo E. Cruvinel*

*Embrapa Instrumentação

Rua XV de Novembro 1452, São Carlos, SP, Brazil

[§] Universidade de São Paulo

Av. Trabalhador São-carlense 400, São Carlos, SP, Brazil

Email: heitor@usp.br, caio.fujiwara@usp.br, egambo@usp.br, vilma@sc.usp.br, paulo.cruvinel@embrapa.br

Abstract—In pesticide application based on direct injection systems, the sprayer response time plays an important role for the spraying quality, mainly when operating in real time. The response time is defined as the time elapsed from the time of injection until the concentration of the mixture (water mixed with herbicide) reaches 95% of its regime value in the spray nozzles. Therefore, in the response time the transport delay and the rise time for achieving the desired concentration are considered. This paper describes an intelligent sensor mounted near the spray nozzles to measure the concentration response time in a herbicide direct injection system, which uses a highly stable sinusoidal excitation signal. The sensor calibration was performed with NaCl solutions at concentrations similar to those found in actual application conditions. Using an integrated system based on the Arduino platform, an algorithm was developed to relate the measurements to the response time. The integrated system comprises the sensor with its own sensing hardware, A/D converter, processing and storage capabilities, software drivers, self-assessment algorithms and communication protocols. The immediate application of the integrated system is in the monitoring of the response time of a precision pesticide application. The results point to the next generation of smart devices that have embedded intelligence to support decision making in precision agriculture.

Keywords—direct injection; response time; electrical conductivity; intelligent sensors

I. INTRODUCTION

Brazil has experienced in the last two decades a significant increase in the use of pesticides for agricultural production. Despite the significant growth of the area cultivated with transgenic seeds, a technology that promises to reduce chemical use in agricultural production, sales of these products increased by over 72% between 2006 and 2012 and is still rising up according to data from the Brazilian National Union of the Industry of Agricultural Defense Products [1], association which represents the pesticide manufacturers in the country.

In the same period, the area planted with grains, fiber, coffee and sugar cane grew by less than 19%, from 68.8 million to 81.7 million hectares, according to the Brazilian National Company for Supply [2]. This means that the average consumption of pesticides, which was just over 7 kilograms per hectare in 2005, rose to 10.1 kilograms in 2011, an increase of 43.2%. Although this amount indicates more protection for products and higher incomes, the uniform rate of application leads to soil and water contamination. A key approach to reduce environmental pollution is to use variable-rate application.

An approach to develop variable-rate sprayer technologies is to install automation and control procedures on conventional sprayers. In this direction the direct injection type of sprayer systems have been used along with electronic controllers. In order to adjust the sprayer operation, reference for variables such as working pressures, traveling speeds, and spraying concentration change rates can be selected to achieve the quality for spraying drop distribution.

The agricultural machinery and technologies available today enable variable-rate chemical application based on prescription maps or sensors [3]. Variable-rate application can be performed by varying the concentration of the chemical on-the-go using a direct injection system [4]. The direct injection system is an electronically controlled system in which the chemical is injected into the carrier stream. The direct injection system has separated chemical and carrier reservoirs and the chemical can be injected into the carrier stream in different positions.

In the literature, reports of systems to inject concentrated pesticides into diluent stream began to appear in the 70th decade [5]. In [6], Vidrine and collaborators tested the feasibility of injecting concentrated pesticides. In [7], Reichard and Ladd developed a field sprayer which included injection of pesticides at specific rates accounting for variations in travel speed. In [8], Chi and collaborators developed a flow rate control system which allowed the measurements of concentrated pesticides. In [9], Ghate and Perry developed a field sprayer based on the use of a compressed air to inject chemical into the carrier stream. In [10], Miller and Smith reported on development of a direct nozzle injection system. In general, during the spraying process errors can be observed. Research works on the evaluation of the application rate errors has been shown that errors are not only due to the deviations from the target flow rates but also due to interaction between the dynamics of the systems and sprayer response time. By now, is quite well known that the direct injection system sprayer response time depends on the sprayer dynamics and on the transport delay [11].

The transport delay is due to the flow rate and distance of the nozzle from the injection point. The farther the nozzle is from the injection point larger the mix uniformity and lower the cost but higher the transport delay of the sprayer. Several studies have appeared regarding to the performance of the direct injection sprayers and reducing their response time [12]–[20]. Therefore, the conventional implements can be reorganized to operate into variable-rate ones using control

systems [21].

An advantage of the injection type variable rate application over pressure-based variable rate application is the ability to perform instantaneous changes in the concentration, as well as the herbicide type [22]. One of the most important injection-type systems is the direct injection, in which ingredients are pumped into a carrier fluid carrying them to the boom. The direct injection system advantage is in mixing the required amount of chemicals with water, saving the excess amount for later use [23]. A key indicator to determine the precision of a direct injection sprayer is the control system response time. The shorter its response time, the higher its field precision.

This paper presents an intelligent and customized electrical conductivity sensor (ICCS) for evaluation of the response time of direct injection sprayers. With the response time measurements in variable rate sprayers, a looking-ahead approach, which is useful to increase competitiveness and support sustainability in agriculture, can be performed.

After this introduction, this paper is organized as follows. Section II presents the theoretical background on the measurements of electrical conductivity, Section III presents the used materials and the methods for the development of the ICCS and the procedures for its validation. Finally, the results and discussions are presented in Section IV, followed by the conclusion in Section V.

II. THEORETICAL BACKGROUND

The electrical conductivity, also called specific conductance, is the ability of a solution to conduct an electric current. The mechanism for the electrical current conduction in electrolyte solutions is not the same as for metals. In liquids, this process is performed based on the movement of solvated ions, which are attracted by an electrical field. Therefore, the physical-chemical process is related to the occurrence of combination between the molecules of a solvent with molecules or ions of the dissolved substance. However, electrolyte solutions obey Ohm's law in the same way as the metallic conductors. When powered by direct current passing through the body of the solution, the conductance denoted G is defined as the inverse of the resistance expressed in Ω^{-1} or Siemens (S). However, the conductance G of a homogeneous body having uniform section is proportional to the sectional area A and inversely proportional to the length ℓ , then:

$$G = \frac{\sigma A}{\ell} \quad (1)$$

where the proportionality constant σ is the conductivity and given in S/m . The ratio ℓ/A is called the conductivity cell constant and depends on the instrumentation used. The conductivity increases with increasing temperature. Furthermore, the conductivity of a solution depends on the number of ions present and for this reason the most common is the use of the molar conductivity defined as:

$$\Lambda_m = \frac{\sigma}{M} \quad (2)$$

where Λ_m is the equivalent conductivity or the molar conductivity in $S\,m^2/mol$ and M is the molarity or molar concentration in mol/L . The molar conductivity varies with the concentration of the electrolytes. A major reason for this effect is the change in the number or mobility of the ions present. The first case

occurs in weak electrolytes, where the dissociation of ions in a solution is not complete. The second case occurs on strong electrolytes, where in the solution the dissociation of the molecule into ions is total, resulting in a very strong interaction between the oppositely charged ions, and can reduce your mobility.

The study of electrical conduction in ionic solutions would be useful for a quick and routine analysis of solutions, since it is a simple measure related to the properties of the solution. In this context, the conductivity of a solution in a cell having an arbitrary dimension can be obtained by determining the cell constant by measuring the resistance of a solution of known concentration. After the cell constant is determined, the values of conductivities of different solutions can be obtained from experimental measurements data. For devices that do not have the automatic temperature compensation system, the conductivity must be determined at $25^\circ C$ which is the reference temperature.

In solutions, yet it is necessary to correct the conductivity observed by subtracting the conductivity of the solvent, i.e., to get the value of $\sigma_{corrected}$. Therefore, the molar conductivity Λ_m shall be written as:

$$\Lambda_m = \frac{\sigma_{corrected}}{M} \quad (3)$$

Thus, turning the unit concentration mol/L to mol/cm^3 , the equivalent conductivity Λ_m between two electrodes spaced 1 cm away due to 1 mol of substance may be given as:

$$\Lambda_m = \frac{1000\sigma_{corrected}}{M} \quad (4)$$

Then, for a parallel plate sensor, the conductance G can be determined based on the molar conductivity Λ_m , the corrected specific conductivity of the electrolyte $\sigma_{corrected}$, the total ionic concentration M (mol/cm^3) of the substance in the electrolyte solution, and the conductivity cell constant ℓ/A in the form:

$$G(A, \ell, \Lambda_m, M) = \left(\frac{\Lambda_m M}{1000} \right) \left(\frac{\ell}{A} \right) \quad (5)$$

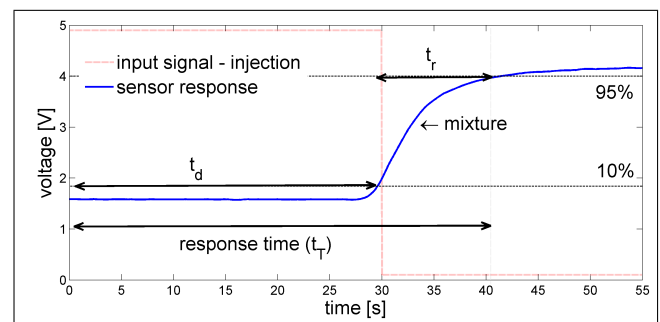


Figure 1. The delay time t_d , rise time t_r and response time t_T involved in a typical injection system as defined in [24]. The red line indicates the behavior in time of the concentrated mixture (water-NaCl) as an injection input.

Peck and Roth defined response time (t_T) as the period from the instant the injection begins until the chemical concentration rate reaches 95% of the equilibrium rate [24]. The rise time t_r and transport delay t_d characteristics of a sprayer proposed by these authors are shown in Figure 1. A 95% concentration rate corresponds to the chemical concentration of

the spraying, which is necessary for satisfactory weed control [25].

III. MATERIAL AND METHODS

The components of the customized smart sensor designed to measure the response time in spraying systems using direct injection of pesticides are shown in Figure 2. For the construction of the smart sensor, voltage regulators, an integrated circuit for a function generator having the capability of frequencies adjustment, opto-isolators and filters were used. Operational amplifiers were used in the active analog filters, non-inverting amplifier drives and isolators circuits. A power transistor was used to drive the injection pump and optocouplers were used to isolate the power circuit from the control circuitry.

A. Excitation Circuit

An excitation circuit for the conductivity sensor was constructed to provide a sinusoidal signal with stability, appropriate frequency and magnitude (Figure 3). The circuitry comprises a sine wave oscillator, a high-pass filter, two insulators and an inverting amplifier circuit (Figure 3). The circuitry was developed to produce signals with high stability and accuracy in an operating frequency range of 0.01 Hz to 1 MHz (Figure 4).

For the generation of the sinusoidal signal an XR2206 integrated circuit which produces sinusoidal signals with considerably low harmonic distortion was used [26]. The oscillator frequency was set to 1.0684 kHz, which is suitable for the application and useful to reduce the electrolysis and the polarization of the solution. In order to tailor the signal for the sensor application considered, a high-pass filtering and a signal amplification module were also used. After conditioning, the signal was appropriate for use presenting voltage values limits as $V_{max} = 4.96\text{ V}$ and $V_{min} = -4.92\text{ V}$.

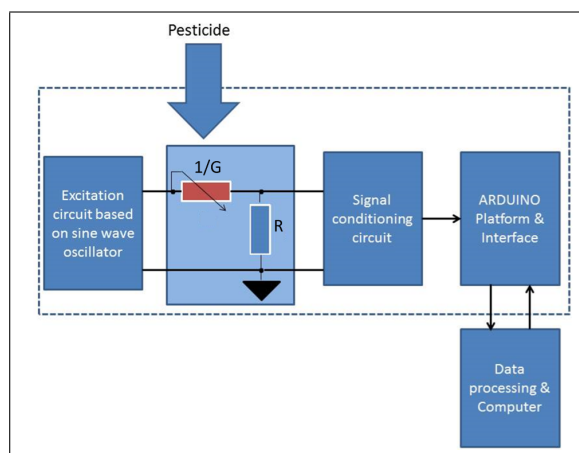


Figure 2. Block diagram of the customized intelligent sensor for response time measurements in spraying systems based on direct injection of pesticides.

B. Signal Conditioning

For signal conditioning, the operational amplifier LF347 integrated circuit, which presents broad bandwidth range (4 MHz), high Slew-Rate (13 V/s), high impedance input ($10^{12}\ \Omega$) and fast settling time (2 μ s), was used [27]. The

use of the OPA344 operational amplifier (low voltage) with an output type Rail to Rail [28] was considered to isolate and protect the Arduino Uno platform against voltage surges or malfunctioning of the mounted circuits.

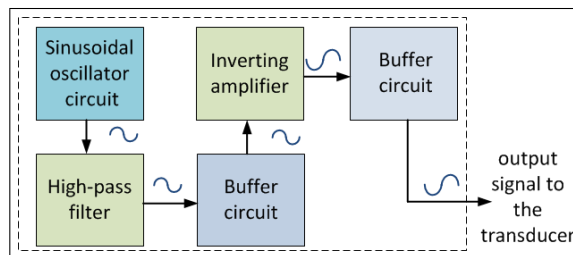


Figure 3. Block diagram of the excitation circuitry.

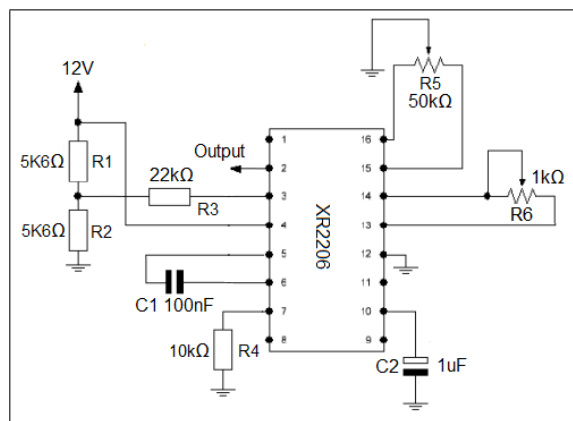


Figure 4. Circuit for the excitation signal generator.

The output of the isolator circuit is limited to voltages from 0 V to 5 V, safe input voltage range for the analog/digital converter (ADC) of the Arduino Uno platform. This ADC has 6 channel 10-bit resolution with absolute accuracy of ± 2 LSB ($\approx 15\text{mV}$), and maximum sample rate of 15 kS/s. The Arduino Uno is an electronic prototyping platform, hardware open and single board, designed with an Atmel AVR microcontroller with built-in input-output support and a standard programming language with origin in Wiring projects, essentially based on C/C ++ [29]. The Arduino Uno platform was used for data acquisition, signal conditioning, computational processing, intelligence aggregation [30], and also for activating the sprinkler system of the injection pump through the LabVIEW[®] software. The use of a buffer circuit, commonly called unity gain buffer, ensures isolation between the two separate stages of the circuit, and the electrical characteristics of a stage does not influence the characteristics of the other. The frequency response and impedance characteristics of the isolation circuit were analyzed through computer simulations, performed in LTspice[®] software. The output signals of each of the stages of excitation circuitry were obtained using an oscilloscope Tektronix TDS2012B and graphics were later built in the Matlab[®] software.

C. Sensor Mounting

Based on the theoretical backgrounds previously presented, a set of parallel plates conductivity type transducers have been built and analyzed for measuring the response time based on the electrical conductivity of the herbicides present in an

agricultural direct injection spraying system. Two stainless steel electrodes with a diameter of 5 mm were used. These transducers were constructed by using a polyacetal base and assembled direct into the nozzle bodies equipped with a diaphragm check valves. For the analysis of the sensor with a static fluid, the electrodes were coupled to the base and spaced at three different distances chosen as 0.5 mm spacing, 1.5 mm and 1 mm, resulting in a set of constant of cells equal to $0,255 \text{ cm}^{-1}$, $0,500 \text{ cm}^{-1}$ and $0,764 \text{ cm}^{-1}$, respectively. The Figure 5 illustrates the positioning and location of the sensor for response time measurements.

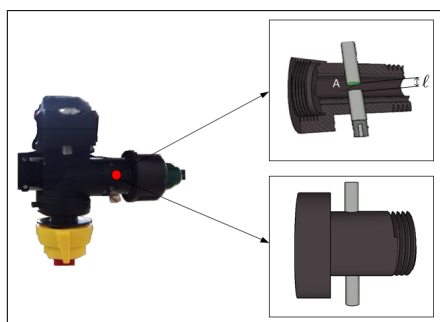


Figure 5. Details of the smart sensor customized to measure the response time of a system of direct injection of pesticides.

D. Sensor Calibration

In order to validate the developed sensor, a real experiment to measure the response time of a sprayer system based on direct injection was performed. The experiment was set for a cell constant of 0.500 cm^{-1} . Furthermore, the sensor was directly assembled into a spray nozzle holder arranged as shown in Figure 6.

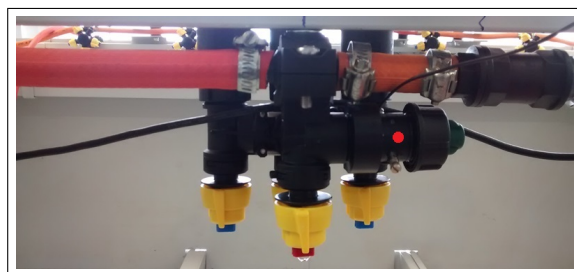


Figure 6. Instrumental arrangement for validation of the intelligent sensor to measure response time of a direct injection sprayer with TeeJet® QJS Multiple Nozzle Bodies e-ChemSaver.

For analysis in real time, the conductivity was measured and the results were processed via LabVIEW® software. Additionally, an Arduino Uno platform was used to capture the analog signals from the sensor, which were previously conditioned for digital measurements, and further processed by computational methods.

The calibration was performed using a commercial conductivity meter from the Tecnonon mCA150 with an operating range of 0 to $200 \mu\text{S}/\text{cm}$, resolution of $0.1 \mu\text{S}/\text{cm}$ (for solutions in the range of 0 to $200 \mu\text{S}/\text{cm}$), 2% of full scale accuracy and 1% of full scale precision [31]. The measurements performed with the commercial conductivity meter were checked with a standard KCl solution (0.02000 mol/L). Static tests were carried out for the analysis of solutions consisting of water

and NaCl. The procedures were performed for three different cell constants.

IV. RESULTS AND DISCUSSION

The computational processing of data and analysis with the developed conductivity sensor was performed using the LabVIEW® software, after the analog/digital conversion and signal conditioning with the Arduino Uno platform. The use of the electronic Arduino Uno platform and the LabVIEW® interface allowed the aggregation of intelligence for self-diagnostic of the ICCS, as well as its self-assessment based on the use of a specific pseudo-code algorithm (Figure 7). The data valid flag was determined experimentally, i.e. based on the dynamic range of the ICCS, defined by $0.50\text{V} \pm 2\text{LSB} < V_{ICCS} \leq 4.90\text{V} \pm 2\text{LSB}$, which is related with the accuracy allowed by the internal ADC of the Arduino Uno platform.

```

Initialization (TIMER, SERIAL, ADC);
if  $0.50\text{V} < V_{ICCS} \leq 4.90\text{V}$  then
    | data valid flag = true;
else
    | data valid flag = false;
end
while true do
    | if data valid flag == true then
        | read temperature ADC;
        | read conductivity ADC;
        | calculate CONDUCTIVITY;
        | send CONDUCTIVITY to SERIAL;
    | else
        | send ERROR to SERIAL;
    | end
end
    
```

Figure 7. Pseudo-code of the algorithm for self-assessment and self-diagnostic.

The calibration results identified the relation for a better accuracy for the conductivity sensor, which is dependent on the conductivity cell constant of the transducer. The shorter the distance between the faces of the electrodes for a same section greater will be the accuracy of the measurements. The calibration curves are shown in Figures 8, 9 and 10 for constant cells given by 0.255 cm^{-1} , 0.500 cm^{-1} and 0.764 cm^{-1} . The individual time responses and the transport delay time for each repetition (Figure 11) were analyzed based on the use of the conductivity sensor and its application in an actual spraying system with a water-NaCl solution flow of $16 \text{ l}/\text{min}$ and pressure equal to 200 kPa. Table I shows the experimental values obtained for determining the response time and the delay times.

TABLE I. EXPERIMENTAL VALUES OF DELAY AND RESPONSE TIMES.

Flow (l/min)	Repetitions	V_{min} (0%)	V_{max} (100%)	t_d (s)	t_T (s)
16	1 st	1.583	4.160	29.560	42.480
	2 st	1.574	4.170	28.800	41.550
	3 st	1.568	4.150	28.360	41.400
23	1 st	1.558	3.989	22.530	32.810
	2 st	1.534	3.964	22.520	33.010
	3 st	1.548	3.969	23.090	33.770

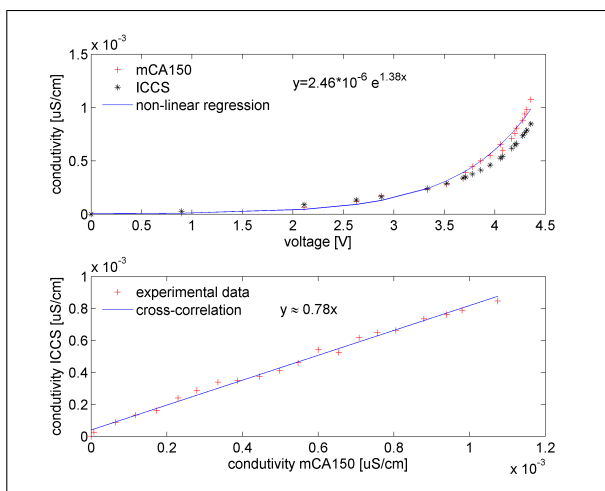


Figure 8. Calibration curves and comparison of measurements of the electrical conductivity from experimental solutions obtained with the intelligent and customized sensor with cell constant of 0.255 cm^{-1} .

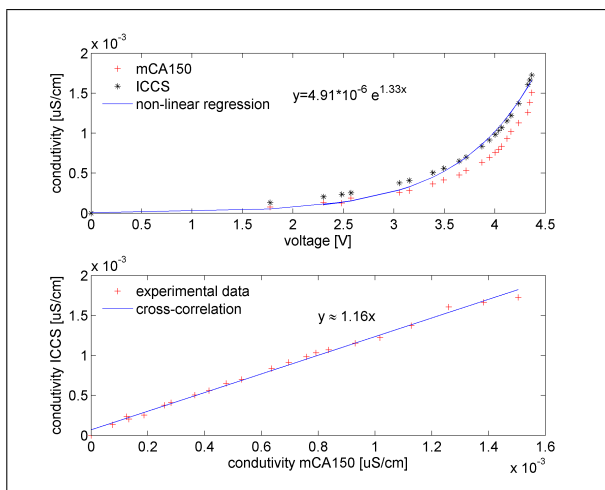


Figure 9. Calibration curves and comparison of measurements of the electrical conductivity from experimental solutions obtained with the intelligent and customized sensor with cell constant of 0.500 cm^{-1} .

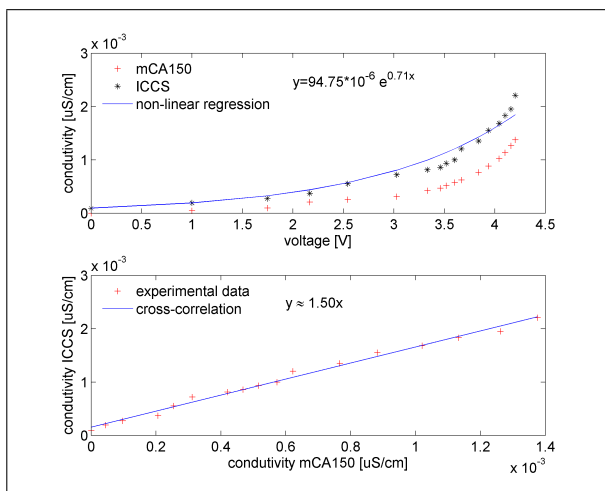


Figure 10. Calibration curves and comparison of measurements of the electrical conductivity from experimental solutions obtained with the intelligent and customized sensor with cell constant of 0.764 cm^{-1} .

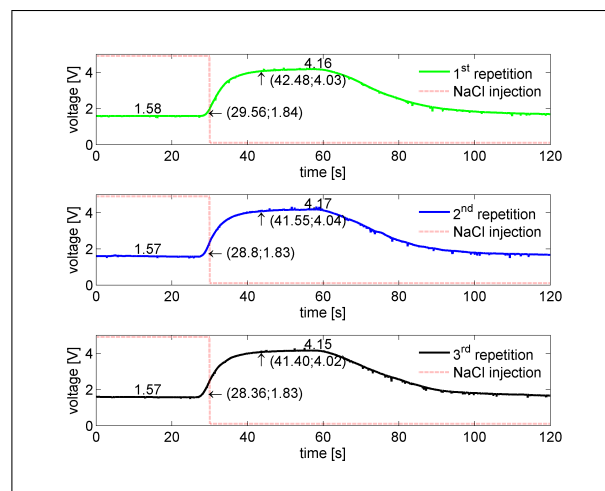


Figure 11. Transients and transport delay times of the sprayer with the conductivity sensor assembled in an actual spraying system with water-NaCl solution flow of 16 l/min and pressure equal to 200 kPa .

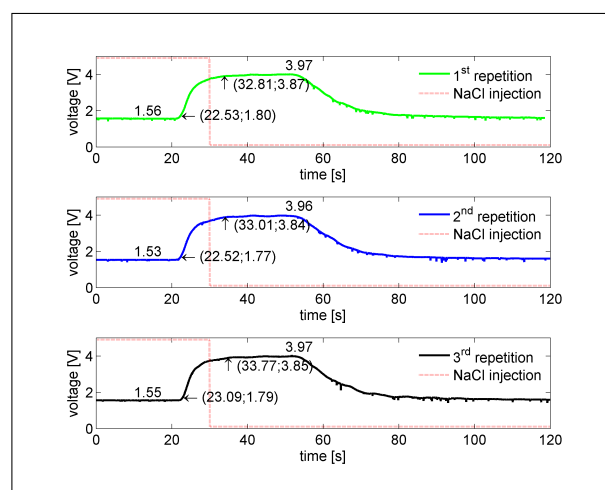


Figure 12. Transients and the transport delay times obtained with the intelligent conductivity sensor assembled in an actual spraying system with water-NaCl solution flow of 23 l/min and pressure equal to 400 kPa .

The obtained results of the dynamic responses for the three repetitions demonstrated the sensor accuracy and reliability. For this experimental arrangement, the average delay time was 28.91 s and the average response time 41.81 s .

A second set of experiments was conducted and the results are shown in Figure 12. In this case, a water-NaCl solution flow of 23 l/min and pressure of 400 kPa were used.

Also, is important to observe that reliability effects and faster circuits have higher current densities, lower voltage tolerances and higher electric fields, which make integrated circuits more vulnerable to electrically failure. The integrated circuits used for the intelligent sensor represent new generations of electronic devices and they provided good performance. Furthermore, the use of the polyacetal base for the intelligent sensor requires a failure analysis.

These procedures for reliability assessment are crucial for the end user as adjustments to electrical conditions and thermal management, since the electrical conductivity is dependent of the temperature of the flows related to the mixture of water plus pesticide.

The results obtained for the sprayer system having a flow rate equal to $23 U_{\min}$ and pressure of 400 kPa, as occurred previously, have shown again, accuracy and reliability in achieving results based on the developed sensor. The average delay time was of 22.71 s and the average response time 33.20 s.

V. CONCLUSION

An intelligent sensor to measure the response time of spray systems based on direct injection was presented. The results have shown its usability in real time applications. The decision to embed the smart sensor directly in the sprayer nozzle provides a scenario, where the input data from the physical sensor could be analyzed by various knowledge-based routines. The sensor output could be raw data or preprocessed information. This information could be in the form of a flag, which shows a confidence level of the response time for pesticide applications.

The results based on the calibration curves for the sensor in three different assemblies showed that the accuracy of measurements depends directly on the conductivity cell constant. However, to determine the response time of a direct injection system of pesticides, one can use a customized sensor with greater spacing between its electrodes to get an adequate sensitivity for sensing the degree of the mixture involving pesticide plus water. Thus, the time involved in the path traversed by the mixture in the sensor can be minimized.

The results of the sprayer system response time with direct injection obtained in this research work have shown that the smart sensor developed has good repeatability, reliability and practicality. Therefore, the results also show the decreasing of the response time with the increasing of the flows, resulting from the increased speed, in which the mixture of water plus the pesticide goes through the system.

The use of intelligent sensor is anticipated to provide additional information than that of traditional sensors. The information provided by an intelligent sensor can include actual data, corrected data, validity of the data, and reliability of the sensor.

Furthermore, such ICCS development attend future perspectives for practical applications, potential benefits for sustainability, as well as precision agriculture processes.

ACKNOWLEDGMENT

The authors acknowledge the financing support from the Brazilian Agricultural Research Corporation (Embrapa Instrumentation, Process MP2 No. 02.11.07.0.25.00.00) as well as from the CNPq Brazilian agency under grant 306477/2013-0.

REFERENCES

- [1] SINDAG. SINDAG and Embrapa study agchem aerial application in Brazil. Accessed at March 5, 2015. [Online]. Available: <http://news.agropages.com/News/NewsDetail—13170.htm> (2014)
- [2] CONAB, "Monitoring of the Brazilian grain crops - season 2013/14 (original in portuguese)," Brazilian National Company for Supply, Tech. Rep., 2014.
- [3] M. Sökefeld, "Variable rate technology for herbicide application," in Precision Crop Protection - the Challenge and Use of Heterogeneity. Springer Verlag, 2010, pp. 335–347.
- [4] J. Vondrica, "Study on the process of direct nozzle injection for real-time site-specific pesticide application," Ph.D. dissertation, Institut für Landtechnik der Rheinischen Friedrich-Wilhelms-Universität, 2008.

- [5] K. L. Hughes and A. R. Frost, "A review of agricultural spray metering," Journal of Agricultural Engineering Research, vol. 32, no. 3, 1985, pp. 197–207.
- [6] C. G. Vidrine, C. E. Goering, C. L. Day, M. R. Gebhardt, and D. B. Smith, "A constant pesticide application rate sprayer model," Transaction of the ASAE, vol. 18, no. 3, 1975, pp. 439–443.
- [7] D. L. Reichard and T. L. Ladd, "Pesticide injection and transfer system for field sprayers," Transactions of the ASAE, vol. 26, no. 3, 1983, pp. 683–686.
- [8] L. Chi, R. L. Kushawara, and F. W. Gigsby, "Chemical flow rate control in injection-type sprayers," Canadian Agricultural Engineering, vol. 30, no. 1, 1988, pp. 19–26.
- [9] S. R. Ghate and C. D. Perry, "Ground speed control of pesticide application rates in a compressed air direct injection sprayers," Transaction of the ASAE, vol. 37, no. 1, 1994, pp. 33–38.
- [10] M. S. Miller and D. B. Smith, "A review of application error for sprayers," Transactions of the ASAE, vol. 35, no. 3, 1992, pp. 787–791.
- [11] P. S. Lammers and J. Vondricka, "Direct injection sprayer," in Precision Crop Protection - the Challenge and Use of Heterogeneity. Springer Verlag, 2010, pp. 295–310.
- [12] R. S. Budwig, J. M. McDonald, and T. J. Karsky, "Evaluation of chemical injection system for mobile agricultural spray equipment," Transaction of the ASAE, 1988, Paper No. 88-1592.
- [13] F. D. Tompkins, K. D. Howard, C. R. Mote, and R. S. Freeland, "Boom flow characteristics with direct chemical injection," Transaction of the ASAE, vol. 33, no. 3, 1990, pp. 737–743.
- [14] K. A. Sudduth, S. C. Borgelt, and J. Hou, "Performance of chemical injection sprayer system," Applied Engineering in Agriculture, vol. 11, no. 3, 1995, pp. 343–348.
- [15] Y. M. Koo and H. R. Sumner, "Total flow control for a direct injection sprayer," Applied Engineering in Agriculture, vol. 14, no. 4, 1998, pp. 363–367.
- [16] H. Zhu, R. D. Fox, H. E. Ozkan, R. D. Brazee, and R. C. Derksen, "A system to determine lag time and mixture uniformity for inline injection sprayers," Applied Engineering in Agriculture, vol. 14, no. 2, 1998, pp. 103–110.
- [17] E. A. Anglund and P. D. Ayers, "Field evaluation of response times for a variable rate (pressured-based and injection) liquid chemical applicator," Applied Engineering in Agriculture, vol. 19, no. 3.
- [18] P. Hloben, "Study on the response time of direct injection systems for variable rate application of herbicides," Ph.D. dissertation, Universitäts- und Landesbibliothek Bonn, 2007.
- [19] A. EL Aissaoui, F. Lebeau, M.-F. Destain, and K. Houmy, "Applying control volume finite element for modeling direct injection boom spraying." Reno, USA: 7th World Congress of Computer in Agriculture, June 22-24 2009, pp. 190–198.
- [20] N. S. Hassen, C. S. Nor Azwadi, and J. M. Sheriff, "Advanced techniques for reducing spray losses in agrochemical application system," Life Science Journal, vol. 11, no. 3, 2014, pp. 56–66.
- [21] M. Jafari, A. Hemmat, and M. Sadeghi, "Development and performance assessment of a DC electric variable-rate controller for use on grain drills," Computers and Electronics in Agriculture, vol. 73, no. 1, 2010, pp. 56–65.
- [22] M. L. Stone, D. K. Giles, and K. J. Dieball, "Distributed network system for control of spray droplet size and application rate for precision chemical application," Toronto, Canada.
- [23] A. Landers. The theory and constituent parts of a direct injection sprayer. Accessed at January 27, 2015. [Online]. Available: <http://vivo.cornell.edu/individual/AI-24241250305> (1998)
- [24] D. R. Peck and L. O. Roth, "Field sprayer induction system development and evaluation," Transaction of the ASAE, 1975, Paper No. 75-1541.
- [25] K. A. Bennet and R. B. Brown, "Direct nozzle injection and precise metering for variable rate herbicide application," Transaction of the ASAE, 1997, Paper No. 97-1046.
- [26] Exar Corporation, Datasheet XR2206. Accessed at February 24, 2015. [Online]. Available: https://www.sparkfun.com/datasheets/Kits/XR2206_104_020808.pdf (2008)

- [27] Texas Instrument, Datasheet LF147, LF347-N. Accessed at February 24, 2015. [Online]. Available: <http://www.ti.com/lit/ds/symlink/lf147.pdf> (2013)
- [28] Texas Instrument, Datasheet OPA344. Accessed at March 04, 2015. [Online]. Available: www.ti.com/lit/ds/symlink/opa344.pdf (2008)
- [29] Arduino, Arduino Uno. Accessed at March 16, 2015. [Online]. Available: <http://arduino.cc/en/Main/ArduinoBoardUno> (2015)
- [30] R. Taymanov and K. Sapozhnikova, "Metrological self-check and evolution of metrology," *Measurement*, vol. 43, no. 7, 2010, pp. 869 – 877.
- [31] Tecnopon, Instructions manual mCA150. Accessed at February 24, 2015. [Online]. Available: <http://www.tecnopon.com.br> (2014)

Underwater Oil Spill Imaging via UV LED-induced Fluorescence

Sangwoo Oh, Moonjin Lee

Maritime Safety Research Division
Korea Research Institute of Ships and Ocean Engineering (KRISO)
Daejeon, Republic of Korea
e-mail: swoh@kriso.re.kr

Abstract—In this research, we describe the concept of underwater oil spill imaging technology based on the UV-induced fluorescence. This imaging system is composed of the ultraviolet LED (Light Emitting Diode) lights and the CCD (Charge-Coupled Device) image sensor. For the identification of the proposed imaging system, we conducted the lab-scale validation tests to classify the difference between the oil samples and the background. For the comparison between oil samples and seawater, we analyzed the images acquired from tests which were performed in different conditions. Through these tests, we can visualize the shape of underwater oil and also distinguish the oil samples from seawater. From this experiment using the proposed setup, we can confirm the possibility of this system for the underwater oil spill imaging system by UV LED-induced fluorescence.

Keywords—Underwater oil; Oil spill imaging; UV LED; Fluorescence

I. INTRODUCTION

Oil spill incidents occur frequently at the sea, despite various efforts to reduce the oil spill from ships and underwater oilfield facilities. Spilt oil is very harmful for every organism in the ocean. For the reduction of oil spread on the ocean, rapid monitoring and exact analysis of oil spill are considerably essential.

Until now, a number of in-situ oil spill monitoring systems have been developed and some of them have been realized [1][2]. They can be largely divided into two parts by means of sensing mechanism. The first one is the sensor which uses the fluorescence method by UV (Ultraviolet) excitation [3] and another is the sensors using electrical capacitance detection by RF signals [4]. These sensors have the functions to analyze their components down to the ppb level. However, these sensors cannot get the image of underwater oil scene, but only detect the presence of oil in the seawater.

In the first step of oil spill accident, oil normally exists on the surface of seawater. But as time goes on, oil frequently forms the ball shape, so-called tar ball, and it goes down from sea surface. So, to identify the underwater oil spill like tar ball oil, it is essential to use the visualization tool for the identification of the underwater oil. In the case of oil spill from underwater oilfield facility, such as oil leak, the monitoring of underwater oil status is necessary for the prevention of it.

To achieve the visualization of the underwater oil spill, we propose a novel underwater oil imaging system which is based on the fluorescence phenomenon. This system is composed of the UV-LED (Light Emitting Diode) lights and the CCD (Charge-Coupled Device) image sensor. For the monitoring of the aquatic organism such as phytoplankton and coral reef, there are some researches which are related to the multispectral imagery in the sea [5][6]. However, in the case of underwater oil spill monitoring, there are a few studies.

In this research, we describe the novel underwater oil imaging system and an initial experiment to acquire the underwater oil image.

II. MATERIAL AND METHODS

A. Underwater oil spill imaging system

The underwater oil spill imaging system which is proposed in the research, is composed of the CCD image sensor (Basler scA1000-30gm) and UV-LED lights. In general, oils which consist of hydrocarbon compounds are excited by ultraviolet wavelengths (300-400 nm) and fluoresce in the visible wavelength range from 400-600 nm. The function of UV-LED lights is to excite the fluorescence of underwater oil. In this research the CCD image sensor is used to capture the fluorescence image of underwater oil. The CCD image sensor has a spectral range of 400 nm to 900 nm. For filtering the emission of reflected light from the underwater oil, we used the lens-type emission filter. The cutoff bandwidth of it is 400 nm. Most reflected light of fluorescent oil have the wavelength above 400 nm wavelength, so we used the emission filter having the cutoff wavelength of 400 nm. The numerical aperture of lens adapted to the CCD image sensor is 2.8.

B. Experiment

At the final development step of proposed imaging system, the water-proof housing is necessary. However, because the purpose of this experiment is to verify the sensing methodology which is newly suggested in this setup, we simplify the experiment condition. Figure 1 shows the experimental setup for the verification of the oil fluorescence by the proposed underwater imaging system. In this experiment, we used the bunker C oil samples

For the excitation of oils, we blocked the external lights (sunlight and artificial light) by a black box and only the UV LEDs can illuminate the oil samples.

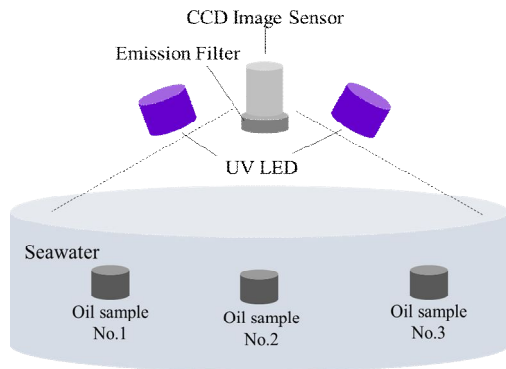


Figure 1. Experimental setup to identify the underwater oil spill imaging using UV LED-induced Fluorescence.

Three oil samples were contained in the cylindrical shape reservoir and the size of it is 3 mm (diameter) x 5 mm (height). This reservoir is made by polyethylene and it is transparent for the UV lights and visible lights. The reservoirs were put on the bottom of small scale basin which is filled with seawater.

In this research, we positioned the UV LED lights at the same position with CCD image sensor (see Figure 1), and captured the image of the fluorescent oil samples by the CCD image sensor. (see Figure 2).

For the quantification between oil samples and seawater, we analyzed the spectrum profile of captured images. Through it, we can see that the similarity level in this experiment is 92%. This analysis was performed in the total pixels of acquired image. These calculations of quantification process were performed by the verified image processing algorithm using MATLAB image process module.

From the processed result of the experiment, we can instinctively recognize the difference between the bunker C oil samples and seawater.

III. RESULT AND DISCUSSION

In this research, we describe the novel underwater oil imaging system and an initial experiment to get the underwater oil image. For the verification of the proposed underwater oil imaging system, we conducted the lab scale experiments to identify the difference between oil samples and seawater.

For the quantification between oil samples and seawater, we analyzed the spectrum profile of captured images. Through it, we can instinctively recognize the difference between the bunker C oil samples and seawater. From this experiment, we can confirm the possibility of this system for the underwater oil spill imaging system by UV LED-induced fluorescence.

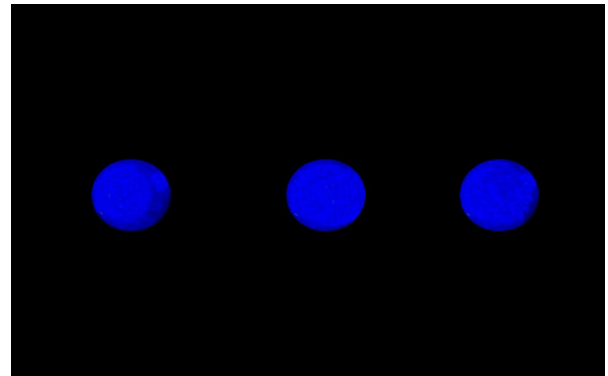


Figure 2. Fluorescent oil imageries acquired by CCD image sensor in the experiments (processed by MATLAB).

IV. CONCLUSION

In this research, a novel underwater oil imaging system was suggested. The basic performance of the proposed system was identified by conducting the lab scale experiment using bunker C oil and seawater. From the result of this experiment we can instinctively recognize the difference between the bunker C oil samples and seawater. Although this experiment is on the first step among the whole development process, if we do some more development, we can expect that this suggested system can be applied to the underwater oil spill imaging system in real site.

ACKNOWLEDGMENT

This work was supported by the Korea Research Institute of Ships and Ocean Engineering (KRISO) Endowment-Grant (PES1870).

REFERENCES

- [1] A. MacLean, C. Moran, W. Johnstone, B. Culshaw, D. Marsh and P. Parker, "Detection of hydrocarbon fuel spills using a distributed fibre optic sensor," *Sensors and Actuators A*, vol. 109, 2003, pp. 60-67.
- [2] G. Griffiths, "Review of oceanographic equipment and sensors for the detection and measurement of pollutants," *Southampton Oceanography Center Research and Consultancy Report*, 2005, no. 99, pp. 1-24.
- [3] C. Henry and P.O. Roberts, "Background fluorescence values and matrix effects observed using smart protocols in the Atlantic Ocean and Gulf of Mexico," *International Oil Spill Conference*, 2001, pp. 1203-1207.
- [4] J. Andrews, "Automated marine oil spill detection system development update," *Marine Environmental Update*, US Navy SPARWAR Systems Centre, 1997, vol. 97, no. 1, pp. 1-10.
- [5] A. C. R. Gleason, R. P. Reid and K. J. Voss, "Automated classification of underwater multispectral imagery for coral reef monitoring," *Oceans 2007*, Vancouver, 2007, pp. 1-8.
- [6] D.G. Zawada, "Image processing of underwater multispectral imagery," *IEEE Journal of Oceanic Engineering*, 2003, vol. 28, no. 4, pp. 583-594.

New Methods for the Preparation of Partial Selective Redox Electrodes for the Determination of H₂O₂

Winfried Vonau, Manfred Decker, Jens Zosel,
 Kristina Ahlborn, Frank Gerlach
 Kurt-Schwabe-Institut für Mess- und Sensortechnik
 Waldheim, Germany
 vonau@ksi-meinsberg.de

Steffen Weißmantel
 Hochschule Mittweida, Fakultät Mathematik/ Naturwissen-
 schaften/ Informatik
 Mittweida, Germany
 steffen.weissmantel@hs-mittweida.de

Abstract— In the paper, new possibilities for the preparation of partially selective redox electrodes based on passivated metals of the subgroups IV to VI of the periodic system are presented. The gas phase oxidation at controlled oxygen partial pressures (CPO) and the pulsed laser deposition (PLD) as an HV method are utilised as alternative methods beside the well established electrochemical passivation which leads usually to the highest possible oxidation state of the passivated metal. These newly available methods enable in principle the tailoring of oxidation states in the sensitive layer and therefore the optimisation of the electrochemical sensitivity and selectivity of sensors equipped with it.

Keywords—partial selective redox electrode; hydrogen peroxide, gas phase oxidation; pulsed laser deposition; electrochemical passivation

I. INTRODUCTION

Measurements of the oxidation/reduction potential (ORP) are suited for online determination of oxidising agents like halogens or hydrogen peroxide in process and waste waters, if the electrode materials provide a partial selectivity [1]. It is already known that systems made of passivated metals of the subgroups IV to VI of the periodic system are suited for this purpose [2]. The favourable sensory behaviour is related to the semiconducting and corrosion properties of the oxide layers with electronic and ionic defects.

The preparation of these layers was carried out so far by anodic oxidation [M(ethod 1)] in half concentrated acids (sulfuric and nitric acid) [3], leading usually to the highest possible valence state of the metal in use at the outer electrode surface. The inner oxide layer near the metal bulk can contain also lower valence states.

In Table I, appropriate metals for the construction of potentiometric sensors with partial selectivity are presented. Figure 1 shows a possible design for the described electrode according to the state of the art.

Generally, electrodes made of these materials exhibit a cross sensitivity to the pH value which should be known and considered. As an example for such a behaviour results of the determination of nitrite by means of a tungsten based indicator electrode at pH values between -1.4 ... 9 are given in Figure 2. There are two ranges with negligible influence

of the pH value (range 1: pH= -1.4 ... 1; range 2: pH= 4 ... 9) on the nitrite concentration related electrode potential. Therefore, a simultaneous pH determination is always advantageous, whereupon the existing problems of pH measurement with glass based or other pH electrodes in strong acidic media should be considered.

TABLE I. MEMBRANE MATERIALS FOR THE FABRICATION OF PARTIAL SELECTIVE ELECTRODES

analyte in aqueous phase	electrode material				
	Ti	Ta	W	Nb	V
Cl ₂	x	x	x		
Br ₂	x	x	x	x	
I ₂			x		
NO ₂ ⁻			x		
H ₂ O ₂					x
Fe ³⁺	x				

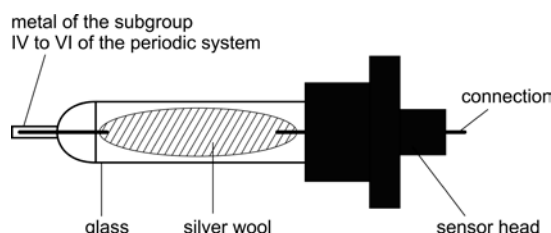


Figure 1. Redox electrode with passivated metal rod as partial selective membrane

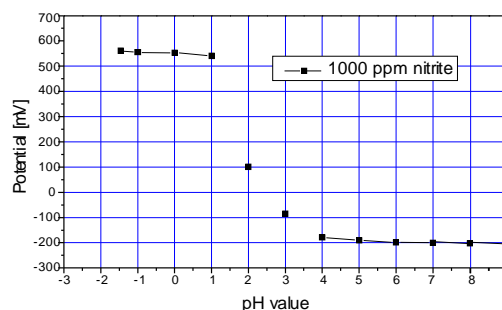


Figure 2. Nitrite determination with tungsten oxide electrodes

To tailor the most important parameters sensitivity and selectivity of the described partial selective electrochemical sensors it might be advantageous to prepare oxide layers in contact with the electrolyte which possess several lower oxidation states with sufficient chemical stability.

In section II, the preparation of the redox electrode by PLD and CPO is described. SEM pictures of the generated vanadium oxide layers and the results of the potentiometric determination of H_2O_2 are presented in section III.

II. NEW METHODS

For the determination of H_2O_2 with partially selective redox electrodes of the above mentioned type vanadium based electrodes are used [4]. Figure 3 shows an electrochemical polarisation curve in sulfuric acid obtained with a vanadium electrode (purity > 99.8 %) within the range of $U_p = 0 \dots 6$ V vs. Ag/AgCl, $Cl^-_{(sat.)}$ at the scan rate 100 mV/s. The observed colour changes of the vanadium surface seem to be related with the formation of VO (green), VO_2 (blue-black) and V_2O_5 (orange) as the final state.

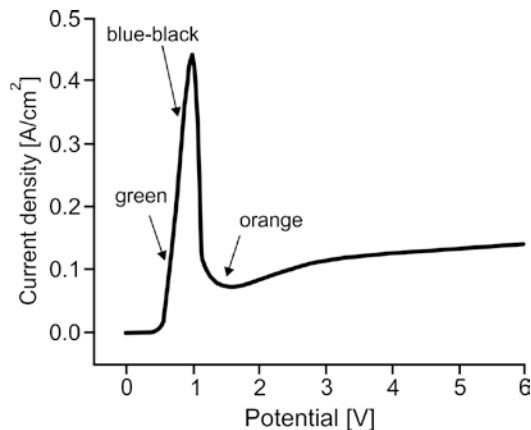


Figure 3. Anodic polarisation curve of pure vanadium in 50% H_2SO_4 measured vs. Ag/AgCl, $Cl^-_{(sat.)}$

A further possibility for the preparation of vanadium oxide layers with tailored valence state is the gas phase oxidation at controlled temperature and oxygen partial pressure [CPO (M2)] according to Figure 4 [5].

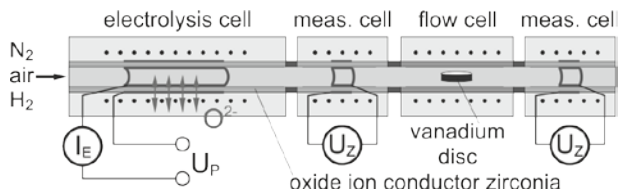


Figure 4. Schematic drawing of the experimental setup for gas phase oxidation of vanadium

The oxygen partial pressure of a mixture of $N_2/air/H_2$ is adjusted precisely within the range $p(O_2) = 10^{-30} \dots 0.2$ bar by a combination of a solid electrolyte pump cell and a solid

electrolyte measuring cell [6]. After gas passage of the vanadium sample positioned in a separately heated transparent flow through cell, the oxygen partial pressure can be controlled again to measure the oxygen uptake by the vanadium surface [7]. Polished vanadium discs were placed inside the transparent cell and treated at different partial pressures and temperatures up to the point, where an oxide layer was visible by the unaided eye.

Vanadium oxide films with defined oxidation states were realised also by using pulsed laser deposition (PLD) either in oxygen background gas or with oxygen ion beam bombardment of growing films (M3) [8] (see Figure 5).

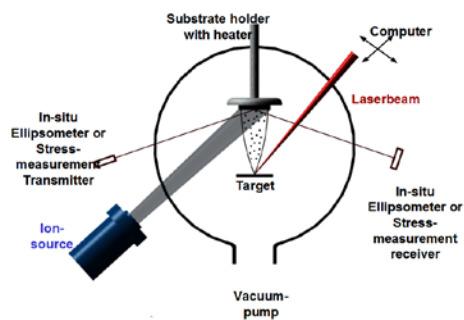


Figure 5. High-vacuum pulsed laser deposition system used for the preparation of vanadium oxide films

The method was used because it allows the preparation of metastable phases of vanadium oxide.

III. EXPERIMENTAL RESULTS, DISCUSSION, OUTLOOK

Figure 6 shows microscopic/ SEM shootings of the surfaces of the vanadium oxide based membranes generated on metallic structures demonstrating that the methods result in functional films that cover the whole surface but differ significantly in their microscopic appearance.

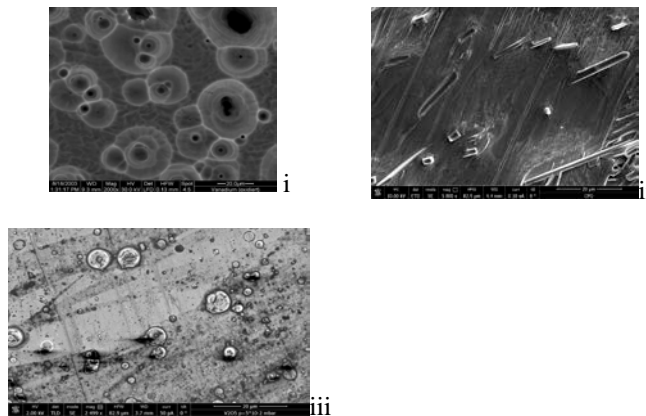


Figure 6: SEM images of vanadium oxide films fabricated by different preparation methods; i: V_2O_5 formed by M1 in 50% H_2SO_4 with a scan rate $U_p = 4,3$ V vs. Ag/AgCl, Cl^-_{sat} at $\theta = 25$ °C; ii: VO_2 prepared by M2 iii: VO formed by M3

Apart from the method-specific created different chemical compositions of the oxides this fact mainly is caused by varying layer thicknesses. Furthermore, the layer presented in Figure 6iii contains a number of droplets, a known disadvantage of the PLD method.

Figure 7 shows that with all mentioned methods sensory active systems of the type V/V_xO_y with partial sensitivity to H_2O_2 are realisable. The electrode functions vary widely. While with M1 there are method-conditioned restrictions in relation to the stoichiometry of the functional oxide, M2+M3 deliver clearly more options concerning the sensor optimisation.

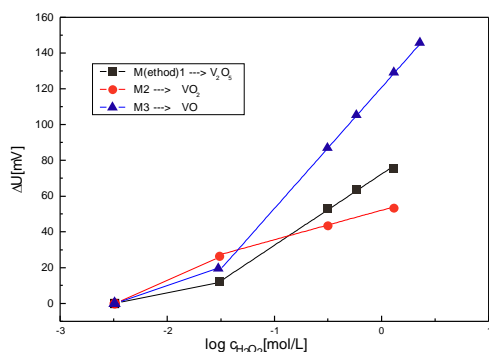


Figure 7. Potentiometric determinations of H_2O_2 with systems of the type V/V_xO_y vs. $Ag/AgCl, Cl^-_{(sat.)}$ realised by different preparation methods (M1, M2, M3) at $\vartheta = 25^\circ C$ in 5% Na_2SO_4 with additives of H_2O_2 at $pH \approx 2$; M1: anodic oxidation, M2: CPO; M3: PLD

Experiences gained from previous work on indicator electrodes for the determination of H_2O_2 based on anodic oxidation of vanadium have demonstrated that a use of the pure transition group metal is unfavourable since the functional layers corrode quickly during the measurement.

It has proved an advantage to alloy vanadium with titanium before passivation [9]. By adjusting an optimal alloy-ratio of both metals, it is possible to retain the functionality of the electrode over a very long period. In this context, results of corrosion measurements given in Figure 8 clearly indicate that the corrosion stability of the electrode membrane can be increased significantly by adding titanium to the alloy.

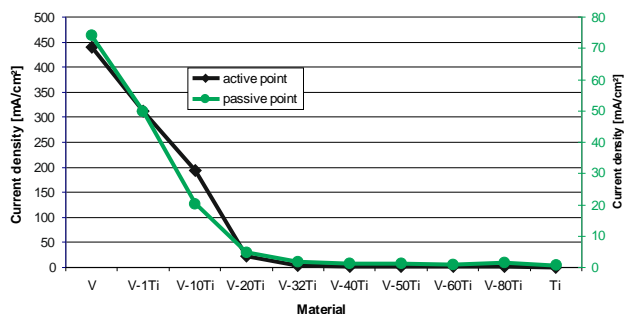


Figure 8. Current density for activation j_a and passivation j_p of V-Ti-alloys

For the choice of an appropriate alloy composition, it is necessary to investigate the upper alloying level of Ti at which the partial selectivity for hydrogen peroxide is maintained at the required level.

Further studies within the scope of the work in process presented here include the following activities:

- creation and evaluation of oxidised alloy coatings based on M2+M3
- examination of the thesis supported in [10] that in the use of vanadium-titanium alloys as membrane material there is no need for an oxidation of the metals and realisation of such alloys by means of M2+M3

IV. CONCLUSIONS

Beside anodic passivation, also CPO and PLD deliver suitable vanadium oxide based membranes for the potentiometric determination of H_2O_2 . The last two mentioned methods allow in principle a largely variable realisation of oxidation states for the vanadium differing from the value +5. This has an impact on the performance of resulting electrochemical indicator electrodes. In future work, these effects shall be examined more closely and the new manufacturing methods for the specific application are to be improved, too.

REFERENCES

- [1] W. Habermann, "Partial selective redox electrodes for the on-line determination of oxidising agents", Ph.D. Thesis, Martin Luther University, Halle, Germany, 1990.
- [2] W. Habermann, P. John, H. Matschiner, and H. Spähn, "Partially selective semiconductor redox electrodes", *Fresenius J. Anal. Chem.*, vol. 356, 1996, pp. 182-186, ISSN: 0937-0633.
- [3] T. Bachmann, U. Guth, and W. Vonau, "Physical and electrochemical properties of vanadium alloy oxide layers prepared by anodic passivation", *Ionics*, vol. 7, 2001, pp. 172-177, ISSN: 0947-7047.
- [4] T. Bachmann, W. Vonau, and P. John, "Hydrogen Peroxide Concentration in Acid Etching Baths", *GIT Laboratory Journal*, vol. 7, pp. 2003, 149-150, ISSN: 1611-6038.
- [5] W. Brückner, H. Oppermann, W. Reichelt, J. I. Terukow, F. A. Tschudnowski, E. Wolf, *Vanadiumoxide. Darstellung, Eigenschaften, Anwendung*. Akademie-Verlag, Berlin 1983.
- [6] M. Schelter, J. Zosel, W. Oelbner, U. Guth, and M. Mertig, "A solid electrolyte sensor for trace gas analysis," *Sens. Actuators B: Chemical*, vol. 187, 2013, pp. 209-214, ISSN: 0925-4005.
- [7] V. Vashook et al., "Crystal structure and electrical conductivity of lanthanum-calcium chromites-titanates $La_{1-x}Ca_xCr_{1-y}Ti_yO_{3-\delta}$ ($x=0-1, y=0-1$)," *J. Solid State Chem.*, vol. 177, 2004, pp. 3784-3794, ISSN: 0022-4596.
- [8] G. Reißer et al., "Influence of ion bombardment on the refractive index of laser pulse deposited oxide films", *Appl Surf. Sci.* vol. 86, 1995, p. 107, ISSN: 0169-4332.
- [9] T. Bachmann, "Electrochemical investigations of oxide layers consisting of vanadium and vanadium alloys", Ph.D. Thesis, University of Technology, Dresden, Germany, 2008.
- [10] P. John, "Indicator electrode with sensitive surface and application therefor", German Patent DE 199 53 218 C2.

Design, Analysis and Modelling of a Capacitive-Based Collision Detector for 3-DOF Hybrid Robotic Manipulator

Dan Zhang

Department of Automotive, Mechanical and
Manufacturing Engineering
University of Ontario Institute of Technology
Oshawa, Ontario, Canada
Email: Dan.Zhang@uoit.ca

Bin Wei

Department of Automotive, Mechanical and
Manufacturing Engineering
University of Ontario Institute of Technology
Oshawa, Ontario, Canada
Email: Bin.Wei@uoit.ca

Abstract—A capacitive based collision detector is proposed and designed in this paper for the purpose of detecting any collision between the end effector and peripheral equipment (e.g., fixture) for the three degrees of freedom hybrid robotic manipulator when it is in operation. The new design is illustrated and modelled. The capacitance, sensitivity and frequency response of the detector are analyzed in detail, and finally, the fabrication process is presented. The proposed collision detector can also be applied to other machine tools.

Keywords- collision detection; sensor; capacitance; robotic manipulator; modelling.

I. INTRODUCTION

A capacitor is defined as two conductors that can hold opposite charges. If the distance and relative position between two conductors change due to the external force, the capacitance value will be changed. This is the basic principle of capacitive sensing, which belongs to electrostatic sensing. The major advantages of electrostatic sensing can be concluded as follows: firstly, it is simple. No special functional materials are required. The sensing principle is easy to implement, requiring only two conducting surfaces. Secondly, it has the characteristic of a fast response. Capacitor-based sensing has high response speed due to the fact that the transition speed is controlled by the charging and discharging time constants that are small for good conductors [1]. There are two kinds of capacitive electrode geometries: parallel plate capacitor and interdigitated finger capacitor. For the interdigitated finger capacitor, it can be regarded as many parallel plate capacitors combining together. One side of the finger is fixed and the other side is suspended, and can move in one or more axes.

Parallel mechanisms have been widely used in different kinds of areas, such as machine tools as shown in Figure 1. When machine tools are in operation, it is sometimes unavoidable to hit the peripheral equipment (e.g., fixture) by the tool, which can damage cutting tools,

clamps and fixtures as shown in Figure 2, or cause damage to the machine itself, which undermines the performance of the whole parallel robotic system, and delays the productions. Therefore, how to prevent the collisions during machining is very important for the machining process. When the end-effector/tool of parallel robotic machine tool accidentally hits the peripheral equipment, e.g., fixture, an operator usually finds it, and hits the emergency stop button, but there is always a time delay. The machine tool should ideally stop immediately when the tool hits the peripheral equipment so that it does not cause further damage. Based on this need and motivation, a sensor should be developed to address this goal. Some computer aided manufacturing software has the ability to perform a machine collision check, but some machine tools do not have this function. Most computer aided manufacturing programs determine the cutter paths, considering sometimes just the tool. In machine tools, it is likely to drive the end effector outside the bounds, resulting in a collision with others. Many machine tools are not aware of the surrounding environment. The end effector just follows the code and it is totally dependent on an operator to detect if a crash occurs.

Imagine the following scenario: when the tool hits the fixture, there should be a vibration produced. So, the question is how to harness this vibration and convert the vibration to an electrical signal that can be recognized by a computer. Capacitive based sensor depends on the physical parameter changing, e.g., the space between the plates and the dielectric constant between them, etc. For example, in the vehicle air bag deployment system, a crash acceleration makes one plate closer to the other, and therefore triggers the bag to deploy. Inspired by this idea, a capacitance-based collision detector/sensor is designed that can sense the vibration and convert the vibration to an electrical signal.

In [2], vibration on a rotating spindle is generated by the sum of the variations in weight distribution. The

corrective action is needed to have a force with an equal but opposite direction to cancel the imbalance condition. The first step to achieve this is to measure the vibration. There, a vibration sensor is installed in a grinding machine spindle, and the vibration is measured using a vibration sensor that is composed of a seismic mass that is connected to a piezoelectric transducer which converts the vibration into an electric signal. The above scenario mainly measures the amount of vibration that the rotating spindle produced and it is not appropriate to use here as a collision detector. In [3], the chatter vibration is detected by using three different acceleration sensors that are attached to three different axis of the machine tool. In [4], a web learning tool with 3D simulation for axial table collision detection was proposed, but no device has been designed. In [5], a vibration detection algorithm was proposed and a speed regulator was designed for the backlash vibration of a machine tool. In [6], a new approach was presented to detect and avoid hard and soft collisions caused by user errors, and a capacitance based sensor was briefly mentioned for the collision of the machine tools, but it did not explicitly design and propose the capacitance based collision sensor. In [7], a six-dimensional wrist force/torque sensor based on E-type membranes is designed and fabricated, and it is applied onto the five-axis parallel machine tool to measure the tool forces and torques. The previous one is force/torque sensor (used to detect forces and moments), but that is not a vibration sensor.

In this paper, a collision detection sensor is designed that can sense the vibration that the end-effector caused when the tool accidentally hits the fixture. When the tool accidentally hits the ground or an object, it will produce vibration, the vibration will make the distance of the capacitor change, and therefore trigger the machine to stop immediately. No one has ever designed the collision detector that gears towards the situation that the machine tool should stop immediately when the end-effector hits the peripheral equipment.

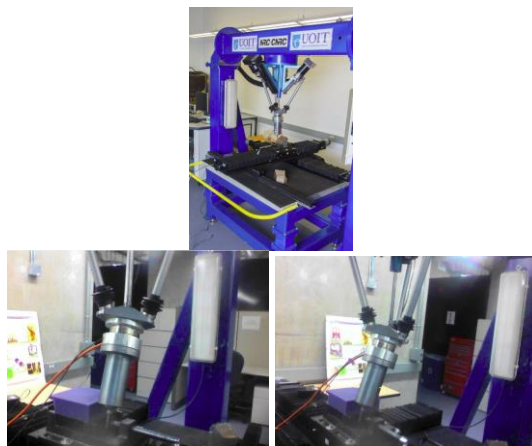


Figure 1. 3-DOF parallel robotic machine tool developed in the R&A Lab in UOIT

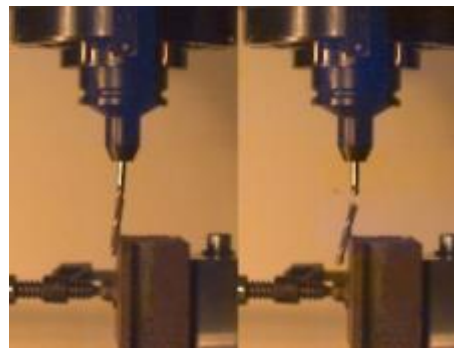


Figure 2. Collision occurred during machining [6]

The structure of the paper is as follows. In Section 2, the new design will be illustrated. The capacitance and sensitivity will be discussed in Section 3. Section 4 analyzes the resonant frequency of the detector, and finally fabrication process is presented in Section 5.

II. NEW DESIGN

Capacitive sensing depends on the physical parameter changing either the spacing between the two plates or the dielectric constant. Our vibration sensing method is based on this idea.

One side of the finger-like capacitor is attached to the moving platform of the hybrid robotics manipulator, and the other side of the finger-like capacitor is attached to the tool as shown in Figure 3. The details and its dimensions are shown in Figures 4 and 5. When the tool accidentally hits the ground or an object, it will vibrate and the distance between the fingers will change and therefore, the capacitance will change and trigger the machine to stop.

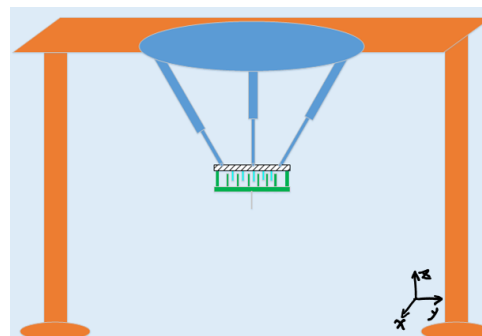


Figure 3. Vibration detector/sensor used in 3-DOF hybrid robotic manipulator

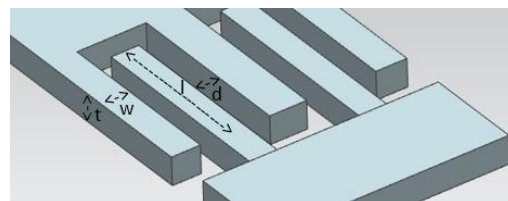


Figure 4. Dimensions of the detector

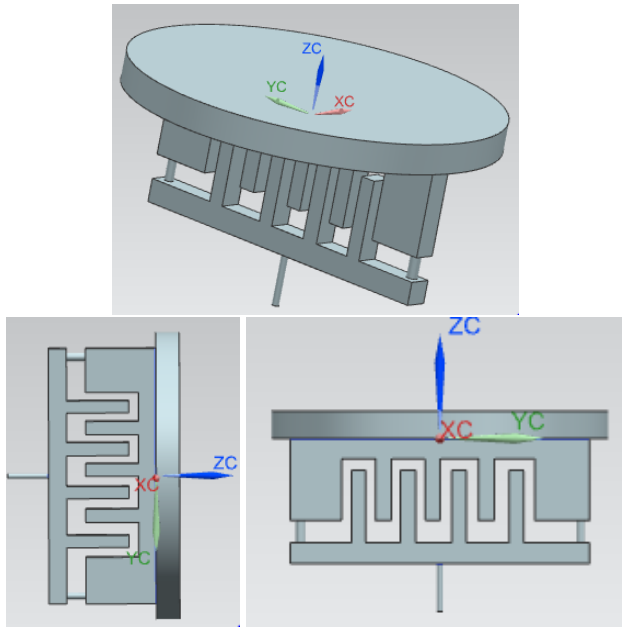


Figure 5. Capacitance based collision detector

The capacitance between a pair of fingers is contributed by the surface of fingers in the overlapped region. Capacitance derived from multiple pairs are connected in parallel, so the total capacitance is the summation of capacitance contributed by neighboring fingers.

III. CAPACITANCE AND SENSITIVITY

For a single fixed finger and its two neighboring moving fingers, there are two capacitances associated with each finger pair, one is the left-side of the finger, denoted as C_l , and the other is the right-side of the finger, denoted as C_r . When the tool is not vibrating, the values of these two capacitance is the same, i.e.,:

$$C_l = C_r = \frac{\varepsilon_0 l t}{d} \quad (1)$$

where ε_0 is the permittivity of the vacuum, l is the engaged overlapping distance of the fingers, t is the thickness of the fingers, d is the distance between a fixed-comb finger and its neighboring movable finger.

A. Movement along y direction

When the tool accidentally hits the fixture, the tool will vibrate, the free finger will move by a distance, say x , and then the capacitance values of these two capacitors become the following:

$$C_l = \frac{\varepsilon_0 l t}{d - x} \quad (2)$$

and

$$C_r = \frac{\varepsilon_0 l t}{d + x} \quad (3)$$

The total value of capacitance is:

$$C = \frac{\varepsilon_0 l t}{d - x} + \frac{\varepsilon_0 l t}{d + x} = \frac{2d\varepsilon_0 l t}{d^2 - x^2} \quad (4)$$

For a case study, suppose there are 13 fingers, which means there are 12 capacitors, so the 12 capacitors will contribute the total capacitance of the device. So the above can be rewritten as follows:

$$C = 12 \frac{2d\varepsilon_0 l t}{d^2 - x^2} \quad (5)$$

This change can be transferred to the electrical signal, and under a certain value, it means the machine tool is in the process of manufacturing. Even though there are small vibrations, the capacitance change is under that value, and the capacitance will not trigger the electrical controller to stop the machine. When, however, the capacitance change is very large, then the capacitor will trigger the controller to stop the machine immediately. This takes place if the condition of the pieces is softer than the fixture. When the pieces are stiffer than the fixture, we need to set the condition so that when the capacitance is under that value, the capacitor needs to trigger the controller to stop the machine. When the vibration is above that value, the capacitor will not trigger the controller to stop the machine. In other words, under a certain value range, the capacitance change is not sensitive (big) enough to trigger the controller to stop the machine, which is under the condition that the piece is softer than fixture. Also, that certain value needs to be determined by experimentation.

$$\text{If: } C = 12 \frac{2d\varepsilon_0 l t}{d^2 - x^2} < \text{Value 1}$$

Value 1 needs to be determined by experiment
The capacitor will not trigger the controller to stop the machine

$$\text{If: } C = 12 \frac{2d\varepsilon_0 l t}{d^2 - x^2} > \text{Value 1}$$

The capacitor will trigger the controller to stop the machine

Above a certain value range, the capacitance change is not sensitive (small) enough to trigger the controller to stop the machine, which is under the condition that the piece is stiffer than fixture. Also, that certain value needs to be determined by experimentation.

$$\text{If: } |C = 12 \frac{2d\varepsilon_0 l t}{d^2 - x^2}| < |\text{Value 1}|$$

The capacitor will not trigger the controller to stop the machine

$$\text{If: } |C = 12 \frac{2d\varepsilon_0 lt}{d^2 - x^2}| > |\text{Value 1}|$$

The capacitor will trigger the controller to stop the machine

Set the decision logic to a certain value, the decision logic will receive a signal from the capacitor/sensor to determine if it is actually manufacturing or a collision. We can set the logic to negative value when the pieces are stiffer than fixture. The sensor will not decide if the contact is the beginning of a collision or simply defines the manufacturing pieces. This is the function of the decision logic [6]. If the value is larger or smaller than a certain value that was given to the logic, then the detector/sensor will trigger the machine to stop or not to stop. It is related to the decision logic module design, which has been out of the authors' research scope, and can be done as a future work. The main purpose of this paper is the idea of using the capacitive principle based method to design the collision sensor.

In terms of when the cutting tool breaks the moment it hits the fixture, this must be the condition that the fixture is harder than the piece. If it is in that case, as being said above, i.e., under certain value range, the capacitance change is not sensitive (big) enough to trigger the controller to stop the machine when the tool is in the process of manufacturing. Also, that certain value needs to be determined by experimentation. Ideally, when the tool hits the fixture, the detector/sensor will trigger the machine to stop immediately, so the tool will not break. The worst case scenario is when the tool breaks, at which point the capacitance will also change, so it will trigger the machine to stop. Either way, no matter if the tool breaks or not, if the capacitance change is above that value, then it will trigger the machine to stop.

However, during motions, the rate of capacitance change can be measured; this rate of change can also be called the displacement sensitivity. It is obtained by taking the derivative of C with respect to x , and we can have the following,

$$S(x) = \frac{\partial C}{\partial x} = \frac{48d\varepsilon_0 lt x}{(d^2 - x^2)^2} \quad (6)$$

The above is under the movement along the y direction (transverse). Transverse comb drive devices are frequently used for sensing the sensitivity and they are easy to fabricate.

B. Movement along x direction

When the movement is along the x direction, we have the following, (note that the movement along z direction is

very small or none because the suspension beam is along the z direction, which blocks the movement along z direction), there are 13 fingers, which means there are 12 capacitors, so the 12 capacitors will contribute the total capacitance of the device. At rest, the total capacitance is:

$$C = 12 \frac{\varepsilon_0 lt}{d} \quad (7)$$

When there is force in x direction, which will make the fingers move in the x direction, this will cause the effective thickness t' to change. Suppose the change value is x . Under the above changed condition the capacitance will change to the following:

$$C = 12 \frac{\varepsilon_0 l(t-x)}{d} \quad (8)$$

The relative change of capacitance w.r.t. displacement x (i.e., displacement sensitivity, or the change of capacitance as a function of applied displacement) can be expressed as follows:

$$\frac{\partial C}{\partial x} = -\frac{12\varepsilon_0 l}{d} \quad (9)$$

IV. FREQUENCY RESPONSE

The device can be seen as a fixed-free cantilever beam, and the resonant frequency can be expressed as:

$$f_1 = \frac{1.732}{2\pi} \sqrt{\frac{EIg}{Fl_1^3}} \quad (10)$$

$$I = \frac{wt^3}{12} \quad (11)$$

There are two suspension beams, so the force/spring constant can be expressed as follows [1]:

$$F = k \cdot x \quad (12)$$

$$k = 2 \times \frac{Ewt^3}{4l_1^3} \quad (13)$$

Plug in the above F and I , resonant frequency can be finally derived as follows:

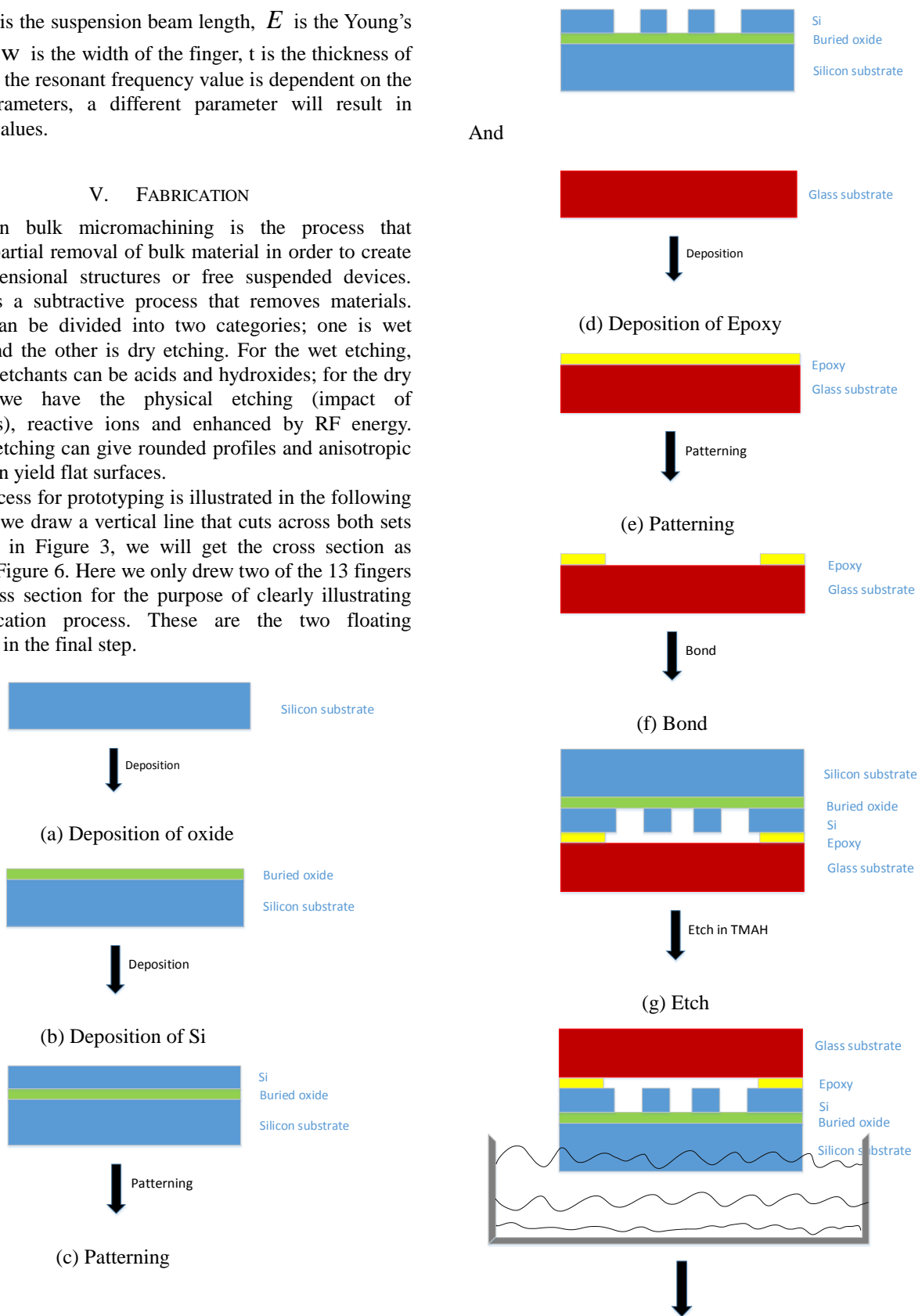
$$f_1 = \frac{1.732}{2\pi} \sqrt{\frac{EIg}{Fl_1^3}} = \frac{1.732}{2\pi} \sqrt{\frac{g}{6x}} \quad (14)$$

Where l_1 is the suspension beam length, E is the Young's modulus, W is the width of the finger, t is the thickness of the finger, the resonant frequency value is dependent on the above parameters, a different parameter will result in different values.

V. FABRICATION

Silicon bulk micromachining is the process that involves partial removal of bulk material in order to create three dimensional structures or free suspended devices. Etching is a subtractive process that removes materials. Etching can be divided into two categories; one is wet etching and the other is dry etching. For the wet etching, the liquid etchants can be acids and hydroxides; for the dry etching, we have the physical etching (impact of atoms/ions), reactive ions and enhanced by RF energy. Isotropic etching can give rounded profiles and anisotropic etching can yield flat surfaces.

A process for prototyping is illustrated in the following Figure. If we draw a vertical line that cuts across both sets of fingers in Figure 3, we will get the cross section as shown in Figure 6. Here we only drew two of the 13 fingers in the cross section for the purpose of clearly illustrating the fabrication process. These are the two floating rectangles in the final step.



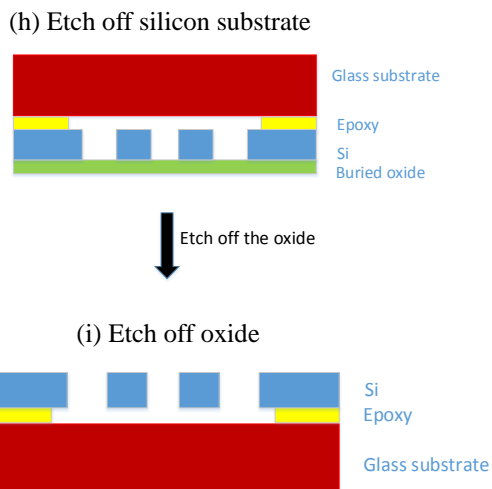


Figure 6. Fabrication process

Compared with parallel-plate capacitors, the capacitance between two neighboring sets of fingers are relatively small. However, one can achieve large capacitance and force by increasing the number of comb pairs. The proposed collision detector can also be used in other machine tools.

VI. CONCLUSION

In this paper, a capacitance based collision detector is designed in order to detect any collisions between tool and peripheral equipment to prevent further damage to the machines. The new design is illustrated and modelled. The capacitance, sensitivity, and frequency response of the detector are analyzed in detail, and the fabrication process is finally presented. The proposed collision detector can also be applied to other machine tools. Future work will build the prototype to test the proposed detector in the real application scenarios.

ACKNOWLEDGEMENT

The authors would like to gratefully acknowledge the financial support from the Natural Sciences and Engineering Research Council of Canada (NSERC) and Canada Research Chairs program.

REFERENCES

- [1] C. Liu, *Foundation of MEMS*, ISBN-13: 978-0-13-249736-7. Pearson Prentice Hall, 2006.
- [2] MARPOSS, "Sensors for Grinding Machines Monitoring," http://www.marposs.com/technology.php/eng/sensors_grinders_monitoring [retrieved: March, 2015]
- [3] D. Kim, J. Song, S. Cha, and H. Kim, "Real-Time Compensation of Chatter Vibration in Machine Tools," *I.J. Intelligent Systems and Applications*, 06, 2013, pp. 34-40.

- [4] C. Chen, R. Lin, and R. Chang, "Efficient Web-Learning Collision Detection Tool on Five-Axis Machine," *World Academy of Science, Engineering and Technology*, Vol. 7 No. 7, 2013, pp.1053-1057.

- [5] E. Mohammadias, "Vibration Detection and Backlash Suppression in Machine Tools," *The 2009 IEEE/RSJ International Conference on Intelligent Robots and Systems, USA, 2009*, pp. 972-977.

- [6] T. Rudolf, C. Brecher, and F. Possel-Dölken, "Contact-based Collision Detection – A New Approach to Avoid Hard Collisions in Machine Tools," A. Donmez, L. Deshayes (Eds.), *International Conference on Smart Machining Systems, 2007*, pp. 1-4.

- [7] Q. Liang, D. Zhang, Q. Song, Y. Ge, H. Cao, and Y. Ge, "Design and fabrication of a six-dimensional wrist force/torque sensor based on E-type membranes compared to cross beams," *Measurement, Volume 43, Issue 10, 2010*, pp. 1702–1719.

Capillary Rise Multiparametric Sensor for Testing of Diesel and Biodiesel Fuel

Michał Borecki, Jan Szmidt
 Institute of Microelectronics and Optoelectronics
 Warsaw University of Technology
 Warsaw, Poland
 email: borecki@imio.pw.edu.pl

Mariusz Duk, Andrzej Kociubiński
 Lublin University of Technology
 Department of Electronics
 Lublin, Poland.
 email: akociub@semiconductor.pl

Michael L. Korwin-Pawłowski
 Département d'informatique et d'ingénierie
 Université du Québec en Outaouais
 Gatineau, Québec, Canada
 email: Michael.Korwin-Pawłowski@uqo.ca

Jarosław Frydrych
 Automotive Industry Institute
 Warsaw, Poland.
 email: j.frydrych@pimot.eu

Przemysław Prus,
 Blue Oak Inventions
 email: przemyslaw.prus@forcate.pl

Abstract-There are many fuel quality standards introduced by national organizations and fuel producers. Usual techniques for measuring fuel parameters like viscosity, density, cetane index, fraction composition and flash point, require relatively complex and expensive laboratory equipment. On the fuel user side, fast and low cost sensing of useful state of biodiesel fuel is important. The main parameters of diesel fuel compatibility are: density and viscosity. Diesel fuel surface tension is one of the main properties for characterization of the quality of the fuel atomization process that affect fuel quality. The present paper concentrates on the construction of the sensor which enables the examination of the mentioned parameters in one arrangement. Results of development of a capillary photonic sensor working on the principle of multipoint monitoring of capillary rise of fuel in inclined capillary are presented. We discuss the principle of the sensor's operation, the construction of the head, and the experimental results of testing biodiesel fuels for their parameters. We conclude that the proposed construction may be in future the base of low cost commercially marketable instruments.

Keywords-biodiesel fuel; diesel fuel quality; surface tension of diesel fuel; multiparametric sensor; capillary sensor.

I. INTRODUCTION

The paper consists of 5 sections. First section was the introduction where the diesel fuel, diesel engine properties as well as known sensors for diesel fuel testing were discussed and the aim of work is presented. Second section describes the proposed idea of multiparametric sensor for diesel fuel testing. Developed sensor construction presented in section three. In the section four the discussion of obtained results of characterized diesel fuels examination in developed sensor is presented. The method of fuels classification is proposed. The short conclusion is gathered in section five.

Classical diesel fuels are made from distilled products of crude oil with addition of improvers. Biodiesel fuel is a mixture of classical diesel fuel and bio-components.

One of the most important diesel fuel quality parameters is ignition quality. The ignition quality depends on the molecular composition of the fuel and is characterized by the ignition delay time, which is the time between the start of injection and the start of combustion. For standardization reasons, measurements of ignition quality of fuel (CN) have to be carried out in the Cooperative Fuel Research engine (CFR-5) or ignition quality tester (IQT™). The basic disadvantage of such approach to fuel quality measurements is the high cost of the measurement device and the complexity of the procedure.

Nowadays, producers define the useful state of diesel fuel by several parameters: cetane number, density, and distillation parameters, kinematic viscosity. Other diesel fuel parameters characterize its operability: amount of carbon residue, water and sediment, cloud point, conductivity, oxidation stability, acidity, copper corrosion, flashpoint, lubricity, appearance, and color [1]. For the ordinary fuel user, such collection of parameters is often too complex. In this situation the user requires the simplest possible answer to a question: is that fuel useful for my engine?

A. Diesel fuel and engine

The challenge for diesel engine designers is to match the combustion chamber size with the diesel fuel injection characteristics [2]. The diesel fuel must be introduced into the combustion chamber, vaporize and react with oxygen at an assumed speed. The fuel properties that have greatest effect on injection process are viscosity, density and surface tension. If the injection is made at a constant pressure, the viscosity affects the fuel spray formation by limiting the speed of fuel flow. If the injection system is designed to

meter the volume of injected fuel, the density of fuel defines the fuel injected mass that is linked with the useable portion of energy. The surface tension is the one of main factors that describes the fuel tendency to form drops, known also as the fuel atomization process or spray forming.

It was postulated that the surface tension of most liquid hydrocarbons is very similar. For example, for HydroCal 300 - a hydrotreated naphthenic medium grade lubricant oil and IFO-120, an intermediate fuel oil, the measured surface tensions at 25°C are the same and equal 31.8 mN/m, while their viscosities differ significantly: 162mPa for HydroCal and 487mPa for IFO-120 [3]. It should be noted that contemporary diesel fuels components are not only pure hydrocarbons. Present-day diesel fuel may include some biodiesel which is obtained from vegetal oils or the bio-mass, and other additives. These supplements may significantly change surface tension and other diesel fuel parameters [4].

In a European study, it was observed that using the biodiesel fuel at low environment temperatures can lead to the degeneration of engine [5]. Therefore, production standards for biodiesel fuel were introduced: density at 15°C (ISO3675) and low-temperature fluidity for the transitional seasonal periods and winter (DIN EN 116). Important disadvantages of biodiesel fuel can be overcome by fuel processing. A new generation of biodiesel fuel can be made with bio-component isomerization or hydrogenation [6].

It has been proven that surface tension is one of the most important of inhomogeneous fluid properties. It reflects the range of interactions in a fluid more directly than the bulk properties do [7]. The relationship between the surface tensions of different real vegetable oils and their fatty acid composition was postulated in [8]. Predicting the surface tension of biodiesel fuels from their fatty acid composition showed that the differences in surface tension between biodiesel types are not the only cause of the reported differences in engine tests [9].

There are few basic methods of surface tension measurements: the capillary rise method, the drop weight method, the ring or plate method, the maximum bubble pressure method, the method of analyzing the shape of the hanging liquid drop, and the dynamic methods [10].

The capillary rise method is the oldest method used for surface tension determination. For the surface tension measurement a capillary is dipped into the tested liquid. If the interaction forces of the liquid with the capillary walls are stronger than those between the liquid molecules, the liquid wets the walls and rises in the capillary to a defined level. If the cross-section area of the capillary is circular and its radius is sufficiently small, then the meniscus is semispherical. When the capillary is filled in the vertical position the surface tension may be calculated with following equation:

$$\gamma \cong \frac{1}{2\cos(\theta)} r \cdot g \cdot \left(h + \frac{r}{3} \right) \cdot (\rho_l - \rho_v), \quad (1)$$

where: γ is the surface tension, θ is the contact angle, r is the inner radius of capillary tube, g is the gravity constant, h is the height of meniscus, ρ_l is the density of liquids, and ρ_v is

the density of vapor [11]. For standard temperatures, the density of liquid is much greater than of the density of vapor, therefore presence of the vapor phase is ignored. The contact angle may have different values in the static or dynamic situations. Such situations for a capillary being filled are presented in Figure 1.

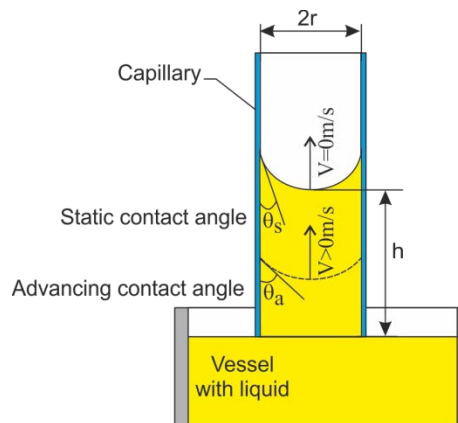


Figure 1. Static and advancing contact angle in capillary flow.

Since a film of oil remains on the inner surface of the capillary after the receding phase, representing complete wetting, the static contact angle was considered to be equal to 0° [12].

Advancing contact angles between a glass slide and different hydrocarbon oils differ significantly depending on the temperature, the speed of liquid creep and the type of liquid hydrocarbon. For example, measured at 25°C and 264µm/s the advancing angle of HydroCal 300 is 36° while of IFO-120 is 54° [3].

The simplest technique for measuring the capillary rise is using a ruler with an optical reading, but its automation requires a camera, a mechanical device as lift or a liquid injector coupled with an additional light source to improve the optical reading of the meniscus position.

Because of its relative simplicity, the drop weight method, is one of the most common methods used for surface tension automated measurements. In this method drops formed at the tip of the glass capillary are weighted and counted. The pendant drop at the tip starts to detach when its weight reaches the value balancing the surface tension of the liquid. The advantage of the method is the possibility to measure surface tensions between liquids and other than optically transparent materials [13]. The disadvantage of this method is the necessity to calculate the corrections for the capillary tip parameters and the volume of the drop, which are characteristic of a given device.

The ring method and the Wilhelmy plate method are similar. In these methods an object is moved perpendicularly into or out of the liquid. The plate is moved towards the surface until the meniscus connects with it, or the submerged ring is pulled out of the liquid. The additional force acting on the plate or ring due to its wetting by liquid is measured.

In the maximum bubble pressure method an air or gas bubble is blown at constant rate through a capillary submerged in the tested liquid. The maximum measured

pressure that is required to insert the bubble of gas into the liquid may be used for surface tension determination.

The shape analyzing methods of liquid drop is based on the effect of the liquid's deformation caused by the gravitation force action. The surface area of a drop is proportional to its squared radius and the gravitational deformation depends on its volume, which is proportional to the third power of the radius [14].

One of dynamic methods for surface tension determination is based on the analysis of the shape of an oscillating liquid jet. The jet flows out from an elliptic orifice and therefore it oscillates. Mathematical analysis of such a jet was given for the first time by Lord Rayleigh in 1879. One can conclude from these considerations that the surface tension may directly affect fuel injection characteristics.

B. Sensors for diesel fuel testing

Nowadays, optical sensors are introduced into the fuel testing market. Some known optical sensors enable the examination of a set of fuel parameters, but the possibility of easy measurement comes with a high price of the devices [15]. On the other hand, some proposed multiparametric sensors may be low cost, but using them requires trained operating personnel. The possibility of diesel fuel quality testing using an optoelectronic set-up implementing a multiparametric method was shown in [16] [17].

II. IDEA OF MULTIPARAMETRIC SENSOR FOR DIESEL FUEL TESTING

The idea of the sensor was inspired by the need to come up with a measurement method of a set of diesel fuel parameters in one system that would require the minimum of automated mechanical elements. The aimed at set of diesel fuel parameters includes: density, viscosity, surface tension and wetting represented by the contact angle between fuel and glass. Such a set of parameters may be observed using the classical capillary rise method (Figure 1) with three capillaries of different inner diameters. The data obtained in the measurement enable solving of a three equation system derived from (1). To obtain the additional viscosity measurement data one needs to measure the capillary rise speed. An increase of the liquid movement distance in the capillary to improve the precision of the measurement is possible by the inclination of the capillary. When capillary's axis is inclined at the α angle to the horizontal, a liquid is drawn in by capillary forces according to equation (2).

$$\frac{dl}{dt} = \frac{2\gamma \cos(\theta) - g \cdot l \cdot \rho_l \sin(\alpha)}{8 \cdot \eta \cdot l} \cdot r^2, \tag{2}$$

where: γ is the surface tension, θ is the contact angle, r is the inner radius of the capillary tube, g is the gravity constant, l is the length coordinate of meniscus at capillary axis, t is the time of measurement, α is the angle of inclination, ρ_l is the density of liquid, and η is its viscosity. Eq. 2 may be solved for the sensor application in two ways.

The first solution is for local speed measurement at a set length coordinate of meniscus with the formula:

$$\frac{\Delta l_s}{\Delta t_s} = \frac{2\gamma \cos(\theta) - g \cdot l_s \cdot \rho_l \sin(\alpha)}{8 \cdot \eta \cdot l_s} \cdot r^2, \tag{3}$$

where: l_s and Δl_s are presented in Fig 2.

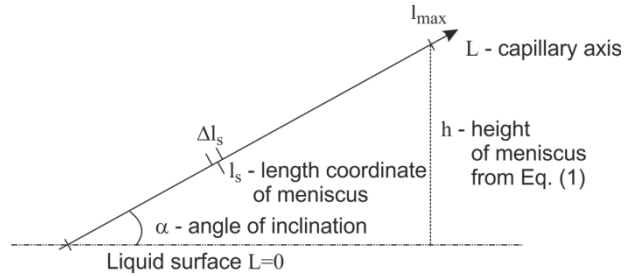


Figure 2. Parameters reading of local speed determination for (3).

The second solution of (2) is based on integration:

$$t_2 - t_1 = \int_{l_1}^{l_2} \frac{8 \cdot \eta \cdot l}{r^2 [2\gamma \cos(\theta) - g \cdot l \cdot \rho_l \sin(\alpha)]} dl, \tag{4}$$

where: l_1 and l_2 are presented in Figure 3.

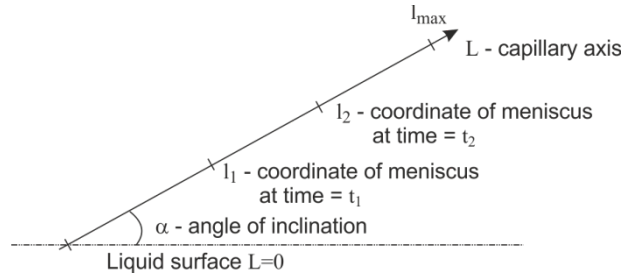


Figure 3. Parameters reading for integral solving of (3).

For the sensor application, (4) may be solved numerically by inputting in the measured time of rise $t_2 - t_1$ at corresponding coordinates of meniscus.

III. SENSOR CONSTRUCTION

A. Sensor head

The sensor's head consists of two functional blocks: the base and the optrode, shown on Figure 4.

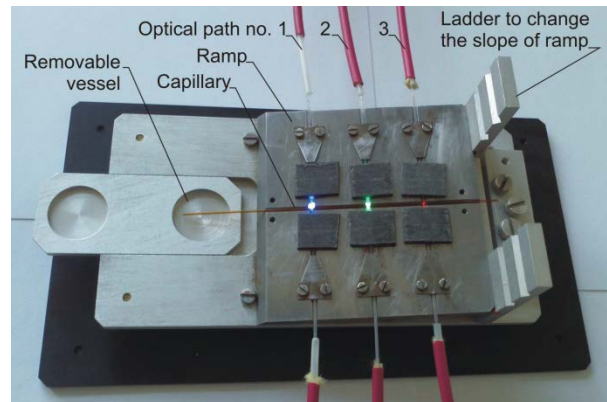


Figure 4. View of the ramp sensor head.

The base is used to integrate the removable vessel for the examined liquid, the three optical paths of the source and the receiver, as well as for positioning the optrode at one of the three possible inclination angles.

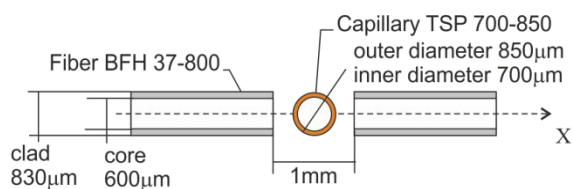


Figure 5. Optical path geometry.

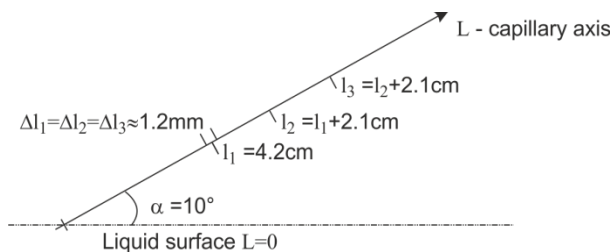


Figure 6. Ramp geometry

The replaceable optrode is made from 15cm sections cut from the TSP 700-850 capillary from Polymicro Inc. In the optical paths large core optical fibers BFH 37-800 from Thorlabs were used. They are characterized by the core radius of 800μm and the hard clad outer diameter of 830μm, which is similar to the capillary’s outer diameter. The tips of the fibers are positioned at the distance of 1mm, where in the middle of the distance between the tips is positioned the capillary (Figure 5). The geometry of the optical path provides the value of Δls, required in equation (3). As the optical paths are the same, Δls=Δl1=Δl2=Δl3≈1.2mm, the experiment ramp geometry may be presented as in Figure 6.

B. Optoelectronic signal processing

As light source, three fiber coupled LEDs with three different emission wavelengths were used. The lowest-power LEDs were selected from Thorlabs list of high power devices: M490F2, blue with the 490 nm wavelength; M565F1, green/yellow - 565 nm wavelength; and M625F1, red - 625 nm wavelength. The diodes were connected to DC2100 controllers operating in the light modulation mode. The receiving fibers were inserted into the optoelectronic detection unit of our own design, presented previously in [18]. The optoelectronic unit was connected to a PC by an analog input of IOtech Personal daq 3000 data acquisition system. That system was also used to monitor the ambient temperature with two LM35DT circuits and control it with a radiant heater at 25°C.

To operate the system, at the 0.1s sampling rate, a script in DasyLab 10 was designed [19]. The raw data collected for acetone is presented in shown on Figure 7. The initial values of signals for different paths are off set on Figure 7 for clarity of visualization. Moreover, the differences of the initial values do not matter, as the sensor operation is based on the differences of the measured time values. The time differences presented for acetone are in agreement with (3)

$\Delta t_1 < \Delta t_2 < \Delta t_3$, and time intervals are in agreement with (4) $[(t_2-t_1)=0.9s] < [(t_3-t_2)=2.6s]$. The t_1 measurement value is uncertain, as the filling of the vessel may not be repeatable when a hand held pipetor is used.

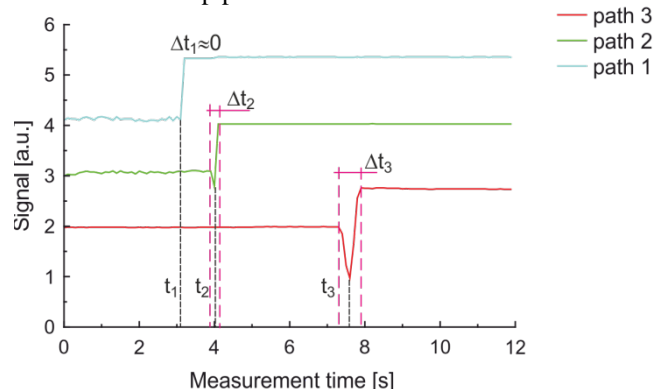


Figure 7. Acetone characteristics.

IV. EXPERIMENTAL RESULTS

In this section are presented the experimental procedure and the results of examination of different diesel and biodiesel fuels.

A. Diesel and biodiesel fuels used for examination

The operation of the sensor was examined with fuels that are mixtures prepared from components according to the European Union standards. The fuels were fresh or stored in room condition for two years.

Base oil (BO) was prepared from crude oil distillation products. The petrodiesel (PD) was prepared with additives according to the EN-590 norm. Biodiesel fuels (BDx – x is the volume ratio of the biocomponent) were prepared from PD with addition of fatty acids methyl esters (FAME) and other additives according to the EU standard. The results of classical laboratory examination of prepared fuels are presented in Tab. 1. Density measurement accuracy was ±2.0 kg/m³ while resolution was ±0.1 kg/m³. Viscosity measurement accuracy was ±1 %.

TABLE I. SELECTED PARAMETERS OF PREPARED FUELS

Fuel acronym	Parameter			
	FAME [%]	Density at 15°C [kg/m ³]	Kinematic viscosity at 40°C [mm ² /s]	CN
BO	0	805.0	1.581	49.8
PD	0	832.6	3.367	59.6
BD02	2	833.6	3.3825	58.4
BD04	4	834.5	3.394	58.3
BD06	5.8	835.4	3.401	58.6
BD08	7.8	836.4	3.413	57.3
BD10	9.7	837.4	3.432	57.3
BD30	28.8	847.0	3.595	54.9
BD50	48.9	857.4	3.813	53.6
BD70	68.6	867.3	4.058	53.7
BD100	100	883.2	4.509	51.2
EN-590*	0-7	820-845	2-4.5	>51

Abbreviations used: FAME – Fatty acids methyl esters (bio-component), CN – cetane number, EN-590 – diesel fuel standard.

The fuels BO, BD30, BD50, BD70 and BD100 do not meet the standards of density, viscosity and FAME ratio, but meet the quality test of CN.

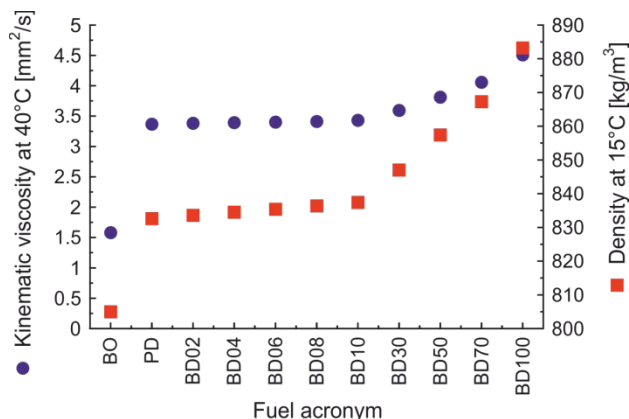


Figure 8. Viscosity and density of examined fresh fuels. ± 0.01 lb/ft³

The densities and the viscosities of the examined fuels change almost monotonically with their content of FAMEs, as presented in Figure 8.

B. Examination of biodiesel fuels using the developed sensor

We examined at least 3 times samples of each fuel, and on the following figures we present representative measurement signals. The results of measurement of fresh PD presented in Figure 9 show that, contrary to acetone, the Δt_s are measurable in each optical patch $\Delta t_1=0.2s$, $\Delta t_2=0.3s$, $\Delta t_3=0.7s$, and that the time intervals $(t_2-t_1)=6.5s$ and $(t_3-t_2)=13s$ are greater than for acetone, as fuel viscosity is much greater than that of acetone.

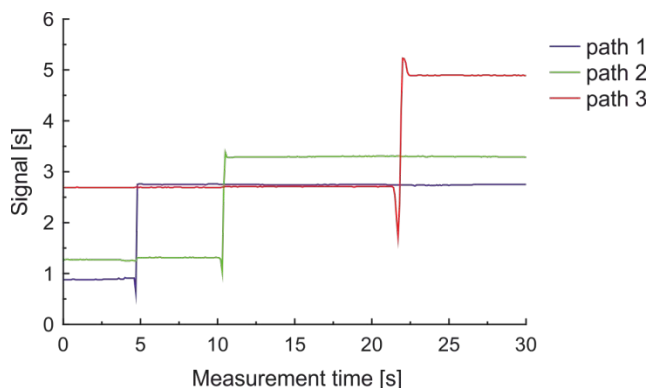


Figure 9. Measurement signals of fresh premium quality petrodiesel PD.

From our experimental results we saw that fresh BO, BD70 and BD100 fuels differ significantly from other fuels when the t_3-t_2 parameter is considered, as is shown on Figure 10. The difference in (t_3-t_2) times from one fuel to another varies much greater than the fuels densities or viscosities. Calculated values of surface tension of fuels, with the assumption that contact angle is 0° , are presented in Figure 11. These results show that the values of surface tensions are probable and that the advancing contact angles differ significantly for the analyzed fuels.

The next test performs the analysis of time interval values of fuels stored in a closed tank for two years in dark room conditions. The volumes of fuels seem to be constant, no presence of resins was observed, but the fuels seem to be more transparent. The results presented in Figure 12 in comparison to the results seen in Figure 10 indicate that the measured times intervals increase for stored fuels, but not monotonically.

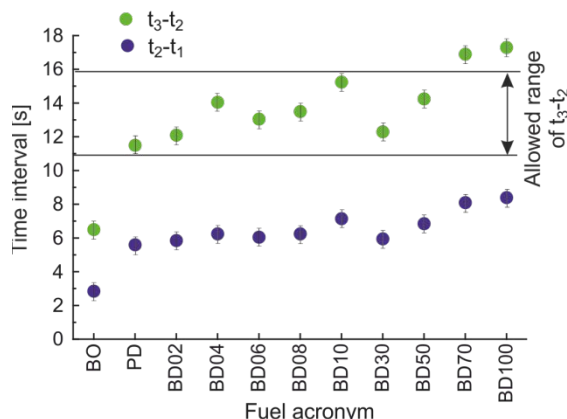


Figure 10. Measurement data of fresh diesel fuels for solving (4).

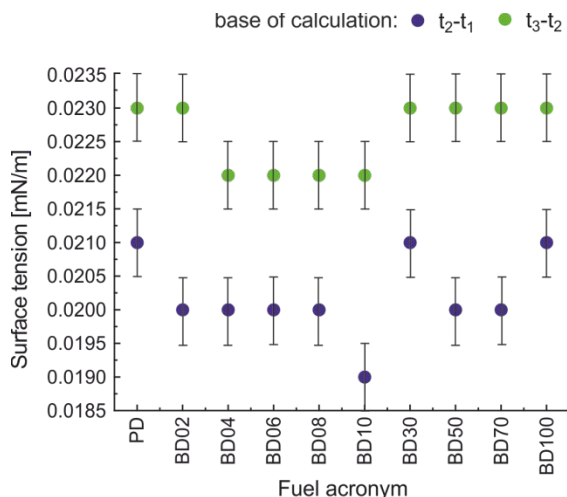


Figure 11. Calculated surface tensions of fresh fuels.

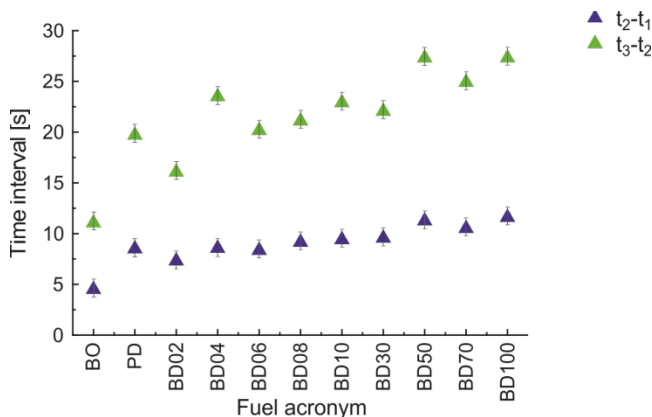


Figure 12. Measurement data of diesel fuels stored for 2 years.

The results of examination of time differences Δt_3 for fresh and stored fuels are presented in Figure 13. The summarized results of the experiments led us to the conclusion that Δt_3 time measurement data differences and t_3-t_2 time intervals relate more clearly to the acceptable quality fuels than the set of surface tension, contact angle, viscosity and density data. On the base of data collected in the experiments we can set the parameters determining the useful state of biodiesel fuel as the limits of the time intervals t_3-t_2 and the limits of time differences Δt_3 .

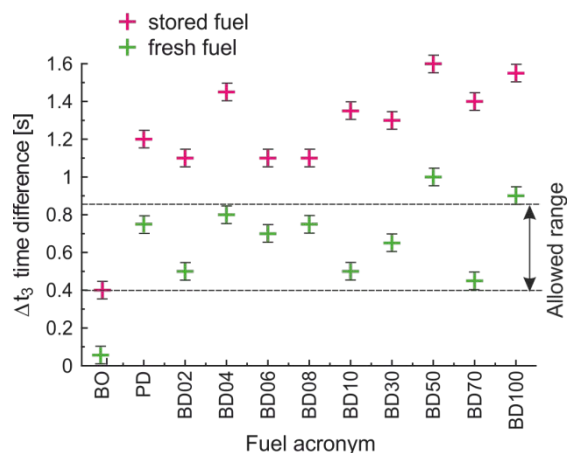


Figure 13. Measured time differences Δt_3 for fresh and stored fuels.

The analysis of data showed that in the presented method the useful state of diesel biodiesel fuel was not determined as precisely as presented in [20], but the construction of the head is much simpler and its use is easier.

V. CONCLUSIONS

We proposed a sensor working on the principle of optical examination of diesel fuel with capillary rise. The presented device has been tested with ground truth data and it shows great promise.

The analysis of the measured signals of diesel and biodiesel fuels showed the relationship of the times of fuel flow in the capillary with the useful state of diesel fuels. We showed that the information on useful state of diesel fuel could be presented in the form of recommended ranges of times of the fuel crossing sections of an inclined capillary during the capillary fill. It is not as accurate as other methods yet, but its intrinsic advantages of simplicity of design and cheap manufacture could make the technology viable in the near future.

The future work will consist of integration of the LEDs and photodiodes in a common unit with the ramp.

ACKNOWLEDGMENT

This work was partially supported by the NCBiR/PGNiG grant Polish Technology for Shell Gas, task T3.1.

REFERENCES

[1] Department of Industry, Science and Resources, "Setting national fuel quality standards - Discussion paper 4", in

"Operability fuel parameters (petrol and diesel)," Environment Australia, 2001.

[2] T. W. Rayan, "Diesel Fuel Combustion Characteristics," in G.E. Totten ED., Fuels and Lubricants Handbook; properties, performance, and testing, ASTM International, West Conshohocken, 2003, pp. 717–720.

[3] A. A. Keller, V. Broje, and K. Setty, "Effect of advancing velocity and fluid viscosity on the dynamic contact angle of petroleum hydrocarbons," Journal of Petroleum Science and Engineering, vol. 58, 2007, pp. 201–206.

[4] F. Wang, J. Wu, and Z. Liu, "Surface Tensions of Mixtures of Diesel Oil or Gasoline and Dimethoxymethane, Dimethyl Carbonate, or Ethanol," Energy Fuels, vol. 20(6), 2006, pp. 2471–2474.

[5] M. Balat, and H. Balat, "A critical review of biodiesel as a vehicular fuel," Energy Convers Manag., vol. 49, 2008, pp. 2727–41.

[6] A. Malinowski, J. Czarnocka, and K. Biernat, "An Analysis of Physico-Chemical Properties of the Next Generation Biofuels and Their Correlation with the Requirements of Diesel Engine," in Biodiesel - Feedstocks, Production and Applications, Z. Fang, Ed., InTech, Rijeka, Croatia, 2012, pp. 435–459.

[7] H. W. Xiang, "Surface Tension" in The Corresponding-States Principle and its Practice Thermodynamic, Transport and Surface Properties of Fluids, Elsevier, Amsterdam, 2005, pp. 215–228.

[8] E. A. Melo-Espinosa, et al., "Surface tension prediction of vegetable oils using artificial neural networks and multiple linear regression," Energy Procedia, vol. 57, 2014, pp. 886 – 895.

[9] C. A. W. Allen, K. C. Watts, and R. G. Ackman, "Predicting the surface tension of biodiesel fuels from their fatty acid composition," Journal of the American Oil Chemists' Society, vol. 76(3), 1999, pp. 317–323.

[10] P.G. de Gennes, F. Brochard-Wyart, and D. Quéré, "Capillary and Wetting Phenomena—Drops, Bubbles, Pearls, Waves," Springer-Verlag New York, ISBN 978-0-387-21656-0 (eBook), 2004, pp. 1–292.

[11] D. L. Katz, and W. Saltman, "Surface Tension of Hydrocarbons," Ind. Eng. Chem., vol. 31(1), 1939, pp 91–94.

[12] B. Jańczuk, E. Chibowski, and T. Białopiotrowicz, "Influence of N-alkanes on contact angle and flotability of quartz," Journal of Materials Science, vol. 25, 1990, pp. 1353–1356.

[13] M. Borecki and J. Kruszewski, "Intelligent high resolution sensor for detecting of liquid mediums," Optica Applicata, vol. 31, 2001, pp. 691–699.

[14] K. D. Danov, et al., "Capillary meniscus dynamometry – Method for determining the surface tension of drops and bubbles with isotropic and anisotropic surface stress distributions," Journal of Colloid and Interface Science, vol. 440, 2015, pp. 168–178.

[15] M. Włodarski, A. Bombalska, M. Mularczyk-Oliwa; M. Kaliszewski, and K. Kopczyński, "Fluorimetric techniques in analysis and classification of fuels," Proc. SPIE vol. 8703, 2012, pp. 87030B.

[16] M. Borecki and M. L. Korwin-Pawlowski, "Optical capillary sensors for intelligent microfluidic sample classification," in Nanosensors: Theory and Applications in Industry, Healthcare and Defence, T.C. Lim, Ed., CRC Press, Boca Raton, FL, USA, 2011, pp. 215– 245.

[17] M. Borecki, et al., "Fiber Optic Capillary Sensor with Smart Optode for Rapid Testing of the Quality of Diesel and Biodiesel Fuel," IJASM, vol. 7, 2014, pp. 57–67.

[18] M. Borecki, et al., "Sensing of Essential Amino Acids Behaviour Under Fast Thermal Shocks in Liquid Water Environment," IARIA, Proc. Sensordevices, 2014, pp. 32–38.

- [19] P. Prus, M. Borecki, M. L. Korwin-Pawłowski, A. Kociubiński, and M. Duk, "Automatic detection of characteristic points and form of optical signals in multiparametric capillary sensors," Proc. SPIE, vol. 9290, 2014, pp. 929009.
- [20] M. Borecki, et al., "Sensing Method and Fiber Optic Capillary Sensor for Testing the Quality of Biodiesel Fuel," IARIA, Proc. Sensordevices 2013, pp. 19–24.

UV Irradiation to Increase the Spectral Sensitivity of a-SiC:H pi'n/pin Photodiode Beyond the Visible Spectrum Light

M. Vieira, M.A. Vieira, V. Silva, P. Louro, A. Fantoni
 CTS/UNINOVA
 Monte de Caparica, Portugal
 e-mail: mv@isel.ipl.pt

M. Vieira, M.A. Vieira, I. Rodrigues, V. Silva, P.
 Louro, A. Fantoni
 DEETC/ISEL
 Lisbon, Portugal
 e-mail: mv@isel.ipl.pt

Abstract— In this paper, we experimentally demonstrate the use of near-ultraviolet steady state illumination to increase the spectral sensitivity of a double a-SiC/Si pi'n/pin photodiode beyond the visible spectrum (400 nm-880 nm). The concept is extended to implement a 1 by 4 wavelength division multiplexer with channel separation in the visible/near infrared ranges. The device consists of a p-i'(a-SiC:H)-n/p-i(a-Si:H)-n heterostructure, sandwiched between two transparent contacts. Optoelectronic characterization of the device is presented and shows the feasibility of tailoring the wavelength and bandwidth of a polychromatic mixture of different wavelengths. Results show that the spectral current under steady state ultraviolet irradiation depends strongly on the wavelength of the impinging light, and on the background intensity and irradiation side allowing controlled high-pass filtering properties. If several monochromatic pulsed lights, in the visible/ Near infrared (VIS/NIR) range, separately or in a polychromatic mixture illuminate the device, data shows that, front background enhances the light-to-dark sensitivity of the medium, long and infrared wavelength channels, and quench strongly the low wavelengths channels. Back background has the opposite behavior; it enhances only channel magnitude in short wavelength range and strongly reduces it in the long ones. This nonlinearity provides the possibility for selective tuning of a specific wavelength. A capacitive optoelectronic model supports the experimental results. A numerical simulation is presented.

Keywords- *amorphous SiC technology; optoelectronics; spectral sensitivity; UV irradiation; photodiode; multiplexer device; VIS/NIR decoding; numerical simulation.*

I. INTRODUCTION

The LED is a very effective lighting technology due to its high brightness, long life, energy efficiency, durability, affordable cost, optical spectrum and its colour range for creative purposes. Their application as communication device with a photodiode as receptor, has been used for many years in hand held devices, to control televisions and other media equipment, and with higher rates between computational devices [1]. This communication path has been employed in the near infra-red (NIR) range, but due to the increasing LED lighting in homes and offices, the idea to

use them for visible light communications (VLC) has come up recently. Newly developed technologies, for infrared telecommunication systems, allow increase of capacity, distance, and functionality, leading to the design of new reconfigurable active filter [2], [3], [4]. To enhance the transmission capacity and the application flexibility of optical communication, efforts have to be considered, namely the fundamentals of Wavelength Division Multiplexer (WDM) based on a-SiC:H light controlled filters, when different visible signals are encoded in the same optical transmission path [5]. They can be used to achieve different filtering processes, such as: amplification, switching, and wavelength conversion.

In this paper, it is demonstrated that the same a-SiC:H device under front and back controlled near ultraviolet optical bias acts as a reconfigurable active filter in the visible and near infrared ranges, making the bridge between the infrared and the red spectral ranges. In consequence, bridging the visible spectrum to the telecom gap offers the opportunity to provide alternative and additional low cost services to improve operative production processes in office, home and automotive networks.

In Section I, an introduction is given and in Section II, some experimental results are presented. In Section III, the bias controlled selector is analyzed and in Section IV, the Wavelength Division Multiplexed (WDM) based on SiC technology is described. In Section V, the optoelectronic model gives insight the physics of the device and finally in Section VI, the conclusions are presented.

II. EXPERIMENTAL DETAILS

A. Device configuration

The light tunable filter is realized by using a double pi'n/pin a-SiC:H photodetector produced by Plasma Enhanced Chemical Vapor Deposition (PECVD).

The device has Transparent Conductive Oxide (TCO) front and back biased optical gating elements as depicted in Figure 1.

The active device consists of a p-i'(a-SiC:H)-n/p-i(a-Si:H)-n heterostructure with low conductivity doped layers. The deposition conditions and optoelectronic characterization of the single layers were described elsewhere [6].

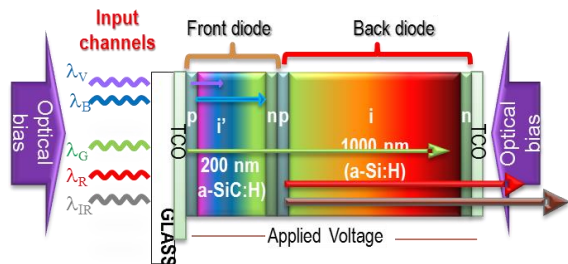


Figure 1. Device configuration and operation.

The thicknesses and optical gap of the front i' (200 nm; 2.1 eV) and back i (1000 nm; 1.8 eV) layers are optimized for light absorption in the blue and red ranges, respectively [7].

B. Device operation

Monochromatic (infrared, red, green, blue and violet; $\lambda_{IR,R,G,B,V}$) pulsed communication channels (input channels) are combined together, each one with a specific bit sequence, impinge on the device and are absorbed accordingly to their wavelengths (see arrow magnitudes in Figure 1).

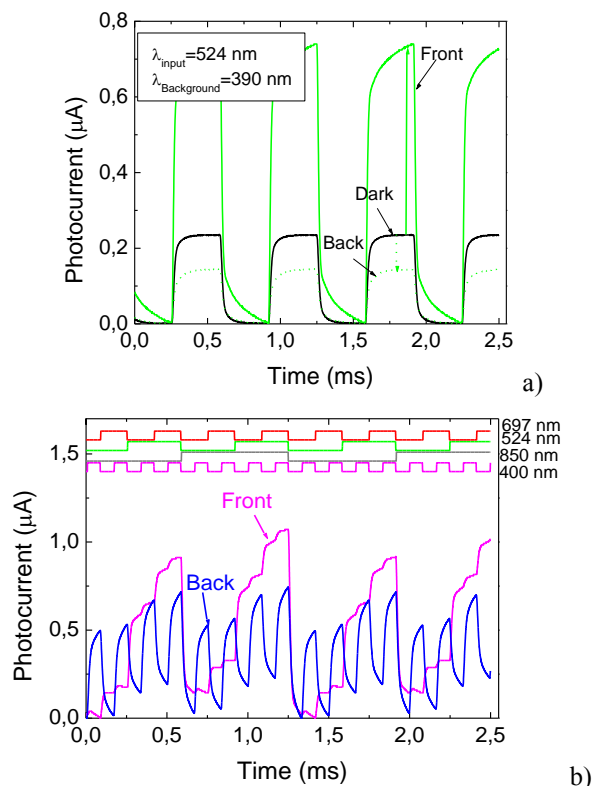


Figure 2. a) 524 nm input channel under front, back and without (dark) background irradiation. b) MUX signals and under front and back $\lambda=390$ nm irradiation and different bit sequences.

The combined optical signal (multiplexed signal; MUX) is analyzed by reading out the generated photocurrent under negative applied voltage (-8V), without and with near ultraviolet background ($\lambda_{Background}=390$ nm) and different intensities, applied either from the front (λ_F) or the back (λ_B) sides. The device operates within the visible range using as input color channels the square wave modulated low power light supplied by near-infrared/visible (VIS/NIR) LEDs. In Figure 2a, the 524 nm input channel is displayed under front, back and without UV irradiation. The arrows indicate the enhancement (solid line) or quenching (dot line) of the dark signal, respectively under front and back irradiation. In Figure 2b, the polychromatic mixture of four different input channels (400 nm, 524 nm, 697nm and 850 nm) under front and back $2800 \mu Wcm^{-2}$ irradiation, is displayed. At the top, the input channels wavelengths and their bit sequences guide the eyes.

III. BIAS CONTROLLED SELECTOR

A. Optical bias controlled filter

The spectral sensitivity was tested through spectral response measurements [8] without and under 390 nm front and back backgrounds of variable intensities. The spectral gain (α), defined as the ratio between the signal with and without irradiation was inferred.

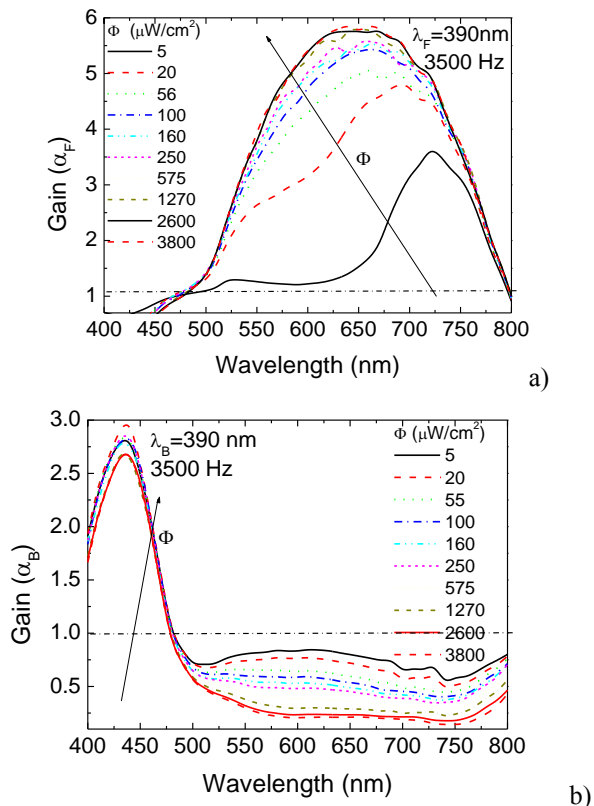


Figure 3. Front (λ_F) and back (λ_B) spectral gains ($\alpha_{F,B}$) respectively, under $\lambda=390$ nm irradiations.

In Figure 3, the spectral gain (α) is displayed under steady state irradiations. In Figure 3a, the light was applied from the front (λ_F) and in Figure 3b, the irradiation occurs from the back side (λ_B). The background intensity (ϕ) was changed between $5\mu\text{Wcm}^{-2}$ and $3800\mu\text{Wcm}^{-2}$.

Results show that, the optical gains have opposite behaviors. Under front irradiation (Figure 3a) and low flux, the gain is high in the infrared region, presents a well-defined peak at 725 nm and strongly quenches in the visible range. As the power intensity increases, the peak shifts to the visible range and can be deconvoluted into two peaks, one in the red range that slightly increases with the power intensity of the background and another in the green range that strongly increases with the intensity of the ultraviolet (UV) radiation. In the blue range, the gain is much lower. This shows the controlled high-pass filtering properties of the device under different background intensities. Under back bias (Figure 3b) the gain in the blue/violet range has a maximum near 420 nm that quickly increases with the intensity. Moreover, it strongly lowers for wavelengths higher than 450 nm, acting as a short-pass filter. Thus, back irradiation, tunes the violet/blue region of the visible spectrum whatever the flux intensity, while front irradiation, depending on the background intensity, selects the infrared or the visible spectral ranges. Here, low fluxes select the near infrared region and cuts the visible one, the reddish part of the spectrum is selected at medium fluxes, and high fluxes tune the red/green ranges with different gains.

B. Nonlinear spectral gain

To analyze the effect of the background intensity in the input channels, several monochromatic pulsed lights separately (850 nm, 697 nm, 626 nm, 524 nm, 470 nm, 400 nm; input channels) or combined (MUX signal) illuminated the device at 12000 bps [9].

Steady state optical bias with different intensities was superimposed separately from the front and back sides and the photocurrent measured. For each individual channel the photocurrent gain under irradiation was determined. In Figure 4, these gains are displayed as a function of the background lighting under front (Figure 4a) and back (Figure 4b) irradiation.

Results show that, even under transient conditions and using commercial visible and NIR LEDs, the background side and intensity alters the signal magnitude of the input channels.

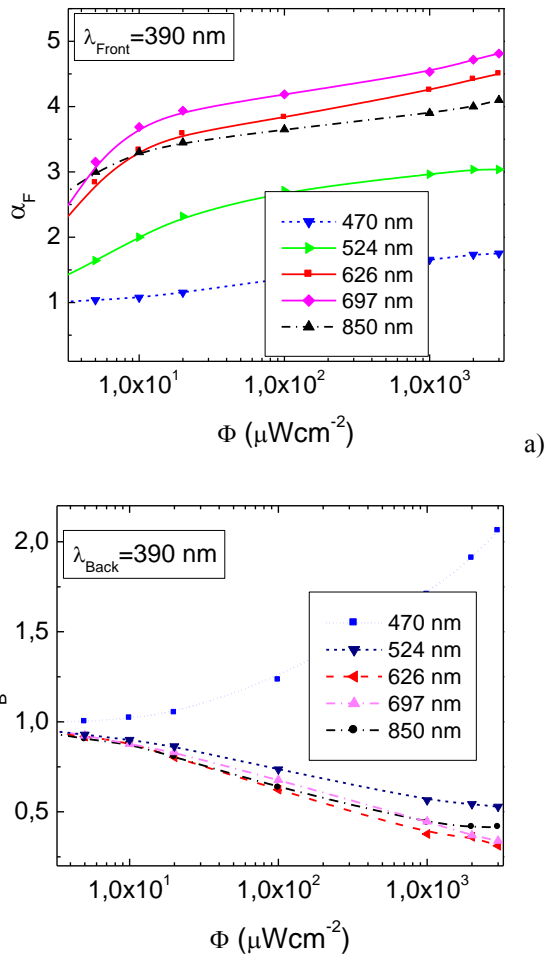


Figure 4. Front (a) and back (b) optical gains as a function of the background intensity for different input wavelengths in the VIS/NIR range.

The gain depends mainly on the channel wavelength and to some extent on the lighting intensity. Even across narrow bandwidths, the photocurrent gains are quite different. This nonlinearity allows identification of the different input channels in the visible/infrared ranges.

IV. WAVELENGTH DIVISION MULTIPLEXER

A. Input channels

Four monochromatic pulsed lights with different intensities, separately (400 nm, 470 nm, 697 nm and 850 nm; input channels) or combined (MUX signal) illuminated the device at 12000 bps.

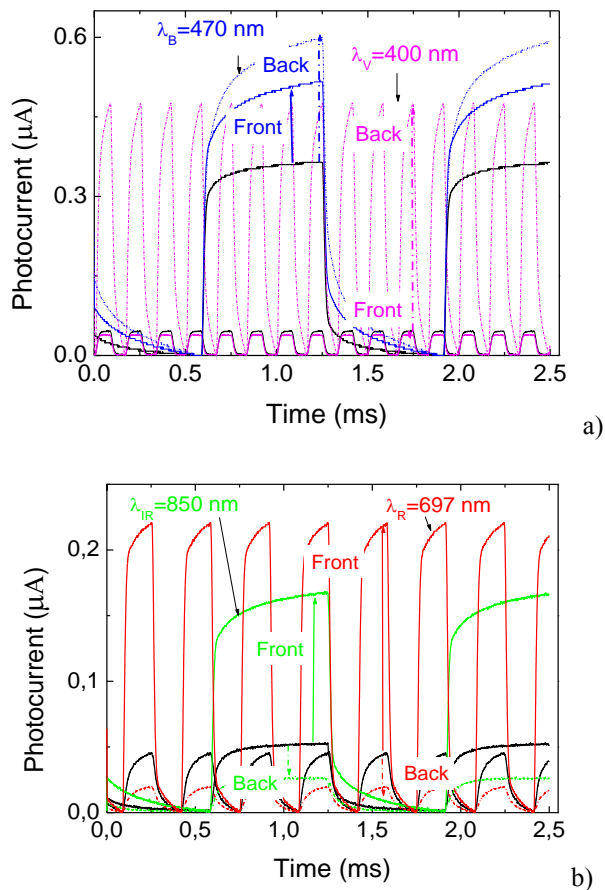


Figure 5. Input signals under front and back 390 nm background irradiation. a) violet and blue channels. b) red and infrared channels.

Steady state 390 nm front and back optical bias with $2800 \mu\text{Wcm}^{-2}$ intensity was superimposed separately and the photocurrent was measured. In Figure 5a, the blue and violet transient signals are presented under front and back irradiations while in Figure 5b, the red and infrared signals are displayed.

In Table I, the measured optical gains for five different input channels are displayed.

TABLE I OPTICAL GAINS UNDER 390 NM FRONT (α_{FRONT}) AND BACK (α_{BACK}) IRRADIATIONS.

	$\lambda=400$ nm	$\lambda=470$ nm	$\lambda=524$ nm	$\lambda=697$ nm	$\lambda=850$ nm
α_{Back}	11.6	1.8	0.61	0.46	0.44
α_{Front}	0.9	1.5	3.2	4.3	3.5

Back irradiation enhances, differently, the input signals in the short wavelength range (Figure 5a) while front irradiation increases them otherwise in the long wavelength range (Figure 5b). This side dependent effect is used to enhance or to quench the input signals allowing their recognition and providing the possibility for selective tuning of the visible and IR input channels.

B. MUX signal

In Figure 6, two MUX signals due to the input signals of Figure 2a and Figure 5 are displayed without (dark) and under front and back irradiation. On top, the signals used to drive the input channels are shown to guide the eyes into the on/off channel states.

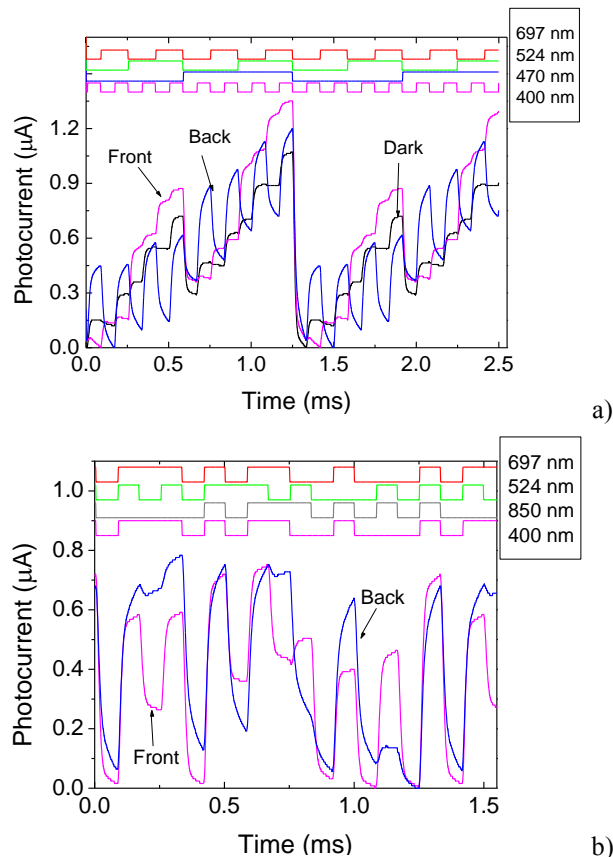


Figure 6. MUX signals: a) without and under front and back $\lambda=390$ nm irradiation and different bit sequences. b) Front and back irradiation and two channels (400 nm and 697 nm) with the same bit sequence.

Results show that, the background side alters the form of the MUX signal, enhancing or quenching different spectral ranges. In Figure 6a all the on/off states are possible so, without optical bias, 2^4 ordered levels are detected and correspond to all the possible combinations of the on/off states. Under, either front or back irradiation, each of those four channels, by turn, are enhanced or quenched differently (Figure 6, Table I) resulting in an increase magnitude of red/green under front irradiation or of the blue/violet one, under back lighting. Since the gain of the four input channels is different ($\alpha_{F,B}$; Table I) this nonlinearity allows identifying the different input channels in a large visible/infrared range. In Figure 6b, both 400 nm and 697 nm channels have the same bit sequence which corresponds to only 2^3 ordered levels, however once the optical gains of both channels are quite different under front and back irradiation (Table I) it is possible to identify them. Under back irradiation the MUX

signal receive its main contribution from the 400 nm channel while under front irradiation it is mainly weighed buy the long wavelength channels. By comparing front and back irradiation is possible to decode the transmitted information.

Under front irradiation, near-UV radiation is absorbed at the beginning of the front diode and, due to the self-bias effect, increases the electric field at the back diode where the red/infrared incoming photons (see Figure 1) are absorbed accordingly to their wavelengths (see Figure 3) resulting in an increased collection. Under back irradiation the electric field decreases mainly at the back i-n interface enhancing the electric field at the front diode quenching it at the back one. This leads to an increased collection of the violet/blue input signals.

So, by switching between front to back irradiation the photonic function is modified from a long- to a short-pass filter allowing, alternately selecting the red/infrared channels or the blue and violet ones, thus, making the bridge between the visible and the infrared regions.

V. OPTOELECTRONIC MODEL

Based on the experimental results and device configuration a two connected phototransistors model (Figure 7a), made out of a short- and a long-pass filter was developed [5] and upgraded to include several input channels. The *ac* circuit representation is displayed in Figure 7b and is supported by the complete dynamical large signal Ebers-Moll model with series resistances and capacities. The charge stored in the space-charge layers is modelled by the capacitor C_1 and C_2 . R_1 and R_2 model the dynamical resistances of the internal and back junctions under different *dc* bias conditions. The operation is based upon the following strategic principle: the flow of current through the resistor connecting the two transistor bases is proportional to the difference in the voltages across both capacitors (charge storage buckets). The modified electrical model developed is the key of this strategic operation principle. Two optical gate connections ascribed to the different light penetration depths across the front (Q_1) and back (Q_2) phototransistors were considered to allow independent blue (I_1), red/infrared (I_2) and green (I_3, I_4) channels transmission. Four square-wave current sources with different intensities are used; two of them, I_1 and I_2 , with different frequencies to simulate the input blue and red channels and the other two, I_3 and I_4 , with the same frequency but different intensities, to simulate the green channel due to its asymmetrical absorption across both front and back phototransistors.

In Figure 7c, the block diagram of the optoelectronic state model is displayed. The resistors (R_1, R_2) and capacitors (C_1, C_2) synthesize the desired filter characteristics. The input signals, $\lambda_{IR,R,G,B,V}$ model the input channels and $i(t)$ the output signal. The amplifying elements, α_1 and α_2 are linear combinations of the optical gains of each impinging channel, respectively into the front and back phototransistors and account for the enhancement or quenching of the channels (Figure 3) due to the steady state irradiation. Under front irradiation we have: $\alpha_2 \gg \alpha_1$ and under back irradiation $\alpha_1 \gg \alpha_2$. This affects the reverse photo

capacitances, $(\alpha_{1,2}/C_{1,2})$ that determine the influence of the system input on the state change.

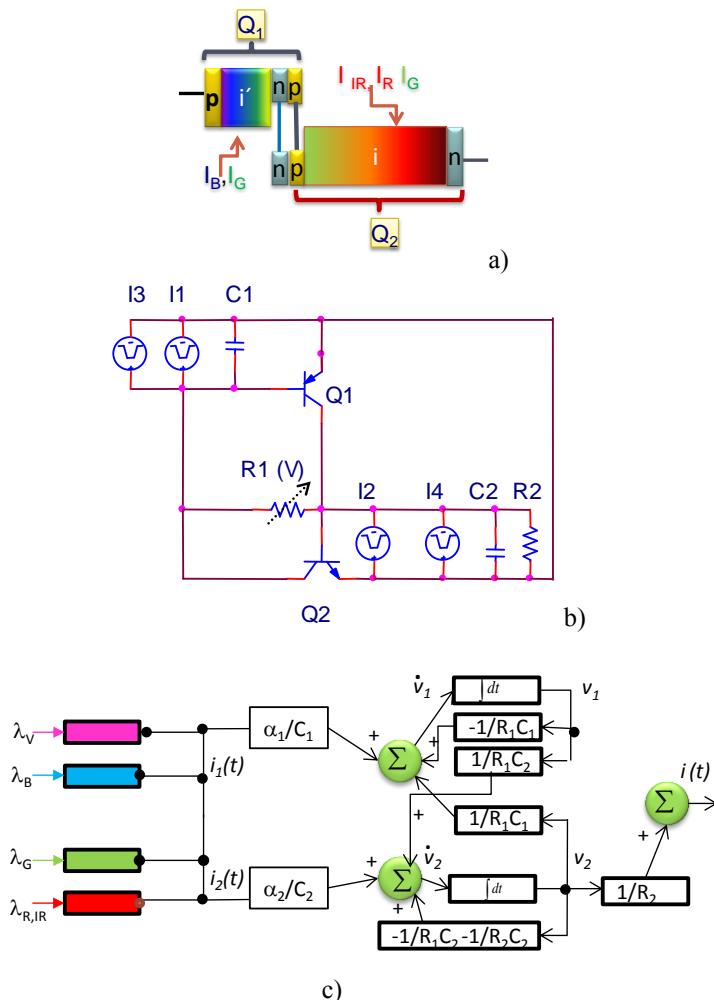


Figure 7. a) Two connected transistor model, b) equivalent electric circuit, c) block diagram of the optoelectronic state model.

A graphics user interface computer program was designed and programmed within the MATLAB® programming language, to ease the task of numerical simulation. This interface allows selecting model parameters, along with the plotting of bit signals and both simulated and experimental photocurrent results. To simulate the input channels we have used the individual magnitude of each input channel without background lighting (Figures 2 and 5), and the corresponding gain at the simulated background intensity (Table I). Figure 8, presents results of a numerical simulation with $3000 \mu\text{W}/\text{cm}^2$ front and back $\lambda=390 \text{ nm}$ irradiation and the experimental outputs of Figure 2b and Figure 6b, respectively.

Values of $R_1=10 \text{ K}\Omega$, $R_2=1 \text{ K}\Omega$, $C_1=1000 \text{ pF}$, $C_2=20000 \text{ pF}$ were used during the simulation process (Figure 7c). On top of the figures, the drive input LED signals guide the eyes into the different *on/off* states and correspondent wavelengths

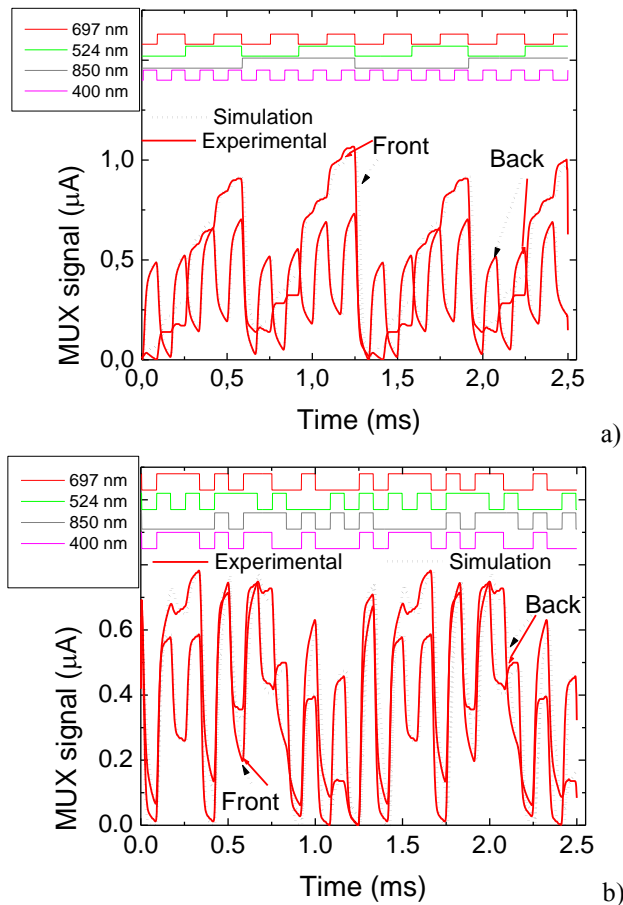


Figure 8. Numerical simulation with front and back $\lambda=390$ nm irradiation, and different channel wavelength combinations and bit sequences.

A good fitting between experimental and simulated results was achieved. The plots show the ability of the presented model to simulate the sensitivity behavior of the proposed system in the visible/infrared spectral ranges. The optoelectronic model with light biasing control has proven to be a good tool to design optical filters. Furthermore, this model allows for extracting theoretical parameters by fitting the model to the measured data (internal resistors and capacitors). Under back irradiation higher values of C_2 were obtained confirming the capacitive effect of the near-UV radiation on the device that increases the charge stored in the space charge layers of the back optical gate of Q_2 modelled by C_2 .

VI. CONCLUSIONS

We experimentally and theoretically demonstrate the use of near-ultraviolet steady state illumination to increase the spectral sensitivity of a double a-SiC/Si pi'n/pin photodiode beyond the visible spectrum (400 nm-880 nm). The concept is extended to implement a 1 by 4 wavelength division multiplexer with channel separation in the visible/near infrared ranges.

Results show that, the pi'n/pin multilayered structure becomes reconfigurable under front and back irradiation, acting as data selector in the VIS/NIR ranges. The device performs WDM optoelectronic logic functions providing photonic functions such as signal amplification, filtering and switching. The opto-electrical model with light biasing control has proven to be a good tool to design optical filters in the VIS/NIR. An optoelectronic model was presented and proven to be a good tool to design optical filters in the VIS/NIR range.

ACKNOWLEDGEMENTS

This work was supported by FCT (CTS multi annual funding) through the PIDDAC Program funds (UID/EEA/00066/2013) and PTDC/EEA-ELC/120539/2010.

REFERENCES

- [1] T. Komiyama, K. Kobayashi, K. Watanabe, T. Ohkubo, and Y. Kurihara, "Study of visible light communication system using RGB LED lights," in Proceedings of SICE Annual Conference, IEEE, 2011, pp. 1926–1928.
- [2] S. S. Djordjevic et al. "Fully Reconfigurable Silicon Photonic Lattice Filters With Four Cascaded Unit Cells" IEEE photonics Technology Letters, 23, NO. 1, january 1, 2011, pp. 41-44.
- [3] P. P. Yupapin and P. Chunpang, "An Experimental Investigation of the Optical Switching Characteristics Using Optical Sagnac Interferometer Incorporating One and Two Resonators," Optics & Laser Technology, Vol. 40, No. 2, 2008, pp. 273-277.
- [4] S. Ibrahim et al., "Fully Reconfigurable Silicon Photonic Lattice Filters With Four Cascaded Unit Cells" 21 Mar 2010, paper OWJ5. Optical Fibre Communications Conference, OSA/OFC/NFOEC, San Diego.
- [5] M. Vieira, P. Louro, M. Fernandes, M. A. Vieira, A. Fantoni, and J. Costa, "Three Transducers Embedded into One Single SiC Photodetector: LSP Direct Image Sensor, Optical Amplifier and Demux Device", Advances in Photodiodes", InTech, Chap.19, 2011, pp. 403-425.
- [6] M. Vieira, P. Louro, M. Fernandes, M. A. Vieira, A. Fantoni, and J. Costa Advances in Photodiodes, InTech, Chap.19, 2011, pp:403-425.
- [7] M.A. Vieira, P. Louro, M. Vieira, A. Fantoni, and A. Steiger-Garção, "Light-activated amplification in Si-C tandem devices: A capacitive active filter model" IEEE sensor jornal, 12, NO. 6, 2012, pp. 1755-1762.
- [8] M. A. Vieira, M. Vieira, P. Louro, V. Silva, and A. S. Garção, "Photodetector with integrated optical thin film filters" Journal of Physics: Conference Series, 421, 012011 March 2013. doi:10.1088/1742-6596/421/1/012011
- [9] M. Vieira, M. A. Vieira, I. Rodrigues, V. Silva, and P. Louro, "Tuning optical a-SiC/a-Si active filters by UV bias light in the visible and infrared spectral ranges", Phys. Status Solidi, C, 2014, pp. 1-4 Article first published online: 25 JUL 2014. DOI: 10.1002/pssc.201400020.

Silicon Based Temperature Sensors with Extended Temperature Range and Simple One-Point Calibration

I. Tobehn¹, A. Steinke¹, A. Albrecht¹, H. Hansch², M. Kunze³, and T. Ortlepp¹

¹ CiS Forschungsinstitut für Mikrosensorik GmbH, Erfurt, Germany

² IL Metronic Sensortechnik GmbH, Ilmenau, Germany

³ Hahn-Schickard, Villingen-Schwenningen, Germany

e-mail: itobehn@cismst.de

Abstract— Temperature is the most important parameter to be measured in industry, automation, environment and many other fields. Almost any silicon diode can be used as a temperature transducer. Its main advantages are the high precision and the high long-term stability while the drawbacks are the limited operation temperature and the parameter spread due to fabrication uncertainties. We propose a dedicated fabrication technology for silicon-based temperature diodes, specifically designed and optimized to overcome these limitations. It is designed for higher temperature sensing applications where simple calibration, high accuracy and high long-term stability are most important. We demonstrate test results to evaluate the obtained process stability and discuss potential application fields in hybrid multi-sensor systems and more complex feedback-based sensor-actor systems.

Keywords—silicon temperature sensor; one-point calibration; platforms; building blocks; pressure sensor; dew point sensor.

I. INTRODUCTION

The demand for high performance sensors in the field of process and environmental control, automation and security is obvious. Here, sensors for pressure, humidity, concentration [1], play the most important role. But high accuracy and long term stability of those sensors must be seen in context with the performing of temperature. Another trend goes conform to the accuracy: the spatial distance between the main sensor (e.g. pressure) and the temperature sensor or the distance between the temperature sensor and the measuring substance (air, liquid, solid matter) must be as small as possible. From another perspective, [2] classifies this fact regarding the invasive, semi-invasive and non-invasive principle. Miniaturization and integration are the strategy in the future. Therefore, in the last years the sensing of temperature has played an ever increasing role in different fields of smart sensor systems and system integration. With the silicon-diode based temperature sensor described in [3] a common denominator has been found for all these challenges. In following we describe three typical designs and technologies of silicon temperature sensors.

First of all the design and technology of single-chip temperature sensors including proposals for a higher temperature range will be described. Advantages regarding stability, working range, size, cost, ease of use, are compared

to the well established thermocouple, resistive and thermistor based temperature sensors. To enter this market with single-chip silicon temperature sensors is more difficult but possible. Decisive advantages should be the compatibility of the electrical interfaces and signal processing [2] and the potential for an easy-to-integrate assembly process in chip-on-board or flip-chip technologies.

Secondly the silicon diode as temperature sensor is described forwarding full or hybrid integration close to the signal processing. The main advantages should be the technology compatibility from the process point of view and the assembly as close as possible to other devices. Sensors measuring environmental parameters such as humidity, pressure, force, gas and liquid concentration have typically strong temperature dependencies. This temperature cross sensitivity has in most cases the effect, that the higher the working temperature is, the lower the resulting accuracy for the primary quantity under investigation. Temperature measurements at the point of primary detection system (for the purpose of temperature compensation) are absolutely necessary.

The third case is of increasing importance for sensor-actor-systems where integrated temperature sensors decide about accuracy and expense for calibration. One predestined system is the dew point sensor system [4]-[6]. Such a sensor system consists of two different transducers (temperature and condensation) and a heating-cooling system. The temperature sensor has to measure the water temperature as the result of a closed-loop conducted by the cooling element.

For all these applications an integrated silicon temperature sensor can have the same dominator and enough potential for extended temperature applications. Trends in application fields like smart mobility, smart health, smart security, and smart manufacturing [7] go conform to the progressive trends of microelectronic, micro system technique [8] and key enabling technologies [9].

In Section II, the technology strategy is described under the point of view of possible kinds of silicon integration. Basis for this integration is the typical current-voltage characteristic of a silicon p-n junction (see Section III). Section IV covers different temperature sensors and applications. Section V concludes the paper.

II. TECHNOLOGY STRATEGY

Already in [4][10], the monolithic integration of temperature sensors in a CMOS- process had been described. Up to now, some of these concepts have been realized by products on the market.

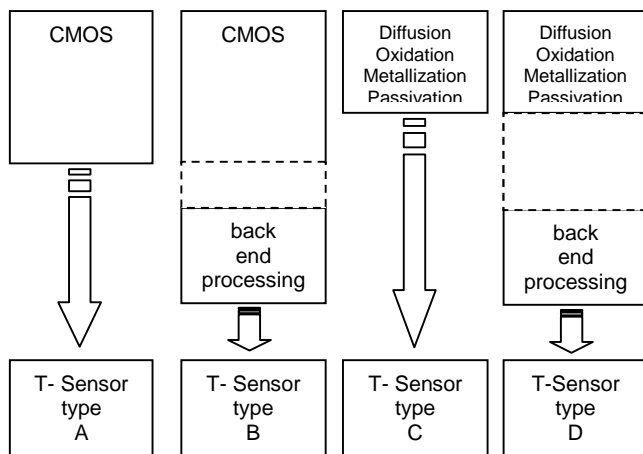


Figure 1. Selection of different sensor integration

Fig. 1 presents an overview of different integration concepts for temperature sensors into systems. Type A is part of a complete CMOS process realized e.g. in [11]-[13]. After the CMOS process, no further back end technology steps are necessary. The CMOS electronics can be used for signal processing of the temperature signal [14].

In case of type B temperature sensor the CMOS process is added by back end processing steps. Typically, Micro-electro-mechanical systems (MEMS) technology steps like membrane etching or realization of electrodes including deposition of functional layers are described by this technology chain. Both realizations have limitations due to the temperature range of CMOS electronics.

Type C is similar to A, except that the temperature sensor fabrication is based on selected CMOS steps only (diffusion, metallization and passivation). Substrates, diffusion parameters and metallization can be selected to obtain a higher operation temperature of the sensor [15]-[16]. In the same matter, Type D is the most commonly used technology in micro sensor systems. From the main sensor point of view, the temperature sensor stands for front end processing followed by the sensor specific MEMS steps.

III. SILICON P-N JUNCTION TEMPERATURE SENSORS

The electrical potential difference (at a given current) at p-n junctions shows pronounced temperature dependence. With increasing temperature the current-voltage characteristics shifts to lower voltages. This relationship is shown in Fig. 2. This correlation between current, voltage and temperature is the base for the use of p-n-junctions in temperature measurements.

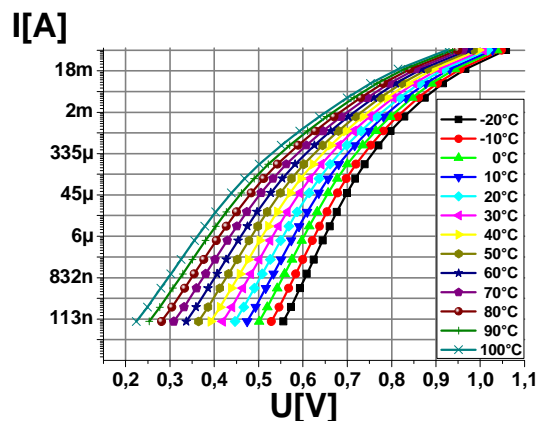


Figure 2. Current-voltage characteristic of a temperature diode at different temperatures

IV. DESIGN AND RESULTS

A. Single p-n junction Temperature Sensor

In Fig. 3 a typical layout is shown. In order to minimize the voltage deviation by using higher currents, a four-wire measurement is possible. Since n-substrate is used, the effective diode is formed by the p-type implantation in the middle of the structure.



Figure 3. Typical sensor layout for four-wire measurement

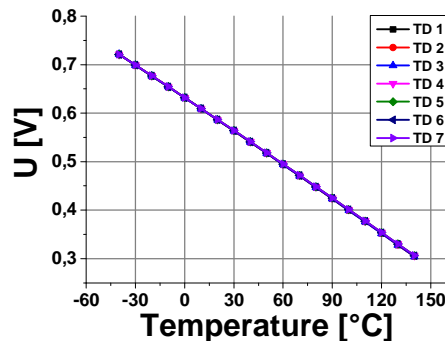


Figure 4. Voltage-temperature characteristics of seven different temperature diodes of one type

Fig. 4 shows the voltage versus temperature for seven diodes fabricated in the same process. A constant supply is used in this case. The slope of these characteristics is almost identical within a certain margin.

This allows a single-point calibration. By modifying the preparation using silicon-in-insulator (SOI) technology, the measuring range can be extended up to 250 °C. In this case, the manufacturing tolerance, i.e. the deviation of the characteristic curve of a sensor from the mean value, is minimal. The biggest differential illustrated in Fig. 5 at 140 °C corresponds to a relative error of 0.5 %.

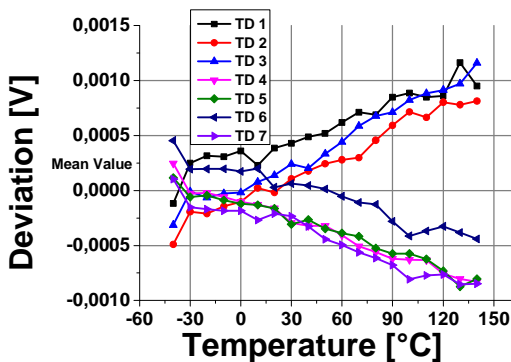


Figure 5. Deviations from the mean voltage in the temperature range from -40 °C to 140 °C

B. p-n junction temperature sensor for error compensation (using the example of a pressure sensor)

A silicon based piezoresistive pressure sensor is a good example for a monolithic integration of a MEMS component with a temperature sensor. Temperature variations influence parameters like linearity, sensitivity and accuracy. The on-chip temperature measurement is essential for a compensation of these cross sensitivities. An integrated silicon temperature sensor realized as p-n junction does not need further technology steps, but its integration has further advantages.

Firstly the sensor can be placed close to the piezoresistors and measures the temperature direct without artefacts, secondly the p-n junction does not need additional layers such as metal depositions which could cause mechanical effects and affect the performance of the piezoresistors. Fig. 6 shows a typical design where the Wheatstone bridge and the temperature sensors (left hand corner) are integrated on one chip. The integration of several diodes at different places does not cause additional cost but does e.g. not provide further improvements of this concept.

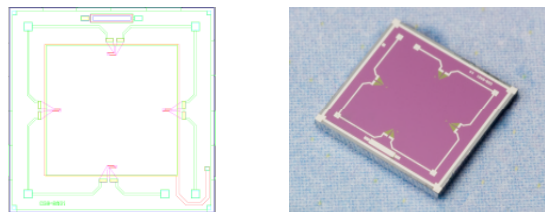


Figure 6. Design of a piezoresistive pressure sensor with integrated p-n junction as temperature sensor [17]

C. p-n junction temperature sensor as part of a sensor-actor-system (using the example of a dew point sensor)

Temperature sensors are of central importance in the realization of a thermal detecting dew point sensor [5][18]. On the one hand temperature sensors are used to determine the state of condensation on a sensitive sensor membrane, on the other hand to detect the temperature of the sensing spot.

Water has a high heat capacity and a high enthalpy of vaporization. Thus, it makes up a high energy conversion in the evaporation even of smallest water droplets. The heat capacity of a micro mechanic membrane with heating and temperature sensing elements, however, is extremely small. Comparing the heat capacity of a dewy and not dewy spot on the membrane can determine condensation qualitatively. For this task it is ideal to use Seebeck elements. These allow the determination of a temperature profile in response to a transient heating pulse.

In a balance of condensation and evaporation, located on a water-surface, the surface temperature is corresponding to the dew point temperature. To determine the temperature of the condensing surface of the thermal dew point sensor, two measurements are required. By means of a diode, implanted in the silicon bulk, is the bulk-temperature determined. The temperature dependence of the diode forward voltage (approximately 2.3 mV/K) is calibrated at several points in order to achieve a high accuracy. Furthermore, the temperature difference between the silicon bulk and the sensitive condensation spot on the membrane is determined by using Seebeck elements. The two determined temperature values are added and result in the absolute temperature of the sensitive condensation spot. In Fig. 7 the design of the dew point sensor is presented and both temperature sensors are marked.

Further technology modules e.g. thinfilm peltier modules [19] increase the value chain and the potential of further miniaturization.

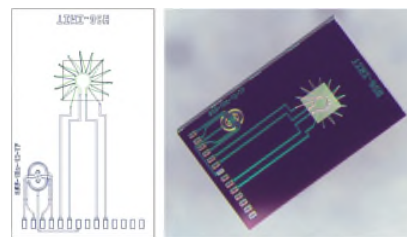


Figure 7. Design (left) and photograph (right) of the silicon sensor chip including sensor for absolute (left hand corner) and condensed water (in the middle) temperature measurement [20]

V. CONCLUSION

Silicon based temperature sensors are of increasing importance for the actual and next generation of smart sensor systems. Single temperature devices as well as integrated device for process automation and environmental conditions are not possible without temperature sensing. Current development in this field addresses the extension of the working range to higher temperatures. Next generation of

process sensors are focused more and more on in-situ and on in-line applications and are exposed harsh environments and higher temperatures. To keep pace with the advantages of cost effective microelectronic technology the implementation of silicon temperature sensor as front end or backend process is still the most promising way.

ACKNOWLEDGMENT

We acknowledge the support the federal government by means of the framework of the High-Tech Initiative Germany, the support program Innovation Competence East as well as the support of the European Union.

The authors thank for support Federal Ministry of Research and Education FKZ 16SV5346 and for the Federal Ministry for Economic Affairs and Energy FKZ MF120073. A part of the research leading to the presented results has received funding from the HORIZON 2020 program via grant 644596, project SMARTER-SI.

REFERENCES

- [1] AMA Fachverband für Sensorik e.V.: Sensor Trends 2014. Trends in Future-Oriented Sensor Technologies“, [Online]. Available from: [http://www.ama-sensorik.de/fileadmin/Publikationen/AMA_Study_Sensor_Trends\[1\].pdf](http://www.ama-sensorik.de/fileadmin/Publikationen/AMA_Study_Sensor_Trends[1].pdf) (2015.07.09).
- [2] M. Mansoor, I. Haneef, S. Akhtar, A. D. Luca, and F. Udrea, “Silicon diode temperature sensors - a review of application”, *Sensors and Actuators A*, vol. 232, pp. 63-74, 2012.
- [3] A. L. Spetz, A. Baranzahi, P. Tobias, and I. Lundström, “High Temperature Sensors Based on Metal-Insulator-Silicon Carbide Devices”, *Physica Status Solidi (A)*, Applied Research, vol. 162, iss. 1, pp. 493-511, 1997.
- [4] D. Heinze, H. Hansch, D. Hofmann, B. March, and A. Steinke, „Monolithisch integrierter Taupunkt-Sensor mit hoher Genauigkeit und Langzeitstabilität unter industriellen Bedingungen“, *Sensoren und Messsysteme / Fachtagung Sensoren und Meßsysteme ; 8 (Bad Nauheim) : 1996.03.11-13. - Düsseldorf : VDI-Verl. (1996)*, pp. 319-325.
- [5] M. Kunze, J. Merz, W. J. Hummel, H. Glosch, S. Messner, and R. Zengerle, “A micro dew point sensor with a thermal detection principle”, *Measurement Science and Technology*, vol. 23, pp. 014004, 2012.
- [6] IL Metronic Sensortechnik GmbH, [Online]. Available from: <http://www.il-metronic.de> (2015.7.6).
- [7] EPoSS, “Strategic research Agenda of the European Technology Platform on Smart Systems Integration”, Version 2, March 10, 2009, [Online]. Available from: <http://www.smart-systems-integration.org/public/documents/publications/EPoSS Strategic Research Agenda 2009.pdf> (2015.07.09)
- [8] P. Coge, “More-than-Moore Roadmapping. Update”, ITRS Summer Public Conference, San Francisco, July 13, 2010, [Online]. Available from: <http://www.itrs.net/ITRS 1999-2014 Mtgs, Presentations & Links/2011Summer/PublicPresentations/MoreThanMoore.pdf> (2015.07.09)
- [9] European Commission, “High-Level Expert Group on Key Enable Technologies”, Final Report, June 2011, [Online]. Available from: http://ec.europa.eu/enterprise/sectors/ict/files/kets/hlg_report_final_en.pdf (2015.07.09)
- [10] A. Steinke, B. March, D. Heinze, and H. Hansch, “The CCC-dewpoint sensor as a concrete example of design and industrial realization of monolithic transducers”, *Proceedings SENSORS Expo 1989, Chicago, October 6-8*, pp. 417-422, 1998.
- [11] A. L. Aita, M. A. Pertijs, K. A. A. Makinwa, J. H. Huijsing, and C. M. Meijer, “Low-Power CMOS Smart Temperature Sensor With a Batch-Calibrated Inaccuracy of ± 0.25 °C (± 3 σ) from 70 °C to 130 °C”, *Sensors Journal, IEEE*, vol. 13, no. 5, pp. 1840-1848, 2013.
- [12] K. Souri, Y. Xhae, F. Thus, and K. Makinwa, “A 0.85V 600nW all-CMOS Temperature Sensor with an Inaccuracy of ± 0.4 °C (3σ) from -40 to 125°C”, *Solid-State Circuits Conference Digest of Technical Papers (ISSCC), 2014 IEEE International*, Feb. 2014, p. 222-223, doi: 10.1109/ISSCC.2014.6757409
- [13] K. A. A. Makinwa, “Smart temperature sensors in standard CMOS”, *Electron Devices Meeting, 2008. IEDM 2008. IEEE International*, Dec. 2008, pp. 1, doi: 10.1109/IEDM.2008.4796714
- [14] STMicroelectronics, “LM135 Precision Temperature Sensor”, data sheet, [Online]. Available from: http://www.st.com/web/catalog/sense_power/FM89/SC294/PF63662 (2015.07.09)
- [15] C. P. L. v. Vroonhoven and K. A. A. Makinwa, “An SOI thermal-diffusivity-based temperature sensor with $\pm 0,6$ °C (3σ) untrimmed inaccuracy from -70°C to 225°C”, *Sensors and Actuators A*, vol. 188, pp. 66-74, 2012.
- [16] S. Santra, P. K. Guha, S. Z. Ali, I. Haneef, and F. Udrea, “Silicon on Insulator Diode Temperature Sensor - A Detailed Analysis for Ultra-High Temperature Operation”, *Sensors Journal, IEEE*, vol. 10, no. 5, pp. 997-1003, 2010.
- [17] CiS Forschungsinstitut für Mikrosensorik GmbH, [Online]. Available from: <http://www.cismst.org> (6.7.2015).
- [18] M. Kunze, S. Billat, H. Glosch, M. Ashauer, E. Keßler, A. Ihring, U. Dillner, and U. Schinkel, “Thermisch detektierender Taupunktsensor mit integrierter Peltierkühlung“, *Temperatur 2013: Fachtagung; PTB Institut Berlin, 5./6. Juni 2013; [Verfahren und Geräte in der Temperatur- und Feuchtemesstechnik; Tagungsband]*.
- [19] “Smart Access to Manufacturing for Systems Integration”, Project Website, [Online]. Available from: <http://www.smarter-si.eu>, (6.7.2015).
- [20] Hahn-Schickard-Gesellschaft für angewandte Forschung e.V., [Online]. Available from: www.hahn-schickard.de (6.7.2015).

Performance Analysis of Commercial Accelerometers of Different Technologies

Stephan Elies, Stefan Ebenhöch

Dept. Reliable Systems

Fraunhofer Institute for High-Speed Dynamics, Ernst-Mach-Institut, EMI

Freiburg, Germany

e-mail: stephan.elies@emi.fraunhofer.de

Abstract—This paper points out the performance and limits of commercial resistive, piezoresistive, piezoelectric, capacitive, thermal and optical accelerometers and can be used as a reference work. Therefore, datasheets of 118 accelerometers from 27 manufacturers of eight countries have been analyzed. Focus of the analysis were the parameters overload shock limit, measurement range, frequency response, resonance frequency, volume, weight, power consumption and operating temperature of both uniaxial and triaxial accelerometers. Accelerometers with overload shock limits in the range of 50 g to 200×10^3 g and within a measurement range of 2 g to 110×10^3 g have been analyzed. The unit g stands for the gravity acceleration defined as 9.81 meters per square second. A strict overload shock limit of 10×10^3 g for accelerometers with proof mass and a measurement range of less than 2×10^3 g was found. Also, that the performance of uniaxial and triaxial accelerometers differs. Especially uniaxial piezoelectric accelerometers show a better performance with regard to overload shock, measurement range, resonance frequency, frequency response and operating temperature in contrast to triaxial ones. Piezoelectric accelerometers show the highest overload shock limits, measurement range and operating temperature, capacitive accelerometers the lowest power consumption and volume, piezoresistive accelerometers the widest frequency response.

Keywords; *accelerometers; measurement range; frequency response; resonance frequency; overload shock limit.*

I. INTRODUCTION

Within the conducted review, seven transduction principles used in commercial accelerometers today could be identified. The capacitive, piezoresistive and piezoelectric (with charge and with voltage output) principles are most common [1]-[4]. Further principles are the resistive, optical and thermal ones. Reviews of state of the art accelerometers [1][2] are mostly focused on the first three mentioned technologies. This fact and the general lack of reviews of accelerometers as stated in [1], especially comparing different commercial technologies with each other, have been the motivation of the present work. Furthermore, a review including the useful parameters volume, weight, power consumption and operating temperature is missing.

In this paper, we point out the performance of commercial accelerometers by analyzing: a number of 118 accelerometers from 27 manufacturers of eight countries; piezoresistive, resistive, piezoelectric with charge and also

with voltage output, capacitive, optical and thermal accelerometers; the parameters overload shock limit, measurement range, frequency response, resonance frequency, volume, weight, power consumption and operating temperature for both uniaxial and triaxial accelerometers. All parameters were stored in a database to identify limits of technologies and correlation between parameters by data mining.

The review includes accelerometers with overload shock limits within the range of 50 g to 200×10^3 g and within a measurement range of 2 g to 110×10^3 g. The unit g stands for the gravity acceleration defined as 9.81 meters per square seconds. Our review covers commercial accelerometers used in numerous fields, such as consumer, automotive, railway and aerospace industries, with cost per unit within the range of between 1 and 3000 Euro, excluding restricted accelerometers.

In Section 2, the transduction principles of the analyzed accelerometers are explained. The database and the process of data acquisition is addressed in Section 3. In Section 4, the analyzed parameters of accelerometers are discussed and finally, the results are summarized in Section 5.

II. TRANSDUCTION PRINCIPLES OF ACCELEROMETERS

Most accelerometers can be modelled as a spring-mass-damper system. Acceleration applied to the accelerometer leads to a mass displacement or to a bending of a cantilever beam caused by the inertial force. There are a number of transduction principles to detect the displacement of the mass or the bending of the cantilever beam. Common commercial accelerometers detect the change of resistance, capacitance, charge, temperature or optical characteristics caused by mass displacement or bending. Further principles are the resonant, tunneling and electromagnetic principle [2]. But we found no manufacturer selling such accelerometers off-the-shelf.

Each transduction principle needs electronics to convert, e.g., the change in resistance into a voltage signal. Also, for, signal amplifying and processing, electronic circuits are needed. Depending on the transduction principle, either external electronics has to be connected or is combined in one housing. Fundamentally, accelerometers are classified into two types with regard to their frequency response [3]. So called AC accelerometers can only measure dynamic acceleration. The second type that can measure static acceleration, such as gravity acceleration as well as dynamic acceleration is called DC accelerometer.

A. Piezoelectric accelerometers with charge output

They comprise piezoelectric materials as natural quartz crystals bonded with a proof mass. Acceleration leads to a mass displacement and causes stress in the crystal subsequently. Under stress, the piezoelectric effect causes a charge transfer in the crystal. The amplitude of charge can be measured. Electronics is not integrated so these accelerometers provide a charge signal which has to be transferred by special low noise cable. They work only for AC measurement [3].

B. Piezoelectric accelerometers with voltage output

They work exactly the same way as piezoelectric accelerometers with charge output, but the electronics is integrated to amplify and convert the charge signal into a voltage signal. So they provide a voltage output signal and work only for AC measurement [3].

C. Resistive accelerometers

They detect the change of resistance of a metal strain gauge bonded to a cantilever beam. An acceleration leads to a bending of the cantilever beam and thus to a change in resistance of the strain gauge. For metal foil the geometric effect dominates the piezoelectric effect [5]. Up to four strain gauges are normally configured in a Wheatstone bridge circuit. So they provide a voltage signal and work for DC measurement.

D. Piezoresistive accelerometers

They work exactly the same way as resistive accelerometers, but the strain gauge is fabricated from semiconductor materials. Single crystal silicon is about 100 times more sensitive to strain because for semiconductors the piezoresistive effect dominates the geometric effect [5]. Configured in a Wheatstone bridge circuit, they provide a voltage signal and work for DC measurement [1].

E. Capacitive accelerometers

They detect changes of capacitance of a plate capacitor. The plates are composed of semiconductor material, such as silicon. The capacitor consists of a moveable plate in-between two stationary plates. The center plate deflects due to acceleration and leads to a change of the capacitance. Configured in a Wheatstone bridge circuit, they provide a voltage signal and work for DC measurement [2][3].

F. Optical accelerometers

Usually, they detect the change of optical characteristics in an optical fiber. There are a variety of technics for fiber optical measurement [6]. The Fiber Bragg Grating (FBG) principle has become widely known [7] and FBG accelerometers seem to be the popular fiber optical technology. Bragg Gratings are interference filters written into optical fibers. The gratings reflect only a narrow spectral component of induced light. This characteristic is used for FBG accelerometers. Acceleration leads to a deformation of an optical fiber attached to a suspension

beam. The deformation of the optical fiber changes the reflection characteristic of the Bragg gratings. This change can be detected by comparing the spectral component of the reflected with the induced light. Because usually, electronics is not integrated, they provide an optical signal. They work for DC measurement. In the present work we only analyzed FBG accelerometers.

G. Thermal accelerometers

Thermal accelerometers based on mass displacement have been studied in [8]. We found no manufacturer selling these accelerometers off-the-shelf. Thermal accelerometers without mass displacement have been reported among others in [9]. These types of accelerometers consist of a heater and thermocouples located around the heater in a hermetic chamber. Without acceleration, the heater creates a symmetric temperature profile. When acceleration is applied, the hot air in the chamber moves and the temperature profile gets asymmetric. The asymmetry can be detected by the thermocouples around the heater. There is one manufacturer that patented and commercialized this transduction principle [10]. Electronics is integrated and these accelerometers provide a voltage signal and work for DC measurement. In the present work, we only analyzed thermal accelerometers without moving parts.

III. DATABASE AND PROCEDURE OF DATA ACQUISITION

For this paper, we considered accelerometers worldwide with regard to high overload shock limit, high measurement range, low power consumption and low volume. Table I lists the number of accelerometers classified by their country of origin into European Union and worldwide. We chose the headquarters of manufacture as country of origin because of globalization, engineering, manufacturing, etc., could be distributed across several locations worldwide. For this review, we think the headquarters is the most suitable parameter to compare the performance of accelerometers by countries because from 27 manufactures, 15 manufacture their accelerometers at the headquarters, and 7 manufacture at the headquarters and one or more locations worldwide. Only for 5 manufactures, the location of manufacture is not explicitly specified.

TABLE I. NUMBER OF ANALYZED ACCELEROMETERS CLASSIFIED BY HEADQUARTER OF COMPANY INTO EUROPEAN UNION AND NON EU.

Country of origin	Number of Accelerometers	Classification by country of origin
Germany	35	European Union (EU)
UK	11	
Denmark	11	
USA	37	Worldwide (Non EU)
Switzerland	13	
China	9	
Canada	1	
Hong Kong	1	

Table I is not exhaustive, but we found no commercial accelerometers with higher overload shock limit, higher measurement range and so on.

Table II shows the number of analyzed accelerometers classified by their transduction principle and classified by frequency response into AC and DC measurement.

TABLE II. NUMBER OF ANALYZED ACCELEROMETERS CLASSIFIED BY TRANSDUCTION PRINCIPLE AND FREQUENCY RESPONSE.

Transduction principle	Number of accelerometers	Classification by frequency response
Capacitive	40	DC
Piezoresistive	15	
Resistive	7	
Optical	4	
Thermal	2	
Piezoelectric voltage output	30	AC
Piezoelectric charge output	20	

Resistive and especially optical and thermal accelerometers are not very common in contrast to the other transduction principles. Due to small samples, we will highlight only special characteristics of these three principles in the next section.

IV. ANALYSES OF PARAMETERS

In this section, we will analyze the parameters overload shock limit, measurement range, power consumption, volume, weight, frequency response, resonance frequency, and operating temperature of accelerometers specified on their datasheets.

A. Measurement range of accelerometers

In datasheets, the measurement range is mostly specified for a symmetric range of acceleration, e.g., -500 g to 500 g. Rarely the lower limit is restricted, e.g., -200 g to 500 g. In this review, the parameter measurement range stands for the positive upper limit of acceleration, for the last given example 500 g, because for 95 of 118 accelerometers, the measurement range is symmetric. For 24 accelerometers, the lower limit is not specified and only for one accelerometer, the lower limit is restricted. In Figure 1, the measurement range is plotted against the accelerometer-ID. A number of 118 different accelerometers have been analyzed, so there are 118 IDs where each ID is a unique identifier. That means an accelerometer, e.g., with the ID 50 in Figure 1 has the same ID in Figure 2 to Figure 8. These figures were designed to correlate the analyzed parameters among each other. Among 118 accelerometers, there are only three capacitive accelerometers with two measurement axes. Because of that small number, they were classified into the class of triaxial accelerometers, annotated in Figure 1.

Capacitive accelerometers are limited to a measurement range of 500 g and resistive accelerometers to 10×10^3 g.

Only piezoelectric and piezoresistive accelerometers are capable of measuring more than 10×10^3 g with the restriction that piezoresistive accelerometers are the only ones capable of DC measurement above 10×10^3 g.

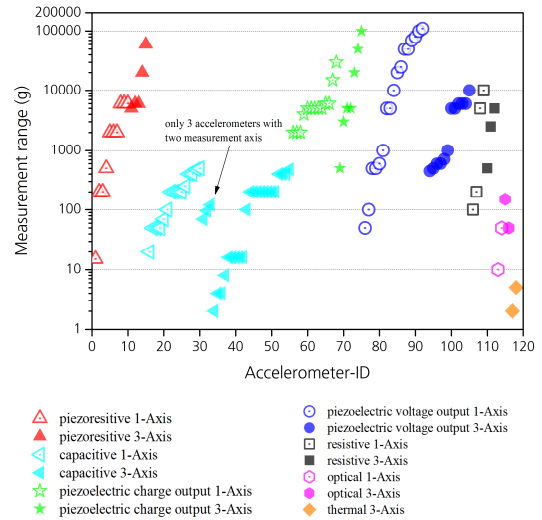


Figure 1. Measurement range of 118 accelerometers classified by transduction principle, number of measurement axis and sorted by measurement range in ascending order.

For measuring 100×10^3 g and more, uniaxial piezoelectric accelerometers are capable. However, triaxial piezoelectric accelerometers with voltage output are limited to 10×10^3 g.

B. Overload shock limit

Figure 2 presents the overload shock limit against the ID. Except for piezoelectric accelerometers, most accelerometers cannot be used for overload shock limits beyond 10×10^3 g. Especially the capacitive principle is strictly limited to the 10×10^3 g threshold.

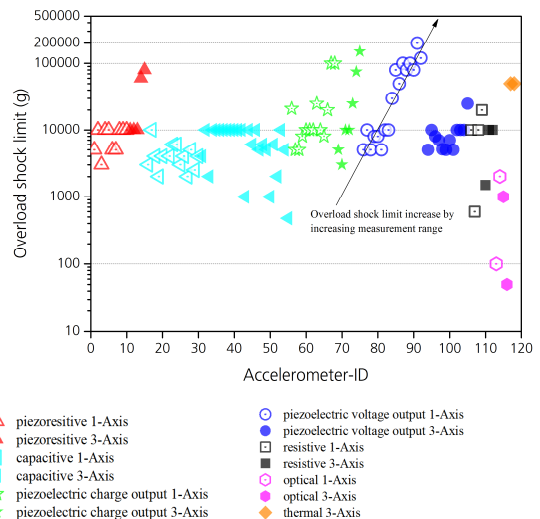


Figure 2. Overload shock limit of 118 accelerometers classified by transduction principle, number of measurement axis and sorted by measurement range in ascending order.

The review also shows that a general comparison of overload shock limits for different accelerometers is only possible to a limited degree, due to the fact that this parameter is only valid for a specified profile of acceleration and a defined period of time. Usually, the overload shock limit is specified as the peak of a semi sinusoidal profile of acceleration. But a uniform specification of the period of time on datasheets is missing. The period of time is specified as the maximum or the minimum time or the rise time of a semi sinusoidal profile. For altogether 85 of 118 accelerometers, the period of time is not specified on their datasheets.

C. Power consumption of accelerometers

Figure 3 shows the power consumption against the ID. Note that piezoelectric accelerometers with charge output and optical accelerometers are excluded because electronics is not integrated and therefore no power is used. Of course, both principles also need electronics, but in this review, we did not focus on external electronics. Furthermore, for 13 of 118 accelerometers, no power consumption was specified on the datasheet.

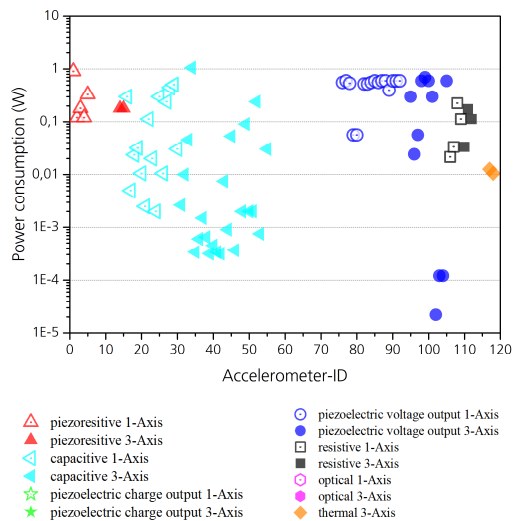


Figure 3. Power consumption of 81 accelerometers classified by transduction principle, number of measurement axis and sorted by measurement range in ascending order.

The upper limit of power consumption is about 1 watt. Generally, the majority of capacitive accelerometers show the minimal power consumption beside some piezoelectric accelerometers with voltage output. Our analyses show that there is no significant correlation between power consumption and measurement range. The power consumption for uniaxial piezoelectric accelerometers with voltage output is nearly constant.

D. Volume of accelerometers

Figure 4 illustrates the volume plotted against the ID. Note that the volume for piezoelectric accelerometers with charge output and optical accelerometers does not comprise

integrated electronics as explained in the section before. The volume of capacitive accelerometers covers a range of five decades, but this transduction principle has the minimal volume in total. Tendentially, the volume of piezoresistive

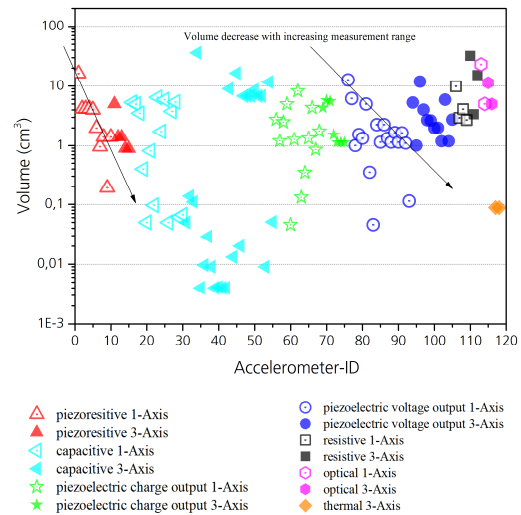


Figure 4. Volume of 118 accelerometers classified by transduction principle, number of measurement axis and sorted by measurement range in ascending order.

and piezoelectric accelerometers with voltage output decreases by increasing measurement range. However, optical accelerometers have the largest volume.

E. Weight of accelerometers

Figure 5 shows the weight plotted against the ID. For 18 of 33 capacitive and for the two thermal accelerometers, the weight is not specified on the datasheet. Note again that electronics for piezoelectric accelerometers with charge output and optical accelerometers are excluded.

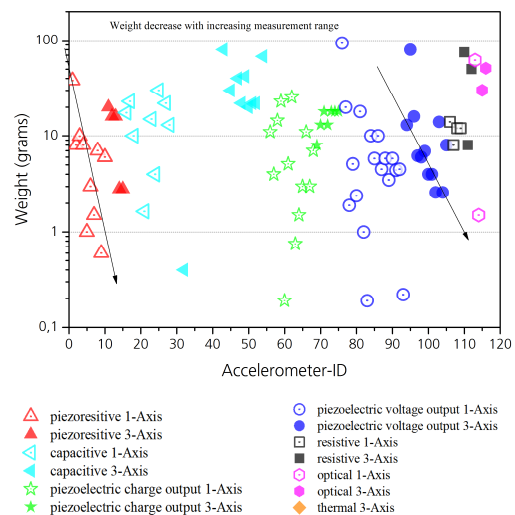


Figure 5. Weight of 98 accelerometers classified by transduction principle, number of measurement axis and sorted by measurement range in ascending order.

Almost all transduction principles cover a range of three decades from 0.1 grams to 100 grams. According to the volume, there is a clear tendency of decreasing weight with increasing measurement range for piezoresistive accelerometers and piezoelectric accelerometers with voltage output.

F. Resonance frequency of accelerometers

Figure 6 shows the resonance frequency plotted against the ID. For altogether 40 accelerometers (21 capacitive and 10 piezoresistive ones), this parameter was not specified on the datasheet. Due to sparse data, we exclude these two principles from discussion.

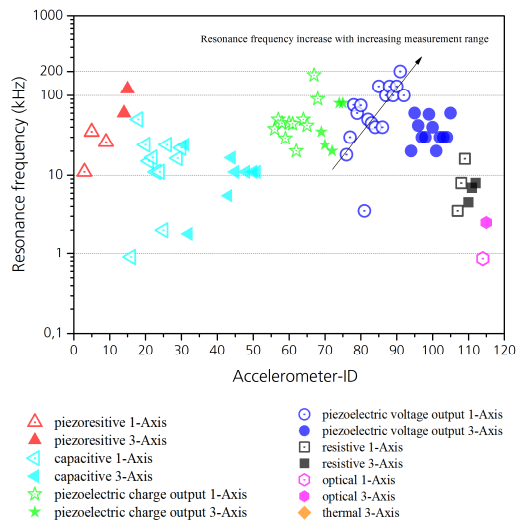


Figure 6. Resonance frequency of 78 accelerometers classified by transduction principle, number of measurement axis and sorted by measurement range in ascending order.

Tendentially, for uniaxial piezoelectric accelerometers with voltage output, the resonance frequency correlates with increasing measurement range and is limited to a range between 10 kHz up to 200 kHz. For triaxial piezoelectric accelerometers with voltage output, the maximum resonance frequency is significantly lower and limited to 80 kHz.

G. Frequency response of accelerometers

Figure 7 presents the range of the frequency response plotted against the ID. Notice that the axis of ordinate combines a logarithmic and linear scale. A comparison of the frequency responses of accelerometers is only possible to a limited degree because a uniform specification of the tolerance of the output signal on datasheets is missing. For only 54 of 118 accelerometers, the frequency response is specified for a tolerance of the output signal within ± 3 dB. For 56 accelerometers, the tolerance for the output signal is specified non-uniformly, e.g., for -18% , $+15\%$, $\pm 10\%$, $\pm 7\%$, $\pm 5\%$, ± 10 dB, ± 2 dB or not specified. For 8 accelerometers, the specification is completely missing.

With few exceptions, piezoresistive and resistive accelerometers are limited to 5 kHz and capacitive to 1 kHz.

Most piezoelectric accelerometers are capable for a range of 1 Hz to 20 kHz, and a few are capable for a frequency response down to 0.2 Hz. By tendency, uniaxial piezoelectric accelerometers show a wider frequency response than the triaxial ones. The thermal accelerometers

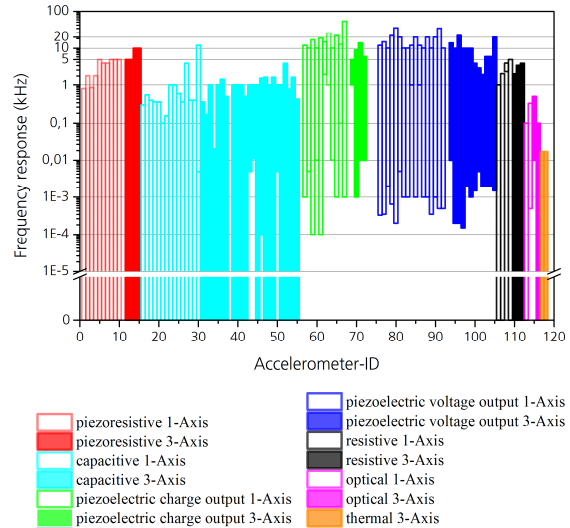


Figure 7. Range of frequency response of 110 accelerometers classified by transduction principle, number of measurement axis and sorted by measurement range in ascending order.

are limited to 17 Hz and by frequency extension circuits, this limit can be pushed to 100 Hz [10].

H. Operating temperature of accelerometers

Figure 8 presents the operating temperature against the ID. For piezoelectric accelerometers with charge output, the standard operating temperature is in the range of $-54\text{ }^{\circ}\text{C}$ to $150\text{ }^{\circ}\text{C}$. But they are capable to work up to $250\text{ }^{\circ}\text{C}$ because

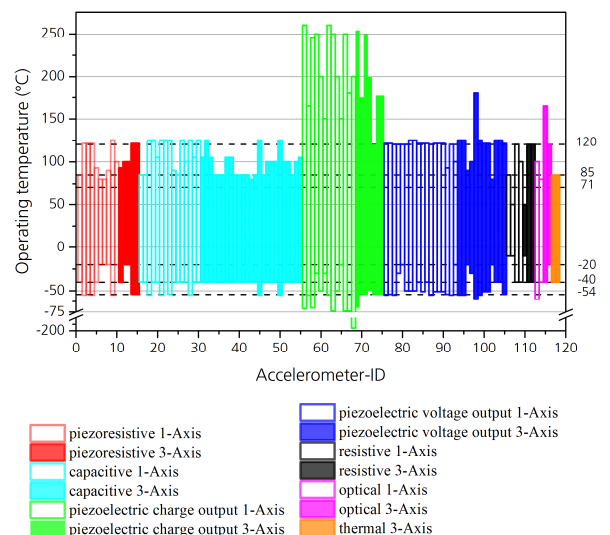


Figure 8. Range of operating temperature of 118 accelerometers classified by transduction principle, number of measurement axis and sorted by measurement range in ascending order.

the electronics as limiting factor is excluded. In contrast, uniaxial piezoelectric accelerometers with voltage output are limited to a standard temperature of 120 °C. For capacitive accelerometers, the standard temperature is in the range of -40 °C up to 85 °C. For piezoresistive accelerometers, the standard temperature is only in the range of -20 °C up to 85 °C. By tendency, the positive operating temperature for the most uniaxial capacitive and piezoelectric accelerometers is higher than for the triaxial ones.

I. Performance of accelerometers by country of origin

For the last figure of this paper, we chose another design to illustrate two interesting facts. Therefore, a distinction between uniaxial and triaxial accelerometers has not been made. Figure 9 presents the overload shock limit plotted against the measurement range.

First, accelerometers from manufacturers of the European Union are limited to an overload shock limit of 100×10^3 g and to a measurement range of 80×10^3 g.

Second, there is a strict threshold for accelerometers based on a proof mass. Within a measurement range of up to 2×10^3 g, they are strictly limited to overload shock limits of 10×10^3 g. Remember that the thermal principle works without a proof mass, so it is less fragile to overload shocks.

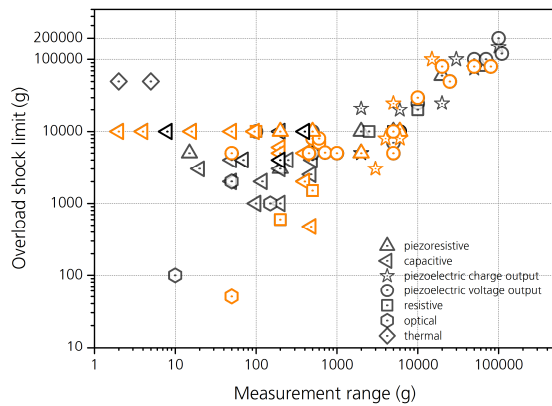


Figure 9. Overload shock limit versus measurement range of 118 accelerometers. The transduction principles are highlighted by the shape of the symbols. Accelerometers from the EU are highlighted in orange and the non-EU ones are highlighted in black.

Beside accelerometers capable of measuring more than 10×10^3 g, it is very difficult to find such with overload shock limits beyond the 10×10^3 g limitation.

V. CONCLUSION

A variety of commercial accelerometers have been analyzed. Performance and limits of accelerometers were presented and can be used as a reference work for choosing the right technology.

The paper shows that accelerometers from manufacturers of the European Union are nearly state of the art with regard to measurement range and overload shock limit. It was found

a strict overload shock limit of 10×10^3 g for accelerometers with proof mass and a measurement range of up to 2×10^3 g.

We ascertain that the performance of uniaxial and triaxial accelerometers is slightly different. Especially uniaxial piezoelectric accelerometers show a better performance with regard to measurement range, overload shock, resonance frequency, frequency response and operating temperature than the triaxial ones.

A general comparison of accelerometer parameters is not always easy due to a lack of uniform or missing specification in datasheets. In this context, important parameters, such as overload shock limit, frequency response and resonance frequency are affected.

In summary, piezoelectric accelerometers show the highest measurement range, shock limits and operating temperature, capacitive accelerometers the lowest power consumption and volume, and piezoresistive accelerometers the widest frequency response.

VI. ACKNOWLEDGMENT

The author thanks Mr. M. Weber for the support in extracting accelerometer parameters from datasheets.

REFERENCES

- [1] V. Narasimhan, H. Li, and M. Jianmin, "Mircomachined high-g accelerometers: a review", *Journal of Micromechanics and Microengineering*, vol. 25 (3), Feb. 2015, pp. 1-18, doi:10.1088/0960-1317/25/3/033001.
- [2] G. Krishnan, C. U. Kshirsagar, G. K. Ananthasuresh, and N. Bhat, "Micromachined high-resolution accelerometers", *Journal of the Indian Institute of Science*, vol. 87 (3), Jul.-Sept. 2007, pp. 333-361.
- [3] A. Chu, "Choosing the right type of accelerometers", *Application Notes*, Measurement Specialties Inc., May 2012.
- [4] O. B. Degani, D. J. Seter, E. Socher, S. Kaldor, E. Scher, and Y. Nemirovsky, "Comparative study of novel micromachined accelerometers employing MIDOS", *Sensors and Actuators A: Physical*, vol. 80 (2), March 2000, pp. 91-99, doi:10.1016/S0924-4247(99)00253-8.
- [5] S. Beeby, G. Ensell, M. Kraft, and N. White, "MEMS mechanical sensors", Artech House, Inc., Boston London, 2004, ISBN 1-58053-536-4.
- [6] K. T. V. Grattan and T. Sun, "Fiber optic sensor technology: an overview", *Sensors and Actuators A: Physical*, vol. 82 (1-3), May 2000, pp. 40-61, doi:10.1016/S0924-4247(99)00368-4.
- [7] A. Méndez, "Fiber Bragg grating sensors: a market overview", *Proc. SPIE6619, Third European Workshop on Optical Fibre Sensors*, vol. 6619, July 2007, pp. 661905-1-661905-6, doi:10.1117/12.738334.
- [8] U. A. Dauderstädt, P. H. S. de Vries, R. Hiratsuka, and P. M. Sarro, "Silicon accelerometer based on thermopiles", *Sensors and Actuators A: Physical*, vol. 46 (1-3), Jan.-Feb. 1995, pp. 201-204, doi:10.1016/0924-4247(94)00890-T.
- [9] A. M. Leung, J. Jones, E. Czyzewska, J. Chen, and B. Woods, "Micromachined accelerometer based on convection heat transfer", *Proc. IEEE Micro Electro Mechanical Systems Workshop (MEMS'98)*, Jan. 1998, pp. 627-630, doi:10.1109/MEMSYS.1998.659830.
- [10] J. Fennelly, S. Ding, and J. Newton, Y. Zhao, "Thermal mems accelerometers fit many applications", *Sensor Magazin*, Mar. 2012, pp. 18-20.

2D and 3D Phononic Crystals - A New Class of (Bio)Chemical Microsensors and Sensor Networks

Ralf Lucklum, Mikhail Zubtsov
Institute for Micro and Sensor Systems
Otto-von-Guericke-University
Magdeburg, Germany
ralf.lucklum@ovgu.de, mikhail.zubtsov@ovgu.de

Yan Pennec
Inst. d'Electronique de Microelectr. et de Nanotechnologie
University Lille 1
Lille, France
yan.pennec@univ-lille1.fr

Frieder Lucklum
Institute for Microsensors, -actuators and -systems
University Bremen
Bremen, Germany
flucklum@imsas.uni-bremen.de

Abstract—We introduce concepts of a new class of acoustic sensor devices, so-called phononic crystal sensors. Small volumes of a complex liquid act as network of individually addressable acoustic resonators in its most promising realization. Resonance frequency reveals bulk properties of the mixture, for example the concentration of a compound. We furthermore suggest an acoustic analog to Photonic Crystal Enhanced Microscopy, PCEM, a spatially distributed metamaterial microacoustic sensor network for visualization of liquid and recognition layer properties.

Keywords-*phononic crystal; metamaterial; acoustic microsensors; (bio)chemical sensor*

I. MOTIVATION

Phononic crystals (PC) have been introduced in the early 1990s [1][2]. There are a lot of different phononic crystal realizations accomplishing translation symmetry in 2D and 3D designs. Bulk phononic crystals have a periodic modulation in their density and sound velocities for longitudinal and transverse polarization, creating band gaps at wavelengths commensurate to their lattice constant, i.e., acoustic (through liquids) or elastic mechanical (through solids) waves with certain frequencies cannot travel through the crystal at least in certain crystallographic directions. Since one can design properties not known in nature they are sometimes described as metamaterials. Major efforts in phononic crystal studies have been devoted to the search of absolute band gaps in perforated solids or solid/solid structures. Only recently reports on technical applications have been published, including sensing. The ability to magnify the interaction of acoustic waves with matter through specific geometries that are capable of confining acoustic waves in a small volume provides the basis for this novel type of sensor.

Linear or point defects are the characteristic feature of phononic crystal sensors. Defect modes can be designed to create a well separated mini-transmission band within the band gap and appear as transmission peak within the

transmission spectrum of phononic crystals. The position of the respective mode on the frequency scale, shortly called peak frequency, f_p , is sensitive to defect properties, specifically geometry and material properties of the confined matter. They can be changed by the measurement value of interest. Promising applications are the measurement of concentration of some compound, x_i , in a liquid confined in the cavity, concentration of a component, conversion rate during a chemical reaction, (bio)chemical activity or size of associates or molecule conformation etc. These values should become effective via a distinct change in speed of sound, v [7]-[9], of the liquid mixture:

$$f_p = f(v) = f(v(x_i)) \quad (1)$$

or in terms of sensitivity, S_f :

$$S_f = \frac{\partial v}{\partial x_i} \frac{\partial f_p}{\partial v} \quad (2)$$

The key difference to competing microacoustic sensors is that phononic crystal sensors give access to **volumetric** mechanical properties of the mixture whereas most classical sensors measure properties at the **interface** to the sensor element. Since the first term in (2) must be expected to be small at concentrations relevant to (bio)chemical applications, key design objective of phononic crystals sensor development is a large second term in (2). It can be realized by strong confinement of acoustic energy in a high- Q cavity resonator. A second important issue is that the respective acoustic cavity mode is the only allowed mode or that it is at least well separated from other modes. Finally, the modes must 'survive' under experimental conditions.

II. REALIZATIONS

The first phononic crystal sensor version has been introduced in [3]. A 2D phononic crystal fabricated in steel and having a slit cavity perpendicular to the propagation direction of longitudinal acoustic waves has been published

in [4]. The 4-row phononic sub-crystals provide optimized boundary conditions for the slit cavity resonator. This sample has been applied to a first technical application [5]. On-going research deals with the introduction of a disposable liquid container in response to medical needs [6]. Key design challenge is insensitivity to unavoidable variations in the coupling layer between phononic crystal and glass capillary.

A metamaterial sensor applies the so-called extraordinary transmission through a perforated plate [7]. We have shown that dynamic metastructures are created, defined by bi-medium oscillatory states at a certain frequency at normal incidence of plane longitudinal waves. On-going research is motivated by PCEM [8]. We focus on the acoustic analog. It is a spatially distributed sensor array for visualization of liquid and recognition layer properties based on an individually addressable network of metamaterial microacoustic elements. Acoustic waves are generated and detected by phased array US transducers, Figure 1.

A very challenging project is the development of a tubular phononic crystal [9] and its application as network of tubular phononic sensors, the so-called tubular bell. This development is motivated by the fact that pipes and vessels are the most prominent elements in modern technical environment and in nature to transport fluids like water or blood. By keeping the inner surface of the tube cylinder free of any obstacles, one of the major concerns in chemical, biochemical, and petrol or food industry, as well as in medicine, will be overcome. Figure 2 shows the first ever published result of a simulation of one of our ideas. Additional structural elements are periodically arranged at the outer wall of the pipe only. We can demonstrate the appearance of band gap and sharp resonance-like transmission peaks. The latter are governed by properties of the liquid inside the pipe.

Another aspect which must be considered at early stage is the fabrication technology of the sensor element. High-resolution stereolithography-printing technology enables the maskless, single-step fabrication of freeform 3D microstructures. This allows rapid prototyping of novel designs, fast optimization and finally customized products. Figure 3 shows a proof-of-concept 3D design extending the established 2D array of holes in a solid matrix to all three Cartesian directions.

III. CONCLUSIONS

First results prove the excellent perspectives of phononic crystals as new sensor class. They merge unique features of ultrasonic sensors and resonant sensors, specifically usage of ultrasonic wave propagation allowing for separation between electronics and measurement ‘cell’ and resonant cavities giving access to high resolution frequency measurement. However, application as chemical or biosensor introduces new challenges, e.g. volume and shape of the measurement cell, disposable materials, and highly variable fabrication technology.

All these specific aspects again have major influence on the design of the phononic crystal, the theory behind and the

models to compute band diagram and transmission spectrum.

On the other hand photonic crystal sensors, the optical counterpart having a longer history have already found their application as chemical and biosensors because of their excellent features like sensitivity, selectivity and reliability. The obvious analogy of the basic sensor principle, despite their also obvious difference, justifies further efforts in this still very young research field.

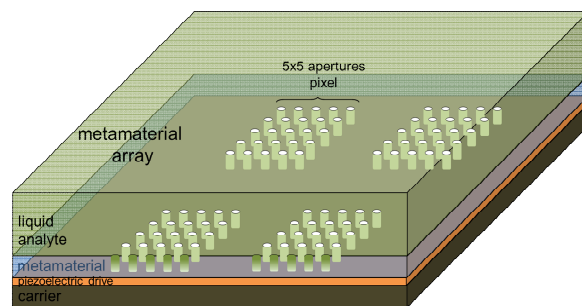


Figure 1: Idea of the metamaterial microacoustic array

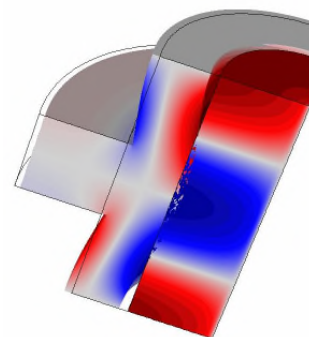


Figure 2: Quarter of a single element of a tubular bell. Colors represent deformation/pressure results of a numerical analysis (Comsol). Geometric dimensions scale with wavelength; here the mid-frequency is 1 MHz.

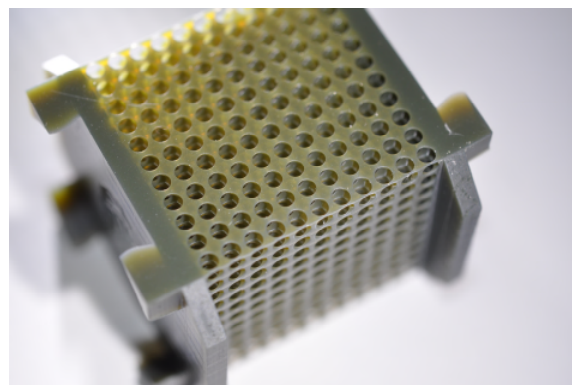


Figure 3: Stereolithography fabrication sample: 11x11x11 3D phononic crystal with 2 mm lattice constant [10]

REFERENCES

- [1] M. M. Sigalas and E. N. Economou, "Elastic and acoustic wave band structure," *Journal of Sound and Vibrations*, 158, 377-382, 1992.
- [2] M. S. Kushwaha, P. Halevi, G. Martinez, L. Dobrzynski, and B. Djafai-Rouhani, "Theory of acoustic band structure of periodic composites," *Phys. Rev. B*, 49, 2313-2322, 1994.
- [3] R. Lucklum and J. Li, "Phononic crystals for liquid sensor applications," *Meas. Sci. Technol.*, 20, 124014, 2009.
- [4] R. Lucklum, M. Ke, and M. Zubtsov, "Two-dimensional phononic crystal sensor based on a cavity mode," *Sens. Actuators B*, 171-172, 271-277, 2012.
- [5] A. Oseev, M. Zubtsov, and R. Lucklum, "Gasoline properties determination with phononic crystal cavity sensor," *Sens. Actuators B*, 189, 208-212, 2013.
- [6] R. Lucklum, M. Zubtsov, and S. Villa Arango, "Cavity Resonance Biomedical Sensor," *ASME Proceedings*, doi:10.1115/IMECE2014-38222.
- [7] M. Zubtsov, R. Lucklum, M. Ke, A. Oseev, B. Henning, and U. Hempel, "2D phononic crystal sensor with normal incidence of sound," *Sens. Actuators A*, 186, 118-124, 2012.
- [8] Y. Zhuo et al., "Single nano particle detection using photonic crystal enhanced microscopy," *Analyst*, 139, 1007-1015, 2014.
- [9] M. Zubtsov and R. Lucklum, "Phononic crystal wave mechanics in periodically modulated tubular structures," *ICSV22, proc.*, in press
- [10] R. Lucklum and M. Vellekoop, "Rapid Prototyping of 3D Phononic Crystals using High-Resolution Stereolithography Fabrication", *Euroensors 2015, proc.* in press.

A Dual Grating Fiber Sensor to Discriminate Axial and Radial Strains

Romain Guyard, Dominique Leduc, Yann Lecieux and Cyril Lupi

Institut de Génie Civil et de Mécanique (GeM), l'UNAM Université,
 Université de Nantes, UMR CNRS 6183,
 Email: Romain.Guyard@univ-nantes.fr

Abstract—When a fiber Bragg grating strain sensor is embedded inside a structure, the interaction of the sensor with the host material can lead to spurious results if the radial strain is neglected. In this article, we use numerical simulations to show that the axial and radial strains can be simultaneously measured with a single fiber in which a Bragg grating and a long period grating are superimposed. Moreover, we present an optimal architecture of the sensor.

Keywords—Strain; Embedded sensors; optical fiber gratings.

I. INTRODUCTION

Fiber Bragg gratings (FBG) are made of periodic modulation of the refractive index of the core of an optical fiber. As a consequence they behave as bandpass filters and reflect a very narrow spectral band of the incoming light, centered on the Bragg wavelength : $\lambda_B = 2n_{\text{eff}}\Lambda_0$ where n_{eff} is the effective index of the light propagating inside the core and Λ_0 the period of the grating. Any change in the period of the grating or in the effective index induces a shift in the Bragg wavelength.

FBGs are often used as strain sensors (see for example [1]–[5]). Indeed, when the fiber is strained, the period of the grating is modified. Moreover, due to the photo-elastic effect, the effective index also varies. What should be underlined is that the variation of the effective index depends on the strains in all directions. There is a tensorial relation between strain and refractive index change.

When the fiber is glued at two points on the surface of the monitored structure, its *axial* strain, ϵ_z , is exactly the same as the strain of the structure. Moreover, as the fiber is free to deform in the transverse plane, its *radial* strain ϵ_r is driven by the axial strain: $\epsilon_r = -\nu\epsilon_z$, where ν is the Poisson's ratio of the fiber. In this case, the axial strain is the only unknown and the measurement of a single Bragg wavelength shift is then sufficient. This is why FBG strain sensors are usually mounted at the surface of the structure.

When the fiber is embedded, it is not free anymore to deform in the transverse plane. Its radial strain then depends in a non trivial manner on the interaction between the fiber and the host material. It can not be deduced simply from the axial strain. Consider for example a sensor embedded in a cylinder of heat hardening resin (Young modulus: 3100 MPa, Poisson's ratio: 0.4; thermal expansion coefficient: $114 \times 10^{-6} \text{ K}^{-1}$) as used in the composite material. The initially liquid resin is heated. During cooling, it imposes mechanical stress on the fiber axially as well as radially. Assume that a drop of 100 K in temperature is imposed on the structure, with two different boundary conditions (BC): BC 1: the cylinder is free to undergo axial and radial deformation; BC 2: the cylinder external surface is free to move radially while the upper and

lower sections are fixed. Table I shows the calculated axial and radial strains together with the radial strain that would be measured by a single FBG under the assumption that: $\epsilon_r = -\nu\epsilon_z$. These results show that a single embedded FBG

TABLE I. Comparisons between calculated and measured strains

	BC 1		BC 2	
	axial strain	radial strain	axial strain	radial strain
Calcul	-11400 $\mu\epsilon$	1562 $\mu\epsilon$	0 $\mu\epsilon$	-438 $\mu\epsilon$
FBG	-11200 $\mu\epsilon$		209 $\mu\epsilon$	

gives at best approximate measurements (BC 1) and sometimes erroneous measurements (BC 2). A real case is in between BC 1 and BC 2. This underlines that the axial and the radial strains must be simultaneously determined. Then two linearly independant measurements have to be performed at the same point. It has been recently proposed to use the superposition of a long and a short period grating to achieve this task [6]. In this paper we study numerically more deeply this architecture and show that some configurations can fulfill the following requirements:

- The sensor has to measure simultaneously the radial and axial strains with the same precision on the axial strain as the FBGs mounted on surface.
- The transmission spectrum of the sensor has to exhibit only two peaks in the range [1400 nm; 1600 nm], one associated to the FBG and one to the Long Period Grating (LPG) in order to avoid any ambiguity in the order of the mode of the LPG.
- The response of the sensor must be linear in the range $\epsilon_{r,z} \in [-5000 \mu\epsilon; +5000 \mu\epsilon]$.

Section 2 is devoted to the description of the sensor and of the principle of measurement. In Section 3, we present the evolution of the behavior of the sensor as a function of relevant parameters and we determine the best architectures. Then we conclude and discuss briefly the results in Section 4.

II. THE DUAL GRATING SENSOR

In this section, we present the structure of sensor and we describe the principle of measurement.

A. Architecture of the sensor

The sensor is made of the juxtaposition of two gratings of same length inside the core of a fiber, surrounded by two concentric claddings (see Figure 1). Both gratings can be written using UV light with the same phase mask technique. The best is to write first the Bragg grating with one mask and then the long period grating with another mask [7].

We call a_1 the radius of the core and n_1 its refractive index, a_2 the radius of the inner cladding and n_2 its index, and a_3 the

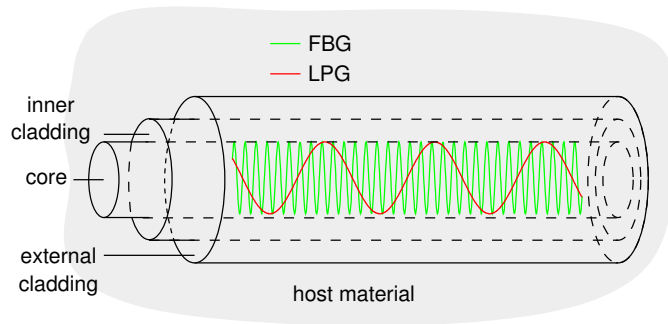


Figure 1. (a) Geometry of sensor. The red and green lines represent the variation of the refractive index of the core corresponding to the LPG and the FBG.

radius of the external cladding and n_3 its index. In order that only one mode propagates in the core of the fiber, the values of a_1 , n_1 and n_2 are fixed to that of a classical SMF28 fiber:

$$a_1 = 4.2 \mu\text{m} \quad \text{and} \quad n_1 = 1.0036n_2 \quad (1)$$

where n_2 is given by the Sellmeier's law:

$$n_2^2(\lambda) = 1 + \sum_{i=0}^3 \frac{A_i \lambda^2}{\lambda^2 - \lambda_i^2} \quad (2)$$

with $A_1 = 0.696750$, $A_2 = 0.408218$, $A_3 = 0.890815$, $\lambda_1 = 0.069066 \mu\text{m}$, $\lambda_2 = 0.115662 \mu\text{m}$ and $\lambda_3 = 9.900559 \mu\text{m}$ [8].

The first grating is a classical fiber Bragg grating. It reflects a narrow bandwidth of the incoming light centered on the Bragg wavelength λ_B . As a consequence, its transmission spectrum exhibit a hole around λ_B . The value of λ_B is given by the condition of resonance:

$$\lambda_B = 2n_{\text{eff}}^{\text{core}}(a_1, n_1, n_2, \lambda_B) \Lambda_B \quad (3)$$

where Λ_B is the period of the grating and $n_{\text{eff}}^{\text{core}}$ the effective index of the mode that propagates inside the core. It is given by the dispersion equation [9]:

$$F_c(a_1, n_1, n_2, n_{\text{eff}}^{\text{core}}, \lambda) = 0 \quad (4)$$

The second grating is a long period grating which couples the mode inside the core to resonant inner cladding modes. The wavelengths of resonant cladding modes are given by:

$$\lambda_{LPG} = [n_{\text{eff}}^{\text{core}}(a_i, n_i, \lambda_{LPG}^m) - n_{\text{eff},m}^{\text{clad}}(a_i, n_i, \lambda_{LPG}^m)] \Lambda_{LPG} \quad (5)$$

where Λ_{LPG} is the period of the grating and $n_{\text{eff},m}^{\text{clad}}$ the effective index of the m^{th} cladding mode. It is given by the dispersion equation of the cladding modes [9]:

$$F_g(a_1, a_2, n_1, n_2, n_3, n_{\text{eff}}^{\text{core}}, n_{\text{eff}}^{\text{clad}}, \lambda) = 0 \quad (6)$$

The light propagating inside the cladding gradually vanishes because of inhomogeneities and micro-bending. The transmission spectrum of the LPG exhibits then holes around each λ_{LPG} .

The coupling coefficient κ^m between a cladding mode m and the core mode [10]:

$$\kappa^m = \frac{\omega \epsilon_0 n_1^2}{2} \int_0^{2\pi} d\theta \int_0^{a_1} r dr E_t^m \cdot E_{0t}^* \quad (7)$$

gives the strenght of the coupling and then the depth of the hole in the spectrum.

B. Principle of measurement

When the fiber is strained, the period of the gratings, the radii and the indices of the three layers change. The variation of the period of each grating depends on the axial strain:

$$\Lambda = (1 + \epsilon_z) \Lambda_0 \quad (8)$$

where Λ_0 is the period of the grating at rest, while the changes of the radii depend on the radial strain:

$$a_i = (1 + \epsilon_r) a_{0i} \quad i = \{1, 2, 3\} \quad (9)$$

where a_{0i} is the radius at rest of the layer i . The variation of the refractive indices depends on both strains, due to the photo-elastic effect:

$$n_i = n_{i0} - \frac{n_{i0}^3}{2} [(p_{11} + p_{12}) \epsilon_r + p_{11} \epsilon_z] \quad i = \{1, 2, 3\} \quad (10)$$

where $p_{11} = 0.113$, $p_{12} = 0.252$ are the components of the photoelastic tensor of silica [11]. According to (4) and (6), the variations of the radii and the refractive indices induce a variation of the effective indices of the core mode and the cladding modes. All these changes cause a shift in λ_B and λ_{LPG} which can be expressed in the linear regime as:

$$\begin{cases} \Delta \lambda_B &= \alpha_{1r} \epsilon_r + \alpha_{1z} \epsilon_z \\ \Delta \lambda_{LPG} &= \alpha_{2r} \epsilon_r + \alpha_{2z} \epsilon_z \end{cases} \quad (11)$$

where α_{1r} and α_{1z} are respectively the sensitivity of the FBG to the radial and axial strain, and α_{2r} and α_{2z} are respectively the sensitivity of the LPG to the radial and axial strain. In a real experiment, one would measure these two shifts in wavelength and deduce the strains by inverting the system given by (11):

$$\begin{cases} \epsilon_z &= \frac{\alpha_{1r} \Delta \lambda_{LPG} - \alpha_{2r} \Delta \lambda_B}{D} \\ \epsilon_r &= \frac{\alpha_{1z} \Delta \lambda_B - \alpha_{2z} \Delta \lambda_{LPG}}{D} \end{cases} \quad (12)$$

where $D = \alpha_{1r} \alpha_{2z} - \alpha_{2r} \alpha_{1z}$.

The smallest measurable axial $\Delta \epsilon_z$ and radial $\Delta \epsilon_r$ strains can be derived from (12) using an uncertainty calculation:

$$\begin{cases} \Delta \epsilon_z &= \frac{|\alpha_{1r}| + |\alpha_{2r}|}{|D|} \delta \lambda_{\min} \\ \Delta \epsilon_r &= \frac{|\alpha_{1z}| + |\alpha_{2z}|}{|D|} \delta \lambda_{\min} \end{cases} \quad (13)$$

where $\delta \lambda_{\min}$ is the smallest measurable wavelength shift. It is usually of the order of 1 pm. Equation 13 shows that the largest D is, the better the resolution is.

C. Method to determine optimal architecture

The aim of the study is to find an architecture that meets the specifications. The parameters are a_1 , a_2 , a_3 , n_1 , n_2 , n_3 , λ_B and λ_{LPG} . The number of parameters can be reduced with the help of physical considerations. As stated above, the characteristics of the core and the refractive index of the inner cladding are chosen to be the same of a single mode SMF28 fiber. The outer cladding serves to isolate the modes of the inner cladding from the environment of the fiber. Its radius must be sufficiently large so that the cladding modes amplitudes falls to zero well before the interface between the outer cladding and the external medium. In practice, $a_3 = a_2 + 15 \mu\text{m}$ is enough. In contrast, the refractive index of the outer cladding n_3 influences very little the properties of

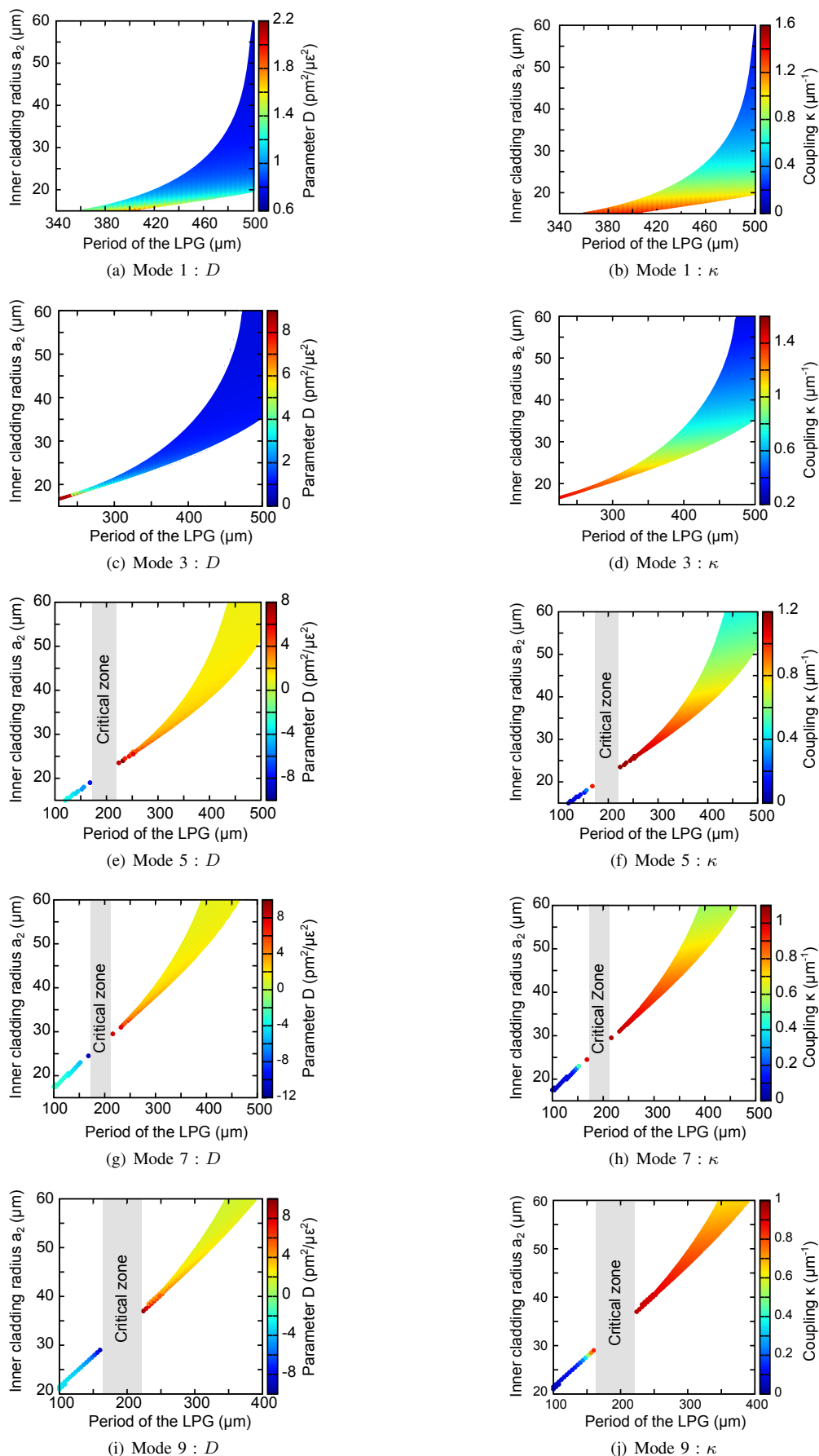


Figure 2. Evolution of D and κ as a function of a_2 and Λ_{LPG} .

the grating. It can be chosen arbitrarily in the range $[1.; n_2[$. We use the value $n_3 = 0.95n_2$ compatible with silica. The period of the Bragg grating is fixed to 501 nm in order to obtain a Bragg wavelength of 1.45 μm . Finally, the only free parameters are a_2 and Λ_{LPG} .

In order to determine the best couples of parameters $\{a_2, \Lambda_{LPG}\}$, we proceeded to a systematic exploration of the parameters space, with Λ_{LPG} varying from 100 μm to 500 μm by steps of 5 μm and a_2 varying from 15 μm to 70 μm by steps of 0.5 μm . Values of a_2 smaller than 15 μm were not considered because in this case the inner cladding is not large enough to isolate the core mode from the outer cladding.

For each couple $\{a_2, \Lambda_{LPG}\}$, we first determined the wavelength of the resonant cladding modes of the unstrained sensor using (5) and (6). We only kept the couples for which only one mode was present in the range [1400 nm, 1600 nm]. Then we applied a radial strain comprised in the range $[-5000 \mu\epsilon; +5000 \mu\epsilon]$, the axial strain remaining null. For each strain, the new radii and indices were calculated with the help of (9), (10), (4) and (6). This led to the new λ_B and λ_{LPG} from which were deduced the shifts $\Delta\lambda_B$ and $\Delta\lambda_{LPG}$. Then a linear regression gave the sensitivity α_{1r} of the Bragg wavelength and α_{2r} of the long period grating to the radial strain. The same procedure was used to calculate the sensitivity of the FBG and the LPG to the axial strain.

III. RESULTS

Figure 2 shows a cartography of the coupling coefficient κ and the parameter D for the first five odd cladding modes, as a function of a_2 and Λ_{LPG} . Even modes are not considered since their coupling coefficient is almost zero.

The white areas in each graph correspond to configurations where λ_{LPG} is outside the range [1400 nm; 1600 nm]. For each mode and for both D and κ , the shape of the coloured area looks like a comma, which tip is close to the lowest Λ_{LPG} and the lowest a_2 . Above mode 5, the tip is splitted into two parts, with a dead zone where no mode falls in the desired range. The sign of D changes through the critical zone and the coupling coefficient abruptly falls to zero. This corresponds to a change of modal properties of the cladding.

As stated by (13), the highest sensitivity is obtained with the largest values of D . For each mode, the largest values of D are located in the tip of the comma, *i.e.*, for the smallest values of Λ_{LPG} and the smallest values of a_2 . What is very interesting is that the highest coupling coefficients are also localised in the tip of the comma. This means that a couple $\{a_2, \Lambda_{LPG}\}$ can provide at the same time a good resolution and a good coupling.

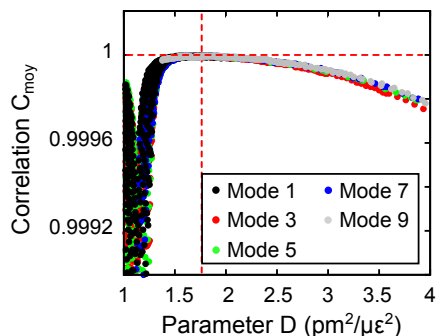


Figure 3. Evolution of C_{moy} as a function of D .

However, it is not possible to choose the configuration with the highest D since others specifications have to be fulfilled. In particular, the shifts of wavelength must evolve linearly with the strain in the range $[-5000 \mu\epsilon; +5000 \mu\epsilon]$. In order to quantify the linearity of the behavior of the long period grating, we use the estimate $C_{moy} = (|C_{\epsilon_r}| + |C_{\epsilon_z}|)/2$ where C_{ϵ_r} and C_{ϵ_z} are defined as:

$$C_{\epsilon} = \frac{\sum_{i=0}^N (\epsilon_i - \bar{\epsilon}_i) (\Delta\lambda_{LPG}^m - \overline{\Delta\lambda_{LPG}^m})}{\sqrt{\sum_{i=0}^N (\epsilon_i - \bar{\epsilon}_i)^2 (\Delta\lambda_{LPG}^m(\epsilon_i) - \overline{\Delta\lambda_{LPG}^m})^2}} \quad (14)$$

where N is the number of samples of strain ϵ_i for which $\Delta\lambda_{LPG}^m$ was calculated and \bar{x} is the mean value of x .

The Figure 3 shows the estimate C_{moy} as a function of D for modes 1 to 9. Surprisingly the values are placed on the same curve for all the modes. This curve presents a maximum for $D = 1.75 \text{ pm}^2/\mu\epsilon^2$. We choose this value for the sensor. This is not a sufficient condition to fix the couple $\{a_2, \Lambda_{LPG}\}$, so we require a complimentary condition: $\lambda_{LPG} = 1.55 \mu\text{m}$. This value is far enough from λ_{FBG} , so that no collapsing can occur between the FBG and the LPG resonant wavelengths when the strain increases.

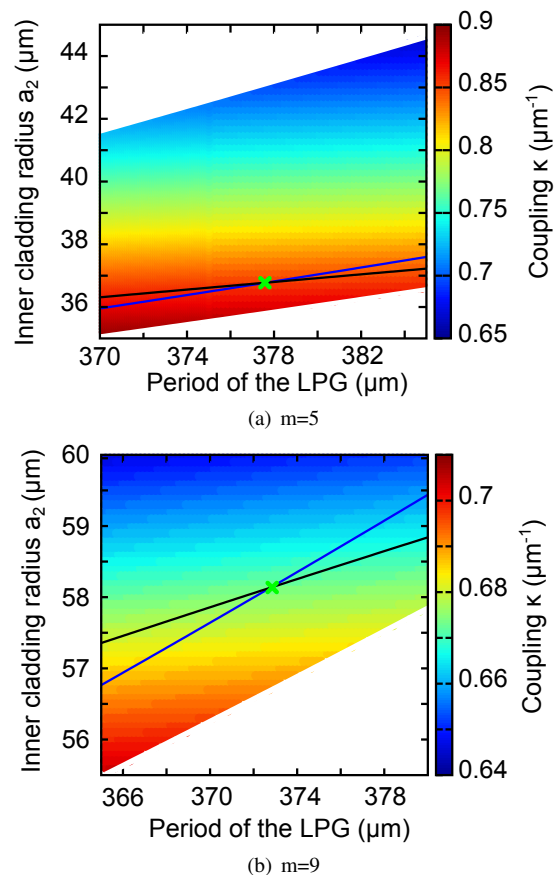


Figure 4. Determination of the optimal configuration for different modes.

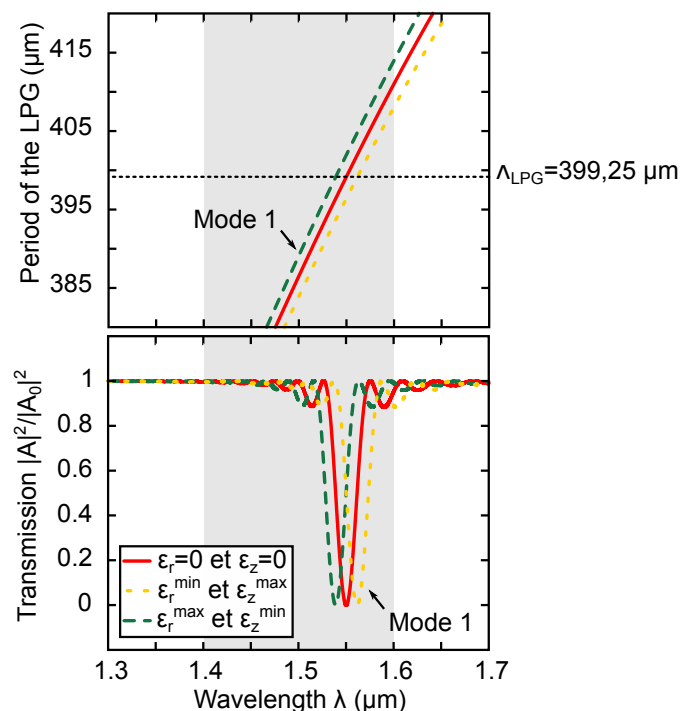
The dark lines on the graphics of Figure 4 correspond to the points where $D = 1.75 \text{ pm}^2/\mu\epsilon^2$ and the blue lines the points where $\lambda_{LPG} = 1.55 \mu\text{m}$. The intersections between these lines give the couples $\{a_2, \Lambda_{LPG}\}$ that meet all the requirements. The table II summarises the characteristics of

long period gratings given by these intersections for the five first modes. All these gratings present very similar sensitivities α_{2r} and α_{2z} and close periods Λ_{LPG} . In contrast, they exhibit quite different coupling coefficients. The coupling coefficients of mode 1 is almost twice the coupling coefficient of mode 9. Moreover, the radius of the inner cladding for mode 1 is smaller than that of other modes which makes it less sensitive to bending. And that is an other interesting feature.

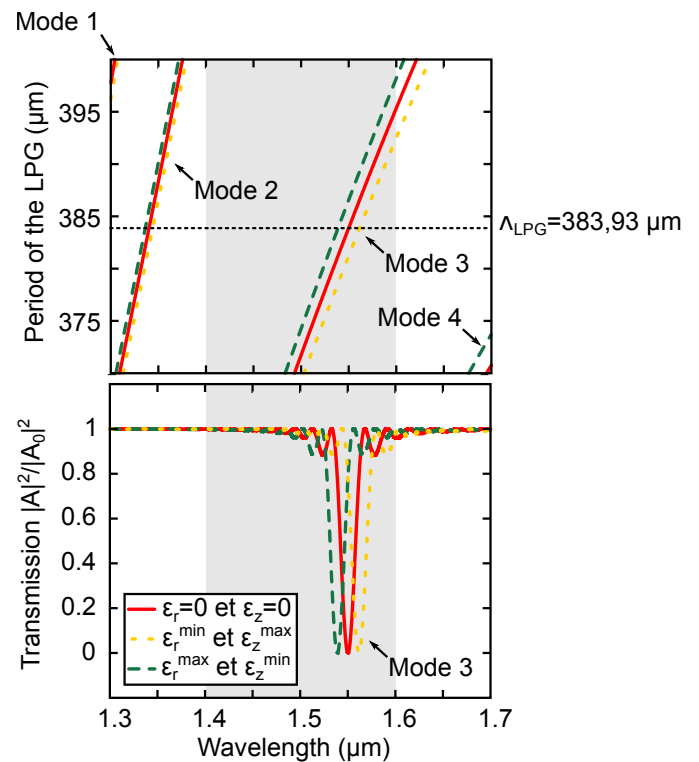
TABLE II. Characteristics of the optimal long period gratings

m	1	3	5	7	9
a_{20} (μm)	15.45	26.14	36.78	47.45	58.13
Λ_{LPG} (μm)	399.25	383.93	377.65	374.55	372.77
n_{eff}^m	1.442996	1.442772	1.442707	1.442672	1.442653
κ^m (μm^{-1})	1.328	1.020	0.850	0.750	0.680
α_{2r} ($\text{pm}/\mu\epsilon$)	-1.895	-1.860	-1.852	-1.847	-1.750
α_{2z} ($\text{pm}/\mu\epsilon$)	0.434	0.420	0.410	0.407	0.410

At this step, we retain two configurations: LPG1 : $\{a_{20} = 15.45 \mu\text{m}, \Lambda_{LPG} = 399.25 \mu\text{m}\}$ with mode $m = 1$ and LPG2: $\{a_{20} = 26.14 \mu\text{m}, \Lambda_{LPG} = 383.93 \mu\text{m}\}$ with mode $m = 3$. The last requirement that they have to fulfill is to present a single peak in the range [1400 nm; 1600 nm] whatever the strain.


 Figure 5. Evolution of λ_{LPG} with Λ_{LPG} and transmission spectrum for LPG1.

The figures 5 and 6 show the transmission spectrum of LPG1 and LPG2 together with the variation of the resonant wavelength as a function of the period of the grating: the straight line correspond to variation when the grating is at rest and the dashed lines to the maximum red-shift and the maximum blue-shift. The lengths of the gratings have been chosen to maximize the depth of the hole in the transmission spectrum. For LPG1, the mode 1 is the only one resonant in the desired wavelength range. In fact, no other mode is resonant in the [1300 nm, 1700 nm] for the considered range of strain. For LPG2, we can see that the modes 2 and 4 are close to


 Figure 6. Evolution of λ_{LPG} with Λ_{LPG} and transmission spectrum for LPG2.

the border. However, these modes do not interfere since their coupling coefficients are negligible. These two configurations can then be used.

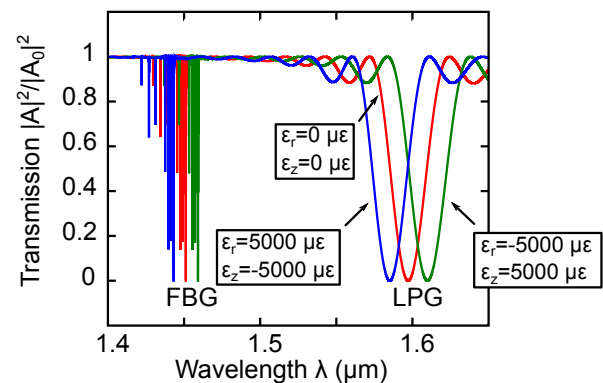


Figure 7. Transmission spectrum of optimal sensor.

We finally present on Figure 7 the whole spectrum of the sensor with LPG1. The red line correspond to the sensor at rest, the blue line to the strain that gives a maximal blue-shift and the red line to the strain that gives a maximal red-shift. We can notice a slight shift of λ_{LPG} in the absence of strain. This shift is due to the juxtaposition of the FBG. We can also notice the apparition of several narrow holes for wavelength smaller than λ_B . These holes correspond to the coupling between cladding modes and the core mode induced by the FBG. However these complementary holes do not induce confusion since their wavelengths are always smaller than λ_B .

Figure 8 shows the variation of the wavelength shifts of the FBG and the LPG as a function of ϵ_z and ϵ_r . As expected, the response of the sensor is quite linear. The deviation from

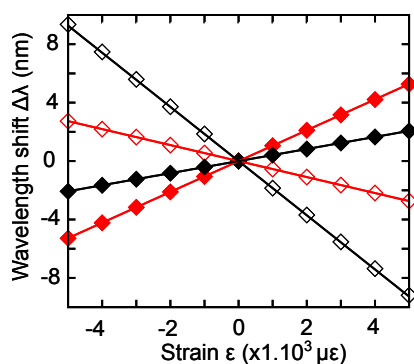


Figure 8. Response of the sensor to axial and radial strain.

linearity is drawn on Figure 9. It does not exceed 50 με for a strain of 5000 με, i.e., 1%. The sensitivity of the FBG to the axial strain is $\alpha_{1z} = 1,068 \text{ pm}/\mu\epsilon$, and that of the LPG is $\alpha_{2z} = 0,434 \text{ pm}/\mu\epsilon$. The sensitivity of the FBG to the radial strain is $\alpha_{1r} = -0,555 \text{ pm}/\mu\epsilon$ and that of the LPG is $\alpha_{2r} = -1,895 \text{ pm}/\mu\epsilon$. From this values, and assuming that the smallest measurable wavelength shift is 1 pm, we deduce from (13) that the smallest measurable radial strain is $\Delta\epsilon_r = 1,4 \mu\epsilon$ and the smallest measurable axial strain is $\Delta\epsilon_z = 0,85 \mu\epsilon$.

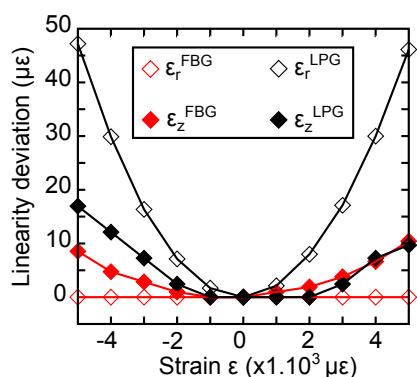


Figure 9. Deviation from linearity.

IV. CONCLUSION

In this article, we studied an optical fiber sensor designed to discriminate axial and radial strains when embedded in a material host. The sensor is made of the juxtaposition of a fiber Bragg grating and a long period grating inside the core of a three layer optical fiber. The specifications were to obtain a linear response of the sensor and a resolution similar to classical strain Gauge for the axial strain resolution, i.e., 1 micro-strain. Among all the parameters we identified two relevant parameters : the radius of the inner cladding and the period of the long period grating. We then searched optimal values of these parameters and found several configurations. The most promising are associated to cladding mode orders 1 and 3. These configurations present smaller radii of inner cladding which makes the sensor less sensitive to bending, and higher coupling coefficients which allows smaller lengths for the gratings. They allow to measure the axial strain with a resolution of $0,85 \mu\epsilon$ and the radial strain with a resolution of $1,4 \mu\epsilon$. This result is a real advance in strain measurement since a classical embedded strain fiber sensor can not discriminate axial and radial strain. Moreover, the resolution on axial strain of a FBG mounted on surface is of the order of $1 \mu\epsilon$. The range of measurable strain with a linear response is $[-5000 \mu\epsilon; +5000$

$\mu\epsilon]$. In this range, the deviation from linearity is less than 1%. All these properties can make this sensor a very useful tool for the measurement of strain inside structures. The next step is to investigate its sensitivity to bending.

REFERENCES

- [1] T. Chan, L. Yu, H. Tam, Y. Ni, S. Liu, W. Chung, and L. Cheng, "Fiber bragg grating sensors for structural health monitoring of tsing ma bridge: Background and experimental observation," *Engineering Structures*, vol. 28, no. 5, 2006, pp. 648 – 659. [Online]. Available: <http://www.sciencedirect.com/science/article/pii/S0141029605003421>
- [2] R. Ramly, W. Kuntjoro, and M. K. A. Rahman, "Using embedded fiber bragg grating (fbg) sensors in smart aircraft structure materials," *Procedia Engineering*, vol. 41, no. 0, 2012, pp. 600 – 606, international Symposium on Robotics and Intelligent Sensors 2012 (IRIS 2012). [Online]. Available: <http://www.sciencedirect.com/science/article/pii/S1877705812026185>
- [3] F. Surre, R. H. Scott, P. Banerji, P. Basheer, T. Sun, and K. T. Grattan, "Study of reliability of fibre bragg grating fibre optic strain sensors for field-test applications," *Sensors and Actuators A: Physical*, vol. 185, no. 0, 2012, pp. 8 – 16. [Online]. Available: <http://www.sciencedirect.com/science/article/pii/S0924424712004153>
- [4] Y. Gebremichael, W. Li, W. Boyle, B. Meggitt, K. Grattan, B. McKinley, G. Fernando, G. Kister, D. Winter, L. Canning, and S. Luke, "Integration and assessment of fibre bragg grating sensors in an all-fibre reinforced polymer composite road bridge," *Sensors and Actuators A: Physical*, vol. 118, no. 1, 2005, pp. 78 – 85. [Online]. Available: <http://www.sciencedirect.com/science/article/pii/S0924424704005461>
- [5] M. Bocciolone, G. Bucca, A. Collina, and L. Comolli, "Pantograph-catenary monitoring by means of fibre bragg grating sensors: Results from tests in an underground line," *Mechanical Systems and Signal Processing*, vol. 41, no. 12, 2013, pp. 226 – 238. [Online]. Available: <http://www.sciencedirect.com/science/article/pii/S0888327013003142>
- [6] D. Leduc, Y. Lecieux, P.-A. Morvan, and C. Lupi, "Architecture of optical fiber sensor for the simultaneous measurement of axial and radial strains," *Smart Materials and Structures*, vol. 22, no. 7, 2013, p. 075002. [Online]. Available: <http://stacks.iop.org/0964-1726/22/i=7/a=075002>
- [7] S. Triollet, L. Robert, E. Marin, and Y. Ouerdane, "Discriminated measures of strain and temperature in metallic specimen with embedded superimposed long and short fibre bragg gratings," *Measurement Science and Technology*, vol. 22, no. 1, 2011, p. 015202.
- [8] V. Bhatia, "Proprieties and sensing applications of long period gratings," Ph.D. dissertation, Faculty of the Virginia Polytechnic Institute, November, 1996.
- [9] T. Erdogan, "Cladding-mode resonances in short- and long-period fiber grating filters," *Journal of the Optical Society of America A*, vol. 14, Aug. 1997, pp. 1760–1773.
- [10] H. Kogelnik, "2. theory of dielectric waveguides," in *Integrated Optics*. Springer, 1975, pp. 13–81.
- [11] P. FERDINAND, "Capteurs fibres optiques rseaux de bragg," *Techniques de l'ingnieur CND : mthodes surfaciques*, vol. base documentaire : TIB586DUO., no. ref. article : r6735, 2015.

A Multi-Directional Thermal Flow Sensor Fabricated On Flexible Substrate

Anastasios Moschos, Dimitrios Barmpakos, Grigoris Kaltsas

Department of Electronics Engineering
 Technological Educational Institute of Athens
 Athens, Greece
 e-mail: G.Kaltsas@ee.teiath.gr

Abstract—A multi-directional thermal flow sensor was developed and preliminary evaluation was made. The presented device utilizes simple manufacturing techniques and commercially available components. In addition, the sensing elements are completely isolated from the flow channel and therefore the device is ideally suited for a wide range of applications. Preliminary experimental results indicate adequate flow rate and direction sensitivity.

Keywords—thermal flow sensor; directional; plastic substrate

I. INTRODUCTION

Directional flow sensors are used in a variety of applications, including meteorology [1], avionics [2], wind turbine design and monitoring [3], building ventilation systems design [4], agricultural production optimization [5] and the automotive industry [6]. Thermal directional sensors, in particular, have been developed and studied more extensively since the introduction of relative silicon-based devices [7] and various implementations have been presented, introducing diverse designs in order to enhance sensor performance. Additional sensing elements in varying distances from the heater have been shown to widen the flow rate detection range, [8] [9], while the addition of sensing elements in tighter angles, as expected, provides a more accurate flow direction estimation [10] and the incorporation of more than one heater improves sensitivity [11] [12]. However, most of the existing implementations require complicated MEMS manufacturing technology and are relatively fragile due to bonding wire connections and exposed sensing elements.

In this work a simple, inexpensive implementation of a thermal multi-directional flow sensor based on previously published work [13] is presented, resulting in a robust, maintenance-free device suitable for harsh environments.

II. PRINCIPLE OF OPERATION

The present device incorporates a quadruplet of orthogonally placed sensing elements equidistant in respect to a centered heater (Figure 1a). This configuration allows for determination of the two main flow parameters (flow value and direction).

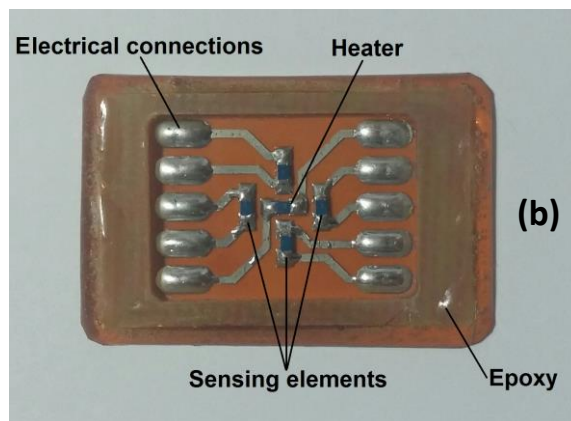
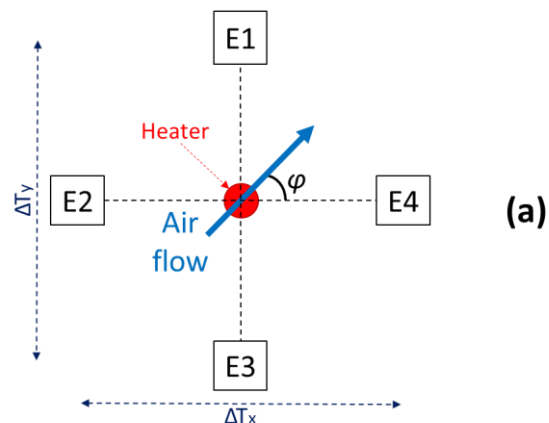


Figure 1. a) Sensor layout representation. ΔT_x and ΔT_y are the temperature differences measured between sensing element pairs E2-E4 and E1-E3 respectively.

b) Actual device layout, shown before encapsulation. The center heater and the surrounding sensing element pairs are visible.

The heater is operated in constant current mode in order to simplify the sensor interface. The flow rate value can be extracted from the temperature drop of the heater, while the flow angle ϕ is derived from the differential signals of the sensing elements, which are correlated to the flow direction according to the following functions [11]:

$$\Delta T_x = \Delta T_0 \cos\phi \tag{1}$$

$$\Delta T_y = \Delta T_0 \sin\phi \tag{2}$$

$$\phi = \arctan (\Delta T_y / \Delta T_x) \tag{3}$$

ΔT_0 represents the temperature drop induced on the sensing element pairs by the applied flow (Figure 1b). The signs of ΔT_y and ΔT_x must be taken into account when calculating the inverse tangent in order to obtain four-quadrant results.

III. SENSOR FABRICATION

The sensor is based on standard Printed Circuit Board manufacturing technology and readily available components, thus producing a simple, cost-effective approach with highly repeatable results.

A 100 μ m thick polyimide film is used as substrate. After patterning of conductive traces and soldering the sensing elements at a distance of 2,5mm from the heating element, the device was sealed using epoxy materials and flipped vertically (Figure 2), thus the heater/sensing elements are completely chemically and mechanically isolated from the fluid while allowing thermal interaction via the thin polyimide membrane. Despite the sensing element isolation, sufficient thermal coupling is attained due to the small thickness of the membrane, hence adequate sensitivity and detection range are achieved. It should be underlined that flow is applied on the external surface of the substrate (Side 2 in Figure 2e).

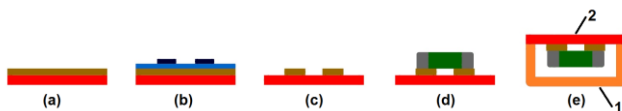


Figure 2. Fabrication steps: (a) pre-laminated substrated, (b) masking & definition, (c) patterning and copper etching, (d) PT100 element soldering, (e) sensor encapsulation in epoxy material < 1 >, allowing thermal coupling of the flipped sensor to the fluid only via the polyimide membrane < 2 >. note: dimensions are not to scale

IV. RESULTS

Device characterization was made using a measurement setup consisting of a controllable flow rate source providing the reference flow, whereas the device was mounted to a turntable controlled by a stepper motor. A 30mA current was applied to the heater by a Keithley 2612 sourcemeter, corresponding to 110mW under zero flow conditions. The sensing elements' response was constantly monitored by a multi-channel Keithley 2000 multimeter. Figure 3 illustrates the device response as a function of the flow, for rates in the region 0-50 Standard Liters Per Minute.

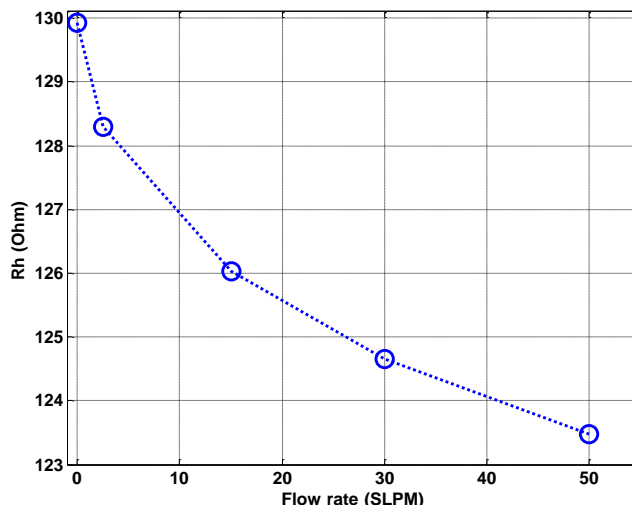


Figure 3. Heater resistance as a function of the applied flow

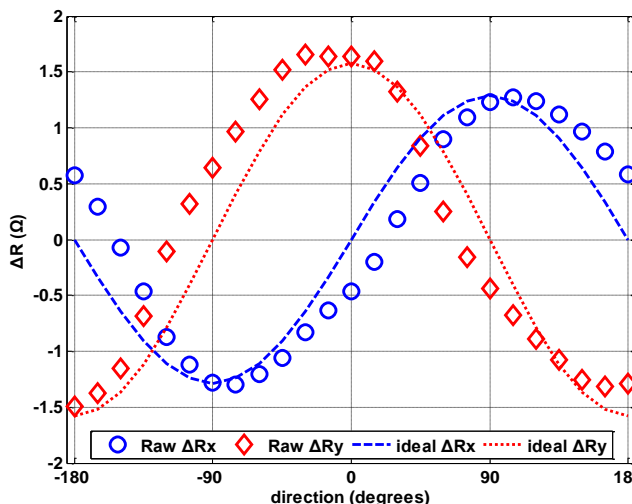


Figure 4. Heater resistance as a function of the applied flow

The aforementioned response corresponds to the heater's resistance change under hot-wire principle of operation. As mandated by the IEC60751 standard the PT100 sensing elements' resistance presents an effectively linear correlation to temperature for $T > 0^{\circ}\text{C}$ and a small temperature variation, therefore ΔT_x and ΔT_y in equations (1), (2) and (3) can be substituted by $k\Delta R_x$ and $k\Delta R_y$ respectively, where ΔR_x represents the difference in resistance of the element pair along the x and y axis accordingly and k a linear constant factor. The device response as a function of flow direction is presented in Figure 4, where the parameters ΔR_x and ΔR_y are plotted in relation to the turntable angle in the range -180 to 180 degrees in 15 degree steps. A constant flow rate of 40 SLPM was applied during the directional response evaluation. Experimental results indicate that the flow angle

can be extracted with sufficient accuracy. Although a phase difference and a small vertical offset is observed in comparison to ideal response curves, the deviations can be attributed to slight asymmetries in the device layout. Partial compensation can be made by subtraction of the phase offset from the data waveform and amplitude normalization around zero as indicated in Figure 5. In this case, improved direction estimation can be obtained (Figure 6), resulting in a mean error in the order of ± 3.5 degrees.

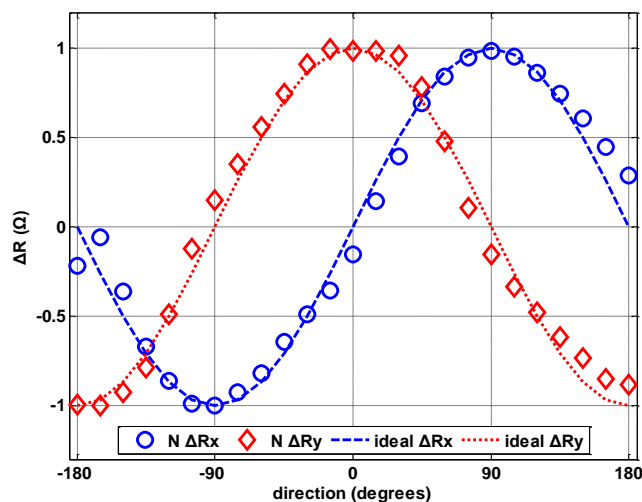


Figure 5. Compensated differential data as a function of the flow angle

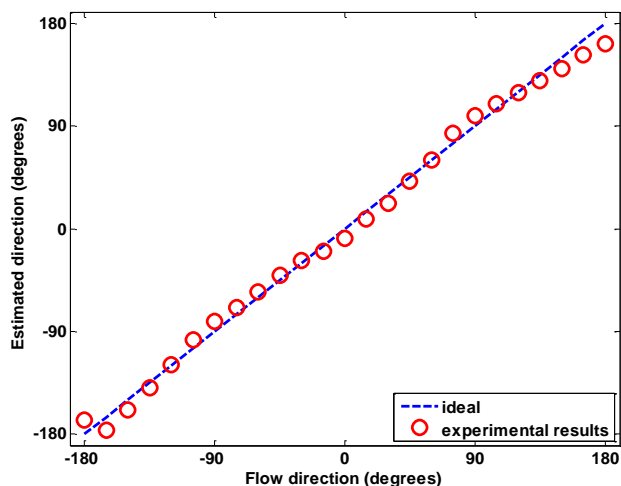


Figure 6. Estimated flow angle as a function of the actual values

V. CONCLUSION

In this research, a thermal gas flow sensor for measuring two-dimensional flow was developed and a preliminary evaluation in constant current mode was performed. In the proposed approach the flow is completely isolated from the active elements of the device. Obtained measurements show promising results considering the low cost and complexity of

the implementation with a measurable flow rate range extending from about 2 up to more than 50 SLPM and a mean absolute angle error of $\pm 3,5$ degrees, after applying simple software phase compensation on the measurements. Further sensor development with improvement of the layout precision and additional processing of the measurements is expected to provide a solid low-cost alternative option, especially for harsh environment applications.

ACKNOWLEDGMENTS

This work is partially supported by the IKY Fellowship of Excellence for Postgraduate Studies in Greece- Siemens Program (2013-2015).

REFERENCES

- [1] E. van Doorn, et al., "Statistics of wind direction and its increments," *Physics of Fluids* (1994-present) 12.6 (2000), Pages 1529-1534.
- [2] J.R. Platt, "Wind detection in a microcosm: ship/aircraft environment sensors," *Aerospace and Electronic Systems Magazine*, IEEE 13.2 (1998), Pages 26-33.
- [3] I. Abohela, N. Hamza, and S. Dudek, "Effect of roof shape, wind direction, building height and urban configuration on the energy yield and positioning of roof mounted wind turbines," *Renewable Energy*, Volume 50, February 2013, Pages 1106-1118.
- [4] T. van Hooff, B. Blocken, "On the effect of wind direction and urban surroundings on natural ventilation of a large semi-enclosed stadium," *Computers & Fluids*, Volume 39, Issue 7, August 2010, Pages 1146-1155.
- [5] E. Gil, M. Gallart, P. Balsari, P. Marucco, M. P. Almajano, and J. Llop, "Influence of wind velocity and wind direction on measurements of spray drift potential of boom sprayers using drift test bench," *Agricultural and Forest Meteorology*, Volume 202, 15 March 2015, Pages 94-101.
- [6] M. F. Yassin, M. Ohba, "Experimental study of the impact of structural geometry and wind direction on vehicle emissions in urban environment," *Transportation Research Part D: Transport and Environment*, Volume 17, Issue 2, March 2012, Pages 161-168.
- [7] J. H. Huijsing, J. P. Schuddemat, and W. Verhoef, "Monolithic integrated direction sensitive flow sensor," *IEEE Trans. Electron Dev.*, ED-29 (1982), Pages 133 – 136.
- [8] N. T. Nguyen, "A novel wind sensor concept based on thermal image measurement using a temperature sensor array," *Sensors and Actuators A: Physical* 110.1 (2004), Pages 323-327.
- [9] Yarali, Milad, and S. K. Khanna, "Microfabrication of a variable range and multi-directionally sensitive thermal flow sensor," *Sensors and Actuators A: Physical* 220 (2014), Pages 159-167.
- [10] Keplinger, Franz, et al., "Highly sensitive sensor for flow velocity and flow direction measurement," *Sensors*, 2006. 5th IEEE Conference on Sensors, IEEE, 2006, Pages 1436-1439.
- [11] B. W. Van Oudheusden, J. H. Huijsing, "Integrated silicon flow-direction sensor," *Sensors and Actuators* 16.1 (1989), Pages 109-119.

- [12] K. A. Makinwa, J. H. Huijsing, "A smart wind sensor using thermal sigma-delta modulation techniques," *Sensors and Actuators A: Physical* 97 (2002), Pages 15-20.
- [13] A. Moschos, A. Petropoulos, E. Zervas, S. Athinaios, and G. Kaltsas, "Thermal Flow Measurements by a Flexible Sensor, Implemented on the External Surface of the Flow Channel," *Procedia Engineering*, Volume 87, 2014, Pages 1366-1369.

Development of a Novel Approach for Detecting Wood Decays in Living Trees Using Gas-Sensor Arrays

Manuela Baietto, Sofia Aquaro, Daniele Bassi
Dipartimento di Scienze Agrarie e Ambientali (DISAA)
Università degli Studi di Milano
Milano, Italy
e-mail: manuela.baietto@unimi.it

Alphus Dan Wilson
Forest Insect and Disease Research
USDA Forest Service, Southern Hardwoods Laboratory
Stoneville, MS, USA
e-mail: dwilson02@fs.fed.us

Letizia Pozzi
Demetra Società Cooperativa Sociale ONLUS
Besana in Brianza, Italy
e-mail: pozzi@demetra.net

Abstract— Wood rot is a serious fungal disease of trees. Wood decay fungi penetrate and gain entry into trees through pruning cuts or open wounds using extracellular digestive enzymes to attack all components of the cell wall, leading to the destruction of sapwood which compromises wood strength and stability. On living trees, it is often difficult to diagnose wood rot disease, particularly during extreme weather conditions when trees can fail, causing tree parts to fall onto people and property. Today, tree stability evaluation and inner decay detection are performed visually and by the use of commercial instruments and methods that are often invasive, time-consuming and sometimes inadequate for use within the urban environment. Moreover, most conventional instruments do not provide an adequate evaluation of decay that occurs in the root system. A long-term research project, initiated in 2004, was aimed at developing a novel approach for diagnosing inner tree decays by detecting differences in volatile organic compounds (VOCs) released by wood decay fungi and wood from healthy and decayed trees. Different commercial electronic noses (ENs) were tested under laboratory conditions and directly in the field, on healthy and artificially-inoculated stem wood chips, and root fragments. For the final stage, soil air was evaluated for the presence of VOCs released by root-decaying fungi on diseased standing trees cultivated in the urban environment.

Keywords- *electronic nose; decay detection; urban forestry; VOCs; tree.*

I. INTRODUCTION

Trees in urban environments are cultivated under conditions that are extremely hostile (causing many stresses and negative effects) and consequently inadequate to sustain healthy plant life. Frequently, trees must face high levels of air, soil and water pollution [1]. Root development is often limited by permanent water stress and very small soil volume for root expansion, providing inadequate support of above-ground plant parts [2][3]. Moreover, road works, hasty or poor pruning methods, and vandalism increase tree stress in the urban environment. These adverse environmental factors

dramatically increase physiological stresses that decrease tree fitness and increase susceptibility to attack by pathogenic agents [4].

Wood decay fungi are some of the worst microbial pathogens because they can take advantage of tree physiologic stresses by attacking and destroying all woody components, reducing tree structural stability, leading to failure (breaks) especially during severe weather events [5][6]. Root rots (decays) are even more dangerous and severe, due to difficult detection and the possibility of causing wind throw to the ground (complete tree loss). Trunk and root rot diagnoses in standing trees currently are performed primarily by electrical conductivity meters, constant feed drills, single pulse sonic and ultrasonic techniques, core samples, computerized tomography, and molecular methods for identification of decay fungi [7]. These tools and methods are pensive, invasive, require very skilled personnel, and do not provide systemic information. For these reasons, a multi-year study aimed at developing a novel approach for diagnosing inner tree decays using several gas sensor arrays or ENs was tested.

Section II of this paper is focused on presenting a small bibliographic review on recent findings about VOCs emitted by wood and wood decay fungi. Section III presents all the electronic noses tested in our experiments. Section IV represents results and discussions of our experiments, supported by graphic outputs.

II. VOCs EMITTED BY WOOD AND DECAYING FUNGI

Live standing trees containing decayed wood release a particular mixture of volatile organic compounds (VOCs) consisting of fungal metabolites, tree metabolites, and fungus-induced tree antimicrobial defense compounds (e.g. phenolic metabolites, terpenoids, isoprenoids, and phytoalexins). The composition of metabolites released by individual fungi is controlled largely by the types and combinations of metabolic pathways specific to microbial

species, which are regulated by genetic, substrate and environmental factors [8]. Korpi *et al.* [9] found microbes that released pinenes, acrolein, ketones and acetylenes that were irritants to mice. Other investigations have focused on the identification of VOCs released by food spoilage fungi [10][11]. The compound 1-octen-3-ol was detected in damp houses containing various mold fungi [12]. Numerous other chemical species have been reported as fungal metabolites, including complex acids, sesquiterpenes, methyl ketones and alcohols [13]. Relatively few recent studies have reported on the release of VOCs by healthy and decayed trees. An analysis of healthy *Populus* spp. and *Pinus* spp. indicated the presence of mainly monoterpenes, acetone and small amounts of isoprene [14]. Other studies have indicated increases in toluene and α -pinene emissions associated with *P. sylvestris* under pathogen attack [15], and a decrease in isoprene emissions from diseased *Quercus fusiformis* L. and *Q. virginiana* L. [16]. The bacteriostatic role of plant VOCs was studied by Gao *et al.* [17] who found emissions of terpenoids, alcohols, aldehydes, organic acids, and esters released by five healthy coniferous species in which α -pinene, β -pinene, 2,(10)-pinene, myrcene and d-limonene represented more than 95% of total VOC emissions. Increased levels of α -pinene, limonene, nonaldehyde and benzaldehyde also were found in artificially-inoculated wood shaves in the same study.

III. ELECTRONIC NOSES

The EN is an instrument that mimics the human olfactory apparatus to detect VOCs through a series of sensors (sensor array) that provide digital signatures (sensor patterns) of all volatile chemicals present in the aroma bouquet of the sample analyte. In this experiment, we employed three different commercially available ENs.

A. AromaScan A32S Electronic nose

The AromaScan 32S (Osmetech Inc., Wobum, MA, USA) is a conducting polymer (CP) EN that contains an organic matrix-coated polymer-type 32-sensor array designed for general use applications with 15 V across sensor paths. The sensor array response to different VOCs was tested previously [8]. Sensors responses are measured as a percentage of electrical resistance changes to current flow in the sensors relative to baseline resistance ($\% \Delta R/R_{base}$). The sorption of headspace volatiles, composed of specific VOC mixtures, to the CP sensor surfaces induces a change in the electrical resistance to current flow, which is detected and measured to produce the sensor array output. Sensor responses varied with the type of plastic polymer used in the sensor matrix coating, produced by electropolymerization of either polypyrrole, polyaniline or polythiophene derivatives, which have been modified with ring substitutions of different functional groups and with the addition of different types of metal ions to the polymer matrix in order to improve and modulate

sensor response. All measurements were statistically compared using normalized sensor outputs from the sensor array. Conducting polymer analysis methods used with this instrument employ application-specific reference libraries for aroma pattern recognition and neural-net training algorithms.

B. Lybranose 2.1 Electronic nose

Operation of this EN is based on the quartz crystal microbalance (QCM) technology, which can be described as an ultrasensitive sensor capable of measuring small changes in mass on a quartz crystal recorded in real-time. The heart of the QCM is the piezoelectric AT-cut quartz crystal sandwiched between a pair of electrodes. The electrodes are attached to an oscillator. When an AC voltage is applied over the electrodes, the quartz crystal starts to oscillate at its resonance frequency due to the piezoelectric effect. If sample volatiles are evenly deposited onto one or both of the electrodes, the resonant frequency will decrease proportionally to the mass of the adsorbed layer according to the Sauerbrey equation [18]. The LibraNose 2.1 (Technobiochip, Pozzuoli, NA, Italy) sensor array consists of eight 20 MHz AT-cut QCM sensors with a gold surface (Gambetti Kenologia, Binasco, PV, Italy) coated with either metalloporphyrines, deposited by solvent casting, or by polypyrrole polymer) films (Technobiochip patent. no. 04425560.2-2102) deposited by means of Langmuir-Blodgett technology using a KSV 5000 film-deposition device (KSV Instruments, Helsinki, Finland). This process utilizes 0.3 mg/mL polymers dissolved in chloroform and ultrapure, distilled water as a subphase.

C. PEN3 Electronic nose

The PEN3 EN (Airsense Analytics GmbH, Schwerin, Germany) is a very compact instrument (255 × 190 × 92 mm), light-weight (2.1 kg) and portable olfactory system. It consists of an array of 10 different doped metal-oxide semi-conductive (MOS) gas sensors positioned into a very small chamber with a volume of only 1.8 ml. The instrument operates with filtered, ambient air as a carrier-gas at a flow rate of 10-400 ml min⁻¹, sample-chamber temperature of 0-45 °C, and sensor array operating temperature of 200-500 °C. The sensing reaction is based on an oxygen exchange between the volatile gas molecules and the metal coating material. Electrons are attracted to the loaded oxygen and result in decreases in sensor conductivity. Instrument sensitivity to various gas analytes ranges from 0.1-5.0 ppm.

IV. MAIN GOALS

This research project, a pioneer in the field of plant pathology and urban forestry, is based on following steps starting from basic research to be applied to finalized research solution. In every phase we have formulated a hypothesis derived from a question, with the aim to verify if the instrument could give positive answers.

A. Can the EN discriminate between healthy and inoculated wood samples?

The first step of the research was aimed at determining if wood decay fungi emit certain combinations of VOCs that can be detected and recognizable by ENs [19]. 11 wood decay fungi (WDF) strains were selected, cultivated and inoculated on wood chips samples (sapwood) taken from 19 tree species: *Fraxinus pennsylvanica* Marsh., *Liquidambar styraciflua* L., *Pinus taeda* L., *Platanus occidentalis* L., *Populus deltoids* Bartr. ex Marshall, *Quercus nuttallii* Palm., *Quercus lyrata* Walt., *Thuja occidentalis* L., *Taxodium distichum* L. *Acer negundo* L., *A. saccharinum* L., *Aesculus hippocastanum* L., *Castanea sativa* Mill., *Cedrus deodara* (D. Don) G. Don fil., *Celtis australis* L., *Platanus x acerifolia* Brot., *Quercus rubra* L., *Robinia pseudoacacia* L., and *Tilia* spp.. Species were selected from among the hardwood and conifer species most common in the lower Mississippi Delta and Northern Italy urban and forest environment, where the experiments were conducted. After 6, 12 and 24 months of incubation under standard conditions we evaluated the discrimination ability of all three selected ENs. Figures 1-3 show some results of this step.

Figure 1.a reports about the ability of Lybranose 2.1 in discriminating healthy and inoculated wood samples of all tree species with all fungal species. Although some zones of the graph show some overlaps between the two types, it is possible to assert that WDF emit volatiles which are clearly discriminable for the instrument. PEN3, differently, but clearly discriminated healthy and inoculated wood samples (Fig. 1.b).

Running Principal Component Analysis (PCA) on samples belonging to one single tree species inoculated with different fungal strains, it is clear as the EN (Fig. 2) can easily discriminate the different WDF species.

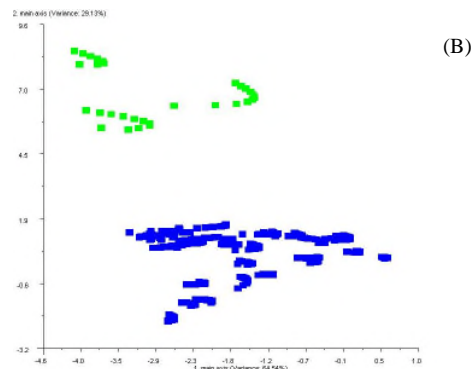
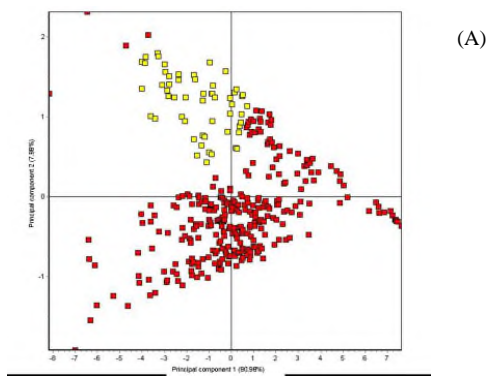


Figure 1(A-B). Discrimination of volatiles from healthy and decayed wood block using PCA. Labels are as follows: yellow and green labels indicate volatiles from healthy controls and red and blue labels indicate volatiles from decayed samples

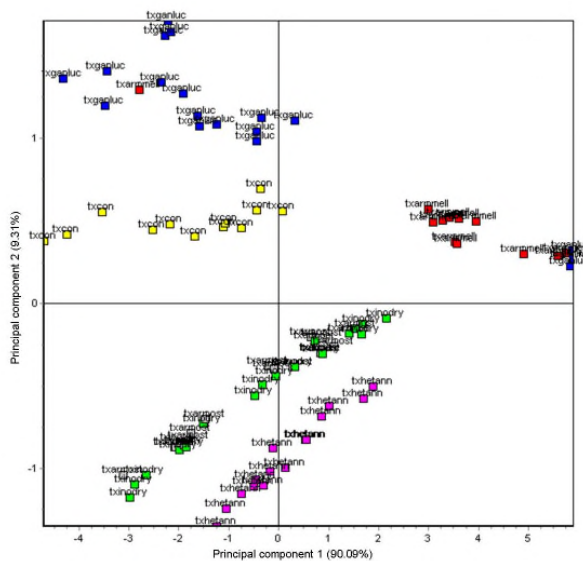


Figure 2. Discrimination of volatiles from artificially-inoculated decayed wood samples of *Tilia* spp. by PCA. Different color labels indicate different wood decay fungi responsible for decay. Undecayed (control) wood block are labeled in yellow

B. Can the EN discriminate between healthy and inoculated root samples under soil conditions?

The root system is the most important organ for initiating plant growth as it is dedicated to the uptake of water and minerals. In trees, structural roots give mechanical support to the heavy woody structure. The root system is by nature the least known of all tree organs as it is not assessable other than by destructing methods. As far as root decay diagnoses are concerned, there are not commercially available tools capable of assessing and diagnosing decays in the root system.

This phase of the research, aimed at determining if the presence of VOCs emitted by wood decaying fungi or decayed living wood can be detected even under-soil conditions, utilized root tissue from four species of shade trees [7]. Parts of 1 cm healthy roots were sampled from each tree in which roots were prepared and inoculated with four

different WDF strains (two strains of *Armillaria mellea*, one of *Ganoderma lucidum* and one of *Heterobasidion annosum*). Inoculated root chips were then incubated under two different kinds of soils (very poor urban soil and professional soil for horticulture) for 12 months at standard laboratory conditions.

Our results show that: (1) PEN 3 EN could easily discriminate between inoculated and non-inoculated root chips after 12 months of incubation; (2) PEN 3 EN could not discriminate the inoculated samples from the healthy ones after only 6 months from the inoculation. This means that under soil conditions, wood decay fungi take a little more time to develop enough VOCs to be detected from the EN (Fig. 3); (3) Soil type does have an influence on the discrimination capability of the instrument. This is probably due to the fact that professional soil type, which is still rich in microorganisms, emits a strong aroma bouquet.

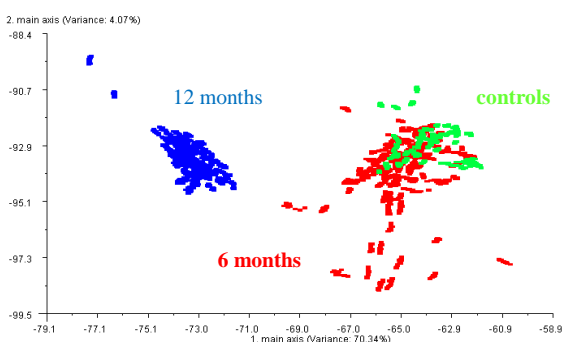


Figure 3. Discrimination of VOCs from healthy controls (green labels) and artificially-inoculated root chips after 6 months (red labels) and 12 months (blue labels) from inoculation using PCA.

C. Can the EN detect the presence of a decay in the root system of standing trees directly in the field?

All previous steps of this long research were aimed at evaluating the diagnostic feasibility of EN under the stable and standardized conditions of the laboratory environment. In this stage, the EN was employed directly in the field to detect the presence of VOCs emitted by wood decay fungi attacking the root system.

A very important postulate of this research is that the diagnostic system (tool as well as sampling method) should be totally non-invasive for the plant. Wounds caused by sampling, diagnosis or analysis method could eventually be preferred entry points for further pathogenic attack. According to this, a revolutionary sampling method was tested based on detecting decay fungi that emit VOCs which diffuse in soil air macropores. To sample and analyze soil air, a pump system was designed and built as seen in figure 4, in which soil air is sucked in by the pump and directly carried to Nalophan bags for e-nose analysis.

For this final stage of the research, more than 60 trees planted in the city of Milano, Italy, belonging to five different species [*Acer negundo* L., *A. negundo* 'Variegatum', *A. pseudoplatanus* L., *Aesculus*

hippocastanum L., and *Platanus x acerifolia* (Aiton) Willd were sampled].



Figure 4. The automatic pump employed in the field to put directly soil air in Nalophan bags

All of these trees were previously assessed via conventional methods for the presence of stem and root decays. Soil air was sampled six times over a period of two years.

Our preliminary results, shown in figures 5-7, demonstrate that WDF VOCs can be found in soil macropores, and that their concentration in the zone of the root system is high enough to be detected by EN sensors. Figure 5 shows a linear discriminant analysis (LDA) performed on soil air samples taken about 30 cm from the bole of healthy and decayed trees. The etiologic agent causing decays in sample trees, previously recognized via traditional methods, was also recognized by the EN. Figure 6 shows the diagnostic feasibility of the PEN 3 EN in discriminating between different WDF species. Soil air or healthy control trees also were used to check if healthy root systems release the same VOCs as those released by trunk sapwood; and if ENs can discriminate between species on the basis of those VOCs. Figure 7 shows the discrimination feasibility of the PEN 3 EN between different healthy tree species on the basis of VOC analysis in the aroma bouquet released by root systems sampled at about 30 cm from the bole by the use of an air pump.

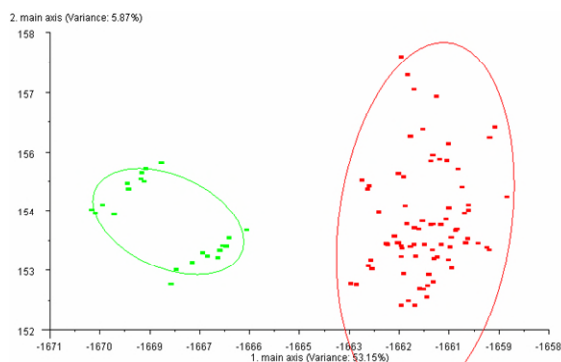


Figure 5. Linear Discriminant Analysis performed on volatiles in soil air samples taken 30 cm from the bole of healthy (green labels) and decayed (red labels) standing trees.

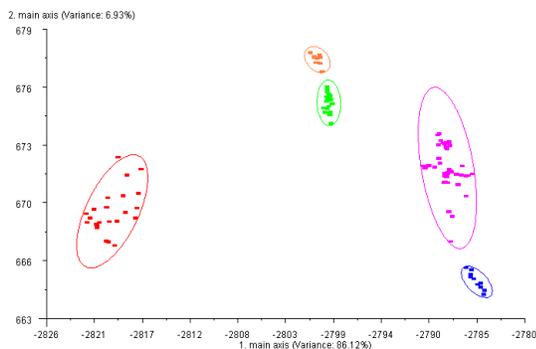


Figure 6. PCA performed on volatiles in soil air samples taken 30 cm from the bole of healthy (green labels) and decayed standing trees. Different colors correspond to main etiologic decay agent: *Armillaria* spp. (red labels), *Meripilus giganteus* (orange), *Ganoderma* spp. (pink) and *Perenniporia* ssp. (blue labels).

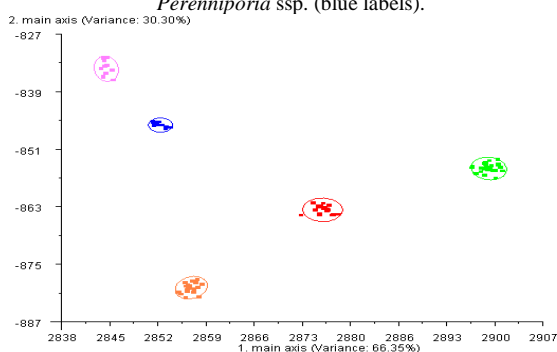


Figure 7. PCA performed on volatiles in soil air samples taken 30 cm from the bole of healthy standing trees. Different colors correspond to different species as following: *Metasequoia glyptostroboides* (pink labels), *Fagus sylvatica* (blue), *F. sylvatica* 'Pendula' (red), *Aesculus hippocastanum* (green) and *Quercus rubra* (orange).

V. CONCLUSIONS

Tree cultivation in the urban environment requires some agronomic works which are particularly important and expensive for Public Administrators. Among these, pruning and maintaining tree stability most influence the annual budget of ordinary management. Tree stability assessment, a fundamental duty to prevent sudden tree failures so ensure citizen's safety, is performed by very skilled personnel who employ commercial instruments and tools which are, in most of cases, invasive and very expensive. Decay assessment of the root system is not currently performed, as there are no commercially available instruments besides ENs capable of these assessments.

Our experimental research started about 10 years ago, was aimed at developing a sampling and analysis methodology to determine the presence of active wood decay and root rots on standing trees, in a rapid and non-invasive way, applicable in all situations and usable by non-skilled operators. Through multiple stages of research, we have demonstrated that three different commercial ENs can discriminate: between different tree species and WDF species by analyzing the VOCs in the aroma bouquet

released by healthy (non-inoculated) and inoculated trunk wood chips; between healthy (non-inoculated) and inoculated root chips incubated under two different kinds of soils; between healthy and decayed living and standing trees, between different species of healthy standing trees, and between etiologic agents of diseased standing trees on the basis of the analysis of the aroma bouquet present in the soil air (macropores) sampled near the tree bole.

The EN system is not fully ready to be employed daily in the field yet, as it is necessary to build application-specific aroma signature databases of healthy tree species at different stages of growth, development and phenologic phase, as well as diseased tree species, decayed by different wood decay fungi species, in order to train ENs to yield immediate answers directly in the field.

ACKNOWLEDGMENT

This multi-year research was funded by Comune di Milano – Sett.re Tecnico Arredo Urbano e Verde, and from Demetra Società Cooperativa Sociale Onlus (Besana in Brianza, MB, Italy). The Authors would like to thank Dr. Daniele Guarino, Charisse Oberle, Luca Maccabelli, Raffaello Brambilla and Lorenzo Presicce for their help in sampling and analyzing data.

REFERENCES

- [1] B. Skrbic, M. Snezana, and M. Matavulj, "Multielement profiles of soil, road dust, tree bark and wood-rotten fungi collected at various distances from high frequency road in urban area," *Ecol. Indicat.*, vol. 13, pp. 168-177, 2012.
- [2] T. B. Randrup, "Urban soils as a growing medium for urban trees," in *Urban Forestry in the Nordic countries. Proceedings of a Nordic Workshop on Urban Forestry*, T.B. Randrup, K. Nilsson, and P. Nilsson, Eds., Danish Forest and Landscape Research Institute: Hoersholm, 1996, p. 59.
- [3] S. D. Day, J. R. Seiler, and N. Persaud, "A comparison of root growth dynamics of silver maple and flowering dogwood in compacted soil at differing soil water content," *Tree Physiol.*, vol. 20, pp. 257-263, 2000.
- [4] C. J. Luley, *Wood Decay Fungi Common to Urban Living Trees in the Northeast and Central United States*, Urban Forestry LLC: Naples, 2005.
- [5] D. Lonsdale, *Principles of tree hazard assessment and management*. Forest Commission: Farnham, 1999.
- [6] N. P. Manthey and J. R. Clark, J. R., *A Photographic Guide to the Evaluation of Hazard Trees in Urban Areas*, 2nd ed., International Society of Arboriculture: Savoy, 1994.
- [7] M. Baietto, L. Pozzi, A. D. Wilson, and D. Bassi, "Evaluation of a portable MOS electronic nose to detect root rots in shade tree species," *Computer and Electronics in Agriculture*, vol. 93, pp. 117-125, 2013.
- [8] A. D. Wilson, D. G. Lester, and C. S. Oberle, "Development of conductive polymer analysis for the rapid detection and identification of phytopathogenic microbes," *Phytopathology*, vol. 94, pp. 419-431, 2004.
- [9] A. Korpi, J. P. Kasanen, Y. Alarie, V. M. Kosma, and A. L. Pasanen, "Sensory irritating potency of some microbial volatile organic compounds (MVOCs) and a mixture of five MVOCs," *Arch. Environ. Health.*, vol. 54, pp. 347-352, 1999.

- [10] N. Magan and P. Evans, "Volatiles as an indicator of fungal activity and differentiation between species, and the potential use of electronic nose technology for early detection of grain spoilage," *J. Stored Prod. Res.*, vol. 36, pp. 319-340, 2000.
- [11] B. J. P. de Lacy Costello, R. J. Ewen, H. E. Gunson, N. M. Ratcliffe, and P.T.N. Spencer-Phillips, *Sensors for early warning of postharvest spoilage in potato tubers*, British Crop Protection Council: Farnham, UK, pp. 425-432, 2002.
- [12] G. Strom, J. West, B. Wessen, and U. Palmgren, "Quantitative analysis of microbial volatiles in damp Swedish houses," in *Health Implications of Fungi in Indoor Environments*, R.A. Samson, B. Flannigan, M.E. Flannigan, A.P. Verhoefl, O.C.G. Adan, and E.S. Hoekstra, Eds. Elsevier: Amsterdam, The Netherlands, 1994, pp. 291-305.
- [13] R. J. Ewen, P. R. H. Jones, N. M. Ratcliffe, and P. T. N. Spencer-Phillips, "Identification by gaschromatography-mass spectrometry of the volatile organic compounds emitted from the woodrotting fungi *Serpula lacrimans* and *Coniophora puteana*, and from *Pinus sylvestris* timber," *Mycol. Res.*, vol. 108, pp. 806-814, 2004.
- [14] I. Villanueva-Fierro, C. J. Popp, and R. S. Marin, "Biogenic emissions and ambient concentration of hydrocarbons, carbonyl compounds and organic acids from ponderosa pine and cottonwood trees at rural and forested sites in Central New Mexico," *Atmos. Environ.*, vol. 38, pp. 249-260, 2004.
- [15] J. Faldt, H. Solheim, B. Langstrom, and A. K. Borg-Karlson, "Influence of fungal infection and wounding on contents and enatiomeric compositions of monoterpenes in phloem of *Pinus sylvestris*," *J. Chem. Ecol.*, vol. 32, pp. 1779-1795, 2006.
- [16] L. J. Anderson, P. C. Harley, and R. K. Monson, "Reduction of isoprene emissions from live oak with oak wilt," *Tree Physiol.*, vol. 20, pp. 1199-1203, 2000.
- [17] Y. Gao, Y. Jin, H. Li, and H. Chen, "Volatile organic compounds and their roles in bacteriostasis in five conifer species," *J. Integr. Plant Biol.*, vol. 47, pp. 499-507, 2005.
- [18] G. Sauerbrey, "Verwendung von Schwingquarzen zur Wägung dünner Schichten und zur Mikrowägung (The use of quartz oscillators for weighing thin layers and for microweighing)," *Z. Phys.*, vol. 155, pp. 206-222, 1959.
- [19] M. Baietto, A. D. Wilson, D. Bassi and F. Ferrini, "Evaluation of three electronic noses for detecting incipient wood decay," *Sensors*, vol. 10, pp. 1062-1092, 2010.

Bayesian Inference using Spike Latency Codes for Quantification of Health Endangering Formaldehyde

Muhammad Hassan and Amine Bermak

School of Engineering
Hong Kong University of Science & Technology, Hong Kong
Emails: mhassan@ust.hk, eebermak@ece.ust.hk

Amine Ait Si Ali and Abbes Amira

College of Engineering
Qatar University, Doha, Qatar
Emails: amine.aitsiali@qu.edu.qa, abbes.amira@qu.edu.qa

Abstract—Recently, the exposure to formaldehyde has appeared as a major concern since it is listed as a human carcinogen. Conventional methods for its long-term monitoring are not feasible due to their high operational cost, long analysis time and the requirement of specialized equipment and staff. In this paper, we use an electronic nose, containing an array of commercially available Figaro gas sensors, to estimate formaldehyde concentration. A hardware friendly bio-inspired spike latency coding scheme has recently been employed for gas classification by using relative time between spikes. We use this scheme to estimate formaldehyde concentration by utilizing absolute spike timings. However, there is no straightforward relationship between the spike latency and the formaldehyde concentration. Instead, stochastic variability in the sensor array response, corresponding to repeated exposure to the same formaldehyde concentration, implies that latency patterns of the sensor array encode probability distribution over the formaldehyde strength. We use a Bayesian inference approach to estimate the formaldehyde concentration, and its performance is successfully validated by acquiring data for formaldehyde with our sensor array at twenty different concentrations in the laboratory environment.

Keywords—Formaldehyde exposure; Sensor array; Spike latency coding; Bayesian inference.

I. INTRODUCTION

Formaldehyde (CH_2O) is one of the most ubiquitous and reactive aldehydes in the environment. It is a colourless and rapidly polymerizing gas at room temperature and is widely used in consumer products to protect them from spoilage by microbial contamination. It can also be found in pressed wood products, tobacco smoke and fuel burning appliances [1]. Recently, formaldehyde received great attention when it was considered as a human carcinogen in the report of International Agency for Research on Cancer [2]. This was based on sufficient evidence of carcinogenicity from studies of human cancers and exposure to formaldehyde. Higher concentration levels of formaldehyde in the indoor environment pose a serious health hazard to occupants of buildings. A recent study [3] reported increased concentration levels in urban areas. This alarming situation highlights the importance of formaldehyde monitoring with a low cost and robust solution on a long-term basis for healthy living. Unfortunately, traditional methods [3]-[6] can not be used for the long-term monitoring of formaldehyde because specialized equipment and staff are required for the analysis of air samples collected from the area being monitored. Moreover, the cost and analysis time associated with these methods is very high.

An electronic nose system, containing an array of gas sensors, emerged as a successful platform for the fast identification of gases in the last two decades and it is targeted for many applications like food quality checking [7], diseases diagnosis [8], bacteria identification [9], environmental monitoring [10], beverages classification [11], paper quality inspection [12] and identification of health endangering indoor gases [15]. In this paper, we use an electronic nose system, containing an array of six commercially available Figaro gas sensors, to acquire the signature of CH_2O at twenty different concentration values spanning from 0 to 5 parts per million (ppm).

Motivated by the recent experimental findings in the field of neuroscience which report a logarithmic relationship between the odor concentration and the spike latency of the mitral cell [13], a logarithmic time domain scheme is used for gas classification by translating a sensor array response into a spike latency pattern [14]. Hardware friendly rank order based classifiers are developed for gas identification by using this technique [14]-[17]. In these classifiers, the relative time between spikes is utilized to distinguish gases. We use this scheme to retrieve concentration information by using absolute spike latencies. However, there is no straightforward relationship between the absolute spike latency and the formaldehyde concentration as there is in the rank order based classifiers where the change in relative times between spikes does not change the classification performance as long as their temporal order is not changed. Generally, gas sensors exhibit randomness in their responses due to multiple reasons and as a result, stochastic variability is observed in the latency patterns.

In this paper, we use a probabilistic inference approach [18] to deal with this randomness in the latency patterns in order to estimate CH_2O concentration. Probabilistic models have been successfully used in neuroscience to build computational theories for perception and action [19]. There are two major steps in this approach. The first step is to learn the probability encoding model or the tuning curve for the spike latency patterns at each concentration value of the CH_2O from the experimental data obtained through the sensor array. The second step is to use a bayesian decoding model to estimate the formaldehyde concentration for a new test latency pattern by using the probability encoding model. The performance of this approach is evaluated by acquiring the data of twenty different concentration values of CH_2O in the laboratory environment.

The paper is organized as follows. Section II explains probabilistic inference approach for CH_2O concentration estimation. Section III describes the experimental setup for data

acquisition and evaluates the performance of our approach. Finally, the conclusion is drafted in Section IV.

II. PROBABILISTIC INFERENCE

A logarithmic time-domain encoding scheme has been used for gas identification in rank order based classifiers [14]-[17]. In these classifiers, the spike latency l_i of the i -th sensor corresponding to a target gas is represented as

$$l_i = \frac{\log x_i}{m_i} \quad (1)$$

where x_i denotes the sensitivity of the the sensor i and m_i is a sensor dependent parameter which is extracted through linear regression between the average log sensitivity of the sensors across the array as an explanatory variable and the sensitivity of the i -th sensor as an output variable. This spike latency carries information about the gas identity and its concentration. In rank order based classifiers, a temporal sequence of spikes referred to as a rank order is used for gas identification. Absolute spike latency is shifted with the change in the concentration but the temporal sequence of spikes remains fixed. In this paper, we use this logarithmic time-domain encoding scheme to retrieve concentration information by using absolute spike latency.

The potential challenge with this scheme is that the gas sensors usually exhibit randomness in their responses because of drift and as a result, stochastic variability is observed in the latency patterns. In this paper, we present a probabilistic inference approach to retrieve concentration information from the random latency patterns. Probabilistic approaches have been successfully used in developing computational paradigms for biological sensory systems [19].

The main objective of using probabilistic inference is to find the most probable concentration value of the new test latency pattern by learning the distribution of latency patterns corresponding to each concentration value from available measurements taken with the electronic nose. Let us consider the following notations for this probabilistic inference problem: suppose we have a set of concentrations $c=\{c_j\}$ and latency patterns obtained through the experiments where each latency pattern is denoted as $l=\{l_1, l_2, \dots, l_n\}$, where l_i represents the latency of the i -th sensor.

Probabilistic inference is a two step process [19]. In the first step, we learn a model fitting that captures the mapping from l to c from available sensor array measurements. In the second step, we use bayesian decoding to estimate the concentration value c_i from the new observed latency pattern l .

In order to learn model fitting, we need to know the distribution or probability encoding model of the latency pattern conditioned on the CH₂O odor intensity. With a particular model, parameterized by a vector θ , we can use maximum likelihood (ML) to obtain the optimal estimate $\hat{\theta}$ for which the latency patterns are most likely

$$\hat{\theta} = \operatorname{argmax}_{\theta} p(l|c, \theta) \quad (2)$$

In our application, we assume that latency patterns follow a Gaussian distribution $\mathcal{N}(\mu, \Sigma)$ and hence second order statistics, that is, mean and covariance, is sufficient to learn this distribution. We use ML to estimate these parameters from

sensor array measurements. If \mathbf{m} is the ML estimate of the true mean and \mathbf{S} is the ML estimate of the true covariance matrix then the conditional density of latency patterns with a given CH₂O odor intensity (c_i) is given by

$$p(l|c_i) = \frac{1}{(2\pi)^{n/2} |\mathbf{S}_i|^{1/2}} \exp\left[-\frac{1}{2}(\mathbf{l} - \mathbf{m}_i)^T \mathbf{S}_i (\mathbf{l} - \mathbf{m}_i)\right] \quad (3)$$

In order to estimate a new latency pattern, Bayesian decoding is used to compute the posterior probability $p(c_i|l)$ of every concentration value c_i in the set with a given latency pattern l . It can be described as

$$p(c_i|l) = \frac{p(l|c_i)p(c_i)}{p(l)} \quad (4)$$

Finally, the concentration with maximum posterior probability is selected as an estimated concentration of the new observed latency pattern.

$$\hat{c} = \operatorname{argmax}_i p(c_i|l) \quad (5)$$

III. EXPERIMENTAL SETUP AND PERFORMANCE EVALUATION

We use six commercially available Figaro gas sensors to build an array for CH₂O concentration estimation. The description of these sensors is listed in Table I. The experimental setup for acquiring the response of CH₂O at different concentrations is shown in Figure 1. The sensor array is embedded in a glass container with an inlet valve for CH₂O exposure and outlet valve for its outflow. The cylinders of CH₂O and dry air are connected to mass flow controllers (MFCs) which are used to control the CH₂O concentration by mixing it with air in different proportions. A computer with a data acquisition board is used for MFCs programming to achieve the desired concentration of CH₂O and for acquiring the response of the sensor array.

TABLE I. GAS SENSORS USED TO ESTIMATE CH₂O CONCENTRATION.

Sensor	Target Compounds
TGS 826	Ammonia
TGS 2600	Air contaminants
TGS 2602	Volatile organic compounds
TGS 2610	Liquefied petroleum gas
TGS 2611	Methane
TGS 2620	Solvent vapors

We expose the sensor array to twenty different concentration values of CH₂O in the range between 0.25 ppm to 5 ppm with a 0.25 ppm increment step. The sensor array is exposed to CH₂O for 500 seconds to obtain its response and then dry air is used for 750 seconds to recover the baseline response, i.e., the response without CH₂O vapors. All the sensors in the array respond to the target concentrations of CH₂O with different values of sensitivity. A typical response of a sensor in the array to CH₂O at ten different concentrations is shown in Figure 2. In the figure, from left to right the concentration is increased which results in decreased sensor resistance. Notice that drift also appears, i.e., the sensor does not recover to its original state (baseline response) during dry air exposure.

Drift is the major issue with current gas sensor technology, which may occur due to changes in operational conditions,

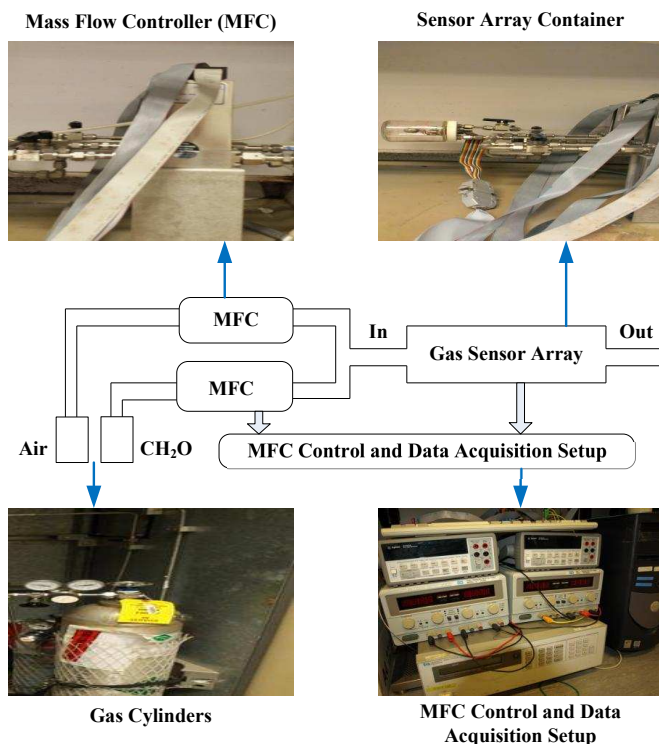


Figure 1. An Experimental setup to acquire the sensor array response to CH₂O exposure at different concentrations.

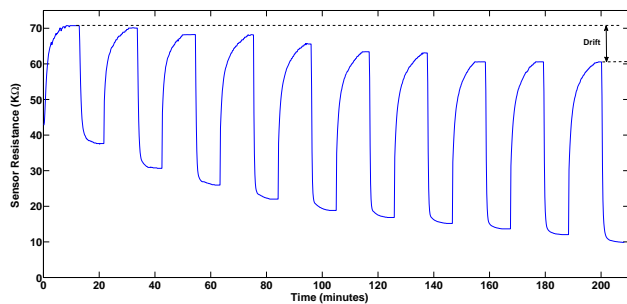


Figure 2. Typical sensor response to formaldehyde at ten different concentrations.

poisoning, and aging. Stochastic variability is observed as a result of this drift. From these resistance values, the sensitivity of each sensor is computed by dividing the steady state sensor resistance during the gas exposure by the baseline resistance. Regression coefficients m_i of each sensor are computed through linear regression, as shown in Figure 3. These parameters are used to transform the sensitivity pattern of the sensor array into a spike latency code (SLC) or pattern.

The Bayesian inference approach is applied on these spike latency codes in order to estimate the CH₂O concentration, and a 92.75% performance is achieved. This is slightly higher as compared to other state of the art methods, which include Gaussian mixture models (GMM), multi-layer perceptron (MLP) and support vector machines (SVM) with linear and radial basis function (RBF) kernel. The performances of all these methods are summarized in Table II. The Bayesian inference approach with spike latency codes not only performs

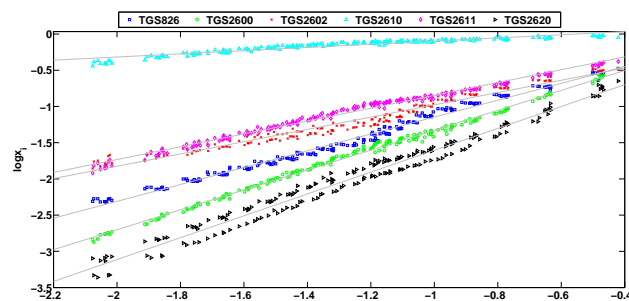


Figure 3. Extraction of regression coefficients for each sensor through linear regression.

better but it also does not require any tuning of parameters, which is extensively used in other methods.

TABLE II. PERFORMANCE COMPARISON OF CH₂O QUANTIFICATION ALGORITHMS.

Classification method	Classification Performance (%)
GMM	91.25
MLP	89.25
SVM (Lin)	88.5
SVM (RBF)	92.5
Bayesian Inference with SLC	92.75

IV. CONCLUSION

In this paper, we developed a low cost and compact solution to estimate the concentration of health endangering formaldehyde in the indoor environment by integrating commercially available gas sensors. Spike latency codes are used in the hardware friendly rank order based classifiers for gas classification. We use these codes to retrieve concentration information. Stochastic variability is observed in the spike latency codes due to inherent issues in the existing gas sensor technology. A probabilistic inference approach is used with spike latency codes to reliably estimate formaldehyde concentration. This scheme requires no manual tuning of the parameters as compared to other commonly used state of the art methods.

ACKNOWLEDGMENT

This paper was made possible by National Priorities Research Program (NPRP) grant No. 5 - 080 - 2 - 028 from the Qatar National Research Fund (a member of Qatar Foundation). The statements made herein are solely the responsibility of the authors.

REFERENCES

- [1] M. N. Indang , A. S. Abdulamir , A. A. Bakar , A. B. Salleh, Y. H. Lee, Y. N. Azah, "A review: methods of determination of health-endangering formaldehyde in diet," Res. J. Pharmacology, vol. 3, no. 2, 2009, pp. 31-47.
- [2] International Agency for Research on Cancer, "IARC classifies formaldehyde as carcinogenic to humans," Press release. Jun. 2004, URL: <http://www.iarc.fr/en/media-centre/pr/2004/pr153.html> [accessed: 2015-07-07].
- [3] P. Guo, K. Yokoyama, F. Piao, K. Sakai, "Sick building syndrome by indoor air pollution in Dalian," Int. J. Environ. Res. Public Health, no. 2, Apr. 2013, pp. 1489-1504.

- [4] T. Salthammer, S. Mentese, R. Marutzky, "Formaldehyde in the indoor environment," *Chemical Reviews*, vol. 110, no. 4, Apr. 2010, pp. 2536-2572.
- [5] J. G. Dojahn, W. E. Wentworth, and S. D. Stearns, "Characterization of formaldehyde by gas chromatography using multiple pulsed-discharge photoionization detectors and a flame ionization detector," *J. Chromatogr. Science*, vol. 39, no. 2, Feb. 2001, pp. 54-58.
- [6] H. L. Pinheiro, M. V. de Andrade, P. A. de Paula Pereira, J. B. de Andrade, "Spectrofluorimetric determination of formaldehyde in air after collection onto silica cartridges coated with Fluoral P," *Microchem. Journal*, vol. 78, no. 1, Sep. 2004, pp. 15-20.
- [7] S. Capone, P. Siciliano, F. Quaranta, R. Rella, M. Epifani, L. Vasanelli, "Analysis of vapours and foods by means of an electronic nose based on a sol-gel metal oxide sensors array," *Sensors Actuators B Chemical*, vol. 69, no. 3, Oct. 2000, pp. 230-235.
- [8] A. P. F. Turner and N. Magan, "Electronic noses and disease diagnostics," *Nature Reviews Microbiology* 2, no. 2, Feb. 2004, pp. 161-166.
- [9] M. Trincavelli, S. Coradeschi, A. Loutfi, B. Sderquist, P. Thunberg, "Direct identification of bacteria in blood culture samples using an electronic nose," *IEEE Trans. Biomed. Engineering*, vol. 57, no. 12, Dec. 2010, pp. 2884-2890.
- [10] R. E. Baby, M. Cabezas, and E. N. Walse de Reça, "Electronic nose: a useful tool for monitoring environmental contamination," *Sensors Actuators B Chemical*, vol. 69, no. 3, Oct. 2000, pp. 214-218.
- [11] M. Penza and G. Cassano, "Classification of food, beverages and perfumes by WO₃ thin-film sensors array and pattern recognition techniques," *Sensors Actuators B Chemical*, vol. 73, no. 1, Feb. 2001, pp. 76-87.
- [12] M. Holmberg, F. Winquist, I. Lundström, J. W. Gardner, E. L. Hines, "Identification of paper quality using a hybrid electronic nose," *Sensors Actuators B Chemical*, vol. 27, no. 1, Jun. 1995, pp. 246-249.
- [13] T. W. Margrie and A. T. Schaefer, "Theta oscillation coupled spike latencies yield computational vigour in a mammalian sensory system," *J. Physiology*, vol. 546, no. 2, Nov. 2002, pp. 363-374.
- [14] H. T. Chen, K. T. Ng, A. Bermak, M. K. Law, D. Martinez, "Spike latency coding in biologically inspired microelectronic nose," *IEEE Trans. Biomed. Circuits and Systems*, vol. 5, no. 2, Apr. 2011, pp. 160-168.
- [15] M. Hassan, S. Brahim Belhaouari, A. Bermak, "Probabilistic rank score coding: A robust rank-order based classifier for electronic nose applications," *IEEE Sensors Journal*, vol. 15, no. 7, Jul. 2015, pp. 3934-3946.
- [16] M. Hassan and A. Bermak, "Threshold detection of carcinogenic odor of formaldehyde with wireless electronic nose," in *IEEE Sensors*, Valencia, November 2014, pp. 1368-1371.
- [17] J. A. Yamani, F. Boussaid, A. Bermak, D. Martinez, "Glomerular latency coding in artificial olfaction," *Front. Neuroengineering*, vol. 4, art. 18, Jan. 2012, pp. 1-9.
- [18] E. Alpaydin, *Introduction to Machine Learning*, MIT Press, 2010.
- [19] D. C. Knill and A. Pouget, "The Bayesian brain: the role of uncertainty in neural coding and computation," *Trends in Neuroscience*, vol. 27, no. 12, Dec. 2004, pp. 712-719.

Application of Cavity Enhanced Absorption Spectroscopy in Detection of Selected Gas Pollutants

Zbigniew Bielecki, Jacek Wojtas, Janusz Mikołajczyk, Sylwester Chojnowski

Institute of Optoelectronics
 Military University of Technology
 Warsaw, Poland
 email: zbigniew.bielecki@wat.edu.pl

Abstract— The paper presents applications of cavity enhanced absorption spectroscopy in detection of nitrogen dioxide (NO₂), nitrous oxide (N₂O), nitric oxide (NO) and carbon monoxide (CO). In the constructed portable sensor of nitrogen dioxide, blue-violet laser was used. The sensor sensitivity reaches a level of single ppb. Additionally, successful monitoring of N₂O, NO and CO was demonstrated in the laboratory air. These sensors required high precision mid-infrared spectroscopy. All of the developed sensors are able to measure concentration at the ppb level using quantum cascade lasers. It makes it possible to apply these instruments in monitoring the atmosphere quality.

Keywords— laser absorption spectroscopy; cavity enhanced spectroscopy; CEAS; gas sensors; QCL.

I. INTRODUCTION

Detection of various gases and measurement of their concentration are very important for monitoring of industrial processes and investigation of their environmental impact. Within the last decades, many methods were developed for stand-off and in-situ detection of volatile substances. They are dominated by mass spectrometry, gas chromatography, chemiluminescence, semiconductor gas sensors or electrochemical devices. Their main inconveniences are size and cost of the apparatus, complicated maintenance, drifts and cross-response issues, e.g., high-sensitive to humidity, poor detection limit and limited lifetimes.

Optoelectronic sensors employing cavity enhanced absorption spectroscopy (CEAS) are very useful in the effort to minimize the level of the environment contamination [1]. These sensors use the phenomenon of optical radiation absorption to detect and measure the concentrations of the molecules, provide achieving low detection limits and high selectivity. For this purpose, it is necessary to apply radiation, the wavelength of which is matched to the spectral range characterized by strong absorption of the tested molecules. Such sensors are more sensitive and selective than many other detection techniques [2]. The rest of this paper is organized as follows. Section II describes CEAS in atmosphere monitoring. Section III describes experiments results. The acknowledgement and conclusions close the article.

II. CAVITY ENHANCED ABSORPTION SPECTROSCOPY IN ATMOSPHERE MONITORING

In practice, nitrogen oxides together with sulfur dioxide are the main gas air pollution. They cause strong

acidification of precipitation, the formation of photochemical smog and highly toxic secondary pollutants (ozone, aromatic hydrocarbons). They also rapidly accelerate corrosion of stone buildings and metal structures, threaten human health, irritate the respiratory system and general weaken the body's resistance to infectious diseases. That is why, the preliminary research was focused on the development of nitrogen oxides sensors providing the detection limit as low as possible. Detection limits at the ppb-level and short measurements time (< 3 s) were demonstrated.

CEAS was proposed by R. Engeln in 1998. The principle of its operation is very similar to cavity ring down spectroscopy one (CRDS). In both setups there is applied an optical cavity with a high quality factor that is made up of two concave mirrors with very high reflectivity R . This results in a long optical path, even up to several kilometers [5]. The idea of the CRDS method is shown in Figure 1.

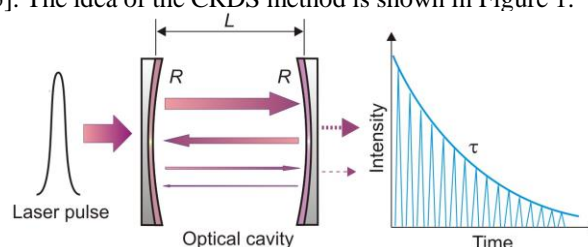


Figure 1. Cavity ring down spectroscopy idea

A pulse of optical radiation is injected into the cavity through one of the mirrors. Then inside the cavity multiple reflections is observed. After each reflection, part of the radiation exiting from the cavity is registered with a photodetector. The output signal from the photodetector determines the intensity of radiation propagated inside the optical cavity. If the laser wavelength is matched to the absorption spectra of gas filling the cavity, the cavity quality decreases. Thus, parameters of the photodetector signal are changed. Thanks to this, the absorption coefficient and concentration of gas can be determined. These calculations will be discussed in a subsequent section.

The main difference relates to the laser beam and the optical cavity alignment. In this technique the light is injected at a very small angle in respect to the cavity axis (Figure 2). As a result, dense structure of weak radiation modes is obtained or modes do not occur due to overlapping. Sometimes, a piezoelectric-driven mount that modulates the cavity length (position of the output mirror) is used in order

to prevent the establishment of a constant mode structure within the cavity [3].

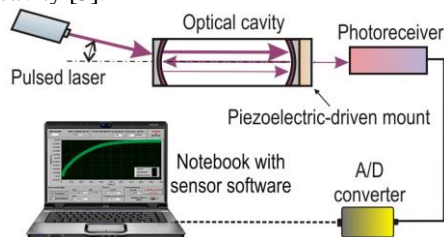


Figure 2. The scheme of CEAS setup

The weak mode structure causes that the entire system is much less sensitive to instability in the cavity and to instability in laser frequencies. Additionally, due to off-axis illumination of the front mirror, the source interference by the optical feedback from the cavity is eliminated. CEAS sensors attain the detection limit of about 10^{-9} cm^{-1} [4]. Therefore, this method creates the best opportunity to develop a portable optoelectronic sensor of nitrogen oxides.

III. EXPERIMENTS

In the applied methods, determination of the gas concentration is performing by measuring the decay time of the photodetector signal [2][3]. If the laser pulse duration is negligibly short and only the main transverse mode of the cavity is excited, then exponential decay of radiation intensity can be observed. The decay time of signal in the cavity (τ) depends on the reflectivity of mirrors, diffraction losses and the extinction coefficient α :

$$\tau = \frac{L}{c(1-R+\alpha L)} \quad (1)$$

where L is the length of the resonator, c - speed of light. Determination of the examined gas concentration is a two-step process. First, measurement of the decay time (τ_0) of radiation in the optical cavity without tested gas is performed. During next step, the same measurements is made (decay time τ) for the cavity filled with the gas. Knowing the absorption cross section (σ) of the examined gas, its concentration can be calculated from the formula

$$C = \frac{1}{c\sigma} \left(\frac{1}{\tau} - \frac{1}{\tau_0} \right), \text{ where } \tau_0 = \frac{L}{c(1-R)} \quad (2)$$

In our experimental setups, we applied visible and mid-IR semiconductor lasers. The first one was constructed using a blue-violet semiconductor laser (414 nm) developed at the Institute of High Pressure of the Polish Academy of Sciences. It was applied in outdoor tests consisting in determination its applicability for measuring NO_2 concentrations in the atmosphere. During the test, the developed sensor demonstrated a low detection limit (1 ppb) and a short measurement time (~ 3 s).

The mid-IR lasers were applied to investigate gases, the absorptions lines of which are located in the infrared region

of spectrum [5]. There were applied quantum cascade lasers (4.53 μm and 5.27 μm) from Alpes Lasers SA, Switzerland and the prototype quantum cascade laser (4.78 μm) from the Institute of Electron Technology, Poland. The achieved results using the constructed CEAS systems in some gas pollutants detection are summarized in Table 1. The developed setups were enabling laboratory research a few gases: nitric oxide, nitric dioxide and carbon monoxide.

TABLE I. THE TEST RESULTS OF OUR SENSORS

Type of sensor	Operation Wavelength	Detection Limit	Measurement Uncertainty	Comments
NO_2	414 nm	1 ppb	5%	Outdoor tests
N_2O	4.53 μm	45 ppb	13%	Laboratory tests
NO	5.27 μm	70 ppb	12%	Laboratory tests
CO	4.78 μm	Approx. 150 ppb	-	Under laboratory tests

IV. CONCLUSIONS

CEAS sensors are able to measure concentration of atmosphere gases at ppb level. Their sensitivity is comparable with the sensitivities of instruments based on other methods, e.g., gas chromatography or mass spectrometry. Observation of NO_2 molecules can be done at electronic transitions which are characterized by a broad absorption spectra providing a relatively large mean absorption cross section within the range of several nanometers. Therefore, using broadband multimode lasers it is possible to detect this gas. However, for other compounds (like N_2O , NO and CO) mid-IR absorption lines are also very promises.

ACKNOWLEDGMENT

The presented work was supported by The National Centre for Research and Development in the scope of Project ID: 179616.

REFERENCES

- [1] M. Miczuga, K. Kopczyński, J. Pietrzak, and R. Owczarek, "Measuring system for detection and identification of hazardous chemicals," Proc SPIE, 2012, vol. 8703, doi: 10.1117/12.2010663
- [2] T. Stacewicz, J. Wojtas, Z. Bielecki, M. Nowakowski, J. Mikołajczyk, R. Mędrzycki, and B. Rutecka, "Cavity ring down spectroscopy: detection of trace amounts of substance," Opto-Electron. Rev., 2012, vol. 20, pp. 34-41.
- [3] J. B. Paul, L. Lapson, and J. G. Anderson, "Ultrasensitive absorption spectroscopy with a high-finesse optical cavity and off-axis alignment," Applied Optics, 2001, vol. 40, pp. 4904-4910.
- [4] I. Courtillot, J. Morville, V. Motto-Ros, and D. Romanini, "Sub-ppb NO_2 detection by optical feedback cavity-enhanced absorption spectroscopy with a blue diode laser," Appl. Phys. B, 2006, vol. 85, pp. 407-412.
- [5] J. Wojtas, J. Mikołajczyk, and Z. Bielecki, "Aspects of the Application of Cavity Enhanced Spectroscopy to Nitrogen Oxides Detection," Sensors, 2013, vol. 13, pp. 7570-7598.

Reducing System Response Time and Noise of Electrochemical Gas Sensors - Discussed for Propofol Monitoring in Breathing Gas

Dammon Ziaian^{*†}, Philipp Rostalski^{†‡}, Andreas Hengstenberg^{†§} and Stefan Zimmermann^{*}

^{*}Institute of Electrical Engineering and Measurement Technology,
Leibniz University Hannover, Germany,
Email: dammon.ziaian@web.de, zimmermann@geml.uni-hannover.de

[†]Research Unit, Draegerwerk AG & Co.KGaA, Luebeck, Germany

[‡]Now at Institute for Electrical Engineering in Medicine,
University of Luebeck, Germany

Email: rostalski@ime.uni-luebeck.de

[§]Now at SICK AG, Hamburg, Germany

Email: andreas.hengstenberg@online.de

Abstract—Electrochemical sensors are used in various gas measurement applications and are available for different gases. Depending on the application, the sensor might need to be installed far away from the actual measurement site, requiring the use of long sampling lines. Examples are portable gas measurement devices in which remote locations like tanks and chemical reactors need to be monitored. But also medical applications, where the sensors cannot be positioned in close vicinity to the patient, are common like, e.g., the side-stream measurement of breathing gas. Due to the characteristics of electrochemical sensors and to the adsorption and desorption behavior of sampling lines for different gases, the electrical sensor signal may indicate long response times. In this paper, we propose an on-line signal processing algorithm which is capable to significantly improve the performance. After characterizing the dynamic behavior of the sensor system, a properly designed deconvolution filter is used to reduce response time and signal noise. Within this article, we also provide an example of this algorithm for a novel electrochemical sensor for the measurement of the anesthetic agent propofol in exhaled air. For this application, the acceleration is prerequisite for the measurement chain to be of practical use in a clinical setting. Our goals, to establish a measurement three times faster than the physiologic parameter might change and to reduce non-physiological disturbances, were achieved with additional reserves.

Keywords—deconvolution; electrochemical sensor; propofol; response time; noise reduction.

I. INTRODUCTION

Electrochemical sensors [1] are widely used for measuring gases in various industries, most notably process industry, oil and gas, but also in medical applications. Various research and development activities have gone into optimizing the design, material and electrochemical properties of this type of gas sensor in order to improve response time, selectivity, accuracy, precision, minimizing the drift and other adverse effects. However, a certain delay in the response due to the diffusion, chemical reaction but also adsorption/desorption is inherent in any sensor.

Referring to the topics "Electrochemical Gas Sensors", "Signal Conditioning" and "Signal Processing", we will discuss a specific medical application for an electrochemical gas sensor, but similar techniques may be used in other areas.

After describing the specific application and measurement chain for the physiological signal considered for the remainder of this article, we will discuss the design of a deconvolution filter to accelerate the system response while filtering non-physiological disturbances. The performance of the filter is analyzed both theoretically and based on laboratory measurement.

In Section II, the specific application and the experimental setup are declared. Furthermore, mathematical explanations on modeling and the design of the algorithm are given. Results of the signal acceleration and noise reduction are presented in Section III. At the end, the application of advanced signal processing is discussed and concluded in Section IV.

II. MATERIAL AND METHODS

A. Specific application

As a practically relevant example, an electrochemical gas sensor which is used to quantify the concentration of 2,6-Diisopropylphenol, also known as propofol, is considered [2]. Propofol is applied as an anesthetic agent for humans and animals. It is intravenously administered in the formulation of a lipid emulsion. Its volatile characteristics allow detecting propofol in the breathing gas after injection [3]. During anesthesia the exhaled concentration appears in the order of around 20 ppb (parts per billion) [4][5]. As a result, the required sensitivity and accuracy of the sensor need to be suitable to ensure a reliable measurement.

When handling substances in such low concentrations, effects of adsorption and desorption along the measurement chain have a particularly strong impact. In the case discussed here, the carrier gas is drawn through a 2.5 m long sampling line from the propofol source which happened to be a gas cylinder (carrier gas: N₂, propofol concentration: 40 ppb±30% rel. standard deviation). Since the true concentration of one cylinder lies between 28 ppb and 52 ppb according to the vendor, the sensitivity of the sensor cannot be stated based on the actual data. The schematic of the setup is presented in Figure 1. A sampling flow of 180 ml/min is generated with the help of a pump. Hence, the carrier gas is led through the sampling line to interact with the sensor.

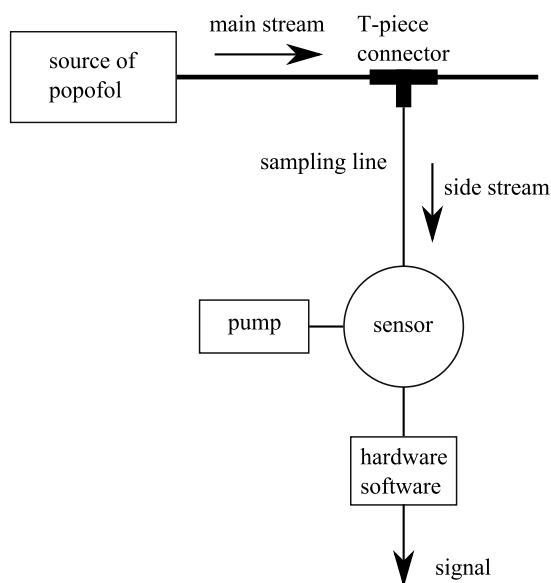


Figure 1. Schematic of the experimental setup. The side stream is driven through the sampling line to pass the electrochemical sensor for detection. A T-piece connector is used for switching.

The saturation of propofol on the inner surface of the line leads to a major dynamic delay in time before the electrochemical sensor is able to detect the absolute concentration. Besides the delay caused by the sampling system, the response characteristics of the electrochemical sensor itself adds further major delay. It is assumed that these two effects are responsible for the main delay. Another cause refers to the volume of the line which the gas has to pass before reaching the sensor leading to a constant, non-dynamic delay. Considering an inner tubing diameter of 3.2 mm, given flow rate and given length of the sampling line, a dead time of 5.4 sec is created. However, 5.4 sec are negligible in contrast to the major dynamic delay reasons. Recorded signals are usually corrupted by noise. Owing to the pump, to thermal noise within the electronic components and other effects, all measured values possess a specific variance. Besides the minimization of the response time, another objective of the signal processing algorithm proposed in this article is to increase signal quality in real-time. We have been aware of the fact that signal acceleration might lead to over-proportional amplification of non-physiological disturbances. In the light of the aforesaid, it is mandatory to seek for this goal.

B. System identification

Any signal processing procedure needs to be tailored to the specific application. This can be either done heuristically by following tuning rules or by using a model-based procedure. In this publication we follow the latter route. System identification is the necessary first step to identify the underlying system model.

1) *Recording the step response:* A step change of propofol gas was applied in order to excite the measurement system. Data was recorded using the setup illustrated in Figure 1. At defined times the propofol-free sampling line was connected and disconnected to the main stream which contained propofol-saturated gas of approximately 40 ppb. One standardized cy-

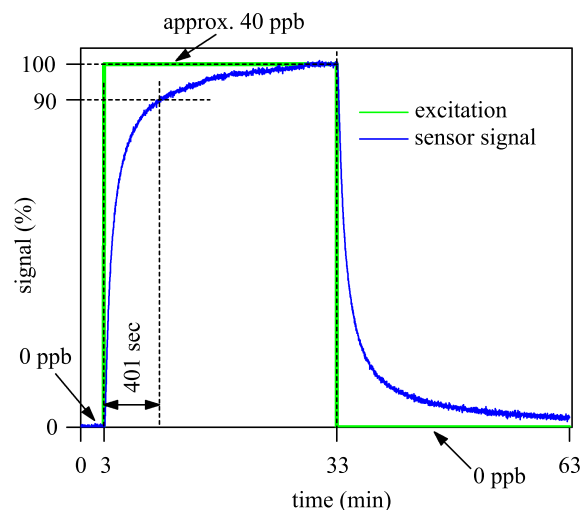


Figure 2. Result of one measurement cycle. Excitation sequence is shown in green and sensor signal in blue. 90% of the ultimate value is reached within 401 sec after connecting to the main stream.

cle consists of three minutes of recording the baseline with propofol-free room air, followed by 30 minutes of connection to the main stream. And finally, the system was purged for 30 minutes with room air by disconnection from the T-piece connector. In Figure 2, the input excitation is shown in green and the resulting step response of the sensor system in blue. Dotted lines indicate the 90% value and the steady state of the response. In this particular measurement it takes

$$t_{90} = 401 \text{ sec} \tag{1}$$

to reach 90% of the steady state value.

To quantify the precision of each measurement the signal to noise ratio (SNR), here defined as

$$\text{SNR} = \frac{\text{amplitude}}{\text{standard deviation}} \tag{2}$$

is calculated. The *amplitude* derives from the mean value of a short time period towards the end of exposure to propofol gas and is thus equal to the steady state value. The SNR may be understood as an intra-measurement precision, whereas the evaluation of a set of multiple measurements leads to the overall precision of the sensor system. A higher SNR reflects a better precision. For the measurement shown in Figure 2 the resulting ratio appears as 367, indicating a rather low noise situation. Again, the actual noise situation is not the reason for seeking a better SNR, but the signal acceleration, explained in what follows, makes it mandatory.

2) *Modeling and parameter identification:* System identification can be done using different methods, ranging from white box modeling based on first-principles with parameters derived using physically measures to black box modeling, where no prior knowledge about the model is available. We will follow the latter approach with two assumptions on the model structure. The step response from Figure 2 suggests a first or second order response, without overshoot and no oscillatory components. A reasonable model structure (second

order) in the time domain is thus given by

$$f_{model}(t) = k \left(1 + e^{-\frac{t}{T_1}} \frac{T_z - T_1}{T_1 - T_2} + e^{-\frac{t}{T_2}} \frac{T_z - T_2}{T_2 - T_1} \right). \quad (3)$$

Therein k represents the static gain. T_1 , T_2 and T_z characterize the dynamics of the system and t is set to be the time variable. By means of the *Laplace* transformation [6] the same relationship may be stated in the frequency domain as

$$f_{model}(t) \circ \bullet F_{model}(s) \quad (4)$$

$$F_{model}(s) = k \frac{T_z}{T_1 T_2} \frac{s + \frac{1}{T_z}}{\left(s + \frac{1}{T_1}\right) \left(s + \frac{1}{T_2}\right)} \quad (5)$$

$$= k \frac{T_z s + 1}{(T_1 s + 1)(T_2 s + 1)}, \quad (6)$$

wherein s is defined as the complex angular frequency.

The parameters of this model are computed using an optimized fitting procedure. With the help of a least squares method the set of parameters k , T_z , T_1 and T_2 are determined which yield the smallest sum of squares error between the modeled and the actual response. The best values found for this particular setup are as follows:

$$k = 1 \quad (7)$$

$$T_z = 413.03 \text{ sec} \quad (8)$$

$$T_1 = 536.95 \text{ sec} \quad (9)$$

$$T_2 = 52.49 \text{ sec} \quad (10)$$

In Figure 3 the result of the modeling and parameter identification is illustrated. The blue line represents the measurement as displayed in Figure 2. After finding an appropriate model structure and reasonable parameters the modeled signal, drawn in orange, can be calculated. The visual matching indicates that the fitted curve agrees well with the measurement. The remaining mismatch is likely to be a result of the inherent non-linearity of different dynamics for rising and falling concentrations. With a hybrid model including two switching dynamics for rising and falling signal response respectively the fitting curve would show a better match, albeit at the price of mathematical complexity and a non-linear behavior.

C. Design of algorithm

In [7], the physiological lung dynamics regarding the propofol exchange from blood plasma to breathing gas are described by a first order differential equation. Its time constant T , which is defined as the time to reach 63% of the final propofol concentration in the lung due to a sudden change in the blood plasma propofol level, is estimated using clinical patient data to be $T = 414$ sec in mean, approximately corresponding to a respond time of $t_{90,breath} = 952$ sec. We expect that a proper metering for anesthesia monitoring is performed when the detection happens three times faster than the parameter might change. Considering this, the sensing system should not exceed a maximal response time of $t_{90,max} = 317$ sec for a clinically relevant measurement of propofol in breath.

As mentioned before, the main issue of the electrochemical measurement system for propofol is its long response time. Major causes for this are adsorption/desorption effects in the sampling system as well as the inherent measurement dynamics of the electrochemical sensor itself. All of these

elements lead to a delayed response between the propofol concentration in breath and the signal provided by the sensor with a typical response time of $t_{90} = 401$ sec. Fortunately in a clinical environment most of the factors determining the delay are almost constant over time and depend only on the measurement chain. The delay can thus be compensated by using linear signal processing. The design of such an algorithm is the content of this section.

1) *Deconvolution*: The measured signals $\phi(t)$ are the result of the time course of the propofol concentration in the breathing gas $c_{breath}(t)$ and $f_{system}(t)$, which is meant to be the unknown response characteristic of the measuring system,

$$\phi(t) = f_{system}(t) * c_{breath}(t), \quad (11)$$

where $*$ denotes the convolution operator.

During a measurement, $f_{model}(t)$ (identified in Section II-B2) and all past values of $\phi(t)$ are known. The aim is to compute the original source signal $c_{breath}(t)$ with these known information. It is possible to estimate the delayed signal by inverting the slow dynamic components of the measurement chain. Mathematically, this means that we need to invert the effect of the convolution through deconvolution with all transfer elements between source and electrical signal of the sensor. Deconvolution is best understood in frequency domain. Each frequency component is delayed and damped individually by the measurement chain

$$\Phi(s) = F_{system}(s) C_{breath}(s). \quad (12)$$

The idea of deconvolution is simply to shift and amplify each frequency component accordingly to reverse this effect. Based on the model identified in Section II-B2, we can approximate $C_{breath}(s)$ through deconvolution as

$$\hat{C}_{breath}(s) = \Phi(s) \cdot \text{inv}(F_{model}(s)) \quad (13)$$

$$= F_{system}(s) C_{breath}(s) \frac{1}{F_{model}(s)}, \quad (14)$$

where $\Phi(s)$ denotes the frequency transform of the measured signal, $F_{model}(s)$ is the model identified in the previous section

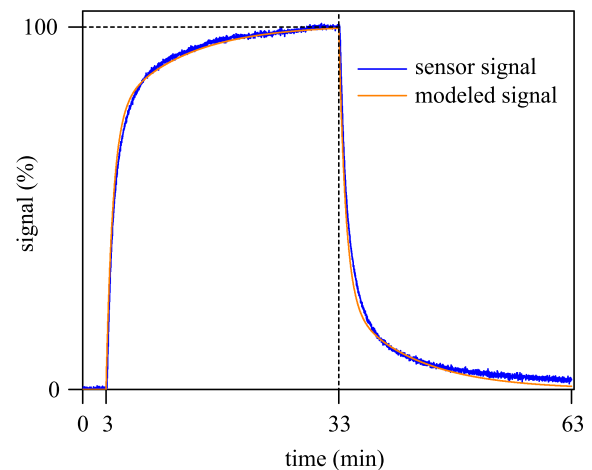


Figure 3. Result of the modeling and parameter identification. The measured time course is displayed in blue and the modeled signal in orange.

and $\hat{C}_{breath}(s)$ provides the estimated propofol concentration. This procedure, however, is not realizable for a number of reasons in practical setting requiring real-time computation in a medical device. First and foremost, the deconvolution equation (14) as given above cannot be realized, at least not without modification. Any causal system satisfies the property that its numerator order is equal or lower than its denominator order. This translates into the fact that at each point in time we only measure the next signal value but not its time derivatives.

$$\begin{aligned} \text{inv}(F_{model}(s)) &= \frac{1}{F_{model}(s)} \\ &= \frac{(T_1 s + 1)(T_2 s + 1)}{k(T_z s + 1)} \end{aligned} \quad (15)$$

Not keeping causality would incorrectly imply that an effect may appear before its cause.

Another potential issue of a simple inversion is noise. In reality, (12) can be rewritten as

$$\Phi(s) = F_{system}(s) C_{breath}(s) + R(s), \quad (16)$$

where $R(s)$ denotes the Laplace transform of the noise. The estimation of $\hat{C}_{breath}(s)$ considering the noise term results in

$$\hat{C}_{breath}(s) = \frac{F_{system}(s) C_{breath}(s)}{F_{model}(s)} + \frac{R(s)}{F_{model}(s)}. \quad (17)$$

Most real systems, including the measurement chain in question, have a low-pass behavior which dampens high frequency noise. Inverting the transfer function of such a system would result in a high-pass behavior which highly amplifies non-physiological signal components such as noise and distorts the actual propofol signal. Our aim, to increase the SNR, addresses this over-proportional amplification of noise during deconvolution.

2) *Causality and noise treatment*: One potential solution to overcome the issues mentioned above is to augment the deconvolution filter in (17) by a low-pass filter

$$\underbrace{\hat{C}_{breath}(s)}_{\text{estimation}} = F_{system}(s) C_{breath}(s) \frac{F_{filter}(s)}{F_{model}(s)} + R(s) \frac{F_{filter}(s)}{F_{model}(s)} \quad (18)$$

$$= (F_{system}(s) C_{breath}(s) + R(s)) \frac{F_{filter}(s)}{F_{model}(s)} \quad (19)$$

$$= \underbrace{\Phi(s)}_{\text{measurement}} \underbrace{\frac{F_{filter}(s)}{F_{model}(s)}}_{\text{algorithm}}. \quad (20)$$

If the filter order is chosen high enough, the causality of the overall system is satisfied. Since $\text{inv}(F_{model}(s))$, see Equation 15, has a numerator order of two and a denominator order of one, a low-pass filter $F_{filter}(s)$ with an order of at least one would therefore fulfill the need for causality.

3) *Low-pass filter*: Dedicated to the electrochemical measurement system and to the application requirements the following low-pass filter –a second order Butterworth filter [8]– has shown sufficient performance. Its flatness and linearity in the pass band and the uncomplicated design are beneficial

in our case. Other types of filtering may be more favorable depending on the application.

In order to determine a suitable cut-off frequency we considered the appearing dynamics. The dynamics of propofol exhalation in breathing gas can be derived from [7][9]. In a subsequent adjustment procedure our filter parameters have been fine-tuned during application to obtain a satisfying compromise between noise rejection and response time. With the resulting cut-off angular frequency of

$$\omega = 2\pi f = 4 \cdot 10^{-2} \frac{\text{rad}}{\text{sec}} \quad (21)$$

the transfer function of the Butterworth filter is given as

$$F_{filter} = \frac{0.0016 \frac{\text{rad}^2}{\text{sec}^2}}{s^2 + 0.05657 s \frac{\text{rad}}{\text{sec}} + 0.0016 \frac{\text{rad}^2}{\text{sec}^2}}. \quad (22)$$

4) *The resulting algorithm and its software implementation*: As implied in (20), the algorithm for the signal processing is composed as

$$F_{algorithm}(s) = \frac{F_{filter}(s)}{F_{model}(s)}. \quad (23)$$

For our particular case, the algorithm results in

$$F_{algorithm}(s) = \frac{(T_1 s + 1)(T_2 s + 1)}{k(T_z s + 1)} \frac{0.0016 \frac{\text{rad}^2}{\text{sec}^2}}{s^2 + 0.05657 s \frac{\text{rad}}{\text{sec}} + 0.0016 \frac{\text{rad}^2}{\text{sec}^2}} \quad (24)$$

due to the model characterized in Section II-B2 and due to the filter described in Section II-C3. All poles of $F_{algorithm}(s)$ are negative, thus stability is ensured. The continuous frequency domain is helpful for design matters. But for the implementation as a real-time capable algorithm few more steps are required. Since the sensors output is available digitally it exists of discrete values appearing in a specific rate. Therefore, it is necessary to transform into the discrete time domain. With the use of the bilinear transform [10] and the properties of the z -transform [11] the algorithms output at a certain point in time can be stated as a sum. (25) depicts a general description. Therein, $y(k)$ expresses the algorithms output and $x(k)$ the measured value, while k denotes the discrete time variable.

$$y(k) = \frac{1}{a_0} [b_0 x(k) + b_1 x(k-1) + \dots + b_n x(k-n) - a_1 y(k-1) - \dots - a_n y(k-n)] \quad (25)$$

Hence, $y(k)$ is calculated as a linear combination of previous calculations and measurements, whereas $a_{0...n}$ and $b_{0...n}$ denote the coefficients characterizing the algorithm.

Applied on $F_{algorithm}$ of (24), we find a compact description to be implemented in any software as a real-time capable signal processing algorithm:

$$y(k) = \frac{1}{a_0} [b_0 x(k) + b_1 x(k-1) + b_2 x(k-2) + b_3 x(k-3) - a_1 y(k-1) - a_2 y(k-2) - a_3 y(k-3)] \quad (26)$$

After transformation for a sampling rate of 1 Hz the coefficients can be found in Table I. The given precisions of decimal places are required for stability, when the algorithm is programmed to perform.

III. RESULTS

Due to the concise description of the algorithm presented in the previous section it is possible to calculate an accelerated signal in real-time as well as retrospectively. Further on, results are presented for a step change of the propofol concentration as displayed in Figure 2 of Section II-B2 and for repeated measurements.

In Figure 4, the post-processed signal is illustrated in red. This example visualizes the improvement possible through signal processing. In this particular case, the response time t_{90} is notably reduced from 401 seconds to 104 seconds. In Section II-C, the maximal tolerated response time is mentioned to be $t_{90,max} = 317$ sec. Therefore, this requirement is fulfilled with an additional reserve. The secondary objective stated is an increase of precision. By noise treatment consideration during the filter design the SNR is enhanced from 367 to remarkably 1482. As the measuring system is afflicted with non-linearity the algorithm shows a different result for rising and falling signals. Both overshooting and undershooting lead to higher (102.3%) and lower (-1.1%) values. However, the error stays below $\pm 5\%$, which is an acceptable result compared to the enhancements in response time and noise reduction.

To express the performance and the repeatability of the algorithm, repeated measurements were evaluated. The same setup was used at different times whereas the algorithm was executed online in real-time. As an example, the results for three repetitions are displayed in Figure 5. Pairwise-colored curves denote sensor signals and their related real-time processed estimation of the input excitation. It might be that a drift of the propofol source concentration or of the sensor sensitivity have occurred during the repetitions. Even though, the algorithm has performed stable and with expected results. Summarized, we observe that results are highly reproducible and that the algorithm performs similarly in real-time as long as main parameters of the system do not significantly change and linearity is given for the tolerated concentration range. This result is valid for the discussed clinical practice and also for several other applications of electrochemical and other sensors.

IV. DISCUSSION AND CONCLUSION

In various practical applications of electrochemical sensors a sampling line is required to transport the gas from the sampling site to the sensor. This together with the dynamics of the sensor itself might lead to significant delays and adverse measurement dynamics, rendering the electrochemical measurement signal useless for the application. To overcome this obstacle, a solution in form of an accelerating algorithm is presented.

TABLE I. DISCRETE TIME COEFFICIENTS FOR A 1 HZ-CLOCKED DECONVOLUTION FILTER

coefficient	value
a_0	1
a_1	-2.9551616730526264
a_2	2.9113070363222864
a_3	-0.95614323255658584
b_0	0
b_1	0.060676477761667597
b_2	-0.12009490846751848
b_3	0.059420561418924996

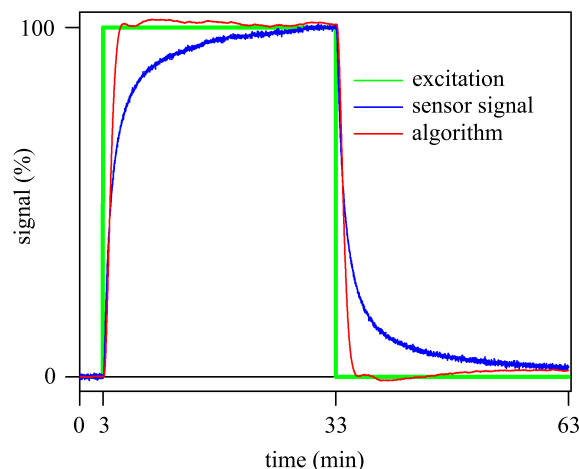


Figure 4. The result of the signal post-processing is displayed in red, the sensor signal used for the calculation in blue.

In this article, we have demonstrated that the application of advanced signal processing can help to optimize the performance of electrochemical measurement systems with long sampling lines. For the example of an electrochemical propofol sensor, the response time could significantly be reduced by a factor of 9.2 while the SNR could be increased at the same time by a factor of 4. Furthermore, the proposed procedure involves only straight forward model-based design steps and should thus easily be transferable to other applications. Starting with a modeling and system identification step, the characteristics of the sensor system are identified. Here, a second order equation is used to model the sensor response. Noise considerations lead to the specification of a second order low-pass Butterworth filter and to the design of a deconvolution algorithm.

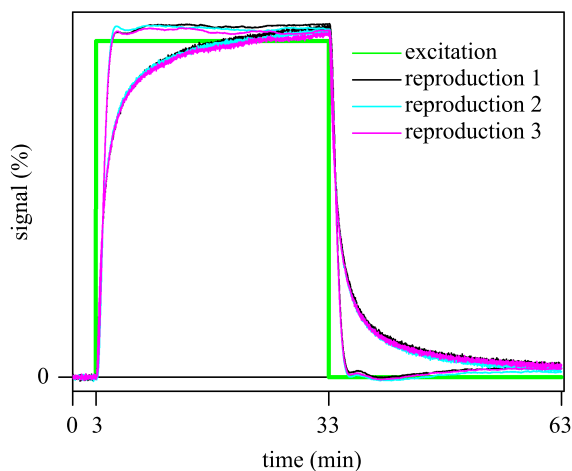


Figure 5. Three reproduced measurements 1-3 are illustrated to express the repeatability. The algorithm was applied in real-time during each measurement. Pairs of the same color represent related sensor and algorithm signals.

Our primary objective has been to realize a detecting system able to observe the propofol concentration in patients exhaled breath at least three times faster than this physiological parameter might change. With the help of the presented algorithm the accelerated response time of $t_{90} = 104$ sec is 9.2 times faster than the patients average breath propofol concentration change with $t_{90,breath} = 952$ sec.

The patient with the fastest exhalation dynamic observed in [7] does have a time constant of $T = 227$ sec. This implies a maximal permitted response time of $t_{90,max} = 174$ sec for the measuring device. Thus, using the presented acceleration algorithm the propofol sensors system is even suitable to monitor such, probably exceptional, fast exhalation dynamics.

Another issue discussed in the paper relates to noise. On the one hand more accurate signals are advantageous in general and on the other hand we are aware of the fact that deconvolution might lead to exceedingly higher noise levels. With a proper choice of a low-pass filter, this effect could be coped with, resulting in a significantly improved SNR, albeit the SNR has been acceptable before processing. The results of a bad-dimensioned filter for comparison would show nothing but noise.

It is worth mentioning that the application of the presented signal processing is not limited to the clinical setting. Especially, portable gas detection devices are often used in conjunction with long samplings reaching up to 30 m and thus leading to remarkable delays beside the dead time delays due to volume.

Technologically, other more advanced signal processing algorithms come to mind such as Wiener Filter [12], (linear/non-linear) Kalman Filter [13] or moving horizon estimation, however at a price of a higher complexity. It will be part of ongoing research activities to evaluate these techniques in the context of electrochemical sensors with long sampling lines and to compare the results against the surprisingly simple and effective solution provided here.

One difference to a clinical setup is regarded to the relative humidity conditions of the gas, which appear much higher when patients' breathing gas is sampled. Influences of humidity were not observable during other investigation. Thus, the impact is not part of this work and might be a topic to

address in future.

REFERENCES

- [1] P. J. Gellings and H. J. Bouwmeester, *The CRC Handbook of Solid State Electrochemistry*. CRC Press, 1997, chapter 10, ISBN: 978-0849389566.
- [2] "Package leaflet: Information for the user Diprivan 10 mg/ml (1%) Emulsion for Injection or Infusion," 2015, URL: <https://www.medicines.org.uk/emc/medicine/8375> [accessed: 2015-06-19].
- [3] M. Grossherr, A. Hengstenberg, T. Meier, L. Dibbelt, K. Gerlach, and H. Gehring, "Discontinuous Monitoring of Propofol Concentrations in Expired Alveolar Gas and in Arterial and Venous Plasma during Artificial Ventilation," *Anesthesiology*, vol. 104, pp. 786–790, 2006.
- [4] M. Grossherr et al., "Propofol concentration in exhaled air and arterial plasma in mechanically ventilated patients undergoing cardiac surgery," *Br J Anaesth.*, vol. 102, no. 5, pp. 608–613, 2009, doi: 10.1093/bja/aep053.
- [5] A. Takita, K. Masui, and T. Kazama, "On-line Monitoring of End-tidal Propofol Concentration in Anesthetized Patients," *Anesthesiology*, vol. 106, pp. 659–664, 2007.
- [6] H. Dwyer, "The Laplace Transform: Motivating the Definition," *CODEE Journal*, vol. 125, pp. 1231–1238, 2011, URL: <http://www.codee.org/ref/CJ11-0116> [accessed: 2015-06-19].
- [7] D. Ziaian et al., "Pharmacokinetic modeling of the transition of propofol from blood plasma to breathing gas," in *2014 IEEE International Symposium on Medical Measurements and Applications, MeMeA 2014, Lisboa, Portugal, June 11-12, 2014*, pp. 80–84. [Online]. Available: <http://dx.doi.org/10.1109/MeMeA.2014.6860035>
- [8] D. Gordon, E. Robertson, and J. J. Dowling, "Design and responses of Butterworth and critically damped digital filters," *Journal of Electromyography and Kinesiology*, vol. 13, pp. 569–573, 2003.
- [9] C. Hornuss, D. Wiepcke, S. Praun, M. Dolch, C. Apfel, and G. Schelling, "Time course of expiratory propofol after bolus injection as measured by ion molecule reaction mass spectrometry," *Anal Bioanal Chem*, vol. 403, no. 2, pp. 555–561, April 2012.
- [10] G. Zhang, X. Chen, and T. Chen, "Digital redesign via the generalised bilinear transformation," *Int. Journal of Control*, vol. 82, no. 4, pp. 741–754, April 2009, doi: 10.1080/00207170802247728.
- [11] J. R. Ragazzini and L. A. Zadeh, "The analysis of sampled-data systems," *American Institute of Electrical Engineers, Part II: Applications and Industry, Transactions of the*, vol. 71, no. 5, pp. 225–234, Nov 1952.
- [12] N. Wiener, Ed., *Extrapolation, Interpolation, and Smoothing of Stationary Time Series*. New York: Wiley, 1949, ISBN: 0-262-73005-7.
- [13] R. E. Kalman, "A New Approach to Linear Filtering and Prediction Problems," *J. Fluids Eng.*, vol. 82, no. 1, pp. 35–45, March 01 1960, doi: 10.1115/1.3662552.

Early Detection of Emissions Preceding Fires from Overloaded Electric Cables: Approach with Thermo-Cyclically Operated MOG Sensor Arrays and Numerical Signal Analysis

Rolf Seifert and Hubert B. Keller
 Institute of Applied Informatics (IAI)
 Karlsruhe Institute of Technology
 e-mail: rolf.seifert@kit.edu

Navas Illyaskutty, Jens Knoblauch and Heinz Kohler
 Institute for Sensor and Information Systems (ISIS)
 Karlsruhe University of Applied Sciences
 e-mail: heinz.kohler@hs-karlsruhe.de

Abstract—A thermodynamically operated multi metal oxide sensor array is introduced together with a novel signal analysis approach for early detecting the emissions from overheated isolation cable materials used in electrical cabinets. The principal sensor element is a thermo-cyclically operated four sensing layer array, which can yield conductance signatures appropriate to specifically identify gases. The obtained conductance profile shapes bear good capability for detection and identification of pyrolysis gas emissions at relatively low sample heating temperatures even before a color-change of the polyvinyl chloride (PVC)-isolation is visible. The dynamic conductance signals were evaluated using SimSens, a numerical analysis tool designed for simultaneous evaluation of conductance profiles. The results show promising pyrolysis gas identification and concentration determination capabilities in relation to the conductance profile shapes of model gases like carbon monoxide (CO) and propene.

Keywords—metal oxide gas sensor; sensor array; early fire detection; pyrolysis; data analysis.

I. INTRODUCTION

In the current scenario, developing sensor systems for early detection of fires instigated by overloaded electrical circuits has gained great attention due to increased sensibility for security aspects. Metal oxide gas sensors (MOG) can be used as appropriate candidates for detection of conventional fires and smoke [1]. This type of gas sensor could be utilized for early detection of fires in electrical installations, as pyrolysis of cable materials leads to emission of distinct gas mixtures depending on insulation material composition [2]. Identification of those typical gas mixtures by thermo-cyclic operation of MOG sensor arrays and simultaneous sampling of conductance over time profiles (CTPs) together with numerical analysis of these profiles has been shown in the past to be an elegant and reliable method for detection of fires [3]-[7].

The present study proposes a thermo-cyclically operated four-layer sensor array, which yields gas specific dynamic conductance profiles, as well as a signal analysis approach using SimSens [8]; both together could open new applications as e.g. in the field of early detection of overloaded cables and fire.

In Section II, the program SimSens for simultaneous evaluation of sensor data is briefly introduced. Section III

gives a survey over the experimental set up of the sensor system. The results of the experimental set up are discussed in context with the results of the numerical data analysis for identification of pyrolysis gases in Section IV. Section V involves the conclusions and gives an outlook.

II. OUTLINE OF THE SIMSENS PROGRAM

In many applications, a multitude of different gases may occur, which have to be identified and analyzed simultaneously. One application of great interest is the above mentioned detection of fires due to electrical overload of cables at early stages of development. Depending on the various coating materials of the cables a variety of gases or gas mixtures can be emitted. These gases or gas mixtures according to the related coating materials have to be simultaneously identified and analyzed for early detection of such developing risk. The term “simultaneously” in this context means that the measurements are performed with only one sensor system and the instantaneous analysis is performed with only one analysis procedure covering all the different gases or gas mixtures, which may occur at a certain time but not at once.

The calibration and evaluation program SimSens was designed to meet these demands on simultaneous gas identification capability. SimSens is an extension of the well-introduced program ProSens [9],[10], which was designed to analyze only one target gas or gas mixture under consideration.

Like ProSens, SimSens consists of a calibration part and an evaluation part. In the calibration part SimSens provides the mathematical calibration models for every gas to be analyzed. Each calibration model consists of functions for determination of the component concentration and of functions for calculating the related so-called theoretical CTP for substance identification. This means the calibration part of SimSens provides calibration models for every gas or gas mixture under consideration, whereas ProSens calculates only one calibration model. The functions included in the calibration part of SimSens are parametric functions and the parameters are determined by multiple linear regressions of the CTP sample values versus concentration.

These parameters are transferred to the evaluation part of SimSens for the analysis of an unknown gas sample. Based on these parameters and the CTP of an unknown gas sample

the evaluation part of SimSens calculates theoretical CTPs for each calibrated gas and compares these CTPs with the measured CTP.

If the measured CTP and one of the theoretical CTPs are close together, i.e., a difference value calculated from the sum of quadratic differences of every sample point of the measured CTP and the theoretical CTP is smaller than a pre-determined decision value, SimSens identifies the unknown gas sample as the related calibrated target gas.

Otherwise SimSens recognizes that the gas sample is none of the calibrated target gases. In case of identification, SimSens calculates the concentration of the gas sample based on the related calibration model.

Using these algorithms of numerical sensor signal analysis, SimSens has the capability to identify and analyze a variety of target gases or gas mixtures. This is due to the fact that in the calibration part of SimSens more than only one calibration model can be determined, namely one calibration model for each gas or gas mixture, which may occur in the considered application. Furthermore, in the evaluation part of SimSens, not only one gas or gas mixture can be identified, but all gases or gas mixtures, which are calibrated.

III. EXPERIMENTAL SET UP

The principal sensing element used for pyrolysis gas identification studies is a four-fold sensor array on a 4x4 mm² alumina chip (Figure 1), which comprises four micro-dispensed thick-film sensing layers of different SnO₂/additive-composites [3]. In operation, the sensor-chip is thermally modulated by applying a steady slope heater-voltage, which results in a periodic, nearly triangular temperature profile between 100 °C and 450 °C, at a cycle time of three minutes (Figure 2). Operating MOG sensors thermo-cyclically and sampling of the conductance simultaneously yields gas specific CTPs [3]-[6], which enable identification of the gas atmosphere from the characteristic CTP shapes.

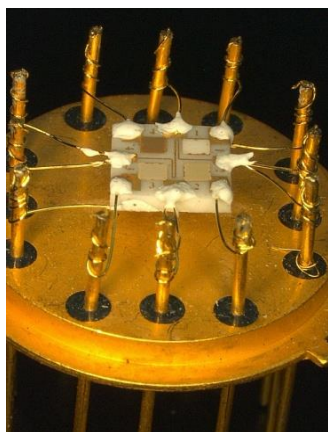


Figure 1. Multi-sensor-array with four different layers dispensed on thin-film Inter-Digital-Electrodes. The chip is mounted on TO 8 header.

Pure SnO₂, SnO₂/2%ZnO-, SnO₂/1%PtO- and SnO₂/1%PdO-composites were selected systematically from

a variety of material combinations by investigating their sensitivity performance. The various material combinations were investigated towards their specific conductance behavior to propene (C₃H₆), carbon monoxide (CO) and methane (CH₄) at different concentrations in synthetic air and 37.5 % (21°C) relative humidity (r.H.) and were later exposed to pyrolysis gases as described in the following sections. These model gases were particularly selected as they are found to be the main components evolved during the pyrolysis of standard PVC-insulation cable materials. The selected sensing materials show optimal sensitivity, stability and gas identification capabilities towards model gases like CO and propene and to pyrolysis gases. The sensitivity to methane is very low and not further reported.

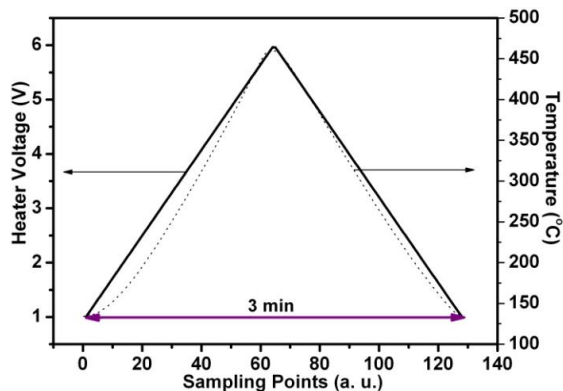


Figure 2. Triangular heater voltage profile applied to operate the sensor array at thermo-cyclic mode (left ordinate) and corresponding temperature monitored by IR camera (right ordinate).

A detailed description of the sensor fabrication, experimental set up and generation of pyrolysis gases is depicted in refs [3], [5], [6]. Pyrolysis experiments were conducted with 3.5 g of PVC isolated litz copper wires (LiY – 0.14mm², AWG26, 2A current rating, yellow). The pyrolysis gases were generated by heating the samples in a quartz tube reactor and the evolving gas is carried to the sensor by a constant synthetic air flow. After the reactor, the constant flow is mixed with another adjustable flow of synthetic air in order to get varied gas concentrations. The reactor temperature was increased in a stepwise fashion starting from room temperature up to 170 °C. This fixed temperature was selected after several systematic experiments conducted below and above 170 °C. Evidently, the wire sample showed no visible change up to temperatures of 150°C and even at 170°C only a slight change of the sample by shrinking of insulation diameter is observed. At 200°C discoloring takes place, the sample turns brown.

IV. RESULTS AND DISCUSSION

A. Sensor Response

An overview of the pyrolysis experiment with sensing pattern of a pure SnO₂ layer towards pyrolysis gas at different concentrations is given in Figure 3. The pyrolysis gas was transported by a constant primary gas flow and diluted by a dilution flow of synthetic air. It is demonstrated

that at 170 °C, an almost constant emission from the polymer material is observed over more than five hours. The absolute conductance-values presented here vary greatly depending on experimental parameter values. Several CTPs were recorded at a reactor temperature of 170°C, while changing the dilution level to set defined relative concentrations. The CTPs at each concentration are highly reproducible at the repeated cycling by showing similar baseline and peak conductance values (Figure 3, inset).

The CTPs measured by different sensitive materials to model gases (CO and propene) and pyrolysis gases at different concentrations are visualized in Figure 7 for comparison. In the very most cases they show very specific features with respect to gas identification capabilities.

The thermo-cyclically driven array of four different gas sensitive SnO₂/additive-composites exhibits four different profiles to an exposed gas, which in fact can enhance the gas identification capability compared to conventional mono-sensors operated at isothermal mode. For example, in consideration of propene and CO response, the different sensing materials show completely different CTP shapes (Figure 7, 1st and 2nd column). In case of pyrolysis gas, although the profile shapes of all materials look similar with two distinctive conductance peaks at the temperature rising and dropping regions, the conductance peak positions are dependent on temperature. Also, by the CTP-features of each sensor the pyrolysis gases can be clearly distinguished from the model gases (Figure 7, rows).

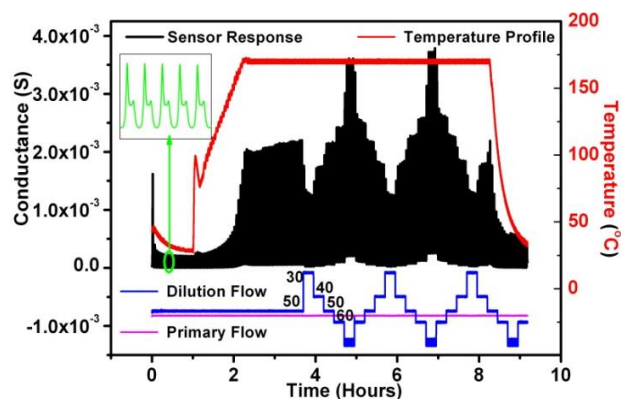


Figure 3. Measurement sequence of a pure SnO₂ layer exposed with pyrolysis gas of a heated PVC-coated wire with temperature profile and gas flows. The numbers relate the pyrolysis gas concentrations in percent. At each concentration, the heater cycles 10 times. The inset and the oval in green show the reproducibility of the profiles with stable baseline and maximum conductance at repeated temperature cycles.

B. Data Analysis

To demonstrate the performance of the sensor system and the procedure SimSens, it was assumed that besides

pyrolysis gases propene and CO as interfering atmospheres may occur. The goal is to distinguish between the different gas atmospheres, this means to recognize whether an unknown gas sample is one of the considered gases. In case of identification, additionally, the concentration of the gas has to be determined. The analysis model is based on the CTP-data of all four gas sensitive layers of the chip (Figure 7), which are simply linked together to one “extended CTP” (ECTP) as visualized in Figs. 4-6.

For the calibration model of pyrolysis gas, the CTPs of pyrolysis gases at 30%, 40% and 60% relative gas concentrations (Figures 3 and 7) were used and for the calibration model of propene and CO, the CTPs were taken at the corresponding concentrations 125ppm, 250ppm and 500ppm.

To test the capability for identifying, the gas component/mixture and to determine the associated concentrations, three gas samples were measured and evaluated by SimSens. These are pyrolysis gas at 50% relative concentration, propene and CO at 375ppm.

The following figures show that the pyrolysis gas sample at 50% relative concentration could be clearly recognized as a pyrolysis gas. This is due to the fact that in Figure 4 the difference between measured CTP and calculated CTP on the basis of the pyrolysis calibration model is very small. In Figure 5 and in Figure 6, the differences between measured CTP and calculated CTP based on the calibration model of propene, respectively CO, are much higher. Analogous results were obtained when evaluating the propene sample and the CO sample.

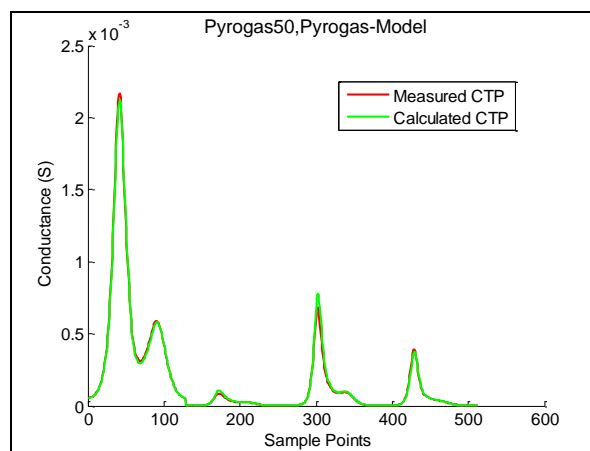


Figure 4. Measured ECTP of pyrolysis sample at 50% dilution and associated calculated ECTP based on the pyrolysis calibration model.

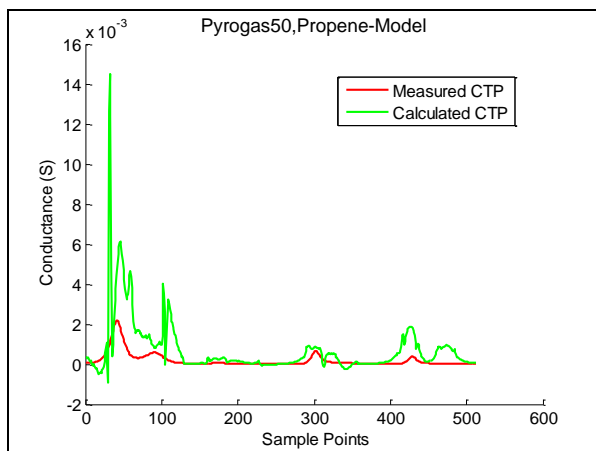


Figure 5. Measured ECTP of pyrolysis sample at 50% dilution and associated calculated CTP based on the propene calibration model.

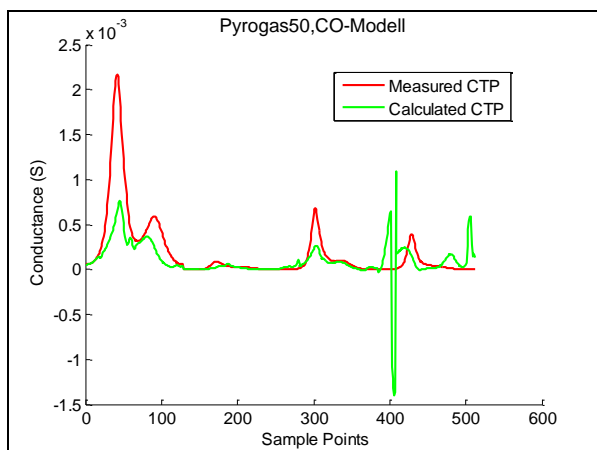


Figure 6. Measured ECTP of pyrolysis sample at 50% dilution and associated calculated CTP based on the CO calibration model.

TABLE I. DIFFERENCE VALUES BETWEEN MEASURED CTPS AND THEORETICAL CTPS

	Pyrolysis Model	Propene Model	CO Model
Pyrolysis-50%	2.2e-03	6.6e+02	8.7e+06
Propene 375ppm	9.9e+01	1.3e-02	1.5e+05
CO 375ppm	1.0e+00	4.3e+02	1.7e-01

Of course, the decision of identification is not based on a visual impression. For substance identification, a difference value D is calculated as a measure of the difference between measured CTP and calculated CTP. D is the relative sum of quadratic differences of every sample point of the measured CTP and the theoretical CTP. If the difference value is smaller than a so-called decision threshold value eps, the

sample under consideration is identified as the associated gas. In this investigation, the decision threshold value was set to $\text{eps}=4.e-01$.

In Table I, only the red bold numbers are smaller than the decision threshold value. Therefore, the pyrolysis sample could be identified as a pyrolysis gas, the propene sample as a propene gas and the CO sample as a CO gas.

After identifying the gas samples, SimSens calculates the associated gas concentrations. The evaluation results are given in Table II.

TABLE II. COMPARISON OF DOSED AND ANALYZED CONCENTRATION VALUES AND RELATIVE DEVIATION. ABOUT THE MEANING OF CONCENTRATIONS IN % SEE FIGURE 3.

Sample	Dosed concentrations	Calculated Concentrations	Relative Error
Pyrolysis 50	50%	47,6%	4,7%
Propene 375ppm	375ppm	388,8ppm	3,7%
CO 375ppm	375ppm	379,6ppm	1,2%

The concentration values estimated by the calibration model deviate from the experimentally adjusted values by less than 5% in all cases.

V. CONCLUSIONS AND OUTLOOK

The thermo-cyclic operation of a MOG array combined with simultaneous numerical analysis of the CTPs has been shown to be an elegant way for identification of gas mixtures. In this study, the pyrolysis gases emitted by heated PVC-based insulation materials are registered by well reproducible CTPs, even at temperatures where no color change of the sample material could be observed. These CTPs are well distinguishable from those obtained for two model gases, CO and propene. The results look promising considering the aim of early fire detection with high sensitivity.

The acquired CTPs were numerically analyzed employing the SimSens algorithm and the results showed very good identification capabilities and concentration estimation accuracy, which can lead to better incident identification and a very sensitive, more robust detection with a low false alarm rate.

In case of field applications, gas detection experiments for fire or any other dangerous gases using MOG sensors may have to be conducted in a real environment, where indefinite and unspecific but typical gas mixtures are present. In such cases, the numerical analysis of data using SimSens of a thermo-cyclically operated MOG-array will be of great advantage because the CTPs of four sensitive layers provide numerous gas specific features. To enable these advanced field applications, a microprocessor-based sensor system has to be devised, featuring the necessary means. This work has already been started.

ACKNOWLEDGMENT

The authors would like to thank German Federal Ministry of Education and Research (BMBF) for financial support of this work (Project Nr. 16N12262).

REFERENCES

- [1] D. Gutmacher, C. Foelml, W. Vollenweider, U. Hofer, and J. Wöllenstein, "Comparison of gas sensor technologies for fire gas detection", *Procedia Engineering* 25, 2011, pp. 1121–1124
- [2] G. Korotchenkov, V. Brynzari, and S. Dmitriev; SnO₂ thin film gas sensors for fire-alarm systems, *Sensors and Actuators B* 54, 1999, pp. 191-196
- [3] N. Illyaskutty, J. Knoblauch, M. Schwotzer, and H. Kohler, "Thermally modulated multi sensor arrays of SnO₂/additive/electrode combinations for gas identification", *Sensors and Actuators B* 217, 2015, pp. 2-12.
- [4] K. Frank, V. Magapu, V. Schindler, H. Kohler, H. B. Keller, and R. Seifert, "Chemical analysis with tin oxide gas sensors: choice of additives, method of operation and analysis of numerical signal", *Sensor Letters* 6, 2008, pp. 908–911
- [5] J. Knoblauch, N. Illyaskutty, and H. Kohler, "Early detection of fires in electrical installations by thermally modulated SnO₂/additive-multi sensor arrays", *Sensors and Actuators B* 217, 2015, pp. 36-40.
- [6] J. Knoblauch et al., "Sensor system applying thermally modulated MOG for early detection of fires in electrical cabinets", 15. Internationale Tagung über Automatische Brandentdeckung, 15th International Conference on Automatic Fire Detection, Proceedings Vol. II, pp 105-112, 14. - 16. Oktober 2014, Duisburg
- [7] H. Kohler, R. Becker, N. Link and J. Röber;; "Apparatus and process for identifying and/or determining the concentration of at least one gas component", EP 0 829 718 B1 (2004)
- [8] H. B. Keller, R. Seifert, and H. Kohler, "SimSens – a New Mathematical Procedure for Simultaneous Analysis of Gases with Resistive Gas Sensors", *Sensors & Actuators: B. Chemical* (2015), DOI information: 10.1016/j.snb.2014.10.133, pp. 203-207
- [9] R. Seifert, H. B. Keller, K. Frank, and H. Kohler, "ProSens - an Efficient Mathematical Procedure for Calibration and Evaluation of Tin Oxide Gas Sensor Data", *Sensor Letters* 9/1, 2011, pp. 7-10
- [10] R. Seifert, H. B. Keller, "Verfahren zur Klassifikation und zur Bestimmung der Einzelkonzentrationen eines Stoffgemisches (Procedure for Classification and Determination of the Concentration of the Components of a Gas Mixture)", Patentschrift DE10 2004 057 350

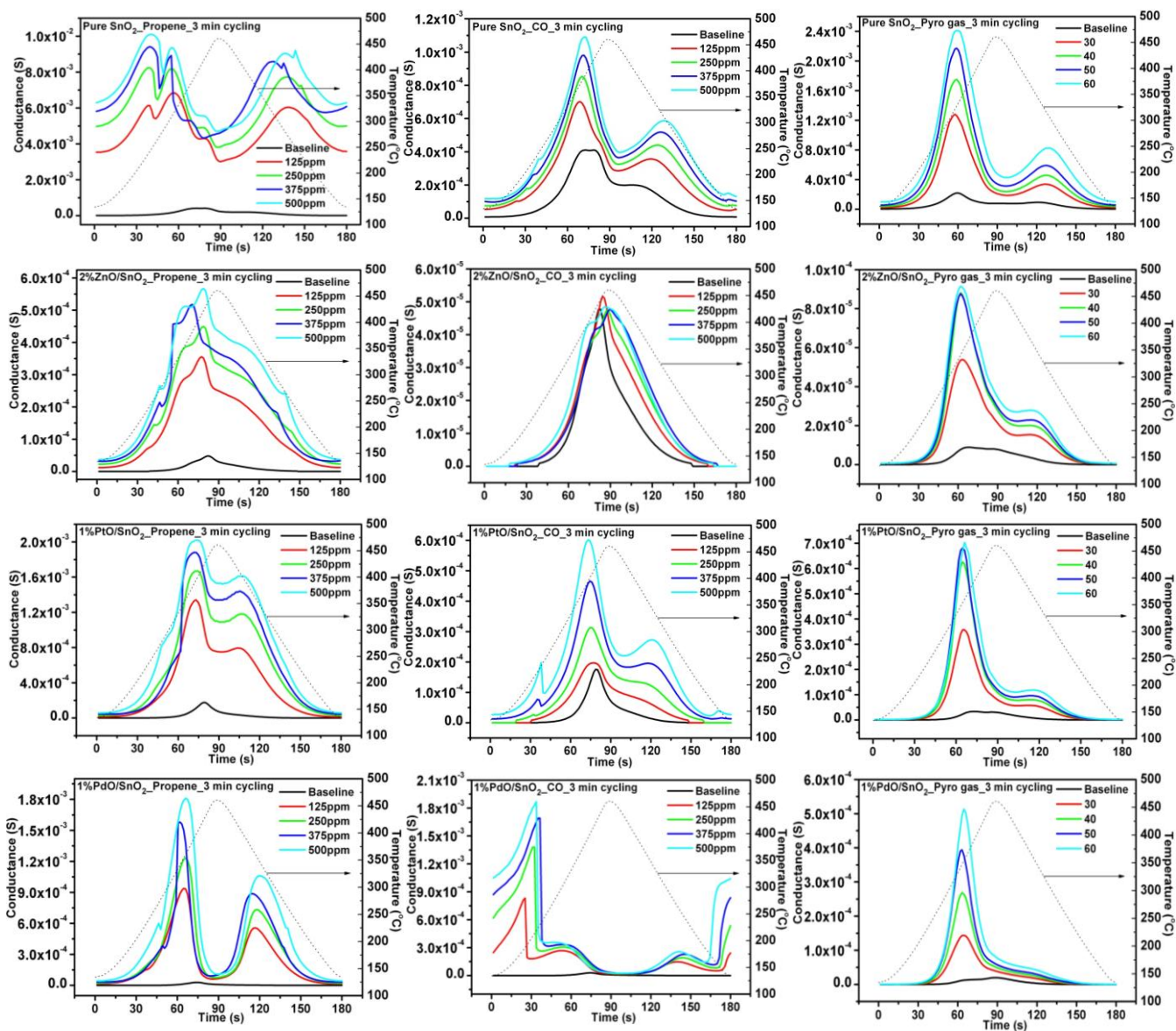


Figure 7. Matrix representation of the comprehensive sensor responses: Conductance over time profiles (CTP) of the four sensing layers (in columns) when exposed to various concentration of propene, CO and pyrolysis gas (in rows). The propene and CO concentrations are given in ppm and the pyro gas concentration is given in percentages in relation to the dilution flow used, (see caption of Figure 3 for more details).

Highly Sensitive Pt-TiO₂-Pt Sandwich-type Metal Oxide Gas Sensors of Hydrogen

Influence of the electrode design on the gas sensing properties

O. Krško, T. Plecenik, A. A. Haidry, P. Ďurina, M. Truchlý, B. Grančič, M. Gregor, T. Roch, L. Satrapinskyy, M. Mikula, P. Kúš, A. Plecenik

Department of experimental Physics
Faculty of Mathematics, Physics and Informatics, Comenius University
Bratislava, Slovak Republic
e-mail: krsko@fmph.uniba.sk

M. Moško, A. Mošková
Institute of Electrical Engineering
Slovak Academy of Sciences
Bratislava, Slovak Republic

Abstract – In this paper, we present a metal oxide-based hydrogen gas sensor with high sensitivity and short response time, operating at room temperature. Our sensors have a sandwich-like structure with a thin metal oxide layer in between the top and bottom electrode. The electrodes are in a shape of long narrow bridges, perpendicular to each other. It has been shown that narrowing the top electrode down to ~100 nm causes the sensitivity to substantially increase and reduces the response time. The sensor response (ratio R_{Air}/R_{H_2}) to 1% H_2 in synthetic air can be as high as $\sim 10^5$ at room temperature, with response time of only a few seconds. A theoretical model explaining such a behavior is also proposed. The increased sensitivity of sensors with narrow top electrode is explained by non-trivial abrupt change of the charge carrier transport mechanism from thermoemission to electron drift. This change is caused by the hot electron temperature instability induced by combination of the H_2 diffusion profile under the top electrode and high intensity of electric field between the electrodes.

Keywords-hydrogen gas sensor; metal oxide; high sensitivity; room temperature.

I. INTRODUCTION

Pursuit of alternative fuels and energy carriers causes hydrogen to attract more and more attention. However, the use of hydrogen also brings its safety risks what makes the leak detection crucial. Demand for highly sensitive, fast, stable and reasonably priced hydrogen gas sensors therefore increases [1]. Operation of the chemiresistive MOS gas sensors is based on the change of conductivity due to contact with oxidizing and reducing gases [2]. Although these devices are already being used for years, their further research and improvement is possible thanks to development in the field of nanotechnology. One of the problematic properties of the MOS gas sensors is their relatively high operating temperature, usually ranging approximately from 200 to 400 °C. Heating to such temperatures is undesirable for use in hazardous explosive environments and significantly rises the power consumption. The work presented here is therefore focused on development of highly sensitive metal oxide gas sensors operating at room temperature.

In Section 2, the sample preparation process is described. In Section 3, the results of measurements performed on the prepared samples are presented and discussed.

II. SENSOR FABRICATION

The sensors were prepared as follows: On the sapphire substrate, the 100 μm wide and 20 nm thick bottom Pt electrode was formed by lift-off photolithography and DC (direct current) magnetron sputtering. The 35 nm thick TiO₂ layer was then deposited by DC reactive magnetron sputtering. Subsequently the upper Pt electrode (width ranging from 100 nm to 1100 nm on different samples) was formed on top of the TiO₂ layer by DC magnetron sputtering followed by electron beam lithography and ion beam etching. The whole sensor structure was then annealed at 600 °C for 1 hour. During the annealing process, the TiO₂ crystallizes and ohmic contacts are formed at the metal-semiconductor interfaces. The TiO₂ grain diameter was determined by XRD (X-ray diffraction) and AFM (atomic force microscopy) to be approximately 10 nm. A sketch of the final sensor profile is shown on Figure 1.

III. RESULTS AND DISCUSSION

Responses of the sensors to presence of H_2 in technical air were measured in a closed chamber in a gas flow regime, with possible target gas concentration ranging from 300 ppm to 10 000 ppm (parts per million) regulated by two Red-y mass flow controllers. For wider (over ~300 nm) top electrodes,

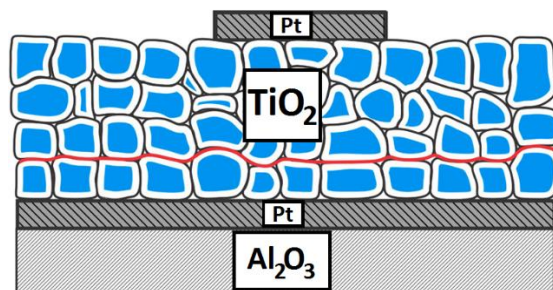


Figure 1. Illustration of the sensor cross section. Schematic figure of the sandwich-type sensor with crossed electrodes.

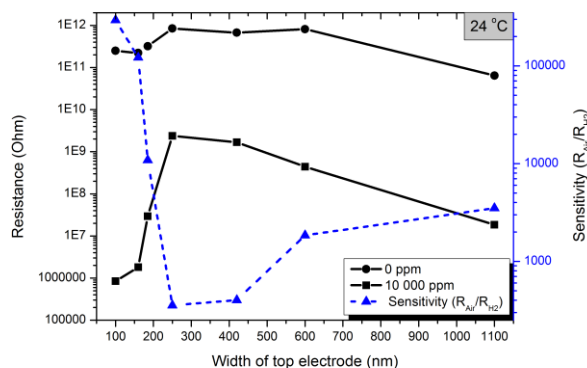


Figure 2. Dependence of the sensor resistance on the top electrode width for 0 and 10000 ppm H₂ in technical air (left y axis). Dependence of sensitivity on the top electrode width (right y axis).

the resistance of the sensors was observed to slightly increase with the decreasing width of the top electrode due to its smaller cross section. However, a steep decrease of the sensor resistance at 10000 ppm of H₂ was observed for sensors with the top electrode width below ~200 nm even at room temperature (Figure 2). Response of the sensor (ratio R_{Air}/R_{H₂}) with 100 nm wide top electrode to 10000 ppm H₂ in synthetic air was higher than ~10⁵. We explain such high response of the sensors with narrow (~ 100 nm) top electrode by a combination of two effects. First, for such narrow electrodes the diffusion length of H₂ molecules is large enough to create high concentration profile even directly under the top electrode and the height of the inter-grain energy barriers in this region is decreased. At the same time, the intensity of the electric field reaches its maximum in this region. Combination of these two effects induces the hot electron temperature instability, which will be explained further. In general, relation between the temperature of electron gas and the temperature of crystal lattice is given by the energy balance equation [3]

$$\frac{k_b T_e}{2} = \frac{k_b T}{2} + j_e F \tau_e$$

where j_e is the electron current density, F is the electric field intensity and τ_e is the energy relaxation time. The term $j_e F \tau_e$, which represents the electric field induced heating of the electron gas, is usually negligible. In our situation, this term rises significantly and the electron temperature T_e is no more equal to the temperature of the crystal lattice T .

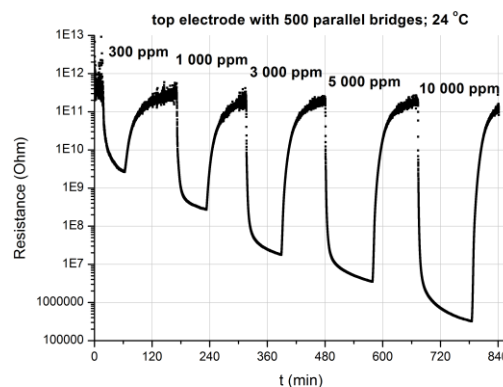


Figure 3. Response of the sensor with 500-bridge top electrode on different concentrations of H₂ in technical air at room temperature.

Rise of the electron gas temperature well above the level of crystal lattice temperature causes the abrupt change of the charge carrier transport mechanism from thermionic emission to electron drift [4].

Problematic is the high resistance of our sensors, which reaches values over our measurement limit of ~ 10¹¹ Ohm without the presence of hydrogen. This decreases the measurable response of such sensors, especially for low H₂ concentrations. A solution for too high resistivity of TiO₂ material has been proposed through doping [5]. To solve this problem in our case, sensors with the top electrode consisting of many parallel bridges were fabricated. This type of electrode is expected to decrease the overall resistance of the whole structure and allows us to detect lower concentrations of hydrogen. Preliminary results obtained on the sensor of this type, with a 500-bridge top electrode, are shown in Figure 3.

REFERENCES

- [1] T. Hübert, L. Boon-Brett, V. Palmisano, M. A. Bader, "Developments in gas sensor technology for hydrogen safety" International Journal of Hydrogen Energy, 2014, pp. 1-10
- [2] N. Barsan, U. Weimar, "Conduction model of metal oxide gas sensors" Journal of Electroceramics, 2001, pp. 143-167
- [3] K. Hess, "Advanced Theory of Semiconductor Devices" Prentice-Hall, Englewood Cliffs, NJ, 1988.
- [4] T. Plecenik, M. Mosko, et al., "Fast highly-sensitive room-temperature semiconductor gas sensor based on the nanoscale Pt-TiO₂-Pt sandwich" Sensors and Actuators B 207, 2015, pp. 351-361
- [5] Z. Li, D. Ding, Q. Liu, C. Ning, "Hydrogen Sensing with Ni/Doped TiO₂ Nanotubes" Sensors, 2013, pp. 8393-8402

High Frequency Thick Film Ultrasonic Transducers Used for Estimation of Flow-Mediated Vasodilation of the Radial Artery

Andrzej Nowicki, Marcin Lewandowski, Ihor Trots

Department of Ultrasound
Institute of the Fundamental Technological Research
Warsaw, Poland
email: anowicki@ippt.pan.pl, mlew@ippt.pan.pl,
igortr@ippt.pan.pl

Robert Olszewski

Cardiology and Internal Medicine
Medical Military Institute
Warsaw, Poland
email:rolszewski@wim.mil.pl

Abstract - Preceding atherosclerosis is an endothelial dysfunction. Therefore there is a growing interest in the application of non-invasive clinical tools to assess endothelial function. Commercially available ultrasound machines can measure flow-mediated vasodilatation of the brachial artery using maximum 10-12 MHz linear probes. The higher the probe frequency, the better the axial resolution. Recently, a new technology of piezoelectric transducers based on PZT thick film technology has been developed in Meggitt (Denmark) as a response to a call for devices working at higher frequencies. The thick films exhibited at least 30% bandwidth broadening comparing to the standard PZ 27 transducers, resulting in an increase in match filtering encoding output by a factor of 1.4-1.5 and finally resulting in a signal to noise gain of the same order. The introduction of a high frequency 25-30 MHz ultrasound scanner to measure radial artery diameter after reactive hyperemia opens a new window for more precise imaging of endothelial function.

Keywords-thick film transducers, atherosclerosis, flow mediated vasodilation.

I. INTRODUCTION

High frequency (HF) ultrasonography is gaining increased interest in skin, eye and small animals imaging. However, an excessive attenuation of ultrasound at HF limits the range of the available frequencies, considering the permissible peak pressure of the probing beam. Our motivation was to develop the dedicated wobbler scan head with the transducer exhibiting wide-bandwidth behavior and enabling transmission of wide-band encoded probing pulses with peak pressure not exceeding the acceptable levels.

The issue of maximizing penetration depth with concurrent retaining or enhancement of image resolution constitutes one of the time invariant challenges in ultrasound imaging. Concerns about potential and undesirable side effects set limits on the possibility of overcoming the

frequency dependent attenuation effects by increasing peak acoustic amplitudes of the waves probing the tissue. To overcome this limitation, a pulse compression technique employing 16 bit Complementary Golay Code (CGS) was implemented at 25-35 MHz. In comparison with the other, earlier proposed, coded excitation schemes, such as chirp, pseudo-random chirp and Barker codes, the CGS allows virtually side lobe free operation, [1, 2]. Section II describes the influence of the transducer bandwidth on the overall gain of the compressed ultrasonic echoes. Section III describes the method and the preliminary results of measurements of the radial artery diameter. The conclusions close the article.

II. WIDE BAND THICK FILM PROBE

The bandwidth of a Golay coded sequence often exceeds fractional bandwidth of the available imaging transducer. It results in final gain of the compressed echo signal for different spectral widths of CGS. For example, in the case of 80% fractional transducer bandwidth, the peak-to-peak amplitude in compressed signal decreases to 90%. For 60% and 50% fractional bandwidth the compressed signals decrease to 57% and 50%, respectively. Also, with the narrowing of the transducer bandwidth the pulse width elongates. In the case of 80% fractional transducer bandwidth, the full width at half maximum (FWHM) in compressed signal is equal to 37ns. Following transducer bandwidth decreasing leads to FWHM widening and for 60% and 50% fractional transducer bandwidth, the FWHM in compressed signal is equal to 61.4ns and 63.5ns, respectively. Assuming speed of sound in tissue equals to 1540 m/s the corresponding spatial FWHM would be equal to 57 μm , 94.5 μm and 97.8 μm respectively [1]. The bandwidth of the used transducer is shown in Fig. 1.

The proper material for wide band thick film flat and concave transducers was developed by Insensor® - Meggitt (Copenhagen, Denmark). The technology based on screen or pad printing process offers not only flexibility of defining the thickness (i.e., resonant frequency) of the transducers through printing the specified number of film layers, but also the option of readily selecting the shape of the

transducer and semi assembling of the final device since the film can be deposited on the appropriate substrate, e.g., of porous ceramic with well defined acoustic properties acting as backing for the transducer. The printing process offers possibility to deposit the piezoceramic film on a focusing substrate. The piezoceramic film will follow the curvature of the backing forming an active layer of well defined and uniform thickness. The top and bottom electrodes are deposited as a part of the printing process and provided with leads for electrical connections.

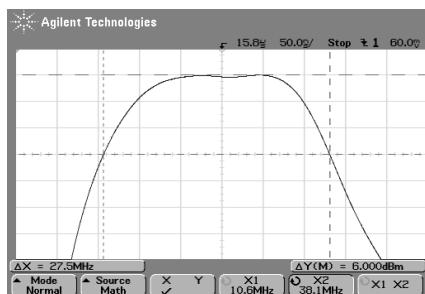


Figure 1. FFT spectrum of the ultrasonic echoes for the thick film transducer; central frequency close to 27 MHz, bandwidth=27.5 MHz.

Piezoceramic thick films have relatively low acoustic impedance of approx. 18 MRayls and the acoustic properties of the substrate/backing material have been optimized to match it.

III. METHODS AND RESULTS

Compression of the received coded sequences effectively resulted in very short, one wavelength long, probing pulses and allowed for very precise measurements of internal diameter of the radial artery. In 1994, Celermajer et al [3] described the technique to test the endothelium and smooth muscle dependent dilation capability by producing the reactive hyperemia in brachial artery. In 2002, Corretti et al [4] published the initial guidelines for the ultrasonic assessment of flow-mediated vasodilatation (FMD) of the brachial artery. Since then numerous reports on the technique were published [e.g., 5, 6]. In general enthusiastic, however due to the limited axial resolution of the commercial US scanners working in 10 MHz frequency range, the precision of the diameter measurements was not better than 0.2 mm. resulting in considerable ambiguity in final estimation of artery diameter dilation. That is why we have decided to modify the technique increasing the scanning frequency up to about 30 MHz and tracking the dilation of the radial artery instead of brachial one.

FMD of radial artery was examined in total 12 healthy young volunteers (25-35 years) men. The longitudinal scan of the radial artery of 36 year old volunteer is shown in Fig.2. In vivo and in vitro examinations were performed using a high frequency ultrasound scanner uScan developed at IPPT PAN. The device operates with a single element mechanically wobbling thick film transducer at the frequency 25-35 MHz.

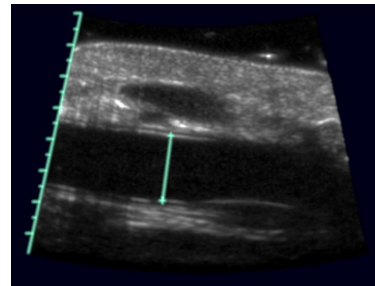


Figure 2. Longitudinal scan of the radial artery, systolic diameter= 2 mm

The Radial Artery Reactive Response (RARR) was induced by a five minute artery ischemia through the inflated tourniquet on the arm or forearm. Restoration of blood flow in the artery is strongly promoting the release of nitric oxide NO. The measured initial internal radial artery diameter was in range of 1.59-2.25 mm; the maximum diameter 2.01-2.60 mm was observed 40-60 seconds after tourniquet deflation.

IV. CONCLUSIONS

In the pilot study, the model of the brachial artery ultrasound demonstrated that using HF scanning ultrasound allowed to precisely register an increase in the diameter dimension of the radial artery ultrasound model already by 5%. RARR in healthy volunteers, using a transient ischemic calling stimulation has shown changes from 30 to 40 %, while in the four volunteers after cardiac incidents, these changes did not exceed 10 %.

REFERENCES

- [1] A. Nowicki, I. Trots, P. Lewin, W. Secomski, R. Tymkiewicz, "Influence of the ultrasound transducer bandwidth on selection of the complementary Golay bit code length," *Ultrasonics*, vol. 47, 2007, pp.64 – 73, 2007.
- [2] A. Nowicki et al., "Thick Film Transducers for High Frequency Coded Ultrasonography," *Archives of Acoustics*, 36, 4, pp.945–954, 2011.
- [3] D. S. Celermajer et al, "Non-invasive detection of endothelial dysfunction in children and adults at risk of atherosclerosis," *Lancet*, 340, pp.1111–1115, 1992.
- [4] M. C. Corretti et al, "Guidelines for the ultrasound assessment of endothelial-dependent flow-mediated vasodilation of the brachial artery: a report of the International Brachial Artery Reactivity Task Force," *J Am Coll Cardiol*, 39, pp.257–265, 2002.
- [5] R. A. Harris, S. K. Nishiyama, D. W. Wray and R. S. Richardson, "Ultrasound Assessment of Flow-Mediated Dilation," *Hypertension*, 5, pp.1075-1085, 2010.
- [6] K. E. Pyke, M. E. Tschakovsky, "Peak vs. total reactive hyperemia: which determines the magnitude of flow-mediated dilation," *J Appl Physiol*, 102, pp.1510 -1519, 2007.

Figuring Out Conscientious Degree from Brightness Distribution in IADL

Shota Shimayoshi, Shun Okamura

Graduate School of Information Science and Engineering
Ritsumeikan University
Shiga, Japan
Email: shimayoshi@de.is.ritsumei.ac.jp
shun_kamu@de.is.ritsumei.ac.jp

Yusuke Kajiwara, Hiromitsu Shimakawa

College of Information Science and Engineering
Ritsumeikan University
Shiga, Japan
Email: kajiwara@de.is.ritsumei.ac.jp
simakawa@de.is.ritsumei.ac.jp

Abstract—Because of the rapid increase of the elderly, the lack of helpers to take care of the elderly has become a serious problem in Japan. A way should be found to enable the elderly to be independent as long as possible. The paper refers to the motivation to keep the quality of life high as living willingness. The elderly with living willingness would keep their living environments comfortable. On the contrary, the elderly losing their living willingness are likely to make disorder in their house keeping, such as lazy cleaning and skipping of dish washing. The detection of the disorder of their daily activities makes it possible to find the decline of their living willingness early, because the disorder implies their physical and mental health get worse. Instrumental Activities of Daily Living (IADL) plays an important role to find the disorder. The activities are conducted to improve the quality of life. The laziness of the elderly in IADL implies they are losing their motivation to improve the quality of life. The paper proposes a method to recognize IADL, preserving the privacy of the elderly. It also figures out conscientious degree the elderly take IADL. The method uses the brightness distribution sensor. It provides a classifier of IADL from the brightness distribution. In an experiment for the elderly, the f-measure with which the method has recognized activities of cleaning, cooking, and washing are 0.975, 0.912, and 0.927, respectively. The experiment shows 0.599 in Nagelkerke R^2 , which indicates how well the method figures out conscientious degree in the activities. It reveals the method is precise enough to measure the decline of the elderly in the living willingness.

Keywords—Elderly; Daily Living; Privacy; Brightness; Sensor;

I. INTRODUCTION

Japan is suffering from a rapid progress of declining birth rate and increasing an aging population. As a result, it is worried that Japan will be short of nursing care staff by 2025. It is highly required to take measures to improve the self-supporting degree of each of the elderly, which means how an elderly person can spend his or her daily life independently [1]. Especially, it is essential to prevent the elderly from running into a condition where they require long-term and constant care in daily activities. To achieve the goal, it plays a vital role to find symptoms of the decline of their health condition from their daily activities. We should pay special attentions to the elderly living alone, because it is difficult to find symptoms of their decline. As one of the symptoms of the decline, the elderly tend to lose their motivation to keep high quality of their life. The paper refers to the motivation to keep the quality of life high as a “living willingness.” The decrement in the living willingness of the elderly appears in their daily life. It is verified that the elderly could be in unhealthy condition

physically and mentally when a living rhythm changes into disordered manner. Moreover, a lazy lifestyle negatively affects the self-supporting degree and the health of the elderly [2].

If we could notice that one’s lifestyle is becoming disordered manner, various measures can be taken to recover their living willingness. Lawton [3] has pointed out the Instrumental Activities of Daily Living (IADL) are effective to judge the self-supporting degree of the elderly. IADL are not essential to keep our life. However, if we carry out them, we can improve the quality of our life. Examples of IADL include cleaning and washing. Let us consider to measure the degree of carrying out IADL in terms of not only the frequency of the execution, but also the conscientiousness in the execution. If the degree of a specific elder person is high, we can estimate he or she is willing to enjoy daily life. On the contrary, an elderly person whose degree is getting worse is worried to lose the living willingness. The degree of carrying out IADL is considered to imply symptoms of the decline of the elderly. It is expected that we can find the elderly who have just started losing their living willingness. Furthermore, it is also expected to provide some measures to recover their living willingness. There are many works that apply IADL to detect the changes of the elderly such as abnormality in health conditions [4][5]. They examine the frequency and the execution time in each IADL action. This paper proposes to use IADL as an index of the living willingness of the elderly. It examines the conscientious degree of IADL in addition to the frequency and the execution time. It is thought that the elderly who carry out IADL less conscientiously is going to stop IADL actions eventually. The examination of the conscientious degree of IADL will contribute to the detection of the declines of the elderly in the earlier stage with higher accuracy.

This paper focuses on cleaning actions among the IADL actions. First, cleaning action is identified with the machine learning and extracted from many living daily activities. The conscientious degree of a cleaning action is figured out from the characteristics of the action during the cleaning period. This paper proposes a model to identify the conscientious degree. The method uses the brightness distribution sensors [6] to collect movement logs in order to protect the privacy of the elderly. The brightness distribution acquired by the sensors brings information significant enough for a machine to discern living activities, while it makes no meanings for humans to perceive what the elderly are doing.

This study figures out the conscientious degree with the difference of the body trunk movement of the person carrying

out of the living activities. The method can discover symptoms of the decline in the early stage, using both of the execution degree and the conscientious degree.

The remainings of the paper are organized in the following way. Section II describes the related works. Section III explains the method to discern the living activity, using brightness distribution sensors. It also states how to figure out the conscientious degree of discerned cleaning actions. Section IV illustrates the process of an experiment to evaluate the proposed method along with its result, followed by discussion of the result in Section V. Section VI concludes this paper.

II. RELATED WORKS

There is a method to automatically recognize activities of the elderly in daily life with cameras set up in their house [7]. The camera acquires a lot of information unrelated to activities of them from their daily life. Since the method pays little attention to the privacy of the elderly, it causes the elderly to be stressed. It is not preferable to set up a camera in a house. A method to recognize living activities with a Kinect sensor [8] also has the problem in the viewpoints of the privacy protection, because it acquires a lot of irrelevant information as well as the camera. Techniques to recognize actions at home protecting the privacy are proposed with acceleration sensors [3], infrared sensors [9], and laser range finders [10]. Acceleration sensors measure the movement of persons who wear them in their body. They cannot acquire any data unless they are worn. Some of the elderly feel resistance to wear them, while others forget to wear them. The amount of data infrared sensors acquire is small and its accuracy is poor. It is difficult to figure out living willingness with the sensors due to the poor accuracy. Though they can be applied to the detection of emergency such as accidents and spasms, it costs high to set up many of them in various places to overcome their poor accuracy. Laser range finders implement data acquisition in a wide range. However, it is unrealistic to install many of the sensors to detect actions, because they are expensive sensors.

III. FIGURING OUT CONSCIENTIOUS DEGREE FROM BRIGHTNESS DISTRIBUTION

A. Brightness Distribution Sensor

The method uses brightness distribution sensors [6] to protect privacy of the elderly. Figure 1 shows the difference of the acquired data between a Web camera and a brightness distribution sensor. The brightness distribution sensor acquires

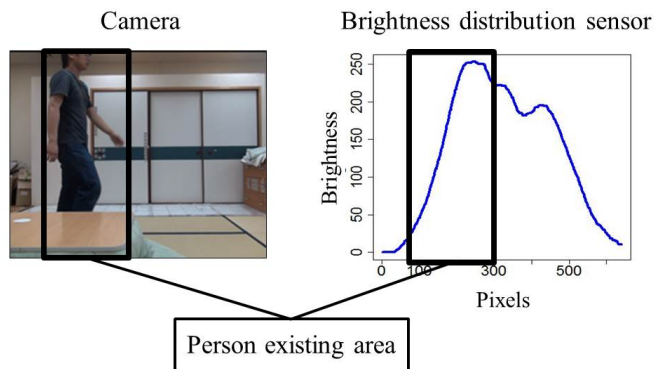


Figure 1. Difference between Web camera and brightness distribution sensor.

only the brightness value in the horizontal dimension. It recognizes a person, utilizing the fact a brightness value changes largely at the position where the person moves. Two brightness distribution sensors are settled so that the center lines of the data acquisition areas of each sensor should cross almost orthogonally. The volume of information of the sensors is less than that of cameras because they acquire only brightness. Privacy is threatened with malaise of the acquired information by outsiders. Even if outsiders get the brightness information showing activities of a specific person, they do not understand what the person does. Brightness distribution sensors can be set up inexpensively, because we can covert commercial web cameras into brightness distribution sensors, exchanging their lenses into rod lenses. A lot of sensors are not required because they acquire as wide range data as the web cameras. The sensors save space, because a small sensor covers a wide range.

B. Activity Classification from Local Features

The method uses the Bag-of-Features method [11] to extract a peculiar feature from the brightness data of each living activity. Each pixel of figures has various properties. First, the Bag-of-Features method clusters pixels of figures into several groups, based on the properties. It figures out the histogram of each figure, counting points in every cluster. The distinguishes images with the features in the shape of the histogram. The proposed method calculates the three local features for each pixel, consisting of background difference values, pixel difference values, and frame difference values. Three local features are the main elements that can be taken from the brightness data. The background difference values are picked up from the difference of the target image from an image containing no living activity. The pixel difference values and the frame difference values are derived from special difference and temporal difference of the background difference value. These local features compose a three dimensional space. Let a brightness value be $b(f, p)$, where p and f denotes the pixel number and the frame number, respectively. Let us denote the background difference value, the pixel difference value, and the frame difference value with $B_s(f, p)$, $P_s(f, p)$, and $F_s(f, p)$, respectively. Three local features can be expressed in (1)-(3), when the number of the frame showing the background is assumed to be 0.

$$B_s(f, p) = b(f, p) - b(0, p) \tag{1}$$

$$P_s(f, p) = B_s(f, p) - B_s(f, p - 1) \tag{2}$$

$$F_s(f, p) = B_s(f, p) - B_s(f - 1, p) \tag{3}$$

The background difference value is a feature corresponds to the existence of a person. The pixel difference value expresses the edge of position where a person exists. The frame difference value shows the movement of a person. Pixels represented with the three values are plotted in the three dimensional space. All points are clustered using k-means++ [11]. The histogram indicating the number of points included in each cluster is constructed to show the distribution of points for each image. The histogram does not provide any location information, which is important to identify living activities. For instance, the information is important when we want to distinguish living activities in which a person moves around the entire room like cleaning from living activities executed at specific locations like washing. The method reflects the location information dividing the image into parts equal in

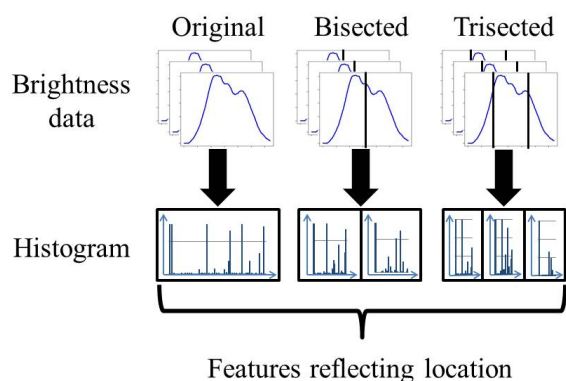


Figure 2. Constructing histogram from division brightness data.

their width. A histogram is constructed from each of them [12]. Figure 2 depicts the outline when the division is applied to the original brightness data. The original brightness data corresponding to the whole of the acquisition area are bisected and trisected in the proposed method. Eventually, six histograms are constructed from a single sensor. The method acquires 12 histograms from one living activity because it uses two sensors. Due to the division of brightness data, features representing person movement appears in all of the six histograms in living activity where a person moves around the entire room like cleaning, while those features appears in specific histograms in case of washing in which a person stays in a specific location. The proposed method constructs a model to identify features of each living activity with the Random Forest method [13]. The model calculates which living activity has been executed, given features in an actual living activity.

C. Figuring Out Conscientious Degree from Flow Line

The proposed solution pays attention to the conscientious degree in the living activity to find a smaller change in the living willingness. Each living activity has its own index to represent its conscientious degree. The method figures out the conscientious degree of each living activity where the person would move around in the room. Among various kinds of living activities, it focuses on cleaning, because it is an essential activity to improve the quality of the life. It pays an attention on the body trunk, which is the most important part for human beings in various living activities.

First, the method presumes the location of the body trunk of a target person from the brightness value in each sensor. Since the brightness value greatly changes at the position the person exists within the range of the sensor, the location of the body trunk is estimated at the position where the change of the brightness value is largest, that is, the position with the maximum background difference value. The position of the body trunk, T , is given by (4).

$$T = \arg \max_{0 \leq p \leq 639} |B_s(f, p)| \tag{4}$$

Next, the flow line of the body trunk is constructed, arranging the position of the body trunk all over the frames in the time series order. The proposed method figure out the conscientious degree of the living activities where a person moves around in the room like cleaning. Using the Hidden Markov Model (HMM) [14], the method derives a state change diagram to consider staying and movement of the person in a

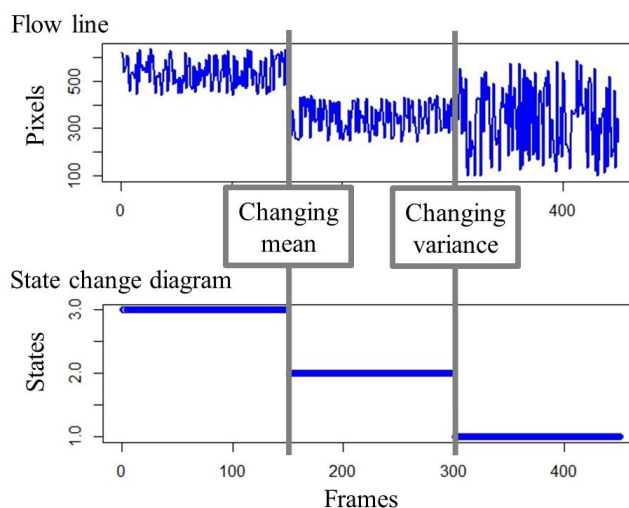


Figure 3. State change diagram converts from flow lines.

flow line. The example of the state change diagram the HMM converts from flow lines is shown in Figure 3. The graph of a flow line in the figure indicates the position of the body trunk in the course of the time, assuming the horizontal axis and the vertical axis are the time line and the pixel number, respectively. The state change diagram implies the flow line in the figure roughly has three states. The change of the mean and the variance expresses a significant state change. The change of the mean means the body trunk moves to another position, while that of the variance corresponds to the change in the width of operation of the body trunk. The conscientious degree of the living activity is figured out from the two kinds of state changes. The transition probability is used to examine the relevance among states. The transition probability to a different state is considered to represent the movement order and the work procedure in the living activity, because it is influenced by the position of the body trunk and the change in the width of operation. It is not considered as the feature of each person, because it varies easily with the order and the combination of living activities. The proposed method values the transition probability from one state to the same state, which is referred to as the self transition probability. When the person stays in a specific point, the self transition probability is considered to indicate the location and the time period of the stay, because it gets little influence from the position of body trunk and the change in the width of operation.

Regarding the self transition probability as the feature of the living activity of each person, the proposed method calculates the self transition probability of each state from the two state change diagrams associated with the two sensors. A model is constructed to figure out the conscientious degree of a specific cleaning activity where the person move around the room. The model assumes the self transition probability in each state is the explanatory variable while the conscientious degree is the objective variable. The model uses the logistic regression [15], because the objective variable is a qualitative variable. The combination that minimizes the Akaike Information Criteria (AIC) [15] is selected from two or more explanatory variables, to construct a model which predicts the conscientious degree of the living activity.

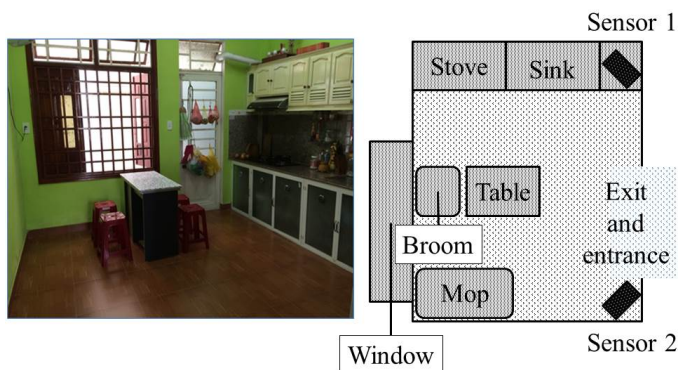


Figure 4. Experimental environment.

IV. EXPERIMENT

A. Purpose and Process

We have verified living activities can be identified with the brightness distribution with an experiment. Using the data collected in the experiment, we examine whether the conscientious degree is able to be estimated from the difference of the body trunk. Figure 4 shows the experimental environment, which is an actual dining-and-kitchen space. The photograph in the left side shows the view taken from the exit and entrance of the floor plan in the right side. The movable space of the experimental environment is a 3 meter square. To decrease the blind spot, a brightness distribution sensors is installed at each of the 2 corners of the space. Each of them is mounted at a point of 80 centimeters in height. Subjects of the experiment are 20 elderly people consist of 8 men and 12 women whose ages range from 60 to 70 years old. In the experiment, subjects conduct three living activities: cleaning, cooking, and washing, according to the standard of IADL. In the cleaning, each of them wipes the entire floor with a mop, after sweeping with a broom. In the cooking, each of them breaks an egg into a bowl to mix with favorite seasonings. The subject fries it and dishes it up. The washing makes each of them keep washing tablewares at the sink. Each of the subjects repeats every living activity 3 times, each of which is finished within 3 minutes. A whole experiment for one subject is organized within 60 minutes so as to prevent the conscientious degree of the activities from varying with their tiredness. The number of times and the length of the activity time is determined in consideration of the load of the subjects.

B. Evaluation

With the Bag-of-Features method, we detect living activities from features in the brightness distribution values sampled in the experiment. We have determined to classify the brightness distribution values into 25 groups after the examination of all combinations. We have used the 20 fold cross validation so that all 20 experiment participants may become test data to evaluate the generalization performance. The algorithms used for the detection are the Random Forest [13], the Naive Bayes classifier [16], and the linear Support Vector Machines [17]. These algorithms are suitable for the detection of living activities because they are known to provide high performance under a lot of objective variables. The performance of the proposed method is evaluated by the f-measure, which is the harmonic average of the precision and the recall. The precision

is an index that shows the accuracy of the result because it is the ratio of target actions in actions detected by the method. Recall is an index that shows the coverage of the result because it is the ratio of detected target actions in target actions to be detected by the method. We should take a good balance of the precision and the recall. Even if the precision is high, we are not sure how many target actions to be detected are covered by the detected actions. The f-measure presents the balance of the precision and the recall.

We have paid a special attention to the cleaning to know the conscientious degree of each subject, because it is one major instance of IADL a lot of people take in daily life. It is thought that the cleaning is effective to judge the conscientious degree for almost all persons. In the experiment, cleaning of each subject is recorded with as a video movie to ask people watching it on the conscientious degree of the subject as a questionnaire. The questionnaire asks 15 twenties consisting of 12 males and 3 females to evaluate the conscientious degree of the cleaning of each subject with 5 ranks. Based on the rounded average of their evaluation, we regard the elderly ranked at 4 or more as highly conscientious, while ones ranked 2 or less as poorly conscientious. We have also examine common features for subjects of high conscientious degree and ones of low conscientious degree, to find a criterion to distinguish subjects with the conscientious degree. Focusing on the movement of subjects in the experiment space, we apply the HMM to find the criterion. The HMM decides the state transition in the time series with the Viterbi algorithm after presuming parameters concerning to the state with the Baum-Welch algorithm [14]. Applying the Baum-Welch algorithm to all subject flow line, states are identified in the flow lines representing the movement of subjects. The transition of identified states in each flow line is figured out with the Viterbi algorithm to each flow line of all participants. In the HMM, when we assume too few states, we cannot see any difference among subjects, because each subject stays in specific states too long. On the contrary, too many states make subjects stay in every state too short. In both case, we cannot find any difference among subjects. After trials for all combinations, we have determined 5 is the best number of states to find difference in each subject. If many subjects of high conscientious degree stay in a specific state, the state indicates the feature of the high conscientious degree. The proposed method examines the self transition probability of each state. To predict whether each subject is conscientious or not, it builds a Logistic regression model whose explanatory variables are the self transition probability. It selects combinations of two or more explanatory variables which minimize AIC. The combination of the explanatory variables provides the laargest influence on estimation of the conscientious degree. We calculate Nagelkerke R^2 [18], which shows the degree of fit of the model made by Logistic regression. Nagelkerke R^2 takes the value between 0 and 1. The more it approaches to 1, the better the degree of fit of the model.

C. Result

Table I shows the f-measure values in the detection using the three Supervised learning algorithm. As the table shows, Random Forest is superior to the others. In all kinds of the living activities, the f-measure values exceeds 90 percent when Random Forest is used. The conscientious degree is high in 6 subjects and low in 3 subjects from the result of the question-

TABLE I. F-MEASURE VALUES IN THE DETECTION USING THE THREE SUPERVISED LEARNING ALGORITHM.

	Cleaning	Cooking	Washing
Random Forest	0.975	0.912	0.927
Naive Bayes classifier	0.830	0.793	0.705
Linear Support Vector Machines	0.942	0.897	0.874

TABLE II. CRITERIA OF THE CONSCIENTIOUS DEGREE IN THE QUESTIONNAIRE.

	Number of cases
Fineness in movement of hands	10
How to put force	8
Area within the range of action	7
Fineness in movement of body trunk	7
Repetition degree within the area of action	4
Length of time	3
How to wash mop	3
Presence of periodicity	1
Good quality of posture	1
Dustpan after sweeping with broom	1
Whether the cleaned place is seen or not	1

naire to 15 twenties. Table II shows the summary of the result in the criteria of the conscientious degree in the questionnaire. The table indicates the fineness of movement of hands and the body trunk are adopted as the criterion a lot of people. The conscientious degree decreases when the movement is too large. It justifies the proposed method uses the self transition probability to figuring out the conscientious degree, because the amount of movement influences on the staying time of each point. 5 states are derived, applying the HMM to the movement of each subject. The brightness distribution sensors used in the experiment represent the position of the body trunk with the angle ranging from 0 to 639, where 0 corresponds to the left side while 639 to the right side. Table III shows the mean and the variance of the position in each state for Sensor 1 and Sensor 2. We build several Logistic regression models to calculate the conscientious degree, specifying various combination of the self transition probability in states as explanatory variables. Among the models, the AIC gets minimum for the one in which we specify only the self transition probability of State 4 of Sensor 2 as an explanatory variable. It means the conscientious degree is best discriminated when subjects stay in State 4 of Sensor 2. The model figures out the conscientious degree, Pr_i , with

$$Pr_i = \frac{1}{1 + \exp(107.4 - 113.4s_i)} \quad (5)$$

where s_i is the explanatory variable. The fitting degree of the model is fairly good because Nagelkerke R^2 is 0.599. For each of subjects with the high and the low conscientious degree, Figure 5 shows the difference of the self transition probability of each state derived from Sensor 1, when the subject stay in State 4 of Sensor 2. In figure, a horizontal axis shows the IDs of the status of Sensor 1. The vertical axis shows the average probability of the subject staying in each state for both of the high and the low conscientious degree. In State 1 and State 5, there is a big difference of the average probability between subjects of the high and the low conscientious degree. Suppose a subject stays in State 4 of Sensor 2. From Table III, the subject staying State 1 derived from Sensor 1 should be located around B in Figure 5, while the location of the subject staying State 5 of Sensor 1 should be around A. These results

TABLE III. MEAN AND VARIANCE OF THE POSITION IN EACH STATE FOR SENSOR 1 AND SENSOR 2.

	Sensor 1		Sensor 2	
	Mean	Variance	Mean	Variance
State 1	231	540	120	672
State 2	303	406	174	140
State 3	366	281	222	294
State 4	444	792	337	1507
State 5	551	1845	489	3777

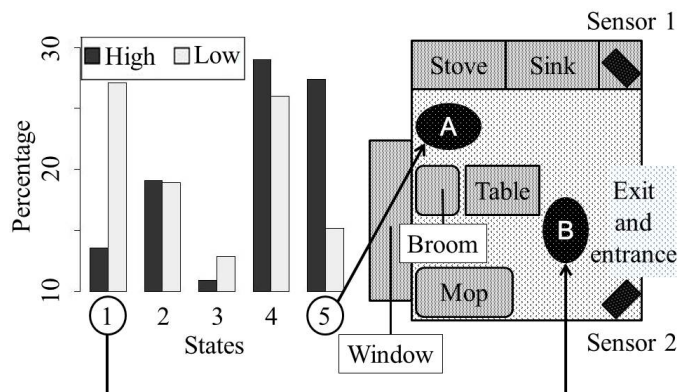


Figure 5. Difference of the self transition probability of each state derived from Sensor 1, when the subject stay in State 4 of Sensor 2.

imply subjects with the high conscientious degree are likely to stay around A, while ones with the low conscientious degree often stay around B. It can be said that the conscientious degree is judged high for subjects cleaning corner spots emphatically, while that of subjects staying in spacious parts is regarded low. The conscientious degree is understood from the length of the staying time in specific locations.

V. DISCUSSION

From the f-measure, it is thought that Random Forest is the best machine learning algorithm to be applied to detect living activities. The f-measure with Random Forest has reached over 90 percent for any examined activities. The method measures the living willingness from the transition of the execution degree calculated from actual living activities for the long term. For instance, suppose the elderly have engaged in specific activities regularly. It is thought that their living willingness decreases, if they get lazy for the activities for some time. The laziness is expected to be found without loss, because the detection accuracy exceeds 90 percent. The proposed method is practical enough. Among the examined activities, the cleaning is detected with the highest f-measure, 0.975. The cooking and the washing are inferior to the others, because the location of the subjects is similar in the activities. Since people cook or wash tablewares in the location far from the sensors, it is difficult for the sensors to recognize small movement of hands and arms in the activities. The activities might fail to match with pre-acquired features of any activity. It is necessary to select better sensor positions to make them recognize the small movement in the cooking and the washing.

In the model to discriminate the conscientious degree, we found State 4 of Sensor 2 has the best self transition probability. In the questionnaire, the conscientious degree of the cleaning is low when the movement of body trunk is too large. There are a lot of answers which value the width of

the movement area to judge the conscientious degree. It is thought the high conscientious degree is related to the staying time in the corner of the room. In the mean time, the time length of the cleaning is not mentioned as a criterion to judge the conscientious degree. It does not work as a criterion because we have specified the time length of each activity in the experiment, which makes the difference among subjects small. Nagelkerke R^2 of the model is 0.599. We can expect the improvement of its value, if we can add factors which are picked up as the criteria, but not incorporated in explanatory variables of the model. For example, we can incorporate the force subjects put during the cleaning, as shown in the second line of Table II, if we can sense it. It has been revealed subjects with the high conscientious degree differ from those of the low conscientious degree in terms of the location they stay. Subjects with the high conscientious degree stay longer in the corner of the room, because they clean the room carefully. On the contrary, subjects low in the conscientious degree stay longer in a spacious part of the room. It implies we can figure out the conscientious degree from the location subjects stay longer.

The proposed method assumes to learn the floor plan of the room beforehand. Even in the case the floor plan is changed, the method is applicable without trouble, if we specify the floor plan to the algorithm.

VI. CONCLUSION

The paper has proposed to detect living activities with brightness distribution sensors. It has also presented a method to figure out the conscientious degree of the detected activities. An experiment to evaluate the method reveals it can detect cleaning, cooking, and washing with 0.975, 0.912, and 0.927 in the f-measure, respectively. The method implies the conscientious degree can be figured out from the location of cleaning people. Our future work is to apply the method to more kinds of living activities in various places, to expand the coverage of the method.

REFERENCES

- [1] H. Kanai, G. Tsuruma, T. Nakada, and S. Kunifuji, "Notification of Dangerous Situation for Elderly People using Visual Cues," IUI '08 Proceedings of the 13th international conference on Intelligent user interfaces, Jan. 2008, pp. 345-348.
- [2] F. Portet, M. Vacher, C. Golanski, C. Roux, and B. Meillon, "Design and evaluation of a smart home voice interface for the elderly: acceptability and objection aspects," Personal and Ubiquitous Computing, vol. 17, no. 1, Jan. 2013, pp. 127-144.
- [3] M. P. Lawton and E. M. Brody, "Assessment of older people: Self maintaining and instrumental activities of daily living," Gerontologist, vol. 9, 1969, pp. 179-186.
- [4] S. M. Hwang, et al., "Multi-modal sensing smart spaces embedded with WSN based image camera," PETRA '10 Proceedings of the 3rd International Conference on Pervasive Technologies Related to Assistive Environments, no. 63, Jun. 2010.
- [5] R. Jain, L. Jalali, and M. Fan, "From health-persona to societal health," WWW '13 Companion Proceedings of the 22nd international conference on World Wide Web companion, May. 2013, pp. 1329-1334.
- [6] S. Nakashima, Y. Kitazono, L. Zhang, and S. Serikawa, "Development of privacy-preserving sensor for person detection," Procedia Social and Behavioral Sciences, vol. 2, Jan. 2010, pp. 213-217.
- [7] Z. Zhou, et al., "Activity Analysis, Summarization, and Visualization for Indoor Human Activity Monitoring," IEEE Transactions on Circuits and Systems for Video Technology, vol. 18, no. 11, Nov. 2008, pp. 1489-1498.
- [8] T. Banerjee, J. M. Keller, and M. Skubic, "Building a Framework For Recognition of Activities of Daily Living from Depth Images Using Fuzzy Logic," 2014 IEEE International Conference on Fuzzy Systems(FUZZ-IEEE), Jul. 2014, pp. 540-547.
- [9] J. H. Shin, B. Lee, and K. S. Park, "Detection of Abnormal Living Patterns for Elderly Living Alone Using Support Vector Data Description," IEEE Transactions on Information Technology in Biomedicine, vol. 15, no. 3, May. 2011, pp. 438-448.
- [10] T. Matsumoto, M. Shimosaka, H. Noguchi, T. Sato, and T. Mori, "Pose Estimation of Multiple People using Contour Features from Multiple Laser Range Finders," The 2009 IEEE/RSJ International Conference on Intelligent Robots and Systems(IROS 2009), Oct. 2009, pp. 2190-2196.
- [11] M. R. Abid, P. E. Meszaros, R. F. d. Silva, and E. M. Petriu, "Dynamic Hand Gesture Recognition for Human-Robot and Inter-Robot Communication," 2014 IEEE International Conference on Computational Intelligence and Virtual Environments for Measurement Systems and Applications(CIVEMSA), May. 2014, pp. 12-17.
- [12] Y. Peng, Y. Yan, W. Zhu, and J. Zhao, "Vehicle Classification Using Sparse Coding and Spatial Pyramid Matching," 2014 IEEE 17th International Conference on Intelligent Transportation Systems(ITSC), Oct. 2014, pp. 259-263.
- [13] L. Breiman, "Random Forests," Machine Learning, vol. 45, no. 1, Oct. 2001, pp.5-32.
- [14] A. Mohamed and K. N. R. Nair, "Continuous Malayalam Speech Recognition Using Hidden Markov Models," A2CWIC '10 Proceedings of the 1st Amrita ACM-W Celebration on Women in Computing in India, no. 59, Sep. 2010.
- [15] H. Chen, L. Chen, T. P. Albright, and Q. Guo, "Improved Logistic Regression Approach to Predict the Potential Distribution of Invasive Species Using Information Theory and Frequency Statistics," Sixth IEEE International Conference on Data Mining - Workshops(ICDMW'06), Dec. 2006, pp. 873-877.
- [16] G. H. John and P. Langley, "Estimating Continuous Distributions in Bayesian Classifiers," UAI'95 Proceedings of the Eleventh conference on Uncertainty in artificial intelligence, Aug. 1995, pp. 338-345.
- [17] T. Joachims, "Training Linear SVMs in Linear Time," KDD '06 Proceedings of the 12th ACM SIGKDD international conference on Knowledge discovery and data mining, Aug. 2006, pp. 217-226.
- [18] N. J. D. Nagelkerke, "A Note on a General Definition of the Coefficient of Determination," Biometrika, vol. 78, no. 3, Sep. 1991, pp. 691-692.

Tactile Handle for an Instrumented Cane

Andrés Trujillo-León, Fernando Vidal-Verdú
 Departamento de Electrónica, Universidad de Málaga
 Instituto de Investigación Biomédica de Málaga (IBIMA)
 Málaga, Spain
 {atrujilloleon, fvidal}@uma.es

Ragou Ady, Wael Bachta
 Sorbonne Universités, UPMC Univ. Paris 06
 CNRS UMR7222, INSERM U1150
 Paris, France
 {ragou.ady, wael.bachta}@upmc.fr

Abstract—Tactile sensors are useful input devices to implement human machine interfaces in areas such as rehabilitation or assistance. They can prevent damage from accidents or bad usage, and also provide rich information to infer human behavior from the pressure distribution at the contact interface. This paper introduces an instrumented cane handle equipped with a tactile sensor. The electronics devoted to data acquisition, pre-processing and communication is described. Furthermore, results from tests with different users are shown to illustrate how the information provided by the tactile sensor is related to the gait and can be exploited for research or as control input in an active cane.

Keywords—tactile sensors; rehabilitation; gait assistance.

I. INTRODUCTION

Population aging is a major concern in Western Societies. The increase in life expectancy and the low birth rate make that average age increases. Societies get older and this is changing the way of living [1]. Moreover, challenges arise to extend the autonomy of people as much as possible. This is mandatory since there will not be enough young people to take care of the elder, and it is obviously desirable to increase the quality of life and self-esteem. Besides of progresses in medicine that will heal and preserve our bodies, robotics and smart systems can be a great source of assistive devices that provide solutions to the new needs. Assistive robots or devices should be designed with a first restriction in mind: safety. Human robot interaction is a broader field of interest and research that shares this concern.

Tactile sensors or artificial skins have implemented a way to protect humans against accidental damage caused by machines, and they are also a mean to implement interaction between robots and humans. However, tactile sensors can play a more advanced role in implementing a human-assistive device interface. This can be done by taking advantage of the fact that tactile sensors are arrays and they provide information not only from the aggregated output but also from its spatial distribution [2]. This is done in manipulation with robotic hands or grippers, where the tactile moments are computed to obtain information like contact size and shape, or contact location [3]. Similar information from the contact between the human and the machine can be exploited to build the interface. For instance, tactile information is used in [4] to implement a device that aims a natural and intuitive driving of a wheelchair or trolley. Another assistive device that targets the issue of mobility in old populations is an active or smart cane [5]. It is preferable to a wheelchair as long as possible, since the user keeps more active. Tactile sensors can be used in this context in two senses. First, they are a mean to obtain knowledge

about the force distribution on the handle, so they can provide information about how the cane contributes to the balance in the gait process. Second, similarly to the usage pointed out in [4], they can work as an interface to infer the user intention and help to design intuitive and friendly assistive canes.

This paper intends to show that it is certainly possible to get useful information for these purposes from a tactile sensor. Specifically, a simple tactile sensor was built with an array of commercial force sensing resistors [6]. Then, it is exploited to find which relevant data can be extracted during its use as a cane handle. The obtained results confirm that the sensor provides information about two basic parameters involved in the gait process: the load force on the cane when the user leans on it and the orientation of the cane shaft. Therefore, the potential use of tactile sensors in these assistive devices, as for example the instrumented cane shown in [7], is proved.

The structure of this paper is the following. In Section II, the developed device is introduced. Firstly, the tactile handle is described. Then the electronics conditioning for the latter is covered. In Section III, the experiments, the materials involved in them as well as the analysis of the extracted data are detailed. Section IV is dedicated to present and discuss the obtained results. Finally, the paper is closed with Section V in which the conclusions of this work are exposed.

II. DEVELOPED DEVICE

This section describes the device this document focuses on. Firstly, an introduction of the design of the tactile handle is given. Secondly, the hardware in charge of the sensor acquisition is described in detail.

A. Tactile handle

The shape of the developed handle intends to emulate a 'T' cane handgrip. This kind of handles is specially suitable for people who have suffered a loss of strength in their hand. Figure 1 shows the physical implementation of the handle. Commercial force sensing resistor (FSR) sensors from Interlink Electronics [6] have been chosen as tactile sensing units. Their output is less linear and sensitive if the sensors are placed on a rough surface. Therefore, in order to have a good performance, they must lie on a flat surface [8]. This constraint explains the square profile of the handle. Five FSR sensors have been placed on the upper, left and right faces of the handle. Only three sensors have fitted in the lower side since it is where the cane shaft and the handle join. The eighteen tactels have been interconnected forming a matrix of four rows by five columns (Figure 2). Note that in the lower face, the number of columns is reduced to three. The matrix configuration is



Figure 1. Tactile handle implementation.

optimal since it minimizes the resources needed to address and digitize the tactels.

Moreover, soft pads have been placed on the active area of the FSR sensors to enhance the response by concentrating the force. Finally, the whole structure is covered with a layer of foam to make the grasp more comfortable.

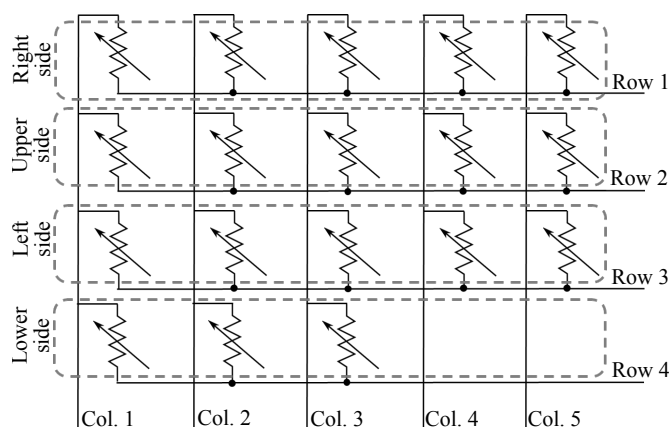


Figure 2. Matrix of FSR sensors schematics.

B. Conditioning electronics

The acquisition board (Figure 4) is based on a PIC18F4680 from Microchip Electronics. This microcontroller possesses a wide range of input/output interfaces and a considerable number of Analog-to-Digital (A/D) channels at an affordable price. Figure 3 shows the circuit scheme. The columns of the FSR matrix are wired to the A/D channels of the microcontroller through a trans-impedance stage. On the other hand, the rows are connected to analog switches controlled by generic digital input/output ports of the PIC. These activate the switches in order to ground the row that is going to be read and to connect the others to a reference voltage (V_{ref}). Note that the output of the amplifier for the chosen tactel can be calculated as shown:

$$V_{out_{i,j}} = V_{ref} \left(1 + \frac{R_G}{R_{S_{i,j}}} \right) \quad (1)$$

Where $R_{S_{i,j}}$ the resistance of the FSR sensor in (i, j) position.

Besides, the feedback resistance R_G is implemented with a potentiometer so the gain of every column can be tuned independently. The output for the rest of the tactels will be zero as the voltages in the amplifier inputs are the same, V_{ref} , due to the negative feedback. This way, $V_{out_{i,j}} \in [V_{ref}, V_{DD}]$ being V_{DD} the supply voltage (the amplifiers saturation voltage, actually). Note that V_{ref} should be a low value in order to have a good dynamic range.

Once the voltage given by (1) has been digitized for every tactel, the information is ready to be sent to other devices through the communication interfaces. In the experiment that will be described in this paper, the tactile handle readings are sent to a computer using a serial-to-USB converter. Nevertheless, they can be also transmitted through the I^2C bus with a level conversion in case the board is embedded, for example, in an active cane as the one described in [5].

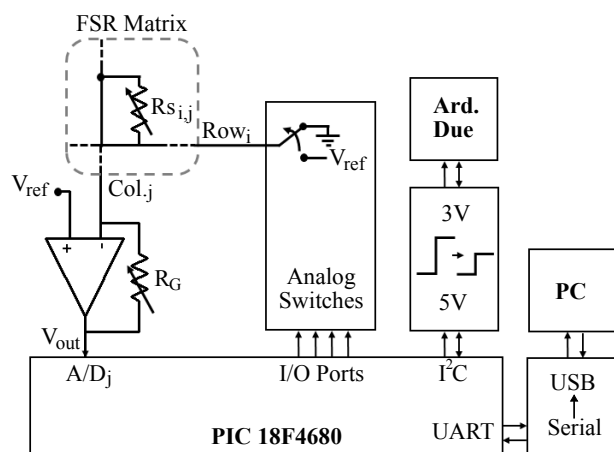


Figure 3. Conditioning electronics scheme.

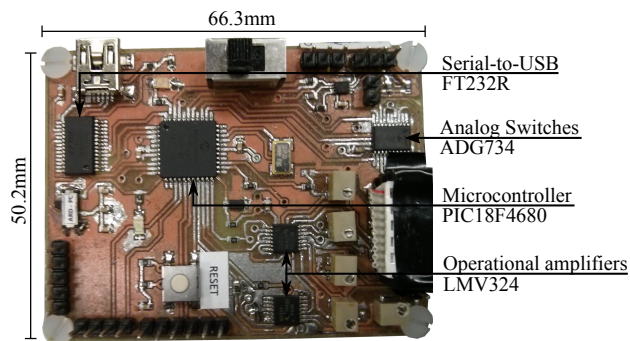


Figure 4. Conditioning electronics board.

III. MATERIALS AND METHODS

This section introduces the experimental setup. Furthermore, the protocol followed to carry out the experiments and the parameters under analysis are described.

A. Experimental setup

In order to test the device introduced in the previous section, an experimental setup was built (Figure 6). In addition

to the tactile handle, two more sensor are used. Firstly, an inertial module unit (IMU) measures the yaw angle in the walking direction, that is to say, the angle with respect to the vertical in the sagittal plane. An Arduino Due board gathers the data from the IMU. Secondly, a Mini45 Force/Torque sensor, from ATI Industrial Automation, obtains the load force in the cane shaft axis (F_z). The acquisition card that processes the data from the Mini45 is the National Instruments USB-6211.

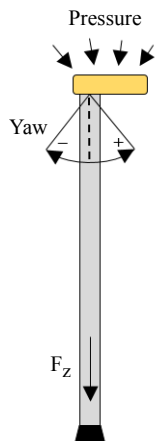


Figure 5. Parameters captured during the experiments.

The tactile handle acquisition board, the Arduino Due and the USB-6211 are connected to a computer through an USB hub. The computer synchronizes the capture of the three sensors at a rate of 40Hz.

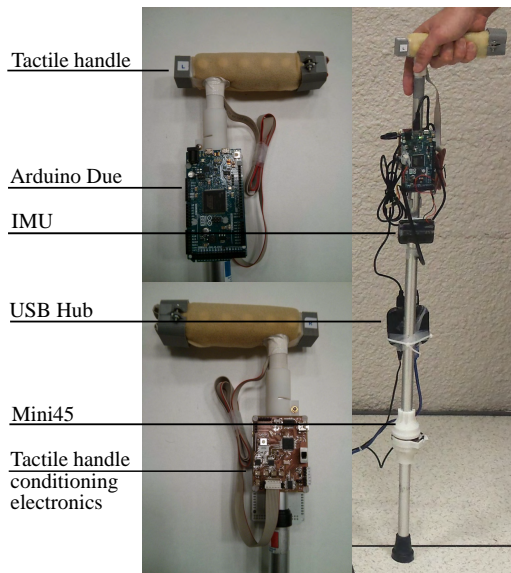


Figure 6. Experimental setup.

B. Experiments and analysis

Ten healthy subjects aged between 21 and 32 took part in the tests. They wore a brace in one of their legs and a modified sole in order to simulate walking impairment [9]. They were naive about the experiment purpose. They were asked to use

the cane walking straight for 5.5m. Every subject repeated the test four times.

As it was introduced in the previous section, the parameters from the external sensors that have been analyzed are F_z and the yaw angle (Figure 5). With respect to the tactile handle, the pressure map (Figure 7) can be processed in several ways. One of them consist in obtaining the center of mass (CoM) of the tactile image. This parameter can be calculated either taking into account the whole FSR matrix or just considering the rows one by one. In the latter case, the CoM of one side of the tactile handle is determined by (2).

$$CoM_{side} = \frac{\sum_{i=1}^5 p(i) \times x(i)}{\sum_1^5 p(i)} \quad (2)$$

Where $p(i)$ and $x(i)$ are the position and the pressure value of the i^{th} tactel in the handle side, respectively.

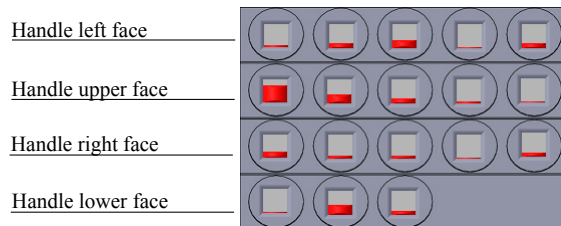


Figure 7. Example of pressure map from the tactile handle.

On the other hand, the tactile handle can also provide information about the grip pressure. Again, this can be estimated either in a global way, that is to say, including all the tactels or considering each row separately. Thus, the component of the grip pressure in one row of the FSR matrix could be calculated as the mean pressure on that side of the handle:

$$\bar{P}_{side} = \frac{\sum_{i=1}^5 p(i)}{5} \quad (3)$$

In the analysis carried out in this paper, the parameters in (2) and (3) have been estimated for the upper side of the handle (Figure 1 and 7). Furthermore, in order to remove the noise, all the data have been low-pass filtered.

IV. RESULTS AND DISCUSSION

To assess the associations between, on the one hand, the CoM_u and F_z and, on the other hand, the \bar{P}_u and the cane yaw angle, Pearson correlation coefficients are computed for each subject using the mean trajectories across the four trials. All the coefficients are close to 1 with a statistical significance. This states a strong linear correlation between the observed parameters.

Looking at the results of the experiments presented in Figure 8, it can be indeed observed that the yaw angle and the center of mass of the upper side of the handle (CoM_u) are strongly coupled. The figure shows the mean of these parameters for the four test performed by one the subjects. This subject can be considered representative of the results obtained in the experiments. Note that CoM_u has been amplified and

shifted vertically to ease the visual comparison. This way, CoM_u unit (mm) and scale must be ignored since they have been altered. In addition, computing the tests mean requires that all of them have the same number of samples. Thus, they have been interpolated and, consequently, the time scale deformed. That is the reason why there are no values in the time axis. Lastly, the first and last step have been removed since they are a transient component and are not relevant in the analysis of the steady gait.

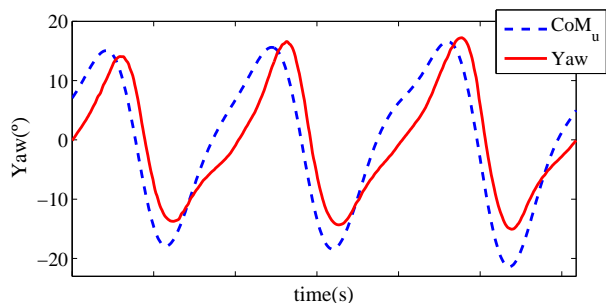


Figure 8. Yaw and CoM_u for a representative subject.

The same happens if we look at the pair formed by F_z and \bar{P}_u . Figure 9 shows the mean of these parameters for all the tests carried out by the same subject as before. \bar{P}_u has been pre-processed in the same way as CoM_u to make the graphic comparison easier.

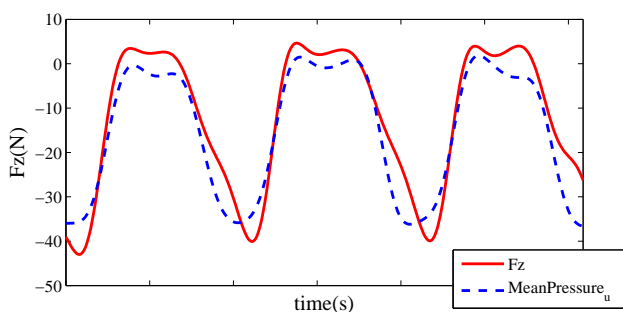


Figure 9. F_z and \bar{P}_u for a representative subject. Note that the same as in Figure 8 happens with time axis and, in this occasion, with the \bar{P}_u unit (V) and scale.

The pattern in the latter figures repeats for every subject in the experiments to a greater or lesser extent. Therefore, it is certainly feasible to reach an estimation of the angle of the orientation of the cane and the load force exerted on it based on the data acquired by the tactile handle presented in Section II.

V. CONCLUSIONS

A device composed of a tactile handle and its conditioning electronics has been presented. Experiments have been realized in order to test it. According to the results analyzed in Section IV, a tight coupling between two parameters involved in the gait process and two parameters extracted from the tactile handle has been found. These are, on the one hand, the load force applied on the cane and the mean pressure on the upper part of the handle and, on the other hand, the angle of the

orientation of the cane shaft and the center of mass of the upper side of the handle.

The preliminary results show the operation and viability of the tactile handle as a tool to monitor the assisted gait as well as a sensor device in a smart or robotic active cane.

Future work could involve the implementation of a second prototype with a miniaturised conditioning electronics. In it, the data could be either transmitted by a wireless protocol as Bluetooth or stored locally. Thus, wires would no longer be necessary and the system would be more comfortable to use. Another possible point to address could be the realization of a more ergonomic handle. Finally, apart from the variables shown in this work, the coupling between other parameters could be studied.

ACKNOWLEDGMENT

This work was partly accomplished within the laboratory of excellence SMART supported by French state funds managed by the ANR within the Investissements d'Avenir programme ANR-11-IDEX-0004-02. It has been also partially funded by the Spanish Government under contract TEC2012-38653, FPU Program and European ERDF funds.

REFERENCES

- [1] "Demographic change and work in Europe ," 2010, URL: http://www.eurofound.europa.eu/sites/default/files/ef_files/ewco/surveyreports/EU0902019D/EU0902019D.pdf [accessed: MAY, 2015].
- [2] R. Dahiya, P. Mitterdorfer, M. Valle, G. Cheng, and V. Lumelsky, "Directions Toward Effective Utilization of Tactile Skin: A Review," *Sensors Journal, IEEE*, vol. 13, 2013, pp. 4121–4138, ISSN: 1530-437X.
- [3] A. Schmid, N. Gorges, D. Goger, and H. Worn, "Opening a door with a humanoid robot using multi-sensory tactile feedback," in *Robotics and Automation, 2008. ICRA 2008. IEEE International Conference on*, May 2008, pp. 285–291.
- [4] A. Trujillo-León and F. Vidal-Verdú, "Driving Interface Based on Tactile Sensors for Electric Wheelchairs or Trolleys," *Sensors*, vol. 14(2), 2014, pp. 2644–2662, ISSN: 1424-8220.
- [5] R. Ady, W. Bachta, and P. Bidaud, "Development and control of a one-wheel telescopic active cane," in *Biomedical Robotics and Biomechanics (2014 5th IEEE RAS EMBS International Conference on*, Aug. 2014, pp. 461–466.
- [6] "Interlink Electronics. FSR402®," 2011, URL: <http://www.interlinkelectronics.com/FSR402.php> [accessed: JUNE, 2015].
- [7] C. Perez, A. Oates, L. Hughey, and J. Fung, "Development of a force-sensing cane instrumented within a treadmill-based virtual reality locomotor system," in *Virtual Rehabilitation International Conference*, 2009, June 2009, pp. 154–159.
- [8] F. Vidal-Verdú, M. Barquero, J. Castellanos-Ramos, R. Navas-González, J. Sánchez, J. Serón, and A. García-Cerezo, "Large Area Tactile Sensor Patch Based on Commercial Force Sensors," *Sensors*, vol. 11(5), 2011, pp. 5489–5507, ISSN: 1424-8220.
- [9] M. Ackermann and W. Schiehlen, "Dynamic Analysis of Human Gait Disorder and Metabolical Cost Estimation," *Archive of Applied Mechanics*, vol. 75, 2006, pp. 569–594, ISSN: 0939-1533.

Analysis of the Effect of Visuals on the Stabilization of Trunk Muscles During Rotational Motion

Nika Zolfaghari, Kristiina M. Valter McConville, and Shahini Sirikantharajah

Electrical and Computer Engineering
Ryerson University
Toronto, Canada
e-mail: kmconvi@ee.ryerson.ca

Abstract— Seated balance, especially for the application of wheelchair users, has become an area of interest for researchers. Numerous studies have been done to date, which analyze the effects of wheelchair propulsion on shoulders and limbs, but little study has been done in regards to trunk muscles and their stabilization effects. Therefore, for this study, motorized rotational motion at a rotational angle of 45 degrees was performed on nine subjects in both the forward and backwards directions of motion. Eight abdominal and back trunk muscles (rectus abdominis, external oblique, thoracic erector spinae, and lumbar erector spinae) were analyzed via electromyography (EMG). In addition, the effect of the presence of virtual reality was analyzed on the muscle activity. Each trial was made up of four randomized test, and were performed three times each on each subject for accuracy purposes. The acquired raw signals were processed in MATLAB, and their results were analyzed. It was found that the most muscle activity was present in the forward rotational direction while visuals were playing on the screen in front of the subject. This indicates, that it is under that condition that the muscles work their hardest in order to stabilize the body and maintain balance.

Keywords-*Electromyogram (EMG); electrode; virtual reality; muscle activity; seated balance.*

I. INTRODUCTION

The study of seated balance with rehabilitation engineering has been an area of great interest to many researchers. One of the reasons for this is its wide are of application. Understanding seated balance and the factors which affect it become increasingly valuable when dealing with individuals in wheelchairs. Although wheelchairs were revolutionary in helping disabled individuals get around, they are not without their drawbacks, as their prolonged use can lead to possible injuries [1]. When a wheelchair travels over uneven surfaces, the inevitable motions which it causes the human body to endure can lead to tendinitis, carpal tunnel syndrome, and even back pain [2]-[6]. Moreover, when these users utilize ramps to go from one level to another, their bodies lean towards the direction opposite to the direction of motion in order to reduce tipping and maintain stability [7]. However, since these individuals tend to have weaker stabilizing trunk muscles either due to spinal cord injury, or atrophy [8]. This limits the amount of directional leaning their body can perform in order to shift their centre of mass and remain balanced [2].

Fortunately, a vast number of studies have been performed to date which assess the effect that wheelchair propulsion has on muscles [9, 10]. However, the focus of these studies has been on shoulder and upper limb muscles, and very little study has been done on trunk muscles, which is surprising as it has been suggested that these trunk muscles play a vital role in stabilization of balance during wheelchair propulsion [11][12].

Yang, et al. [11], and Howarth, et al. [13] both performed studies examining lower back and abdominal muscle contractions through electromyography (EMG). They did so while subjects were in forward wheelchair propulsion, and they found that the initial stages of motion produced the highest muscle activity. Moreover, other studies such as the ones mentioned have focused on manual wheelchair propulsion, and only on even surfaces. It is important to note though that as technology rapidly advances, motorized wheelchairs, as well as scooters are becoming more widely used. Furthermore, they travel over uneven surfaces and ramps on a regular basis.

This became the motivation behind our study, in which decided to focus on the effects of motorized rotational motion on the stabilizing trunk muscles. Specifically, the muscles which we focused on were the Rectus Abdominis (RA), External Oblique (EO), Thoracic Erector Spinae (TE), and Lumbar Eector Spinae (LE). To add another layer to this study, we decided to combine the motion with visuals achieved through virtual reality, which allowed us to perform a comparison on the effects that visuals have on stabilization.

All of the studies were performed on healthy subjects in order to set the baseline in determining how a healthy individual's muscles should be contracting. As a further step in the future, the study could be expanded to wheelchair users in order to analyze their muscle deficiencies as compared to a healthy individual.

Virtual reality allows for the study of the link between physical human behaviour and perception [14]. Furthermore, it allows for the recreation and analysis of the outside world in a lab setting which can be controlled [15]. Although virtual reality has been extensively studied for the purpose of training and rehabilitation, little has been done in the field to date in regards to seated balance for wheelchair users [16][18]. However, when testing during rotational motion, the chances of experiencing motion sickness increase according to the sensory conflict theory. This theory states

that when there are conflicting visual and vestibular inputs, disequilibrium occurs, resulting in motion sickness [19][20].

This paper will proceed by looking at the methods used for this study in section II, including subject selection, experimental setup, and trials. Section III will move on to outlining the produced results of the trials. The results will be discussed in section IV and compared to previous studies, and finally section V will wrap up with the concluding remarks.

II. METHODS

A. Subjects

This study was performed on nine healthy subjects (two males, and seven females), between the ages 20 and 30 years old. None of the recruited subjects had any pre-existing medical conditions or injuries. Approval from the Ryerson University Research Ethics Board had been sought after and received prior to the commencement of this study.

B. Experimental Setup

For this study, a motorized rotational device, the MaxFlight FS-VC Dual System motion simulator, was used to mimic the motions that a typical wheelchair goes through on a daily basis. This world class simulator is the only one of its kind which can rotate a full 360 degrees in both the pitch and roll directions. It has an option in which the angle and direction of motion can be manually set to any value between 0 and 360 degrees. Figure 1 illustrates the simulator with an open cockpit, and Figure 2 shows the simulator while in motion.



Figure 1. MaxFlight Motion Simulator with an Open Cockpit

Once a subject has met the eligibility requirements, their muscles were wiped with alcohol swabs in preparation for electrode attachment. Two Ag/AgCl electrodes (3M™ Red Dot™ Monitoring Electrodes) were placed on each of the following trunk muscles with an approximate interelectrode distance of 3 cm: Rectus Abdominis (RA) – 3 cm lateral to the umbilicus (belly button), External Oblique (EO) – 5 cm

lateral to the rectus abdominis, Thoracic Erector Spinae (TE) – 5 cm lateral to the T9 spinal disk, and Lumbar Erector Spinae (LE) – 3 cm lateral to the L4 spinal disk. As previously mentioned, these muscles play a key role in seated balance, and were chosen for that reason.



Figure 2. MaxFlight Motion Simulator During Motion

The electrodes were then connected to the CleveMed Bioradio 150 data acquisition device via snap-leads. The CleveMed Bioradio then transmitted the acquired signals to a nearby computer wirelessly.

C. Trials

Trials were performed in both the forward and backwards directions, each at a rotational angle of 45 degrees. Additionally, each trial in each direction was performed both while visuals were playing on the screen in front of the subject, and also when visuals were not present. Moreover, each trial was performed three times for accuracy assurance. As subjects were not told which direction they were about to travel, and the order of the trials was randomized, this was a blind study. Subjects were given a ten minute break halfway between the study in order to minimize any possible motion sickness.

D. Signal Processing

A sampling frequency of 960 Hz was used for data acquisition of the raw signal. Once the raw signal had been

obtained, it was rectified, and a low-pass Butterworth filter (4th order) with a cut-off frequency of 6 Hz was used to filter out the noise from the signal.

$$|H(\Omega)|^2 = \frac{1}{1+(\Omega/\Omega_c)^{2N}} = \frac{1}{1+\varepsilon^2(\Omega/\Omega_p)^{2N}} \quad (1)$$

Where N is the order of filter, Ω_c is the corner frequency, Ω_p is the pass-band edge frequency, and $1/(1+\varepsilon^2)$ is the band edge value of $|H(\Omega)|^2$.

Next, in order to visualize the overall shape and amplitude of the muscle activity, the envelope of the rectified signal was obtained. Subsequently, the three trials for each condition were averaged in order to reduce noise due to biological factors during data acquisition. This resulted in a single signal, which was representative of the muscle.

In order to analyze the amount of muscle activity, the root mean square (RMS) of the averaged signal was obtained.

$$x_{rms} = \sqrt{\frac{1}{n}(x_1^2 + x_2^2 + x_3^2 + \dots + x_n^2)} \quad (2)$$

Finally, the work done by the muscle (related to the amount of contractions) was determined by finding the integral of the signal, referred to as the iEMG.

$$iEMG = \int_0^t EMG dt \quad (3)$$

III. RESULTS

All of the calculations were performed in MATLAB, including the production of the figures. Since eight muscles of nine subjects were recorded under four conditions, a plethora of results and figures were produced. In the interest of saving space, the figures for subject 2, and the RMS and iEMG values for subject 5 will be displayed only, as they were the most representative of the results overall. To recap, each of the previously mentioned eight muscles were analyzed under the following four conditions:

- Forwards direction, visuals present (FV)
- Backwards direction, visuals present (BV)
- Forwards direction, visuals not present (FN)
- Backwards direction, visuals not present (BN)

Furthermore, each of the eight channels represents the following muscles:

- Ch.1: Right Rectus Abdominis (RA)
- Ch.2: Left Rectus Abdominis (RA)
- Ch.3: Right External Oblique (EO)
- Ch.4: Left External Oblique (EO)
- Ch.5: Right Lumbar Erector Spinae (LE)
- Ch.6: Left Lumbar Erector Spinae (LE)
- Ch.7: Right Thoracic Erector Spinae (TE)
- Ch.8: Left Thoracic Erector Spinae (TE)

Figures 3-7 represents the produced results as a signal goes through the signal processing algorithm (FV used as an example).

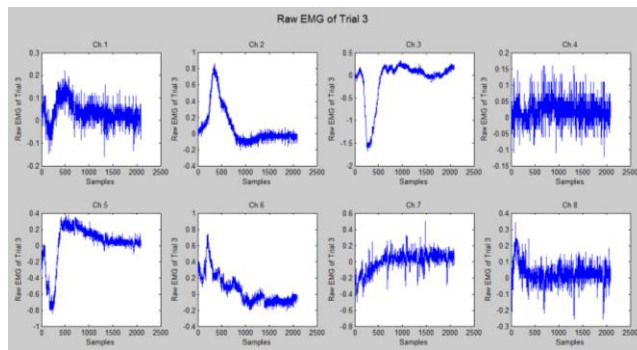


Figure 3. Raw EMG of Trial 1 for FV, Subject 2

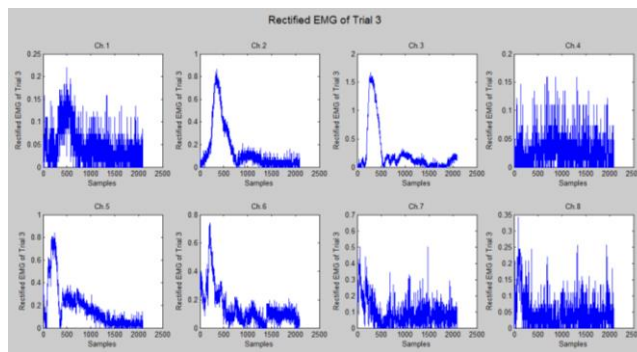


Figure 4. Rectified EMG of Trial 1 for FV, Subject 2

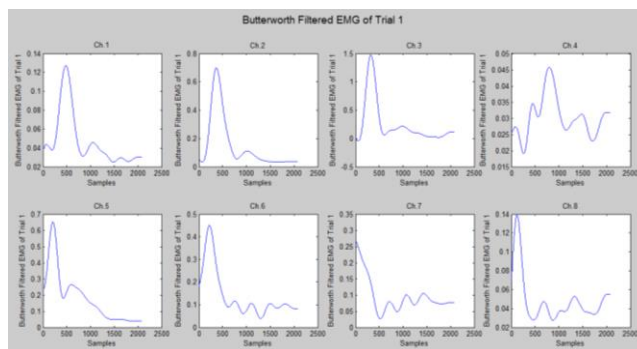


Figure 5. Butterworth Filtered EMG of Trial 1 for FV, Subject 2

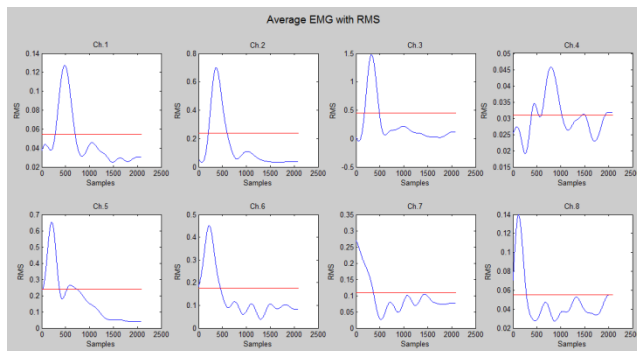


Figure 6. Averaged EMG with RMS for FV, Subject 2

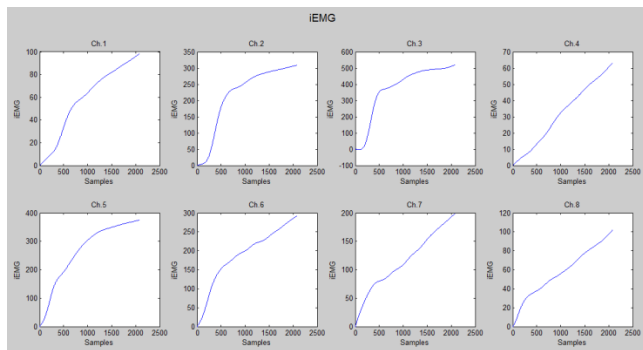


Figure 7. iEMG for FV, Subject 2

When comparing the raw signal in Figure 3 to the filtered averaged signal in Figure 6, it can be seen just how effective the signal processing algorithm was in cleaning the signal and removing unwanted excess noise from the signal.

As the RMS and iEMG values represent the work done by each muscles, they will be compared under the various conditions, as illustrated by Tables I and II.

TABLE I. RMS OF SUBJECT 5

	Ch.1	Ch.2	Ch.3	Ch.4	Ch.5	Ch.6	Ch.7	Ch.8
BV	0.03	0.03	0.03	0.03	0.06	0.17	0.11	0.05
BN	0.03	0.04	0.03	0.04	0.20	1.18	0.72	0.41
FV	0.03	0.03	0.04	0.03	0.06	0.11	0.10	0.06
FN	0.08	0.12	0.07	0.06	0.09	3.11	0.07	0.05

TABLE II. iEMG OF SUBJECT 5

	Ch.1	Ch.2	Ch.3	Ch.4	Ch.5	Ch.6	Ch.7	Ch.8
BV	59.4	60.5	60.0	61.3	92.3	310	124	86.4
BN	187	199	172	205	598	4817	2166	1388
FV	125	133	144	131	205	277	254	208
FN	3756	545	349	322	461	9486	402	287

IV. DISCUSSION

Upon analyzing the produced graphs of all nine subjects, it was noted that amongst the different conditions the overall shape of the muscle response was very similar for the same subject, which was expected.

Moreover, when looking at all of the RMS and iEMG tables for all nine subjects, it can be seen that the RMS values of the back muscles (Ch. 5-8) are consistently lower than those of the front abdominal muscles (Ch. 1-4). This finding illustrates the fact that it is the posterior back muscles that play a larger role in upper body stabilization.

Furthermore, higher RMS and iEMG values were produced when the subjects were travelling in the forwards rotational direction. It is important to note that when the subjects are travelling in the backwards direction, the back of the seat is there to support them, a possible reason as to why the trunk muscles do not need to work as hard to stabilize.

The final trend is that the RMS and iEMG values of the muscles tend to be higher when visuals were playing on the screen as opposed to when the screen was turned off. This was expected, as when the visuals are playing on the screen, it gives the subject the feeling that they are travelling/displaying more than they actually are. If the subject perceives their fall to be steeper, their muscles will work harder to stabilize the body, resulting in higher RMS and iEMG values. Moreover, when the screen was turned off, it was pitch black inside of the motion simulator cabin, so the subject was not able to place themselves in relation to the surrounding environment, and likewise, their muscles did not feel as though they had to work as hard to stabilize balance

V. CONCLUSION

When looking at the findings overall and summarizing them, it can be concluded that the FV (forward direction, visuals present) condition had the highest muscle activity, as determined by the RMS and iEMG values, and thus, the muscles had to work the hardest in that condition in order to stabilize and maintain balance. All of the findings could be used for the development of effective rehabilitation programs, including virtual reality training.

ACKNOWLEDGMENT

We would like to thank the Natural Sciences and Engineering Research Council of Canada for funding the study. We would also like to thank all of the subjects for providing their time during data acquisition.

REFERENCES

- [1] K. Samuelsson, H. Larsson, M. Thyberg, and B. Gerdle, "Wheelchair seating intervention," *Disabil Rehabil*, vol. 23, 2001, pp. 677-682,.
- [2] D. J. Sanderson, and H. J. Sommer, "Kinematic features of wheelchair propulsion," *J Biomech*, vol. 18, 1985, pp. 423-429,.

- [3] K. A. Curtis, G. A. Drysdale, R. D. Lanza, M. Kolber, R. S. Vitolo, and R. West, "Shoulder pain in wheelchair users with tetraplegia and paraplegia," *Arch. Phys. Med. Rehabil.*, vol. 80, 1999, pp. 453-457.
- [4] D. H. Rintala, P. G. Loubser, J. Castro, K. A. Hart, and M. J. Fuhrer, "Chronic pain in a community-based sample of men with spinal cord injury: prevalence, severity, and relationship with impairment, disability, handicap, and subjective well-being," *Arch. Phys. Med. Rehabil.*, vol. 79, 1996, pp. 604-614.
- [5] K. A. Samuelsson, H. Tropp, E. Nylander, and B. Gerdle, "The effect of rear-wheel position on seating ergonomics and mobility efficiency in wheelchair users with spinal cord injuries: a pilot study," *J. Rehabil. Res. Dev.*, vol. 41, 2004, pp. 65-74.
- [6] K. A. Sinnott, P. Milburn, and H. McNaughton, "Factors associated with thoracic spinal cord injury, lesion level and rotator cuff disorders," *Spinal Cord*, vol. 38, 2000, pp. 748-753.
- [7] J. W. Chow, T. A. Millikan, L. G. Carlton, W. S. Chae, Y. T. Lim, and M. I. Morse, "Kinematic and electromyographic analysis of wheelchair propulsion on ramps of different slopes for young men with paraplegia," *Arch Phys Med Rehabil.*, vol. 90, 2009, pp. 271-278.
- [8] A. Bjerkefors, M. G. Carpenter, A. G. Cresswell, and A. Thorstensson, "Trunk muscle activation in a person with clinically complete thoracic spinal cord injury," *J Rehabil Med*, vol. 41, 2009, pp. 390-392.
- [9] S. J. Mulroy, J. K. Gronley, C. J. Newsam, and J. Perry, "Electromyographic activity of shoulder muscles during wheelchair propulsion by paraplegic persons," *Arch Phys Med Rehabil*, vol. 77, 1996, pp. 187-193.
- [10] S. de Groot, H. E. Veeger, A. P. Hollander, and L. H. van der Woude, "Short-term adaptations in co-ordination during the initial phase of learning manual wheelchair propulsion," *J Electromyogr Kinesiol*, vol. 13, 2003, pp. 217-228.
- [11] Y. S. Yang, A. M. Koontz, R. J. Triolo, J. L. Mercer, and M. L. Boninger, "Surface electromyography activity of trunk muscles during wheelchair propulsion," *Clin Biomech*, vol. 21, 2006, pp. 1032-1041.
- [12] A. J. Dallmeijer, L. H. van der Woude, H. E. Veeger, and A. P. Hollander, "Effectiveness of force application in manual wheelchair propulsion in persons with spinal cord injuries," *Am. J. Phys. Med. Rehabil.*, vol. 77, 1998, pp. 213-221.
- [13] S. J. Howarth et al, "Trunk Muscle Activity During Wheelchair Ramp Ascent and the Influence of a Geared Wheel on the Demands of Postural Control," *Archives of Physical Medicine and Rehabilitation*, vol. 91, 2010, pp. 436-442.
- [14] W. H. Warren et al, "Optic flow is used to control human walking", *Nature Neuroscience*, vol. 4, 2001, pp. 213-216.
- [15] E. A. Keshner, "Virtual reality and physical rehabilitation: a new toy or a new research and rehabilitation tool?" *Journal of NeuroEngineering and Rehabilitation*, vol. 1, 2004, pp. 1-2.
- [16] D. P. Inman, K. Loge, and A. Cram, "Learning to drive a wheelchair in virtual reality", *Journal of Special Education Technology*, vol. 26, 2011, pp. 21-34.
- [17] G. Di Gironimo, G. Matrone, and A. Tarallo, "A virtual reality approach for usability assessment: case study on a wheelchair-mounted robot manipulator", *Engineering with Computers*, vol. 29, 2013, pp. 359-373.
- [18] S. Virk, and K. M. V. McConville, "Virtual reality applications in improving postural control and minimizing falls", *Proceedings of the 28th IEEE EMBS Annual International Conference*, 2006, pp. 2694-2697.
- [19] K. E. Money, "Motion Sickness", *Am. Psychol. Soc*, vol. 50, 1970, pp. 1-39.
- [20] J. F. Golding, "Motion Sickness Susceptibility", *Autonomic Neuroscience: Base and Clinical*, vol. 129, 2006, pp. 67-76.

Controlled Cryogenic Ablation Using Ultrasonic Sensing

Assaf Sharon

Robots and BioMedical Micro Systems (RBM²S) research laboratory, School of Mechanical Engineering, Faculty of Engineering, Tel Aviv University, Tel Aviv, Israel.
e-mail: assaf.a1@post.tau.ac.il

Dr. Gabor Kosa

Robots and BioMedical Micro Systems (RBM²S) research laboratory, School of Mechanical Engineering, Faculty of Engineering, Tel Aviv University, Tel Aviv, Israel.
e-mail: gkosa@post.tau.ac.il

Abstract—The Cryoablation process is one of the methods for treating various tissue abnormalities. Cryoablation devices are mostly minimally invasive and are used in open loop control, monitored by additional imaging devices. In this study, we monitor the growth of the ablated area by using a miniature ultrasonic transducer that is collocated with the tip of the cryogenic device. The 20 MHz ultrasonic sensor is capable of measuring the size of the ice sphere that is created in front of the needle. In addition to real time monitoring of the ablation process, the ultrasonic sensor will be able to determine the local thickness of the tissue prior to the treatment (thus enabling the setting of the power of the ablation treatment). The combined device will shorten the ablation treatment and will eliminate the need for additional ablation treatments or monitoring devices. The proof of concept was done in water, ultrasonic gel and muscle tissue. In the experiments we found that, in the frequency domain one can identify at 10-12 MHz the increase of the intensity of the returned echo in the ice and the decrease of the signal after the ice-tissue boundary. One can correlate the increase of the intensity with the growth of the ice sphere.

Keywords – Cryogenic, Ablation, Control, Ultrasound, Piezo, Ice

I. INTRODUCTION

Cryosurgery, also referred to as Cryotherapy or Cryoablation, is a minimally invasive surgical technique in which freezing is used to destroy undesirable tissue. Cryoablative techniques have persistently improved over the past forty years with the development of successive generations of devices including Cryoneedles, Cryoballoons, intraoperative ultrasound and vast knowledge of the mechanisms by which cells are affected by low temperature exposure [1]. We now recognize two mechanisms causing cell death following a freezing cycle: direct mechanism adjacent to the ablating device of cell rupture due to intracellular ice crystal formation and cellular dehydration with associated osmotic damage, and indirect mechanism of ischemia and necrosis throughout the tissue/tumor peripheral zone [2, 3]. To perform a cryosurgical procedure successfully, it is important to monitor precisely and evaluate accurately the extent of freezing. Failure to do so can lead to either insufficient or excessive freezing, and consequently, to recurrence of malignancies treated by cryosurgery or to

destruction of healthy tissues [4]. Most of the Cryoablation devices are used in an open loop control. The results of the treatment are inspected by additional imaging devices such as ultrasound, camera, temperature sensors and other sensors according to the relevant application [1].

In this study, we intend to add a miniature ultrasonic sensor to a cryoablation device in order to determine the treatment progress in real time, observing the ice sphere's boundary growth. This capability allows controlling directly the ablation process by closed loop control. Such a device, will be able to determine much more effectively (faster, more accurately and more precisely). The close loop controlled cryogenic device will be more efficient and safe than the current treatment. In addition to real time monitoring of the ablation process, the ultrasonic sensor will be able to determine the local thickness of the target area before treatment and will enable a more accurate setting of the device's parameters (freezing power and period). The system will shorten the ablation treatment and eliminate the need for recurrence treatments.

To the best of our knowledge, there is no Cryoablation device with collocated sensor that monitors in-situ the progress of the target tissue's freezing.

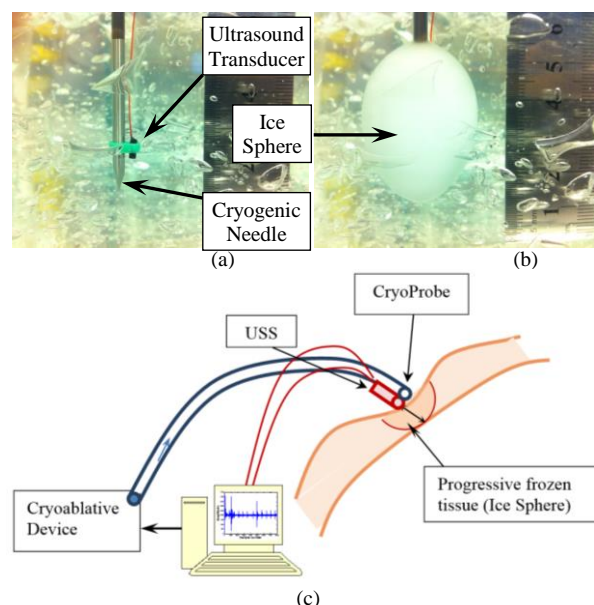


Figure 1: CryoProbe to sensor connection before (a) and after (b) freezing; Schematic overview of the system (c)

The purpose of the present study is to show feasibility of detecting the ice sphere growth from within the ice sphere during Cryoablative therapy without using additional monitoring devices. We assume that by transducing a high frequency ultra-sound wave we will be able to determine the location of the ice sphere outer boundary due to the impedance differences between frozen and unfrozen tissue. We expect to be able to distinguish the frozen tissue's returning echo's (inside the ice sphere) from the unfrozen tissue's returning echo's (at the outer rim of the ice sphere).

In section 2 (Method), we will present an overview of the entire system with detailed description of its two main components; Ablation device and monitoring device, following with an explanation of the monitoring method and the analysis done. Section 3 (Results) will include a summary of the results of different analysis steps and our conclusions will be presented in section 4.

II. METHOD

A. System Overview

The controlled Cryoablation system, that we developed is a device for Cryoablation therapy with an ultrasound transducer attached to it as shown in Figure 1. In the future the ultrasonic sensor will be integrated into the cryogenic needle.

The main components of the system are:

1. A cryoablation device with a Cryoprobe reaching extreme low temperatures (about -170°C) at its tip. Acronymed as CAS.
2. A forward looking ultrasonic sensor that can measure regular and frozen tissue up to 10 mm in depth. Acronymed as USS.

The detailed description of the components is described in the following sections.

B. Ablation Device

We used the Cryo-ablative device designated as IceSense3™ system (Figure 2) manufactured by IceCure Medical. IceCure Medical developed a minimally invasive Cryo-ablation therapy for the Women health market [5].



Figure 2: IceCure's IceSense3™ System (Left) and its CryoProbes with an example of Ice Sphere at their tip (Right)

The IceSense3™ system, provides a minimally invasive, in-office, definitive treatment which uses low temperatures (about -170°C) to destroy (ablate) the targeted tissue in situ. The system uses a closed loop cryogen which reaches a Cryoprobe tip at the center of the ablate tissue and cooled to sub-zero temperatures, removing heat from the targeted tissue by conduction [6] (See Fig 1b and Figure 2). During the Cryo-ablative procedure, an ice spheroid (for convenience we regard to it as a sphere) is formed around the Cryoprobe tip. The ice sphere size varies in time and can reach a diameter of 40 mm and length of around 55 mm after 10 minutes.

C. Monitoring Device

We have used an Ultrasound transducer manufactured by Vermon, France as our monitoring (Figure 3).

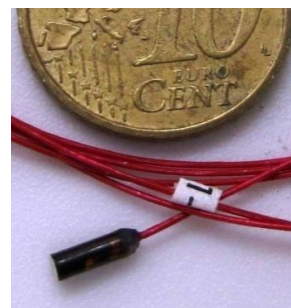


Figure 3: Vermon ultrasonic sensor -Ø2X5.5 mm

The transducer is a single element transducer with outer dimensions of Ø2X5.5 mm and central frequency of 18.5 MHz as shown in the frequency response in Figure 4.

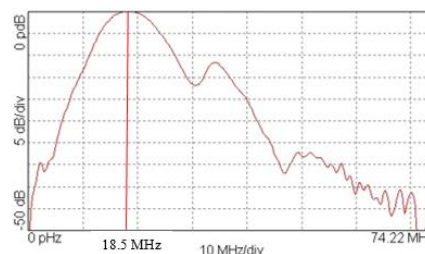


Figure 4: Vermon US sensor frequency response with central frequency of 18.5 MHz

This frequency is equivalent to 0.126 mm axial resolution [7] in water. The frequency response (Figure 4), has a central frequency of 18.5 MHz (at -3dB) bandwidth frequency of 8.7 MHz, low cut frequency 14.2 MHz and high cut frequency 22.9 MHz.

The ultrasound transducer time response in water is noted in Figure 5.

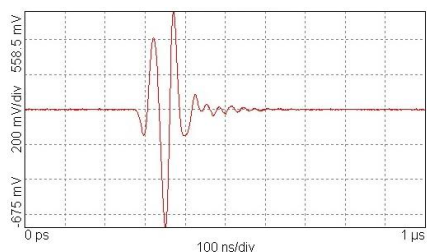


Figure 5: USS time response

The transducer is controlled by USBox system of Lecoeur Electronique Company, transmitting 230 Volts (1 volts step), square pulse. The monitoring was done in A-mode, transmitting and receiving from the same transducer. The returning Echo's were monitored by Matlab software, sampling in 80 MHz in order to observe returning Echo's of up to 40 MHz.

D. Experimental Method

Our main objective, was to recognize the outer contour of the ice sphere in real time (during treatment) when our monitoring device is located at the center of the freezing zone hence allowing us to have both treating and monitoring elements in a single device. The transducer was chosen to be minimally in size to allow in the future positioning inside the ablating element (less than $\varnothing 3$ mm). In this experiment, we connected it to the center of the CryoProbe freezing zone with additional connector placing the transducer adjacent to the CryoProbe outer surface (Figure 1). We have used US Parker gel inside a Standard 1000 ml beaker as our tissue model (ablated medium) and compared it to water and chicken breast tissue.

Several cryogenic treatment simulations were done. The freezing process duration was up to 10 minutes. The ice sphere size was measured using an external camera in time periods of 30 seconds as a reference to the transducer measurements. All returning echoes were received in a time to voltage raw data manner and several analyses were done in order to observe the ice sphere growth as detailed below.

E. Data Analysis

Looking at the time response of the echo (Figure 6), one can observe the large attenuation of the signal in the ice.

The ice-water boundary, cannot be distinguished from direct A-mode inspection of the ice sphere's outer contour.

In order to detect the boundary we transferred the signal to the frequency domain using Matlab software's signal analysis toolbox. We are using the following steps to estimate accurately the ice sphere's contour's distance:

1. The sound velocity in ice is estimated by correlating the signal response near the exit of the transducer (called ringing in the US jargon) in water and ice.
2. Using the sound velocity, the time response is converted into distance and an A-mode US image is derived (Figure 6).

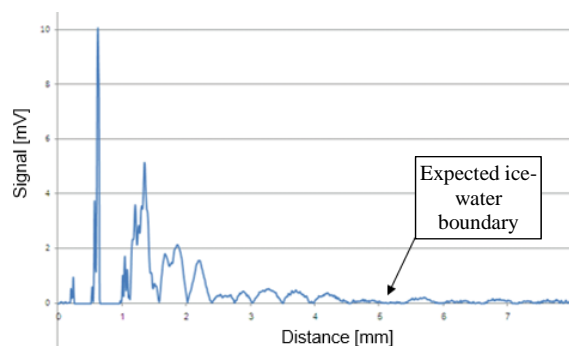


Figure 6: Returning US Echo of 5 mm thick frozen meat slice

3. The time response is also converted to the frequency domain using the short time Fourier transformation. The representation of the data is in a spectrogram that enables identification of significant features in the image (See Figure 7).

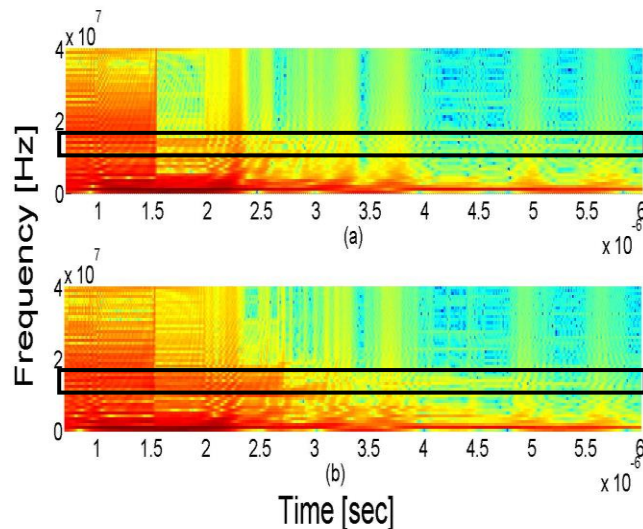


Figure 7: The spectrogram at 3 mm (a) and 4 mm (b) radius Ice sphere (In Parker Gel). The area of interest of 10-12 MHz is in the black frames. The intensity of the echo is depicted by jet colormap.

4. In order to emphasize the growth of the ice sphere we used a binary conversion. This calculation is based on the reduction of the spectrogram according to the derivative of the intensity in the spectrogram (growing intensity black, and vice versa).
5. We also calculated, the sum of the total intensity at the targeted frequency range and found that it is a good indicator of the growth of the ice sphere.

III. RESULTS

Using the correlation analysis, we were able to determine that the frozen gel used has a sound velocity of 2520 m/s (the literature value of ice sound velocity is 3600 m/s and water 1430 m/s) with this property determine we were able to match the returning Echo's with their correct location.

The dynamic process of the growing ice sphere is characterized by the increase of the intensity from the ice layer and the reduction of the intensity of the echo from the water or tissue layer beyond the ice sphere. Figure 7 demonstrates that this process is the most apparent in the bandwidth of 10-12 MHz.

Focusing on the bandwidth we identified in Figure 7 we are able to show a consistence advancing increase of intensity of the echo in time as shown in Figure 8 (red and yellow in the jet colormap).

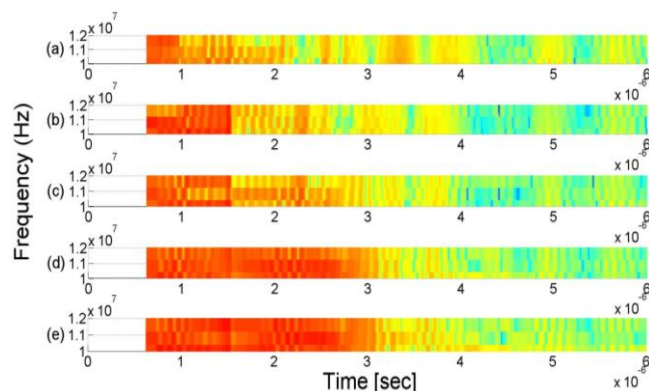


Figure 8: 10-12 MHz Range at different ice sphere sizes: radius of – 0 mm (a), 2 mm (b), 3 mm (c), 4 mm (d) and 5 mm (e) - (In Parker Gel The intensity of the echo is depicted by jet colormap)

This dynamic process can be correlated to the growth of the ice sphere. The increase in the echo from the ice is more emphasized than the decrease in the gel.

To better distinguish the intensity increments, we did additional binary analysis (Figure 9).

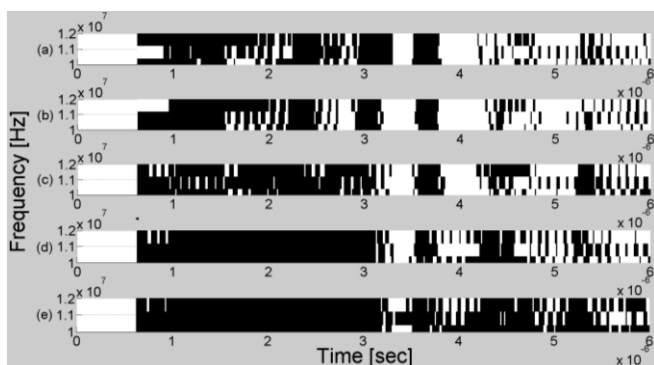


Figure 9: 10-12 MHz Range Binary differences analysis between the base line (0 Sec) and different ice sphere sizes: radius of – 1 mm (a), 2 mm (b), 3 mm (c), 4 mm (d) and 5 mm (e) - (In Parker Gel)

Each signal received at different ice sphere size was compared to the base signal (prior to the freezing cycle) – areas with increased intensity than the base signal are shown in black and areas with lower intensity than the base intensity are shown in white. The advance of the boundary can be detected by the increase of the black area with the growth of the ice sphere. This binary intensity contrast is easier to detect using computerized models in real time.

Finally, we calculated the total intensity of the returning Echo's of different ice sphere sizes during its growth and received an increasing graph for each experiment. We compared all experiments in gel and water in a single graph

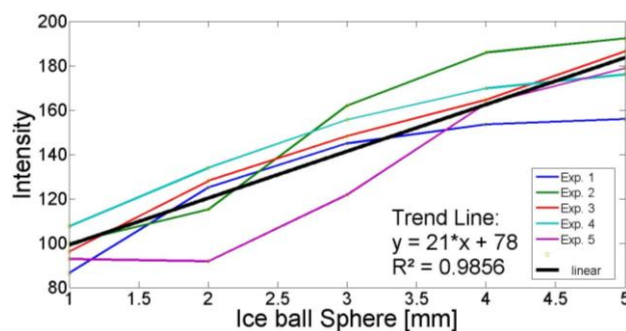


Figure 10: Retrieved signal Total Intensity Vs. different ice sphere sizes – 10-12 MHz Range (All Experiments in water or Parker Gel) with additional combined Linear Trendline (in black).

and receive a linear trend line with R-squared value of 0.9656 (Figure 10).

One can see that the total intensity is a good quantitative measure for the increase of the ice sphere.

The results in the chicken breast tissue show similar results to the gel. There were visible increments with time of

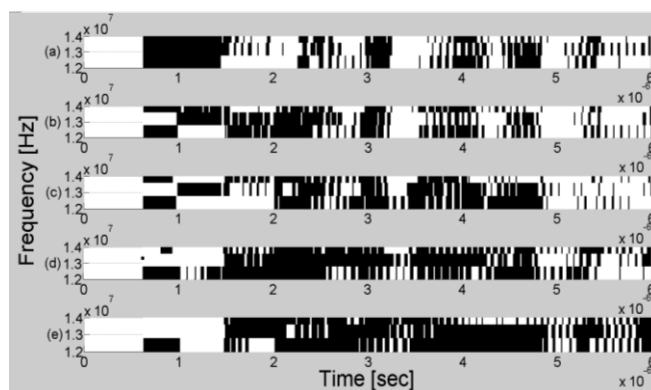


Figure 11: 10-12 MHz Range Binary differences analysis between the base line (0 Sec) and different ice sphere sizes: radius of – 1 mm (a), 2 mm (b), 3 mm (c), 4 mm (d) and 5 mm (e) - (In chicken breast)

the returning Echo's at 10-12 MHz frequency range, better observed when looking at the binary analysis (Figure 11).

We also repeated the returning Echo's total intensity calculation of different ice sphere sizes during its growth and received an increasing graph similar in values to all other experiments (Figure 12).

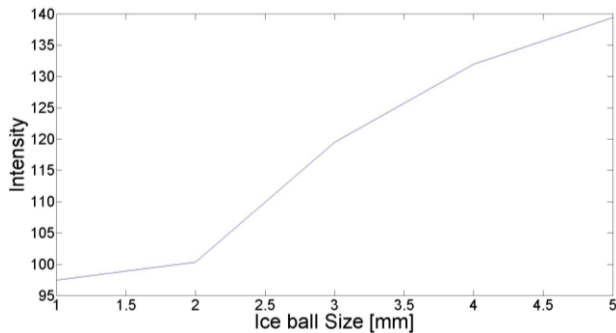


Figure 12: Retrieved signal Total Intensity Vs. different ice sphere sizes – 10-12 MHz Range (In chicken breast)

Combining all the information gathered from the results, we receive a very good indication that measuring the ice ball growth from inside the ice ball is possible even in real time.

IV. CONCLUSIONS

Examining our results, we can clearly distinguish a growing intensity of the signal with the ice sphere growth. We also noticed, that our finding are similar when using ultrasound gel and breast tissue as our ablate model.

With further experiments (using improved ultrasound sensor), we will be able to determine the exact correlation between the intensity growth to the ice sphere real size with high accuracy and precision.

This capability will allow us to monitor the Cryoablation treatment from within the Cryo-ablative device and in the future have a closed loop combined device both treating and monitoring in real time.

REFERENCES

- [1] B. Rubinsky, "CRYOSURGERY," *Annual Review of Biomedical Engineering*, vol. 2, p. 157, 2000.
- [2] A. A. Gage and J. G. Baust, "Cryosurgery-a review of recent advances and current issues," *Cryoletters*, vol. 23, pp. 69-78, 2002.
- [3] M. Maccini, D. Sehart, A. Pompeo, F. A. Chicoli, W. R. Molina, and F. J. Kim, "Biophysiologic considerations in cryoablation: a practical mechanistic molecular review," *International braz j urol*, vol. 37, pp. 693-696, 2011.
- [4] J. G. Baust, A. A. Gage, A. T. Robilotto, and J. M. Baust, "The pathophysiology of thermoablation: optimizing cryoablation," *Current Opinion in Urology*, vol. 19, pp. 127-132, 2009.
- [5] *IceCureMedical Website: <http://icecure-medical.com/>*
- [6] J. Baust, A. Gage, T. B. Johansen, and J. Baust, "Mechanisms of cryoablation: clinical consequences on malignant tumors," *Cryobiology*, vol. 68, pp. 1-11, 2014.
- [7] D. Ensminger and L. J. Bond, *Ultrasonics: Fundamentals, Technologies, and Applications*: CRC Press, Taylor & Francis Group, 2011.

Key Features to Classify Shopping Customer Status from Gait Vectors Acquired with RFID Technology

Yoshihiro Uemura

Graduate School of Information Science and Engineering
Ritsumeikan University, Shiga, Japan
e-mail: y_uemura@de.is.ritsumei.ac.jp

Yusuke Kajiwara, Hiromitsu Shimakawa

College of Information Science and Engineering
Ritsumeikan University, Shiga, Japan
e-mail: {kajiwara, simakawa}@de.is.ritsumei.ac.jp

Abstract—This paper proposes a method to estimate the state of user to provide proactive hospitality from features of their gait pattern acquired with an Radio Frequency Identifier (RFID) system. This method uses RFID readers on each shoe, as well as RFID tags installed on the floor. The ID of each tag is organized as a map, to show the precise position of the user. The reader and tags communicate while the user is walking. We classify tag IDs detected by readers into each step with Ward Method. We calculate stride, walking speed, and so on, as feature components of a gait vector in each step. We recognize the state of the user from these components with the Random Forest. In an experiment, we have imposed subjects on walking under several kinds of conditions. We have evaluated the classification result through F-measure calculated from 10-fold cross-validation. It implies we can classify each state of users. We discuss why we can classify each state of users from gait vector components with the variable importance and their correlation. In addition, we have verified whether we can detect discomfort caused by the way to carry luggage. Finally, we discuss the feasibility of our proposed method.

Keywords—shopping; customer; hospitality; gait; RFID; status;

I. INTRODUCTION

The number of tourists visiting Japan has reached to more than 10 million in 2013. The government aims that every tourist can feel “Omotenashi” in Japan [1]. “Omotenashi” is a Japanese word, which means proactive hospitality. First, an Omotenashi provider grasps the state of customers in advance to provide some services before it is required. There are many tourists who are looking forward to going shopping in Japan [2]. We focus on Omotenashi services in a shopping mall. It is impossible for the shopping mall to provide Omotenashi services for each customer, because it costs too much to train and arrange Omotenashi providers. We need a system that can provide Omotenashi services at a low cost. In this paper, we consider Omotenashi services using the Information and Communication Technology. We propose the two kinds of Omotenashi services in the shopping mall. The first one is to care customers who are suffering from discomfort for luggage, or are fatigued for some reason. The second is to keep safety for distracted customers. For customers who have heavy luggage like electrical appliances as a souvenir, it proposes to use luggage storages and lockers, as well as to inform the location of the elevator. For customers who have fatigue after long shopping, it recommends a resting place like a cafe. It warns distracted customers watching the advertisements or smartphones while walking. We also consider that customers

feel uncomfortable when they hold luggage in a different way than usual. For example, they sometimes have to carry luggage with one hand to hold their baby. In these cases, services should also be changed. It is necessary to identify when they are forced to have luggage with an uncomfortable way by external factors to provide more comfortable services.

Omotenashi services found on grasping the state of a customer in advance. This paper refers to the information as a user status. In this paper, we define the following user status; They are carrying luggage, tired, texting (i.e., using smartphones) while walking, and focusing on advertisements. We assume our services are provided in major streets or in front of display windows. We estimate user status in the areas from their gait patterns. We discuss the variables which play an important role in the estimation. Section 2 introduces existing works. Section 3 explains our method to calculate the feature of customers’ gait. In Section 4 and Section 5, we indicate the experiment and evaluation. In Section 6, the paper discusses the practical possibilities. Section 7 summarizes our work.

II. RELATED WORK

Several methods are proposed to detect user status. Ikeda et al. identify some kinds of luggage like carts and backpacks, using more than one Laser Range (LR) sensors installed around the user [3]. Qi et al. identify whether the user has a suitcase and a backpack from the ratio of left and right contours against the center of the body detected by a camera [4]. Yonekawa et al. detect user fatigue from changes of pressure values measured with sensors installed in shoe insoles [5]. Arif et al. show the fatigue is related to the stability of walking, using 3D accelerometer sensors [6]. Music et al. detect texting while walking from the standard deviation of meter readings from accelerometer sensors [7]. Thepvilojanapong et al. calculate the degree of attention from the staying judgement, the movement of people, discrimination of people, and so on, using LR sensor placed beside walls [8]. Clippingdale et al. detect attention state and estimate interest from direction and expression of the face, direction of the upper body, and so on, using cameras installed in TVs [9]. However, these sensors can only identify one or few kinds of user status. Moreover, positional information is necessary to provide Omotenashi services on the spot. Some of these sensors, pressure sensor and accelerometer sensor, cannot grasp positional information by themselves. Since cameras are poor at shielding privacy, it is difficult to install them in public places like shopping malls. LR sensors are expensive. We need a system to accurately

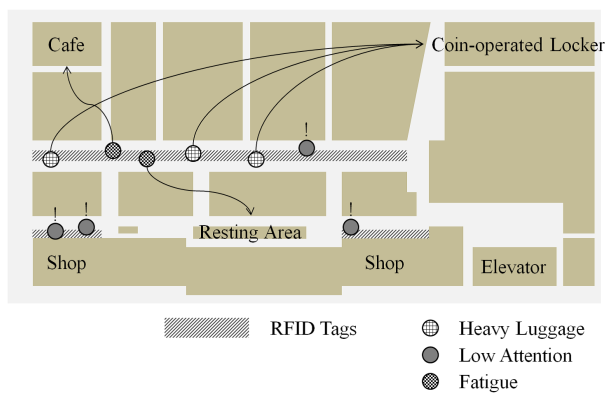


Figure 1. Omotenashi services in actual environment

grasp multiplex status of a user, causing no problem in the issues above.

Gaits vary with user states [10]. We focus on gaits which have positional information as well as are good at shielding. To detect gaits, it is required to grasp accurate positions where the user foots ground. Cho et al. get precise positional information for mobile robot localization with RFID [11]. Wang et al. use hybrid RFID systems to position pedestrians [12]. According to these studies, an RFID can detect accurate positional information. However, it is not studied to detect gaits and to estimate the user status using RFID.

III. GAIT MEASUREMENT WITH RFID

A. Gait Vector

We aim at realizing a system to provide Omotenashi services using RFID. Figure 1 shows how the system works in an actual environment. The system provides services suitable for the current status estimated for every user. An RFID reader and an RFID tag costs about 20 US dollars and several US cents for each, respectively. Our system has high scalability, because the range of our positioning system depends on only the density of RFID tags installed on floors. We assume a shopping mall lends customers readers they wear like anklets, as well as installs tags on areas such as a part of the main street and spaces in front of show windows. Services suitable for each user status make users comfortable, when they are provided before the users request. It realizes Omotenashi services. It leads to acquisition of repeaters and new customers. If every shop installs tags in front of their show windows, it can calculate the degree of attention of users to their merchandise. Understanding constituency, they can improve their services.

In this paper, we estimate user status from a gait, using RFID. Figure 2 shows our method. RFID readers get chronological foot prints based on the foot landing position. 19-dimensional features compose a gait vector for each foot print. Suppose a learner on a computer, which takes gait vectors measured with the RFID system. We train the learner so that it identifies user status. Since there are individual differences in gaits, a learner is trained for each user.

B. Detection of landing position

RFID is a short-range wireless communication technology consisting of a tag with a unique ID and a reader to detect

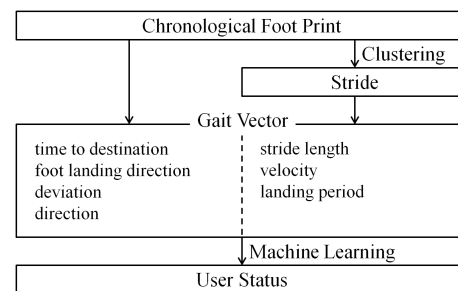


Figure 2. User Status Estimating System

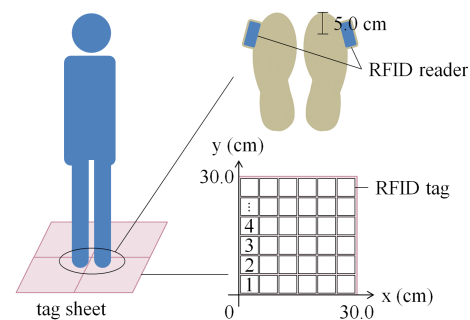


Figure 3. Localization system using RFID

the ID [13]. We use the HF-band RFID technology whose communication distance is several centimeters.

The proposed method uses 45 mm×45 mm square-type RFID tags. It prepares a tag sheet paved with the RFID tags every 50 mm vertically and horizontally. It assumes the tag sheets cover the floor of a specific area. A user wearing an RFID reader on the point 5.0 cm away from the toe walks on the tag sheets as depicted in Figure 3. A unique ID detected by the RFID reader is transformed into the coordinates representing the user position in the area. When the user walks, the coordinates are obtained chronologically.

C. Clustering

The sample rate of the reader is 0.20-0.25 seconds per detection. Generally, the walking speed and a stride is approximately 4.0 km per hour and 1.2-1.8 m [14], respectively. It takes one stride about 1.1-1.6 seconds. The sample rate is high enough to detect it, even if the walking speed has changed up to 5 times faster than the normal one. Depending on the direction in which the reader approaches the tag, more than one tag may be detected in the one step. To understand this reason, let us consider the movement of a foot. Its landing to or rising from the ground at a moderate angle makes some tags meet the communication range. Plural coordinates should be treated as one record, if they correspond to one step. We cluster more than one coordinates corresponding to one step with the Ward method [15], which is a hierarchical cluster analysis method using the ratio of the variance within and between groups. Here, to find one step, we cut out a cluster whose centroid is away by a specific distance from that of the cluster corresponding to the previous step. It allows us to cluster coordinates even if a user takes various steps at a constant interval. We refer to clusters generated by the Ward method as step clusters.

D. Feature Components of the Gait

It is assumed that the user status causes changes in gaits as follows.

Because of heavy luggage,

- Position of the center of gravity is not stable.
- Walking Direction is deviated.
- Walking speed gets slower.

Because of fatigue,

- Stride gets smaller.
- Walking speed gets slower.
- Landing time of the foot gets extended.

Because of low attention,

- Walking speed gets slower.
- Walking Direction is deviated.
- Landing time of the foot gets extended.

This paper defines a gait vector, which presents features of gaits, to identify the user status. We calculate the walking time, the number of detection, the deviation, the direction, the landing period, the stride, and the velocity from recent N step clusters in a fixed interval. The walking time, w_t , is difference between the start point, t_b , and the end point, t_e , of detected time.

$$w_t = t_e - t_b \quad (1)$$

We consider $c_w(i)$ as the j -th detected tag in the i -th detected step cluster. We regard $n_g(i)$ as the number of detection of tags in $c_w(i)$. The total number of detection, w_{nd} , is calculated as follows.

$$w_{nd} = \sum_{i=1}^N n_g(i) \quad (2)$$

We assume the proceeding direction of the user is the positive direction of the y-axis, and the direction turning clockwise it 90 degrees is the positive direction of the x-axis. We refer to $(g_x(i, j), g_y(i, j))$ as a detected coordinate. When a user walks stably, $g_x(i, j) = 0$. Deviation, g_{dev} , is the standard deviation of the x-coordinate.

$$g_{dev} = \sqrt{\sum_x \sum_y g_x(i, j)^2} \quad (3)$$

Let us consider slope a of the regression line, regarding the x-coordinate as the explanatory variables and the y-coordinate as the objective variables. In $c_w(i)$, let the first tag is detected at time $g_t(i, b)$ and the last one at $g_t(i, e)$. The landing period, $g_t(i)$, is calculated as follows;

$$g_t(i) = g_t(i, e) - g_t(i, b) \quad (4)$$

Here, we consider the following distance values to calculate a stride and the walking speed.

w_{w_1} : Cluster center-to-center distance between the current step and the next step.

w_{w_2} : Distance of the landing position between the current step and the next step.

w_{w_3} : Distance of the rising position between the current step and the next step.

w_{w_4} : Distance between the current landing position and the rising position of the next step.

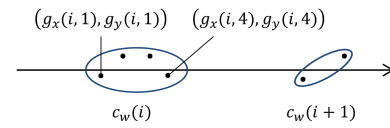


Figure 4. Detail of Step Cluster

w_{w_5} : Distance between the current landing position and the rising position of the next step.

Figure 4 shows details of a step cluster.

We calculate distances between the n -th step cluster and $(n+1)$ -th one. $w_{w_1}(i)$ is an Euclidean distance between coordinates which has central time. $w_{w_2}(i)$ is an Euclidean distance between coordinates which has minimum time. $w_{w_3}(i)$ is an Euclidean distance between coordinates which has maximum time. $w_{w_4}(i)$ is an Euclidean distance between a coordinate which has minimum time of the n -th step cluster and a coordinate which has maximum time of the $(n+1)$ -th one. $w_{w_5}(i)$ is an Euclidean distance between a coordinate which has maximum time of the n -th step cluster and a coordinate which has minimum time of the $(n+1)$ -th one. We also consider the following velocity values using distance values. w_{v_1} is a velocity between coordinates which has central time. w_{v_2} is a velocity between coordinates which has minimum time. w_{v_3} is a velocity between coordinates which has maximum time. n is related from 1 to 3.

$$w_{v_n} = \frac{\sum_1^{N-1} w_{w_n}(i)}{w_t} \quad (5)$$

After we calculate both of the right foot gait vector and the left foot one, we combine them to a single gait vector.

E. Learning and Identification

We examine relationships of the gait vector to the user status. We distinguish features of a gait to identify the user status with the machine learning method, Random Forest (RF) [16]. RF is a group learning method using a tree model, and it is suitable for analysis of the case containing many explanatory variables. RF has two steps, the learning step and the identification step. In the learning step, it creates tree models from pairs of a gait vector and a user status presented as an instruction signal. In the identification step, it identifies the user status corresponding to a new gait vector through the tree model generated in the learning step.

IV. POSSIBILITY OF DETECTION OF USE STATUS

A. Experimental Purpose and Overview

We experiment to identify 4 kinds of user status discussed in chapter 2 from the disturbance of a gait while walking. In the experiment, we use ASI4000USB which is an HF band (13.56 MHz) RFID reader. Its communication distance is about 3.0 cm. We use Tag-It HF-I as an RFID tag. The threshold of clustering shown in session 3.C is 100. Subjects are 11 males and 3 females whose age ranges from 21 to 24. Each of them wears an RFID reader on the point 5.0 cm away from the toe. We install tag sheets on the floor as shown in Section 3.B. The RFID reader attached to each shoe is connected to a laptop PC with USB cables. The walking range is 10.0 m×0.6 m. Among it, the range where tags are installed is 6.0 m×0.6 m, excluding 2.0 m in the both sides as Figure 5 shows. We

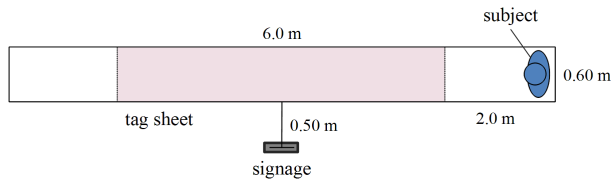


Figure 5. Experimental Environment

record gaits during the following 5 kinds of behavior before and after the physical fatigue uniformly brought by an exercise presented in Section 4.B. We repeat this trial 50 times.

- S_N Walking with no stress.
- S_{LB} Walking with two packages of luggage of 5.0 kg held in both hands.
- S_{LO} Walking with luggage of 5.0 kg held in the right hand.
- S_T Texting while walking, watching a Web site on a smartphone.
- S_A Walking with paying attention to a sign in the middle of the walking range.

Each subject takes a rest for about 30 minutes after each trial. The number of data acquisition per day is less than 100 times to prevent fatigue from affecting on a specific person. After the experiment, we ask the subjects what action is the most uncomfortable.

B. Uniform Fatigue

To artificially make subjects run into a physical fatigue state (S_F), uniformly in each trial, we impose the following exercise on them. We use the exercise intensity calculated from Karvonen method using the heart rate as a measure of S_F [6]. For a subject at age a , the maximum heart rate (M) is calculated with $(220 - a)$. The stable heart rate (R) is measured after a rest for 30 minutes. The real-time heart rate (C) is measured while walking. The exercise intensity (H) is calculated every second with

$$H = \frac{C - R}{M - R} \times 100 \quad (6)$$

Subjects go up and down the stairs at a pace of two steps per second, calculating H every second. They repeat this exercise until the value of H exceeds 60 in total 600 times.

C. Result

We divide input data into 10 groups to take 10-fold cross-validation. We train RF with 9 groups, while measure its performance with 1 group. We evaluate the performance with the F-measure (f) calculated from the precision (p) and the recall (r). The following equation shows how to calculate f .

$$f = \frac{2 \cdot p \cdot r}{p + r} \quad (7)$$

The trained RF classifier distinguishes 5 kinds of behavior: S_N , S_{LB} , S_{LO} , S_T , and S_A . It also discriminates S_F and other user status corresponding to S_{NF} . We show the result in Table I and Table II.

In the upper part of Table I, the table head shows an actual behavior, while each row shows the number of correct

TABLE I. IDENTIFICATION AMONG 5 KINDS OF BEHAVIOR

	S_N	S_{LB}	S_{LO}	S_T	S_A
S_N	960	157	242	46	37
S_{LB}	175	907	271	67	30
S_{LO}	191	259	796	74	36
S_T	41	62	64	1084	167
S_A	33	15	27	129	1130
p	0.666	0.626	0.587	0.764	0.847
r	0.686	0.648	0.569	0.774	0.807
f	0.676	0.636	0.578	0.769	0.827

TABLE II. IDENTIFICATION WHETHER THE USER IS FATIGUE

	men		women	
	S_{NF}	S_F	S_{NF}	S_F
S_{NF}	1746	877	561	228
S_F	1004	1873	189	522
p	0.666	0.651	0.711	0.734
r	0.635	0.681	0.748	0.696
f	0.650	0.666	0.729	0.715

TABLE III. VARIABLE IMPORTANCE

variable	5 behavior	S_{NF} and S_F
w_t	13.899	6.023
w_{nd}	5.499	3.757
g_{dev}	9.592	6.768
M of $g_t(i)$	5.375	4.413
SD of $g_t(i)$	4.672	4.779
w_{v_1}	30.005	8.571
w_{v_2}	17.407	6.383
w_{v_3}	17.899	6.507
M of w_{w_1}	5.763	5.040
M of w_{w_2}	5.553	4.662
M of w_{w_3}	5.317	4.670
M of w_{w_4}	4.365	4.547
M of w_{w_5}	7.464	5.352
SD of w_{w_1}	4.205	4.686
SD of w_{w_2}	4.375	4.796
SD of w_{w_3}	4.253	4.628
SD of w_{w_4}	4.243	4.286
SD of w_{w_5}	4.207	4.723
a	5.503	5.161
mean	8.400	5.250
standard deviation	6.638	1.107

classification. The result reveals the user status is classified fairly correctly.

After experiment, 11 of 14 subjects have told S_{LO} is the most uncomfortable behavior. In spite of the opinion, the uncomfortable behavior does not have the highest classification rate. It implies there are not obvious features in the gait even if the user feels strong discomfort. In Table I, many misclassified cases are found within the group of (S_N , S_{LB} , S_{LO}) and the group of (S_T , S_A). It leads features of S_N , S_{LB} , and S_{LO} are similar, as well as features of S_T and S_A are similar. Through the comparison of the classification result in Table II, the classification is more successful in women. It implies women is likely to show more fatigue features in their gaits than men.

Let us consider the importance of each component of a gait vector in Table III. We simplified the mean and the standard deviation as M and SD for each. w_{v_1} , w_{v_2} , w_{v_3} , and w_t are higher than the mean in the classification among the 5 kinds of behavior. The standard deviation of the variable importance is also large for the 5 kinds of behavior. It implies these are important components for classification. In the discrimination between S_{NF} and S_F , w_{v_1} , g_{dev} , and some of other importance are higher than average. However, standard

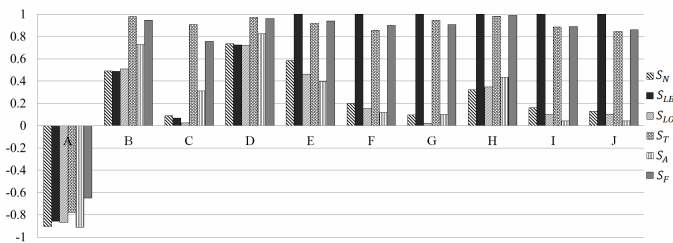


Figure 6. Components with high correlation coefficients

TABLE IV. COMBINATIONS OF COMPONENTS

Combination	
A	w_t w_{v_1}
B	w_t M of $g_t(t)$
C	w_t SD of $g_t(t)$
D	w_t w_{nd}
E	w_{v_1} M of $w_{w_1}(i)$
F	w_{v_1} SD of $w_{w_1}(i)$
G	w_{v_1} a
H	M of $w_{w_1}(i)$ SD of $w_{w_1}(i)$
I	M of $w_{w_1}(i)$ a
J	SD of $w_{w_1}(i)$ a

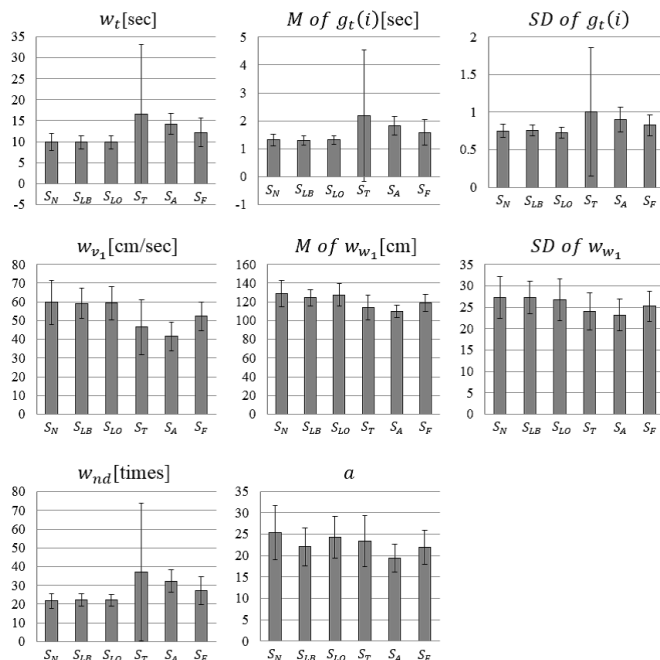


Figure 7. Average and standard deviation of each component

deviation is not large. It indicates each component shows the physical fatigue. Let us discuss each component through the correlation analysis. It is obvious that each stride has strong correlation with the walking time. Excluding these ones, Figure 6 compares combinations of 2 gait vector elements, which has correlation higher than 0.8 or lower than -0.8. In the figure, the symbols from A to J stand for the combinations shown in Table 4. In addition, Figure 7 shows the average and the standard deviation of each component value for all subjects.

Let us discuss every behavior compared with behavior S_N where no load is imposed on subjects. S_{LB} shows negative correlation between w_t and w_{v_1} , and positive correlation among

w_{v_1} , M of $w_{w_1}(i)$, SD of $w_{w_1}(i)$, and a . Compared with S_N , S_{LB} has no difference in average and standard deviation except M of $w_{w_1}(i)$, which means each step gets shorter. These imply subjects slow down with shorter walking cycle. S_{LO} shows negative correlation between w_t and w_{v_1} . It has no difference in average and standard deviation from S_N . These imply S_{LO} is similar to S_N . However, Table I indicates S_{LO} is distinguished from S_N fairly well. It seems each subject feels load in an individual way. S_T has positive correlation among w_{v_1} , M of $w_{w_1}(i)$, SD of $w_{w_1}(i)$, and a as well as positive correlation among w_t , w_{nd} , M of $g_t(i)$, and SD of $g_t(i)$. In cases of S_T where subjects are texting while walking, the standard deviation of some components is much larger than others. It means the walking way varies with persons. The correlation means subjects take smaller strides and longer landing duration when they slow down. S_A shows negative correlation between w_t and w_{v_1} , while positive correlation between w_t and w_{nd} . The average and the standard deviation of strides are smaller than others in S_A . These imply subjects slow down with smaller and fixed strides which increase their stepping. S_F has positive correlation among w_{v_1} , w_{nd} and M of $g_t(i)$, and positive correlation among w_{v_1} , M of $w_{w_1}(i)$, SD of $w_{w_1}(i)$, and a . The observation implies subjects slow down with smaller strides. We can identify each behavior of the user status, if we check the characteristics discussed above.

V. GAIT DIFFERENCE BY WAY OF CARRYING LUGGAGE

A. Experimental Purpose and Overview

Let us see whether some features appear on gaits when people are forced to have luggage with uncomfortable way by some external factors. We examine features of gait vectors under various way of carrying luggage or various feelings of subjects while carrying luggage. Subjects are 1 male and 11 females, whose age ranges from 19 to 22 years old. Experimental conditions are same as session 4.A. We record gaits under the following 3 kinds of behavior.

- S_{LH} Walking with luggage of 4.0 kg holding in the right hand.
- S_{LE} Walking with luggage of 4.0 kg slinging over the right arm.
- S_{LS} Walking with luggage of 4.0 kg slinging on the right shoulder.

Every subject takes each kind of behavior 10 times, interleaving 5 minute break. We have inquired of the subjects what action makes them most comfortable and most uncomfortable.

B. Classification

We have classified 3 kinds of behavior in the same way as section 4.C. The result reveals we can identify each behavior roughly. The F-measure values of S_{LH} , S_{LE} , and S_{LS} are 0.599, 0.516, and 0.562, respectively. The standard deviation of the F-measure among subjects is 0.17804. It implies there is big difference in each individual. As for the importance of components, 2 groups are found; g_{dev} and w_{v_1} are high in one group, while g_{dev} and M of $w_{w_1}(i)$ is high in the other. The 3 variables, g_{dev} , w_{v_1} , and M of $w_{w_1}(i)$, are important for identification. According to the interview after the experiment, all subjects feel S_{LH} and S_{LE} uncomfortable (5 subjects and 7 subjects), while S_{LS} comfortable (12 subjects) for each.

We divide S_{LH} and S_{LE} from S_{LS} to make the two groups, uncomfortable one and comfortable one, respectively. Let us classify the two groups with gait features. Because of the difference of the number of cases in each group, we randomly sample 100 cases. The F-measure values of uncomfortable one and comfortable one are 0.679 and 0.657 for each.

The result implies we can classify each behavior. The importance of components are high at g_{dev} , w_{v_1} , and M of $w_{w_1}(i)$. The way to carry luggage affects gaits, which enables us to guess how subjects feel when walking. In addition, behavior a in this experiment corresponds to S_{LO} in the former experiment. We can distinguish uncomfortable behavior from other kinds of behavior. The interview indicates subjects feel the least load on the body, if they carry luggage slinging on shoulder. The number of sample data might be the reason of variance in the classification. It might be caused by subjects carrying luggage in an unusual way. The importance of components suggests the center of gravity of the body is not stable by the luggage. It seems they slow down or change their steps to ease their uncomfortable feelings.

VI. DISCUSSION

In this paper, we have mentioned the problems of cost, classification ability, and so on in section 2. An RFID reader is about 20 US dollars and a RFID tag is several US cents for each. Our system has high scalability, because the range of our positioning system depends on only RFID tags. The experiment has revealed we can identify all kinds of user status, and whether the user is carrying luggage with uncomfortable way at a certain range, using only the RFID system. If our system is installed in the shopping mall, we can grasp the customer status to provide Omotenashi services suitable for each of them. We assume the shopping mall lends customers a pair of readers, and install tags at some areas like a part of major streets or spaces in front of show windows. Stores in the shopping mall can also easily install the RFID tags, because it is relatively at low cost, and we only have to install them in a specific area of each store.

Since we can know the status of customers from their gaits, we can provide suitable services for each status. We propose the following services for each status. In case of behavior S_{LB} , carrying luggage with both hands, subjects tune various components of the gait vector. It means customers accommodate themselves to the load of luggage. To make the enduring time short, the system should recommend the shortest way to their destination. On the other hand, subjects tune few components of the gait vector in S_{LO} , carrying luggage with one hand. It is too high load for them to carry luggage. The system should recommend to take rests at cafes near them, or to ride on vehicles. The system should call their attention to avoid accidents in advance when they are in S_T , texting, and S_A , low attention. The system provides details of the advertisement customers look at when they are in S_A . Recommendation like S_{LO} is preferable when they are in S_F , fatigue. Customers experience the high level of satisfaction, which lead to increase of customers. In the experiments, subjects are only their age of 20s. However, features of gaits are not different between 20s and 60s [17]. In addition, the rate of foreign visitors to Japan consists of 17.7% men of 30s, 13.5% women of 20s, 13.0% men of 40s,

and 12.8% men of 20s [2]. Our method based on gaits covers many visitors to Japan.

VII. CONCLUSION

In this paper, we have proposed the method to provide customers high quality Omotenashi services using their gait pattern acquired with the RFID technology. In experiment, we have proved the method identifies the state of users from features of their gait. In addition, we have shown we can find out users carrying luggage in unusual ways. However, to classify the state of carrying luggage accurately, we need to train the system individually. We must consider accuracy improvement and generalization from individual as future works. In addition, we consider the RFID readers shape and more specific services.

REFERENCES

- [1] Japan Tourism Agency, "To the realization of the 20 million foreign visitors era", <http://www.mlit.go.jp/common/000059772.pdf> [retrieved: July, 2015] (in Japanese).
- [2] Japan Tourism Agency, "Consumption trends of foreign visitors", 2013, <http://www.mlit.go.jp/common/001032143.pdf> [retrieved: July, 2015] (in Japanese).
- [3] Ikeda, T. et al., "A Method to Recognize 3D Shapes of Moving Targets based on Integration of Inclined 2D Range Scans", IEEE International Conference on Robotics and Automation, 2011, pp. 1237-1240.
- [4] Qi, Y. et al., "Carrying Object Detection and Tracking Based On Body Main Axis", IEEE International Conference on Wavelet Analysis and Pattern Recognition, 2007, pp. 1237-1240.
- [5] Yonekawa, K. et al., "FASH: Detecting Tiredness of Walking People Using Pressure Sensors", Mobile and Ubiquitous Systems: Networking & Services, 2009, pp. 1-6.
- [6] Arif, M. et al., "Analysis of the effect of fatigue on walking gait using acceleration sensor placed on the waist", International Journal of Engineering Intelligent Systems, 2010, pp. 93-103.
- [7] Music, J. et al., "Is it Possible to Detect Mobile Phone User's Attention Based on Accelerometer Measurement of Gait Pattern?", IEEE Symposium on Computers and Communications, 2013, pp. 522-527.
- [8] Thepvilajanpong, N. et al., "Evaluating People's Attention in the Real World", ICROS-SICE International Joint Conference, 2009, pp. 3702-3709.
- [9] Clippingdale, S. et al., "Level-of-Interest Estimation for Personalized TV Program Recommendation", IEEE International Conference on Consumer Electronics, 2013, pp. 11-14.
- [10] Abiko, T. et al., "Influence of Different Methods of Carrying a Load on Gait Parameters of Healthy Young Adults", The Society of Physical Therapy Science, 2014, Vol. 29, No. 1, pp. 147-149(in Japanese).
- [11] Choi, B. et al., "A Hierarchical Algorithm for Indoor Mobile Robot Localization Using RFID Sensor Fusion", IEEE Transactions on Industrial Electronics, 2011, Vol. 58, No. 6, pp. 2226-2235.
- [12] Wang, H. et al., "Hybrid RFID System-based Pedestrian Localization: A Case Study", 2013 10th Workshop on Positioning, Navigation and Communication, 2013, pp. 1-6.
- [13] R. Weinstein, "RFID: a technical overview and its application to the enterprise", IT Professional, 2005, Vol. 7, No. 3, pp. 27-33.
- [14] Perry, J. and Burnfield, J., "Gait Analysis: Normal and Pathological Function", Chapter 20, Slack Inc (2010).
- [15] Ward, J. H., "Hierarchical grouping to optimize an objective function", Journal of the American Statistical Association, 1963, vol. 58, no. 301, pp. 236-244.
- [16] Breiman, L., "Random Forests, Journal of Machine Learning", 2001, vol. 45, pp. 5-32.
- [17] Jin, B. et al., "Walking-Age Analyzer for Healthcare Applications", IEEE Journal of Biomedical and Health Informatics, 2014, pp. 1034-1042.

EEG Sensor Based Semi-Supervised Inattention Prediction Framework For Unmanned Aerial Vehicles

Yerim Choi*, Jonghun Park†

Department of Industrial Engineering
Seoul National University
Seoul, Republic of Korea

Email: *ian4@snu.ac.kr, †jonghun@snu.ac.kr

Dongmin Shin

Department of Industrial and Management Engineering
Hanyang University
Ansan, Republic of Korea
Email: dmshin@hanyang.ac.kr

Abstract—With the advance in sensor devices, electroencephalography (EEG) can be unobtrusively collected enabling the inattention prediction of unmanned aerial vehicle (UAV) operators, which is one solution for reducing the high accident rate of UAVs. Several studies using statistical learning methods on EEG data have shown satisfactory results. However, it is almost impossible to obtain accurate training data containing attention status labels due to the absence of standardized measure for the attention status. Therefore, in this paper, we propose a semi-supervised inattention prediction framework which does not require training data nor any prior information by utilizing the fact that operators keep their attention at the beginning of a task and adopting a cumulative sum algorithm to detect the duration. Moreover, weighted dissimilarity measures are applied to enhance the prediction performance of the proposed framework. From experiments conducted on real-world datasets, the proposed framework showed promising results.

Keywords—EEG sensor; Inattention prediction; Semi-supervised learning; Cumulative sum algorithm; Weighted dissimilarity measures.

I. INTRODUCTION

Unmanned aerial vehicles (UAVs) are known for their high accident rate, which is ten to hundred times higher than that of manned ones [1]. One of the reasons for the high accident rate is the detached cockpits of UAVs, causing frequent inattention of operators [2]. Inattention refers to the status where an operator fails to keep her/his focus on the involved tasks due to external or internal stimuli such as fatigue. Therefore, the accident rate of UAVs can be reduced by predicting the inattention of operators and inducing them to keep their attention.

Among many efforts to predict operators' inattention, electroencephalography (EEG) based statistical learning methods are widely used in various domains including car driving [3] as well as unmanned aerial vehicle maneuvering [4] with satisfactory performances. Particularly, EEG is suitable for inattention prediction of the UAV operators during maneuvering since it can be obtained in less intrusive manner [5] in real time with minimum bias caused by external conditions. Moreover, adopting statistical learning methods is superior to other methods including index based methods [6] or observation based methods [7] in the fact that they enable personalized prediction without human interventions.

Most statistical learning based inattention prediction methods adopt supervised methods such as support vector machines [3] and hidden Markov models [8], which require training data, which is composed of EEG vectors and corresponding attention status labels of an operator. Labels indicate whether

the operator is focused or not during the generation of the corresponding EEG vector. Attention status labels used in previous studies are earmarked by utilizing additional information with imperfect assumptions due to the absence of standardized measure of inattention [9]. For instance, Choi et al. [8] assumed that an operator keeps attention while performing more difficult tasks and labeled EEG generated during performing easy task as inattention status. Several studies assumed that the physical behaviors of operators indicate their attention status and used them as labels. However, these labeling techniques may cause performance degradation since the prediction performance of supervised methods depends on the accuracy of training data. On the other hand, unsupervised methods which do not require labeled data are generally known to show insufficient performances.

To overcome the supervised methods' necessity of training data and unsupervised methods' low performance quality, semi-supervised methods, in which a little portion of labeled data or prior knowledge are used to enhance prediction performances, are proposed [9], [10]. Shi et al. [9] utilize two prior knowledge to classify sleep stages of subjects, one of which are extreme stage labels, which are relatively easy to obtain, and another one is stage changing patterns. Choi et al. [10] assume a certain duration of operators' attention from the beginning of tasks and different contributions of frequency bands depending on attention status, both of which are stated in previous literature. Prior knowledge adopted in both studies are still costly to obtain and require human interventions for determining parameters.

To this end, we propose a semi-supervised framework for inattention prediction of UAV operators, where human interventions or additional information usages are minimized. The same assumptions used in [10] are adopted, which are that operators tend to keep their attention for a certain duration from the beginning of tasks [11] and that contributions of frequency bands differ depending on the attention status. Unlike the previous work, additional methods are employed for automatic parameter determination.

Specifically, inattention prediction is performed by using constrained k-means algorithm [12], which keeps a small portion of labeled data unchanged throughout the clustering procedure. As the small portion of attention labels, instances of a certain duration from the beginning of maneuver are used. The duration is automatically determined by conducting the cumulative sum (CUSUM) algorithm for variance change detection [13], by which unusually fluctuation of EEG is detected. Moreover, weights of the four frequency bands

according to attention status are learned during the clustering procedure by using the weighted dissimilarity measures [14], which determine different weights scheme of features for each cluster.

The rest of paper is organized as follows. In Section 2, the proposed inattention prediction framework for UAV operators is introduced, and its components are presented in detail. Then, performances of the proposed framework are evaluated by using real-world dataset in Section 3, and the paper is concluded in Section 4.

II. INATTENTION PREDICTION FRAMEWORK FOR UAV OPERATORS

A. Problem definition

In this paper, we attempt to predict the attention status of an UAV operator by utilizing EEG generated from the operator while maneuvering. Specially, an EEG sequence of an operator, acquired during performing a task, is denoted by $E = \{\mathbf{e}_n | n = 1, \dots, N\}$, where $\mathbf{e}_n = \langle e_{n,m} \rangle$, $m = 1, \dots, 4$, is the n -th EEG vector composed of $e_{n,m}$, a value of the m -th feature, and N is the total number of EEG vector generated. We note that the four features indicate the four frequencies of EEG power spectral density, alpha (8-12 Hz), beta (13-30 Hz), delta (1-3 Hz), and theta (4-7 Hz), obtained by performing wavelet packet decomposition [15] on original EEG signal.

The purpose of the proposed framework is to determine the attention status of \mathbf{e}_n . Label matrix, $L = [l_{k,n}]$, is a 2-by- N integer matrix, where $l_{k,n}$ indicates whether \mathbf{e}_n is generated during attention status or inattention status, and it can have two values 1 or 0, and $\sum_k l_{k,n} = 1$. If \mathbf{e}_n is generated during the attention status, $l_{1,n}$ is 1 and $l_{2,n}$ is 0, otherwise $l_{1,n}$ is 0 and $l_{2,n}$ is 1.

B. Framework overview

In this section, the proposed inattention prediction framework is introduced. Figure 1 shows an overview of the framework. First, an operator's EEG data is collected using an EEG acquisition device, and, then, a portion of the collected data is labeled by conducting the CUSUM algorithm. The portion of labeled data and the rest of unlabeled data are clustered according to attention and inattention status, and, at last, when new EEG vector of the operator is given, the attention status of the operator during generation of the vector is predicted by using the clustering results.

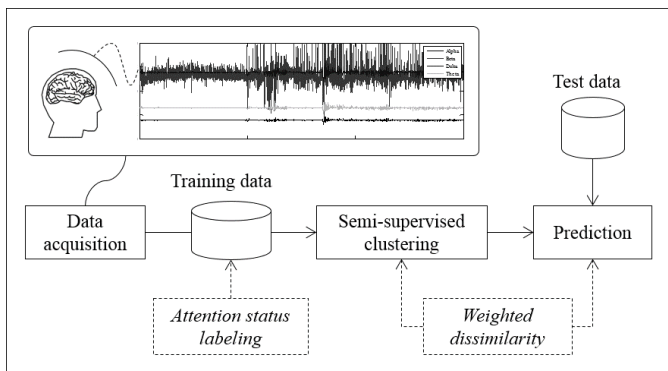


Figure 1. Overview of the proposed framework.

C. Attention labeling using the CUSUM algorithm

To detect the duration, the CUSUM algorithm is adopted, a well-known parameter change detection method for time series data. Particularly, change in variance is detected since there exists a large fluctuation in variance when inattention status occurs as shown in the EEG example from Figure 1. We denote the time, considered as a point where attention is sustained, by d which stands for the duration and call it duration in the rest of the paper.

There exist four time series data, representing the four frequency bands, so that we separately detect their durations and use the minimum value, obtained by (2).

$$d = \min d_m, \quad m = 1, \dots, 4 \quad (1)$$

where d_m is a detected duration of the m -th feature, and it is calculated by (2).

$$d_m = \arg \max_t |D_{t,m}|, \quad (2)$$

where $D_{t,m}$ is defined as (3).

$$D_{t,m} = \frac{\sum_{n=1}^t e_{n,m}^2}{\sum_{n=1}^N e_{n,m}^2} - \frac{t}{N}, \quad (3)$$

D. Inattention prediction using constrained k-means with weighted dissimilarity measures

Using the duration as a small portion of labeled data, constrained k-means [12] is adopted for the proposed semi-supervised inattention prediction. Additionally, different weights of the four frequency bands are learned according to clusters, attention or inattention, by employing the dissimilarity measures [14]. The proposed algorithm combining the above two methods is in the form of the expectation and maximization scheme [16] as shown in Figure 2.

Input: $E, d, \max Iter$

Output: L, C, W

$t \leftarrow 1$

$$c_{1,m} \leftarrow \frac{1}{d-1} \sum_{n=1}^{d-1} e_{n,m}$$

$$c_{2,m} \leftarrow n$$

repeat

if $n < d$ **then**

$$l_{2,n}^{(t+1)} \leftarrow 1 \text{ and } l_{1,n}^{(t+1)} \leftarrow 0$$

else

determine $L^{(t+1)}$ for $n = d, \dots, N$ and $k = 1, 2$

end if

determine $C^{(t+1)}$ for $k = 1, 2$ and $m = 1, \dots, 4$

determine $W^{(t+1)}$ for $k = 1, 2$ and $m = 1, \dots, 4$

$t \leftarrow t + 1$

until $(t = \max Iter)$ || (Equation (4) converges)

Figure 2. Pseudo-code of the inattention prediction algorithm combining constarined k-means with weighted dissimilarity measures.

In Figure 2, C represents a 2-by- m matrix, $m = 1, \dots, 4$, whose elements are $c_{1,m}$ and $c_{2,m}$ indicate the centroid of inattention and attention cluster, respectively. W is also a 2-by- m matrix, and its element, $w_{k,m}$ is a weight of the m -th feature for the k -th cluster. The three determination process of L, C , and W is to minimize the objective function shown in (4).

$$F(E, L, W, C) = \sum_{k=1}^2 \sum_{n=1}^N \sum_{m=1}^4 l_{k,n} w_{k,m} s(c_{k,m}, e_{n,m}), \quad (4)$$

where $s(c_{k,m}, e_{n,m})$ is a similarity measure between $c_{k,m}$ and $e_{n,m}$, calculated by (5).

$$s(c_{k,m}, e_{n,m}) = |c_{k,m} - e_{n,m}|^2 \quad (5)$$

Detailed information of the determination process can be found in [14].

III. EXPERIMENT

A. Data acquisition

To evaluate the performances of the proposed inattention prediction framework, real-world datasets were collected. Four subjects, including a female and three males, maneuvered a flight simulator called Microsoft Flight Simulator XTM [17], which provides tasks and environments similar to those of actual UAVs, using joysticks which are also similar to the controllers of UAVs. Each subject performed a task of maneuvering an UAV from Kagoshima, Japan to Gimhae, Korea for three times in two days with enough rest to avoid fatigue.

A snapshot of data acquisition using the equipments mentioned above is shown in Figure 3. We used a commercial EEG acquisition tool, EmotiveTM EPOC [18]. Using EmotiveTM EPOC, EEG was collected from 14 channels according to the international 10-20 system at frequency of 30 Hz and bandwidth between 0.2 Hz and 45 Hz.

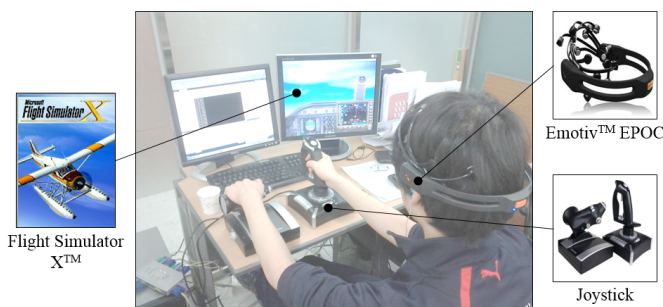


Figure 3. Snapshot of data acquisition procedure by using EmotiveTMEPOC, joysticks, and Microsoft Flight Simulator XTM.

After conducting manual inspection for noise reduction, averaged and normalized magnitudes (in microvolts) across the 14 channels of the four frequency bands were used in the experiments. Subjects were asked to keep certain levels of velocity and altitude while maneuvering, and we assumed that the periods where a subject failed to keep the given standards are the inattention periods of the subject. We note that the information of inattention period only used for model validation purpose.

B. Experiment setting

According to the detection methods for attention durations and weights, nine different models, UM, GW, LW, GD, GWGD, LWGD, DD, GWDD, LWDD, were involved in the experiments. The first three columns in Table II show names and characteristics of the nine models. ‘Non’ indicates that the models do not utilize any duration or weights for inattention prediction, ‘Given’ indicates that the models uses the given values of durations or weights, and lastly, ‘Detected’ or ‘Learned’ indicates that the model uses detected durations or learned weights by performing the CUSUM algorithm or the weighted dissimilarity measure, respectively.

Among the nine models, UM is one that previously exists and the others where duration and weight are utilized are ones that proposed in this paper. Specifically, in the experiments, 5 minutes of duration and weight scheme (1, 2, 1, 1) for (delta, theta, alpha, beta) were used. Those numbers are ones that have proven to show the best performance by comparing a small set of values in the previous study [10], and, also, theta wave is known to be closely related to sleep states. We note that, unfortunately, a previous inattention prediction method based on supervised and semi-supervised approaches cannot be implemented since we assumed that there is no labeled data for training.

As an evaluation criterion, we employed accuracy which is widely used in statistical learning domain [19]. Accuracy is calculated by (6).

$$Accuracy = \frac{TP + TN}{TP + FP + FN + TN}, \quad (6)$$

where TP , FP , FN , and TN receptively represent the number of true positive, false positive, false negative, and true negative instances as shown in Table I. In addition, all experiments are repeated for ten times, and the results are averaged to minimize randomness.

TABLE I. CONFUSION MATRIX FOR INATTENTION PREDICTION.

	Predicted attention	Predicted inattention
Actual attention	True positive (TP)	False negative (FN)
Actual inattention	False positive (FP)	True negative (TN)

C. Experiment results

In this section, experiment results of the proposed inattention prediction framework are presented. Table II shows the summary of the performance comparison results among the nine models. On the average, LWGD model performed the best with an accuracy of 79.71%, while UM model performed the worst with an accuracy of 54.48%. In most cases, better results can be obtained when the attention status labels for the durations or the weights of four frequency bands are used for the inattention prediction.

In addition, prediction accuracies varies among subjects. For instance, while the best accuracy of Subject 4 is 78.00%, that of Subject 3 is 84.37%, and across all subjects, Subject 4 shows the worst accuracies for all models. This implies that for some operators, the proposed framework may not work satisfactorily, and, therefore, additional care should be given for such operators.

By comparing results of models GD and DD, where GD uses a given duration of 5 minutes for all subjects and DD uses a detected duration for each subject and trial, it can be said that prediction quality enhances when using a detected duration with an exception of Subject 3. Moreover, the effectiveness of learning weights varies among subjects, although for most cases using learned weight enhanced the performances. Therefore, in-depth experiments and explorations on the results should be conducted to show appropriateness of the proposed method.

IV. CONCLUSION

In this paper, an inattention prediction framework for UAV operators using statistical learning methods on EEG

TABLE II. PERFORMANCE COMPARISON RESULTS OF THE NINE MODELS ACCORDING TO THE FOUR SUBJECTS IN TERMS OF ACCURACY (IN PERCENT).

Duration	Weight	Model	Subject 1	Subject 2	Subject 3	Subject 4	Average
Non	Non	UM	48.07	65.97	59.64	44.23	54.48
	Given	GW	50.47	62.18	73.31	44.48	57.61
	Learned	LW	47.46	61.93	57.49	48.46	53.83
Given	Non	GD	77.41	78.56	82.07	75.81	78.46
	Given	GWGD	78.56	78.89	81.89	76.67	79.00
	Learned	LWGD	80.15	78.93	84.32	75.41	79.71
Detected	Non	DD	77.90	79.07	81.23	77.20	78.85
	Given	GWDD	78.36	78.92	82.62	77.59	79.37
	Learned	LWDD	77.82	77.97	84.37	78.00	79.54
Average			64.86	71.97	73.65	66.67	69.29

data is proposed. Particularly, it is in the form of a semi-supervised method by utilizing the fact that operators keep their attention at the beginning of tasks to address the problem of no unified attention standard. To minimize human interventions, an automatic method for detecting attention duration, called the CUSUM algorithm, is adopted, and the weighted dissimilarity measures, where weights of four frequency bands are separately learned depending on cluster during clustering process, are applied to further enhance the performances of the proposed method.

For the future work, we plan to conduct in-depth experiments using diverse settings such as durations and weights. Moreover, for the practical usage, advanced methods for both detecting duration and learning weights should be developed to improve accuracy of current model. Eventually, adoption of the inattention framework to a real-world situation will contribute to the lowering the UAV’s accident rate and enhancing UAV operator’s safety.

ACKNOWLEDGMENT

This work was supported by the BK21 Plus Program (Center for Sustainable and Innovative Industrial Systems, Department of Industrial Engineering, Seoul National University) funded by the Ministry of Education, Korea (No. 21A20130012638).

REFERENCES

[1] Department of Defense, “Unmanned aerial vehicles roadmap 2000-2025,” Office of the Secretary of Defense, Tech. Rep., 2001.

[2] T. Nisser and C. Westin, Human factor challenges in unmanned aerial vehicles (uav): a literature review. Lund University School of Aviation, 2006.

[3] M. V. M. Yeo, X. Li, K. Shen, and E. P. V. Wilder-Smith, “Can svm be used for automatic eeg detection of drowsiness during car driving?” Safety Science, vol. 47, no. 1, 2009, pp. 115–124.

[4] Y. Choi et al., “A BCI Based Ground Control Framework for Attention Maintenance of UAV Operators,” *Entrue Journal of Information Technology*, vol. 12, no. 1, 2013, pp. 101–115.

[5] B. Zhang, J. Wang, and T. Fuhlbrgge, “A review of the commercial brain-computer interface technology from perspective of industrial robotics,” in *Proceedings of the IEEE International Conference on Automation and Logistics*, 2010, pp. 379–384.

[6] K. Kaida et al., “Validation of the karolinska sleepiness scale against performance and eeg variables,” *Clinical Neurophysiology*, vol. 117, no. 7, 2006, pp. 1574–1581.

[7] F. Friedrichs and B. Yang, “Camera-based drowsiness reference for driver state classification under real driving conditions,” in *Proceedings of the IEEE Intelligent Vehicles Symposium*, 2010, pp. 101–106.

[8] Y. Choi et al., “Hypovigilance Detection for UCAV Operators Based on a Hidden Markov Model,” *Computational and Mathematical Methods in Medicine*, vol. 2014, 2014.

[9] L.-C. Shi, H. Yu, and B.-L. Lu, “Semi-supervised clustering for vigilance analysis based on eeg,” in *Proceedings of the International Joint Conference on Neural Networks*, 2007, pp. 1518–1523.

[10] Y. Choi, N. Kwon, J. Yoon, S. Jeon, B.-H. Paeng, and a. o. S. Jonghun Park, “A semi-supervised attributes-weighting clustering method for inattention prediction in human-machine interaction systems,” in *Proceedings of the Asia Pacific Industrial Engineering and Management Systems Conference*, 2013.

[11] N. Mackworth, “The breakdown of vigilance during prolonged visual search,” *Quarterly Journal of Experimental Psychology*, vol. 1, no. 1, 1948, pp. 6–21.

[12] S. Basu, A. Banerjee, and R. J. Mooney, “Semi-supervised clustering by seeding,” in *Proceedings of the International Conference on Machine Learning*, 2001, pp. 27–34.

[13] S. Lee, J. Ha, O. Na, and S. Na, “The cusum test for parameter change in time series models,” *Scandinavian Journal of Statistics*, vol. 30, no. 4, 2003, pp. 781–796.

[14] E. Y. Chan, W. K. Ching, M. K. Ng, and J. Z. Huang, “An optimization algorithm for clustering using weighted dissimilarity measures,” *Pattern Recognition*, vol. 37, no. 5, 2004, pp. 943–952.

[15] J.-Z. Xue, H. Zhang, C.-X. Zheng, and X.-G. Yan, “Wavelet packet transform for feature extraction of eeg during mental tasks,” in *Proceedings of the International Conference on Machine Learning and Cybernetics*, vol. 1, 2003, pp. 360–363.

[16] A. Dempster, N. Laird, and D. Rubin, “Maximum likelihood from incomplete data via the em algorithm,” *Journal of the Royal Statistical Society. Series B (Methodological)*, 1977, pp. 1–38.

[17] J. Van West and K. Lane-Cummings, *Microsoft Flight Simulator X For Pilots: Real World Training*. Wiley, 2007.

[18] B. Zhang, J. Wang, and T. Fuhlbrgge, “A review of the commercial brain-computer interface technology from perspective of industrial robotics,” in *Proceedings of the IEEE International Conference on Automation and Logistics*, 2010, pp. 379–384.

[19] K. Kim, B.-s. Chung, Y. Choi, S. Lee, J.-Y. Jung, and J. Park, “Language independent semantic kernels for short-text classification,” *Expert Systems with Applications*, vol. 41, no. 2, 2014, pp. 735–743.

A GSM-based System for the Tracking of Birds

Samuel Matos

University of Trás-os-Montes e Alto Douro
Email: samrmatos@gmail.com

Raul Morais

INESC-TEC and UTAD,
Email: rmorais@utad.pt

P.M. Araújo

MARE, University of Coimbra, Portugal
Email: mmiguelinhu@gmail.com

P.J.Q. Tenreiro

ICNF, Portugal
Email: paulo.tenreiro@icnf.pt

P.J.S.G. Ferreira

DETI/IEETA, University of Aveiro, Portugal
Email: pjf@ua.pt

M. J. C. S. Reis

IEETA and UTAD
Email: mcabral@utad.pt

Abstract—We present a prototype of a system for the tracking of animals, goods or people, by using only Global System for Mobile Communications (GSM) services. The system consists of two parts: a base device and at least one location device. The base device receives the Short Message Service (SMS) sent by the location devices and forwards the messages to an application that decodes and stores the location data in a database. The location device, the part actually attached to the animal, good or person being tracked, combines reduced size and weight with extended range. We present the energy consumption profiles and the computer applications developed to test the system and discuss the results of practical tests with wild and captive birds.

Keywords—GSM-based location, location system, geolocation, tracking system, bird tracking

I. INTRODUCTION

Animal movement and migration has long fascinated man. Due to its scale, bird migration is one of the most striking. The number of birds involved is in the billions, the annual roundtrips of some bird species reach 70,000 km and some birds are known to perform non-stop flights of 10,000 km [1] [2]. Discoveries such as these are in part due to the use of tracking technology, which is of interest for multiple reasons. First, tracking is an important tool to better understand and protect the migrating species. Second, migrant animals are indicators of change. Human activity is having a global impact on the planet and migrant animals modify their behaviour due to human-caused changes and stressors. Birds, being the most mobile of all animals, are of particular interest in this regard. A better understanding of migration patterns also impacts climate change studies, energy generation, airstrike prevention, disease propagation, planning and urbanisation, agriculture, fisheries, and more.

Migration studies were once carried out by observation, but for more than one century they have relied on technological advances and breakthroughs. Bird ringing was one of those advances, and began with the efforts of a school master, Hans Christian C. Mortensen, in Denmark in 1899 [3]. A ring is a light metal band of appropriate size that carries a unique number, by means of which the bird can be identified, if and when recovered.

The relatively small probability of recapturing a ringed bird is a drawback that more recent technologies are helping

to solve. One solution is to use electronic devices to send signals that are then picked up by radio receivers or satellites, enabling scientists to follow the movement of the tagged animals without having to recapture them. In fact, the receiver can be used to home in on the animal to get the device back.

Tracking an animal by radio involves two devices: a transmitter attached to the animal, to send out signals (data); and a receiver to pick up the signal (data). The transmitter can be placed around an animal's ankle, neck, wing, carapace, dorsal fin or it may even be surgically implanted. The advantages of implantation of subcutaneous radio transmitters are discussed in, e.g., [4].

Useful as they are, these devices are far more expensive than the low-tech, non-electronic tags. Also, their size and weight makes them useless for tracking some animals, including many birds species.

Receivers can also be placed in satellites or, more precisely, networks or groups of satellites (e.g., Argos). Satellite tracking has been used to track caribou, sea turtles, whales, great white sharks, seals, elephants, bald eagles, ospreys and vultures [5]. For a review of traditional systems used in the tracking/location of birds, see [6]. In [7], a Global Positioning System (GPS) based tracking system was used in experiments of homing pigeons flying in flocks of up to 10 individuals. The GPS device, based on a commercially available product (u-blox AG, LEA-5H), is able to log 30,000 data points (latitude, longitude, altitude and time), measured 25×45 mm, and weighed 16 g. Upon recapture of the birds the log files are downloaded to a computer and processed. The GPS trackers used in [8] were also applied to study pigeons. The complete device measured $71 \times 41 \times 17$ mm, weighed 35 g. Hand-held, non-differentially corrected 12-channel GPS receivers capable of storing up to 1024 positions were used in central Norway to track hunters and their interactions with Willow Ptarmigan *Lagopus lagopus*, as reported in [9].

The system described in [10] weighs 12 g and includes a GPS receiver, micro-processor, 4 MB of memory for data storage, solar panel and battery. It has a tri-axial accelerometer to monitor behaviour and it is equipped with a radio transceiver for bidirectional communication with a ground-based antenna network, which enables data to be downloaded and new

measurement schemes to be uploaded remotely. It enables the study of fine-scale movements (intervals of 3 s) to long-distance migratory movements (intervals of 20-30 min).

The system used in [11] to study the migratory strategy of herons uses DUCK III Ecotone GPS/GSM transmitters and a battery charged by a solar panel. The transmitters provided accurate information on geographical location every 3, 6, 12 or 24h. No data was provided concerning the device's weight besides the fact that "extra weight of the transmitters and Teflon harness varied from 3.4 to 3.9% of (herons') body mass".

A study concerning seasonal differences in migration patterns of soaring birds in relation to environmental conditions was presented in [12]. Here, 11 adult Booted Eagles were equipped with 22 g GPS-Argos satellite transmitters, and one individual with a GPS data-logger of the same weight. Transmitters were programmed to collect GPS locations on an hourly basis from 6:00 to 20:00 (GMT—Greenwich Mean Time) during migrations.

Other solutions can be considered [13]: data recovery using a VHF beacon data transmitter, radio modem technology, Argos DCLS, mobile communications (GSM/SMS, GSM/GPRS—General Packet Radio Services), LEO satellite telephone data services, Iridium satellites, globalstar satellites, or node-to-node networking. Note that some of these solutions have high power/energy consumption requirements.

The coordinates are the fundamental data in the tracking of birds (or other animals, persons, or goods). In the case of data loggers, they are saved in log files and then downloaded to a computer, upon recapture of the bird.

Light-based geolocation is an alternative when satellite-based systems cannot be used. Theoretically, a light sensor and a clock are sufficient to solve the geolocation problem, at only a fraction of the cost, size and weight of satellite-based systems. On the negative side, the errors increase near the equinoxes and the errors can be in the hundreds of km [14]. The template method [15] improves on this. Light-based geolocators are loggers and the data can be retrieved only if the bird is recaptured.

As far as we know, there is no bird tracking system that relies entirely in GSM technology. In this paper we show that it is possible to track birds in this way, taking advantage of GSM services. To this end we have developed a prototype that combines reduced size and weight with extended range, and that was tested on birds. Since the device is capable of transmitting its data, in the form of text messages, there is no need to recapture the bird.

The remaining of this paper is organized as follows. Section II is used to present the location system, which has two main components: the location device and the base station. Section III is used to explain how data can be viewed and interpreted. In Section IV we present the results achieved with the laboratorial tests. After that, some practical considerations are presented at Section V. The results of the tests carried on birds are presented in Section VI. The paper ends with the major conclusions, presented in Section VII.

II. THE LOCATION SYSTEM

The location system comprises two parts: the location device, attached to the animal (bird); and the base station, to

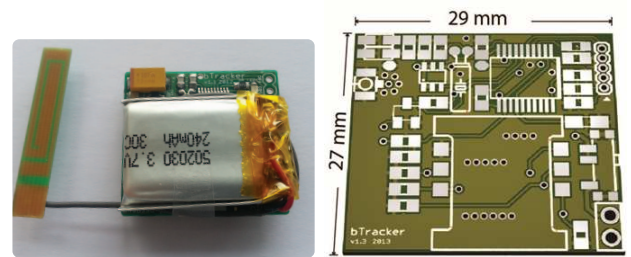


Figure 1. Left—Photo of the prototype with all components; in the PCB underside is just the modem. Right—Top view of the PCB; the lower view contains only the modem connections.

receive the data from the location device.

A. Location device

The prototype uses the following main components:

- **GSM modem**—Allows registration in the GSM cell/network in order to collect the necessary information (in this first phase is also used to send the data for later analysis). We have used a GL865-QUAD Telit modem with the following characteristics:
 - weight: 2.48 g;
 - dimensions: 24.4 × 24.4 × 2.7 mm;
 - connectivity: Quad-band GSM / GPRS stack and Transmission Control Protocol/Internet Protocol (TCP/IP) supported.
- **Antenna**—Print Circuit Board (PCB) antenna with extension and U.FL connector.
- **Micro-controller (MCU)**—The MCU used (PIC24FV32KA301) was chosen considering the energy consumption, size and the presence of certain peripherals. Note, for example:
 - supply voltage: from 2.0 to 5.5 V;
 - Consumption in sleep mode: up to 2.2 μA;
 - 2 UART units;
 - Real Time Clock (RTC).
- **Battery**—The LiPo (Lithium Polymer) technology was chosen due to its weight / capacity relation. As a starting point the battery capacity used was 200 mAh, with an approximate weight of 7 g.
- **Passive Components**—We have used surface-mount technology; surface-mount device, 0805 capacitors and resistors.

We developed a "first" (working) version of the device, which was debugged and improved, both in software and hardware. At the hardware level, the priority was to reduce the weight and dimensions. Figure 1 (left) shows the "second" version, referred to as "bTracker V1.1". To achieve this goal we produced a new design of the circuit with an array of different possible components that reduced the area by 36%, and at the same time reduced thickness from 1.5 mm to 0.5 mm. Some components have been removed or replaced in order to reduce the area and weight, while retaining all the features of the first version. This version weighs about 12 g, with all components and a battery of 180 mAh, and is distributed as follows:

- printed circuit—2 g;

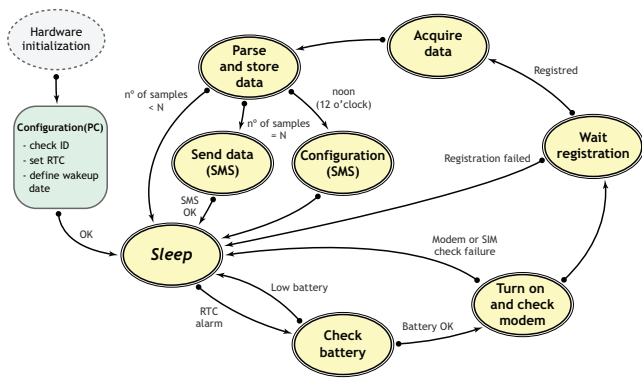


Figure 2. Location device system state diagram.



Figure 3. Photo of the “based device” to receive SMS data and subsequent visualization of the results on the map.

- GSM/GPRS modem—2.5 g;
- battery (180 mAh)—6 g (7 g for a battery of 200 mAh).

Figure 1 (right) shows the appearance and dimensions of the PCB.

At the software/firmware level, the second version represents an improvement in energy consumption, achieved through the reduction of downtime and the use of sleep mode during certain waiting times, leading to a slight reduction in the total energy consumption. We also reduced the clock frequency of the processor from 8Mhz to 2MHz; the consumption difference resulting from this change is presented in Section IV. Figure 2 presents a simplified state diagram of the location device. The complete schematics of the first and second versions of the device can be downloaded from www.mcabral.utad.pt/birds/.

B. Base device

The “base device” is used to receive the SMS sent by the location devices and to forward the messages to a (Java) application that decodes and stores the location data in a MySQL database. It was also used (as an interface card) to test the modem Telit GL865 and the AT commands. It allows commands to be sent directly from the PC to the modem via a terminal. In addition to the modem and SIM card, this base device contains a USB controller (MCP2200, Microchip), which is basically a TTL RS232 to USB converter. A battery, to ensure the 2 A current peaks that the modem used needs (recommended in the datasheet), and a charge controller (MCP73831, Microchip) for LiPo battery technology (charging via the USB port) were also incorporated.

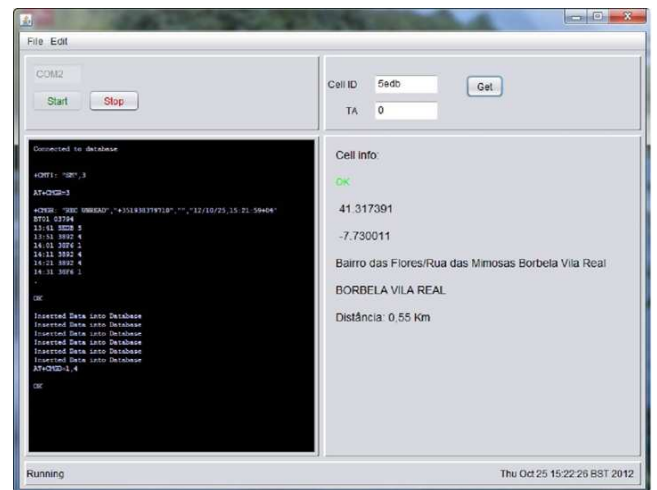


Figure 4. Graphical interface of the Java application responsible for receiving and storing data in the database.

Figure 3 shows a picture of the implemented “base device”, in this case with a 200 mAh LiPo battery. The complete schematic can also be downloaded from www.mcabral.utad.pt/birds/.

At this point a brief description of the application management is in order to help understanding how the base station and location device work together. The application developed for data management performs several tasks. First, it must communicate with the modem via a (virtual) COM port in order to be able to receive SMS and send commands to the modem. After receiving the message, the application identifies the receiver device and sorts out the various fields of the received message. Next, the GSM network cell ID where the location device is linked is searched in the database and the corresponding geographical coordinates, as well as the address where the antenna is located, are retrieved from the database. It is also possible to perform a manual search of a cell ID and retrieve the corresponding data that are stored in a file (Excel). These data are then stored in a database for subsequent online viewing. Figure 4 shows a screenshot of the application.

III. DATA VISUALIZATION

This section explains how the data collected by the devices are presented to the end user.

A. SMS data format

The data collected are sent via SMS. The structure of the SMS is shown in Figure 5 (left).

The message header comprises a unique device identifier (4 characters), followed by the battery voltage in mV. After the header comes the data collected during the operation of the device. To minimise the message size, the date comes first (yy-mm-dd) followed by the complete set of readings on that date. Each line comprises time (hh:mm) followed by the GSM cell ID and Timing Advance. When there is a change in the data collection day a new date is inserted, as can be seen in Figure 5 (left).

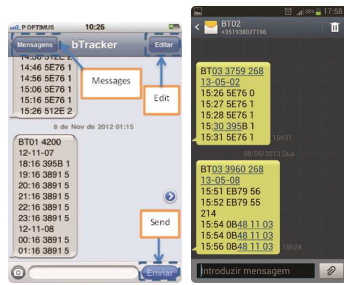


Figure 5. Format of data messages sent by the location device. Left—device identification (BT01), the battery voltage in mV (4200) followed by the date, time, GSM cell ID and Timing Advance (TA). Right—device is in roaming (bottom) and during normal operation (top).



Figure 6. An example of data visualization on map. The bluish circles show the geographical location of the device.

B. View on map

All data received via SMS in the base station are interpreted and stored in the database and can be accessed over the web. The map showing the estimated device location is shown in Figure 6. The bluish circles show the geographical location of the device. As it can be seen, there are bigger circles and smaller circles, showing that the device was further or closer away from the antenna (cell ID). This “distance” is given by the Timing Advance value, and the central values of the circle correspond to the geographical coordinates of the cell ID (antenna).

IV. LABORATORIAL TESTS

The power consumption of the location device is a major concern since it determines the battery capacity, and the battery represents a large fraction of the device weight. We now present results of the energy consumption of the location device in different states and for different tasks. Note that the energy consumption of the base device is not a concern.

The operation of the location device can be divided into three essential states, representing different energy consumptions. All these states are linked by periods when consumption is very low (sleep state), and where a current consumption of less than 20µA was recorded.

A. Device start-up

The first state/task to consider is “start-up” where it is necessary to do some hardware checks and synchronization of the real time clock via the SMS service. Because this task involves sending and receiving SMS, it consumes a significant

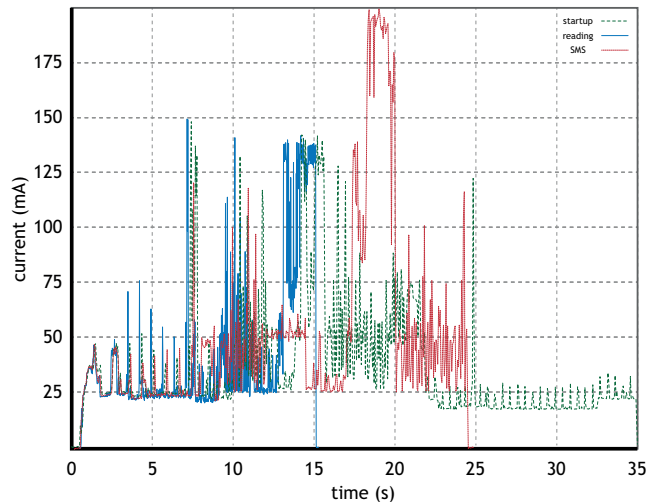


Figure 7. Energy consumption profiles for the three main states: dashed green—boot-up; blue—reading; dotted red—SMS.

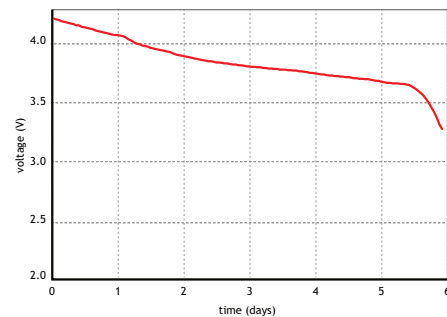


Figure 8. Discharge profile of the 200 mAh battery, for an interval of 10 minutes between acquisitions and every hour uploads (via SMS).

amount of energy. However this is done only once, and its influence on the device’s autonomy is therefore reduced. This profile also includes the first acquisition of the cell ID where the device is connected to. Figure 7 shows the energy consumption profile (dashed green line) for this task.

This state has the following characteristics:

- Average current consumption: 38.8 mA;
- Approximate duration: 36 s;
- Energy consumption: 1.45 mWh;
- Consumed energy fraction (200 mAh battery): 0.195%.

B. GSM cell reading

This state/task directly influences battery life, because it is repeated as a part of the normal operation cycle. The device leaves the state of sleep, does a series of checks, collects the cell information and returns to the state of sleep. The time that the modem needs to log into the network prevents the duration of this task from being shortened. Any change (gain or loss) on energy consumption in this task has a significant influence on the overall battery life and therefore on the frequency with which data can be acquired. Figure 7 shows the energy consumption profile (blue line) for this task.

This state has the following characteristics:

- Average current consumption: 44.2 mA;
- Approximate duration: 15 s;
- Energy consumption: 0.75 mWh;
- Consumed energy fraction (200 mAh battery): 0.101%.

C. Sending SMS

The sending of data via SMS occurs immediately after the “cell reading” task. The extra consumption attributed to the SMS can be calculated as the difference to the previous profile:

- Average current consumption: 51.3 mA;
- Approximate duration: 24 s;
- Energy consumption: 1.38 mWh;
- Consumed energy fraction (200 mAh battery): 0.187%;
- Energy consumption (SMS only): 0.630 mWh;
- Consumed energy fraction (SMS only, 200 mAh battery): 0.085%.

Figure 7 shows the energy consumption profile (dotted red line) for this task.

D. Microcontroller consumption measurements

To obtain a good compromise between performance and power consumption we did a series of consumption measurements, involving only the microcontroller:

- Sleep: 20 μ A;
- 8 MHz: 4.9 mA;
- 4 MHz: 2.8 mA;
- 2 MHz: 1.8 mA;
- 1 MHz: 1.3 mA;
- 500 KHz: 1.0 mA.

The frequency of 2 MHz was selected because it allows a reduced consumption and an acceptable performance.

E. Battery life test

Knowing the energy consumption data it becomes possible to predict, for a given battery capacity, its expected life under various scenarios (depending on the acquisition and data sending frequencies). The quality of the network coverage imposes variations in the power consumption, adding to the difficulty of predicting operating life under real operating conditions. The data to estimate the battery life are:

- Energy consumed at startup: 1.445 mWh;
- Energy consumed by reading: 0.753 mWh;
- Energy consumed by reading SMS: 1.384 mWh;
- Energy consumed by SMS: 0.631 mWh;
- Battery capacity: 200 mAh;
- Battery rated voltage: 3.7V;
- Total energy in the battery: 740 MWh;
- Current consumption in Sleep: 0.02 mA;
- Energy consumption in sleep per day: 1.776 mWh.

For these data, and for intervals between acquisitions of 10 minutes and data uploads every hour (via SMS), we obtain the following:

- Number of acquisitions per day: 144;
- Number of submissions per day: 24;
- Total energy per day: 125.44 mWh;
- Battery: 200 mAh;
- Estimated Duration: 5 days and 20 hours.

The duration (5 days and 20 h) was tested in practice. Figure 8 shows a typical discharge curve for a LiPo battery technology. The test agrees with the predictions. In the last hours the battery condition was already critical, with a cell voltage below 3.5 V.

As another example, imagine that a reading is performed every hour and data is sent every 8 hours (3 times a day). Then,

- Number of acquisitions per day: 24;
- Number of submissions per day: 3;
- Total energy per day: 21.76 mWh;
- Battery: 200 mAh;
- Estimated Duration: 33 days and 23 hours.

V. SOME PRACTICAL CONSIDERATIONS

After encapsulation, the devices are ready to be attached to the birds and cannot be easily turned on or off. To solve this problem we implemented a device configuration schema and a magnetic sensor that allows the device to be started immediately before deploying it.

During the assembly, it is possible to program the starting date and time at which the device starts gathering information. It is also possible to define an operating daily window, e.g., from 11:00 till 20:00. The interval between acquisitions is also configurable with a resolution of one minute. Thus, depending on the particular situation, the device can be switched on immediately after being encapsulated, or a date and time can be set.

A very important feature is the ability to change the operation of the device during its normal operation through a configuration message (SMS). The parameters that can be changed are:

- “Opening hours”—the daily window for location acquisitions;
- “Acquisition interval”—time between each acquisition (in case it is found that the acquisition time is not appropriate to the actual situation);
- “Progress in time”—allows advance in time; for example, with a 20 minute advance the device will sample at 10:20 instead of 10:00.

However, this approach presents the disadvantage of requiring a longer period of activity, so as to ensure that configuration messages are received. This is due to that during normal operation the time that the device is active is not sufficient to receive pending messages. It was then stipulated that every day at 12h00 the device remains active for 40 seconds, the time required to receive pending messages and proceed with the configuration, if this feature is to be used.

Because birds easily cross country borders, at the beginning of each message, immediately after the battery voltage, the country code was added. If the device is in roaming, at the



Figure 9. Left—Photo of devices ready to be used; “encapsulated” using two layers of thermo-contractile sleeve in opposite directions and in between a layer of silicone. Right—Test with cranes; placement of a tracking device.

end of each reading, after the TA field, the network code to which it is connected is also inserted. Only in this way we can determine the device’s location across multiple countries. Figure 5 (right) shows the format of the messages when the device operates in roaming, compared to normal operation.

The device needs to be configured before being encapsulated and placed on the bird. To simplify this task, we have created a simple application that allows editing some important parameters.

The first step is to perform communication with the device so that it returns the parameters that are programmed by default. After that, the device internal clock can be set automatically, using the date and time settings of the PC. If necessary, the device’s ID, the SIM number and the working schedule can be modified. Before leaving the configuration mode, a date and time for the device start-up must be set. After leaving the setup mode, the device stops responding to the application and enters the low-power mode (sleep), to return to the active state only at the scheduled time and date.

In order to adapt the device to the environmental conditions, it is necessary to prevent water and debris from interfering with the electrical circuitry without adding significantly to the final weight. We used thin thermo-contractile plastic film, adding two layers in opposite directions separated by a layer of silicone. Figure 9 (left) shows photos of devices ready to be attached to birds.

VI. TESTS ON BIRDS

We performed three tests with birds in order to evaluate the devices’ performance in real scenarios. Next, we will describe how they were made and the results obtained.

All birds were captured and handled by properly trained and authorised personnel. Two devices were prepared and placed in wild Mallards (*Anas platyrhynchos*) in February 2013. The devices failed soon after the start of the test, probably due to an encapsulation fault and the unforgiving nature of the environment (water). No useful information was collected and we decided to do an experiment with domestic birds, to see if the birds interacted with the device and how the device and the (meanwhile improved) harness and packaging behaved.

The second tests took place in March 2013. The results were positive. Both devices remained fully functional throughout the experiment and sent data as expected. Since the animals were confined to a limited space, there was no variation in position. The devices remained active for two weeks. After recovering them, we found that they were already showing

some signs of water infiltration. This test was important to optimise the harnesses and the packaging.

TABLE I. SUMMARY OF THE LATEST TEST DATA

Device	Date of last SMS	Likely failure cause (Battery level)
BT01	16-07-2013	Battery (3.4 V)
BT02	17-07-2013	credit of the SIM card (3.6 V)
BT03	05-07-2013	credit of the SIM card (3.8 V)
BT04	did not start	Water
BT05	06-07-2013	credit of the SIM card (3.8 V)

The third test began on June 17, 2013. Five devices were placed in Purple Herons *Ardea purpurea*, as seen in Figure 9 (right). Table I shows the date of the last received messages and the possible cause of device failure. As can be seen, one of the devices was damaged by water (possibly as a result of a packaging flaw), in another the battery voltage level suddenly dropped and in the remaining three cases the device did not fail until the budget available for the communications run out. The battery voltage level was still at a level that would have allowed the devices to work as intended. The herons did not leave the nest area during the test.

VII. CONCLUSION

We have presented a prototype of a tracking system that uses only GSM services. The location device transmits messages to a base device, which forwards all received SMS to an application that decodes and stores the location data in a database. The location device, which is the component attached to the bird being tracked, combines reduced size and weight with extended range.

We have presented the energy consumption profiles, the computer applications developed to test it, and the results obtained in practical tests with birds (wild and domestic). The results confirm that GSM-based solutions are entirely capable of tracking, for example, migratory birds.

The accuracy of the system proposed here can be increased using GSM-based triangulation methods, but it cannot match that of GPS-based tracking systems (which are often heavier and more expensive). Light-based geolocators are much smaller and lighter than the GSM-based system proposed, but are much less accurate. Also, as with any data loggers, the data that they collect can be used only if the bird is recovered. With GSM-based tracking, there is no such constraint.

REFERENCES

- [1] C. Minton, K. Gosbell, P. Johns, M. Christie, M. Klaassen, C. Hassell, A. Boyle, R. Jessop, and J. Fox, “Geolocator studies on Ruddy Turnstones *Arenaria interpres* and Greater Sandplovers *Charadrius leschenaultii* in the East Asian-Australasia flyway reveal widely different migration strategies,” *Wader Study Bulletin*, vol. 118, no. 2, 2011, pp. 87–96.
- [2] G. W. Cox, *Bird Migration and Global Change*. Washington: Island Press, 2010.
- [3] I. Newton, *The migration ecology of birds*. Amsterdam: Academic Press, 2008.
- [4] M. Lander, M. Haulena, F. Gulland, and J. Harv, “Implantation of subcutaneous radio transmitters in the harbor seal (*phoca vitulina*),” *Marine Mammal Science*, vol. 21, no. 1, January 2005, pp. 154–161, <http://digitalcommons.unl.edu/cgi/viewcontent.cgi?article=1191&context=usdeptcommercepub>. Accessed: 2015-03-05.
- [5] A. Gavashelishvili and M. J. McGrady, “Radio-satellite Telemetry of a Territorial Bearded Vulture *Gypaetus Barbatus* in the Caucasus,” *Vulture News*, vol. 56, 2007, pp. 4–13.

- [6] R. Wilson, D. Gremillet, J. Syder, M. Kierspel, S. Garthe, H. Weimerskirch, C. Schafer-Neth, J. Scolaro, C. Bost, J. Plotz, and D. Nel, "Remote-sensing systems and seabirds: their use, abuse and potential for measuring marine environmental variables," *Marine Ecology Progress Series*, vol. 228, 2002, pp. 241–261.
- [7] M. Nagy, Z. Akos, D. Biro, and T. Vicsek, "Hierarchical group dynamics in pigeon flocks," *Nature*, vol. 464, no. 7290, Apr 8 2010, pp. 890–U99.
- [8] D. Biro, T. Guilford, G. Dell’Omo, and H. Lipp, "How the viewing of familiar landscapes prior to release allows pigeons to home faster: evidence from GPS tracking," *Journal of Experimental Biology*, vol. 205, no. 24, Dec 2002, pp. 3833–3844.
- [9] H. Broseth and H. Pedersen, "Hunting effort and game vulnerability studies on a small scale: a new technique combining radio-telemetry, GPS and GIS," *Journal of Applied Ecology*, vol. 37, no. 1, Feb 2000, pp. 182–190.
- [10] W. Bouten, E. W. Baaij, J. Shamoun-Baranes, and K. C. J. Camphuysen, "A flexible GPS tracking system for studying bird behaviour at multiple scales," *Journal of Ornithology*, vol. 154, no. 2, Apr 2013, pp. 571–580.
- [11] M. Ledwon and J. Betleja, "Post-breeding migration of Night Herons *Nycticorax nycticorax* tracked by GPS/GSM transmitters," *Journal of Ornithology*, vol. 156, no. 1, Jan 2015, pp. 313–316.
- [12] U. Mellone, J. De La Puente, P. Lopez-Lopez, R. Liminana, A. Bermejo, and V. Urios, "Seasonal differences in migration patterns of a soaring bird in relation to environmental conditions: a multi-scale approach," *Behavioral Ecology and Sociobiology*, vol. 69, no. 1, Jan 2015, pp. 75–82.
- [13] S. M. Tomkiewicz, M. R. Fuller, J. G. Kie, and K. K. Bates, "Global positioning system and associated technologies in animal behaviour and ecological research," *Philosophical Transactions of the Royal Society B-Biological Sciences*, vol. 365, no. 1550, Jul 27 2010, pp. 2163–2176.
- [14] A. M. Fudickar, M. Wikelski, and J. Partecke, "Tracking migratory songbirds: accuracy of light level loggers (geolocators) in forest habitats," *Methods in Ecology and Evolution*, vol. 3, 2012, pp. 47–52.
- [15] P. Ekstrom, "Error measures for template-fit geolocation based on light," *Deep-Sea Research II*, vol. 54, 2007, pp. 392–403.

The Experimental Study of Moving Targets Radio Shadows using GPS Signals

Chr. Kabakchiev
Sofia University
Sofia, Bulgaria
e-mail: ckabakchievr@fmi.uni-sofia.bg

I. Garvanov
ULSIT
Sofia, Bulgaria
e-mail: i.garvanov@unibit.bg

V. Behar
ICT-BAS
Sofia, Bulgaria
e-mail: behar@bas.bg

D. Kabakchieva
UNWE
Sofia, Bulgaria
e-mail: dkabakchieva@unwe.bg

Abstract—This paper focuses on scientific issues related to new application of GPS in radar networks that use the effect of Forward Scattering (FS) of electromagnetic waves to detect and estimate targets on their GPS radio shadows. The aim of the paper is to describe the experimental study of GPS radio shadows of different objects irradiated by GPS signals and to develop a possible algorithm for signal processing of the radio shadows of objects. Registration of FS-GPS radio shadows from moving targets is performed using a small commercial GPS antenna and the stationary receiver. Topology of the experiment meets the requirements for the appearance of the FS effect. The results presented in this article show that from FS-GPS radio shadows of different objects can be extracted information about the parameters of the object including size, speed and direction of movement, distance to the receiver. The information extracted from FS-GPS radio shadows of objects can be used in different applications including radio barriers, security, classification and identification of moving and stationary objects.

Keywords—FS effect; GPS; detection and estimation

I. INTRODUCTION

The main idea is that radio shadows contain valuable information about the objects that can be used to improve the performance of systems with secondary application of wireless technologies. These are FS passive bistatic positioning systems based on radio communication or radio navigation systems, in particular the GPS system. It is normal situation when in conditions of radio shadow of the object these passive radio systems lose the object. When the object is close to the line between the transmitter and the receiver, the receiver loses the reradiated signal from the object (radio shadow). Forward Scatter GPS (FS-GPS) radio shadows formed by different moving objects are investigated in this article. The occurrence of FS radio shadow is the essential physical phenomenon, which can be used to extract some useful information about the objects that generate it.

Forward Scattering Radar operates in the narrow area of the forward scattering effect where the bistatic angle is close to 180° , and the target moves near the transmitter-receiver baseline (Fig. 1) [1]. In forward scatter radar (FSR), the forward scattering effect can be modeled using the Babinet's principle. The Babinet principle says "A plane absorbing

screen of limited dimensions may be replaced by a complementary infinite plane screen with an aperture shaped exactly like the original screen (the complementary screen has openings where the original screen is closed and vice versa. The incident field diffracted at the aperture gives rise to the field coinciding with the shadow field of the original absorbing screen, (except for the sign)".

Due to the forward scattering effect, the Radar Cross Section (RCS) of targets extremely increases (by 2-3 orders) and mainly depends on the target's physical cross section and is independent of the target's surface shape and the absorbing coating on the surface. The use of GPS signals in a passive radar system is very popular as an alternative to traditional radar systems. The idea to apply a GPS L1 receiver to FSR for air target detection is discussed in [2]. Some experimental results of a GPS L1 receiver concerning the detection of air targets are shown and discussed in [3]. A possible algorithm for air target detection in a GPS L5-based FSR system is described in [4], and the detection probability characteristics are calculated in [5] in case of low-flying and poorly maneuverable air targets in the urban interference environment. GPS L1 FSR system for detection of FSR shadows of stationary ground objects is studied in [6][7]. Target detection is indicated if the signal integrated from some satellites exceeds a predetermined threshold.

In this paper, a passive FSR system where GPS satellites are exploited as non-cooperative transmitters is studied. The aim of this study is to verify the possibility to detect FS shadow of moving ground targets when GPS satellites are located at small elevation angles. The experimental scenario includes moving targets and stationary-based FS-GPS system that registers FS shadow of ground moving targets. The experimental results obtained can be used for the design of software applications to a GPS receiver that could measure traffic movement, target velocity and target classification.

The paper is structured as follows. In Section I, the principle of passive Forward Scattering Radar together with its application to FS GPS system is described. In Section II, the description of the experiment with FS GPS system in urban conditions is done. Section III describes the basic stages of signal processing for detection and parameter estimation of moving targets using their FS radio shadows. In Section IV, the

experimental results obtained in result the experiment are discussed.

II. FSR EXPERIMENT DESCRIPTION

The experimental scenario includes targets that are moving into two directions and a stationary-based FS-GPS system that registers FS shadow formed by the moving targets (Figure 1). The GPS receiver is positioned at one side of the road.

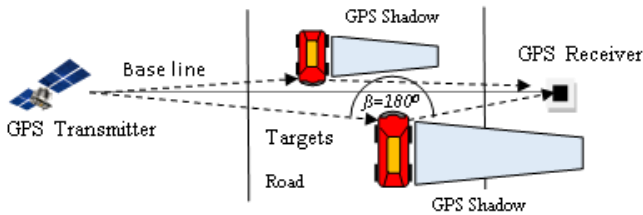


Figure 1. GPS-GSR topology

The purpose of the experiments is to verify that with a small and omnidirectional commercial GPS antenna it is possible to register differences in FS-GPS shadows of moving targets depending on their size and velocity, and also to verify whether the differences in the FS-GPS shadows allows classifying the objects (Figure 2).



Figure 2. Experimental equipment

The paper considers one experimental scenario that includes a stationary-based FS-GPS system that records FS shadows formed by cars moving on the road (Figure 2). During the experiment, the conditions for the occurrence of the FS-GPS effect have been guaranteed. In the experiment, the GPS receiver is positioned from the one side of the road and records the signal from GPS satellites. The signals are recorded from such visible satellites that are located at low elevation angles and when a baseline between satellite and receiver is perpendicular to the road, in order to meet the requirement for the occurrence of the FS effect. During the experiment, the satellite signals are recorded when cars move on the road. The objects passing on the road have different dimensions (cars, vans, buses, trucks, pedestrian etc.). The purpose of these experiments is to check whether the type of the registered FS shadows depends not only on the dimensions of the object, but on the speed of the moving targets as well. The dependence of FS-GPS radio shadows on the size and speed of the marine targets registered by the coastal FSR is firstly shown in [1].

III. SIGNAL PROCESSING

The general block-scheme of a possible algorithm for FS_GPS shadow detection is shown in Figure 3. According to this block-scheme, several visible GPS satellites are acquired and tracked over the complete duration of recorded signals.

Here, we consider the case when the acquisition and tracking algorithms of a GPS receiver are implemented in MATLAB. According to the block-scheme shown in Figure 3, the squared values of the In-phase component at the output of the Code&Carrier tracking block are then filtered by means of the Moving Average Filter with the jumping window. This filter divides the input signal into non-overlapping intervals (jumping windows) of size N milliseconds and calculates the average of samples (integrates) in each interval. This filter not only improves the Signal-to-Noise Ratio (SNR) at the detector input but reduces the number of signal samples as well. Target detection is indicated if the filtered signal exceeds a predetermined threshold H . The Constant False Alarm Rate (CFAR) processor firstly detect single samples and then counts them using a binary nonparametric procedure for detection of sample packages of unknown length, with the decision rule “M/N-L”, in order to estimate their unknown length. The estimated sample package length is proportional to the linear dimension of the target. Next, using the CFAR processor, we use the same approach for estimation of the other target characteristics in the frequency domain. In that way we obtain two important parameters of moving targets – energy and frequency. The obtained target signature can be used for estimation of various target parameters in the time and frequency domains.

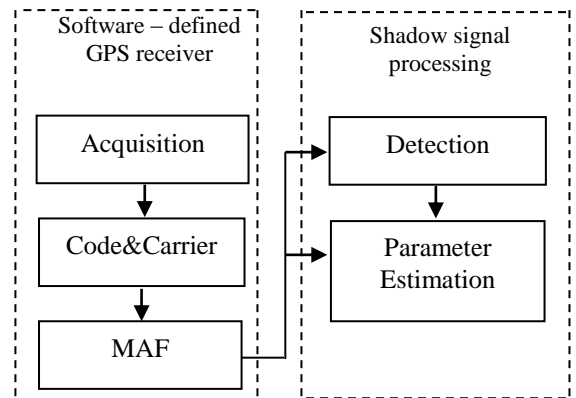


Figure 3. The general block-scheme of signal processing in a FS GPS system

The CFAR processing is a very important procedure, which is very often used especially in real systems, because it allows maintaining the required false alarm rate at the detector output using the adaptive threshold. Next, the extracted target signatures can be used to estimate different target parameters for their classifications.

IV. EXPERIMENTAL RESULTS

The GPS receiver is positioned at the one side of the road, at the height of 1 m from the ground (Figure 2 and Figure 4). The street has four lanes each with the width of 3m, two in one direction. A high building is located on the west of the receiver,

so the GPS receiver receives signals only from the GPS satellites on the east.



Figure 4. Experiment scenario

During the experiment, several cars move at velocity of about 20 - 30 km/h relative to the GPS receiver. The constellation of the visible satellites is shown in Figure 5. It can be seen that during this experiment only four satellites are visible (7, 10, 13 and 28), one of which with the number 13 creates the best conditions for the occurrence of the FS effect.

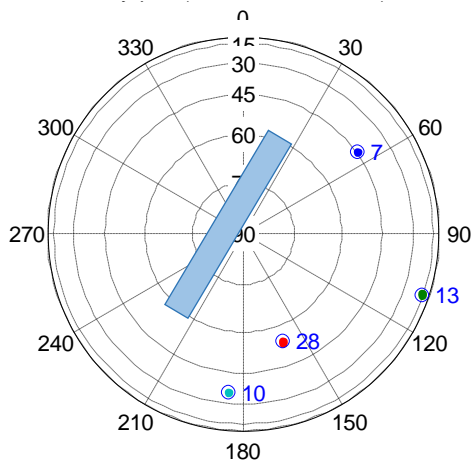


Figure 5. Satellite constellation

This satellite is located most low on the horizon, the bistatic angle between the satellite and receiver is close to 180 degrees, and the car crosses the baseline "satellite - receiver" at the angle of about 90 degrees. The signals from this satellite can be used for detection of the FS-GPS shadow created by targets. The squared in-phase components at the output of the Carrier&Code tracking block are recorded for four satellites (7, 10, 13 and 28) and further filtered by means of the MAF with the moving window of size 200ms. The FS-GPS radio shadows obtained from satellites 7, 10, 13 and 28 are shown in Figure 6. Satellites 7 and 10 are located also low on the horizon, but in their case the car crosses the baseline "satellite-receiver" at an angle different from 90°. These satellites do not meet the requirements for the occurrence of the FS effect. For that reason the signals received from these satellites cannot be used for detection of the FS shadows created by cars. The satellite 28 is located high above the horizon, which worsens the conditions of the occurrence of the FS effect and the FS shadow is small. It is so because the direction of propagation of the signals from the satellite is not orthogonal with respect to the cross section of the vehicle.

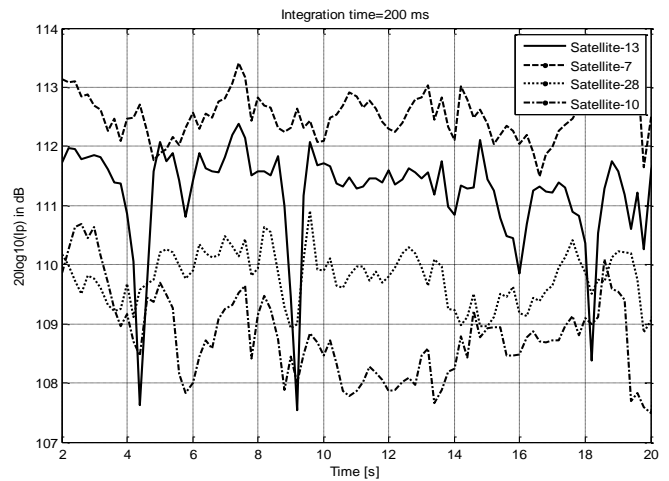


Figure 6. Filtered signals from satellites 7, 10, 13 and 28

The filtered signal from satellite 13 is shown in Fig. 7.

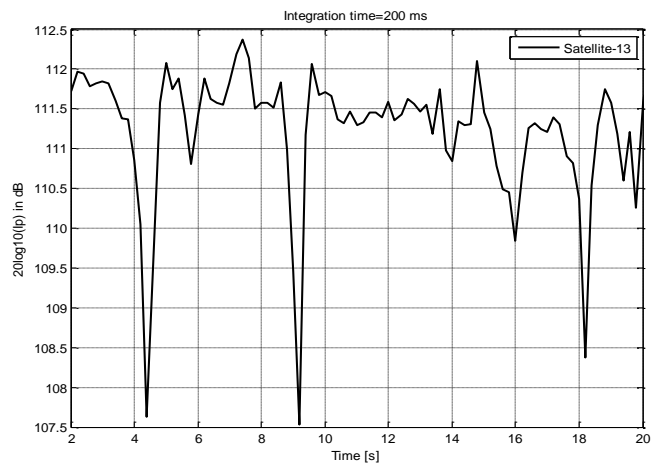


Figure 7. Filtered signal from satellite 7

This figure shows that cars passing near to the receiver have the deepest FS radio shadow (about 8-10 dB). Moreover, the size, the depth and the form of the shadow could serve as information for the development of GPS software applications - for determination of the car velocity and for traffic control. Using the multi-level threshold procedure, it is possible to determine the distance to the vehicle. The shape of the shadow (the first peak) can be used to determine the direction of travel of the vehicle. So, in this way the selection and classification of vehicles can be realized. The parameters of the FS_GPS radio shadow (width and depth) can be used for classification of the type of vehicle. The FS-GPS radio shadows are shown in Figure 8 - for five cars and the van and in Figure 9 - for the car and the bus. Figures 8 and 9 show that the FS-GPS shadow parameters can be used to classify different moving targets. For example, the longer the vehicle, the deeper his radio shadow. The radio shadow width is proportional to the length of the vehicle and his speed of movement. The FS-GPS shadows shown in Figures 8 and 9 are formed by the vehicles moving at almost the same speed of 20-30 km/h.

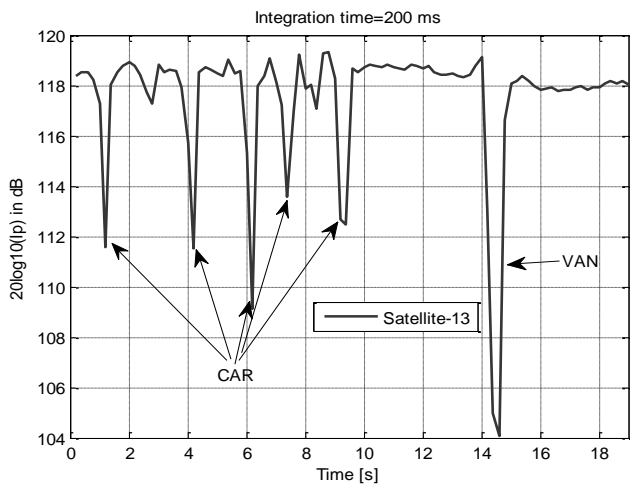


Figure 8. Filtered signals from satellite 13 (five cars and van)

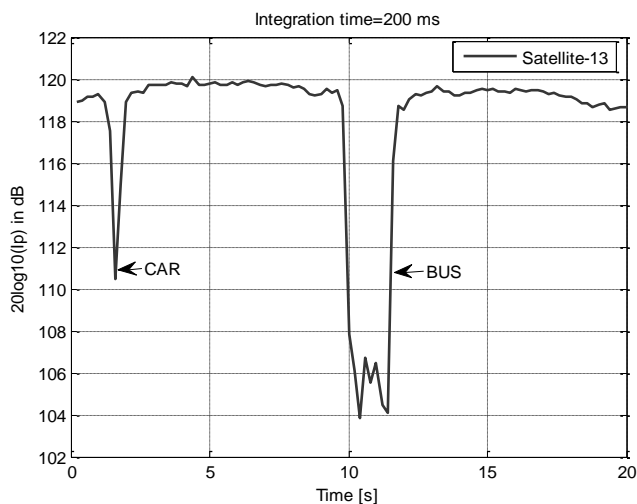


Figure 9. Filtered signals from satellite 13 (car and bus)

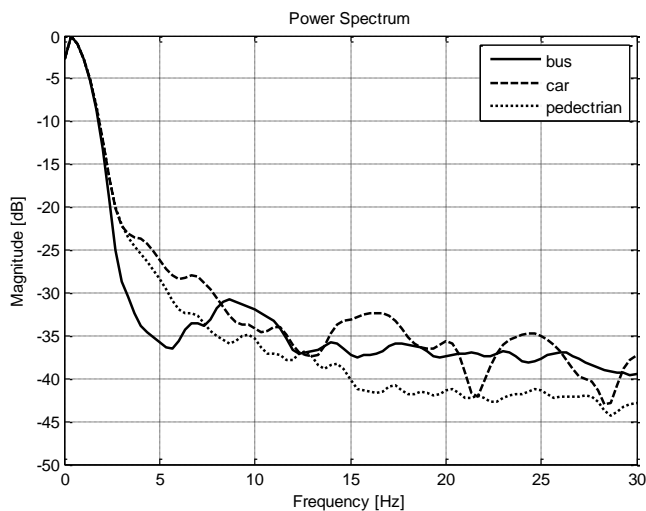


Figure 10. Power spectrum (bus, car and pedestrian)

In this study, it is observed that the FS-GPS shadow depth is proportional to the distance from the object to the receiver. The smaller this distance, the greater the FS-GPS shadow

depth. The greater this distance, the smaller the FS-GPS shadow depth. As mentioned above, the road where the study is realized has four lanes, two in one direction. Figures 8 and 9 also show that the FS-GPS shadow depth in each successive lane of the road is differed by about 2 dB. The length of the car is 4 m, of the van - 6 m, of the bus -12m. Applying the Fast Fourier Transform (FFT) or the Welch method (PWELCH) to the filtered signals from different targets, we obtained the corresponding power spectra (Figure 10). Figure 10 shows that the power spectrum reduces to the level of -40 dB at the frequency of 15 Hz – for the human and at the frequency of 20-30 Hz –for the car and the bus.

V. CONCLUSIONS

It is shown that it is possible to detect different objects on their FS-GPS shadows using a small commercial GPS antenna and the software-defined GPS receiver. Topology of the experiment meets the requirements for the occurrence of the FS effect. This means that the satellite and the GPS receiver are located on the same line, which crosses the object. Experiments show that the FS-GPS shadow can provide information about the object including size, speed, direction of movement, and the distance to the receiver. This information can be extracted from the width, shape and length of the FS-GPS shadows. The occurrence of FS shadow is essential physical phenomenon, which can be used to extract some useful information about the objects that create it. The information obtained can be used in various applications including radar, radio barriers, security, classification and identification of moving and stationary objects.

ACKNOWLEDGMENT

This work is supported by the projects DFNI-T 02/3/2014.

REFERENCES

- [1] M. Cherniakov, (ed.), Bistatic Radar: Principles and Practice, Wiley & Sons, 2007.
- [2] V. Koch, and R. Westphal, "New approach to a multistatic passive radar sensor for air/space defense", IEEE AES Systems Magazine, November 1995, pp. 24-32.
- [3] I. Suberviola, I. Mayordome, and J. Mendizabal, "Experimental results of air target detection with GPS forward scattering radar", IEEE Geoscience and Remote Sensing Letters, vol. 9, no. 1, January 2012, pp.47-51.
- [4] V. Behar and Chr. Kabakchiev, "Detectability of Air Target Detection using Bistatic Radar Based on GPS L5 Signals", Proc. IRS'2011, Leipzig, 2011, pp. 212-217.
- [5] V. Behar, Chr. Kabakchiev, and H. Rohling, "Air Target Detection Using Navigation Receivers Based on GPS L5 Signals", Proc. of ION GNSS, Portland OR, 2011, pp. 333-337.
- [6] Chr. Kabakchiev, I. Garvanov, V. Behar, and H. Rohling, "The Experimental Study of Possibility for Radar Target Detection in FSR Using L1-Based Non-Cooperative Transmitter", Proc. IRS'13, Dresden, Germany, 2013, pp.625-630.
- [7] K. Borre, D. Akos, N. Bertelsen, P. Rinder, and S. Jensen, A Software-Defined GPS and Galileo Receiver: Single-Frequency Approach, Birkhäuser, Boston, MA, 2006.

Synthesis of Amide Functionalized Graphene Oxide for Humidity Sensing Application

(Amide Functionalized Graphene Oxide for Humidity Sensing)

Dinesh Kumar and Sumita Rani

Electronic Science Department, Kurukshetra University

Kurukshetra, Haryana, India

Email dineshelsd2014@gmail.com

Abstract— Amide functionalized graphene oxide (AGO) was synthesized by chemical method at room temperature. Fourier transform infrared spectroscopy, X-ray diffraction and scanning electron microscopy measurements were carried out to verify the functionalization. Thin films of graphene oxide (GO) and AGO were formed by spin coating on SiO₂/p-Si (100) substrate. The variation in the I-V characteristics was recorded at different humidity level. It has been observed that in GO the variation in resistance with humidity is relatively small as compared to AGO. The resistance of the AGO film was approximately 9.87 kΩ at 10% relative humidity (RH), and decreases to 1.5 kΩ at 90% RH.

Keywords- Amide functionalized graphene oxide; relative humidity; I-V characteristics.

I. INTRODUCTION

Humidity plays an important role in every part of the earth processes. To have a desirable surrounding environment, it is necessary to monitor, detect and control the ambient humidity by precise sensors [1]. In today's modern world, there exist various kinds of humidity sensors that have applications in industrial processing and environmental control. Like for fabrication of integrated circuits in semiconductor industry it is essential to monitor moisture levels constantly. In medical field, humidity sensors are essential for respiratory equipment, sterilizers, incubators and biological processing. In agriculture, humidity sensors are used for green-house air-conditioning, plantation protection, soil moisture monitoring, etc. In general, humidity sensors are used for moisture detection by various paper, textile and food processing industries. In modern humidity sensor there is requirement of high sensitivity and wide detection range for fast response and short recovery time to meet industry applications. Thus nanomaterials, such as silicon nanostructures, ceramic nanomaterials, semiconductor nanoparticles and metal oxide are widely used for moisture sensing application due to high surface to volume ratio [2][3].

Graphene oxide (GO) because of its large surface area and electrical properties can be potentially used for ultrasensitive sensor applications [1][3]. As GO has hydroxyl, epoxy and carboxylic acid functional group bonded in two-dimensional network of sp² and sp³ hybridized carbon atoms arranged in a honeycomb structure [2]. The oxygen containing functional groups of GO

enhance hydrophilic properties of it but these groups makes it an insulator by decreasing its conductivity [1][4]. But oxygen functional groups of GO allow fast passage of water within the GO layers [5], which makes fast response of the sensor based on GO. But improving the electrical properties of GO by surface modification via noncovalent or covalent functionalization is a promising way for fabrication of high performance GO-based sensor [6][7]. Already functionalized GO have been successfully used for detection of acetone, hydrogen sulfide, nitrogen dioxide (NO₂), etc [8][9]. Covalent functionalization of GO enhance its physicochemical properties, for instance, isocyanate-treated GO has been exfoliated and form a stable dispersion in polar aprotic solvents [10]. Such functionalization improves the mechanical, electrical, thermal properties [7] and dispersion of functionalization GO in to organic solvents [11].

In view of above observations, heteroaryl/phenyl amine was grafted onto GO sheets by the amide formation between amine functionality of heteroaryl/phenyl amine and oxygen-containing groups (e.g., carboxyl and lactone groups) of GO to give amide functionalized GO (AGO). Section 2, explains the synthesis and amide functionalization of GO. In Section 3, there is discussion about the various characterization of prepared GO and AGO. The effect of surface functionalization on humidity sensing application of GO was also discussed in Section 3. The conclusion of the work is given in Section 4.

II. EXPERIMENTAL

A. Materials

Graphite powder (purity 99.99%), sodium nitrate (99.0%), sulphuric acid, potassium permanganate (99%), hydrogen peroxide, hydrochloric acid, sodium hydroxide (NaOH), hydroxybenzotriazole (HOBt), 2-aminothiazole, N,N'-dicyclohexylcarbodiimide (DCC) were used to prepare GO and AGO.

B. Preparation of GO

Graphite (2 g) and NaNO₃ (1 g) were mixed in cooled concentrated sulphuric acid (46 ml) under stirring in ice bath. KMnO₄ (6 g) was gradually added to the above placed mixture with stirring and cooling so that the temperature of mixture was maintained between 10–15°C [12]. The reaction mixture was then stirred at 40°C for 30 minutes. Subsequently, 80 ml of high purity water was added to the

formed paste, followed by another 90 minutes stirring at 90°C. Successively, to stop the oxidation reaction additional 200 ml water was added. 6 ml of 30% H₂O₂ was added in above mixture sequentially to destroy the excess KMnO₄. The complete removal of KMnO₄ was indicated by color changed to yellow. Sometimes the solution's color was yellow before addition of H₂O₂ which indicated complete reduction of KMnO₄. The solution was then washed with HCl (10%) to remove sulphate. Subsequently, it was filtered and washed several times with DI water. The filtered paste was dissolved in 100 ml DI water. The solution was ultrasonicated for 1 hour and centrifuged for 20 minutes at 4000rpm. GO powder thus obtained was collected and dried at room temperature.

C. Preparation of AGO

The AGO was obtained by condensation of amine group of heteroaryl/phenyl amine with lactone group of GO. AGO was synthesized by dispersing GO (0.3 g) in 30 ml DMF by ultrasonication for 60 minutes at room temperature. Then, NaOH (0.3 g; 7.5 mmol) was added and resulting solution was stirred for 60 minutes at room temperature. Subsequently, 2-aminothiazole (3.1 mmol), HOBt (3.1 mmol) followed by DCC (3.1 mmol) addition to the above reaction mixture and stirred for 24 hours at room temperature. AGO powder collected by centrifugation was added to pure DMF and the resulting suspension was again centrifuged to remove side products. This process was repeated twice with DMF and then with water to remove DMF to give pure AGO. The prepared AGO was dried at 60°C overnight.

D. Characterization

The crystal phase was characterized by X-ray diffraction (XRD) XPERT-PRO diffractometer (45 kV, 40 mA) equipped with a Gionometer PW3050/60 working with Cu K_α radiation of wavelength 1.5406Å in the 2θ range from 5 to 80°. The functional surface group was studied by Perkin Elmer Fourier transform infrared (FTIR) model SPETRUM 65 system. Dried solid samples were mixed with KBr powder and were pelletized before performing the scan from wave number 4000 to 400 cm⁻¹. SEM characterization was carried out by using JSM-6510LV Series Scanning Electron Microscope (SEM) having pre centered W hairpin filament (with continuous auto bias) and equipped with accelerating voltage of 500 V to 30 kV with high magnification of 300,000.

III. RESULTS AND DISCUSSION

The oxygenated GO sheet prepared by the chemical method was treated with NaOH to open the lactone groups (-CO-O-) on the basal plane and convert them into hydroxyl and carboxyl groups. Treatment of resulting reaction mixture with organic amines in the presence of DCC and HOBt leads to the amidation of the carboxyl groups to give AGO. The chemical changes occurring in the GO after treatment with amine can be verified easily by FTIR, XRD, and SEM techniques.

Structural changes of AGO were investigated by comparing the FTIR spectra of GO and AGO (Figure 1). The most characteristic features in the FTIR spectrum of GO was the adsorption bands corresponding to the C=O carbonyl stretching at 1721 cm⁻¹, the stretching bands for C=C bonds at 1591 cm⁻¹, the O-H deformation vibration at 1392 cm⁻¹ and the C-O stretching at 1051 cm⁻¹[13][14]. The FTIR spectra of AGO reveals a new peak at about 1634 cm⁻¹ corresponding to the amide carbonyl (C=O) stretch (amide I) and the peak at about 1585 cm⁻¹ for amide II (C-N in-plane stretching and CHN deformation) [15], which demonstrate that amines has been grafted onto GO as amide bond.

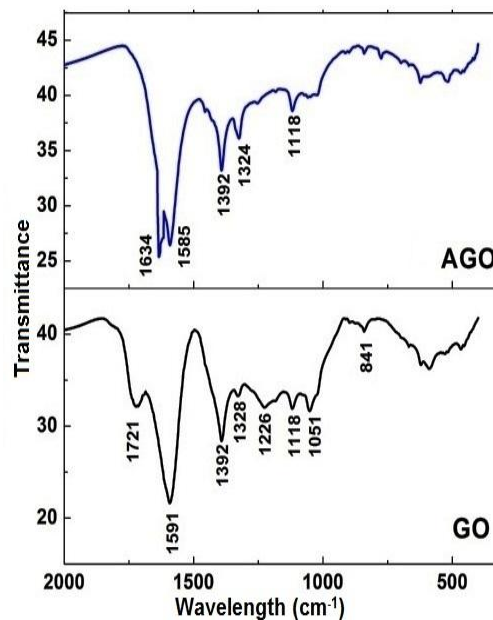


Figure 1. FTIR spectra of GO and AGO

XRD patterns for graphite, GO and AGO are shown in Figure 2. GO shows a diffraction peak at 2θ = 11.42°, which is the characteristic peak of the GO, with increase in interspacing from 0.34 nm (graphite) to 0.77 nm.

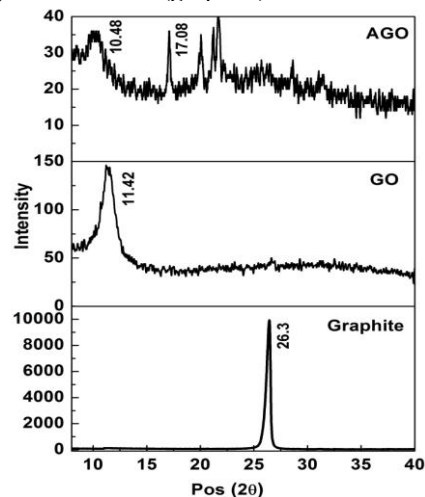


Figure 2. XRD of graphite, GO and AGO

Due to the functionalization of GO the peaks shift to the lower value of angle (2θ) and increase in the interlayer spacing from 0.77 nm (GO) to 0.84 nm for AGO, was observed. The larger value of interlayer spacing suggests the incorporation of additional functionality on the surface of the basal plane of GO. AGO shows peaks at 17.08° , 20.1° and 21.69° correspond to 2-aminothiazole group.

The SEM images represent the surface morphology of the GO and AGO (Figure 3). These images show that the resulting sample of AGO was obviously different from GO. Morphology of GO was observed to have flaky texture indicating its layered microstructure. Different surface morphology of AGO clearly indicates the surface modification of GO after functionalization.

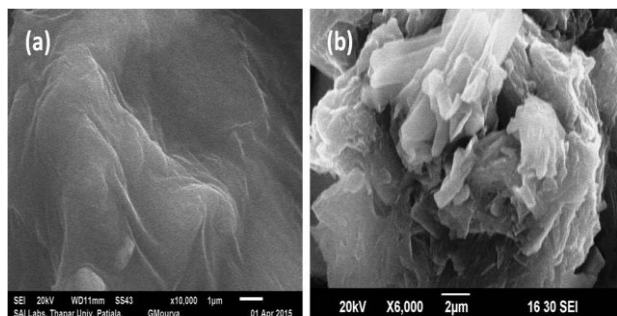


Figure 3. SEM image of GO and AGO

The DC electrical properties, i.e., current–voltage (I-V) characteristics of the GO and AGO films were measured with a voltage sweeping mode at various humidity points. To measure the I-V characteristics one electrode was loaded with the sweeping voltage bias, and the other electrode is grounded. I-V characteristics of GO and AGO films was investigated for 2 to 5 V sweeping voltages at various humidity levels, respectively. The different percentage of humidity level was achieved in sensing chamber by introducing the water vapors.

Figure 4a shows the measured I-V characteristics of GO film in the relative humidity (RH) range of 10% to 90%. From Figure 4a it is clear that the channel current of the GO film increases with increasing RH, indicating that the water adsorption results in a decrease in the resistance of GO films [16]. Water adsorption easily takes place in GO because of presence of large number of oxygen containing functional groups in it. The result revealed that GO is a weak conductor with a continuous water adsorption onto GO films. It is also clear that the current increases with increase in humidity level. At higher humidity (>60%) GO films gives good response.

The sensor resistance (R_s), as a function of humidity is calculated by :

$$R_s = \delta V / \delta I$$

where, δV is incremental voltage and δI is incremental current.

The variation of R_s with humidity is shown in Figure 5. The R_s of the GO film was $0.76 \text{ M}\Omega$ at 10% RH, which decreases to $0.48 \text{ M}\Omega$ at 90% RH. It can be observed from Figure 4b that for AGO, the variation in current is more as

compared to GO. So, AGO is preferred for moisture sensing as compared to GO. The resistance of the AGO film was $9.87 \text{ k}\Omega$ at 10% RH, which decreases to $3.52 \text{ k}\Omega$ at 30% RH. The resistance decrease further with increase in humidity and it become $1.5 \text{ k}\Omega$ at 90% RH. The resistance of film at 90% RH was approximately seven times smaller than that at 10% RH.

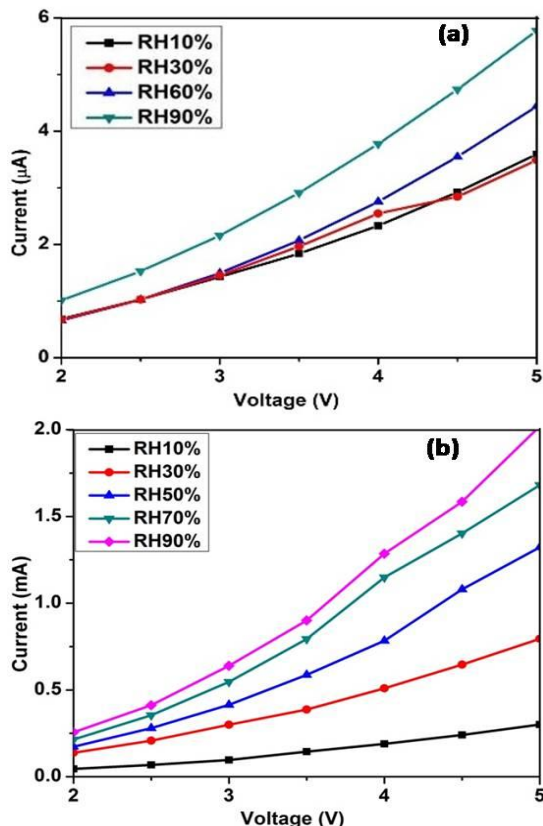


Figure 4. I-V variation in (a) GO and (b) AGO with different humidity from 2V to 5V sweeping voltage

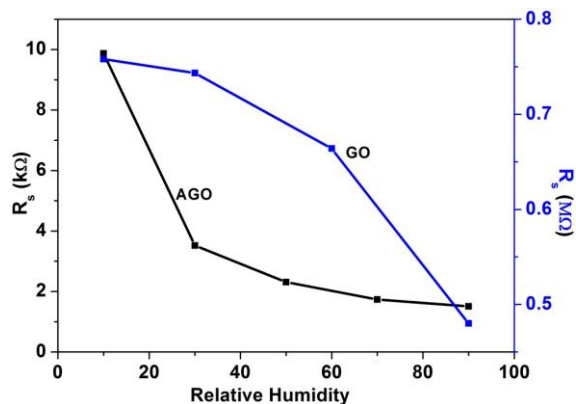


Figure 5. Variation in sensor resistance with humidity

The decrease in the resistance of GO and AGO film can be explained on the basis interaction of water molecules with the film material. At high sweeping voltage, water molecules on the films are ionized and leads to formation of hydrogen ions and hydroxyl ions due to the strong electric

field. The generated hydrogen ions and hydroxyl ions decreases the oxygen containing functional groups of GO and AGO and hence the current increases with humidity. However, in AGO there are less number of oxygen containing groups as compared to GO, so AGO gives better sensitivity. When ambient RH is high, the numbers of adsorbed water molecules are large. As a result, the ionization process generates more hydrogen ions, result in reduction of GO and AGO film. Thereby, AGO exhibits high conductivity at higher applied voltage and at high humidity level.

IV. CONCLUSION

An efficient and easy approach has been used to synthesize the covalent functionalized GO by a simple amidation reaction using 2-aminothiazole. DC measurement method was used to investigate the effect of humidity on the electrical properties of AGO films. Through electrical characterizations, the strong interaction of water molecules with AGO films was observed. The electrical properties of GO and AGO films were affected by humidity and the amplitude of applied voltage. At low RH (<60%), GO films exhibited small variation in current due to the presence of sp³-bonded hybridized carbon atoms and presence of oxygen containing functional groups. AGO shows much better response at lower and higher RH (10% to 90%) indicates its effectiveness as compared to GO. The results are useful for the development of graphene-based sensors.

ACKNOWLEDGMENTS

One of author Sumita Rani is thankful to INSPIRE, Department of Science and Technology (DST), India for funding support.

REFERENCES

[1] S. Borini et al., "Ultrafast Graphene Oxide Humidity Sensors," *ACS Nano*, vol. 7, 2013, pp. 11166–11173.

[2] H. Bi et al., "Ultrahigh humidity sensitivity of graphene oxide," *Sci. Rep.*, doi:10.1038/srep02714, 2013.

[3] U. Mogera, A. A.Sagade, S. J.George, and G. U. Kulkarni, "Ultrafast response humidity sensor using supramolecular nanofibre and its application in monitoring breath humidity and flow," *Sci. Rep.*, doi:10.1038/srep04103, 2014.

[4] I. Jung, D. Dikin, S. Park, W. Cai, S. L. Mielke, and R. S. Ruoff, "Effect of Water Vapor on Electrical Properties of Individual Reduced Graphene Oxide Sheets," *J. Phys. Chem. C*. vol. 112, 2008, pp. 20264–20268.

[5] R. R. Nair, H. A.Wu, P. N. Jayaram, I. V. Grigorieva, and A. K. Geim, "Unimpeded Permeation of Water Through Helium-Leak-Tight Graphene-Based Membranes," *Science*, vol. 335, 2012, pp. 442–444.

[6] C. Marichy et al., "Tin dioxide-carbon heterostructures applied to gas sensing: structure-dependent properties and general sensing mechanism," *J. Phys. Chem.C*, vol. 117, 2013, pp. 19729–19739.

[7] R. Sumita, K. Mukesh, S. Sumit, and K. Dinesh, "Characterization and dispersibility of improved thermally stable amide functionalized graphene oxide," *Material Research Bulletin*, vol. 60, 2014, pp. 143–149.

[8] S. Mao, S. Cui, G. Lu, K. Yu, Z. Wei, and J. Chen, "Tuning gas-sensing properties of reduced graphene oxide using tin oxide nanocrystals," *J. Mater. Chem.*, vol. 22, 2012, pp. 11009–11013.

[9] P. A. Russo, N. Donato, S. G. Leonardi, S. Baek, D. E. Conte, G. Beri, and N. Pinna, "Room-temperature hydrogen sensing with heteronanostructures based on reduced graphene oxide and tin oxide," *Angew. Chem. Int. Ed.*, vol. 51, 2012, pp. 11053–11057.

[10] S. Stankovich, R. D. Piner, S. T. Nguyen, and R. S. Ruoff, "Synthesis and exfoliation of isocyanate-treated graphene oxide nanoplatelets," *Carbon*, vol. 44, 2006, pp. 3342–3347.

[11] E. Fuente, J. A. Menéndez, D. Suárez, and M. A. Montes-Morán, "Basic surface oxides on carbon materials: A global view," *Langmuir*, vol. 19, 2003, pp. 3505–3511.

[12] W. S. Hummers, and R. E. Offeman, "Preparation of Graphitic Oxide," *J. Am. Chem. Soc.*, vol. 80, 1958, pp. 1339.

[13] G. I. Titelman, V. Gelman, S. Bron, R. L. Khalfin, Y. Cohen, and H. Bianco-Peled, "Characteristics and microstructure of aqueous colloidal dispersions of graphite oxide," *Carbon*, vol. 43, 2005, pp. 641–649.

[14] J. I. Paredes, S. Villar-Rodil, A. Martínez-Alonso, and J. M. D. Tasco'n, "Graphene oxide dispersions in organic solvents," *Langmuir*, vol. 24, 2008, pp. 10560–10564.

[15] H. Gunzler, and H. U. Gremlich, "IR spectroscopy," *Winheim: Wiley-VSH*, 2002, pp. 223–227.

[16] H. F. Teoh, Y. Tao, E. S. Tok, G. W. Ho, and C. H. Sow, "Electrical current mediated interconversion between graphene oxide to reduced grapene oxide," *Appl Phys Lett.*, vol. 98, 2011, pp. 173105.

Navigating for Visually Handicapped to Walk Alone with RFID Technologies

Masayoshi Asano

Graduate School of Information Science and Engineering
Ritsumeikan University
1-1-1 Noji-higashi, Kusatsu, Shiga, Japan
Email: asano@de.is.ritsumei.ac.jp

Yusuke Kajiwara, Hiromitsu Shimakawa

College of Information Science and Engineering
Ritsumeikan University
1-1-1 Noji-higashi, Kusatsu, Shiga, Japan
Email: kajiwara@de.is.ritsumei.ac.jp
simakawa@de.is.ritsumei.ac.jp

Abstract—Visually handicapped use their white cane to find obstacles. They follow tactile walking surface indicators to find routes and intersections. They use all sensory organs they can use to acquire the surrounding information. They match the surrounding information with routing information they have, to find their current location and target direction. However, even if tactile walking surface indicators are installed, it is difficult for them to visit unknown places because they have no correct routing information. When they go outside depending on tactile walking surface indicators, they have to follow them. They cannot plan their walking routes for themselves in unknown places. It is impossible for them to walk around various places such as shopping malls and station concourses as sighted persons, which is indispensable to enjoy their daily life. In this work, we propose a method which supports visually handicapped people to visit and walk around in their unknown places. We use RFID technologies to achieve voice navigation with the direction to their destination from their current location and their moving direction. To verify effectiveness of our system, we navigate blindfolded people experimentally. In the experiment, we have confirmed the success rate is 81%

Keywords—RFID; Visually handicapped; Navigation; Sensor;

I. INTRODUCTION

Though people get most of their surrounding information using their eyes, visually handicapped have lost their vision. They cannot spend their life as the same way as sighted persons. In particular, visually handicapped suffer from many difficulties to go out. Tactile walking surface indicators are indispensable for visually handicapped to walk outside. They are paving blocks with uniformly arranged studs. They are "tactile" because they are detectable with feet at walking. They are used to alert visually handicapped of hazards, such as a road cross before moving car traffic or the edge of a drop at subway station platforms. Visually handicapped use not only their feet but also white canes to recognize studs of tactile walking surface indicators. White cane is also used to find the surrounding obstacle. However, tactile walking surface indicators might bring nuisance to people poor at walking such as the elderly and persons on wheelchairs. Because of the nuisance, they not installed all over a town, much less in wide public spaces where many people come and go in various directions. Even if tactile walking surface indicators are installed, it is difficult for visually handicapped to plan their walking courses for themselves. A support method is required for visually handicapped to walk wherever they want like sighted persons.

When visually handicapped go outside, they use all sensory organs which they can use to acquire the surrounding information. To find their current location and target direction, they compare information they acquire with routing information to their destination. However, they do not always have correct routing information in unknown places. Though several methods have been proposed to guide visually handicapped persons[1][2][3], none of them support for them to walk around unknown places. When they go out in unknown places, they have to memorize tactile maps or ask familiar sighted people such as family members or helpers to accompany with them[4]. It is burdensome for them to memorize tactile maps. If they ask familiar people to accompany, it is burdensome for the familiar people to help them. It is necessary to navigate visually handicapped without burden of their familiar people or themselves.

In this work, we propose a navigation method to support visually handicapped persons walking outside like sighted persons even in unknown places which are not covered with tactile walking surface indicators. We guide the visually handicapped, presenting the direction to their destination with voice navigation. We use radio frequency identifier (RFID) technologies to identify the current location and the moving direction of them, from which the direction to their destination is calculated. In the work, a reader is attached on foots to acquire the ID of tags embedded in floors of buildings and roads in outside. Acquired ID of tags allows us to know the exact location, which derives the exact moving direction. To navigate visually handicapped, our system conveys direction to their destination using voice. To verify effectiveness of our system, we have conducted an experimental to navigate blindfolded people. In the experiment, we have confirmed the success rate is 81%.

The following is an outline of the remaining chapters of this paper. Section II summarizes related works to navigate the visually handicapped. Section III proposes a model to navigate the visually handicapped, as well as a method to acquire the current location and the moving direction for the destination.. Section IV. explains an experiment to navigate blindfolded people using the proposed method. We also present results, which are discussed in Section V. Section VI provides the summary of the work.

II. RELATED WORKS

Many navigation systems have been proposed for visually handicapped. To convey information necessary to walk, the

systems have to acquire the current location and the moving direction in a real time manner. A navigation system is proposed to convey surrounding information using RFID technologies[5]. This system installs a reader on a white cane to acquire tags embedded in tactile walking surface indicators. It matches the acquired ID of a tag with a tag map recording the location of all embedded tags in order to the acquire current location and the moving direction. First, visually handicapped specify their destinations using their voice when they use this system. Next, system conveys routes leading to the destinations. They can walk alone using this system. However, this system has some problems, because it installs readers on their white canes. First, increase of the white cane weight enlarges the burden of visually handicapped. Next, searching embedded tags with white cane could cause accidents, because, white canes are also used to detect surrounding obstacles. The visually handicapped have to search embedded tags and surrounding obstacle at the same time, when they use this system. Distracting visually handicapped could cause accidents. Finally, it is difficult for this system to acquire the exact location and the exact moving direction. To plan walking routes, navigation system should acquire the exact location and the exact moving direction in any place in a real time. To achieve it, it is necessary to embed tags in the whole of the floor and roads. If a reader is installed on a white cane, many tags are detected irregularly because the visually handicapped swing it to find surrounding obstacles. Therefore, it is difficult for this system to acquire exact location and the exact moving direction.

Some navigation systems conveys surrounding information using Ultra Wide Band (UWB) technologies[6]. In the systems transmitters are mounted on the ceiling or pillars to transmit current location to users terminals. Terminals which receive signals can recognize the current location and the moving direction anywhere. However, the usage of UWB technologies is limited in Japan. The radio act in Japan constrains the use of UWB system only indoors. Therefore, this system cannot be used in wide public spaces or street in the outdoors.

III. NAVIGATION USING TAG BLOCK

A. Landmark Spot and Navigation Area

In this work, we define a model to allow visually handicapped to walk in a town using flat paving blocks in which tags are embedded. The paving block is studs free to avoid bringing nuisance to poor walkers likely the elderly and people using wheel chairs. It is infeasible to embed tags in all position of a town. We define two kinds of spaces to navigate the visually handicapped in terms of their roles. One is a landmark spot, while the other is a navigation area. To navigate the visually handicapped, we make the best use of them in accordance to purposes of navigation. Figure 1 illustrates Landmark Spots and Navigation Areas. A landmark spot is a space of several meters square to notify the visually handicapped of a town landmark such as a crossroads and a host office. Landmark Spots are settled at surroundings of various landmarks all over the town. The visually handicapped can arrive their destination, traversing one landmark spot to other on the route to the destination. Navigation system acquires the current location and the moving direction of the user in a landmark spot, to convey the direction to the next landmark spot using voice

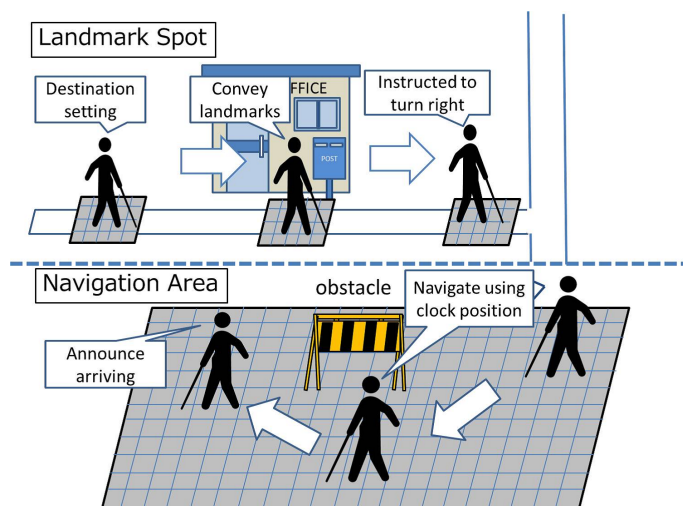


Figure 1. Landmark Spots and Navigation Areas

navigation. Landmark spots are settled, skipping from one to another, to reduce cost. Though it is impossible to navigate the visually handicapped in a fine grade, is effective measures to navigate the visually handicapped according to a specific route, which consists of sidewalks and narrow streets.

On the other hand, in a navigation area, tags are embedded all over it to navigate visually handicapped precisely. A navigation area is effective to navigate them in a shopping mall, the concourse of a big station, and a wide open space like a plaza. The proposed navigation system conveys the direction to their destination in a navigation area. The navigation system acquires the current location and the moving direction of the user in a real time way for the navigation. The navigation system conveys the direction to the destination to the visually handicapped, using a speaker of their handy terminals. The system can navigate them at any position inside the navigation area. Users can avoid obstacles and shorten the path to destination in a navigation area. In this paper, we focus on a navigation area.

B. Navigation method

In this work, we use RFID technologies to achieve voice navigation for the visually handicapped. A navigation system should acquire the current location and the moving direction of the user in a fine grade. To achieve it, we embed tags in flat blocks, while a user wear a reader on user shoes. The detection of tags by the readers attached on shoes allows the navigation system to acquire the current location and the moving direction. The readers attached on shoes also make it possible to use a white cane only for search surrounding obstacle. Compared with the conventional methods[5] [6], our method is safer and more in expensive for the visually handicapped. Figure 2 illustrates the outline of our navigation method. Readers are installed on the tiptoe of shoes, because the tiptoe is touching quite frequently. Tags are embedded in a flat blocks at even intervals like a chessboard. Each tag is associated with a unique number, which is is bound to two-dimensional location information. We refer to this block as a tag block. The navigation system acquires the current location, consulting the location information corresponding to

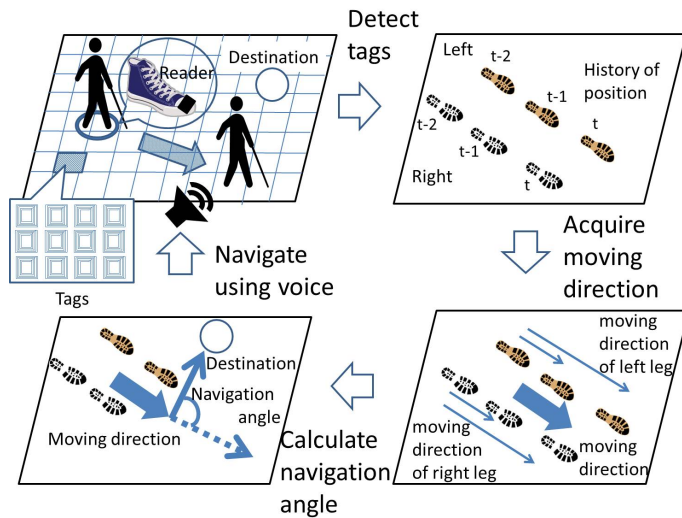


Figure 2. outline of our navigation method

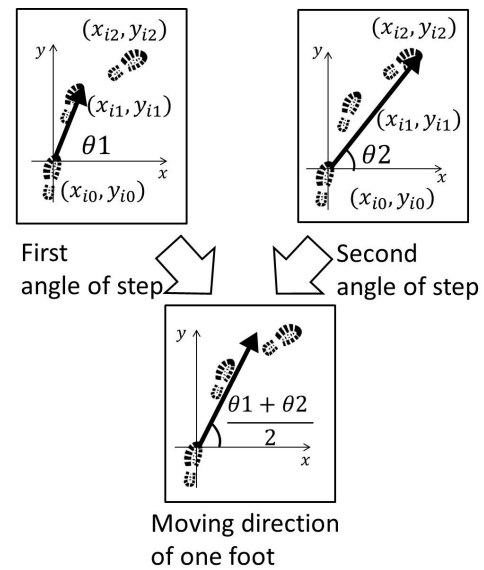


Figure 3. how to derive the angle of the step

the unique number. The position of the both foot is regarded as the location information acquired from the readers attached to the both toes. In each step, the angle from the previous step of one side foot to the current step is calculated to get the current moving direction. It is referred to as the angle of the step. The proposed method calculates it separately left and right. It takes their average of them. The average is the moving direction of the user at that time. The method figures out the difference of the moving direction from the angle to the destination. It is converted to the clock position to convey direction for visually handicapped persons. Clock position is conveyed to the visually handicapped using voice to navigate them. The visually handicapped can understand the direction to destination. The method enables the visually handicapped to walk around like sighted persons.

C. Current location and moving direction

It is important to acquire correctly the current location and the moving direction of a walking visually handicapped person to navigate him. In this work, tags are arranged in a small distance all over the ground to acquire the precise location. A navigation system acquires the current location of the user every step, detecting tags on the ground.

Let $P(X_{in}, Y_{in})$ denote the current location at time point i . Suppose $P_0(X_{i0}, Y_{i0})$ indicates the user location n steps before. The user location at any of these n steps is represented with $P_j(X_{ij}, Y_{ij})$, where $0 \leq j \leq n$. The moving direction of one foot is calculated with (1).

$$\theta_i = \frac{\sum_{j=1}^n \tan^{-1} \left(\frac{x_{ij} - x_{i0}}{y_{ij} - y_{i0}} \right)}{n} \tag{1}$$

Figure 3 illustrates how to derive the angle of the step when $n = 3$. θ_i is derived as follows. $P_0(X_{i0}, Y_{i0})$ is the origin in the calculation of the angle at every step. The navigation system creates coordinate plane at every step. Let P_0 denote the coordinate plane. Its origin is $P_0(X_{i0}, Y_{i0})$. The user stands at $P_j(X_{ij}, Y_{ij})$ after he takes J steps, where $1 \leq j \leq n$.

The navigation system calculates the angle of the vector from P_0 to P_j at every j . It is the angle of the step. Since j varies from 1 to n , n angle values are obtained every i . Each of them corresponds to the angle from the first step(θ_1) to the angle of the n -th step(θ_n). The average from (θ_1) to (θ_n) is the moving direction of one foot at i . The average of the moving direction of both feet is the moving direction of the user at. We define it as (θ_d) . The navigation system calculates (θ_d) every step. Since tags are arranged in a small distance on the ground, a reader detects several tags at one step. It makes an error in the calculation of the moving direction. If a reader detects tags arranging right and left at one step, the navigation system calculate as if the user turns the right or the left. If reader detects tags arranging right and left, the navigation system use only one of them to calculate the moving direction of the user. Let $D(X_g, Y_g)$ denotes the location of the destination. Since the user currently stand at P , the angle of the vector from P to D is the one from the current location to the destination. We refer to it as the destination angle, θ_{ig} , which is calculated using (2).

$$\theta_{ig} = \tan^{-1} \left(\frac{x_g - x_{in}}{y_g - y_{in}} \right) \tag{2}$$

The navigation system derives the navigation angle, θ_t , subtracting θ_d from θ_{ig} . It derives θ_t every step so that it can navigate the visually handicapped in any time.

D. Navigation using clock position

The conveying method is important to navigate the visually handicapped persons. Suppose a visually handicapped person try to reach a specific destination. The destination is not necessarily located in the front of the visually handicapped person. Sometime, it is located in the diagonal right ahead, while it exits in the just left of the visually handicapped person in other time. In an open space like a plaza, it is preferable for him to move to the destination straightforward without any turn. The visually handicapped cannot understand abstract navigation, such as advance the diagonal right ahead.

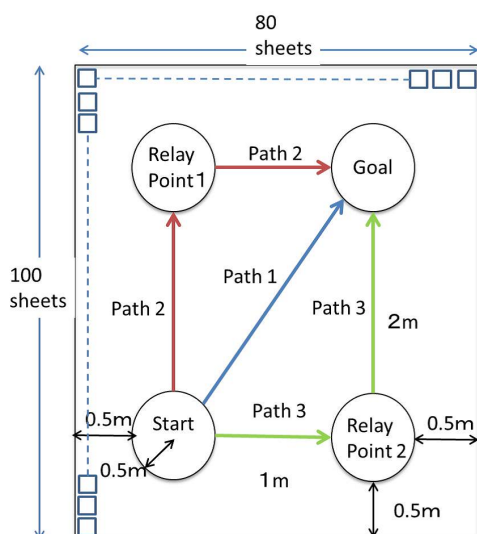


Figure 4. the position of the starting point, goal point and relay points

It is necessary to navigate the visually handicapped using special phrases such as the northeast regarding your front as the north. The clock position is often used by the visually handicapped. In this work, we use the clock position to lead the visually handicapped to their destinations straightforward because we can specify the precise direction with the clock position. The navigation system should convert the navigation angle into the clock position. If the moving direction of a specific visually handicapped person is equal to the destination angle, the navigation angle is equal to 0 degree. In the clock position, 0 degree corresponds to the direction of 12 o'clock. Clock position c is calculated using equations (3) (5), where x is an integer.

$$c = \arg \min_{1 \leq x \leq 12} f(x) \quad (3)$$

$$f(x) = |\theta_l - \theta_x| \quad (4)$$

$$\theta_x = \begin{cases} 30x & \text{if } (1 \leq x \leq 6), \\ -30(12 - x) & \text{if } (6 \leq x \leq 12), \end{cases} \quad (5)$$

IV. EXPERIMENT

A. Experiment environment

We have conducted an experiment to navigate blindfolded people using a navigation system based on the proposed method. We have examined whether the system can navigate blindfolded people from one point to another. We have navigated 13 male and 2 female subjects. Figure 4 illustrates the position of the starting point, the goal point and the two relay points. Before starting, each subject stands at the starting point, facing relay point 1. In this experiment, we prepare three paths as follows.

One of the paths is selected randomly for a subject, to prevent the subject from suspecting the path the subject is following. In this experiment, we have navigated the subjects 15 times in each path. An arrival is regarded as the entrance of a subject within a radius of 50cm from the center of the point. If a subject arrives the goal point using only the navigation system, we regard that the navigation has succeeded. On the contrary, we consider the navigation has failed, if the

navigation is stopped to avoid a danger. The effectiveness of the proposed method is evaluated with the success rate, which is calculated with (6).

$$\text{success rate} = \frac{\text{arriving score}}{15} \quad (6)$$

We have used 5 cm square tags in the experiment. Every tag is installed every 5 cm, being spread over the 4-by-5 meter floor. Tags are covered with a plastic sheet. A reader is attached at the position 5 cm away from the toe of the shoes. In this experiment, the navigation system uses the recent 3 steps to calculate the moving direction of the subject.

B. Results

Figure 5 illustrates the success rate of each subject for every path. The horizontal axis of the graph represents subjects, while the vertical one represents the arriving score. The average of the success rate is 95 %, 80 %, and 68% in path 1, path 2, and in path 3, respectively. The maximum of the success times is 15 in any path. The minimum of the success times is 9, 4, and 3 in path 1, 4 in path 2, and in path 3, respectively. The navigation is highly reliable in path 1, where each of the subjects takes a straight way. However, the navigation is not trustworthy in path 2 and in path 3 where each subject has to take a turn, compared with in path 1.

V. DISCUSSION

It is necessary to improve the success ratio in path 2 and path 3 to navigate the visually handicapped safely. In the experiment, failures mainly attribute to the following three causes.

The first one is misinterpretation of the clock-position by subjects. Failures coming from them are found in all paths. All the subjects are sighted persons, who are unfamiliar with the clock position. They cannot map the clock position specified in navigation messages into the direction to which they should proceed. Because of the failures in the mapping, they have And walked incorrectly, which swerves them from the desired paths.

The second cause is wrong calculation of the navigation angle by the system. The wrong calculation arises in path 2 and path 3. In the experiment, the navigation system calculates the navigation angle uses with the foot location in recent 3 steps, assuming a user walks straightforward during the steps. The calculation gets wrong, if the user changes the direction rapidly during the steps. The moving direction before the change works as the inertia for the calculated moving direction. Actually, a subject turns quickly at the third step in the experiment. At that time, the system calculates a wrong value for the navigation angle, because the first and the second step influence the calculation of the moving direction of the subject. The calculated moving direction is much closer to the one before the rapid turning than the actual one after it. Quick turns of users make the system figure out erroneous values for the navigation direction. To deal with the error, the system should not navigate users when they turns quickly. Rapid turns can be detected from the movement of each foot. We move each foot in turn to take a turn. In the turn, the moving direction of each foot is renewed in turn. When a user walks straightforward, the angle vector from onestep to the

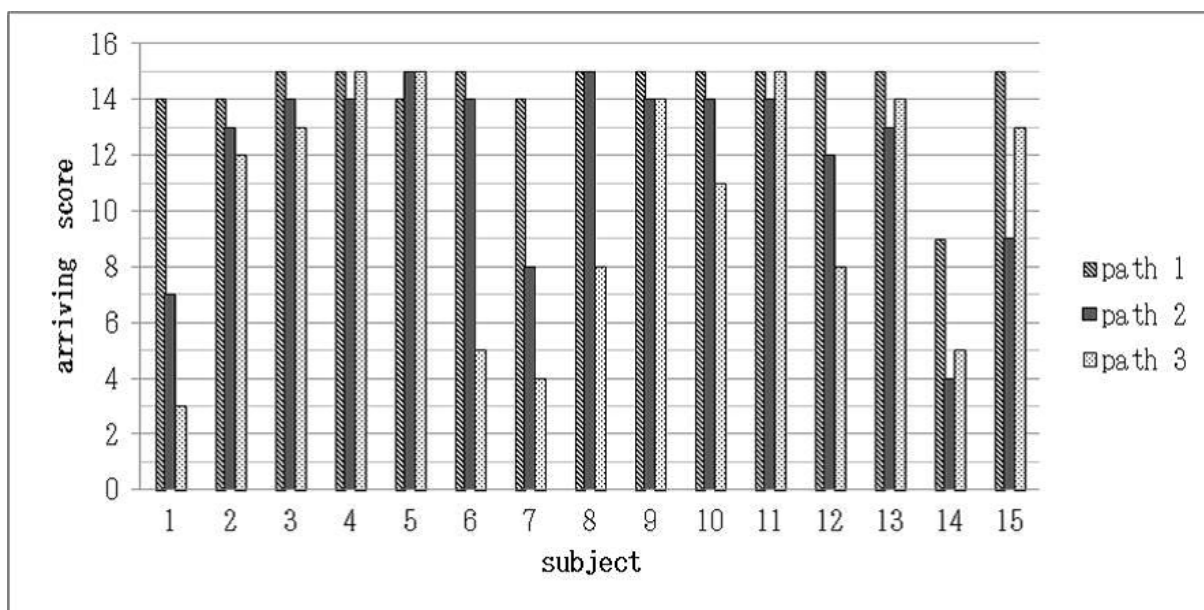


Figure 5. the success rate of each subject for every path

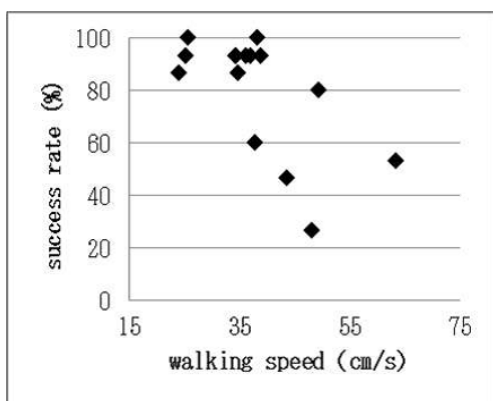


Figure 6. the relationships between the success rate and the walking speed

next of the right foot is close to that of the left foot. On the contrary, the user is considered to take turn, if the vectors differ with each other. In this work, the navigation system averages the vectors of each foot to calculate the moving direction. However, the calculation is valid only when the user walks straightforward. When the vectors of one foot largely differs from that of the other, the navigation system should not issue any navigation message to users to deal with the error in the calculation of the navigation direction.

The final cause is the walking speed of subjects. It takes place in path 2 and 3. In the experiment, the navigation system navigates every 3 seconds. If the walking speed of subjects is fast, the navigation is too late to lead them to desired directions. Figure 5.1 illustrates the relationships between the success rate and the walking speed. The horizontal axis of the scatter diagram is the walking speed, while the vertical axis represents the success rate. The walking speed is negatively correlated with the success rate, where the correlation coefficient is -0.64 . The faster the walking speed,

the lower the success rate. If the walking speed is over 38 cm/sec, the success rate gets worse rapidly. It implies that it is difficult for subjects to turn at relay points, when they are walking the speed over 38 cm/s. To address the problem, the navigation system has to convey voice messages more frequently. However, the visually handicapped persons would get too enormous information to respond properly, if the navigation system conveys voice messages more frequently. The navigation system should change the frequency of the navigation in response to the working speed of users.

VI. CONCLUSION

In this work, we have proposed a navigation method to support the visually handicapped persons walking around like sighted persons in their unknown places. On a landmark spot, the navigation system leads the visually handicapped to proper routes while suppressing cost. In a navigation area, it directly navigates them to the destination with the clock position. The method founds on RFID technologies to get precisely the current location and the moving direction of users. It figures out the navigation direction to their destination from their current location and the moving direction.

To verify effectiveness of the system, we have an experiment to navigate blindfolded people. The average of the success rate in the straightforward path, is 95% ,while that in paths containing turns is 68%. It is necessary to improve the precision to navigate the visually handicapped persons safely routes where they have to turn. The paper has discussed the causes of failures in the navigation to improve the precision. The discussion suggests additional studies to solve issues to improve the precision.

REFERENCES

- [1] V. Kulyukin, C. Gharpure, and J. Nicholson, RoboCart: Toward robot-assisted navigation of grocery stores by the visually impaired, Proceedings. IEEE/RSJ International Conference on Intelligent Robots and Systems, 2005, pp. 2845 - 2850.

- [2] A. Helal, S. E. Moore, and B. Ramachandran, Drishti: an integrated navigation system for visually impaired and disabled, Proceedings. Fifth International Symposium on Wearable Computers, 2001pp. 149 - 156.
- [3] V. Kulyukin, C. Gharpure, J. Nicholson, and S. Pavithran, RFID in robot-assisted indoor navigation for the visually impaired, Proceedings. 2004 IEEE/RSJ International Conference on Intelligent Robots and Systems, (IROS 2004), 2004, pp. 1979 - 1984.
- [4] Syed Rizal Alfam Wan Alwi and Mohamad Noh Ahmad: Survey on Outdoor Navigation System Needs for Blind People, IEEE Student Conference on Research and Development (SCORED),Putrajaya, Malaysia, December 16 -17, 2013, pp. 144 - 148.
- [5] Tatsuya Seto and Kazushige Magatani:A navigation system for the visually impaired using colored navigation lines and RFID tags, IEEE EMBS Minneapolis, Minnesota, USA, September 2-6, 2009, pp. 831 - 834.
- [6] T. H. Riehle,P. Lichter,N. A. , Giudice:An Indoor Navigation System to Support the Visually Impaired, IEEE EMBS Conference Vancouver, British Columbia, Canada, August 20-24, 2008, pp. 4435 - 4438.

Identification of Personal Actions with Brightness Distribution Sensors to Harmonize Domestic Affairs

Nobuaki Takaoka

Graduate school of Information Science and Engineering
Ritsumeikan University
Email: takaoka@de.is.ritsumei.ac.jp

Yusuke Kajiwara, Hiromitsu Shimakawa

College of Information Science and Engineering
Ritsumeikan University
Email: kajiwara@de.is.ritsumei.ac.jp
simakawa@de.is.ritsumei.ac.jp

Abstract—There are many attempts to recognize actions using sensors in homes. Some of them aim to keep watching on the elderly living alone, while others try to bring ecological life, scheduling domestic actions consuming energy. We need an inexpensive method to make it prevail in the society. In the meantime, recognition results threaten privacy, if outsiders obtain them. Almost all people mind whether they are used in malicious ways. The sensor should prevent the leak of the privacy of users. This work proposes a method to recognize various domestic actions with a single kind of sensors, which is not only inexpensive, but also safe enough to protect the privacy. The method uses brightness distribution sensors presenting a sequence of cells, each of which indicates the brightness of one direction in the view area of the sensor. The method gets local features along with the persons who conduct domestic actions. The method enables to recognize both of domestic actions and the period in which they are conducted. To evaluate the accuracy of the method, 10 men and women have participated in an experiment, where they take various domestic actions in their own ways with 4 brightness distribution sensors installed on the wall of an actual kitchen. As a result, the method has marked high performance on the recognition of “vacuuming”, “cooking”, and “taking a rest”, along with their periods. The method also identifies all examinees who conduct them in high accuracy. It is possible to recognize domestic actions in actual home spaces.

Keywords—Domestic action; Brightness distribution sensor.

I. INTRODUCTION

There are many attempts to recognize actions by robots [1], [2], sensing [3] and constructing Internet of Things (IoT) [4] in homes. Among them, recognition of actions by sensors in homes is expected to bring various benefits [5]. It allows us to keep watching of the elderly living alone, as well as to make domestic action schedules reducing energy consumption. In Japan where the ratio of the elderly is increasing rapidly, it is essential to keep watching of the elderly living alone, in order to find fatal accidents and mental decline due to loneliness. Energy saving is also inevitable for people in Japan lacking petroleum production. Inexpensive sensors would realize to keep watching the elderly, even if there are few persons to take care of the elderly. They would also contribute to using electricity efficiently in daily activities. The recognition of actions of each of family members would lead to accommodate the timing of actions of every member so as to minimize the energy consumption, avoiding degradation of the life quality of whole members.

On the other hand, recording of domestic actions has dangers to reveal the privacy of the family members to outsiders. They mind unexpected troubles caused by improper use of the records. Almost all people hate installing sensors which recognize domestic actions from the viewpoint of the privacy.

We need low cost sensors to recognize domestic actions with privacy protection. Nakajima et.al have developed brightness distribution sensors [6] to detect emergencies for the

elderly, protecting their privacy. Using the brightness distribution sensors, this work presents a method to recognize domestic actions. The method identifies domestic actions along with persons who take them. A brightness distribution sensor has a field of vision like a camera. However, instead of a real image of the field, it produces brightness values of the field in one dimension. It protects the privacy because human beings cannot understand the brightness values. Brightness distribution sensors are realized inexpensively, changing lenses of web cameras into rod lenses.

The paper presents the practicability of brightness distribution sensors with the accuracy to recognize each of various daily life actions taken in an actual environment. We have experimented to distinguish 10 persons take various actions in an actual living space. The method has identified both of actors and periods of actions, such as “vacuuming”, “cooking”, and “taking a rest” in high accuracy.

Section 2 presents related works. The proposed method is explained in section 3. Section 4 presents an experiment to verify the effectiveness of the proposed method. In section 5, the paper discusses the experiment results. Section 6 concludes the work.

II. RELATED WORKS

In order to keep watching the elderly, a work presented in [7] has conducted a long term investigation to detect their accidents. Works presented in [8]–[11] utilize ubiquitous sensors to identify domestic actions. The work in [8] recognizes physiological actions, such as sleeping, meal, excreting, and bathing. It detects unusual conditions of the elderly with deviation from usual actions. It costs high for the method presented in [8] to recognize actions, because they use qualified sensors which are specialized to find feature of these actions. The method does not provide ability to generalize actions to be recognized, but recognizes only 4 actions. It also fails to recognize who takes the actions. It does not address the versatility of daily life actions. A visit of a person other than the family members may cause the method to present unexpected outputs. The work explained in [9] is similar to the previous one, because it keeps watching of the elderly, using accelerometers, video cameras, and microphones.

There is also a method to keep watching of the elderly with an integrated platform which manages energy and support for the elderly to live safely and comfortably [10][11]. These method watches the elderly using image data, which a third person can understand.

There are methods to detect domestic actions in smart houses [12]–[15]. Family members can accommodate their energy consumption, following a schedule the method proposes. The methods should not present a schedule which is far from usual daily life [16]. Nakamura et al. proposes the method which integrates data by GPS, smart taps, and laser range

scanners [12]. The method cannot identify who has conducted each of actions, even though it uses several laser range scanners which are expensive. Generally, there are more than family members in a house. The fail of recognition of actors prevents the method to present a schedule acceptable to all members. For example, let us consider a family where a specific person is in charge of house-keeping. If the method cannot recognize actors of actions, it might presents wrong schedule that makes other family members to take care of the house keeping.

There are methods to recognize domestic actions with smart meters which recognize electric power consumption of every electronic appliances[13][14]. There is also a method to recognize domestic actions, measuring energy consumption of each appliance [15]. They cannot recognize domestic actions which do not consume electricity. It cannot provide proper services, due to the lack of the generality.

III. RECOGNITION OF DOMESTIC ACTIONS AND THEIR ACTORS

A. Method overview

In the recognition of domestic actions, we should identify actors of the actions, and the periods in which actors take the actions. Various domestic actions must be recognized with a single kind of sensors to reduce the cost. Since actors are identified, we should provide a method to protect their privacy. The proposed method realizes the recognition with sensors which get brightness distribution. The sensors extract the brightness distribution from original images of target objects. Since it prevents the reconstruction of original images, it protects the privacy.

The method calculates a background difference of the brightness distribution acquired at home. It also calculates a spatial difference and a temporal difference. They include a lot of local features of domestic actions. Base on the Bag-of-Features, the method represents each of brightness distribution data the sensors sample at a specific time as a multi-dimensional vector. Clustering all of the brightness distribution data, the method calculates the centroid of each cluster. The centroids are standards to represent features of all brightness distribution data. For each cell in a specific brightness distribution data, the method searches the cluster nearest to the cell. Voting to the cluster, it constructs a histogram for the brightness distribution data. The features of a domestic action of an actor are represented with the histogram. It is considered features vary with actors and kinds of domestic actions. The shape of histograms is similar with each other when a specific actor takes the same kind of domestic actions. The method constructs a classifier to detect domestic actions and their actors from the shape of histograms. Actors take their domestic actions anytime. The method constructs histograms periodically to recognize domestic actions and their actors.

Figure 1 shows the overview of the method to periodically recognize domestic actions and their actors. Taking the average of the brightness vertically, brightness distribution sensors put out brightness distribution data which consist of an array of cells as many as the number of horizontal pixels of original images. The method installs brightness distribution sensors at home. It gets brightness distribution data of a background image at a situation which contains no target person or target object. The method also gets a time series of brightness distribution data at a situation where a specific actor is conducting each domestic action. The method calculates the background difference, subtracting the brightness distribution data at the domestic action from that of the background image. The background difference expresses values which change when the brightness distribution sensor captures persons and objects different from the background image are captured. We address

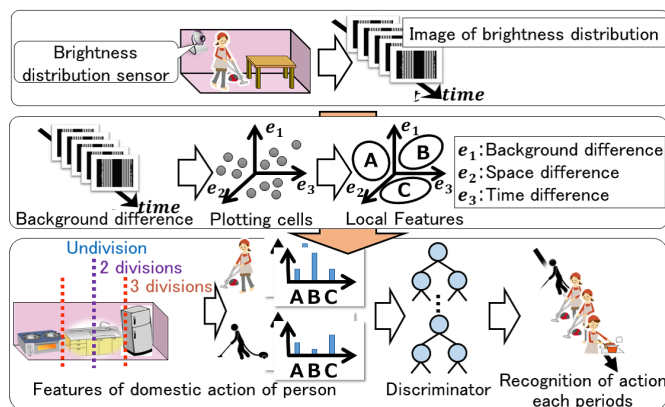


Figure 1. Method overview

three kinds of local elements corresponds to the appearance, the shape, and the motion from the background difference. The appearance is the background difference itself, the difference of the brightness of reflecting light of a target from that of the background. The shape is expressed with the spatial difference of the background difference. It is variation of the brightness of reflecting light affected by the shape of a target. The motion is expressed with the temporal difference of the background difference. The motion is the brightness variation of reflecting light affected by the motion of a target.

The method plots all cells of a time series of brightness distribution data in three dimension space whose axes are three local elements: the background difference, the position difference, and the time difference. The method classifies all cells in the three dimension space into clusters. The centroid of each cluster is the representative value of the cluster. On the basis of the centroids, the method recognizes features of a time series of brightness distribution data. Note that each centroid is also represented with a three dimension vector whose elements are the background difference, the position difference, and the time difference. For example, suppose the background difference and the position difference are 0 while the time difference is 10 in the centroid of a cluster. The cluster represents a feature pattern of motion. The method assigns the vector of each cell to the cluster whose centroid is nearest from the vector. Let us consider chronological brightness distribution data in a domestic action of a specific person. The method constructs a histogram which expresses the number of vectors in a time series of brightness distribution data. The shape of the histograms shows features of the domestic action of the person.

The method also considers where the person takes the action in the viewing field of the brightness distribution sensor. It divides an array of cells from a brightness distribution sensor into two and three parts in each period. It also constructs histograms from the divided cells. The method takes various histograms to construct a discriminator of actions and their actors with the Random Forest. The method gives histograms which are constructed with newly data of chronological brightness distribution into the discriminator. Providing a new time series of brightness distribution data for the discriminator, the method recognizes domestic actions along with their actors.

B. Brightness distribution sensor

The brightness distribution represents how brightness values distribute in an image of a target object. Suppose an image of a target represented with a matrix, like one taken with a Web camera. The brightness distribution is represented with an array of cells, each of which expresses the average

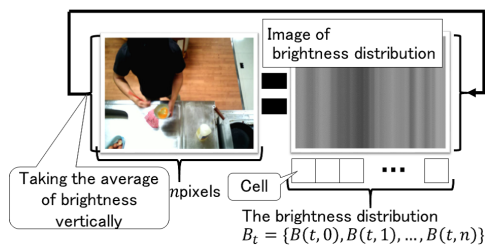


Figure 2. A brightness distribution sensor

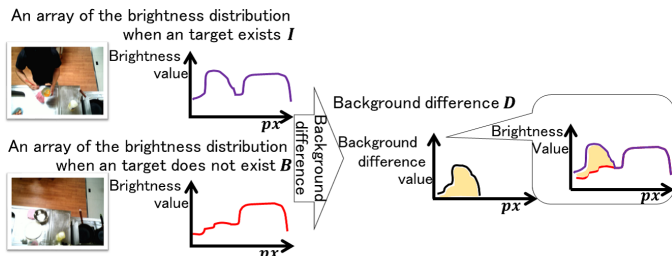


Figure 3. Background difference

of the brightness of the column corresponding to the cell. The result is an array of the brightness which spreads in the row direction. A brightness distribution sensor realizes the calculation optically, condensing vertical brightness with a rod lens [6]. Figure 2 shows information acquired with a brightness distribution sensor. Let n be the number of pixels in the row direction of the sensor. The brightness distribution at time point t , B_t , is formula (1) where $B(t, p)$ is the brightness of the p -th cell.

$$B_t = B(t, 0), B(t, 1), \dots, B(t, n) \quad (1)$$

A brightness distribution sensor has three advantages in the recognition of domestic actions. First, a brightness distribution sensor covers a large angle in a room to recognize various domestic actions. It is programmable so as to recognize various actions with brightness features. It reduces the number of sensors required to recognize domestic actions. The sensor has high versatility to recognize domestic actions. Second, a brightness distribution sensor protects privacy. Since the brightness values are averaged optically for every cell, the third person cannot reconstruct an image of an actor taking a specific domestic action. Third, a brightness distribution sensor is inexpensive. We can implement a brightness distribution sensor, exchanging lenses of a web camera into a rod lenses. Utilizing the CMOS sensor of the web camera, we can make an inexpensive brightness distribution sensor.

C. Background difference

Figure 3 shows how to calculate the background difference. Let I and B are an array of the brightness distribution when an target exists, and that when the target does not exist, respectively. The background difference, D , is the difference of I from B . The recognition of domestic actions should not be affected by a background, such as the wall texture in a room. However, brightness distribution data contains both of moving objects and the background. Since background difference D contains no background information, it contributes to more precise recognition of domestic actions. Like the brightness distribution, background difference D is formula (2) where $D(t, p)$ is the background difference value of the p -th cell at time point t .

$$D_t = D(t, 0), D(t, 1), \dots, D(t, n) \quad (2)$$

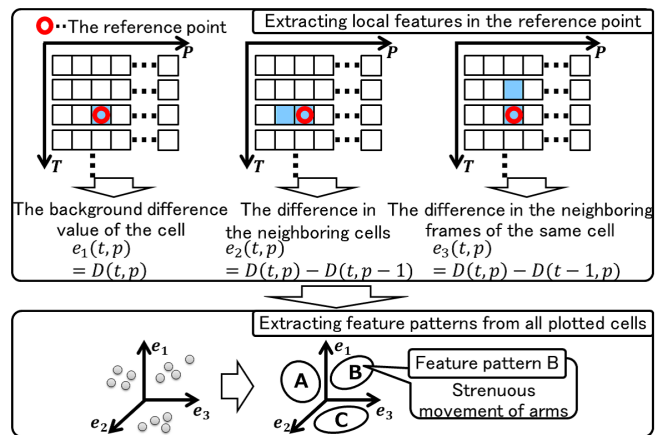


Figure 4. Extracting feature patterns from local elements

D. Extraction of feature patterns with local elements

Figure 4 shows how to extract feature patterns from local elements. Let $D(t, p)$ is the background difference of the p -th cell in the t -th frame of the chronological brightness distribution data recording a specific domestic action. For the cell, the method calculates three local elements: $e_1(t, p)$, $e_2(t, p)$, and $e_3(t, p)$. The first element, $e_1(t, p)$, is the background difference, which is given with (3).

$$e_1(t, p) = D(t, p) \quad (3)$$

It considers only the target, excluding the background, to show the appearance of the target. The second element is obtained with (4).

$$e_2(t, p) = D(t, p) - D(t, p - 1) \quad (4)$$

$e_2(t, p)$ is the difference of the background difference value of the cell from the neighbor one. It corresponds to the spatial difference of the background difference value. Since the equation figures out the brightness difference in the neighboring cells, it contributes to recognizing the shadow of a target to show its shape. The third element is calculated with (5).

$$e_3(t, p) = D(t, p) - D(t - 1, p) \quad (5)$$

Since $e_3(t, p)$ is the brightness difference in the neighboring frames of the same cell, it is the time difference of the brightness to recognize motion of the target. The method performs clustering vectors consisting of the 3 local elements. It regards the centroid vector of each cluster as a feature pattern. Feature patterns allow us to represent motion of the target in various domestic actions. For example, in vacuuming, many cells would show a feature pattern of strenuous movement of arms. The method classifies all cells in the three dimension space with the k-means.

E. Histograms for location

Figure 5 shows how to calculate histograms which show a feature of domestic actions. For example, an actor proceeds vacuuming along a path the actor determines. The path varies with each actor. In addition, rules to determine paths are qualitative and ambiguous. For example, one actor might have a rule to proceed vacuuming around the table clockwise. We should recognize where each feature pattern appears to distinguish actors. The method divides each frame into two and three parts. Combined with the original one, the method gets in total 6 time series of brightness distribution data. For each cell in the 6 time series, the method finds the nearest cluster. The method constructs histograms for each time series. Histograms constructed from the 6 time series

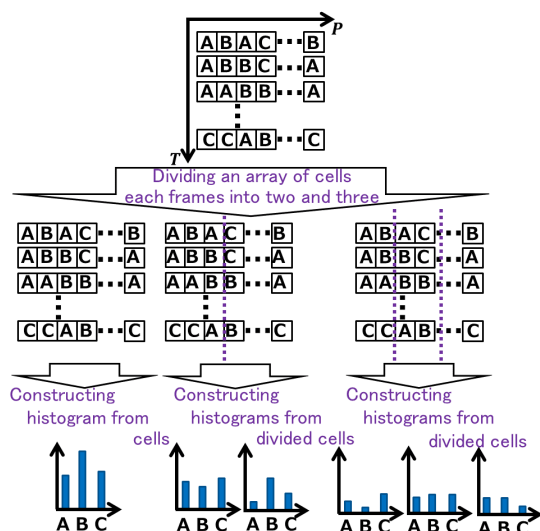


Figure 5. Calculation of histograms

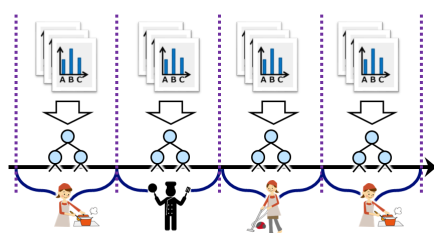


Figure 6. Division of a time series of brightness distribution data

represents features of brightness distribution data. The features include the location where the actor takes the action, such as person X proceeding vacuuming around the table clockwise. Since each actor seems to have his own rule to conduct a specific domestic action, the histograms presents features of domestic actions of a specific actor.

F. Recognition of time series

The proposed method divides a whole time series of the brightness distribution data into several parts. To detect when an actor takes a specific action, it is necessary to recognize domestic actions along with their actors in each part. When an action is recognized, it is not preferable for several actions to be taken in a single time series of brightness distribution data. However, since the timing of each domestic action depends on its actor, it is difficult to find the switching of one domestic action to another. A single time series of brightness distribution data can contain several domestic actions. As shown in Figure 6, the method sequentially recognizes domestic actions for every time series of fixed length, without the consideration of switching of domestic actions. Instead of the considering any switching of domestic actions, the method identifies the domestic action conducted for the longest time in a given duration. It regards the domestic action as the one representing the duration. The method constructs histograms sequentially for every duration of a fixed length. It gives the histograms to a discriminator based on the Random Forest. Through the process, the method recognizes domestic actions, their actors, and the periods in which the actors conduct the domestic actions.

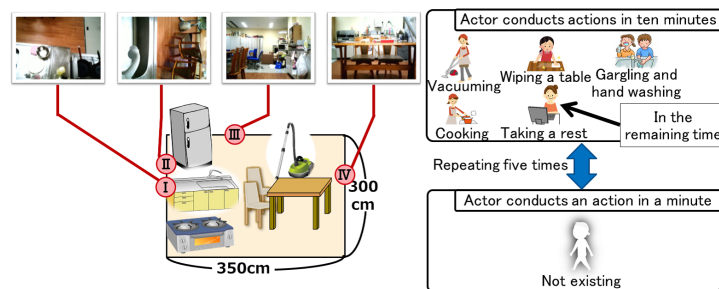


Figure 7. Living space and domestic actions

IV. AN EXPERIMENT IN LIVING SPACE

A. Outline of experiment

We have evaluated the proposed method to identify the actor, the period, and the kind of domestic action conducted in a living space. We validate identification accuracy of the method. Subjects are ten males and females who are all twenties. Each subject conducts domestic actions one by one in the living space. Figure 7 shows a sketch of a living space with a kitchen on floorings, where domestic actions are taken place in the experiment. We install four brightness distribution sensors so that their visual fields covers whole of the living space. Target domestic actions in the experiment should be ones which frequently happen in any living space. We adopt “vacuuming”, “wiping a table”, “cooking”, “gargling and hand washing”, and “taking a rest” as target domestic actions, in addition to “none”, which means there is nobody. The “vacuuming” action is a domestic action that a subject vacuums the floorings. A subject might vacuum under the tables and chairs, moving them. The “wiping a table” is a domestic action that a subject wipes the table with a wet towel placed on the sink. A subject might wipe under objects on the table, moving the objects. The “cooking” is a domestic action in which a subject takes an egg from the refrigerator, stirs the egg inside a bowl, fries the egg with salad oil with a frying pan, serves it on a plate, and washes all the cooking utensils. The cook utensils in the experiment are a bowl, a chopsticks, and a frying pan. Ingredients in the experiment are eggs and salad oil. The “gargling and hand washing” is a domestic action in which a subject washes his own hands with soap and gargles with water in the sink. The “gargling and hand washing” has a peculiar vertical motion in front of the sink. We install sensor B in the sideway at the sink so that it is rotated by ninety degree from the gravity direction. The “taking a rest” is a domestic action in which a subject spends time freely within the visual field of the brightness distribution sensors. It varies with each subject. The “none” is a state in which no subject stays in visual field. We use a brightness distribution data of the “none” to examine the rate of wrong detection of domestic actions. Every subject conducts the 4 kinds of domestic actions within 10 minutes. If they finish them earlier, they can spend the remaining time with the “taking a rest” action. We do not give subjects more specific directions for each kind of domestic actions. We do not specify the time length and the order of domestic actions. Brightness distribution data vary with each subject. We examine the identification accuracy of domestic actions varying with subjects. After the ten minutes, subjects take a rest for one minute outside the visual fields of the brightness distribution sensors. The rest is treated as a “none” state. Every subject repeats the above five times.

B. Evaluation method

We evaluate the ability of the proposed method in terms of identification of kinds and actors of domestic actions. We take a video of all domestic actions. We divide the video data into

slots, which of which lasts twenty seconds. We label every slot with a pair of an actor and a domestic action the actor conducts longest in the slot. Since the “none” has no actor, we do not label any “none” slot. The method divides a set of brightness distribution data from the four brightness distribution sensors into periods. Each of the period lasts 20 seconds synchronized with the video data. The method constructs histograms for each period, according to the way explained in section 3. In the experiment, the number of clusters in the k-means method is 25. Because of the synchronization, each period is associated with a pair of histograms and a label. A discriminator is trained, taking histograms and labels as explanatory variables and response variables, respectively. We use the cross validation to verify the discriminator. In the cross validation, one pair of histograms and a label is used as a test data, while the remaining pairs are used as instruction data. We verify the identification ability of actors by the recall, the precision, and the F measure. Let us consider periods where a specific actor takes a specified action. The recall is the rate of the correctly detected periods out of the periods the actor actually takes the action. The precision is the rate of the correctly detected periods out of all detected periods. The F measure is the harmonic mean of the precision and the recall. The identification ability of domestic actions is also evaluated with the recall, the precision, and the F measure.

C. Result of experiment

TABLE I. IDENTIFICATION OF DOMESTIC ACTIONS

	Precision	Recall	F-measure
not existing	0.782	0.933	0.851
vacuuming	0.743	0.759	0.751
wiping a table	0.605	0.267	0.371
cooking	0.854	0.943	0.897
gargling and hand washing	0.855	0.355	0.461
taking a rest	0.806	0.709	0.754

Table I shows the result of the identification of domestic actions. Domestic actions with the high accuracy are the “vacuuming”, the “cooking”, and the “taking a rest” action, as well as the “none” state. On the contrary, the bad accuracy is found for the “wiping a table” and the “gargling and hand washing” actions.

TABLE II. THE RESULT OF IDENTIFICATION OF ACTORS.

	Precision	Recall	F-measure
actor A	0.770	0.765	0.768
actor B	0.824	0.801	0.813
actor C	0.781	0.791	0.786
actor D	0.877	0.839	0.857
actor E	0.894	0.900	0.897
actor F	0.785	0.780	0.783
actor G	0.852	0.789	0.819
actor H	0.758	0.763	0.760
actor I	0.726	0.558	0.631
actor J	0.793	0.793	0.793

The result of identification of actors is presented in Table II. The accuracy is fairly high for every actor. The results indicate the proposed method recognizes an actor and the period when the actor conducts the “vacuuming”, the “cooking”, and the “taking a rest” actions in the experiment.

The 6 kinds of domestic actions are divided into 2 groups: the “high accuracy” group and the “low accuracy” group in order to examine what conditions cause misidentification. The “high accuracy” group contains actions identified with high accuracy, while the “low accuracy” one consists of actions with low identification accuracy. As shown in Table I, the “high accuracy” group includes the “vacuuming”, the “cooking”, and the “taking a rest” actions, along with the “none” state.

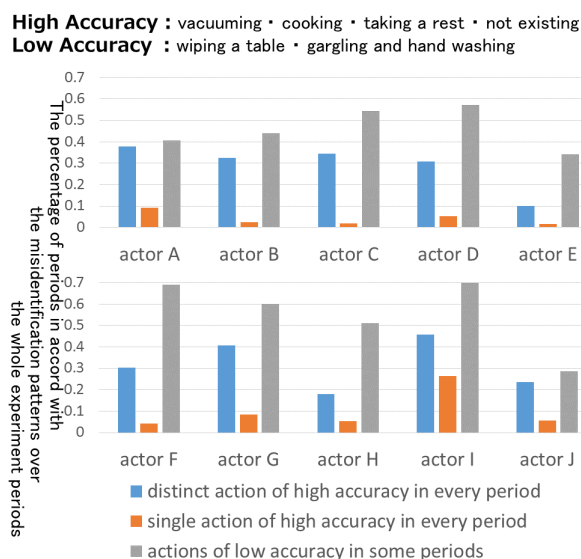


Figure 8. Comparison of misidentification patterns

The “wiping a table” and the “gargling and hand washing” are listed in the “low accuracy” group.

Some actions are identified with high accuracy, while others with low accuracy. Even if the actions of good accuracy take place, the recognition accuracy might get lower in periods where domestic actions switch or periods whose adjacent periods contain domestic actions of low accuracy. We examine how misidentified periods affect the identification ability of the method. We consider the following three patterns for sequential three periods, to see their effects on misidentification.

- 1) An actor conducts distinct domestic actions of high accuracy in each of the period, which is labeled with “distinct action of high accuracy in every period”.
- 2) An actor conducts a single domestic action of high accuracy in all of the three periods, which is labeled with “single action of high accuracy in every period”.
- 3) An actor conducts domestic actions of low accuracy in any of the three periods, which is labeled with “actions of low accuracy in some periods”.

We examine how many times these patterns appear in misidentified periods. We consider what condition makes the method misidentify frequently.

The three patterns are labeled in Figure 8. Neither of the first and the second contains domestic action of low accuracy. In the first and the third pattern, domestic actions are switched. The Figure 8 shows the percentages of periods in accord with the misidentification patterns over the whole experiment periods for every actor. As the result, common to all actors, the patterns are arranged as “actions of low accuracy in some periods”, “distinct action of high accuracy in every period”, and “single action of high accuracy in every period”, in the descending order of their frequency.

V. DISCUSSION

First, we address reasons for the low accuracy for some actions. The “wiping a table” and the “gargling and hand washing” actions are shorter than other domestic actions in their length. In addition to that, hands move in front of a body in the actions. The method fails to extract feature of hands by the background difference. Since those action resemble with each other, the method fails to identify them.

On the contrary, we have expected low accuracy while actors are “taking a rest”, because they can take any action during the period. However, the time prepared for the experiment is so short that actors cannot afford to enjoy their own free behavior when they finish all specified actions. They take similar behavior while “taking a rest”. The method gets an unexpected high accuracy to identify the “taking a rest” actions, even though there is no constraint for their behavior.

For all actors, the method gets the low accuracy of identification in the period where actions are switched or actions of low accuracy are taken place in adjacent periods. Note that we aim to identify the length of a specific domestic action, which contributes to monitoring the elderly and scheduling actions to save energy. To accomplish the aim, the misidentification in the switching of domestic actions brings less harmful impacts than that during a single domestic action. If we consider only domestic actions of high accuracy, we can expect more proper recognition of their period.

VI. CONCLUSION

In this paper, we propose the identification method of domestic actions, along with their actors, and period. The method recognizes domestic actions with brightness distribution sensors. The recognition repeated in a fixed period allows to identify actors conducting domestic actions independent from the timing the actors take the domestic actions.

The method identifies actors and the period of the “vacuuming”, the “cooking”, the “taking a rest” actions in high accuracy, in an experiment. The method contributes to watching of the elderly and effective usage of electricity.

We are going to verify the effectiveness of the method with other kinds of domestic actions.

REFERENCES

- [1] L. Piyathilaka and S. Kodagoda, “Human activity recognition for domestic robots,” in *Field and Service Robotics*. Springer, 2015, pp. 395–408.
- [2] M. Vinagre, J. Aranda, and A. Casals, “An interactive robotic system for human assistance in domestic environments,” in *Computers Helping People with Special Needs*. Springer, 2014, pp. 152–155.
- [3] F. Xie, A. Song, and V. Ciesielski, “Genetic programming based activity recognition on a smartphone sensory data benchmark,” in *Evolutionary Computation (CEC), 2014 IEEE Congress on*. IEEE, 2014, pp. 2917–2924.
- [4] A. F. Santamaria, F. De Rango, D. Barletta, D. Falbo, and A. Imbrogno, “Data analysis and integration of environmental sensors to meet human needs,” in *SPIE Sensing Technology+ Applications*. International Society for Optics and Photonics, 2014, pp. 91 030A–91 030A.
- [5] S. Hattori, Y. Kameda, and Y. Ohta, “A study of multi-sensor correlation toward abnormality recognition,” *IEICE Technical Report MVE*, vol. 104, no. 489, 2004, pp. 19–25, (in Japanese).
- [6] S. Nakashima, H. M. Lu, K. Miyata, Y. Kitazono, and S. Seiichi, “Person localization system using privacy-preserving sensor,” *Applied Mechanics and Materials*, vol. 103, 2012, pp. 622–627.
- [7] A. Hein, E.-E. Steen, A. Thiel, M. Hülsken-Giesler, T. Wist, A. Helmer et al., “Working with a domestic assessment system to estimate the need of support and care of elderly and disabled persons: results from field studies,” *Informatics for Health and Social Care*, vol. 39, no. 3-4, 2014, pp. 210–231.
- [8] H. Tanaka and Y. Nakauchi, “Senior citizen monitoring system by using ubiquitous sensors (mechanical systems),” *Transactions of the Japan Society of Mechanical Engineers, Series C*, vol. 75, no. 760, 2009, pp. 3244–3252, (in Japanese).
- [9] F. Feldwieser, M. Gietzelt, M. Goevercin, M. Marschollek, M. Meis, S. Winkelbach et al., “Multimodal sensor-based fall detection within the domestic environment of elderly people,” *Zeitschrift für Gerontologie und Geriatrie*, vol. 47, no. 8, 2014, pp. 661–665.
- [10] L. Rossi, A. Belli, A. De Santis, C. Diamantini, E. Frontoni, E. Gambi et al., “Interoperability issues among smart home technological frameworks,” in *Mechatronic and Embedded Systems and Applications (MESA), 2014 IEEE/ASME 10th International Conference on*. IEEE, 2014, pp. 1–7.
- [11] I.-H. Bae, “An ontology-based approach to adl recognition in smart homes,” *Future Generation Computer Systems*, vol. 33, 2014, pp. 32–41.
- [12] S. Nakamura, A. Hiromori, H. Yamaguchi, T. Higashimno, Y. Yamaguchi, and Y. Shimoda, “Activity sensing, analysis and recommendation in smarthouse,” in *Multimedia, Distributed, Cooperative, and Mobile Symposium*, vol. 2014, jul 2014, pp. 1557–1566, (in Japanese).
- [13] J. Liao, L. Stankovic, and V. Stankovic, “Detecting household activity patterns from smart meter data,” in *Intelligent Environments (IE), 2014 International Conference on*. IEEE, 2014, pp. 71–78.
- [14] P. Cottone, S. Gaglio, G. L. Re, and M. Ortolani, “User activity recognition for energy saving in smart homes,” *Pervasive and Mobile Computing*, 2014.
- [15] J. Ranjan and K. Whitehouse, “Generating home energy footprint by assigning fixture usage to individuals in homes: poster abstract,” in *Proceedings of the 1st ACM Conference on Embedded Systems for Energy-Efficient Buildings*. ACM, 2014, pp. 226–227.
- [16] S. Hammer, M. Wißner, and E. André, “Trust-based decision-making for energy-aware device management,” in *User Modeling, Adaptation, and Personalization*. Springer, 2014, pp. 326–337.

Macropixel Compressive Sensing Reconstruction of Spectral Images Sensed by Multispectral Filter Array-based Sensors

Yuri H. Mejia, Fernando A. Rojas, and Henry Arguello

Department of Systems Engineering and Computer Science
 Universidad Industrial de Santander

Bucaramanga, Colombia

email: yuri.mejia@correo.uis.edu.co, frojas@uis.edu.co, henarfu@uis.edu.co

Abstract—Spectral images are 3 dimensional data cubes of spectral information from a two-dimensional spatial scene. Traditional acquisition of these data cubes includes complex architectures that involves the use of prisms, tunable filters, and tunable illumination. Technical progress has allowed developing MSFA-based sensors in order to extrapolate the reconstruction of more bands than RGB cameras. However, reconstructing the spectral images with traditional mathematical methods following a least squares or demosaicing approach is unfeasible. Recently compressive sensing technique has been developed that allows reconstructing signals with few measurements than the traditional methods by using the sparse representation of the underlying signal. It is possible to exploit the capabilities of MSFA-based sensors selecting measurements subsets to form macropixels that have spectral information of a single reconstructed pixel. The macropixel size selection leads to a variable reconstructed spatial resolution preserving the filters spectral resolution. This paper presents a model for spectral images reconstruction from macropixels formed with MSFA-based sensor measurements using the principle of compressive sampling. This model selects subsets of the macropixels measurements following a downsampling matrix operation, therefore a reconstruction model is formulated by directly reconstruct a spectral image with the spectral resolution given by the number of filters. To verify the effectiveness of the reconstruction model measurements of the MSFA-based sensor for real spectral images are simulated. An ensemble of random dichroic filters is used. The macropixel compressive sensing reconstruction approach and the traditional scheme reconstruction are compared.

Keywords- spectral images; MSFA-based sensors; compressive sensing; macropixel.

I. INTRODUCTION

Spectral imaging involves the sensing of a scene where at every location of the image plane the spectral information is collected. Its applications are many and cover ocean research, food safety, geology, and medical demands. Some examples involve the characterization of phytoplankton in the ocean [1], quality evaluation in the area of food safety [2], plant stress assessment [3], characterization of different bacterial colonies [4], disease diagnosis, and image-guided surgery [5].

In some spectral imagers, the scene is beamsplit into the wavelength components for example using a prism assembly, and each of these images is captured in a separate detector array. In this method the sensing devices have significant size and weight disadvantages [6]. One of the most intuitive multispectral scanning techniques is the

tunable filter, where a complete spectral image is produced after a sequence of exposures by capturing an image of one spectral band at time. For instance, the spectral image can be sensed by using a filter wheel where some optical filters are installed in a rotatory mechanical structure [7]. Most of the methods are related to scanning operations where multiple exposures are used causing motion artifacts.

On the contrary, some techniques use MSFA and collect multiple wavelength spectra from a single detector array [8]. Nowadays, optical coatings technologies have been miniaturized and optimized such that the creation of multi-patterned arrays of different optical filters, with traditional design and manufacturing methods, is allowed [6]. The optical coatings production methodology combines modern optical thin film deposition techniques with microlithographic procedures. This process enables micron-scale precision patterning of optical thin film dichroic coatings on a single substrate. A dichroic filter is an accurate color filter used to selectively pass light of a small range of wavelengths while reflecting other wavelengths.

Figure 1 shows a representation of a MSFA-based sensor that is a monochrome image sensor covering with a MSFA, each pixel in the sensor is measuring only some spectral components at a specific spatial location. Since there are only some wavelength elements available in each pixel, the missing wavelength elements must be estimated from the adjacent pixels. This process is called multispectral demosaicing, and in most cases is carried out depending on the specific acquisition process.

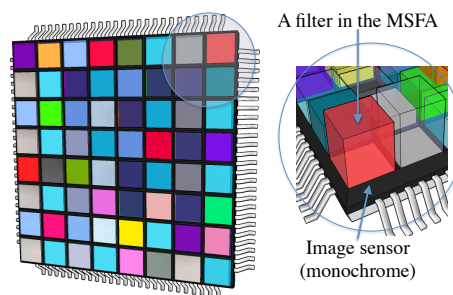


Figure 1. A MSFA-based sensor is illustrated.

For example, Miao et al. [9] generate a MSFA following a binary tree-based method, which starts from a checkerboard pattern. By recursively separating the original checkerboard, the algorithm generates the MSFA given the number of spectral bands and the probability of appearance of each band. Then, they design a demosaicing algorithm based on the same binary tree. Brauers and Aach [10] propose a MSFA that consists of color filter blocks of the

size 3×2 pixels, this configuration allows to use a fast bilinear interpolation with a reconstruction up to 6 spectral bands. Monno et al. [11] propose a five-band MSFA. In the pattern, the green-like channel is distributed as in the Bayer color filter array (CFA), and other channels are arranged following a binary-tree approach. For demosaicing an adaptive kernel can be estimated directly from the raw data. Common to these systems is that the MSFA design is application and number of bands dependent, which reach at most 6.

On the other hand, Compressive Sensing (CS) has emerged as a rising research area that allows the acquisition of signals at sampling rates below the Nyquist-criterion. In CS traditional sampling is substituted by measurements of random projections of the signal. The signals are then reconstructed by solving an l_1 and l_2 minimization problem in a basis where admits sparse representations. CS exploits the fact that hyperspectral images can be sparse in some basis representation.

Mathematically, a multispectral image $\mathbf{F} \in \mathbb{R}^{N \times N \times L}$ in its vector representation $\mathbf{f} \in \mathbb{R}^M$ with $M = N^2 L$, can be expressed as $\mathbf{f} = \mathbf{\Psi} \boldsymbol{\theta}$, where $\boldsymbol{\theta}$ is the coefficients sequence of S elements that represents \mathbf{f} , with $S \ll M$, and $\mathbf{\Psi}$ is a representation basis. Here, $N \times N$ represents the spatial dimensions, and L the number of spectral bands in the data cube. Compressive sensing allows \mathbf{f} recovering from m random projections when $m \geq S \log(M) \ll M$.

Assuming that the MSFA-based sensor performs a linear measurement process that calculate $m \ll M$ internal products between \mathbf{f} and a collection of vectors $\{\mathbf{H}_j\}_{j=1}^m$, as $y_i = \langle \mathbf{f}, \mathbf{H}_j \rangle$, then $\mathbf{y} = \mathbf{H} \mathbf{f}$, where the set of y_i projections form the vector \mathbf{y} of m elements, \mathbf{H} is the measurement matrix with dimensions $m \times M$, with H_j^T rows, and \mathbf{f} is the original signal of size M . For recovering \mathbf{f} from \mathbf{y} , there exist infinite solutions due to the size of \mathbf{y} is much less than the size of \mathbf{f} .

Following the sparse representation of the signal and the MSFA-based sensor, measurements can be expressed as $\mathbf{y} = \mathbf{H} \mathbf{f} = \mathbf{H} \mathbf{\Psi} \boldsymbol{\theta} = \mathbf{A} \boldsymbol{\theta}$, where $\mathbf{A} = \mathbf{H} \mathbf{\Psi} \in \mathbb{R}^{m \times M}$ is the sensing matrix. This underdetermined equation system can be solved if it is satisfied that the measurement matrix \mathbf{H} is incoherent with the sparse transformation $\mathbf{\Psi}$. It is possible to exploit the capabilities of MSFA-based sensors selecting measurements subsets to form macropixels that have spectral information of a single reconstructed pixel. That is, spectral information of a single pixel can be reconstructed based on macropixel measurements. The macropixel size selection leads to a variable reconstructed spatial resolution preserving the filters spectral resolution, reconstructing a spatial decimated data cube. This information can be used in applications requiring higher spectral than spatial image quality, also for a quick view of the scene, for example for purposes of transmission and communication applications

This paper presents a model for spectral images reconstruction from macropixels formed with MSFA-based

sensor measurements using the principle of compressive sampling. This model selects subsets of the macropixels measurements following a downsampling matrix operation, therefore a reconstruction model is formulated by directly reconstruct a spectral image of variable spatial resolution. The maximum spatial resolution is limited by the detector resolution. The number of different filters limits the spectral resolution.

The data cube is then reconstructed as $\tilde{\mathbf{f}} = \mathbf{\Psi} (\operatorname{argmin}_{\boldsymbol{\theta}} \|\mathbf{y} - \mathbf{H}_S \mathbf{\Psi} \boldsymbol{\theta}\|_2 + \tau \|\boldsymbol{\theta}\|_1)$, where \mathbf{y} is the measurement selection, \mathbf{H}_S is the measurement matrix defined as $\mathbf{H}_S = [(\mathbf{D}^0)^T \dots (\mathbf{D}^{q-1})^T]^T \mathbf{H}$, where \mathbf{D}^ℓ is the ℓ^{th} downsampling matrix used for measurement selection, $\boldsymbol{\theta}$ is an S -sparse representation of a low resolution version of \mathbf{f} on the basis $\mathbf{\Psi}$, and τ is a regularization constant.

The rest of this paper is organized as follows. Section II describes the mathematical model of the spectral image acquisition system using MSFA-based sensors. Section III describes the traditional demosaicing process. Section IV addresses the macropixel CS reconstruction approach. Section V describes the mathematical model of the dichroic filters. Section VI shows the simulation results. The conclusion closes the article.

II. SPECTRAL IMAGE ADQUISITION

To analyze the sensor-MSFA system its functions are modeled following the physical sensing phenomena for $L=6$ spectral bands and focusing in the j^{th} -slice in Figure 2. First, the MSFA $T(x, y, \lambda)$ modulates the spatial-spectral data cube $f_0(x, y, \lambda)$, resulting in the coded field $f_1(x, y, \lambda)$, where (x, y) are the spatial coordinates, and λ is the wavelength. Then the coded density impacts on the sensor.

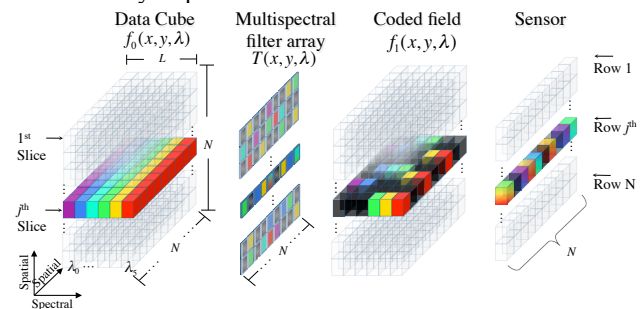


Figure 2. Sensing phenomena representation of the MSFA-based sensor. The j^{th} slice of the data cube is coded by a row of the MSFA.

The coded density integrated into the detector can be expressed as

$$f_2(x, y, \lambda) = \iint T(x', y', \lambda) f_1(x', y', \lambda) h(x' - x, y' - y) dx' dy', \quad (1)$$

where $T(x', y', \lambda)$ is the transmission function representing the MSFA, and $h(x' - x, y' - y)$ is the optical response of the system.

Each pixel in the sensor is a discretized measurement. The source $f_0(x, y, \lambda)$ can be written in discrete form as $F_{i,j,k}$

where i and j index the spatial coordinates, and k determines the k^{th} spectral plane. Let $T_{i,j,k} \in \{0,1\}$ be the discretization of the MSFA.

Then, the discretized MSFA-based sensor measurements can be expressed as

$$Y_{i,j} = \sum_{k=0}^{L-1} F_{i,j,k} T_{i,j,k} + \omega_{i,j}, \quad (2)$$

where $Y_{i,j}$ is the intensity at the $(i,j)^{\text{th}}$ position of the detector, $i, j=0, 1, \dots, N-1$, and the dimensions of the detector are $N \times N$. F is an $N \times N \times L$ spectral data cube, and $\omega_{i,j}$ is the white noise of the sensing system.

The measurements $Y_{i,j}$ in (2) can be written in matrix notation as

$$\mathbf{y} = \mathbf{H}\mathbf{f} + \boldsymbol{\omega}, \quad (3)$$

where \mathbf{y} is an N^2 -long vector representation of $Y_{i,j}$, $\mathbf{f} = \text{vect}([f_0, \dots, f_{L-1}])$ is the vector representation of the data cube \mathbf{F} where f_k is the vectorization of the k^{th} spectral band.

The output \mathbf{y} in (3) can be extended as

$$\mathbf{y} = \underbrace{\begin{bmatrix} \text{diag}(\mathbf{t}_0) & \dots & \text{diag}(\mathbf{t}_{L-1}) \\ \mathbf{H} \end{bmatrix}}_{\mathbf{H}} \begin{bmatrix} f_0 \\ f_1 \\ \vdots \\ f_{L-1} \end{bmatrix} + \boldsymbol{\omega}, \quad (4)$$

where \mathbf{t}_k is the vectorization of the k^{th} MSFA spectral plane, $\text{diag}(\mathbf{t}_k)$ is an $N^2 \times N^2$ diagonal matrix whose entries are \mathbf{t}_k , more specifically $(\mathbf{t}_k)_i = T_{[i/N], [i-1/N]N, k}$ for $i=0, \dots, N^2-1$.

Figure 3 depicts a random MSFA based matrix \mathbf{H} for $N=6$, and $L=4$. Colored squares represent unblocking light elements related to a specific wavelength.

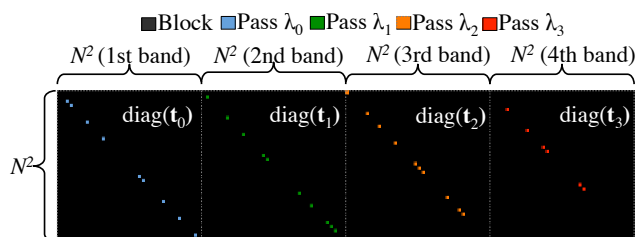


Figure 3. The matrix \mathbf{H} is shown for $N=6$, and $L=4$. Colored squares represent unblocking light elements related to a specific wavelength.

III. TRADITIONAL DEMOSAICING

Given the set of measurements \mathbf{y} a traditional demosaicing algorithm estimates for each reconstructed pixel the intensities for all wavelength components. Common approach minimizes the linear mean square error between the measurements and the vector estimation multiplied by the sensing matrix, that is

$$\tilde{\mathbf{f}} = \underset{\mathbf{f}}{\text{arg min}} \|\mathbf{y} - \mathbf{H}\mathbf{f}\|_2, \quad (5)$$

A closed-form solution to (5) is given by

$$\tilde{\mathbf{f}} = (\mathbf{H}^T \mathbf{H})^{-1} \mathbf{H}^T \mathbf{y} = \mathbf{H}^+ \mathbf{y}, \quad (6)$$

where \mathbf{H}^+ is known as the pseudoinverse of \mathbf{H} , and \mathbf{H}^T is its transpose. For comparison purpose, this approach is implemented.

Also, for the spatial resolution variation of the data cube an average decimation matrix is applied to the reconstructed data cube. The variable q is defined as the macropixel side size; each macropixel in a spectral band is a block of dimensions $q \times q$ pixels, where the ratio N/q is an integer. The decimated reconstruction is given by $\tilde{\mathbf{f}}_q = \mathbf{D}\tilde{\mathbf{f}}$, where \mathbf{D} does a block averaging of size $q \times q$ in each spectral band reducing the size of the vectorized reconstructed data cube to $\frac{N^2 L}{q^2} \times 1$.

The spatial decimation matrix element-by-element can be expressed as:

$$\mathbf{D}_{i,j} = \begin{cases} \frac{1}{q^2}, & \text{if } i = \left\lfloor \frac{j}{q} \right\rfloor - \frac{N}{q} \left\lfloor \frac{j}{N} \right\rfloor + \frac{N}{q} \left\lfloor \frac{j}{qN} \right\rfloor, \\ 0, & \text{otherwise,} \end{cases} \quad (7)$$

where $i = 0, 1, \dots, \frac{N^2 L}{q^2} - 1$, and $j = 0, 1, \dots, N^2 L - 1$.

IV. MACROPIXEL COMPRESSIVE SENSING RECONSTRUCTION

In this model, the macropixel definition is based on the assumption that $q \times q$ neighboring pixels, in an $N \times N \times L$ spectral image, could have a similar spectral response, Figure 4 illustrates this premise. Then, the macropixel, which is formed of $q \times q$ measurement pixels in the sensor, is taken as the spectral response of a single pixel for a decimated reconstruction. For instance, Figure 5 shows an example of the measurement selection for a macropixel side size of $q=2$. In total are taken q^2 subsets of measurements in a single shot of the MSFA-based sensor.

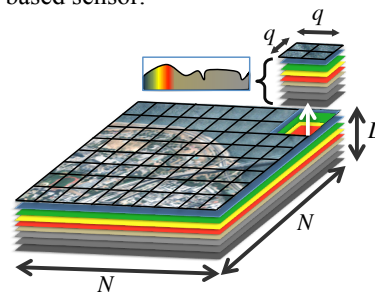


Figure 4. Illustration of the assumption that for $q \times q$ neighboring pixels, in a $N \times N \times L$ spectral image, the spectral response is similar.

In the acquisition model, the matrix product between a downsampling matrix and the total sensor measurements forms each subset of measurements. More specifically, each subset is given by

$$\mathbf{y}^\ell = \mathbf{D}^\ell \mathbf{H}\mathbf{f}, \quad (8)$$

where \mathbf{D}^ℓ does a downsampling in each $q \times q$ square of pixels for taken q^2 different subsets of the total measurements, and \mathbf{y}^ℓ is the ℓ^{th} subset of measurements where $\ell \in \{0, \dots, q^2 - 1\}$. Figure 5 shows an example of a subset measurement selection for $q=2$. Precisely, the function of the decimation matrix \mathbf{D}^ℓ is selecting in each $q \times q$ block of the measurements the ℓ^{th} -element for forming the ℓ^{th} -subset of

measurements. The decimation matrix element-by-element can be expressed as:

$$\mathbf{D}_{i,j}^\ell = \begin{cases} 1, & \text{if } j = iq + (q-1)N \left\lfloor \frac{iq}{N} \right\rfloor + \ell + \left\lfloor \frac{\ell}{q} \right\rfloor (N-q), \\ 0, & \text{otherwise,} \end{cases} \quad (9)$$

where $i = 0, 1, \dots, \frac{N^2}{q^2} - 1, j = 0, 1, \dots, N^2 - 1$, and $\ell = 0, 1, \dots, q^2 - 1$.

Figure 6 depicts the downsampling matrix \mathbf{D}^ℓ for $q=2, N=6$, and $\ell = 0, 1, 2, 3$. The white squares represent one-valued elements.

In this case, the complete set of measurements is given by

$$\mathbf{y} = \begin{bmatrix} \mathbf{y}^0 \\ \mathbf{y}^1 \\ \vdots \\ \mathbf{y}^{q^2-1} \end{bmatrix} = \begin{bmatrix} \mathbf{D}^0 \\ \mathbf{D}^1 \\ \vdots \\ \mathbf{D}^{q^2-1} \end{bmatrix} \mathbf{H} \mathbf{f} = \mathbf{H}_S \mathbf{f}, \quad (10)$$

where subadjacent data cube projection is reconstructed solving an l_1 and l_2 minimization problem, where the decimation process is taken into account. The optimization problem is given by $\tilde{\mathbf{f}} = \Psi(\text{argmin}_\theta \|\mathbf{y} - \mathbf{H}_S \Psi \theta\|_2 + \tau \|\theta\|_1)$, where \mathbf{y} is given by (10), \mathbf{H}_S is the measurement matrix defined as $\mathbf{H}_S = [(\mathbf{D}^0)^T \dots (\mathbf{D}^{q^2-1})^T]^T \mathbf{H}$, θ is an S -sparse representation of a low resolution version of \mathbf{f} on the basis Ψ , and τ is a regularization constant [12].

\mathbf{H}_S is the measurement matrix defined as $\mathbf{H}_S = [(\mathbf{D}^0)^T \dots (\mathbf{D}^{q^2-1})^T]^T \mathbf{H}$, where \mathbf{D}^ℓ is the ℓ^{th} downsampling matrix used for measurement selection, θ is an S -sparse representation of a low resolution version of \mathbf{f} on the basis Ψ , and τ is a regularization constant.

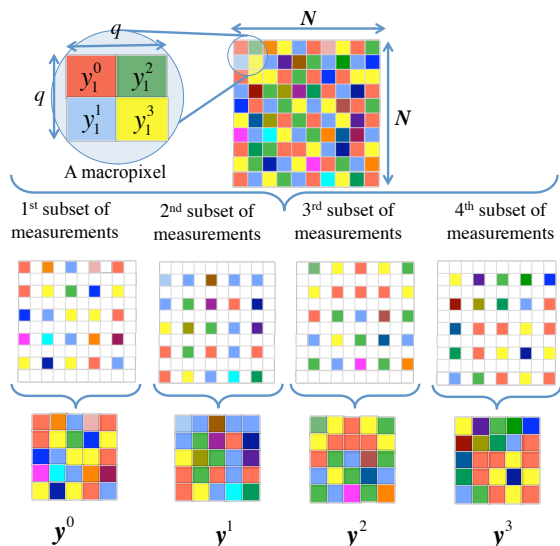


Figure 5. Example of a subset selection for a macropixel size of $q \times q = 2 \times 2$ that forms 4 subsets of measurements in a single shot of the MSFA-based sensor.

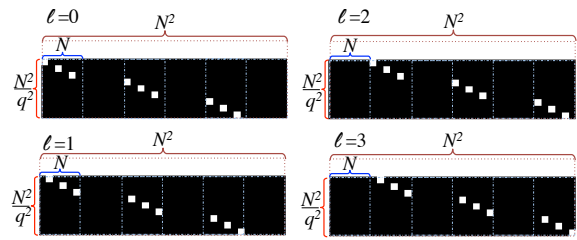


Figure 6. The downsampling matrix \mathbf{D}^ℓ is shown for $q=2, N=6$ and $\ell = 0, 1, 2, 3$. White squares represent ones and the black elements are zero.

V. MULTISPECTRAL FILTERS

For developing this work random dichroic filters were used. Dichroic filters let pass only one spectral band for each sensor pixel. Then, the spectral response for pixel can be selected randomly from a set of spectral bands. The spectral response of the (λ_i^D) dichroic filter pixel can be defined as

$$(\mathbf{t}_k)_i = \begin{cases} 1, & \text{if } k = \lambda_i^D, \\ 0, & \text{otherwise,} \end{cases} \quad (12)$$

for the random variable $\lambda_i^D \in \{0, \dots, L-1\}$, the i^{th} filter where $i=0, \dots, N^2-1$, and $k=0, \dots, L-1$. For example, the first pixel of a MSFA of $L=5$ spectral bands can have the spectral response $(\mathbf{t}_k)_1 = [0 \ 1 \ 0 \ 0 \ 0]$, where the random variable is $\lambda_1^D = 2$.

VI. SIMULATION AND RESULTS

To verify the macropixel CS reconstruction of spectral images sensed by MSFA-based sensors, a set of compressive measurements is simulated using the model of (2). These measurements are constructed employing the Beads spectral image captured with a CCD camera Apogee Alta U260 and a VariSpec liquid crystal tunable filter, in the range of wavelength 400nm-560nm, with steps of 10nm [13]. The resulting test data cube \mathbf{F} has 512×512 pixels of spatial resolution and $L=16$ spectral bands. The RGB image mapped version of the data cube is shown in Figure 7. An ensemble of dichroic filters based on a random selection of spectral bands is used. Compressive sensing reconstruction is realized using the GPSR algorithm [14]. The representation basis Ψ is a Kronecker product $\Psi = \Psi_1 \otimes \Psi_2$, where Ψ_1 is the two-dimensional-wavelet Symmlet-8 basis and Ψ_2 is the cosine basis. The simulations are performed in a desktop architecture with an Intel Core i7 3.6GHz processor, 32GB RAM, and using Matlab R2014a.

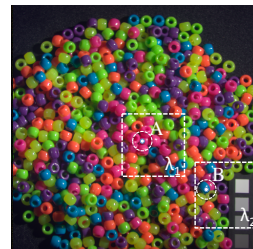


Figure 7. Multispectral image Beads used in simulations (false RGB color).

A. Variation of the macropixel side size q

Figure 8 depicts the PSNR of the reconstructed images as a function of the macropixel side size q , for $q \in \{1, 2, 4, 8\}$. Figure 8(a) shows the results when $L=3$ spectral bands are sensed and reconstructed. Figure 8(b) for $L=8$, Figure 8(c) for $L=12$, and Figure 8(d) for $L=16$. The PSNR comparison is made between the reconstructed image and a spatial decimated version (of size $N/q \times N/q \times L$) of the test data cube. Results show that increasing spectral bands decreases the PSNR for both reconstruction methods. Furthermore, increasing the size of q improves the macropixel CS reconstruction results more than the traditional demosaicing results.

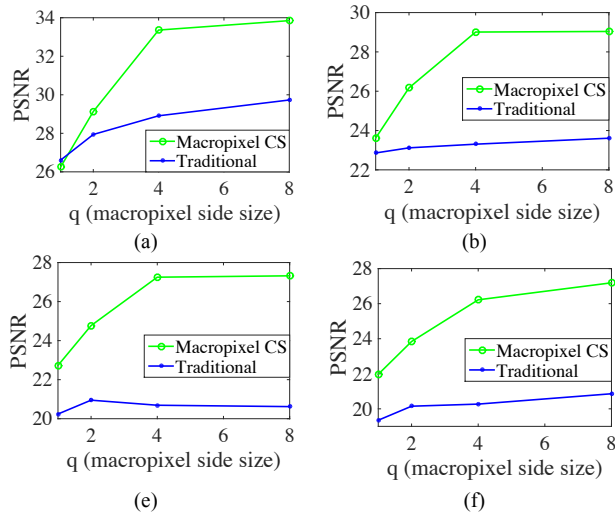


Figure 8. Mean PSNR of the reconstructed data cubes as a function of the macropixel side size q , where L spectral bands are sensed and reconstructed, for (a) $L=3$, (b) $L=8$, (c) $L=12$, and (d) $L=16$.

Figure 9(a) shows a zoomed version of a selected region of the original 2nd spectral band (this region is highlighted in Figure 7 where $\lambda_1=2$). Figure 9 (b) shows its reconstruction when the first $L=3$ spectral bands are sensed and reconstructed using the macropixel CS approach for $q=1$. Figure 9(c) illustrates its reconstruction for the traditional demosaicing method. Figure 9(d) depicts reconstruction along the spectral axis of the spatial pixel location A of the Figure 7, where the intensity is normalized between 0-1. Figure 9 (e)-(h) show similar results for the 3rd spectral band and the second region highlighted in Figure 8 for $\lambda_2=3$. There, it is possible to observe for $L=3$ spectral bands the traditional demosaicing has a comparable performance with the macropixel CS reconstruction (around 26 dB in PSNR for both approaches) for $q=1$ macropixel side size.

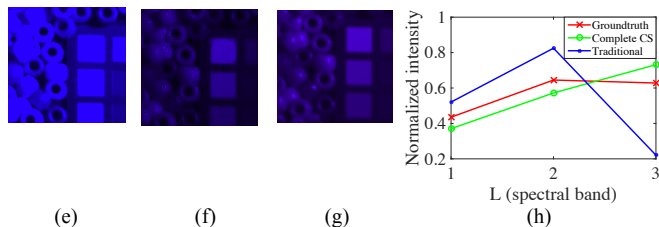
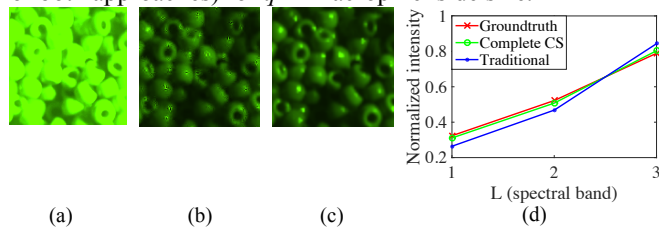


Figure 9. Zoom version of the reconstructions results when $L=3$ spectral bands are sensed and reconstructed, for $q=1$. For the spectral band $\lambda_1=2$: (a) groundtruth, (b) reconstruction by macropixel CS, (c) reconstruction by a traditional approach, and (d) reconstruction along the spectral axis of the spatial pixel location A in the Fig. 8. For the spectral band $\lambda_2=3$: (e) groundtruth, (f) reconstruction by macropixel CS, (g) reconstruction by a traditional approach, and (h) reconstruction along the spectral axis of the spatial pixel location B of the Fig. 8.

Figure 11 shows similar result to those of Figure 10 for $q=4$, and $L=3$. Also, in this case it is possible to observe the better performance of the macropixel CS approach where a PSNR improvement of up to 4 dB is attained for $q=4$ macropixel side size compared with the traditional approach.

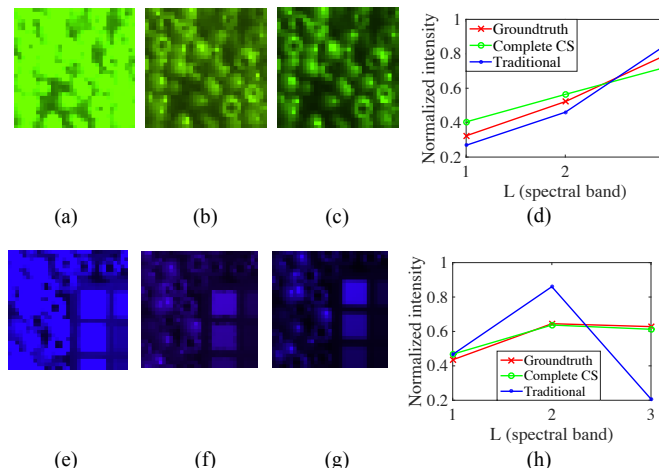


Figure 10. Zoom version of the reconstructions results when $L=3$ spectral bands are sensed and reconstructed, for $q=4$. For the spectral band $\lambda_1=2$: (a) groundtruth, (b) reconstruction by macropixel CS, (c) reconstruction by a traditional approach, and (d) reconstruction along the spectral axis of the spatial pixel location A in the Fig. 8. For the spectral band $\lambda_2=3$: (a) groundtruth, (b) reconstruction by macropixel CS, (c) reconstruction by a traditional approach, and (d) reconstruction along the spectral axis of the spatial pixel location B in the Fig. 8.

Figure 12 (a) shows the selected region of the original 3rd spectral band (in Figure 7 where $\lambda_1=3$). Figure 12 (b) shows its reconstruction when the first $L=8$ spectral bands are sensed and reconstructed using the macropixel CS approach for $q=1$. Figure 12 (c) illustrates its reconstruction for the traditional demosaicing method. Figure 12 (d) depicts reconstruction along the spectral axis for location A. Figure 12 (e)-(h) show similar results for the 8th spectral band and the second region highlighted in Figure 8 for $\lambda_2=8$. The performance of the macropixel CS approach has a PSNR improvement of up to 2 dB for $q=1$ macropixel side size compared with the traditional demosaicing approach.

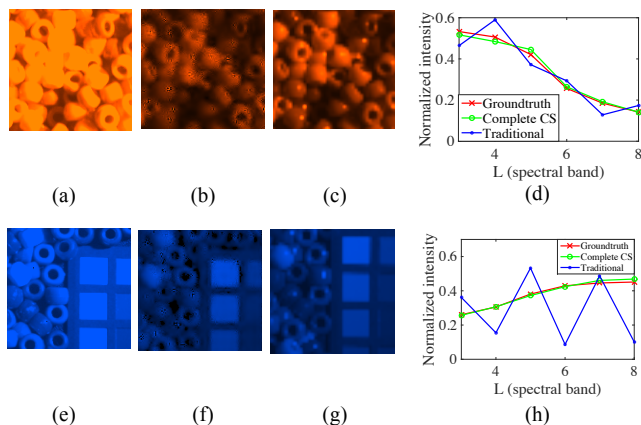


Figure 11. Zoom version of the reconstructions results when $L=8$ spectral bands are sensed and reconstructed. For the spectral band $\lambda_1=3$: (a) groundtruth, (b) reconstruction by macropixel CS for $q=1$, (c) reconstruction by a traditional approach, and (d) reconstruction along the spectral axis of the spatial pixel location A of the Fig. 8. For the spectral band $\lambda_2=8$: (a) groundtruth, (b) reconstruction by macropixel CS for $q=1$, (c) reconstruction by a traditional approach, and (d) reconstruction along the spectral axis of the spatial pixel location B of the Fig. 8.

Figure 13 shows similar result to those of Figure 12 for $q=4$, and $L=8$. Also, it is possible to observe the better performance of the macropixel CS approach where a PSNR improvement of up to 5.7 dB is attained for $q=4$ macropixel side size compared with the traditional approach. For all cases the macropixel CS approach has a better spectral signature reconstruction than the traditional demosaicing.

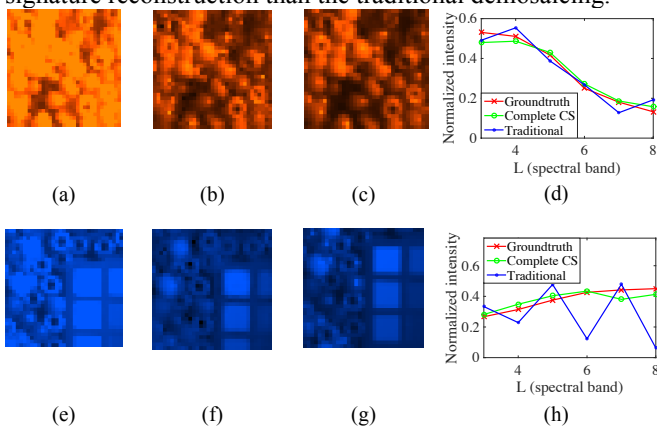


Figure 12. Zoom version of the reconstructions results when $L=8$ spectral bands are sensed and reconstructed, for $q=4$. For the spectral band $\lambda_1=3$: (a) groundtruth, (b) reconstruction by macropixel CS, (c) reconstruction by a traditional approach, and (d) reconstruction along the spectral axis of the spatial pixel location A in the Fig. 8. For the spectral band $\lambda_2=8$: (a) groundtruth, (b) reconstruction by macropixel CS, (c) reconstruction by a traditional approach, and (d) reconstruction along the spectral axis of the spatial pixel location B in the Fig. 9.

VII. CONCLUSION

A model for macropixel CS reconstruction of spectral images sensed by MSFA-based sensors is presented. A selection of measurements subsets to form macropixels that

have spectral information of a single reconstructed pixel is exposed. The macropixel CS reconstruction approach is compared with a traditional least squares reconstruction. For the macropixel CS reconstruction, the PSNR increases rapidly with the macropixel side size. For instance, the improvements range from 1 dB to 6 dB with respect to the traditional approach. Results show that increasing spectral bands decreases the PSNR for both reconstruction methods.

REFERENCES

- [1] J. Ryan, C. Davis, N. Tuffillaro, R. Kudela, and B.-C. Gao, "Application of the Hyperspectral Imager for the Coastal Ocean to Phytoplankton Ecology Studies in Monterey Bay, CA, USA," *Remote Sens.*, vol. 6, no. 2, Jan. 2014, pp. 1007–1025.
- [2] Z. Xiong, A. Xie, D.-W. Sun, X.-A. Zeng, and D. Liu, "Applications of Hyperspectral Imaging in Chicken Meat Safety and Quality Detection and Evaluation: A Review.," *Crit. Rev. Food Sci. Nutr.*, Apr. 2014, pp. 1287-1301.
- [3] G. J. Bellante, S. L. Powell, R. L. Lawrence, K. S. Repasky, and T. a. O. Dougher, "Aerial detection of a simulated CO2 leak from a geologic sequestration site using hyperspectral imagery," *Int. J. Greenh. Gas Control*, vol. 13, Mar. 2013, pp. 124–137.
- [4] M. Mehrübeoglu, G. W. Buck, and D. W. Livingston, "Differentiation of bacterial colonies and temporal growth patterns using hyperspectral imaging," in *SPIE Optical Engineering + Applications*, 2014, p. 922206.
- [5] G. Lu and B. Fei, "Medical hyperspectral imaging: a review.," *J. Biomed. Opt.*, vol. 19, no. 1, Jan. 2014, p. 10901.
- [6] J. D. Barrie, K. a. Aitchison, G. S. Rossano, and M. H. Abraham, "Patterning of multilayer dielectric optical coatings for multispectral CCDs," *Thin Solid Films*, vol. 270, no. 1–2, Dec. 1995, pp. 6–9.
- [7] Z. Frenress, L. C. Young, and H. D. Edwards, "Field Photometer with Nine-Element Filter Wheel," *Appl. Opt.*, vol. 3, 1964, pp. 303–309.
- [8] P. J. Lapray, X. Wang, J. B. Thomas, and P. Gouton, "Multispectral Filter Arrays: Recent Advances and Practical Implementation," *Sensors*, vol. 14, 2014, pp. 21626–21659.
- [9] L. Miao, H. Qi, R. Ramanath, and W. E. Snyder, "Binary tree-based generic demosaicking algorithm for multispectral filter arrays," *IEEE Trans. Image Process.*, vol. 15, no. 11, 2006, pp. 3550–3558.
- [10] J. Brauers and T. Aach, "A Color Filter Array Based Multispectral Camera," 12 *Work. Farbbildverarbeitung*, 2006.
- [11] Y. Monno, M. Tanaka, and M. Okutomi, "Multispectral Demosaicking Using Adaptive Kernel Upsampling," in *In Proceedings of the 18th IEEE International Conference on Image Processing (ICIP)*, 2011, pp. 3218–3221.
- [12] H. Arguello and G. R. Arce, "Colored coded aperture design by concentration of measure in compressive spectral imaging.," *IEEE Trans. Image Process.*, vol. 23, no. 4, Apr. 2014, pp. 1896–908.
- [13] S. K. N. F. Yasuma, T. Mitsunaga, and D. Iso, "CAVE | Projects: Multispectral Image Database," *Generalized Assorted Pixel Camera: Post-Capture Control of Resolution, Dynamic Range and Spectrum*. [Online]. Available: <http://www.cs.columbia.edu/CAVE/databases/multispectral/>. [Accessed: 24-Feb-2015].
- [14] M. A. Figueiredo, R. D. Nowak, and S. J. Wright, "Gradient projection for sparse reconstruction: Application to compressed sensing and other inverse problems.," *Sel. Top. Signal Process. IEEE J.*, vol. 1, no. 4, 2007, pp. 586–597.

Receiver Design of Passive UHF RFID Sensor Platform for Gas Identification

Muhammad Ali Akbar, Amine Ait Si Ali, Abbas Amira, Mohieddine Benammar, Faycal Bensaali
College of Engineering
Qatar University
Doha, Qatar
e-mail: ali.akbar@qu.edu.qa,
amine.aitisali@qu.edu.qa,
abbes.amira@qu.edu.qa,
mbenammar@qu.edu.qa,
f.bensaali@qu.edu.qa

Mohamed Zgaren, Mohamad Sawan
Dept. of Electrical Engineering
Polytechnique Montreal
Montreal, Quebec
e-mail: mohamed.zgaren@polymtl.ca,
mohamad.sawan@polymtl.ca

Amine Bermak
School of Engineering
Hong Kong Uni. of Sci. and Tech.
Clear Water Bay, Hong Kong
e-mail: eebermak@ust.hk

Abstract— The concept of passive Radio Frequency Identification (RFID) sensor tag is introduced to remove the dependency of current RFID platforms on battery life. In this paper, a reader for passive RFID sensor tag is presented along with the processing unit. The RFID system is compliant to Electronics Product Code Generation 2 (EPC-Gen2) protocol in 902-928 MHz ISM band. Whereas the processing unit is implemented and analyzed in software and hardware platforms. The software platform uses MATLAB, whereas a High Level Synthesis (HLS) tool is used to implement the processing unit on a Zynq platform. Moreover, Principal Component Analysis (PCA) and Linear Discriminant Analysis (LDA) based feature reduction approaches are analyzed in detail for efficient classification of gas data. It is found that 90% gases are identified using first three principal components, which is 7% more efficient than LDA. While in hardware, LDA requires 50% less Look-Up Tables than PCA. The RFID tag used for transmission is implemented in 0.13 μm CMOS process, with simulated average power consumption is 2.6 μW from 1.2 V supply. ThingMagic M6e embedded reader is used for RFID platform implementation. It shows an output power of 31.5 dBm which allows a read range of 9 meter.

Keywords—Sensor tag; Pattern recognition; Gas identification; UHF RFID Reader; EPC Gen2; ISM Band

I. INTRODUCTION

Gas identification is one of the most critical challenges in current gas industry because a single leakage of an explosive gas can cause a complete disaster for the whole company. The explosion of a gas container or the leakage of a hazardous gas will also be disastrous for the environment [1]. Therefore, human olfactory based Electronic Nose (EN) systems are introduced, with wide range of applications like milk industry [2] and patient monitoring system [3].

In gas applications, the presence of complex compounds like water vapour with the gases of interest creates one of the challenging issues for the gas identification using EN [4]. The presence of battery further limits the life and durability of the sensor tag. Moreover, the drift and non-selectivity of sensor raise the problem of classification for EN [5]. The possible approaches to deal with the problem of drift and non-selectivity is to increase the number of sensors as adopted by Guo et al. [6] or to introduce the temperature modulation such that a single sensor provides different responses for the same gas due to temperature variations [7]. The purpose of these approaches

is to get more signatures for the same gas, whereas both approaches of multiple-sensors and single sensor-modulation increase the dimensionality of feature vector, thereby increasing the computational complexity. The problem becomes severe if the gas identification system is implemented on any hardware platform because of resource utilization and power consumption which increases with the computational complexity. Therefore, feature reduction approaches like Principal Component Analysis (PCA) or Linear Discriminant Analysis (LDA) is required to reduce the data size and to increase the processing efficiency.

On the other hand, Radio Frequency Identification (RFID) sensing design has been widely explored as a low-cost candidate toward lightweight, reliable and energy-efficient devices for gas detection [8]. There has been permanent evolution toward combining the capabilities of gas sensing and wireless technology in order to collect, process, and transmit time-varying data. This approach leads to RFID-enabled Wireless Sensor Network (WSN) infrastructure. Most of the WSN include a battery [9], which increases their cost and limits their autonomy. The power autonomy can be encountered by using a fully passive (battery-less) UHF RFID design. A typical RFID system is mainly composed by a reader and antenna (also named interrogator), one to several tags (also named electronic labels) and an information systems back-end.

Furthermore, a reconfigurable hardware is required to improve the processing time for run-time classification because a dedicated hardware is faster than the software application. However, gas recognition process requires a complicated training phase and frequent calibration, which is even harder to implement on a dedicated hardware. As a consequence, most EN solution today are software based platforms and the integration of a real-time in-site training and portable EN microsystem is yet to be demonstrated. Therefore, a hardware based processing unit is demonstrated which can be applied in any multi-sensing gas identification platform. The presence of a processor along with a programmable logic based on field programmable gate array (FPGA) has made heterogeneous Zynq platform suitable for our research. A hybrid system can easily be implemented on Zynq using High Level Synthesis (HLS) tool. The other reason for using Zynq board is because the circuit implemented and tested on it can easily be reproduced to application-specific integrated circuit (ASIC).

Therefore, in this paper the reader for a passive Ultra-High Frequency (UHF) RFID sensor platform is presented with a

centralized hardware processing unit to perform feature reduction and classification. The data from multiple sensor tags will be collected using M6e embedded reader at the central processing unit with respect to the Electronics Product Code Generation 2 (EPC-Gen2) protocol in the 902-928 MHz ISM frequency band. Each sensor tag has a 4x4 array gas sensor proposed by Guo et al. [6] and a low power temperature sensor [10]. Moreover, a unique code is associated with all sensor tags individually which helps the processing unit to identify the tag and process the collected data accordingly. The central processing unit is tested on a heterogeneous reconfigurable Zynq platform using High-Level Synthesis (HLS) tools while the tag sensors are implemented in CMOS process to reduce the power dissipation and enhance the full system integration. The presented work is part of an ongoing project in which a low-power multi-sensing gas identification platform is need to be developed for gas identification based on an array of tin-oxide gas sensors.

The remaining sections of this paper are organized as follows. Section II covers the RFID sensor tag along with the experimental setup for data acquisition. The UHF RFID receiver is described in Section III. Section IV is concerned with the processing unit. Simulation results are shown and discussed in Section V. Section VI concludes the paper.

II. RFID SENSOR PLATFORM AND DATA EXTRACTION

The UHF RFID based sensor platform includes a 4x4 array gas sensor [6] and a low power temperature sensor [10]. The main challenge of the RFID sensor design is the power hungry building blocks for which an external power source is required. Whereas, the presence of battery in the sensor tag creates problems by limiting the lifetime of the tag-based sensors. Tags will not be able to communicate with the embedded reader if battery power level goes below a fixed threshold. Therefore, a fully passive UHF RFID approach is adopted such that, the communication link between tags based sensor and reader is guaranteed for longer time. The full tags based sensor system are powered by a remote power through the RF energy received from the reader in order to create autonomous gas measurement micro systems.

The main challenge with the passive RFID tag is the limited range of communication; therefore, hybrid design could be used by adding a battery as power bank in addition to the power harvesting circuit. The power bank will allow to reach higher communication range when needed. Furthermore, 16 gas sensors are used in the tag which results in huge

transmission overhead as tag needs to transmit the data in periodic sessions which in turn further increases the problem of power consumption, therefore a compressive sensing approach such as Orthogonal Matching Pursuit (OMP) algorithm can be adopted for reconstructing the compressed signal [11].

In order to test the sensor tag, data is extracted for 10 concentrations of 20, 40, 60, 80, 100, 120,140, 160, 180 and 200 ppm in air, of three different gases namely Carbon-mono-oxide, ethanol and hydrogen, in a controlled experimental environment. The extraction process of gas data is carried out in a way that the dry air is flushed for 750 s before exposing the sensor to any new concentration of gas. The sensor is then exposed to gas for 250s in a closed glass chamber. This is due to the fact that the sensor reaches steady state after 250s. The experiment is repeated again after obtaining the data for 10 concentrations of each gas such that the obtained data is divided into two parts. The first one is used for training purpose known as learning data (D_l) and the second one for testing purpose known as test data (D_t). The overall model of sensor tag is shown in Figure 1.

III. UHF RFID READER PERFORMANCE

A typical RFID system consists of tags, readers and computer application systems, as shown in Figure. 2. With several excellent characteristics, such as portable, high capacity, long life, security access, and movable recognition, RFID is used more and more widely in logistic systems, production management system, monitoring and tracking system, and so on [12]. The EPC Gen2 protocol was designed based on the minimal features available on an EPC Gen2 RFID tag specifically a 32-bit secret access password, a 16-bit pseudo-random number generator, and limited memory that can store at least two 16-bit random numbers while the tag is powered. An improved authentication scheme is adopted with this standard [13].

The communication range performance of a RFID system depends mainly on the choice of frequency, transmitted power from the reader, sensitivity of tag, tag’s modulation efficiency, data rate, reader receiver sensitivity and location of the tag [14]. Based on the frequency, the RFID system can be considered as Low Frequency (LF), High-Frequency (HF), UHF and Microwave (WF) RFID. Nowadays, the UHF RFID is the most used technology because of its far reading distance (up to 10 meter), passive (battery less) tags, high security, and strong penetrating force features [15].

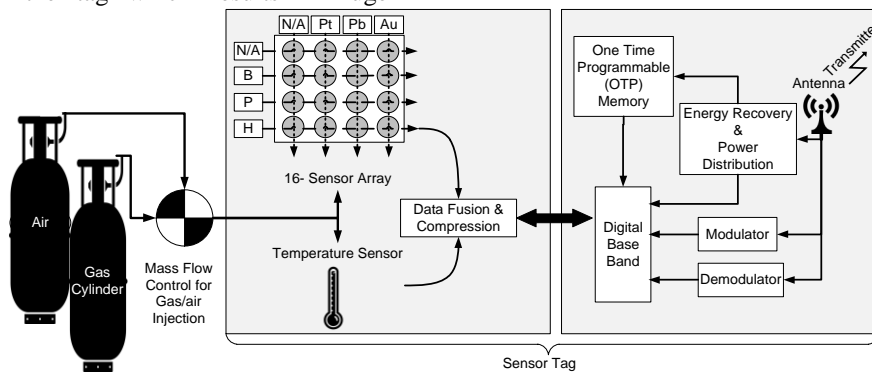


Figure 1. Block Diagram of RFID Sensor tag with data acquisition set-up

As shown in Figure. 2, the controller activates the RFID reader to send RF signals. Tags receive, process and send back the requested data through the tag’s antenna. The tag responds with an identification code using backscattering of modulated received signal. There is no battery as source of energy in the passive tags system, and thereby it gets all the energy needed for running from the electromagnetic wave transmitted by the reader. The reader decodes the received signal through its antenna to be processed by the controller.

In most cases, the reader’s antenna is placed into an external module as presented in Figure. 2 to achieve long read/write ranges also when a circularly polarized reader antenna is used to eliminate tag orientation sensitivity. According to different configurations and parameters , UHF RFID readers can be designed as fixed or handheld readers.

Handheld readers are used in a large number of applications for its portable, and easy to use in shift data collection. It is complicated to design handheld UHF RFID reader, while it includes embedded computer middleware and application, microwave and antenna designs, radio frequency electronic circuits, wireless communications and signal processing, low-power control and many other technical fields. In this research, embedded RFID reader is taken into consideration to reduce the overall system cost and complexity.

A. Antenna Design

Among the important performance characteristic is the maximum range at which RFID reader can detect the backscattered signal from the tag. Because reader sensitivity is typically high in comparison with tag, the reading range is defined by the tag response threshold. Communication range is also sensitive to the tag orientation, the material the tag is placed on, and to the propagation environment. The reader antenna should be a circularly polarized antenna, in order to avoid the polarization loss when the orientation of the identified object is changed. The read range r can be calculated using Friis free-space formula as:

$$r = \frac{\lambda}{4\pi} \sqrt{\frac{P_t G_t G_r \tau}{P_{th}}} \tag{1}$$

where λ is the wavelength, P_t is the power transmitted by the reader, G_t is the gain of the transmitting antenna, G_r is the gain of the receiving tag antenna, P_{th} is the minimum threshold power necessary to provide enough power to the RFID tag chip, and τ is the power transmission coefficient.

B. Link budget

In UHF RFID systems, the forward link depends on the tag sensitivity P_{tag} while the return link depends on the reader sensitivity P_{reader} . The reader can process the tag response data when the tag signal power P_r , received at the reader, is larger than the reader sensitivity. The reader sensitivity is the minimum power of the received tag signal necessary for successful data processing and is mainly defined by the level of self-jammer [16]. One important characteristic is the needed reader sensitivity to detect an arbitrary tag at the maximum possible distance. From [16], the needed reader sensitivity must be better or equal to:

$$P_{reader} = \frac{P_{tag}^2 * K}{P_t} \tag{2}$$

Where K is the tag backscatter gain and P_t is the reader output power. The given equation is valid for any propagation environment. Figure. 3 shows the reader sensitivity requested by the tags to read command at their maximum possible range [16]. The backscatter gain is assumed to be -10dB. The study illustrated in Figure. 3 uses four readers with four levels of output power 30dBm, 20dBm, 10dBm and 0dBm.

C. ThingMagic M6e embedded RFID reader

To further verify the performance of the proposed UHF tag [17] for both near-field and far-field operations, the Thing Magic M6e embedded RFID reader module [18] is studied to be used with a circularly polarized antenna in the free space. This RFID reader module supports the ability to transmit up to 31.5dBm for the UHF RFID band of 902–928MHz and can read more than 750 tags/seconds. This performance makes M6e the recommended RFID reader for challenging applications such as gas identification and temperature monitoring. The M6e has both serial and USB interfaces to support both board-to-board and board-to-host connectivity.

The maximum tags read range can reach up to 30 feet (9 meters) for an operating temperature from -40 °C to 60 °C.

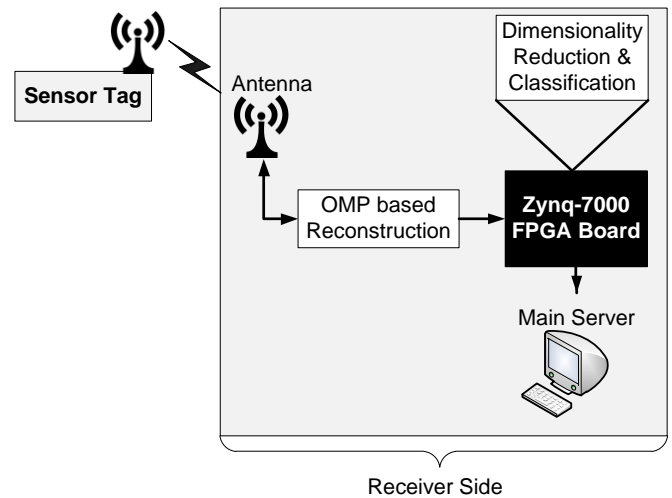


Figure 2. RFID System architecture diagram

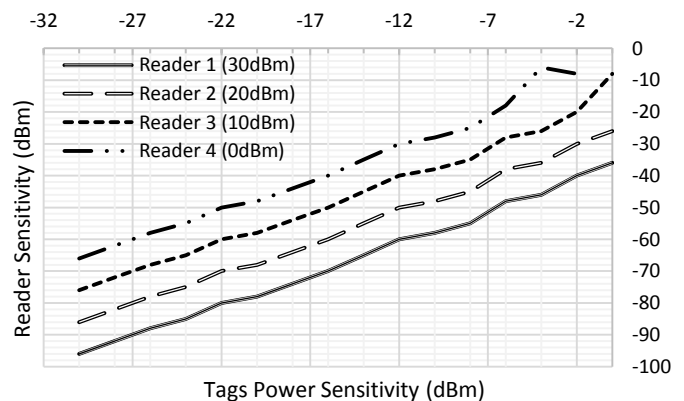


Figure 3. Reader sensitivity comparison at -10dB backscatter gain

IV. PROCESSING UNIT

The data received by the RFID receiver is fed to the processing unit for analysis. The possibility of parallel computation in dedicated hardware makes it much faster than the software at run-time. Therefore the processing unit is implemented on heterogeneous reconfigurable Zynq platform which is having an ARM processor and FPGA chip based on Xilinx 7-series [20]. The reason of selecting the Zynq platform is because of its suitability for hardware/software co-design approach. It is worth noting that the purpose of hardware platform is to process the D_i whereas the training part is done offline using MATLAB. This is to reduce the hardware overhead caused by the complexities of the feature reduction and classification algorithms. Also, the D_i is used one time for training purpose so it is more feasible and efficient to do the training offline. Thus, the hardware processing unit is used to perform real-time feature reduction and classification on D_i of gases.

A. Compressive Sensing Reconstruction

The data acquired by the sensor is compressed before transmission to reduce the power overhead of sensor tag required for transmission purpose. After receiving the RFID signal the processing unit should need to reconstruct the compressed signal to acquire the original sensor data. There are different approaches for reconstruction process, however in this research we utilized the OMP based reconstruction algorithm proposed in [11]. The reason of using this algorithm is due to its scalability and high Peak Signal to Noise Ratio (PSNR).

B. Feature Reduction

After reconstruction a PCA and LDA based feature reduction approaches are applied to check the suitability of the two most common reduction algorithms for gas application. The aim of feature reduction is to reduce the feature size without losing useful information. PCA and LDA-based feature reduction algorithms are summarized in Figure. 4.

In case of PCA the Eigen vectors (E_v) and mean values will be computed offline for training data D_i and then the projection of D_i in new space is obtained by simple multiplication of normalized data with the E_v using MATLAB. Whereas, since the testing part requires only Eigen vectors and mean values, as shown in Figure. 4(a) [19], therefore in case of PCA the computed mean and E_v for D_i are pre-stored in the flash memory of the board and at run-time the hardware will take those values to perform normalization and projection of D_i with lower complexity and faster speed.

In contrast to PCA, LDA is not performed directly on D_i because LDA deals with class boundaries which cannot be identified in D_i . Therefore, D_i is split in to classes such that data for each gas is considered as a single class. The training-data obtained at different concentrations of gas is stored as a train-class (T_c), where sub-script c is representing the type of gas. After computing normalization as well as between and within class-differences, the E_v will be computed. The E_v is then forwarded to the projection block which projects the D_i on reduced feature space. It is worth noticing that LDA testing part requires only Eigen vectors as shown in Figure. 4(b) to project D_i on reduced feature space.

C. Classification

A Binary Decision Tree (BDT) classifier is used to identify the gases after feature reduction. The reason of selecting BDT for classification is because of the simplicity and good performance. The tree formation is carried out on D_i using MATLAB library function whereas the decision nodes will be implemented on hardware using successive if-else condition to classify the gases at run-time from the obtain D_i .

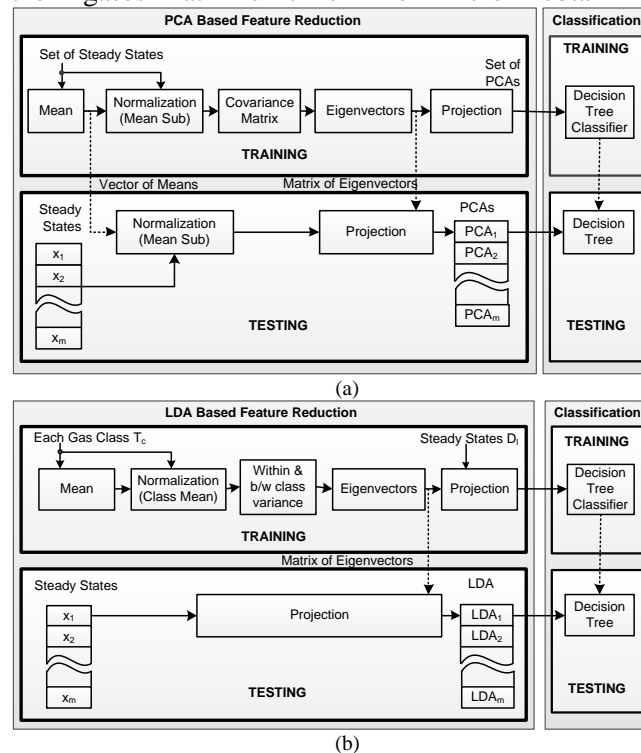


Figure 4. Feature reduction algorithm based on (a) PCA and (b) LDA

V. IMPLEMENTATION RESULTS OF THE PROCESSING UNIT

The software simulation is carried out using MATLAB whereas the hardware implementation is achieved using Vivado HLS tools [21]. It has been observed that for classification BDT with three principal components can classify 90% of gases [19] and is therefore 7% better than using LDA based feature reduction.

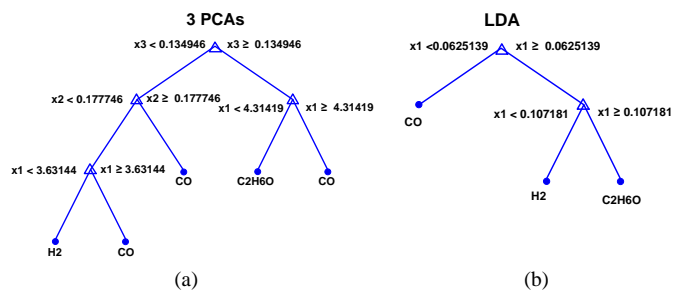


Figure 5. BDT for (a) PCA and (b) LDA

TABLE I. SIMULATION RESULTS FOR GAS-CLASSIFICATION AND HARDWARE OVERHEAD WITH PCA/LDA BASED FEATURE REDUCTION

	Properties	LDA	PCA	
			2-PCA	3-PCA
Classification	Steady State (SS)	83%	80%	90%
Hardware Resources	FF	893	2089	2089
	LUT	1937	3925	3925
	Clock Cycles (CC) (Nano-seconds) ns	8.20	8.20	8.20
	Latency Period (CC)	163	261	261
	Input Interval (CC)	164	262	262

However, for hardware implementation LDA based feature reduction requires 50% less Look Up Tables (LUTs) and 57% less Flip-Flops (FF) than PCA. Moreover, LDA requires 37.5% less latency time than PCA. Where latency time is the period require to produce the final output, as shown in Table. I.

Furthermore, the BDT obtained with LDA based feature reduction algorithm exhibits only 2 decision nodes along with unity depth, while in case of PCA the BDT have 4 decision nodes with three steps in depth. Therefore, LDA offers simplified decision tree which require less time for searching and classification of gas than PCA, as shown in Figure. 5.

VI. CONCLUSION

Since the reader is considered as a key component of the RFID gas application system, therefore a UHF RFID reader is presented with a processing unit implemented on a reconfigurable Zynq platform. The overview of the reader performance characterization is also demonstrated. Whereas, ongoing research focuses on the design and implementation of efficient reconfigurable architectures for OMP algorithm The RFID system is compliant with the EPC-Gen2 protocol in the 902-928 MHz ISM frequency band. ThingMagic embedded M6e reader shows an advantage over existing readers in the market in term of high integration, low power dissipation and low cost.

The designed processing unit at reader is tested with PCA and LDA based feature reduction approaches. It is found that BDT can classify 90% of the gases with three principal components which is 7% more efficient than the identification of gas by BDT using LDA. While in terms of hardware overhead LDA requires 50% less LUTs than PCA and is 37.5% more efficient in terms of latency time.

The presented work is part of an ongoing project in which a low-power multi-sensing gas identification platform is need to be developed for gas identification based on an array of tin-oxide gas sensors. Therefore the system will be tested on real conditions after the completion of the integration process.

ACKNOWLEDGMENT

This paper was made possible by National Priorities Research Program (NPRP) grant No. 5 – 080 – 2 – 028 from the Qatar National Research Fund (a member of Qatar Foundation). The statements made herein are solely the responsibility of the authors.

REFERENCES

- [1] N. Yamazoe, and N. Miura, "Environmental gas sensing", Sensors and Actuators B: Chemical, vol. 20, no. 2-3, 1994, pp. 95-102.
- [2] S. Labreche, S. Bazzo, S. Cade, and E. Chanie, "Shelf life determination by electronic nose: application to milk", Sensors and Actuators B: Chemical, vol. 106, no. 1, 2005, pp. 199-206.
- [3] S. Dragonieri et al. "An electronic nose in the discrimination of patients with asthma and controls", Journal of Allergy and Clinical Immunology, vol. 120, no. 4, 2007, pp. 856-862.
- [4] F. Röck, N. Barsan, and U. Weimar, "Electronic nose: current status and future trends", Chemical reviews, vol. 108, no. 2, 2008, pp. 705-725.
- [5] M. Shi, A. Bermak, S. B. Belhouari, and P.C. Chan, "Gas identification based on committee machine for microelectronic gas sensor", IEEE Transactions on Instrumentation and Measurement, vol. 55, no. 5, 2006, pp. 1786-1793.
- [6] B. Guo, A. Bermak, P.C. Chan, and G.Z. Yan, "An Integrated Surface Micromachined Convex Microhotplate Structure For Tin Oxide Gas Sensor Array", IEEE Sensors Journal, vol. 7, no. 12, 2007, pp. 1720-1726.
- [7] E. Llobet et al. , "Multicomponent gas mixture analysis using a single tin oxide sensor and dynamic pattern recognition", IEEE Sensors Journal, vol. 1, no. 3, 2001, pp. 207-213.
- [8] L. Yang, R. Zhang, D. Staiculescu, C. P. Wong, and M. M. Tentzeris, "A novel conformal RFID-enabled module utilizing inkjet-printed antennas and carbon nanotubes for gas-detection applications", Antennas and Wireless Propagation Letters, IEEE, vol. 8, 2009, pp. 653-656.
- [9] M. Brandl et al. "A low-cost wireless sensor system and its application in dental retainers", IEEE Sensors Journal, vol. 9, no. 3, 2009, pp. 255-262.
- [10] S. Mohamad, F. Tang, A. Amira, A. Bermak, and M. Benammar, "A Low Power Oscillator Based Temperature Sensor For RFID Applications", 5th Asia Symposium on Quality Electronic Design (ASQED), 2013, pp. 50-54.
- [11] H. Rabah, A. Amira, B. K. Mohanty, and S. Almaadeed, "FPGA Implementation of Orthogonal Matching Pursuit for Compressive Sensing Reconstruction", IEEE Transactions on Very Large Scale Integration Systems , DOI: [10.1109/TVLSI.2014.23358716](https://doi.org/10.1109/TVLSI.2014.23358716) .
- [12] R. Weinstein, "RFID: A Technical Overview and it's Application to the Enterprise," IT Professional, vol. 7, no. 3, 2005, pp. 27-33.
- [13] EPCglobal Inc., "EPC Radio-Frequency Identity Protocols Class-1 Generation-2 UHF RFID Protocol for Communications at 860MHz-960MHz Version 1.0.9", EPC global Standards, 2005.
- [14] K. Finkenzeller, "RFID Handbook", New York: Wiley, 2003.
- [15] A. S. Ahson, and M. Ilyas, "RFID Handbook: Applications, Technology, Security, and Privacy", CRC Press, 2008.
- [16] P. Nikitin, K. V. S. Rao, and S. Lam, "UHF RFID tag characterization: overview and state-of-the-art", Antenna Measurement Techniques Association Symposium (AMTA) 34th Annual Meeting and Symposium, 2012, pp. 289-294.

- [17] M. Zgaren, and M. Sawan, "A Front end-EPC Gen-2 Passive UHF RFID Transponder for Embedded Gas Sensor", 4th International Gas processing symposium, 2014, pp. 223-231.
- [18] 'M6e High-Performance 4-Port UHF RFID Module', http://www.dpie.com/manuals/rfid/M6eHardwareGuide_Sept13.pdf, v 1.13.1, accessed May. 12,2015.
- [19] A. Ait Si Ali, A. Amira, F. Bensaali, and M. Benammar, "Hardware PCA for Gas Identification Systems Using High Level Synthesis On The Zynq SoC", IEEE 20th International Conference on Electronics, Circuits, and Systems (ICECS) , 2013, pp. 707-710.
- [20] 'Inc Xilinx. Zynq-7000 All Prog. SoC: Tech. Reference Manual', http://www.xilinx.com/support/documentation/user_guides/ug585-Zynq-7000-TRM.pdf, UG585, v1.8.1, accessed Feb. 20, 2015.
- [21] 'Inc Xilinx Vivado Design Suite User Guide: Embedded Processor H/W Design', http://www.xilinx.com/support/documentation/sw_manuals/xilinx2013_3/ug898-vivado-embedded-design.pdf, UG898, v2014.3, accessed March 9, 2015.

Inspection and Visualization Method for the Internal Structure of Spot-Welded Three-Steel Sheet Using Eddy Current Testing

Keisyu Shiga, Song Nannan, Kenji Sakai, Toshihiko Kiwa, Keiji Tsukada
 Graduate School of Natural Science and Technology, Okayama University
 Okayama, Japan
 E-mail: pcf45clo@s.okayama-u.ac.jp, nnsong84@hotmail.com,
 (sakai-k, kiwa, tsukada)@cc.okayama-u.ac.jp

Abstract— Spot-welding is widely used to assemble parts, such as those of vehicle bodies. To control the quality, safety and productivity of industrial products, a quick and accurate method of inspecting spot-weld is required. In our previous research, we reported an analysis method of examining the strength of spot welded parts by eddy current test (ETC) using a wide range of frequencies from high to low. In this paper, we report a method of analyzing the internal structure of a spot-weld. Magnetic field change showed a good correlation with the destructive shear test to check joint strength. The depth profile of the welded part was obtained by changing the skin depth using a wide range of frequencies. As the magnetic field strength at each frequency was not constant, they were normalized to create the depth profile. The two-dimensional depth profile was obtained by line scanning, and the three-dimensional depth profile was obtained by surface scanning. The three-dimensional internal structure of the welded part, which is nugget-shaped, was constructed from the volume rendering of the three-dimensional map, and it correlated with the shape obtained by cross-sectional observation.

Keywords— eddy current testing (ECT); non-destructive testing; spot-welds; skin depth

I. INTRODUCTION

Spot-welding is widely used to assemble parts, such as vehicle bodies, where thin metal sheets are joined by thousands of spot-welds. In general, the quality of the spot-welds is evaluated by destructive testing of a selected sample. The correlation between weld strength and nugget size has already been established. To confirm nugget size, observation of a cross section is effective [1] [2] [3]. However, destructive testing methods are not applied to all products, and are costly and time consuming. To ensure that all spot-welded products are high quality, a nondestructive testing method is desired. The eddy current test (ETC) of the magnetic method is a convenient, low-cost nondestructive test. However, its application is limited to surface inspection because its high frequency has shallow skin depth penetration [4] [5] [6]. Recently, our group reported two methods: an eddy current test (ECT) using a wide range of frequencies and a magnetic flux leakage test (MFL) using detection of the magnetic flux leakage from the surface of the sample when a low frequency magnetic flux was induced [7] [8]. In this paper, we report a method of analyzing welded parts by ETC using a wide range of frequencies. A spot-welded three-layer steel sheet, which is the same as that used in a real automobile body, was used as the test sample.

Section II describes structure of sample and experimental procedure. Section III describes the result and discussion. Finally, Section IV addresses the conclusion.

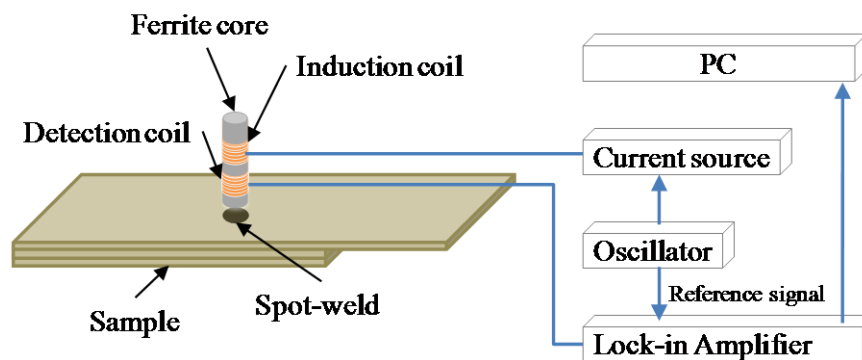


Figure 1. Measurement system for the internal structure of a spot-weld using eddy current testing

II. EXPERIMENTAL

As shown in Figure 1, the measurement system using ETC developed in this study consists of an oscillator, a current source for the induction coil, an induction coil and detection coil with ferrite core, a lock-in amplifier, X-Y stage, and a PC. These coils are composed of a ferrite core of 4.8 mm in diameter, a detection coil of 200 turns, and an induction coil of 50 turns. The pair of induction coil and detection coil with ferrite core is located near the sample surface. The induction coils are operated at 0.3 A (peak-to-peak) sine waveform generated from the current source with frequencies ranging from 100 Hz to 10 kHz.

The measurement method in this study is shown below. The sine waveform that is generated by the oscillator is applied to the current source. An AC current of 0.3 A (peak-to-peak) was applied to the induction coil generating a magnetic field. The secondary magnetic field that occurred on the surface of the sample was measured using the detection coil. Then, the signal was detected as the magnetic field intensity and phase component by a lock-in amplifier. To obtain the magnetic field distribution above the spot weld, the detection coil scans two-dimensionally. Scanning is performed by a XY stage.

The samples used in this study were three spot-welded steel plates of Strength Steel (SS) (40 mm × 200 mm × 0.7 mm), High Tensile Strength Steel (HTSS) (40 mm x 120 mm x 1.2 mm), and High Tensile Strength Steel (HTSS) (40 mm x 120 mm x 1.2 mm), as shown in Figure 2. Several samples with different spot-weld conditions were prepared by changing the number of cycles (5, 10, 15, 20) for the total weld time. One cycle time is the inverse of the commercial power source frequency. Samples were

classified as good quality products when the weld time was long. However, samples were classified as defective products when the weld time was insufficient. To observe the weld nugget structure, samples were cut by a cutting machine, and the cross section of the spot-weld part was observed by an optical microscope.

III. RESULTS AND DISCUSSION

First, we measured the magnetic field at the centerline of the welded part. Scanning was performed at 1-mm intervals by moving the induction and detection coil with ferrite core. Figure 3 illustrates the relation between the total weld time and the magnetic field strength measured at 10 kHz. According to the increments of cycle time, which means the increment of welding time, the magnetic field strength change around the weld position increased. The magnetic field change was considered to be caused by the difference in the nugget size leading to different permeability.

Next, the depth profile was imaged by the line scanned magnetic field change measured at several frequencies. The induction coils are operated in the frequency range from 10 Hz to 10 kHz. The results are shown in Figure 4. The magnetic field intensity at each frequency is not equal as explained by Faraday’s law; therefore, the values obtained at each frequency was normalized. The value of the color scale in Figure 4 shows the normalized value that was the ratio of the magnetic field strength at each point and that at the non-weld position which is the average at both ends of measured area (position of 0 and 9 mm). Although the Y-axis in Figure 4 is frequency, this indicate the depth information. This is because the skin depth δ is defined as follows.

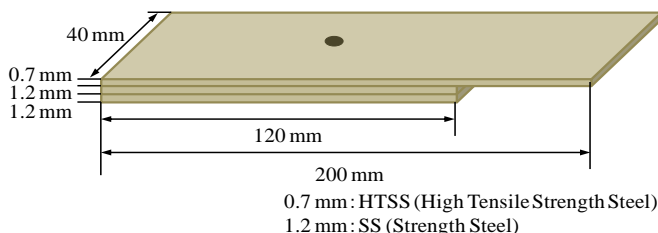


Figure 2. The test sample of spot-welded three-steel sheet.

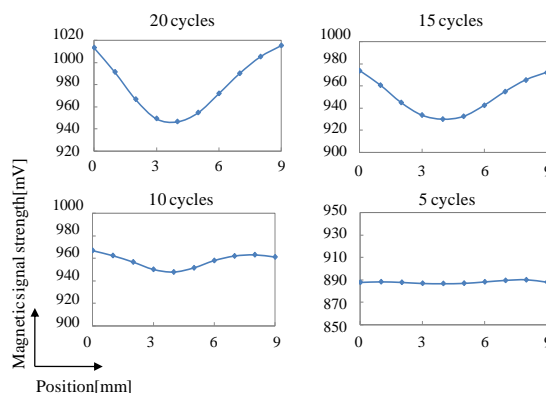


Figure 3. The relation between total weld time and the magnetic field strength measured at 10 kHz.

$$\delta = 1/\sqrt{\pi f \mu \sigma} \tag{1}$$

where μ is the permeability of the specimen and σ is the conductivity of the specimen. The δ is inversely proportional to the square root of the frequency f . This equation means that the magnetic field obtained by applying high frequency indicates the information near the surface and that obtained by applying low frequency indicates that information not only the surface but also inside in the specimen. The amount of change is low in the surface area which corresponds to the top of the image; the amount of change is large in the deep area which is at the bottom of the image. It indicates that a nugget with different permeability was generated inside the plates. In addition, as the cycle time and weld time decreased, the amount of change and size decreased. Therefore, the two dimensional mappings shown in Figure 4 represent the internal structure of spot weld.

To create a three-dimensional mapping of internal structure, we measured the magnetic field at the area of 10×10 mm around the weld in the frequency range from 10 Hz to 10 kHz. Surface scanning was performed at 1-mm

intervals. To obtain volume rendering of the nugget, an arbitrary threshold of normalized value was set at 0.94 and this threshold was adopted for each two-dimensional image. The measured result of three-dimensional image is shown in Figure 5. The measurement positions are x and y axis and z axis shows the frequency. The three-dimensional depth profile denotes the shape of the welds and its size depended on the cycle time. Thus, this three-dimensional image reflects the shape change inside the spot weld caused by different cycle times and non-destructive evaluation of internal structure for spot weld is proposed.

IV. CONCLUSION

We developed an analysis and visualization method for the internal structure of a spot-weld by ECT. The depth profile of the welded part was obtained by usage of multiple frequencies. Furthermore, a three-dimensional nugget shape was constructed by volume rendering of the three-dimensional depth profile. The magnetically measured data is correlated with the optically observed structure.

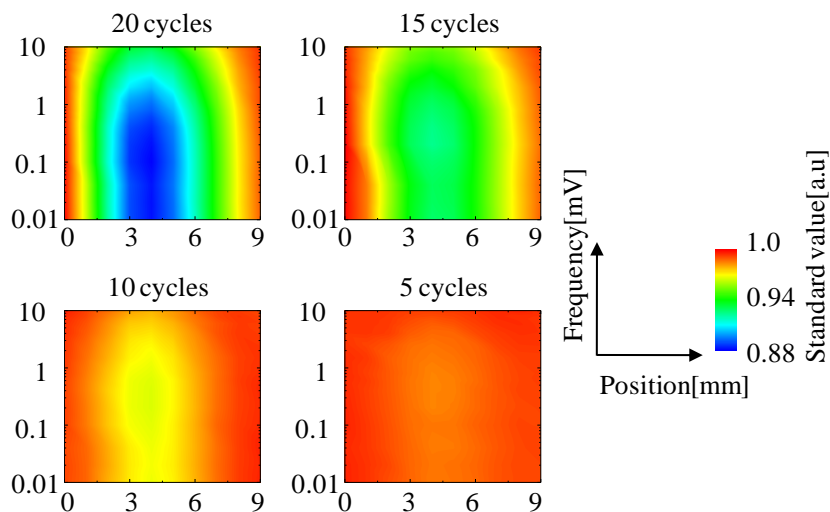


Figure 4. Mapping of the measured magnetic field strength at frequencies from 10 Hz to 10 kHz.

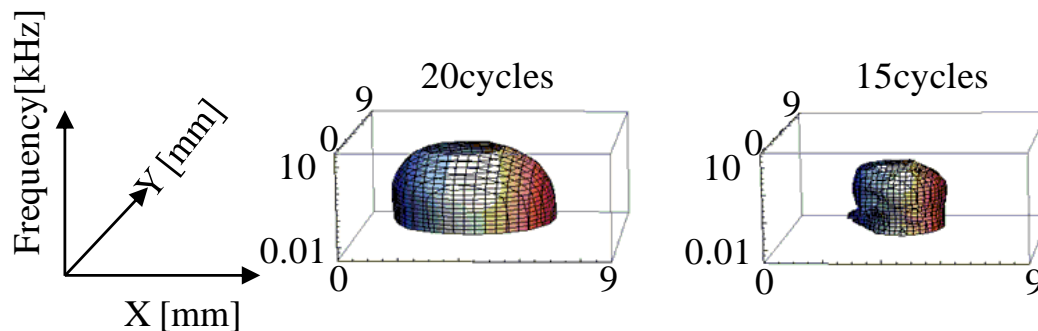


Figure 5. Volume rendered shape of the nugget inside the welded part.

REFERENCES

- [1] P.-C. Lin, S.-H. Lin, and J. Pan, "Modeling of failure near spot welds in lap-shear specimens based on a plane stress rigid inclusion analysis", *Engineering Fracture Mechanics*, Vol. 73, 2006, pp. 2229–2249.
- [2] P.-C. Lin and Z.-L. Lin, "Geometric functions of stress intensity factor solutions for spot welds in cross-tension specimens", *Engineering Fracture Mechanics*, Vol. 78, 2011, pp. 3270-3288.
- [3] S. Dancette, D. Fabrègue, V. Massardier, J. Merlin, T. Dupuy, and M. Bouzekri, "Experimental and modeling investigation of the failure resistance of Advanced High Strength Steels spot welds", *Engineering Fracture Mechanics*, Vol. 78, 2011, pp. 2259-2272.
- [4] R. Hamia, C. Cordier, and C. Dolabdjian, "Eddy-current non-destructive testing system for the determination of crack orientation", *Non-Destructive Testing & Evaluation International*, Vol. 61, 2014, pp. 24–28.
- [5] Y. He, M. Pan, F. Luo, and G. Tian, "Pulsed eddy current imaging and frequency spectrum analysis for hidden defect nondestructive testing and evaluation", *Non-Destructive Testing & Evaluation International*, Vol. 44, 2011, pp. 344–352.
- [6] B. Helifa, A. Oulhadj, A. Benbelghit, I. K. Lefkaier, F. Boubenider, and D. Boutassouna, "Detection and measurement of surface cracks in ferromagnetic materials using eddy current testing", *Non-Destructive Testing & Evaluation International*, Vol. 39, 2006, pp. 384–390.
- [7] K. Tsukada, M. Yoshioka, Y. Kawasaki, and T. Kiwa, "Detection of back-side pit on a ferrous plate by magnetic flux leakage method with analyzing magnetic field vector", *Non-Destructive Testing & Evaluation International*, Vol. 43, 2010, pp. 323–328.
- [8] K. Tsukada, M. Yoshioka, T. Kiwa, and Y. Hirano, "A magnetic flux leakage method using a magnetoresistive sensor for nondestructive evaluation of spot welds", *Non-Destructive Testing & Evaluation International*, Vol. 44, 2011, pp. 101–105.

Development of the Detecting System for Steel Plate with Backside Defect Using an Array of AMR Sensor

Koji Morita, Keishu Shiga, Yuta Haga, Kenji Sakai, Toshihiko Kiwa, Keiji Tsukada
Graduate School of Natural Science and Technology, Okayama University
Okayama, Japan
e-mail: (en422454, pcf45clo, pgtw6b5j)@s.okayama-u.ac.jp
(sakai-k, kiwa, tsukada)@cc.okayama-u.ac.jp

Abstract—Demand for detecting deep defects in the steel plate is increasing. We have reported a magnetic flux leakage testing (MFLT) system to detect deep defects and create magnetic imaging methods that indicate the backside defect. However, the developed system with one magnetic sensor requires XY automatic positioning stage and long measurement time. In this study, to realize fast measurement for practical use, we have developed a new system which can detect the magnetic field at several measurement points simultaneously using a multi-sensor array. Using the developed system, backside corrosion of steel plates having different depth was measured and two-dimensional images were created. The detected vector signal was analyzed by adjusting phase data. As a result, the developed MFLT system showed good performance of detection limit more than 7.2 mm in depth.

Keywords- magnetic flux leakage; magnetic imaging; AMR device; low-frequency field; backside defect

I. INTRODUCTION

Defects or refuge of steel structure, such as infrastructure, bridge legs, power plants, and heavy industry pipeline cause serious accidents. As the decrepit infrastructures are now increasing, it is very important to use non-destructive testing for detecting defects as early as possible. Generally, it is difficult to detect the defects which exist in the internal or on the backside of the steel plate. Therefore, the detection method is required to detect deep defects. In the past, various types of non-destructive testing methods have been investigated such as radiographic testing [1], ultrasonic testing [2], magnetic flux leakage testing (MFLT) [3]-[8], and eddy current testing (ECT) [9]. Ultrasonic testing is affected by the surface state of measurement sample, and it is needed to contact material for testing. Radiographic testing is dangerous for using radiation, thus it needs expert to use. From the above situation, the detecting method that is easy operation and safe is desired. MFLT and ECT testing use magnetic phenomenon, thus, these methods enable contactless, easy operation and safe measurement. MFLT is applied to ferromagnetic material, such as steel and it is a method to detect a magnetic flux from the sample's surface which leaked at defects due to differences in permeability when an external magnetic field is applied to the sample. Although the conventional MFLT system is generally used for surface inspection [10], considering

practice use, it is demanded that the detection of deep defect or backside defect. Therefore, we reported a two-dimensional mapping system for backside defects of a steel plate using MFLT. However, the system consisting of one channel magnetic sensor required two-dimensional stage to obtain the two-dimensional magnetic field mapping and long measurement time. In this study, we have developed a new system which can measure several magnetic signals simultaneously using a multi-sensor array was developed for rapid measurement.

Section II describes the detailed description about system configuration of the developed system. Section III describes the scheme of the experiment and the sample we used. Section IV describes the performance of the developed system was compared with the previous system measuring the steel plate with corrosion. Section V describes the conclusion.

II. DEVELOPED SYSTEM

Figure 1 shows the developed MFLT system. The MFLT system consists of a probe using an 8 channel AMR sensor array and a half-shaped yoke, a pair of excitation coil at both ends of the yoke, preamplifiers, a lock-in amplifier for phase sensitive detection (PSD), a current source, an oscillator, and a PC. Each AMR sensor is located between the both of ends of the yoke, and the interval of sensor is 10 mm. The liftoff between AMR sensor and sample surface was 1 mm. AMR sensors detect the y-axis component of the magnetic field which is parallel to both yoke ends, as shown in Figure 1. The current source applies an electrical current to a pair of induction coil with 25 turns connected to both ends of the yoke. AC magnetic field was induced in the sample between both ends of yoke. The induction coils were operated by sinusoidal wave of 2.5 A from the current source. Using a magnetic field of low frequency, eddy current can be ignored because the skin depth increases with increasing frequency. Thus, the detected magnetic field was mainly due to the magnetic leakage under the operating condition. The yoke is 10 pieces of non-oriented electromagnetic steel plate.

Figure 2 shows the previous MFLT system. The main difference between developed system and previous system is the length of the yoke. The probe consists of a half-shaped short yoke whose section is 10 mm × 10 mm and the induction coils at both ends of the yoke with 30

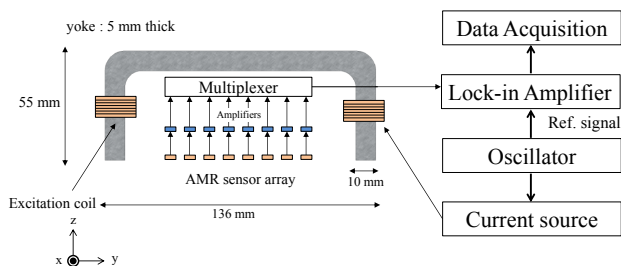


Figure 1. Schematic diagram of the developed MFLT system.

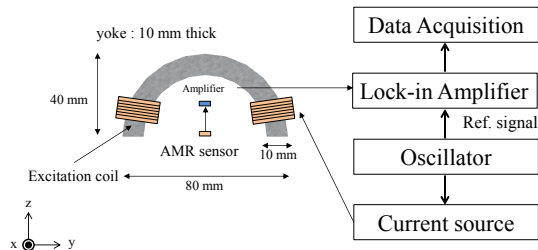


Figure 2. Schematic diagram of the previous MFLT system.

turns. The induction coils were operated by sinusoidal wave of 0.7 A from the current source. The sensor was placed 1 mm away from the sample surface. Both probes are fixed in acrylic case of nonmagnetic material not to affect the AMR sensors.

III. EXPERIMENT

The measurement samples are SS400 steel plates of 12 mm thickness which have different depth of a backside corrosion. The plate had a galvanic corrosion at the center of the plate on the backside. The state of corrosion is shown in Figure 3 and Table 1 shows the detail of the corrosion size of samples.

In the developed system, one line measurement enables multi point measurement. Therefore, the magnetic field was measured in the range of 80 mm × 150 mm around the corrosion, as shown in Figure 4. For the comparison, one line measurement was executed using the previously developed system, and the measurement point was shown as white point in Figure 4.

The magnetic flux leakage generated from the backside corrosion was detected on the front surface by AMR sensors. The interval of measurement point was 10 mm and the y-axis component of the magnetic field was measured in each system.

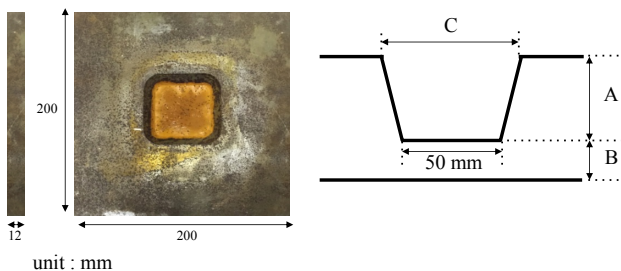


Figure 3. Test plates with corrosion.

TABLE I. THE CORROSION CONDITION OF THE TEST PLATES.

corrosion rates	10 %	20 %	40 %	50 %	60%	80 %
A : depth (mm)	1.2	2.4	4.8	6.0	7.2	9.6
B : depth from surface (mm)	10.8	9.6	7.2	6.0	4.8	2.4
C : Range of corrosion (mm)	59.0	62.05	60.12	62.07	63.89	74.0

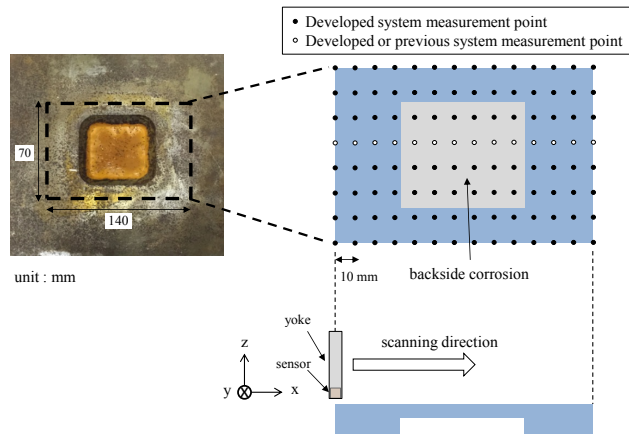


Figure 4. Measurement points for backside corrosion.

The outputs of AMR sensor were measured using a lock-in amplifier to detect the signal intensity and phase, which were synchronized with the oscillator. Overall conditions were adopted for each appropriate condition. Each probe was maintained 1 mm air gap between the yoke heads and the sample. Keeping the constant air gap between the yoke and the sample has an advantage in reproducibility compared with the direct contact method because of the non-smoothness of the sample surface due to oxidization and so on.

At each measurement point, signal intensity and phase was measured. Using the intensity $M_{mes,i}$ and phase α_i , the imaginary part of the signal with the common phase θ is calculated as follows [11].

$$M_{img} = |M_{mes,i}| \times \sin(\alpha_i + \theta) \quad (1)$$

The θ is adjusting phase which adjust shifted phase caused by the system phase shift and the θ depends on the system configuration. Thus, if an optimum θ is obtained by measuring a standard sample, adjustment of θ is not required in other measurement.

IV. RESULTS AND DISCUSSIONS

A. Basic Characteristics of Developed Sensor Array System

Figure 5 and 6 show each system outputs curves for some common phase θ obtained by measurements on the steel plate with corrosion rate of 80 % using 10 Hz sine wave current. The data of Figure 5 is fifth sensor (channel 5) and this is the same position as that of the previous system. Comparing both results, each system can detect the magnetic flux leakage caused by the backside corrosion with the common phase $\theta = 0$ degrees. The previous

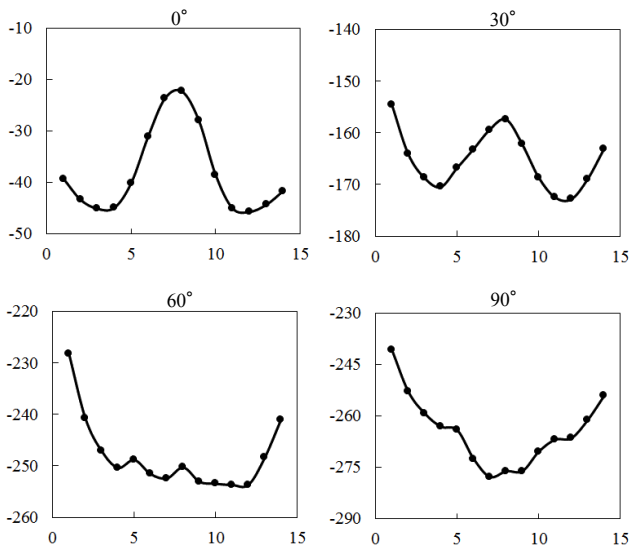


Figure 5. Magnetic flux leakage data with different phase of developed system using multi-sensor array.

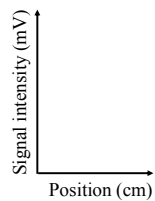
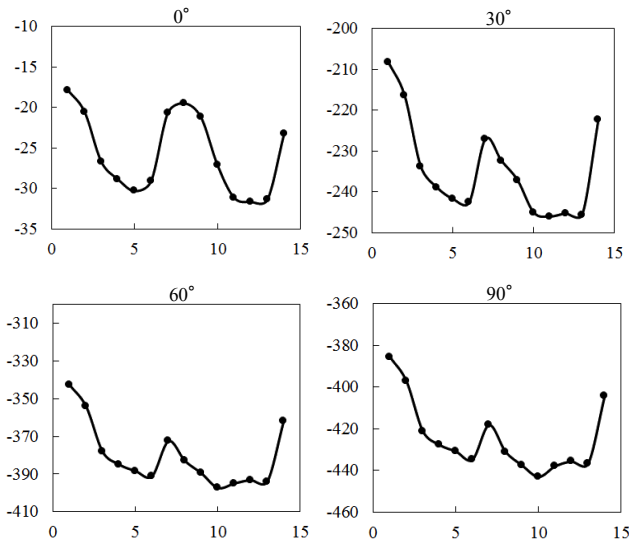


Figure 6. Magnetic flux leakage with different phase of the previous system using one sensor.

system can detect the backside corrosion using above condition. From this result, it was found that the signal changes detected by the developed system are correlated to the backside corrosion. Even if a long yoke was used for applying a magnetic field, the backside corrosion could be curves shown in Figure 5 and 6 showed the same tendency. This means using long yoke enables to detect the magnetic flux leakage using a sensor array. Thus, a measurement system which can realize simultaneous measurement of

multi lines is possible by only carrying out one line measurement using a sensor array.

However, the magnetic field generated by a long yoke was not constant at each position of AMR sensor. Figure 7 shows the magnetic field distribution between the ends of the yoke in the air under the condition that the excitation coil was operated by a current of 10 Hz and 2.5 A sine wave. The magnetic signal was detected by each sensor. The magnetic signal intensity became large and the phase shift was small near by the ends of the yoke. In this condition, the magnetic image created by multi point measurement is affected by the distribution of the magnetic field. Therefore, in this measurement, to reduce the influence of distribution of the magnetic field, the reference signal vector measured with non-defect sample was subtracted from the measured signal vector with defect sample. The measurement point of reference signal was the center line of the non-defected samples. After that, the magnetic images calculated from the subtracted signal vector using (1). Figure 8 shows the magnetic image before subtracting the reference signal (a), and after subtracting the reference signal (b). The corrosion rate is 80 %. Comparing Figure 8 (a) with Figure 8 (b), the influence of the distribution of the magnetic field was reduced by subtracting the signal of non-defect sample, and a clear magnetic image that shows corrosion could be obtained.

B. System Optimization

To optimize the system, the appropriate frequency and common phase using 60 % corrosion rate sample was examined. Figure 9 shows magnetic images using a 5 Hz excitation frequency and various common phases and Figure 10 shows that using a 10 Hz and various common phases. Magnetic images with a common phase 0° showed the clearest corrosion image, and magnetic images with 5 Hz shows the presence of the backside corrosion more clearly than that of 10 Hz. This means that the magnetic

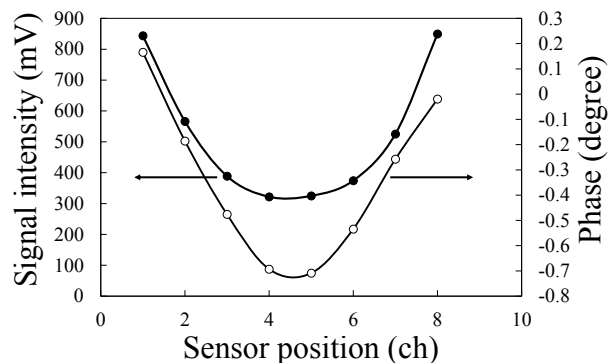


Figure 7. The signal intensity and phase of each sensor caused by the distribution of the magnetic field.

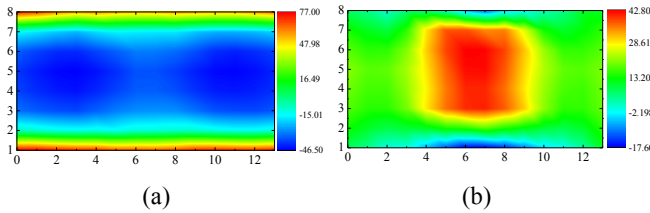


Figure 8. The magnetic images affected with the distribution of the magnetic field (a) and calculated image (b).

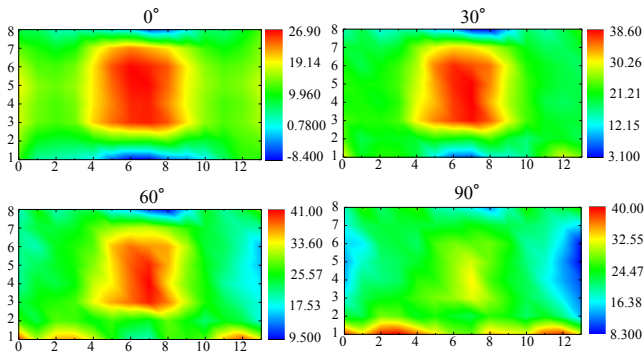


Figure 9. Magnetic images with 5 Hz and different phase.

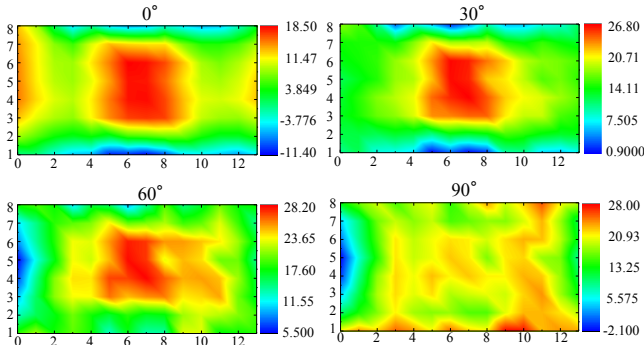


Figure 10. Magnetic images with 10 Hz and different phase.

field penetrated inside the steel plate increased with decreasing the frequency due to the skin effect, and the depth of penetrated magnetic signal with 10 Hz decreased compared to that with 5 Hz. Therefore, the optimum condition was determined as the frequency is 5 Hz and common phase is 0°.

C. Evaluation of Depth Profile

To evaluate the developed system under the optimum condition, we measured magnetic images using the steel plates which have different corrosion rate. The excitation coils were operated with 5 Hz and 2.5 A sine wave from a current source and the common phase was 0°. For all samples, one line measurement was performed and magnetic signal was measured by 8 sensors. Using the

detected magnetic signals, the magnetic images of the samples with different corrosion rates of 10, 20, 40, 50, 60, and 80 % were obtained.

Figure 11 shows the result of magnetic images. The images show the existence of the corrosion and it becomes clear with increasing the actual corrosion rate of more than 40%. On the other hand, the magnetic images with the corrosion rate of 10 and 20 % show unclear images. These unclear images derived from that the magnetic flux leakage did not leak enough when the magnetic field was applied at the sample with low corrosion, and the difference of signal intensity between corrosion part and healthy part was small.

Next, we examined to evaluate the relation between the change of the magnetic field intensity and corrosion rates quantitatively. The change of the magnetic field which is along the dotted line in the Figure 12 (a) is shown in Figure 12 (b). The changes of each corrosion rate of 10, 20, 40, 50, 60, and 80% are shown. The ΔB is defined as the subtracted value between the maximum and minimum values for each sample as shown in Figure 12 (b). The value of ΔB increased according to the increase of the corrosion rates. Comparing ΔB with the magnetic image of 10, 20 %, the magnetic images are unclear and the change of the ΔB for 10 % and 20 % changed little. Therefore, more than 40 % corrosion rate can be detected using the developed system. This corresponds to the depth of approximately 7.2 mm from the surface of the front. Figure 13 shows the relation between the depth of defect and ΔB . The ΔB was chosen thinning rate are 80, 60, 50, 40 % which are ΔB clearly changes. ΔB decreased with the increment of the depth of the defect. Using the magnetic image and ΔB , we can survey the backside defect's size and depth.

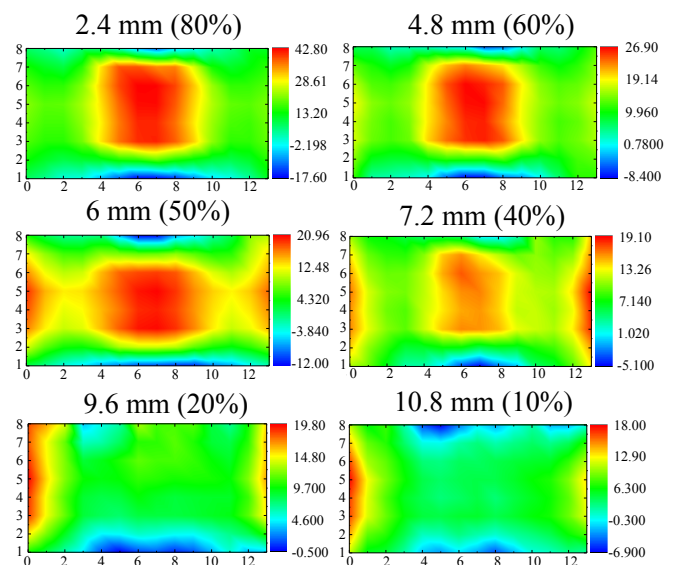


Figure 11. Magnetic images of corrosion with different wall thinning rate.

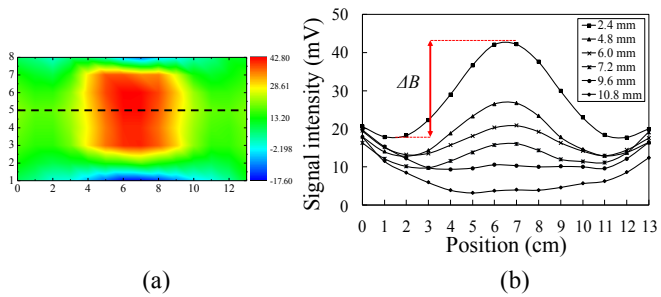


Figure 12. Example of the extracted line (a) and the definition of ΔB (b).

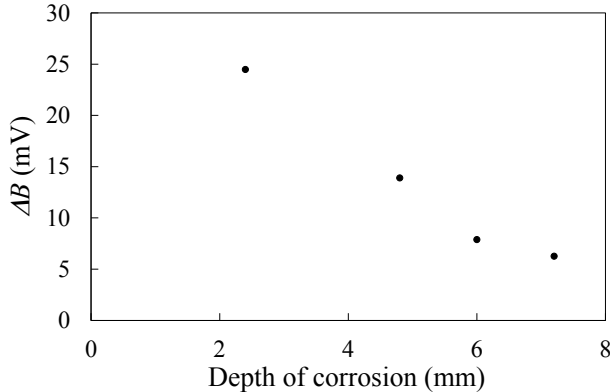


Figure 13. Relationship of the depth of defect and ΔB .

To improve detecting ability for deep corrosion, it is required to gain the enough magnetic flux leakage due to the backside corrosion by increasing the applied magnetic field. To realize this, appressing the sensor probe to a steel plate will be effective to reduce the dispersion of the magnetic flux leakage signals which is derived from the fluctuation of lift-off and leakage of the magnetic flux to the outside.

V. CONCLUSIONS

A new MFLT system with a multi-sensor array for practical use was developed. Arraying the sensors enabled reducing positioning time to settle the sensor probe and sensors, and the system enabled rapid detection of backside defect. When the magnetic field of low frequency was applied, it was possible to detect the deepest defect. In addition, the stronger magnetic field could detect the deep defect. Under these optimized conditions, the developed system showed good detection limit more than 7.2 mm in depth.

REFERENCES

[1] I. G. Kazantsev, I. Lemahieu, G. I. Salov, and R. Denys, "Statistical detection of defects in radiographic images in nondestructive testing," *Signal Processing*, vol. 82, issue 5, May 2002, pp. 791-801.
 [2] M. Kharrat and L. Gaillet, "Non-destructive evaluation of anchorage zones by ultrasonics techniques," *Ultrasonics*, Available online 23 March 2015. vol. 61, August 2015, pp. 52-61.
 [3] T. Bubenik, "Electromagnetic methods for detecting

corrosion in underground pipelines: magnetic flux leakage (MFL)," In *Underground Pipeline Corrosion*, Woodhead Publishing, 2014, pp. 215-226.
 [4] M. M. Tehrani, S. M. Hamidi, H. Eftekhari, M. Karbaschi, and M. Ranjbaran, "The inspection of magnetic flux leakage from metal surface cracks by magneto-optical sensors," *Sensors and Actuators A: Physical*, vol. 172, issue 2, December 2011, pp. 365-368.
 [5] Y. Zhang, Z. Ye, and C. Wang, "A fast method for rectangular crack sizes reconstruction in magnetic flux leakage testing," *NDT & E International*, vol. 42, issue 5, July 2009, pp. 369-375.
 [6] R. Baskaran and M. P. Janawadkar, "Imaging defects with reduced space inversion of magnetic flux leakage fields," *NDT & E International*, vol. 40, Issue 6, September 2007, pp. 451-454.
 [7] J. Atzlesberger and B. Zagar, "Magnetic flux leakage measurement setup for defect detection," *Procedia Engineering*, vol. 5, 2010, pp. 1401-1404.
 [8] P. Wang, Y. Gao, G. Tian, and H. Wang, "Velocity effect analysis of dynamic magnetization in high speed magnetic flux leakage inspection," *NDT & E International*, vol. 64, June 2014, pp. 7-12.
 [9] D. F. He, M. Shiwa, J. P. Jia, J. Takatsubo, and S. Moriya, "Multi-frequency ECT with AMR sensor," *NDT & E International*, vol. 44, issue 5, September 2011, pp. 438-441.
 [10] M. M. Tehrani, M. Ranjbaran, and H. Eftekhari, "Double core giant magneto-impedance sensors for the inspection of magnetic flux leakage from metal surface cracks," *Sensors and Actuators A: Physical*, vol. 170, issues 1-2, November 2011, pp. 55-61.
 [11] K. Tsukada, M. Yoshioka, Y. Kawasaki, and T. Kiwa. "Detection of back-side pit on a ferrous plate by magnetic flux leakage method with analyzing magnetic field vector," *NDT&E International* vol. 43, issue 4, June 2010, pp.232-328.

Analysis of the Planar Electrode Morphology for Capacitive Chemical Sensors

L. E. B. Ribeiro and F. Fruett

School of Electrical and Computer Engineering - FEEC

State University of Campinas – UNICAMP

Campinas, Brazil

e-mail: luizebr@dsif.fee.unicamp.br and fabiano@dsif.fee.unicamp.br

Abstract — Three different electrode structures are compared in this work: conventional interdigitated electrodes (IDE), serpentine electrodes (SRE) and ring-shaped electrodes (RSE). Simulation results and experimental characterization of these electrodes showed that ring-shaped electrodes have a slight capacitance increase per unit of area, thus being more sensitive when used as a capacitive sensor. Furthermore, the ring-shaped electrodes are more suitable in process that requires dripping, for better use of the drop distribution. This is the case of liquid substances or sensors with sensitive elements such as zeolite.

Keywords - interdigitated electrodes; ring-shaped electrodes; serpentine electrodes; capacitive sensors; electrode structure; interdigital electrodes.

I. INTRODUCTION

IDE as capacitive microstructures have been widely used in electronics applications such as surface acoustic wave devices [1], thin-film acoustic electronic transducers [2], tunable devices [3], dielectric spectroscopy [4], dielectric studies on thin films [5][6], humidity and chemical sensors [7][8], etc. They possess interesting features, such as signal strength control by changing its dimensions, multiple physical effects in the same structure, simplified modeling in two dimensions when the aspect ratio of the electrode length to the space wavelength IDE is large, and can be used in a wide range of frequencies [7]. Moreover, it can be manufactured using inert substrates with multiple materials with different fabrication processes, or even microfluidic compatible. Capacitive microstructures used as chemical sensor, typically have one sensitive layer deposited over the electrodes. Polymers have been used for organic vapor sensing because they exhibit rapid reversible vapor sorption and are easy to apply as thin or thick films by a variety of techniques [9]. The polymer layer can be chosen according to its affinity to a particular molecule or set of molecules one wishes to detect. If several sensors with different polymer layers are used to make a sensor array it is then possible to evaluate complex organic vapor samples. These sensor arrays can be part of a so-called electronic nose. Another possibility is the use of flexible substrates such as sensing element. As an example the use of polyimide [10] and plastic foil [11].

Interdigitated electrodes analytical characterization have been received many efforts in order to improve their

capacitance by exploring their geometrical parameters. Igreja et al developed a theoretical model of capacitance for this structure [12]. These capacitors have also been simulated using different tools. They have typically been adopted as a sensor because of the low-power consumption of capacitive transduction mechanism and being compact with a large contact area and relative ease of manufacture. Some authors have analyzed other morphologies such as serpentine, spiral and concentric rings electrodes, in order to improve design performance. Moreover, aside from the different morfologies, several strategies have been employed to increase and improve its ability as a sensor, for example the deposition of a more sensitive layer on the electrodes. The sensor can also have its selectivity improved by the deposition of compounds such as zeolite for detection of air humidity or gases [13].

In this work, we study different geometries of electrodes instead of the materials used to maximize capacitance per area. We can thus improve the sensitivity of capacitive sensors by increasing the total capacitance of capacitive microstructures. Here, we compare the conventional IDE, the serpentine electrodes (SRE) and ring-shaped electrodes (RSE). These electrodes are compared in detail as generic capacitive transducers by numerical simulations. In these simulations, the geometric parameters that most influence on the total capacitance are shown. We measure the capacitance of these thin-film electrodes made of titanium and gold on a glass substrate. Finally, we compare the experimental results with the theoretical analysis, including simulations.

In Section II, the different electrodes designs and their geometrical parameters are shown. They are the main data to the numerical simulation, which is explained in the Section III. The fabrication process is described in section IV. Subsequently, the values of electrical and geometrical characterization are shown in section V. The results are compared and discussed in section VI. Finally, the conclusion is presented in section VII.

II. METHODS AND MATERIALS

The layouts of some interdigitated electrode pairs are shown in Figure 1. Although they were designed with the same area, each structure has a particular capacitance. Therefore, they have different sensitivities as capacitive transducer only because of their different geometric structure.

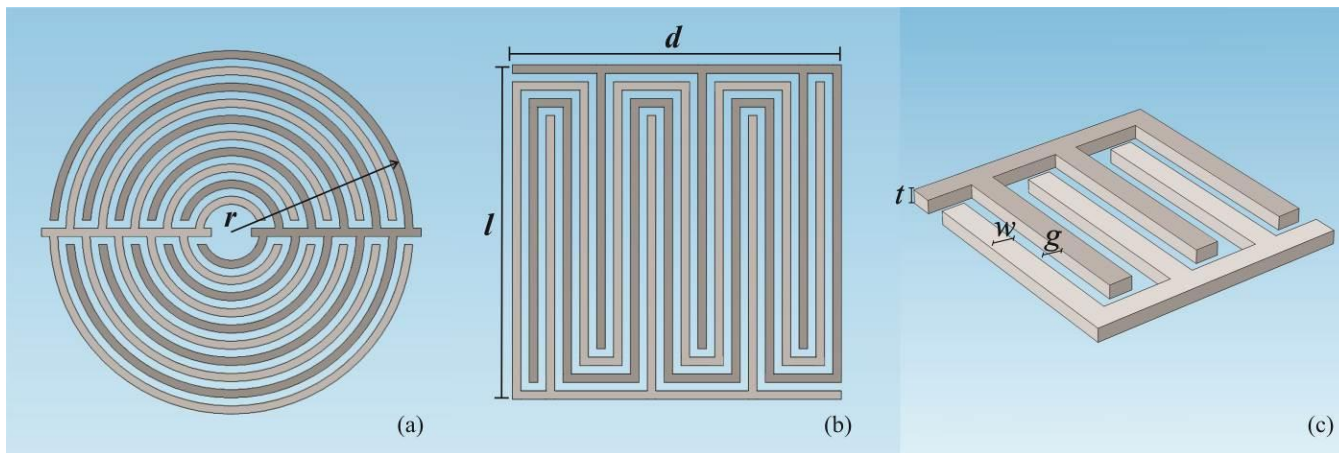


Figure 1. Ring-shape electrode (a), serpentine electrode (b) and interdigitated electrode (c) structures and used parameters.

We simulate the capacitive structures of IDE, SRE and RSE with the same area, same substrate and the same top layer, calculating and comparing the capacitance of each structure using the multiphysics numerical simulator: COMSOL Multiphysics (Comsol Inc., Stockholm, Sweden). This software, based on partial differential equations with the finite element method has been used in the literature to calculate distribution of potential field in similar structures. Figure 2 depicts the simulated structure showing the 3D multislice view of the electrical potential distribution around RSE with 20 fingers.

Multiple simulations were performed to compare dimensions that are relevant to increase the difference between the capacitances. The main geometrical parameters analyzed are the electrode length, the gap between the electrodes, the electrode width (always kept as same value as gap), the thickness of electrodes and the number of fingers. The electrical properties of the substrate and the top layer are also included in the simulator. Because of the differences between the vertical and horizontal dimensions (millimeters to micrometers) critical to reduce the time simulation, we have applied the extrapolation method, presented in the Rivadeneyra work [14]. The thickness has been set to 20% of electrode width.

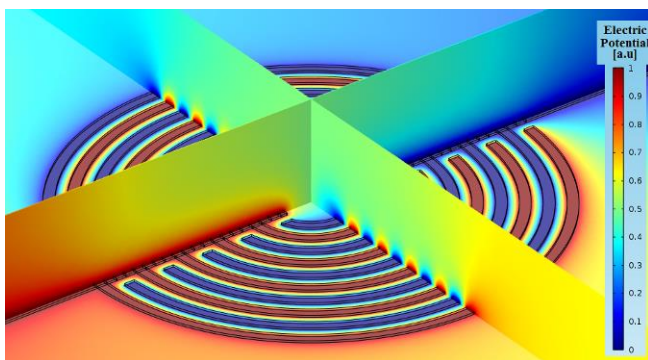


Figure 2. Distribution of potential field in a 3D RSE structure.

III. NUMERICAL SIMULATION

We have performed different numerical simulations comparing the calculated DC capacitance of IDE, SRE and RSE structures always with the same distance between digits, surface area and same materials and manufacturing process. There are multiple geometrical factors that can be varied in the simulations, but for the sake of clarity, we focus on some of them, keeping fixed the rest. Since the goal is maintaining reduced the surface area of electrodes, we define different widths and distances between digits of the structures given that the lowest safe distance to our manufacturing process is 10µm. Therefore, we have used the number, length and width of fingers and the thickness of the deposited metal film as simulation parameters. Table 1 is a summary of these geometric parameters used for simulation. Remember that fabricated structures for each type of electrode, SRE, IDE and RSE, was made with three distances between digits (10µm, 20µm and 50µm) but the number of electrodes and the thickness of the metal thin film was kept constant.

TABLE I. GEOMETRICAL PARAMETERS OF PLANAR ELECTRODE PAIRS

Parameters	Electrode type			Description
	RSE	SRE	IDE	
w	10-50µm	10-50µm	10-50µm	Finger width
g	10-50µm	10-50µm	10-50µm	Gap between fingers
t	2-10µm	2-10µm	2-10µm	Metal film thickness
l	600-800µm	600-800µm	-	Structure length
d	600-800µm	600-800µm	-	Structure width
r	-	-	0.6-3.02mm	Electrode external radius
n	20-50	20-50	20-50	Number of electrodes

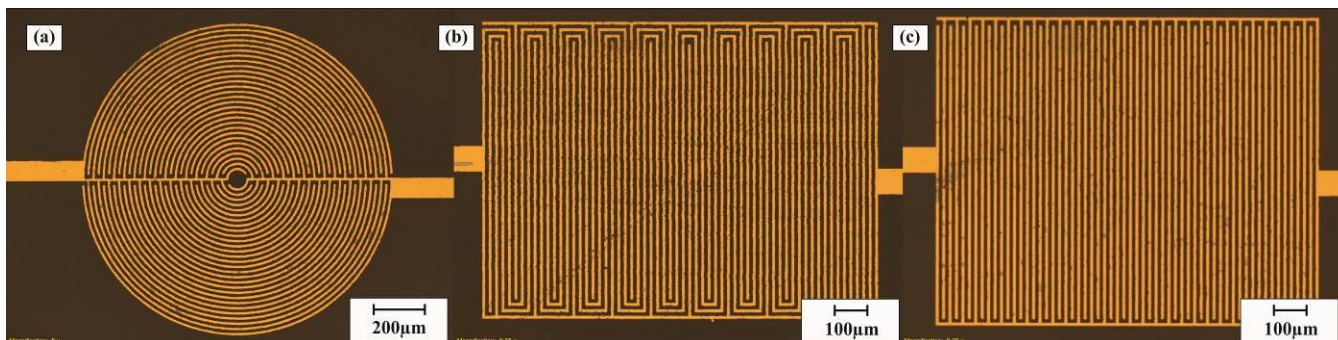


Figure 3. Fabricated RSE (a), SRE (b), and IDE (c) structures.

The first important result was that the capacitance to RSE was the highest in all comparisons. For example, simulating the capacitor with $w = 10\mu\text{m}$, $t = 2\mu\text{m}$ and 20 electrodes we obtain 2.47pF for RSE while the capacitance for the SRE was 2.45pF and the capacitance for IDE was 2.44pF. This means an increase of capacitance of 30fF between the RSE and the IDE. Whereas electrodes are used as capacitive transducers, the fact of the geometrical factor RSE be higher than in other structures means that the sensitivity of the sensor will always be larger using the same area. Furthermore, the capacitance and the increase in sensitivity will increase proportionally. After that, we calculate the numerical capacitances in order to improve the performance of RSE.

Influence of the width of the electrodes (10 to 50 μm) with aspect ratio of the electrode/thickness of the thin film of 5/1 was evaluated for the RSE, SRE and IDE with 20 digits. The results showed a slope of 161.1fF for each micrometer added to the width of the electrodes to the RSE, a slope of 160.7fF/ μm for the SRE and 159.3fF/ μm for the IDE. Remembering that the surface area of each structure was kept the same for each electrode width.

Electrode length contribution (400 to 800 μm) was been evaluated for IDE and SRE electrode with 20 fingers and 10 μm of finger width. Results showed the slope of 4.99fF/ μm for the SRE and 4.74fF for the IDE.

We also have performed the contribution of finger numbers (n) in each structure. The results are presented in Figure 4, as this contribution is nonlinear.

IV. FABRICATION PROCESS

The electrodes fabrication started with the production of the electrode masks where the IDE, SRE and RSE were designed using high-resolution direct writing photolithography with a laser beam. In the next step, a photoresist layer was deposited onto a square optical glass plate (60mm side Kodak 1A High Resolution Glass) and patterned by conventional ultraviolet light (UV) photolithographic method following the electrodes masks. The UV exposures were carried out in a MJB-3 UV300 contact mask aligner (Karl-Suss, Garching, Germany). Titanium-gold (TiAu) thin films, deposited with a Leybold Univex 300 ebeam evaporator (Cologne, Germany), were used as electrode materials. After thin-film depositions, by

the lift-off technic, the devices were immersed in acetone to remove the photoresist layer and excess of metal, leaving the patterned electrodes on the glass surface [6].

V. CHARACTERIZATION

For the experimental characterization the nominal capacitance target was 2pF, taking into account the minimum distance between electrodes of 10 μm . Structures with electrode width of 50 μm have a total area of 28.26mm², and their dimensions are $g = 50\mu\text{m}$, $l = 5.95\text{mm}$, $d = 4.75\text{mm}$ and $r = 3.02\text{mm}$. The area is 4.52mm² for structures with $w = 20\mu\text{m}$, $g = 20\mu\text{m}$, $l = 2.38\text{mm}$, $d = 1.90\text{mm}$ and $r = 1.21\text{mm}$. Structures with $w = 10\mu\text{m}$, minimum secure dimension to our fabrication process, the area is 1.13mm² ($g = 10\mu\text{m}$, $l = 1.19\text{mm}$, $d = 0.95\text{mm}$ and $r = 0.60\text{mm}$).

The geometric inspection of the fabricated structures was performed using the Olympus BX60 microscope as shown in Figure 3. Electrical characterization has been carried out by measuring their capacitance and parallel resistance using the four-wire measurement with a HP 4284A impedance analyzer (Agilent Tech., Santa Clara, CA, USA). The applied excitation voltage was $V_{AC} = 1\text{V}$ and $V_{DC} = 0\text{V}$. The frequency sweep of analysis was from 100Hz to 1MHz. The four-point method was used to minimize the contribution of stray capacitances.

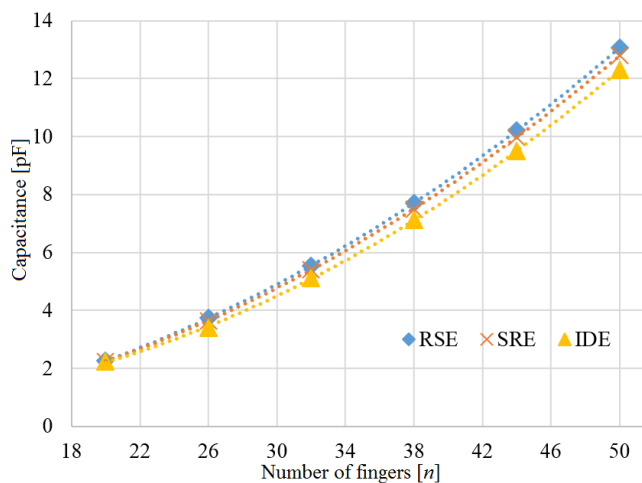


Figure 4. Capacitance vs. number of fingers of RSE, SRE and IDE.

VI. EXPERIMENTAL RESULTS

Measured and the simulated values of the capacitances are in agreement, as shown in Table 2. The measurements were carried out in room conditions (50% RH and 25°C) at 100 kHz.

TABLE II. NUMERICAL VS. EXPERIMENTAL CAPACITANCE.

Finger width (µm)	Numerical simulation (pF)		
	RSE	SRE	IDE
10	2.4667	2.4446	2.4362
20	4.0906	4.0653	4.0345
50	8.9122	8.8723	8.8091
	Experimental measurement (pF)		
	RSE	SRE	IDE
10	2.2332	2.2141	2.1917
20	4.2949	4.2667	4.2412
50	10.5385	9.9979	9.7105

Capacitance measured values have a maximum of 12% discrepancy compared to the simulated results. This difference is due to the capacitance of contacts pads that were not included in the simulation and the variability of the fabrication process.

VII. CONCLUSION

A comparison between the capacitances under different geometric parameters of RSE, SRE and the conventional IDE was shown on this work. Numerical simulations of the capacitance have been carried out to calculate the differences between them due exclusively to their geometrical characteristics at constant area. In these conditions, we have shown a slight capacitance increase for the ring-shaped electrodes against the serpentine electrodes and the conventional interdigitated electrodes.

We have validated the numerical results by experimental characterization of ring-shaped, serpentine and interdigitated structures capacitance. Experimental results verified the capacitive differences between the three structures with same area, for 10µm, 20µm and 50µm of finger width. Moreover, ring-shape electrode presents a geometrical morphology that allows the better usage of its area. It is a promising base electrode mainly when used as sensor in application that involves dripping of substances under analysis or dripping of selective/sensitive substances like zeolite.

ACKNOWLEDGMENT

The authors acknowledge the Center for Semiconductor Components (CCS), the Multi-User Laboratory of IFGW (LAMULT), the Device Research Laboratory (LPD) and the Brazilian Synchrotron Light Laboratory (LNLS). Financial

support for this project was provided by the National Council for Scientific and Technological Development (CNPq) and the São Paulo State Research Support Foundation (FAPESP) inside the National Institute for Science and Technology of Micro and Nanoelectronic Systems (INCT NAMITEC) project.

REFERENCES

- [1] M. I. Rocha-Gaso, C. March-Iborra, Á. Montoya-Baidés, and A. Arnau-Vives, "Surface generated acoustic wave biosensors for the detection of pathogens: A review," *Sensors*, vol. 9, 2009, pp. 5740.
- [2] N. A. Ramli and A. N. Nordin, "Design and modeling of MEMS SAW resonator on Lithium Niobate," 4th International Conference On Mechatronics (ICOM), 2011, pp.1-4.
- [3] M. W. Kim, Y. H. Song, and J. B. Yoon, "Modeling, fabrication and demonstration of a rib-type cantilever switch with an extended gate electrode," *Journal of Micromechanics and Microengineering*, vol. 21, 2011, 115009.
- [4] R. Mahameed, A. M. El-Tanani, and G. M. Rebeiz, "A zipper RF MEMS tunable capacitor with interdigitated RF and actuation electrodes." *Journal of Micromechanics and Microengineering*, vol. 20, n. 3, 2010, 035014.
- [5] Z. Chen, A. Sepúlveda, M. D. Ediger, and R. Richert, "Dielectric spectroscopy of thin films by dual-channel impedance measurements on differential interdigitated electrode arrays," *The European Physical Journal B-Condensed Matter and Complex Systems*, vol. 85, n.8, 2012, pp. 1-5.
- [6] L. E. B. Ribeiro, M. H. Piazzetta, A. L. Gobbi, J. S. Costa, J. A. F. da Silva, and F. Fruett, "Fabrication and Characterization of an Impedance Micro-Bridge for Lab-on-a-Chip." *ECS Transactions*, vol. 31, n. 1, 2010, pp. 155-163.
- [7] A. Rivadeneyra, J. Fernández-Salmerón, J. Banqueri, J. A. López-Villanueva, L. F. Capitan-Vallvey, and A. J. Palma, "A novel electrode structure compared with interdigitated electrodes as capacitive sensor," *Sensors and Actuators B: Chemical*, vol. 204, 2014, pp. 552-560.
- [8] Y. Kim, B. Jung, H. Lee, H. Kim, K. Lee, and H. Park, "Capacitive humidity sensor design based on anodic aluminum oxide," *Sensors and Actuators B: Chemical*, vol 141, n. 2, 2009, pp. 441-446.
- [9] J. W. Grate and G. C. Frye, "Acoustic wave sensors," *Sensors update*, vol. 2, 1996, pp. 37-83.
- [10] J. Virtanen, L. Ukkonen, T. Bjorninen, and L. Sydanheimo, "Printed humidity sensor for UHF RFID systems," *Sensors Applications Symposium (SAS)*, 2010 IEEE, 2010, pp. 269-272.
- [11] D. Briand, A. Oprea, J. Courbat, and N. Bârsan, "Making environmental sensors on plastic foil," *Materials Today*, vol. 14, n. 9, 2011, pp. 416-423.
- [12] R. Igreja and C. J. Dias, "Analytical evaluation of the interdigital electrodes capacitance for a multi-layered structure," *Sensors and Actuators A: Physical*, vol. 112, n. 2, 2004, pp. 291-301.
- [13] M. Urbrizondo, I. Pellejero, A. Rodriguez, M. P. Pina, and J. Santamaria, "Zeolite-coated interdigital capacitors for humidity sensing," *Sensors and Actuators B: Chemical*, vol. 157, Issue 1, 2011, pp. 450-459.
- [14] A. Rivadeneyra, J. Fernández-Salmerón, M. Agudo, J. A. López-Villanueva, L. F. Capitan-Vallvey, and A. J. Palma, "Design and characterization of a low thermal drift capacitive humidity sensor by inkjet-printing," *Sensors and Actuators B: Chemical*, vol. 195, 2014, pp. 123-131.